

Transactions of the ASME®

Technical Editor, **G. K. SEROVY**
Associate Technical Editors
Advanced Energy Systems
M. J. MORAN

Environmental Control
H. E. HESKETH (1995)
Fuels and Combustion Technologies
D. W. PACER (1994)
Gas Turbine
L. S. LANGSTON (1993)
Internal Combustion Engine
J. A. CATON (1995)
Nuclear Engineering
H. H. CHUNG (1995)
Power
R. W. PORTER (1993)

BOARD ON COMMUNICATIONS
Chairman and Vice-President
R. D. ROCKE

Members-at-Large
T. BARLOW, W. BEGELL, T. F. CONRY,
T. DEAR, J. KITTO, R. MATES,
W. MORGAN, E. M. PATTON,
S. PATULSKI, R. E. REDER,
A. VAN DER SLUYS, F. M. WHITE

President, **J. A. FALCON**
Executive Director,
D. L. BELDEN
Treasurer, **ROBERT A. BENNETT**

PUBLISHING STAFF
Mng. Dir., Publ.,
CHARLES W. BEARDSLEY
Managing Editor,
CORNELIA MONAHAN
Sr. Production Editor,
VALERIE WINTERS
Production Assistant,
MARISOL ANDINO

Transactions of the ASME, *Journal of Turbomachinery* (ISSN 0889-504X) is published quarterly (Jan., Apr., July, Oct.) for \$130.00 per year by The American Society of Mechanical Engineers, 345 East 47th Street, New York, NY 10017. Second class postage paid at New York, NY and additional mailing offices. POSTMASTER: Send address change to Transactions of the ASME, Journal of Turbomachinery, c/o THE AMERICAN SOCIETY OF MECHANICAL ENGINEERS, 22 Law Drive, Box 2300, Fairfield, NJ 07007-2300. CHANGES OF ADDRESS must be received at Society headquarters seven weeks before they are to be effective. Please send old label and new address.

PRICES: To members, \$40.00, annually; to nonmembers, \$130.00.

Add \$24.00 for postage to countries outside the United States and Canada.

STATEMENT from By-Laws. The Society shall not be responsible for statements or opinions advanced in papers or . . . printed in its publications (B7.1, Par. 3).

COPYRIGHT © 1993 by The American Society of Mechanical Engineers. Authorization to photocopy material for internal or personal use under circumstances not falling within the fair use provisions of the Copyright Act is granted by ASME to libraries and other users registered with the Copyright Clearance Center (CCC) Transactional Reporting Service provided that the base fee of \$3.00 per article plus 30 per page is paid directly to CCC, 27 Congress St., Salem, MA 01970. Request for special permission or bulk copying should be addressed to Reprints/Permission Department.

INDEXED by *Applied Mechanics Reviews* and *Engineering Information, Inc.*
Canadian Goods & Services
Tax Registration #126148048

Journal of Turbomachinery

Published Quarterly by The American Society of Mechanical Engineers

VOLUME 115 • NUMBER 1 • JANUARY 1993

TECHNICAL PAPERS

- 1 Stall Inception in Axial Flow Compressors (91-GT-86)
I. J. Day
- 10 A Study of Stall in a Low Hub-Tip Ratio Fan (92-GT-85)
M. Soundranayagam and R. L. Elder
- 19 Pressure Fluctuation on Casing Wall of Isolated Axial Compressor Rotors at Low Flow Rate (92-GT-33)
M. Inoue, M. Kuroumaru, and Y. Ando
- 28 The Role of Tip Clearance in High-Speed Fan Stall (91-GT-83)
J. J. Adamczyk, M. L. Celestina, and E. M. Greitzer
- 40 Active Suppression of Rotating Stall and Surge in Axial Compressors (91-GT-87)
I. J. Day
- 48 Active Control of Rotating Stall in a Low-Speed Axial Compressor (91-GT-88)
J. D. Paduano, A. H. Epstein, L. Valavani, J. P. Longley, E. M. Greitzer, and G. R. Guenette
- 57 Evaluation of Approaches to Active Compressor Surge Stabilization (92-GT-182)
J. S. Simon, L. Valavani, A. H. Epstein, and E. M. Greitzer
- 68 Active Stabilization of Compressor Instability and Surge in a Working Engine (92-GT-88)
J. E. Ffowcs Williams, M. F. L. Harper, and D. J. Allwright
- 76 Unsteady Aerodynamic Response of a Cascade to Nonuniform Inflow (91-GT-174)
J. E. Caruthers and W. N. Dalton
- 85 Unsteady Rotor Dynamics in Cascade (91-GT-147)
Y. T. Lee, T. W. Bein, J. Feng, and C. L. Merkle
- 94 Inviscid-Viscous Coupled Solution for Unsteady Flows Through Vibrating Blades: Part 1—Description of the Method (91-GT-125)
L. He and J. D. Denton
- 101 Inviscid-Viscous Coupled Solution for Unsteady Flows Through Vibrating Blades: Part 2—Computational Results (91-GT-126)
L. He and J. D. Denton
- 110 Validation of a Numerical Method for Unsteady Flow Calculations (91-GT-271)
M. Giles and R. Haimes
- 118 On the Propagation of Viscous Wakes and Potential Flow in Axial-Turbine Cascades (91-GT-373)
T. Korakianitis
- 128 Effects of Stator Wakes and Spanwise Nonuniform Inlet Conditions on the Rotor Flow of an Axial Turbine Stage (91-GT-93)
J. Zeschky and H. E. Gallus
- 137 Blade Row Interaction in a Multistage Low-Pressure Turbine (91-GT-283)
N. Arndt
- 147 Wind Tunnel Wall Effects in a Linear Oscillating Cascade (91-GT-133)
D. H. Buffum and S. Fleeter
- 157 Computational Study of Stall Flutter in Linear Cascades (91-GT-5)
A. Abdel-Rahim, F. Sisto, and S. Thangam
- 167 The Effect of Steady Aerodynamic Loading on the Flutter Stability of Turbomachinery Blading (91-GT-130)
T. E. Smith and J. R. Kadambi
- 175 An Unsteady Lifting Surface Theory for Ducted Fan Blades (91-GT-131)
R. M. Chi
- 189 Optical Measurements of Unducted Fan Flutter (91-GT-19)
A. P. Kurkov and O. Mehmed

(Contents Continued on p. 9)

(Contents Continued)

- 197 Rotor Blade Unsteady Aerodynamic Gust Response to Inlet Guide Vane Wakes**
(91-GT-129)
S. R. Manwaring and S. Fleeter

ANNOUNCEMENTS

- 18 Change of address form for subscribers**
Inside Back Cover Information for authors

Stall Inception in Axial Flow Compressors

I. J. Day

Whittle Laboratory,
Cambridge University Engineering
Department,
Cambridge, United Kingdom

Studies have been conducted on two laboratory test compressors to investigate the process leading to the formation of finite amplitude rotating stall cells. The measurements were obtained from circumferential arrays of hot wires and were spatially and temporarily analyzed to show that modal perturbations are not always present prior to stall, and when present, sometimes have little direct effect on the formation of the stall cells. The measurements lead to the conclusion that the occurrence of modal perturbations, and the formation of finite amplitude stall cells, are two separate phenomena, both occurring under roughly the same conditions at the peak of the pressure rise characteristic. The measurements also underline the hitherto unsuspected importance of short length scale disturbances in the process of stall inception. Examples are given of different ways in which stall cells can develop and the conclusions are backed up with a summary of current test data from various machines around the world.

Introduction

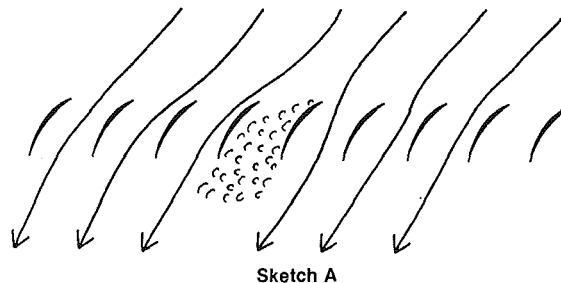
The present trend in aero-engine compressors is toward increased pressure ratio per stage. The need to retain an adequate operating range under these conditions has stimulated renewed interest in compressor instabilities. Rotating stall cells and transient reversed flow (surge) are limiting factors at peak performance of the compressor. New attempts, using better instrumentation and improved analytical models, are therefore being made to understand these complex flow phenomena.

Past efforts in this field have met with limited success. Both rotating stall and surge can be reasonably well described in terms of what happens in the compressor when either disturbance is well established. However, a gap exists in the understanding of how the disturbances come into being and we are still unable to predict the precise operating point at which this instability will occur. In recent years it has become clear that the idea of using only steady-state parameters to determine the stall point of a compressor is too simplistic and the focus of attention has now shifted to problems of aerodynamic stability. The current experimental work on stall inception is aimed at providing a sound physical understanding of the phenomenon on which to base improve modeling of compressor stability.

A heightened interest in stall inception has also been aroused with the recent attempts to extend the compressor operating range through the use of active control techniques. The idea was first published in the open literature by Epstein et al. (1986) and since then successful experiments have been carried out by Day (1992) and Paduano et al. (1992). The objective in applying active control to compressor instabilities is to feed back damping perturbations into the flow field, which will suppress the development of the stalling disturbances.

Contributed by the International Gas Turbine Institute and presented at the 36th International Gas Turbine and Aeroengine Congress and Exposition, Orlando, Florida, June 3-6, 1991. Manuscript received at ASME Headquarters February 19, 1991. Paper No. 91-GT-86. Associate Technical Editor: L. A. Riekert.

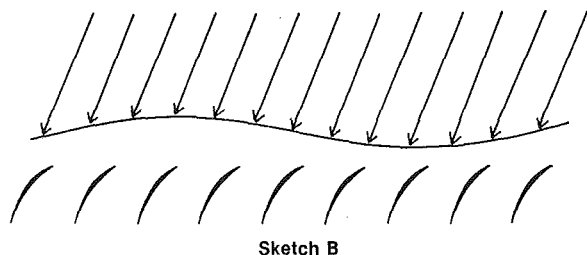
Two flow models of particular interest to the current work can be found in the literature. It will be useful to review these before going on to look at the experimental results. The first flow model is that derived from a picture originally drawn by Emmons et al. (1955). This picture suggests a possible cause of stall inception and offers an explanation of how the stall cell propagates along the blade row.



In a row of highly loaded blades, a minor physical irregularity, or flow nonuniformity, can result in momentary overloading and separation. This separation, or blockage, will restrict the flow through the blade passage and will therefore divert the incoming streamlines. On one side of the blockage the streamline diversion will cause increased incidence, and on the other side decreased incidence. The blade passage subjected to increased incidence, the one on the left in Sketch A, will therefore become stalled, while the one already stalled will unstall. The stall "cell" will thus propagate from blade to blade around the compressor. The propagation speed of the cell is always lower than the rotational speed of the blades and, although the stall cell will move to the left relative to the rotor blades in this picture, both cell and blades move to the right in the absolute frame of reference. Although not origi-

nally intended this way, the above picture has been drawn so as deliberately to emphasize the point that a stall cell such as this need only affect the flow around a few blade passages. A cell like this would be called a disturbance of short length scale.

The second flow model is also found in the above paper by Emmons et al., but has recently been extended to multistage machines by Moore and Greitzer (1986). In this work modal perturbations are of primary interest and these, sometimes referred to as prestall waves, may be visualized as small sinusoidal velocity fluctuations that rotate about the annulus at a steady speed.



In Sketch B only a limited number of blades are shown, but these are intended to represent a complete blade row. A velocity perturbation with a wavelength equal to the circumferential length of the annulus would be referred to as a mode of order 1. Here the blades move to the right and so too does the perturbation, but always at a speed lower than the blade speed. In this view, such a perturbation would grow or decay depending on stability criteria related to the operating point of the compressor. If the compressor were to be throttled toward the stall point, the perturbation would grow in intensity, without any abrupt change in either amplitude or frequency, until a fully developed stall cell is formed. In other words the stall cell would grow smoothly out of the prestall perturbation. Initially the wave amplitude would be infinitely small and not discernible above the background noise, but as the instability point is approached growth of the wave would be rapid, and to the observer the compressor would appear to stall instantaneously.

In recent years the Moore and Greitzer model has received some direct experimental support from work done by McDougall et al. (1990) and by Garnier et al. (1991). McDougall was the first to show that modal perturbations actually exist and his measurements lead him to conclude that localized disturbances of the first type (Sketch A) have no part to play in the stall inception process. Garnier was also able to detect modal perturbations in low and high-speed compressors and examined the buildup of these perturbations prior to stall. His work did not, however, concentrate on the process by which the perturbations ultimately become stall cells. The present work also shows modal perturbations prior to stall, but by looking more closely at the cell formation process it has been found that modal perturbations are not the only path into stall. Disturbances of a shorter length scale (as in Sketch A) have now been identified and their effect on cell formation is evident in the majority of cases tested.

The work documented here focuses on the process of stall cell development and presents detailed measurements from both single stage and multistage machines. It also takes advantage of a compressor facility that incorporates devices by which the onset of stall can be delayed using active control techniques. Using this equipment, the flow field can be perturbed so that different aspects of the transient behavior in the compressor may be studied. The findings undoubtedly reveal a more complicated picture than the accepted picture of stall inception, and provide new details on short length scale disturbances, which will have to be taken into consideration in future modeling of compressor stability. The results also

help explain some of the difficulties encountered in recent active control experiments and underline the fact that methods for active control of stall will need to be more complex than originally thought.

Experimental Facility and Data Processing

The stall inception measurements have been obtained from two low-speed compressors at the Whittle Laboratory, namely the Deverson rig and the C106 compressor. A detailed description of both machines is given by Li (1990) with some additional statistics included in an appendix to this paper. The Deverson rig is a large single-stage low-speed machine ideally suited to detailed measurements of flow in the blade passages (Fig. 1). As a stage it is intended to have axial absolute flow into the rotor and therefore has no inlet guide vanes. The tip clearances of the rotor blades can be varied from 0–3.0 percent, based on chord length, by using spacers under the blades at the hub. The C106 compressor, on the other hand, is a multistage machine with four identical stages (Fig. 1). The blading has been designed to model a modern high-pressure (HP) compressor and the stage loading is comparatively high.

The C106 was used for preliminary studies on the active control of stall and in the course of this work the compressor was fitted with an array of twelve fast-acting air injection valves. These valves were equally spaced around the circumference of the machine between the IGVs and the first rotor and were designed to inject a small puff of air into the flow field near the rotor tips. The velocity of the injected air was about 1.5 times the free-stream velocity and the amount of air from each valve was less than 0.1 percent of the compressor flow rate (a fuller description of these valves is given by Day, 1991). The valves could be individually opened and closed and when linked to a computer could be instructed to inject any desired sequence of disturbances into the compressor.

Data acquisition procedures were essentially the same for both compressors. Hot-wire anemometers were used throughout, although wall static transducers were available to back up the velocity measurements. Where the probes were equally spaced around the circumference of the machine, the number of probes varied between 4 and 8 with 6 being the preferred number. In the four-stage machine the probes could be placed at almost any axial location, but most of the time they were positioned just upstream of the first-stage rotor; about half a chord from the rotor face. In the Deverson rig this spacing was reduced to about a quarter of a chord length ahead of the rotor face. This approach means that the probes were always

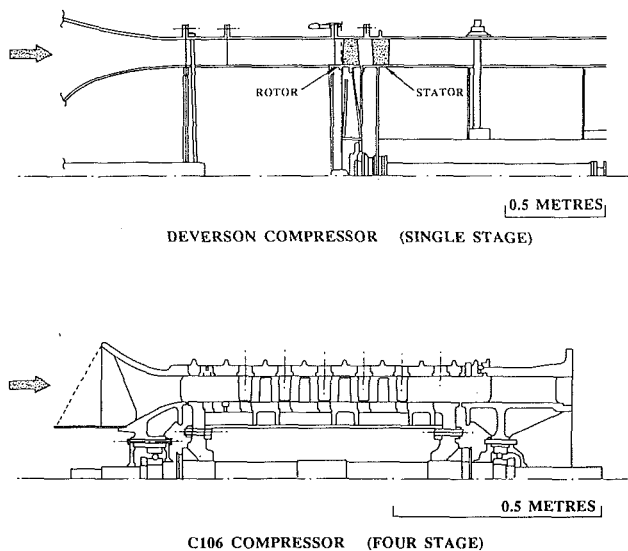


Fig. 1 Cross-sectional views of the Deverson and C106 compressors

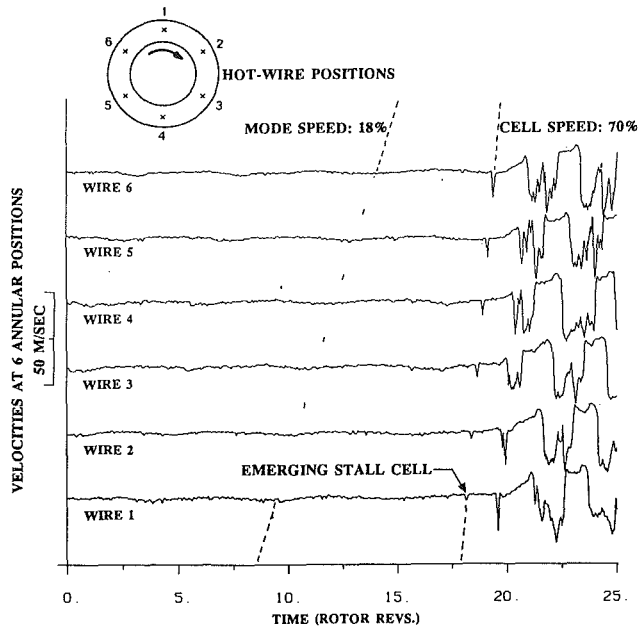


Fig. 2 Hot-wire measurements from the C106 compressor (1.5 percent clearance) showing modal perturbations prior to the formation of a single stall cell (mean flow velocity just before stall: 28 m/s)

in relatively undisturbed flow (as opposed to the turbulent flow behind the rotor), and therefore small changes of blockage or shifts of flow in the rotor passages could easily be detected. Moving the probes farther upstream provides spatial damping from blade-related potential effects, but also reduces the possibility of picking up small disturbances in their early stages.

Numerous processing techniques are available for enhancing various aspects of the transient hot-wire data, but in most cases the examples used in this paper have been specifically chosen so that unprocessed time traces can be used for the sake of clarity. The time taken and the distance traveled around the circumference are easily obtained from these figures to give an indication of speed of rotation. Another useful method of looking at the data is to determine the amplitude and phase angle of circumferential perturbations by Fourier analyzing the velocity distribution around the annulus obtained from the hot-wire probes. Repeated analysis at each sampling time step thus allows waves rotating in the annulus to be tracked as they move and develop with time. This technique was developed by Longley (1988) at the Whittle Laboratory, who first plotted phase angle against time, varying the sizes of dots to indicate the amplitude of the disturbance. In the present work this technique has been used extensively to highlight the coherence of small perturbations that would otherwise have been masked by background noise.

Experimental Results

The experimental results can be roughly divided into two parts, the first dealing with modal perturbations and the second with the formation of finite stall cells. The interaction between these two phenomena will be considered separately.

On a point of terminology, there has been a tendency in the past to refer to modal perturbations as "pre-stall waves." However, as the intention of this paper is to show that the modal perturbations and the formation of finite stall cells are not necessarily consecutive events, the term "pre-stall wave" will not be used. In addition, the nature of the modal perturbations is so closely linked to the idea of aerodynamic resonance that the words "perturbation" and "oscillation" are sometimes interchanged depending on the emphasis required.

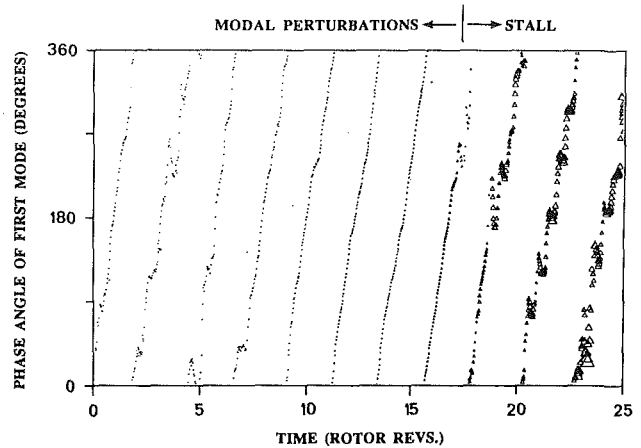


Fig. 3 Results from the Deverson compressor (0.7 percent clearance) showing the phase angle versus time of a first-order modal perturbation

1 Modal Perturbations. Modal perturbations were first observed by McDougall et al. (1990) and since then have been seen in other compressors by Garnier et al. (1991). An example of these perturbations occurring in the C106 compressor is given in Fig. 2. Six hot wires just ahead of the first rotor positioned at midblade span were used to obtain these results. From the beginning of the trace a wavelike disturbance is present in the flow right up to the point where the compressor stalls at rotor revolution 16. By following a trough in the waves as it moves upward and to the right from one wire to the next, it can be seen that the perturbation is traveling in the direction of rotation, and that the incoming flow field must look something like that shown in Sketch B.

Another example of modal perturbations occurring before stall is given in Fig. 3. In this case the data, taken from the Deverson rig at 3.0 percent clearance, have been spatially decomposed using the Longley procedure and are plotted in terms of first-mode phase angle versus time. The size of the dots represents the amplitude of the modal perturbation at each point in time and the grouping of the dots into periodic lines represents the rotation of a coherent modal wave. The unprocessed data from which this plot was derived are shown later in Fig. 10, and it can be seen from both these figures that the stall cell develops smoothly out of the modal wave. [This is not the case in the previous figure (Fig. 2) but this topic will be covered in greater detail later on.]

The growth of the modal perturbations prior to stall in the examples of Figs. 2 and 3 is suggestive of a damped oscillatory system becoming less damped as the compressor is pushed further and further toward the stall point. This is consistent with the Moore and Greitzer (1986) analysis, which shows rapid growth of the oscillations at the peak of the total-to-static pressure rise characteristic.

The C106 test rig with its array of air injection valves offers a unique opportunity to explore the natural resonance of the compressor. To do this a looping sequence of valve openings was employed to give as near as possible a sinusoidal disturbance of constant amplitude to the incoming flow field. The valve sequence was computer generated and the amplitude of the forcing disturbance was kept constant by stabilizing the air injection rate. The compressor was set running at a flow rate as low as possible without prematurely dropping into stall and the looping sequence was set in motion. The disturbance was started at a slow speed, about 10 percent of rotor speed, and slowly accelerated to about 50 percent of rotor speed. Five consecutive sweeps of this frequency range were executed so that an ensemble-averaged result could be obtained. The results from these tests for a single hot wire positioned well away from the immediate influence of the valves are shown in Fig.

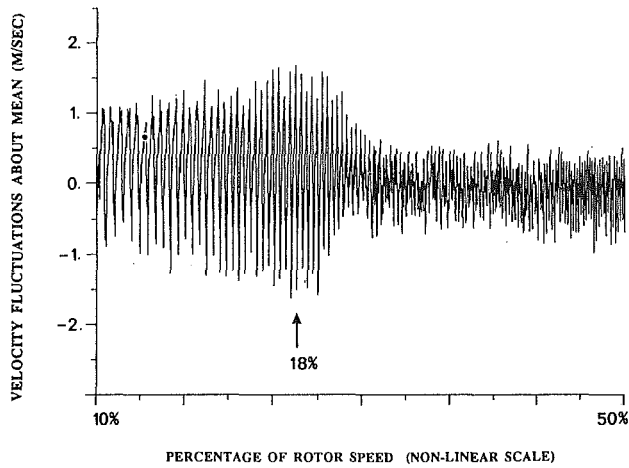


Fig. 4 Velocity fluctuations in the C106 compressor (1.5 percent clearance) induced during unstalled operation by a rotating disturbance of constant amplitude and increasing rotational frequency

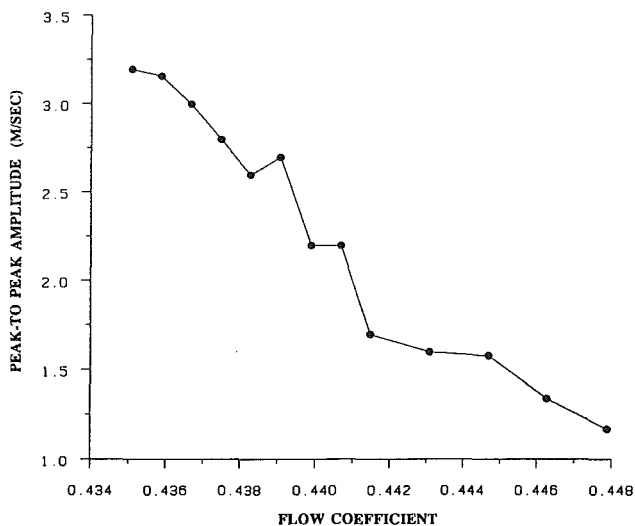


Fig. 5 Amplitude of induced modal oscillations in the C106 compressor at various throttle settings (frequency of forcing disturbance equal to the natural frequency of the compressor, i.e., 18 percent of rotor speed)

4. The abscissa is labeled in percentage of rotor speed and shows that the peak amplitude of the induced disturbance occurs in a frequency range between 15 and 20 percent. This is in close agreement with the modal frequency of 18 percent measured from Fig. 2, where the compressor went into stall naturally.

This experiment was backed up by a series of tests where measurements were taken around the compressor annulus immediately after a short sharp pulse was injected into the flow by one of the valves. The familiar modal disturbance was observed and the frequency was found to be the same as when the mode develops spontaneously. The amplitude of the mode decayed quite quickly after the pulse and was clearly linked to the compressor operating point. Further tests were therefore done to determine how the damping of the system decreases as the peak of the characteristic is approached. Accepting the natural frequency of the system to be about 18 percent of rotor speed, the valves were then used in a sinusoidal fashion at this frequency to excite a response in the compressor while operating at flow rates closer and closer to the stall point. The results are shown in Fig. 5. The amplitude of the excited waves increased almost linearly as the flow rate was reduced. A more interesting point, however, is the limited range over which any

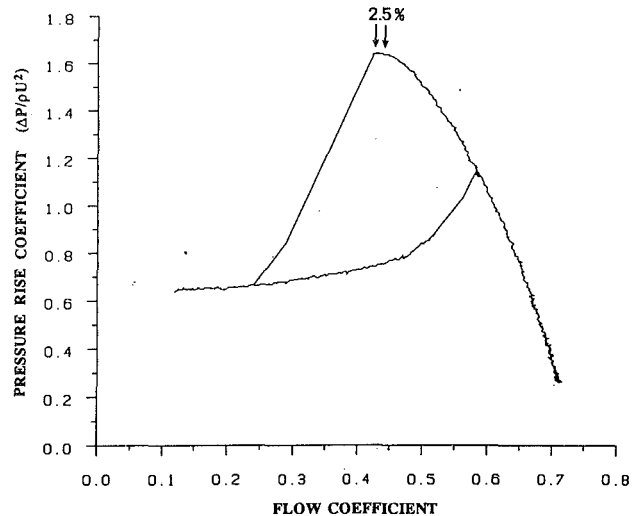
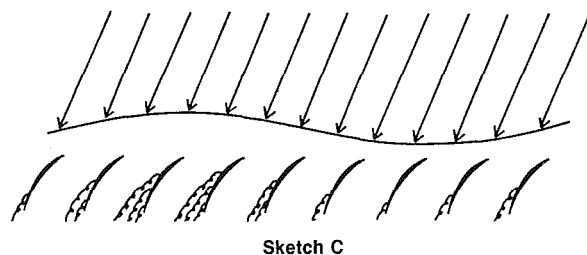


Fig. 6 Total-to-static characteristic of C106 compressor showing how narrow the range is over which modal oscillations can be excited

sign of excitation could be detected. Figure 6 shows this range on the measured total-to-static compressor characteristic. These experiments emphasize the limited range over which modal perturbations can be sustained, and this knowledge will prove useful later on in explaining why modal perturbations are observed prior to stall in some instances and not in others.

During some of the testing on the four-stage compressor, the modal perturbations were of quite noticeable amplitude, even when the air injection valves were not in use. It was therefore reasonable to ask if these waves were not perhaps the manifestation of some other disturbance deeper in the compressor. Measurements were therefore taken with hot wires downstream of the third stator row, i.e., upstream of the last rotor. These probes revealed large periodic velocity fluctuations, which appeared in perfect unison with the modal wave measured simultaneously at the front of the compressor. It was subsequently found that the probes happened to be in such a position relative to the upstream stator blades as to routinely catch the fluctuating wakes shed from these blades. Other probes used at the same time were well clear of the stator wakes and so showed no disturbance at all. The conclusion to be drawn from these tests was that the rise and fall of throughflow velocity occurring with the rotation of the modal wave was causing a sympathetic thickening and thinning of the corner separations attached to each stator blade. The idea is illustrated in Sketch C, where the effect of the velocity perturbation on the wake size is clearly visible.



To demonstrate that this picture is in fact correct, five hot wires were spaced across one blade passage near the outer casing behind the third stage stator row with the first and fifth probes in repeating relative positions. A spanwise position near the outer casing was chosen for this test because the flow separation being examined is usually most marked in the secondary flow regions at the extremities of the blades. The results in Fig. 7 show that hot wire 2, nearest the stator wake, was

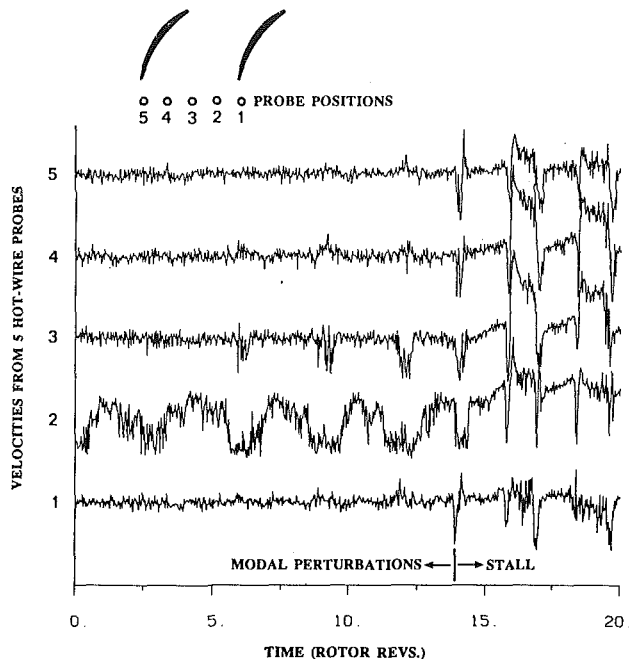


Fig. 7 Data from the C106 compressor showing how the fluctuation in stator wake thickness affects the output from hot wires in various positions relative to the upstream stator blades

indeed picking up the mode associated velocity fluctuations mentioned previously, while wires 1 and 5, which were well clear of the wakes, showed the least disturbance prior to stall. Once the compressor stalled of course the stall cell was picked up equally by all the probes.

It should be noted that corner separations, sometimes quite extreme ones, are a regular feature of the flow in a compressor operating near stall and it is therefore not surprising that the extent of the separation should be influenced by small changes in throughflow velocity. The fact that these separations exist does not imply that the machine itself is stalled nor does the presence of the modal perturbations mean that the compressor is irretrievably on its way into rotating stall. At any point prior to the formation of a finite stall cell, even when strong modal fluctuations are present, the machine can be returned to normal operation simply by backing off the exit throttle. The kind of fluctuating corner separations seen here are present throughout the whole machine and occur in both the rotor and stator blading but with the stators being most severely affected in this compressor, i.e., the C106.

2 The Formation of Finite Stall Cells. In order to discuss the formation of finite (i.e., not infinitesimal) stall cells, it is necessary to be clear about the distinction between a stall cell and a modal wave. A modal wave, as seen experimentally, is a "reversible" disturbance, which can be made to come and go by slight changes in throttle setting and may be visible in the machine for as much as 200 rotor revolutions before stall (Garnier et al., 1991). During this time the pressure rise across the compressor will remain nearly constant. A stall cell, on the other hand, is a comparatively "irreversible" disturbance and once formed will lead inexorably to a collapse of the pressure rise, usually within four to six rotor revolutions.

In the preceding discussion it was shown that modal perturbations may appear in the compressor as the stability line is approached. Alternatively a finite stall cell may also appear in the compressor, independently of the modal perturbations, and at about the same operating condition. It will be shown below that cell formation may precede the occurrence of modal perturbations, in which case the modes are never seen. Alternatively, cell formation may occur after the appearance of

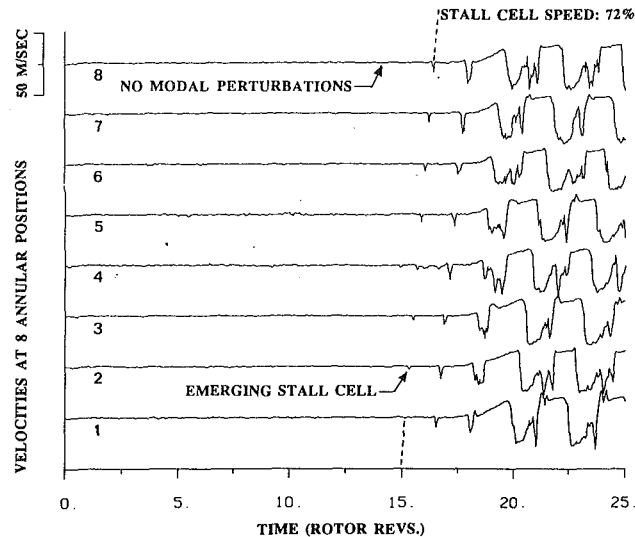


Fig. 8 Hot-wire measurements from the C106 compressor (1.2 percent clearance) showing a stall cell emerging from a flow field in which no modal perturbations can be detected

modal perturbations in which case some degree of coupling between these two phenomena, both rotating in the same direction, may occur.

In a somewhat artificial manner a distinction is drawn below between two types of stall cells that may appear in the compressor: those of short length scale and those of a longer length scale. Although the distinction is made in terms of the size of the cell when it first forms, the real difference between these two types of cell is the speed at which they rotate. The smaller cell will rotate more quickly, while a larger one will rotate more slowly. The importance of this distinction is discussed below.

(a) Cells of Short Length Scale. We start by considering an example from the C106 compressor, set at 1.2 percent tip clearance, in which a stall cell appears before there is any sign of a modal wave. Figure 8 shows the machine operating steadily, with no hint of modal perturbations prior to stall. Modes could not be detected using the Longley FFT procedure either. At approximately $t = 15$ in this figure, a small stall cell of limited extent is formed that rotates around the machine, growing slowly at first and then more quickly to become a fully developed stall cell. Initially the cell starts out moving at about 70 percent of rotor speed but slows down to 38 percent when the cell is fully formed. This pattern of a small localized stall cell rotating fast and slowing as it grows is a dominant feature of the measurements from the C106 compressor and is indicative of a stall inception pattern similar to that suggested in Sketch A.

Another example of cell formation occurring without the presence of modal perturbations comes from the Deverson rig as shown in Fig. 9. It will be recalled that this compressor exhibited modal waves when the tip clearance was set at 3.0 percent (Figs. 3 and 10). Now with the tip clearance at 1.2 percent the picture is quite different. In Fig. 9 the incoming flow is steady and detailed analysis confirms that there is a complete absence of any modal oscillation prior to the formation of the stall cell. Once again the cell is quite localized when it starts out, only two or three blade passages wide, and its speed of rotation is close to 70 percent. The tip clearance for this build is 1.2 percent, as it was in the C106 in Fig. 8, but for want of hard evidence the similarity of clearance may just be a coincidence.

If the tip clearance in the C106 compressor is increased slightly to 1.5 percent by changing the outer casing ring over the first rotor, modal perturbations appear before stall. A clear

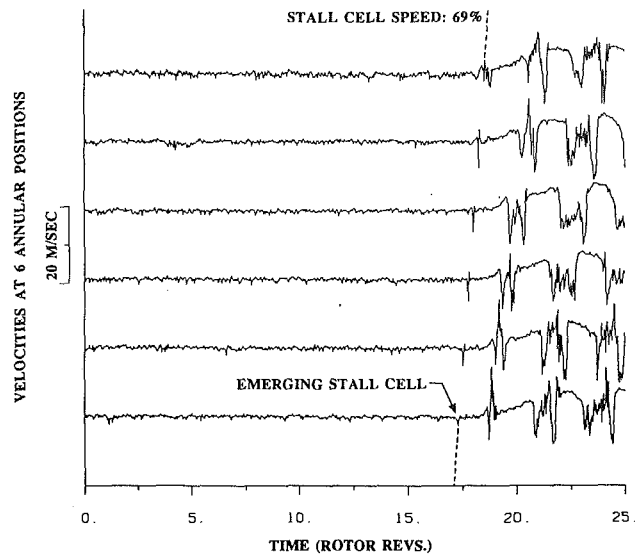


Fig. 9 Hot-wire measurements from the Deverson compressor (1.2 percent clearance) showing a stall cell emerging from a flow field in which no modal perturbations can be detected (mean flow velocity just before stall: 16 m/s)

example of this was given earlier in Fig. 2. Despite the presence of these perturbations the stall cell formation pattern is just as it was in the previous two examples, i.e., a small localized cell, appearing suddenly and rotating fast. The lack of influence of the modal perturbations on the formation of the cell is emphasized by the fact that the modal speed is 18 percent, whereas the stall cell starts out at nearly 70 percent of rotor speed.

In Fig. 2, the stall cell is initially very localized and has a small circumferential length scale compared to that of the preceding modal wave, i.e., $L_{\text{cell}} \sim 0.05 L_{\text{mode}}$. The coupling between the two phenomena would therefore be expected to be small, as is in fact the case. It has been shown by repeated measurements, however, that the modal wave does affect the formation of the stall cell in that the cell usually begins near the trough of the wave where the throughflow velocity is lowest. The stall cell rotates much faster, and is a more vigorous disturbance, than the modal wave and therefore the wave only remains coherent for a very short time after the stall cell appears. Once the stall cell grows in size the modal wave is naturally obliterated.

(b) *Cells of Longer Length Scale.* The above discussion of finite cell development concentrates on what happens when the cell is initially of small length scale, i.e., the disturbance is localized to just a few blade passages. If, on the other hand, the stall cell is larger in circumferential extent when it first forms, it tends to rotate more slowly and coupling between the modal wave and the stall cell will then be more effective.

An example of effective coupling is taken from the Deverson rig at 3.0 percent tip clearance. In this configuration the compressor produces a lower pressure rise for the same flow coefficient than before and the compressor stalls more gently with a much smaller hysteresis loop. The results of the stall inception measurements are shown in Fig. 10 where a modal perturbation appears prior to stall. When the stall cell forms in this case, it is larger in circumferential extent and rotates more slowly. The length scales of the mode and the cell are more comparable here and the cell now appears to grow progressively out of the modal wave. The abrupt change in speed seen previously between the modal wave and the emerging stall cell does not occur in this case. This type of stall inception pattern supports the Moore and Greitzer model shown in Sketch B and is in fact the case studied by McDougall et al. (1990).

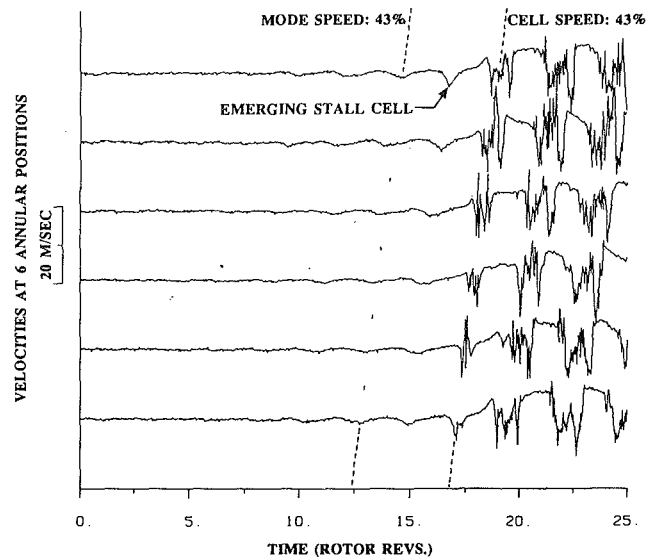


Fig. 10 Hot-wire measurements from the Deverson compressor (3.0 percent clearance) showing a stall cell emerging smoothly out of a flow field containing a modal perturbation

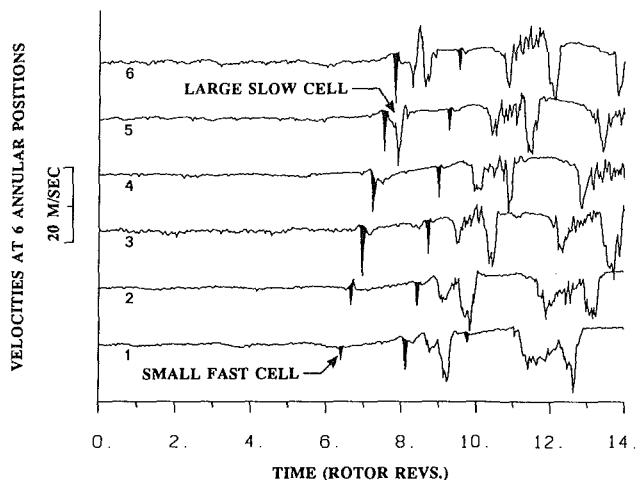


Fig. 11 Hot-wire measurements from the Deverson compressor (0.7 percent clearance) emphasizing the difference in speed between small and large stall cells

(c) *Cells of Both Length Scales.* An unusual example illustrating the difference in rotational speeds of cells of short and long length scales is given in Fig. 11. This data were obtained from the Deverson compressor at 0.7 percent tip clearance when the compressor sometimes stalled in an uncertain manner. Here a short length scale cell is joined soon after inception by a larger cell, which rotates much more slowly. In this figure the smaller cell has been colored in black to make it easier to follow its progress around the machine. Because of its greater speed the small cell quickly catches up with the larger one and after two complete revolutions it runs into the back of the slower moving disturbance. (On closer inspection it can be seen that after one revolution the small cell begins to decrease in size. This is because the part of the flow field through which it is moving is beginning to operate at a higher throughflow velocity due to the blockage caused by the larger cell.)

Supporting Measurements

The examples given above are intended to show that modal perturbations can influence the process of cell formation but

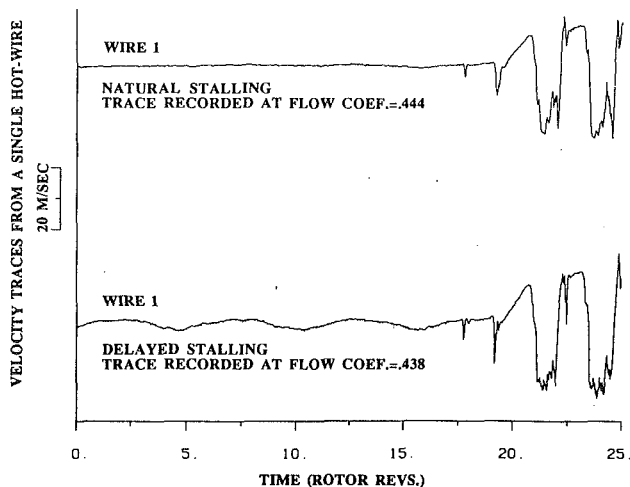


Fig. 12 Hot-wire traces recorded in the C106 compressor (1.5 percent clearance): The upper trace shows natural stalling while the lower trace shows stalling at a flow coefficient 1.5 percent below normal

that these perturbations themselves are not a necessary prerequisite for the formation of stall cells. A number of other experimental observations support this point and these are listed below.

1 It was shown previously how the range over which modal oscillations appear in a compressor is very limited and is restricted to the peak of the characteristic. Since many compressors stall while the characteristic is still rising it is not surprising that the first sign of a disturbance might be the stall cell itself and that the modal oscillations are therefore never seen. This is often the case in the C106 compressor. In this compressor, however, it is possible to inject small quantities of air directly at the tips of the first rotor (in a steady manner) and this has the effect of delaying the formation of the stall cells while creating a nearly horizontal extension to the compressor characteristic (Day, 1992). Any modal oscillation in the compressor can therefore be greatly amplified simply by delaying cell formation and so allowing the compressor to reach an operating point further to the left on the characteristic. The results of such a test are summarized in Fig. 12 where the output from one, rather than six, hot wires is used to illustrate the difference. The upper trace shows the compressor going into stall naturally with only a slight hint of a modal wave before stall. The lower trace shows a much clearer modal wave when the characteristic is extended by just 1.5 percent.

It is worth pointing out again that when the stall cell is small and sharply defined, the coupling between it and the modal perturbation is very weak. The patterns of cell development in the upper and lower traces in Fig. 12 are almost identical despite the fact that a much stronger modal perturbation is present in the lower trace.

A further test along these lines was done using one air injection point only to trip the machine into stall prematurely. By swivelling the chosen injection valve to point in an unfavorable direction, a short sharp puff, effective for about 2.5 ms, is sufficient to trigger the formation of a small finite stall cell of the type seen above, and this causes the compressor to go straight into stall. This premature stalling can be achieved at a flow rate about 5 percent greater than that at the natural stall point. This experiment emphasizes the range over which stalling can occur and implies that, under natural conditions, some minor physical or aerodynamic irregularity could easily stall the machine before the point on the characteristic is reached at which modal oscillations come into play. The data from this last experiment also show that the action of the valve is the immediate cause of cell formation; the valve does not first create a modal oscillation that then turns into a stall cell.

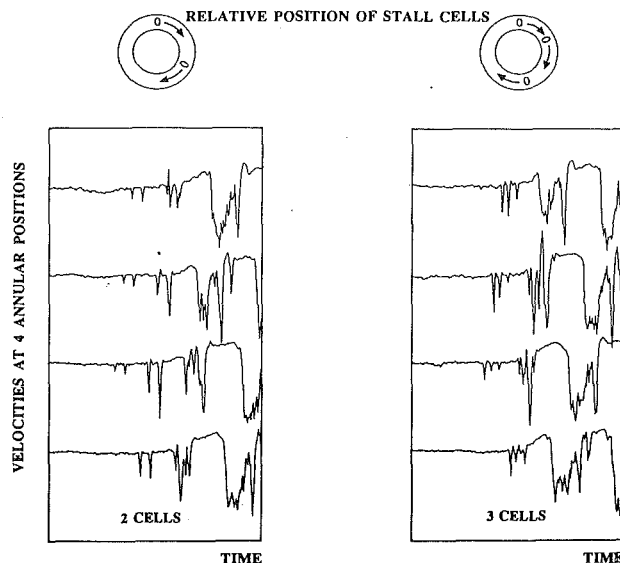


Fig. 13 Examples of the uneven distribution of stall cells around the annulus in the C106 compressor (1.2 percent clearance)

2 The small sharply defined stall cells of the type that appear in the Deverson and C106 compressors have a very short circumferential length scale. The disturbing influence of these cells is restricted to just a few blade passages and therefore any number of cells could form in the compressor, and these could be randomly distributed around the annulus. Figure 13 from the C106 compressor shows some examples of short length scale cells which form in just this way. The random distribution of the cells would be far less likely to occur if organized modal perturbations were a necessary prerequisite for cell formation.

3 In many of the experiments the short-wavelength stall cells appear to originate at precisely the same circumferential position in the annulus each time the machine is stalled. This phenomenon has been observed in the C106 compressor and in the Deverson rig (1.2 percent clearance), but in the Deverson rig particularly, the orientation of the rotor is also involved in the timing of cell formation. A series of 21 consecutive tests were conducted in which six hot wires were used to determine the starting location of the stall cell, and at the same time a once per revolution signal was used to track the orientation of the rotor. In all the tests the stall cell clearly originated near the same spot on the casing and, furthermore, the rotor was always in the same relative position when the cell started. In other words the formation of the stall cell was delayed until a particular part of the rotor was opposite a particular part of the casing. The results of the rotor position measurements are shown in Fig. 14 where relatively little scatter in rotor orientation is observed at the time of cell formation. No measurable eccentricity could be found in the compressor when these tests were done. Again the Sketch A picture of cell formation is most suitable here where, in a highly loaded situation, an imperceptible irregularity would be all that is necessary to trigger the formation of a localized cell.

Some tests were done by McDougall et al. (1990) in the same compressor to try and fix a point on the rotor where the stall cell would begin. Substantial eccentricity (up to eight restaggered blades) had to be built into the rotor before rotor position played a significant part in the timing of cell formation. The difference between their tests and those reported here is that their tests were done at 3.0 percent clearance. At 3.0 percent clearance, modal oscillations of large length scale regulate cell formation (see Fig. 10), whereas at 1.2 percent clearance, the cell length scale is much shorter and localized irregularities are likely to be of greater consequence.

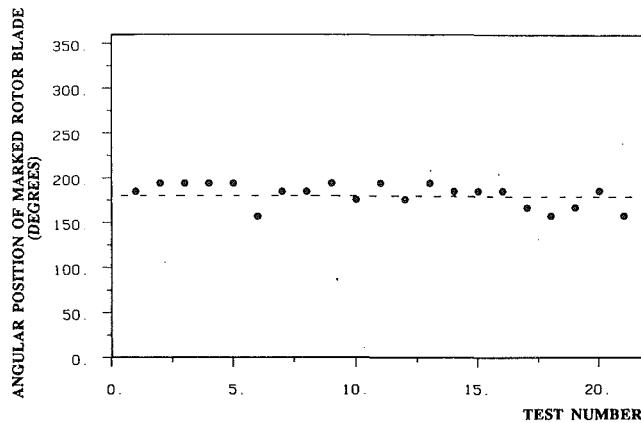


Fig. 14 Series of repeated tests on the Deverson compressor (1.2 percent clearance) showing the angular position of the rotor at the time of stall cell formation

Discussions

The natural occurrence of modal perturbations in a compressor operating near the stability limit has been demonstrated, as has the narrowness of the range over which the perturbations will appear. Finite stall cells of independent origin have also been shown to appear in the compressor under much the same operating conditions. Coupling between the two types of disturbance may occur if the modal perturbation becomes established prior to the formation of the stall cell. If the stall cell forms first, however, the flow field will quickly be disrupted and the modal perturbation will not be seen. The measurements therefore suggest that modal perturbations and the formation of finite stall cells are two separate phenomena.

A modal oscillation is essentially a perturbation superimposed on an underlying axisymmetric flow field. The individual blades in the compressor may all have partly separated flow and the size of the separated region may grow and shrink in sympathy with the oscillation, sometimes even giving the impression of propagation, but still the flow field is essentially axisymmetric. A stall cell, on the other hand, represents a definite break in the symmetry of the flow field. It is not practical to define a stall cell as a disturbance of this or that flow structure, but it is unequivocal to define it as a disturbance that puts an end to the axisymmetric nature of the flow; the crack that stops the bell from ringing.

Two types of stall cells have been observed and these have been classified according to the size of the cell when it first appears, i.e., short or long length scale cells. In the past, part-span and full-span cells have been identified and it might be thought that this classification would perhaps explain the differences observed here. Extensive testing in the C106 and the Deverson compressor has, however, shown that in all cases the first sign of real disruption of the flow field always occurs near the outer casing. In some instances the disturbance spreads to the hub more quickly than in others but in general it may be said that all the stall cells examined here start out as part-span and then become full-span. Some additional information on this topic is given in a discussion by the author to the paper by McDougall et al. (1990). (It is also interesting to note that in the four-stage compressor the stall cell always originates near the tips of the *first* rotor.)

At the present time it is not possible to say which physical features of the compressor are most important in terms of deciding which stall inception scenario will apply. Tip clearance has been found to play an important part, but this is the only parameter that has been varied in any significant way so far and its influence is not clear. Tip clearance is known to affect conditions in the blade passages and therefore its primary effect on stall cell behavior may well be in this part of the flow field.

Table 1

Compressor Build	Modal Speed (%)	Cell Starting Speed (%)	Cell Final Speed (%)
Deverson (3.0%)	43	43	36
Deverson (1.2%)	-	69	36
Deverson (0.7%)	44	65	38
C106 (1.2%)	-	72	38
C106 (1.5%)	18	70	40
Cranfield (4 stage)	-	67	49
Rolls Royce (8 stage)	-	66	48
MIT (build JP)	-	45	22
MIT (build VG)	35	35	38

Some recent tip clearance experiments have produced conflicting results and therefore the references to tip clearance in this paper should be treated as build labels rather than parametric details.

By way of a summary, the stall inception details from the various compressors for which information is available have been tabulated in Table 1.

It can be seen that in only the first and last cases, where the mode and the cell have equal speeds, does a relatively smooth transition take place from the modal perturbation stage right through to the fully developed stall cell. In all the remaining cases, whether modal perturbations are present or not, the stall cells always starts out going relatively fast and only then slow down. Further than this the data as a whole underline the complexity of the problem and highlight the importance of short length scale disturbances in the stalling process.

Conclusions

1 From the experimental results it would appear that modal oscillations and the formation of finite stall cells are separate, and physically different, events. A modal oscillation is a disturbance of circumferential proportions superimposed on a fundamentally axisymmetric flow field. An emerging stall cell on the other hand is a localized disturbance that represents the start of the process by which the symmetry of the flow field is destroyed.

2 The occurrence of modal oscillations and the formation of finite stall cells are not necessarily consecutive events. Both types of disturbance develop near the limit of the pressure rise characteristic, but either one might be the first to appear.

3 If a finite stall cell is the first to appear in the compressor, the symmetry of the flow field is rapidly destroyed and modal oscillations do not develop. If a modal oscillation develops prior to the formation of a finite stall cell, the oscillation may influence the stalling process to a greater or lesser extent depending on the size of the cell when it forms.

4 It would appear that stall cell formation can be divided into two different patterns. In the one case the stall cell is restricted in circumferential extent, and the initial speed of rotation is high. In the second case the cell is larger in circumferential extent, originates less abruptly, and rotates at a speed more like the final stall cell speed. (The separation of cells into categories of small or large is probably artificial, and a continuous spectrum of sizes is more than likely possible.)

5 When cell formation occurs in an already established modal flow field, some measure of coupling between these two phenomena may occur. If the cell is initially of small length scale, its formation will not be affected by the larger length scale modal perturbation. In these circumstances the only influence of the modal waves is to provide a localized dip in the throughflow velocity where the stall cells are most likely to originate. When the stall cell formation is larger in circumferential extent, the stall cell will appear in phase with the modal wave and will develop smoothly without an abrupt change in amplitude or speed.

6 The data seen so far suggest that it is the initial emergence, and subsequent spreading, of a short length scale disturbance that is the most commonly followed route into fully developed stall.

Acknowledgments

I am extremely grateful to Rolls Royce plc. for their financial support of the project and of myself through the Rolls Royce Fellowship at Wolfson College. Significant financial support in the form of a cooperative grant was also provided by the SERC and this is gratefully acknowledged. Messers C. Freeman, A. Cargill, and S. Morgan of Rolls Royce Derby are all to be thanked for their interactive assistance. In Cambridge I would like to thank Prof. N. Cumpsty, the initiator of this work, for his generous collaborative support. I am also appreciative of the help and useful comments received from my colleague, Dr. J. Longley. I would like to thank Prof. E. Greitzer for his interest and encouragement, J. Paduano for useful discussions, and Dr. D. Wisler for recent confirmation of some of my ideas.

References

- Day, I. J., 1993, "Active Suppression of Rotating Stall and Surge in Axial Compressors," *ASME JOURNAL OF TURBOMACHINERY*, Vol. 115, this issue, pp. 40-47.
- Emmons, H. W., Pearson, C. F., and Grant, H. P., 1955, "Compressor Surge and Stall Propagation," *Transactions of the ASME*, Vol. 79.
- Epstein, A. H., Ffowcs Williams, J. E., and Greitzer, E. M., 1986, "Active Suppression of Aerodynamic Instabilities in Turbomachines," AIAA Paper No. 86-1994; also *Journal of Propulsion and Power*, Vol. 5, No. 2, 1989, pp. 204-211.
- Garnier, V. H., Epstein, A. H., and Greitzer, E. M., 1991, "Rotating Waves as a Stall Inception Indication in Axial Compressors," *ASME JOURNAL OF TURBOMACHINERY*, Vol. 113, pp. 290-302.
- Li, Y. S., 1990, "Mixing in Axial Compressors," Ph. D. Thesis, University of Cambridge; Li, Y. S., and Cumpsty, N. A., 1991, "Mixing in Axial Flow Compressors: Part I—Test Facilities and Measurements in a Four-Stage Compressor," *ASME JOURNAL OF TURBOMACHINERY*, Vol. 113, pp. 161-165.
- Longley, J. P., 1988, Whittle Laboratory, Cambridge, United Kingdom, Private Communication.
- McDougall, N. M., Cumpsty, N. A., and Hynes, T. P., 1990, "Stall Inception in Axial Compressors," *ASME JOURNAL OF TURBOMACHINERY*, Vol. 112, pp. 116-125.
- Moore, F. K., and Greitzer, E. M., 1986, "A Theory of Post-Stall Transients in Axial Compression Systems: Part I—Development of Equations, and Part II—Application," *ASME Journal of Engineering for Gas Turbines and Power*, Vol. 108, pp. 68-76, 231-239.

Paduano, J., Epstein, A. H., Valavani, L., Longley, J. P., Greitzer, E. M., and Guenette, G. R., 1993, "Active Control of Rotating Stall in a Low Speed Axial Compressor," *ASME JOURNAL OF TURBOMACHINERY*, Vol. 115, this issue, pp. 48-56.

A P P E N D I X

Table 2 Deverson single stage compressor: midheight blading parameters and other details

	<u>Rotor</u>	<u>Stator</u>
Solidity	1.31	0.95
Aspect Ratio	1.37	1.34
Chord (mm)	111.0	114.0
Stagger (deg.)	47.9	14.3
Camber (deg.)	26.5	42.9
No. of aerofoils	51	36
No. of IGVs		0
Axial Spacing (mm)		50.0
Tip diameter (mm)		1524
Hub/Tip ratio		0.8
Speed of Rot. (rpm)		500
Reynolds Number		3.1×10^5

Table 3 C106 four-stage compressor: midheight blading parameters and other details

	<u>Rotor</u>	<u>Stator</u>
Solidity	1.47	1.56
Aspect Ratio	1.75	1.75
Chord (mm)	35.5	36.0
Stagger (deg.)	44.2	23.2
Camber (deg.)	20.0	40.6
No. of aerofoils	58	60
No. of IGVs		60
Axial Spacing (mm)		13.0
Tip diameter (mm)		508
Hub/Tip ratio		0.75
Speed of Rot. (rpm)		3000
Reynolds Number		1.7×10^5

A Study of Stall in a Low Hub-Tip Ratio Fan

M. Soundranayagam

The National Engineering Laboratory,
East Kilbride, Glasgow, Scotland

R. L. Elder

Cranfield Institute of Technology,
Bedford, England

An investigation has been carried out in order to define the process of rotating stall inception in a low-speed, low hub-tip ratio fan. Based on elementary cascade analysis, the fan would be expected to stall from the root. However, considerable experimental evidence indicates that tip stall is more frequently incurred. Although the analysis has been undertaken for a specific fan, it is considered to be representative of a broad range of machines. The analysis has involved two primary considerations, first the effect of streamtube contraction, which has been studied theoretically, and second, real flow effects (those not contained in the theoretical model), which have been studied experimentally. The study of streamtube contraction indicates that the root rematches to a more stable operating point, thus alleviating some of the problems in that region. The experimental investigation was undertaken on an isolated rotor, with successive build modifications to increase the likelihood of rotating stall inception at the root. It was apparent that real fluid effects tended to steepen the root pressure rise characteristic, thus enhancing the stability in that region. The performance of the fan at the tip tended to be poor, providing a pressure characteristic with a lower negative gradient than anticipated, indicating less stability than simple flow models would suggest. Hot-wire flow mapping at the rotor exit supported the overall conclusion that the rotor showed a strong reluctance to stall at the root apparently due to "centrifuging" of the boundary layer toward the tip.

Introduction

The aerodynamic design of blading for low hub-tip ratio fans is complicated due to the different conditions occurring along the span and the downstream static pressures the various blade sections have to provide (the downstream static pressures being controlled by the performance of the various blade sections and radial equilibrium considerations).

Stall is a widely used term associated with flows that are considered to be partially or completely separated. In the present context, however, the term stall is used to describe the condition where the compressor flow regime changes from a nominally axisymmetric flow to one characterized by one or more cells of reduced throughflow, which rotate in the direction of rotation but at about half rotor speed, i.e., the rotating stall condition. Rotating stall is an undesirable flow condition and research into its prediction and control has been pursued for over forty years (Cheshire, 1945; Dring et al., 1982; Freeman, 1985; Moore and Greitzer, 1986; Greitzer and Moore, 1986; Smith, 1974).

Stability analysis of the compressor flow field, usually employing an actuator disk model of the blade rows, has made a strong contribution to the understanding of stall inception in a two-dimensional sense. Almost any reasonable physical model used in such a stability analysis is able to predict the

growth of circumferential perturbations (i.e., rotating stall). The stability criterion employed is similar for all the models (i.e., the compressor will stall at or near the zero slope point of the pressure rise characteristic (Emmons et al., 1959; Fabri, 1970; Dunham, 1965)), but this is of limited validity since a good proportion of compressors stall while still on the negatively sloped part of their characteristic (Day et al., 1978; Fattner, 1990). It is probable that further improvements would require inclusion of modeling of radial and circumferential effects in considerable detail. This in turn would rely on a more thorough understanding of the stall inception process.

Until recently, experimental knowledge of the inception process had largely been based on correlative studies of conventional steady-state parameters such as the casing boundary layer thickness and the blade row static pressure rise (Koch, 1981; Zika, 1985). While such studies have certainly increased the data available leading to a better general understanding of the factors affecting the process, they are inherently limited in their ability to describe the inception process in more detail. This is due in part to the fact that it is difficult to study the influence of any one factor in isolation. Concepts such as the blade stall/wall criterion (Greitzer et al., 1979) point to the important role that may be played by the different regions of the flow field. The development of transient experimental techniques has also permitted the problem to be analyzed more closely. Recent investigations in a high hub-tip ratio stage (Jackson, 1987) have revealed that forward spillage of the tip clearance vortex can play an important role in the inception process.

Contributed by the International Gas Turbine Institute and presented at the 37th International Gas Turbine and Aeroengine Congress and Exposition, Cologne, Germany, June 1-4, 1992. Manuscript received by the International Gas Turbine Institute February 4, 1992. Paper No. 92-GT-85. Associate Technical Editor: L. S. Langston.

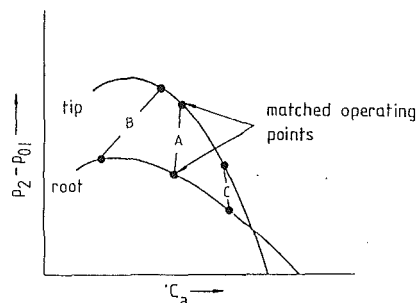


Fig. 1(a) Root and tip matching

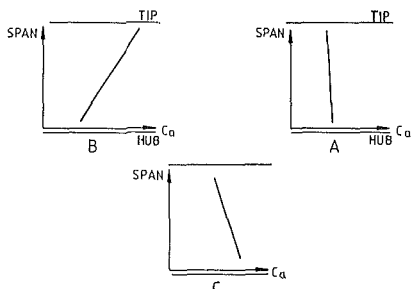


Fig. 1(b) Spanwise velocity profiles at match conditions A, B, and C shown above

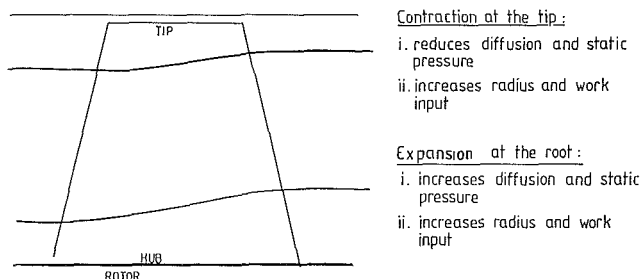


Fig. 1(c) Streamtube contraction/expansion at tip and root

The current paper is concerned with stall in a fan of low hub-tip ratio consisting of rotor and stator, although much of the study has been undertaken on the isolated rotor. Matching of the various streamtubes through a fan is controlled by the downstream static pressure, which in turn is influenced by radial equilibrium. A common design feature of rotors is a uniform radial distribution of work. As a consequence the tip pressure rise characteristic tends to be steeper than those at the root. Therefore the root sections tend to suffer greater variation in local flow condition for a specified change in back pressure. As the mass flow is reduced, therefore, the blade root section tends to reach the peak of its characteristic well before the tip region (Fig. 1a). Operation at, or near, the peak of the total-to-static characteristic is linked, both experimentally and theoretically, to stall inception. Therefore this simple model would suggest the fan would stall at the root before doing so at the tip.

Existing experimental data of stall cell patterns in low hub-tip ratio fans indicates that both part-span and full-span cells may occur. If stable part-span cells occur in isolated rotors, however, then they have generally been found to occur at the tip, although measurements on compressors (rotor and stator)

(Giannissis et al., 1989; Wood et al., 1960) indicate that stable part-span cells at the root can in fact occur in some conditions. The general case, however, is that the stall inception occurs at the tip especially for isolated fan rotors.

There is thus a discrepancy between the predicted radial location of stall inception and the experimental findings. It has been pointed out that consideration of streamtube contraction effects could significantly alter the situation by modifying the local characteristics from those obtained under assumptions of two-dimensional (cascade) flow. Blade boundary layer migration is also known to occur in many compressors and in all probability would have some effect on the local characteristics. It also appears possible that a stall cell originating at the root could be rapidly centrifugal to the tip.

In this study the effects of streamtube contraction have been evaluated and, in addition, measurements have been undertaken on an isolated rotor. It is felt that these studies shed some light on the matter and are described in the following sections.

Streamtube Contraction Effects

To investigate the effects of streamtube contraction, an existing streamline curvature program was used. The program was of the type used for the analysis of multistage compressor flows in the gas turbine industry (Marsh, 1976). The results presented here are for an isolated rotor of free vortex design and hub-tip ratio of 0.4. The rotor geometry corresponds to that of a research fan used for casing treatment studies (Smith, 1980).

It is common to design an axial fan for a uniform axial velocity profile at its design point both upstream and downstream. As the mass flow is reduced, the velocity profile will generally skew, with a larger reduction in axial velocity toward the root than at the tip, Fig. 1(b). In the stage studied, this axial velocity skew was accompanied by diffusion of the root and acceleration of the tip streamtubes across the blade row (i.e., an axial velocity ratio, AVR, less than unity for the root and greater than unity for the tip), Fig. 1(c). There is an associated outward radial shift in the streamtube mean radius for both the hub and tip. The AVR of less than unity at the hub would normally result in an increased loss coefficient and deviation angle, both of which would tend to reduce the negative gradient of the pressure rise characteristic. This would be thought to increase the tendency for the root to stall. However, the outward radial shift in the streamtube mean radius also produces an increased work input (leading to an increased total-to-static pressure rise), tending to increase the level of this root pressure characteristic, making it steeper and more stable. A third factor is that the presence of diffusion will modify the delivery static pressure of the sections and thereby modify the radial matching.

As already noted, the axial velocity skew was accompanied by a contraction of the tip streamtube across the blade row (i.e., an AVR greater than unity) and an outward shift in the streamtube mean radius. The greater than unity AVR at this tip section would result in a decreased loss coefficient and deviation angle, both of which would tend to increase the negative gradient of the characteristic, adding to the effect of the outward radial shift of the streamtube mean radius. It is therefore expected that streamtube contraction effects would tend to make the tip streamtube characteristic steeper and hence more stable.

Nomenclature

AVR = Axial Velocity Ratio (inlet/
outlet)
 \bar{C}_a = mean axial velocity

i = incidence
 P_2 = downstream static pressure
 P_{01} = upstream total pressure

U_m = mean blade speed
 δ = deviation angle
 ϕ = flow coefficient = \bar{C}_a/U_m

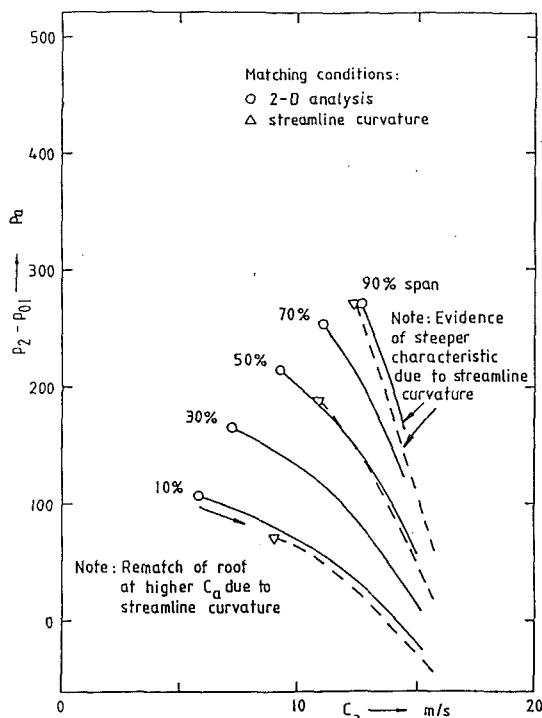


Fig. 2 The effects of streamtube contraction

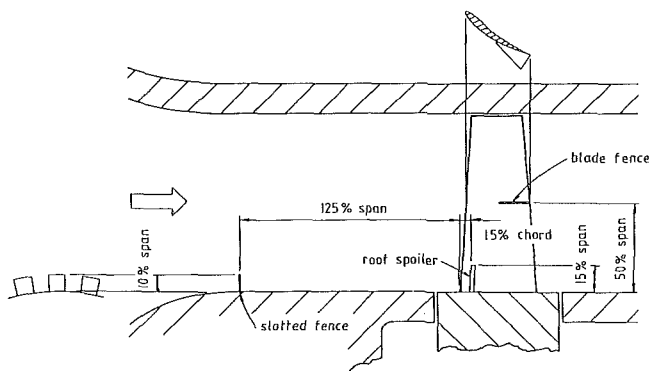


Fig. 3 Build modifications

Streamtube contraction therefore appears to have influences at both the tip and root. To determine the net effect of the full streamline curvature, calculations have been compared with an analysis in which streamtube contraction has been suppressed.

To achieve this the program was first run as a standard streamline curvature calculation for the complete compressor geometry. To simulate a simple axisymmetric analysis (i.e., no streamtube contraction effects) the compressor annulus was divided into five annular sections of equal spanwise extent (i.e., 20 percent span) in which two-dimensional flow was assumed. The performance of each of these sections was then separately determined with the matched operating points of the individual sections obtained from radial equilibrium conditions. A comparison of these results is shown in Fig. 2.

The most significant streamline curvature effect is that the skew in axial velocity (the axial velocity profile from root to tip) has been considerably reduced compared with the two-dimensional analysis, i.e., for the same total-to-static pressure rise of the tip streamtube (overall fan total-to-static pressure rise) the effect of streamtube contraction has been to rematch the operating point of the root streamtube to a significantly higher value of local axial velocity. Streamtube contraction

would therefore seem to reduce the tendency of the root streamtube to stall by matching the root further from stall. It was argued earlier in this section that streamtube contraction will tend to increase the negative slope (and the stability) of the tip characteristic by increasing the local AVR. Careful examination of data used to prepare Fig. 2 showed this to be the case. It would therefore appear that streamtube contraction tends to enhance the stability of both root and tip streamtubes (at least this is the conclusion from this very simple measure of stability).

Experimental Studies

Test Rig and Instrumentation. The experimental studies were carried out on an isolated rotor of free vortex design (Azimian et al., 1990). The hub-tip ratio was 0.5 with a casing diameter of 508 mm. The rotor had 27 blades of aspect ratio 2.66. The rotor was operated at 1500 rpm with a blade Reynolds number of 1.25×10^5 at the tip radius. The measurements presented here were taken in the downstream traverse plane, located at 45 percent of an axial chord downstream of the trailing edge. It should be noted that the rotor was not that used for the theoretical study. This was by way of convenience and the authors do not feel that it significantly influences their finding.

A three-hole cylindrical yawmeter was used to obtain conventional traverse data. In order to obtain greater detail of the flow structure in the blade-to-blade plane, hot-wire anemometry was employed. A single sensor, dual orientation hot-wire technique was used.

An array of up to four hot-wire probes was used to detect disturbances during the inception transient. The hot-wire sensors were tangentially oriented, which allowed them to measure the axial velocity component to a good approximation. The data acquisition system for the hot-wire measurements was based on a microcomputer. In order to meet the requirement for high sampling speeds and high data volume, the sampling routines were written in machine code. A continuous recording routine was used for data capture during the inception transient.

Experimental Study of Five Rotor Builds. From initial tests on the isolated rotor, it appeared that the first disturbance in the stall inception process took place at the tip. The initial (nominal) build, tip clearance 3.2 mm, was modified in four different ways (Fig. 3) in an attempt to cause the first disturbance to occur at the root.

- (i) The tip clearance was first reduced to 0.7 mm to improve the tip performance (reduced tip clearance). This clearance was then maintained for subsequent tests.
- (ii) The hub boundary layer thickness was increased by using a slotted fence to increase the incidence at the root (thick hub boundary layer).
- (iii) Blade suction surface spoilers were fitted to the root to degrade the root performance (root spoiler).
- (iv) A blade fence was used at midspan to impede radial migration of boundary layer material, which possibly aided root performance (blade fence).

The measured overall characteristics are compared in Fig. 4. It is clear that the root spoiler significantly reduces the ability of the rotor to generate pressure rise by, presumably, prematurely separating the flow on the root section blade profile introducing a source of low momentum fluid. Both the large tip clearance and thick hub boundary layer have much the same influence, while the blade fence has a much smaller effect on rotor performance. No great importance has been attached to the different flow rates noted at stall because the coefficient used reflects the average axial velocity involved, which will be significantly influenced by the different blockages and velocity profiles introduced by the different build modifications.

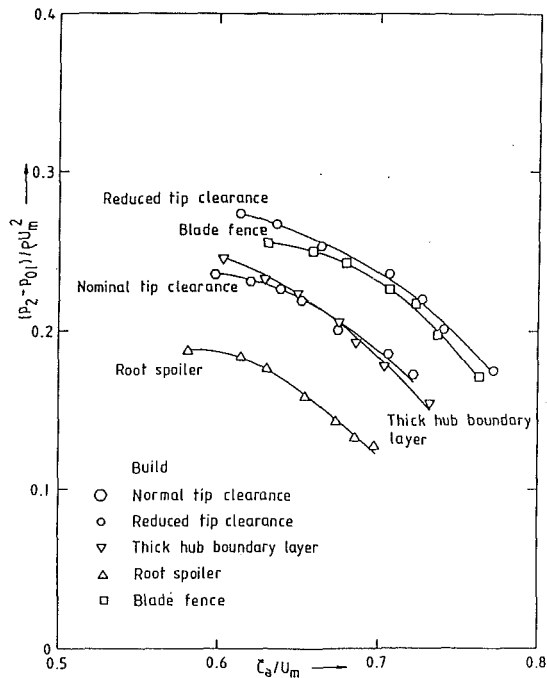


Fig. 4 Overall total-to-static characteristics

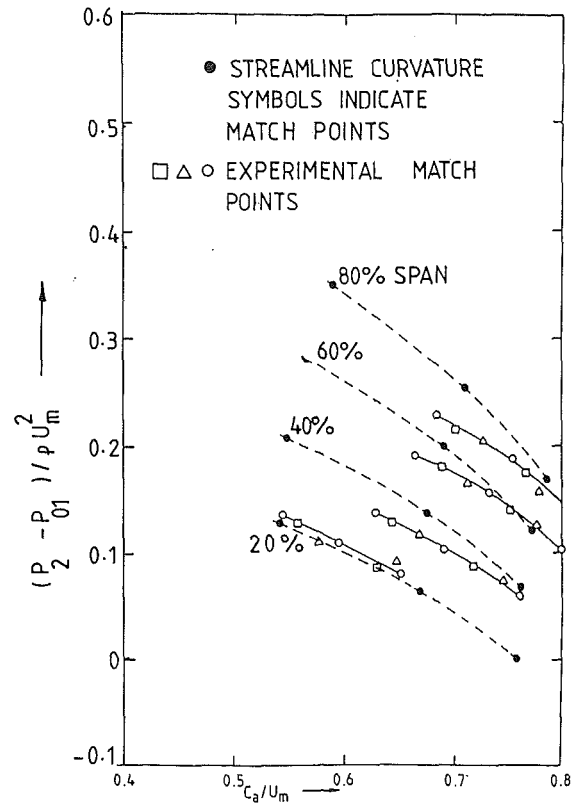


Fig. 6 Thick hub boundary layer: total-to-static characteristics

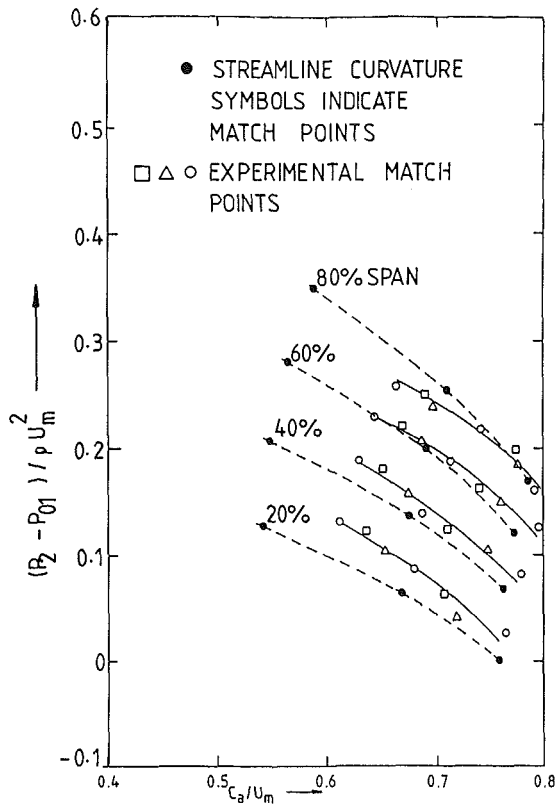


Fig. 5 Reduced tip clearance: local total-to-static characteristics

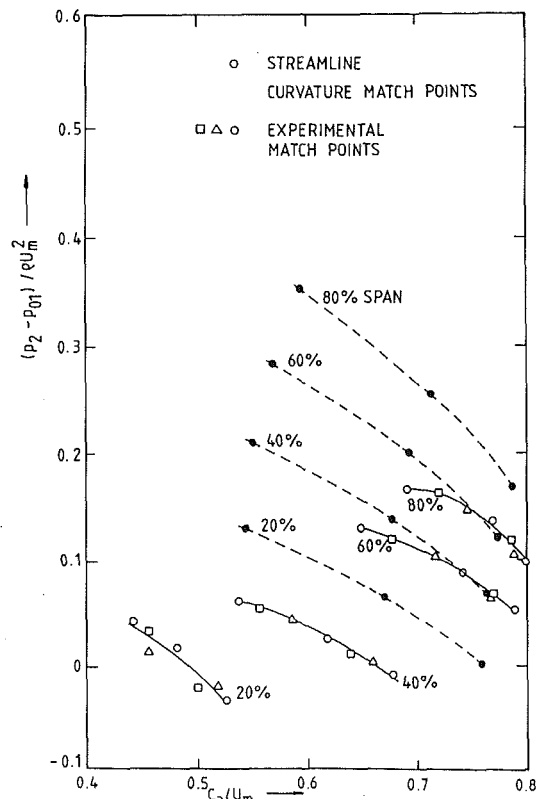


Fig. 7 Root spoiler: local total-to-static characteristics

The measured local characteristics at different spanwise positions are presented in Figs. 5-8. The local characteristics predicted by the streamline curvature method were used as a common reference. It will be noted that the predicted characteristics were most similar to the test characteristics for the reduced tip clearance build, Fig. 5, since this was closest to the ideal situation assumed for the calculation method. The pressure rise characteristics of the tip streamtubes generally

tended to stall in all the builds. The root streamtubes were either of similar slope to the predicted characteristics or steeper. The tendency of the tip streamtube pressure characteristic to stall can at least partly be associated with the effects of tip

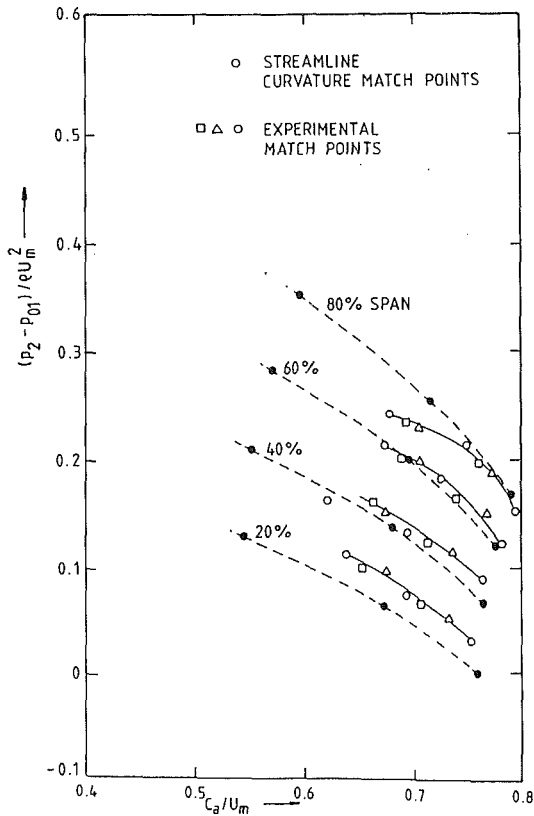


Fig. 8 Blade fence: local total-to-static characteristics

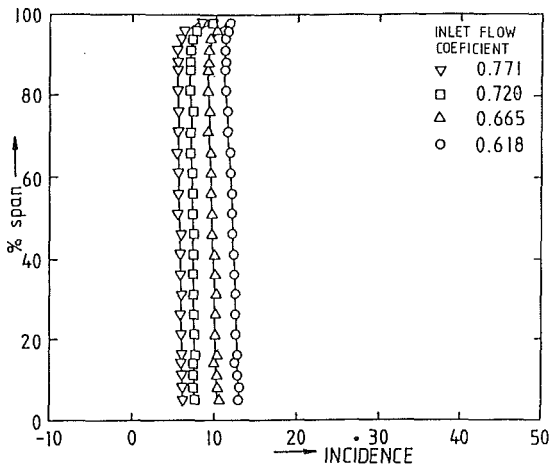


Fig. 9(a) Reduced tip clearance: distribution of incidence angle

clearance, which degrades the rotor performance in the tip region.

Traverse results, Figs. 9-12, indicate a peak in deviation angle for all builds some distance from the hub with a rapid reduction close to the hub (overturning due to the rotating surface). Only one build, Fig. 11, showed a small upturn at the measurement point closest to the hub. At the tip section a region of large deviation (underturning) will be noted for all builds, which most probably arises from the stationary outer casing and tip clearance effects. Each build indicates that in the midheight region the deviation is significantly influenced by incidence (flow rate). It is also noticeable that the change is much smaller in the hub boundary layer region. It is also apparent from these figures that the enlarged hub boundary layer and root spoiler configurations modify the local incidence and deviations quite significantly. The blade fence, however,

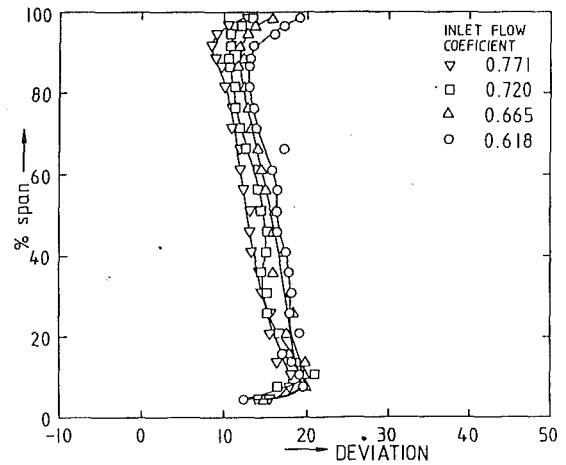


Fig. 9(b) Reduced tip clearance: distribution of deviation angle

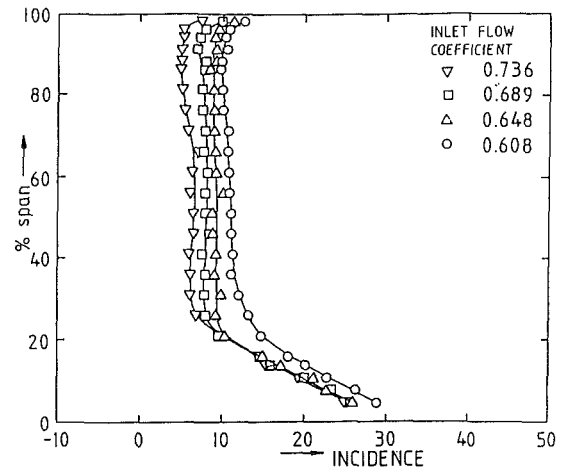


Fig. 10(a) Thick hub boundary layer: distribution of incidence angle

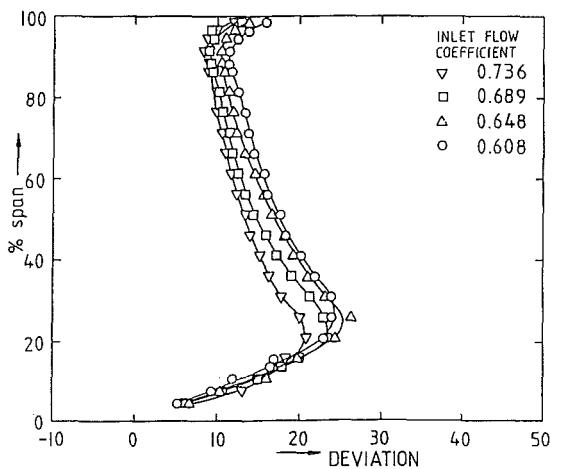


Fig. 10(b) Thick hub boundary layer: distribution of deviation angle

does not appear to influence the hub and tip conditions significantly but disturbs the flow in the midheight region, increasing the deviation inboard of the fence and reducing it outboard of the fence. This suggests that radial migration occurs, increasing the boundary layer thickness inboard and decreasing it outboard of the fence. The effect, however, is only a local redistribution and to influence the hub and tip flows would appear to require blade fences closer to these

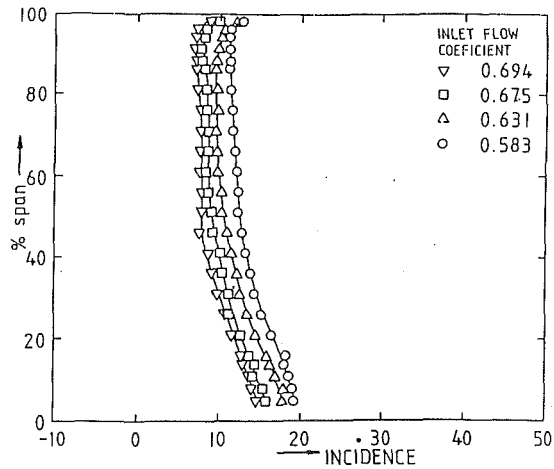


Fig. 11(a) Root spoiler: distribution of incidence angle

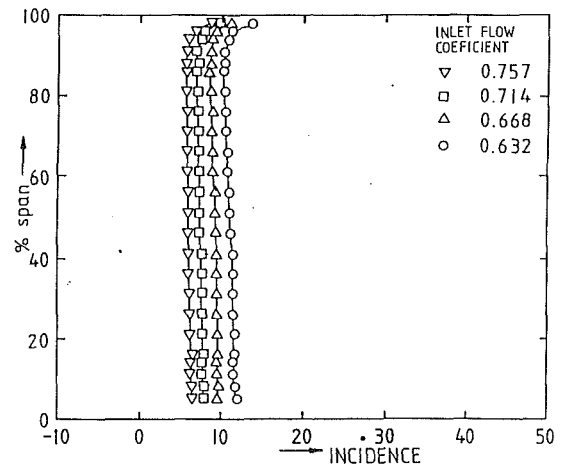


Fig. 12(a) Blade fence: distribution of incidence angle

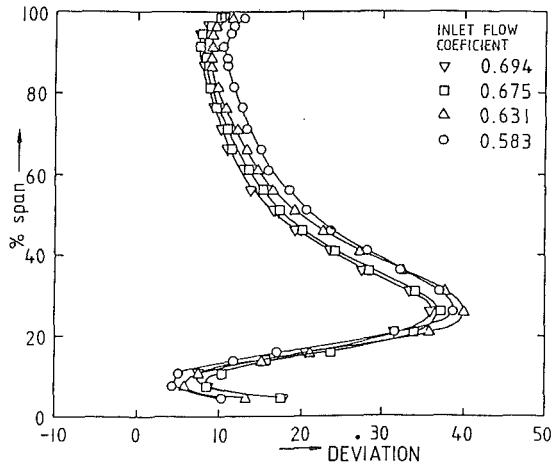


Fig. 11(b) Root spoiler: distribution of deviation angle

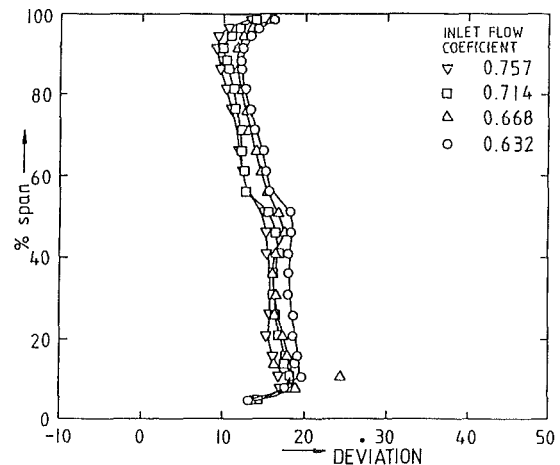


Fig. 12(b) Blade fence: distribution of deviation angle

regions. Figure 4 indicates that the blade fence suffers premature stall. Close study of the data used to prepare Figs. 5 and 8 indicates that this is largely a tip stall problem in the blade fence build, which is difficult to explain with the preceding argument.

The presence of centrifuging of the blade boundary layer to some modest fraction of blade height was supported by the axial velocity contours obtained by hot-wire anemometry at the rotor exit, Figs. 13 and 14. The axial velocity contours indicated that blade boundary layer material had apparently undergone a radial displacement, with visible "necking" at the blade root in some cases. To balance this there was movement of the core flow as it moved inward to occupy the region vacated by the blade boundary layer shift. It appears highly worthwhile advancing these ideas in association with those on mixing (Adkins and Smith, 1982; Gallimore and Cumpsty, 1987; Wisler et al., 1987) but this must remain a subject for the future. The evidence of migration suggests that the tendency to greater stability at the root could be explained by the presence of "centrifuging," the outward radial movement of boundary layer material along the blade surface. This would improve the effective blade profile at the root and thus make the pressure characteristic steeper by reducing deviation (and increasing turning).

It is noticeable that in the root spoiler build, heavily separated flow was observed at 25 percent span (Fig. 11), with a deviation angle locally exceeding 35 deg, yet the fan continued to operate stably. This demonstrates that heavily separated flow does not appear necessarily to trigger rotating stall.

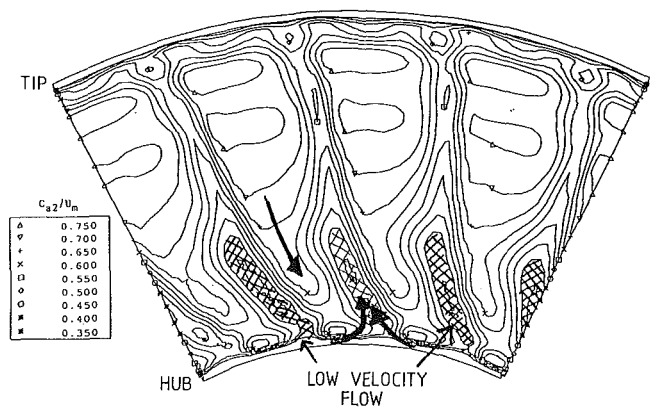


Fig. 13 Axial velocity contours downstream of the rotor with the thick boundary layer and inlet flow coefficient of 0.608

The time records of axial velocity recorded during the inception process by the hot-wire array showed a large degree of variation, for tests on the same build. This points to the difficulties in the development of high reliability methods of detecting stall precursors for active control of rotating stall. Some high hub-tip ratio builds have shown good levels of repeatability (Day, 1992) but in the studies described here this did not prove possible.

Even with these difficulties, stall inception was clearly first detected at the tip in all cases despite the gross build modifi-

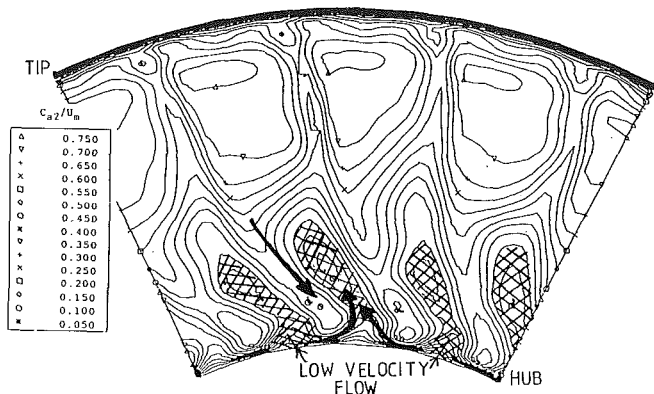


Fig. 14 Axial velocity contours downstream of the rotor with the root spoiler and inlet flow coefficient of 0.583

cations introduced to increase the likelihood of root stall. This seems to indicate that stall inception was dominated by events in the tip region and that the root shows a marked reluctance to stall.

Frequency analysis of the axial velocity signal at different radial locations was used to investigate the possible existence of weak precursors in the prestall flow field at stations other than the tip; however, no such precursors could be clearly identified. These measurements did, however, show that overall unsteadiness levels increased at midspan and tip positions as the flow coefficient was reduced. The unsteadiness at the root, however, did not significantly increase, which again points to the reluctance of the root region to generate unsteadiness.

Conclusion

While streamtube contraction considerably modifies elementary ideas about stall inception in low hub-tip ratio machines, real fluid effects (those not accommodated in our model) appear to play an even more important role in the relative stability of the root and tip regions. There is therefore a need for a clearer knowledge of the actual events taking place before and during stall inception before attempting to develop more reliable prediction models, empirical or numerical.

The evidence from the present study suggests that the root has a very strong tendency to remain stable and that this is largely due to centrifuging of the boundary layer flows and reduction of axial velocity skew caused by streamtube contraction. It was seen that the root resists stall even if gross build changes were introduced to induce root separation. The performance of the root behaves contrary to expectations based on two-dimensional cascade concepts. The tip shows a much larger propensity to stall although it appears that events in the tip region are influenced by flow conditions at other radial stations.

Not unnaturally, the study described above raises questions about the range of validity of any conclusions to machines of different hub-to-tip ratio and to higher speed machines. While it appears to the authors that the phenomena described are relatively independent of hub-to-tip ratio, the extent to which they can be observed will be significantly influenced. The generality of the observations to high-speed machines also appears to be reasonable, although the presence of shocks and a more compressible flow field would be expected to modify the situation. This leads to an observation about the lack of good quality high-speed data on stall and stall inception (rotor, single stages, and compressors) from which such conclusions could possibly be reached.

Previous paragraphs have indicated that the rotor is more tolerant to root flows than might have been anticipated from simple concepts. Perhaps it is worth noting that this tends to focus interest on the tip flow, which suffers boundary layer

flows centrifuged up the blade and tip leakage flows. It is also noteworthy that the static pressure at rotor outlet is highest at the tip due to the radial static pressure gradient caused by swirl. This implies yet more difficulty for the tip section, which, as noted, stalls more readily. Several authors have indicated, however, that the tip flow can be improved using various treatments (Smith, 1980; Azimian et al., 1990). It should perhaps also be noted that the cantilevered stator suffers tip clearance in the hub region, generally a greater static pressure rise than that in the outer casing region (due again to the radial static pressure gradient existing upstream and downstream of the stator) and is often noted to stall. It therefore appears to the authors that studies of stator performance should be undertaken along with the study of stages (rotor and stator combined). In both cases a greater propensity to stall in the region of the hub might well be anticipated.

References

- Adkins, G. G., Jr., and Smith, L. H., Jr., 1982, "Spanwise Mixing in Axial-Flow Turbomachines," *ASME Journal of Engineering for Power*, Vol. 104, pp. 97-110.
- Azimian, A. R., Elder, R. L., and McKenzie, A. B., 1990, "Application of Recess Vaned Casing Treatment to Axial Flow Fans," *ASME JOURNAL OF TURBOMACHINERY*, Vol. 112, pp. 145-150.
- Cheshire, L. J., 1945, "The Design and Development of Centrifugal Compressors for Aircraft Gas Turbines," *IMECHE, War Emergency Issue No. 12*.
- Day, I. S., Greitzer, E. M., and Cumpsty, N. A., 1978, "Prediction of Compressor Performance in Rotation Stall," *ASME Journal of Engineering for Power*, Vol. 100, p. 1.
- Day, I. J., 1993, "Stall Inception in Axial Flow Compressors," *ASME JOURNAL OF TURBOMACHINERY*, Vol. 115, this issue, pp. 1-9.
- Dring, R. P., Joslyn, H. D., and Hardin, L. W., "An Investigation of Axial Compressors Rotor Aerodynamics," *ASME Journal of Engineering for Power*, Vol. 104, pp. 84-96.
- Dunham, J., 1965, "Non-axisymmetric Flows in Axial Flow Compressors," *Mech. Eng. Sci. Monograph No. 3*, IMechE.
- Emmons, H. W., Kronauer, R. E., and Rockett, J. A., 1959, "A Survey of Stall Propagation—Experiment and Theory," *ASME Journal of Basic Engineering*, Vol. 81, pp. 409-416.
- Fabri, J., 1970, "Rotating Stall in Axial Compressors," *Internal Aerodynamics (Turbomachinery)*, IMechE, pp. 96-110.
- Fattner, L., ed., 1990, "Test Cases for Compilation of Internal Flows in Aeroengine Components," AGARD-AR-275.
- Freeman, C., 1985, "Effect of Tip Clearance Flow on Compressor Stability and Engine Performance," *Tip Clearance Effects in Axial Turbomachines*, VKI lecture series 1985-5.
- Gallimore, S. J., and Cumpsty, N. A., 1986, "Spanwise Mixing in Multistage Axial Flow Compressors: Part I—Experimental Investigation," *ASME JOURNAL OF TURBOMACHINERY*, Vol. 108, pp. 2-9.
- Giannisis, G. L., McKenzie, A. B., and Elder, R. L., 1989, "Experimental Investigation of Rotating Stall in a Mismatched Three-Stage Axial Flow Compressor," *ASME JOURNAL OF TURBOMACHINERY*, Vol. 111, pp. 418-426.
- Greitzer, E. M., et al., 1979, "A Fundamental Criterion for the Application of Rotor Casing Treatment," *ASME Journal of Fluids Engineering*, Vol. 101, pp. 237-244.
- Greitzer, E. M., and Moore, F. K., 1986, "A Theory of Post-Stall Transients in Axial Compression Systems: Part II—Application," *ASME Journal of Engineering for Gas Turbines and Power*, Vol. 108, pp. 231-239.
- Jackson, A. D., 1987, "Stall Cell Development in an Axial Compressor," *ASME JOURNAL OF TURBOMACHINERY*, Vol. 109, pp. 492-497.
- Koch, C. C., 1981, "Stalling Pressure Rise Capability of Axial Flow Compressor Stages," *ASME Journal of Engineering for Power*, Vol. 103, pp. 645-656.
- Marsh, H., 1976, "Throughflow Calculations in Axial Turbomachinery—A Technical Point of View," AGARD 47th Meeting of PEP.
- Moore, F. K., and Greitzer, E. M., 1986, "A Theory of Post-stall Transients in Axial Compression Systems: Part I—Development of Equations," *ASME Journal of Engineering for Gas Turbines and Power*, Vol. 108, pp. 68-76.
- Smith, G. D. J., 1980, "Casing Treatment in Axial Compressors," PhD Thesis, Cambridge University, United Kingdom.
- Smith, L. H., 1974, "Some Aerodynamic Design Considerations for High Bypass Ratio Fans," presented at the 2nd International Symposium on Air Breathing Engines, Sheffield, United Kingdom.
- Wisler, D. C., Bauer, R. C., and Okiishi, T. H., 1987, "Secondary Flow, Turbulent Diffusion, and Mixing in Axial-Flow Compressors," *ASME JOURNAL OF TURBOMACHINERY*, Vol. 109, pp. 455-482.
- Wood, M. D., Horlock, J. H., and Armstrong, E. K., 1960, "Experimental Investigation of the Stalled Flow of a Single Stage Axial Flow Compressor," *Aeronautical Quant.*, p. 159.
- Zika, V. J., 1985, "Correlation and Prediction of Rotating Stall Inception by Divergence Method," *ASME Journal of Fluids Engineering*, Vol. 107, pp. 191-196.

N. A. Cumpsty¹

Most of the papers on stall have been directed at machines with high hub-tip ratio and it is welcome to see a paper that considers the much more difficult topic of stall for low hub-tip ratio compressors. With a high hub-tip ratio there are many aspects of stalling behavior that are not understood; this is even more true for machines such as those that are the basis of this paper. Soundranayagam and Elder have tried to explain the observed tendency of low hub-tip ratio compressors to stall when conditions at the tip deteriorate. To this end they have used an axisymmetric calculation method to examine the radial redistribution of flow. They conclude that the radial redistribution, referred to here as streamtube contraction, tends to increase the stability of the flow near both the hub and tip. I believe that their conclusions relating to the flow at the hub are entirely wrong and contrary to experimental evidence, while those for the tip are misleading.

When the flow through a rotor is reduced below its design value, a powerful effect is the drop in axial velocity across the rotor root. This may be thought of as a fundamental trend in the way in which rotors respond. It arises from the more rapid increase in work input near the tip than near the hub as the flow rate is reduced, together with the constraints of radial equilibrium, and can be seen using even elementary arguments. Lower axial velocity near the hub than the casing necessarily leads to a radial shift in the streamsurfaces, and to a contraction in the streamsurfaces near the casing. Because of the axial velocity drop between inlet and outlet across the rotor near the hub, a marked rise in flow blockage or even flow separation can occur there. The large amount of blockage associated with any separation will lead to an additional increase in the radial outward shift of the streamsurfaces.

The rotor geometry used by the authors for the meridional calculations in this paper was tested by Smith (1980) in the White Laboratory. (Much of the information in this PhD thesis is given in the more accessible paper by Smith and Cumpsty 1984.) Smith measured a time-mean reversed flow near the hub (an axial velocity moving in the upstream direction) while the rotor was still operating in a stable manner in its unstalled mode. It is not that some relief occurred to make the hub stable, as Soundranayagam and Elder conclude, but that complete flow separation and reversal there do not lead to instability of the entire flow or a transition to rotating stall. The rotor tested by Smith was very definitely one that stalled following flow deterioration at the tip, because casing treatment proved highly effective in extending the operating range.

Some of the confusion is undoubtedly caused by terminology, since the word "stall" has so many uses and meanings. Many blades have some separated flow near the root, particularly at flow rates below the design value; although this is generally undesirable, it is not necessarily serious, and when it occurs it does not seem appropriate to refer to the blade row as stalled. In some cases, such as that described by Smith and Cumpsty, the extent of separation at the root can be substantial, yet the rotor operates on an unstalled characteristic. It seems to be desirable to avoid terms like root stall, since the effect of this is so very different from stall in the sense of the change in operation of the rotor from unstalled flow to fully developed rotating stall. In any event, whenever the word stall is to be used it is essential to make clear what is meant. The word "stable" also needs to be used with caution: It is not legitimate in the present context to talk, for example, about the flow at a blade root being stable. It is the entire flow field that is stable or unstable. The question should rather be whether the flow near the root is such that the entire flow is stable

when axisymmetric, or whether the axisymmetric flow is unstable with the root flow in this condition so that flow will alter to an asymmetric one in rotating stall. The flow in the rotor tested by Smith was clearly stable when the flow near the hub was severely separated and the flow did not become unstable until conditions near the tip deteriorated.

The first paragraph of Soundranayagam and Elder's conclusions seems to me to be accurate. The second paragraph, however, seems wrong for the following reasons:

1 There is absolutely no evidence that the rotor root has a tendency "to remain stable." The rotor used by the authors for their calculation showed extensive separation and flow reversal near the hub prior to collapse of the whole flow into rotating stall. It would be more appropriate to say that flow separation in the root does not lead to instability of the entire rotor flow.

2 The rotor root does not behave contrary to expectations based on two-dimensional cascade concepts, although it would be unwise to apply these concepts without recognizing the important three-dimensional effects involved.

3 The tip does not show a larger propensity to stall. What it does show is a controlling influence over the stability of the entire flow. In other words it is with a change in the flow at the tip that the overall flow then exhibits a rapid evolution into what is commonly called rotating stall.

References

- Smith, G. D. J., and Cumpsty, N. A., 1984, "Flow Phenomena in Compressor Casing Treatment," *ASME Journal of Engineering for Gas Turbines and Power*, Vol. 106, pp. 532-541.

J. H. Horlock²

The authors rightly point to an effect that should move a root section toward flow separation—the drop in local axial velocity across the blade row. They suggest that the root behaves "contrary to expectations based on two-dimensional blade concepts," possibly due to centrifuging of the boundary layer.

But there is another effect that may invalidate the use of cascade data in the prediction of root performance—the different secondary flow in the two cases. In the cascade test the entry flow is co-lateral and the wall boundary layer is swept into the corner between the wall and the suction surface of the blade, causing a substantial area of separation. In the compressor test the (relative) annulus wall boundary layer is skewed at entry to the rotor root. The streamwise vorticity associated with this entry skew is opposite to that generated in the passage and smaller areas of corner separation may be anticipated (an effect originally observed by Moore and Richardson at M.I.T.). We may however note that if the wall boundary layer grows over an infinitely long rotating hub, then the flow at entry to the rotor root is indeed colateral and the cascade tests will be more representative of compressor performance, as long as the axial velocity ratio is matched.

In the experiments by Wood et al. to which the authors refer, a "rough" rotating stall was observed near the hub of the compressor, but it was on the stator root section. The rotor tip was the first to stall, in a part-span mode.

Authors' Closure

The reduction in axial velocity at the rotor blade root described by Professor Cumpsty is presumably that due to the spanwise rematching of the rotor to satisfy downstream radial equilibrium conditions and he is quite correct in stating that these are independent of viscous effects. The calculations pre-

¹Whittle Laboratory, Cambridge University, Cambridge, United Kingdom.

²Whittle Laboratory, Maddingley Road, Cambridge, CB3 0DY, United Kingdom.

Pressure Fluctuation on Casing Wall of Isolated Axial Compressor Rotors at Low Flow Rate

M. Inoue

M. Kuroumaru

Y. Ando

Kyushu University,
Mechanical Engineering for Power,
Hakozaki 6-10-1, Higashi-ku
Fukuoka, 812, Japan

The pressure fluctuations on the casing wall of two axial flow compressor rotors with various tip clearances have been analyzed by the use of two kinds of correlation functions. The behavior of the pressure fluctuation varies depending on tip clearance and blade solidity. In the case of small tip clearance, the nature of disturbances becomes random as the flow rate is reduced to a stall condition. For moderate tip clearance, coherent-structured disturbances appear intermittently at low flow rate. They appear more frequently as the solidity is increased and the flow rate becomes lower. For large tip clearance, the coherent structured disturbances exist even at considerably higher flow rates. Corresponding to these features, there are peculiar patterns in the correlation designated as "phase-locked correlation functions."

Introduction

In axial flow compressors, the investigation of aerodynamic instabilities is currently highlighted. Some matters of primary concern are the fluid mechanic processes of rotating stall inception and finding a forewarning phenomenon of stall. If an occurrence of stall is foreseeable by a real-time indicator, it is possible to set a compressor operating point with a small surge margin so that it operates under a high loading condition by means of a preview control technique. It would also be possible to extend the operating range by suppressing the instabilities through the use of an active control technique (Epstein et al., 1989; Day, 1993b; Paduano et al., 1993). These techniques are available for increasing pressure ratio per stage to reduce the total number of compressor stages.

Detailed experimental work has been done with improved measuring and analytical methods to elucidate the complex flow phenomena triggering to rotating stall. Reported so far are the existence of disturbances with different wavelengths rotating at speeds slightly lower than the rotor speed (Mathioudakis and Breugelmans, 1985), the occurrence of small stall cells traveling initially at near rotor speed and decelerating rapidly with growth in cell size (Jackson, 1987), the presence of a modal prestall wave propagating at a speed close to the fully developed stall cell speed (McDougall et al., 1990; Garnier et al., 1991), and the coexistence of the formation of finite stall cells and the propagating prestall wave (Day, 1993a).

From a more practical point of view, the authors examined the statistical characteristics of pressure fluctuation on the casing wall of two compressor rotors with various tip clearances, and tried to find a forewarning phenomenon of rotating

stall (Inoue et al., 1991). The pseudo-space correlation maps of pressure fluctuation were drawn in the relative reference frame fixed to the rotating blades by means of the phase-locked multisampling data acquisition technique. According to these phase-locked patterns, it was found that the periodicity in the fluctuation with blade spacing collapsed noticeably from the maximum pressure-rise point to the stall-onset point on the overall performance characteristics. To represent the periodicity of pressure fluctuation, a practical detection parameter was proposed that was easily obtained during operation of a compressor.

However, the detection parameter requires data acquisition over 200 or more rotor revolutions, which results in deterioration of sensitivity in case of a rapid change in flow conditions. It gives no information on the instantaneous nature of the disturbance because it is a kind of statistical value.

The purpose of this study is to examine closely the nature of the disturbance prior to the stall in the previous study (Inoue et al., 1991).

Experimental Facility

A schematic view of the rotating cascade facility in Kyushu University is shown in Fig. 1. An inlet chamber (1500 mm × 1500 mm × 150 mm) with honeycombs and filters is installed on the upstream end of the test section. The downstream end is connected to an outlet chamber (1800 mm × 1500 mm × 2350 mm) followed by a nozzle flow meter, a cone diffuser, and an auxiliary fan. Both chambers are available to avoid a surge condition and to examine the flow behavior at stall inception. The test section consists of a fixed outer casing, a fixed journal box, and changeable assembly including a rotor, a stator, an inlet nozzle, an inner casing, and a hub section to provide for various cascade geometries.

Two rotors tested in this study are the same as in the previous

Contributed by the International Gas Turbine Institute and presented at the 37th International Gas Turbine and Aeroengine Congress and Exposition, Cologne, Germany, June 1-4, 1992. Manuscript received by the International Gas Turbine Institute January 28, 1992. Paper No. 92-GT-33. Associate Technical Editor: L. S. Langston.

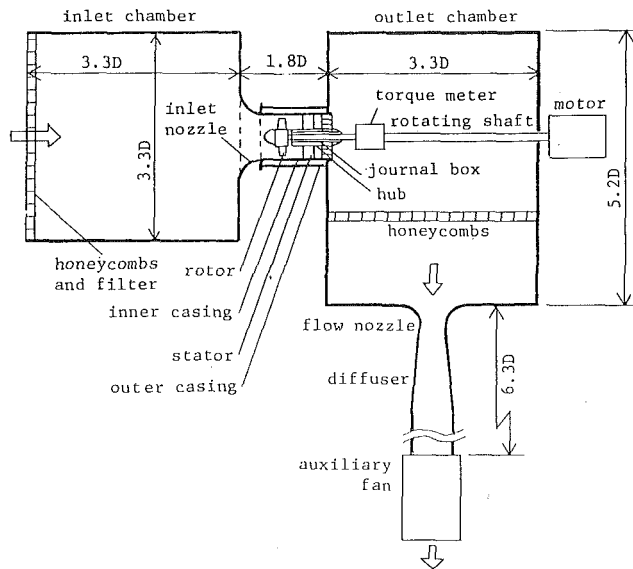


Fig. 1 Low-speed rotating cascade facility

paper (Inoue et al., 1991). The tip diameter, hub/tip, ratio and tip chord length of the blade are 449 mm, 0.6, and 117.5 mm, respectively, for both rotors. Rotor A has low loading with low solidity of 1.25 at midspan and rotor B has high loading with high solidity of 1.67. For each rotor, the tip clearance was varied from $\tau = 0.5$ mm to $\tau = 5.0$ mm by changing the inner casing. Details of the geometry and blading are given by Inoue and Kuroumaru (1989).

Two high-response pressure sensors (Kulite XCQ-080-1G) were mounted on the casing wall to cover the measuring points (IZ, IX) in Fig. 2 by changing the axial location and a phase-locked acquisition technique. Another set of pressure sensors is installed with an interval of 36 deg in the circumferential direction. The interval of 36 deg does not coincide with multiples of blade spacing for either rotor. An estimated error in the pressure measurement is less than 2 percent of the dynamic pressure corresponding to the rotor tip speed.

Technical Approach

Figure 3 shows typical time traces of the pressure transducer outputs under various operating conditions. Near the design point the casing wall pressure changes regularly in the shape of saw-tooth corresponding to the blade passing. Near a stall condition small disturbances appear on the saw-toothed wave, and increase in size as the flow rate is reduced. They remain

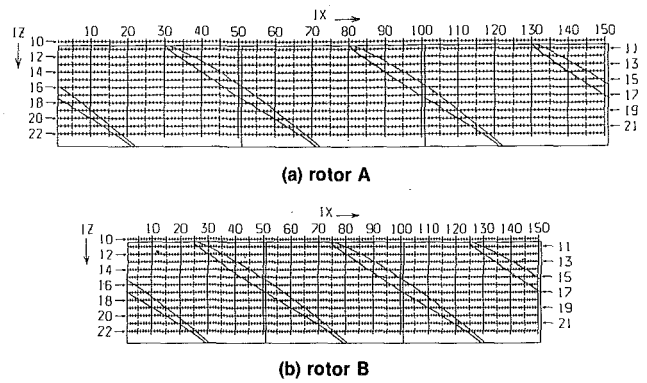


Fig. 2 Measuring point in the relative frame (the circumferential and axial location of each point is identified by the numbers IX and IZ)

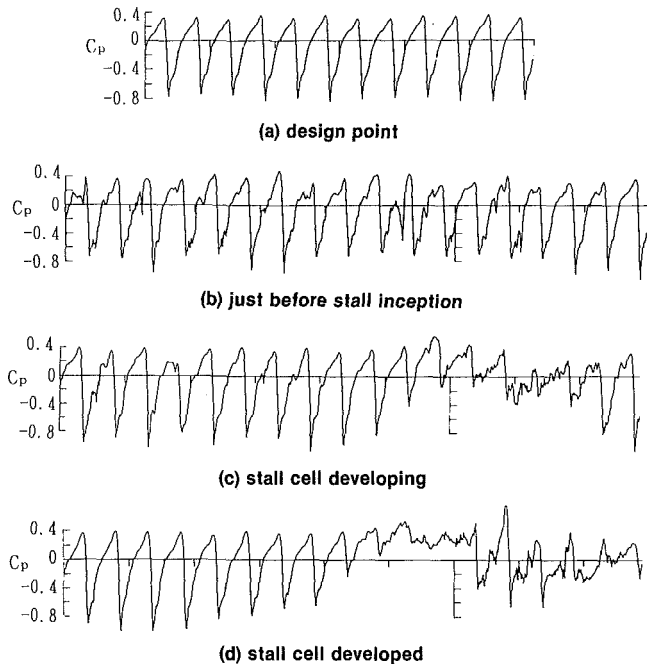


Fig. 3 Typical time traces of pressure for various flow conditions (rotor A, $\tau = 0.5$ mm)

in the developing stall cell, but disappear outside the stall cell once the stall cell is fully developed. In this paper (and in the previous paper, Inoue et al., 1991), the focus is placed on this type of disturbance. It is in contrast with the approach of MIT and Cambridge University groups who focus on the disturb-

Nomenclature

BFM = blade fluctuation moment

(Eq. (4))

BPV = blade pressure variance (Eq. (5))

C_p = wall pressure coefficient
 $= (\bar{p} - p_{0i}) / (\rho u_t^2 / 2)$

C'_p = pressure fluctuation coefficient
 $= p' / (\rho u_t^2 / 2)$

f, g = pressure fluctuation component

IX = identification number of circumferential measuring point (Fig. 2)

IZ = identification number of axial measuring point (Fig. 2)

N = number of rotor revolution

\bar{p} = average pressure on casing wall

p' = pressure fluctuation component

p_{0i} = stagnation pressure at rotor inlet

R = time correlation coefficient

RP = phase-locked correlation coefficient

R_s = two point cross-correlation coefficient

s = blade spacing

T, t = time

u_t = rotor tip speed

Θ, θ = circumferential coordinate

ρ = density of fluid

σ_f, σ_g = standard deviation of f, g

τ = tip clearance

ϕ = flow rate coefficient (mean axial velocity divided by u_t)

ψ = total pressure rise coefficient (total pressure rise divided by $\rho u_t^2 / 2$)

Subscripts

1 = autocorrelation

2 = cross correlation

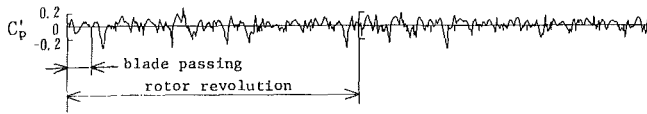


Fig. 4 Time traces of pressure fluctuation excluding blade passing wave (rotor A, $\tau = 0.5$ mm)

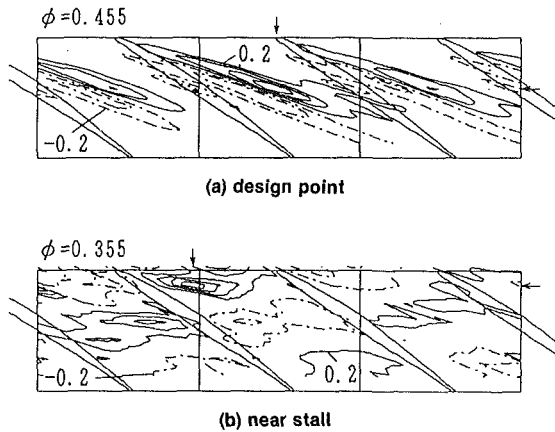


Fig. 5 Phase-locked patterns of pseudospacial correlation at design point and near stall (rotor B, $\tau = 2.0$ mm) (Inoue et al., 1991)

ances of a wavelength much larger than the blade spacing. In an investigation on the longer waves, the blade passing frequency waves are eliminated by a measurement upstream of the rotor or through a low pass filter. In this approach, however, the blade passing waves are eliminated by subtracting the phase-locked and averaging values from the instantaneous signals. Figure 4 is an example of the time trace of a disturbance excluding the blade passing waves.

In the previous paper, the statistical characteristics of the disturbance were clarified by the phase-locked patterns of standard deviation (pressure fluctuation), skewness, and pseudospacial correlation in the reference frame relative to the rotating blades. An interesting feature was found in the pseudospacial correlation maps: Under the normal flow condition the phase-locked pattern is periodic with blade spacing, but the periodicity collapses near the stall inception, as shown in Fig. 5. The periodic nature can easily be observed with a single pressure transducer by the cross-correlation coefficient R_s of pressure fluctuation between two points one blade spacing apart in the relative reference frame. The variations of R_s with flow rate are summarized in Fig. 6 together with the performance curve, on which the hysteretic stall characteristics are indicated by dotted vertical lines: The left-hand lines correspond to the stall points with the throttle closed and the right-hand lines the stall-recovery points with the throttle opened. The correlation R_s decreases rapidly from the maximum pressure-rise point to the stall point except for the rotors with high solidity and extremely large tip clearance. For the cases with large tip clearance, the correlation R_s yields large negative values to suggest the existence of coherent structure in the disturbances, which is also shown in the phase-locked spatial correlation map (Fig. 5).

There are many unknown behaviors in disturbances of this type. The pseudospacial correlations were examined only over three blade flow passages for various tip clearances. Is there any correlation in the whole annulus? Is so, is there any relation to a long wave mode? Does the coherent disturbance actually exist? Does it propagate in the circumferential direction? How does the nature of the disturbance vary with tip clearance? In the phase-locked data acquisition, the intervals of data sampling are too large in comparison with the time scale of the

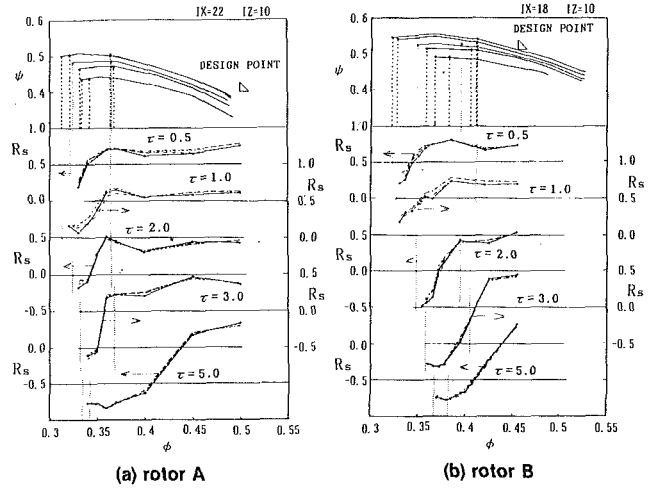


Fig. 6 Variations of two-point correlation function with flow rate

disturbance, because the statistical value at each relative point is obtained by one data sampling per rotor revolution and averaging over 200 ~ 500 revolutions. What does the pseudospacial correlation mean physically? Does it have any relation to a time correlation of pressure fluctuations during one revolution of the rotor?

A correlation function is widely used to examine the scale and propagating speed of flow disturbances. In this study, to answer the above questions, the casing wall pressure fluctuation is analyzed by two kinds of correlation functions: One is similar to that in the previous paper (Inoue et al., 1991) and the other is a common time correlation.

If f and g are the pressure fluctuations of two pressure sensors mounted on the casing at an interval of θ_p in the circumferential direction, they are functions of time t and the circumferential coordinate θ . Here, θ is measured in the relative reference frame of the rotor. A time-space correlation coefficient is written by

$$R(\theta, T) = \frac{f(\theta, t)g(\theta - \theta_p + \theta, t + T)}{\sigma_f \sigma_g} \quad (1)$$

where σ_f and σ_g are the standard deviations of f and g .

$$\sigma_f = \sqrt{\overline{f^2}}, \quad \sigma_g = \sqrt{\overline{g^2}}$$

In the phase-locked multisampling data acquisition technique, Eq. (1) is obtained as follows: (1) θ is fixed to a reference point θ_0 ; (2) θ is changed with $\theta = i\Delta\theta$ where i is the number of the measuring point corresponding to IX in Fig. 2 and $\Delta\theta$ is the distance between two measuring points; (3) a set of f_n and g_n (suffix n denotes the number of rotor revolutions) are acquired by increasing i one by one during one rotor revolution; (4) then, $f_n g_n$ is averaged over N rotor revolutions ($N = 200 \sim 500$). That is,

$$RP = R(i\Delta\theta) = \left\{ \frac{1}{N} \sum_{n=1}^N f_n(\theta_0) g_n(\theta_0 - \theta_p + i\Delta\theta) \right\} / \sigma_f \sigma_g \quad (2)$$

Equation (1) is a spatial correlation if $T = 0$. In this technique, however, T varies with $\theta = i\Delta\theta$ since $\theta = \omega T = i\omega \Delta t$ ($\omega =$ angular velocity of rotor, $\Delta t =$ interval of data sampling). It was called the pseudospacial correlation coefficient on the assumption of frozen events during sampling time in Inoue et al. (1991). The phase-locked patterns in Fig. 5 are obtained by placing $\theta = \theta_p$ and changing the axial location (IZ in Fig. 2) of the pressure sensor of g . The correlation coefficient is unity at the reference point, which is denoted by an intersection point of extensions of two arrows on the upper and right line in Fig. 5. The two point cross-correlation coefficient R_s in Fig.

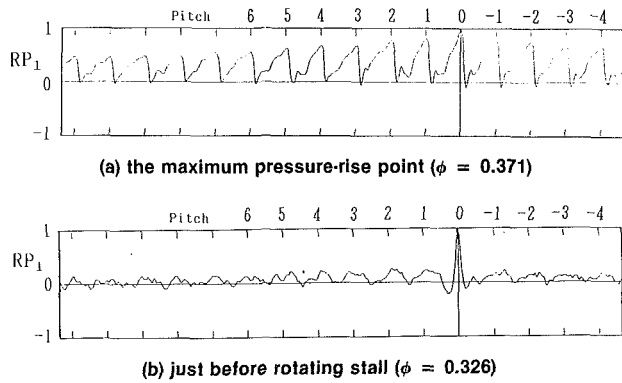


Fig. 7 Phase-locked autocorrelations for small tip clearance (rotor B, $\tau = 0.5$ mm)

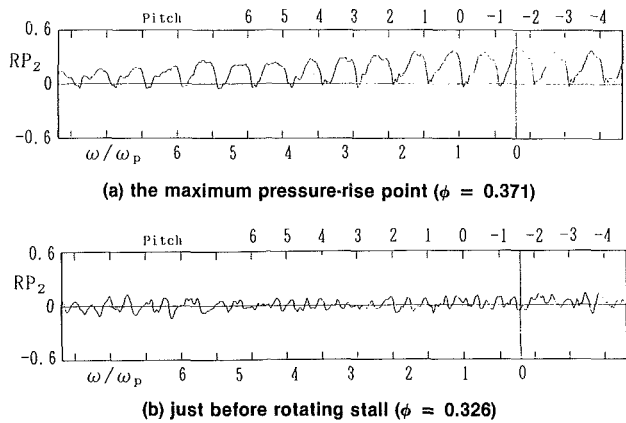


Fig. 8 Phase-locked cross correlations for small tip clearance (rotor B, $\tau = 0.5$ mm)

6 is obtained with a single pressure sensor by substituting $g = f$, $\theta_p = 0$ and a fixed interval of $i\Delta\theta = s$ ($s =$ blade spacing) into Eq. (2). The values of IX and IZ on the upper part of Fig. 6 denotes the location of reference point.

In this study, Eq. (2) is examined over a rotor revolution ($i\Delta\theta = 0 \sim 2\pi$). It is called "phase-locked correlation" because the sampling time during a rotor revolution is too long for calling it "pseudospacial correlation" on the assumption of frozen events. The phase-locked autocorrelation coefficient with $g = f$ and $\theta_p = 0$ is denoted by RP_1 and the phase-locked cross-correlation coefficient with $\theta_p = 36$ deg by RP_2 .

On the other hand, Eq. (1) is a time correlation in the absolute frame of the casing. By means of the multisampling technique without phase-lock, it can be obtained by replacing t and T by $j\Delta t$ and $i\Delta t$.

$$R = R(i\Delta t) = \left\{ \frac{1}{M} \sum_{j=1}^M f(j\Delta t)g(i\Delta t + j\Delta t) \right\} / \sigma_f \sigma_g \quad (3)$$

where M is the total sampling number acquired during several blade passing periods. The autocorrelation coefficient denoted by R_1 is obtained with a single sensor by substituting $g = f$ into Eq. (3). The cross-correlation coefficient denoted by R_2 is obtained with two sensors 36 deg apart from each other.

These correlations are mainly investigated on the casing wall near the rotor leading edge ($IZ = 10$ or 12 in Fig. 2).

Experimental Results and Discussion

Rotors With Small Tip Clearance. Figures 7 and 8 show the typical phase-locked autocorrelation RP_1 and the phase-locked cross correlations RP_2 in the case of small tip clearance ($\tau = 0.5$ mm). The short vertical lines on the upper and lower

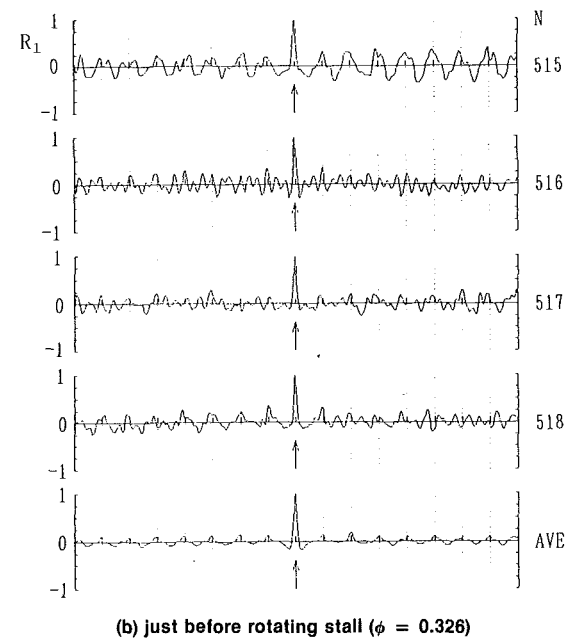
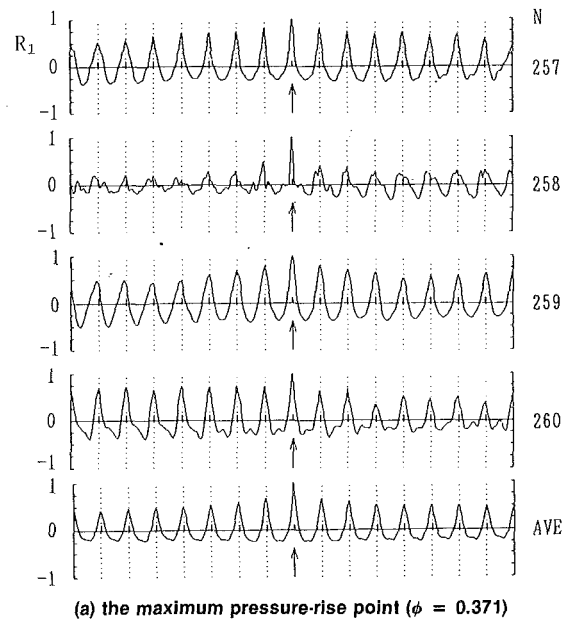


Fig. 9 Time autocorrelations for small tip clearance (rotor B, $\tau = 0.5$ mm)

frame line indicate the relative distance from a reference point ($\theta = \theta_0$) with multiple of blade spacing. The vertical dotted lines in Fig. 8 are multiples of distance between two sensors. As the distributions of RP_1 and RP_2 at design point were essentially similar to those at the maximum pressure-rise point in the case of small tip clearance, the latter is compared with the correlation just before the stall inception in the figures. The data just before the rotating stall were obtained by a pretrigger data acquisition system by Inoue et al. (1991), in which a required number of the data samples before a trigger of stall inception are acquired in a microcomputer. The trigger pulse of stall inception is taken by setting a threshold level for the low pass filtered signal of a pressure sensor.

The phase-locked correlation RP_1 and RP_2 are periodic with blade spacing at the maximum pressure-rise point. This phenomenon suggests that the time scale of dominant disturbances is the same order or considerably large in comparison with the

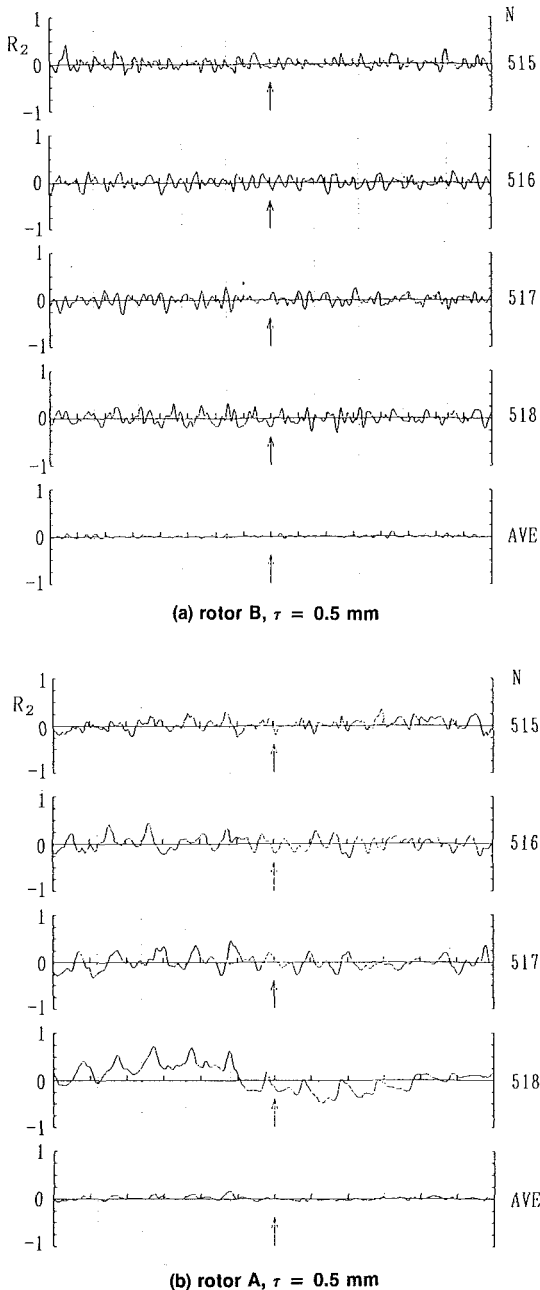


Fig. 10 Time cross correlations just before stall inception for small tip clearance

time of one rotor revolution. As the fluctuation level is very low in the case of small tip clearance under the normal flow condition, this behavior of disturbances may be due to variations in tip clearance or fluctuations in inlet or outlet conditions.

The periodicity of RP_1 and RP_2 rapidly degenerates toward stall and nearly disappears just before stall inception due to the appearance of random disturbances with high amplitude. It is shown in Fig. 7(b) that the scale of the disturbance is less than half of the spacing. There is no evidence indicating the propagation of disturbance in the RP_2 correlation (Fig. 8(b)).

Figures 9(a) and 9(b) show the variation of the autocorrelation with the numbers of rotor revolutions. Figure 9(a) is at the maximum pressure-rise point, Fig. 9(b) is several revolutions before the trigger of stall inception. In Fig. 9(b), the trigger pulse is taken at $N = 520$ under the fixed throttle condition. In each case, the average over 20 revolutions is shown on the lowest line. The intervals of vertical dotted lines

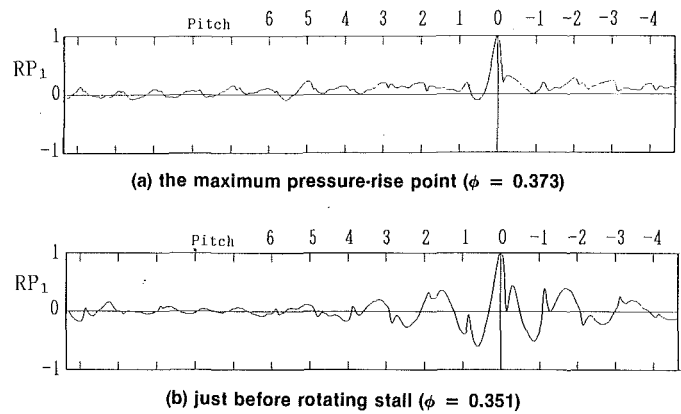


Fig. 11 Phase-locked autocorrelations for moderate tip clearance (rotor B, $\tau = 2.0$ mm)

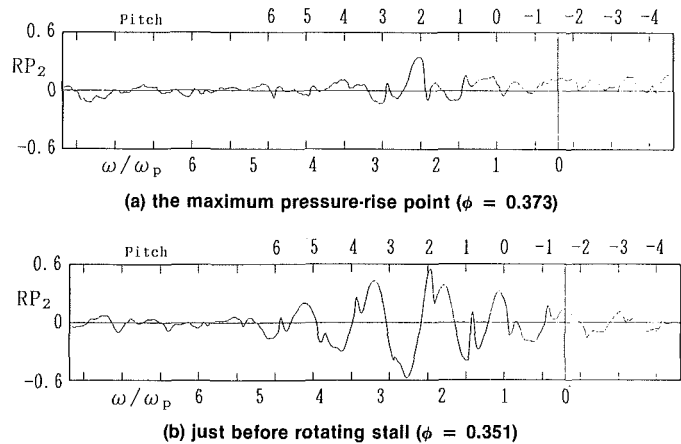


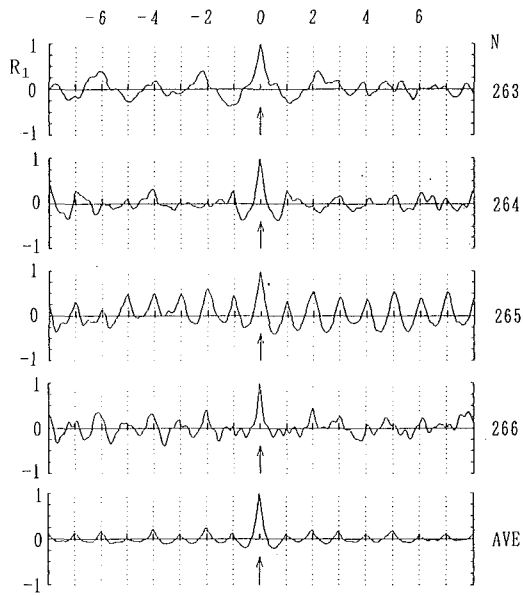
Fig. 12 Phase-locked cross correlations for moderate tip clearance (rotor B, $\tau = 2.0$ mm)

correspond to blade spacing. In the case of maximum pressure-rise, R_1 is periodic with blade spacing for most of the revolutions. Just before rotating stall, there are a few cases where R_1 is periodic, but over most of the rotation, the time correlation is weak and random, which results in disappearance of correlation in the average case. No essential difference was found in R_1 between 500 and several revolutions before the stall inception (the figure is omitted).

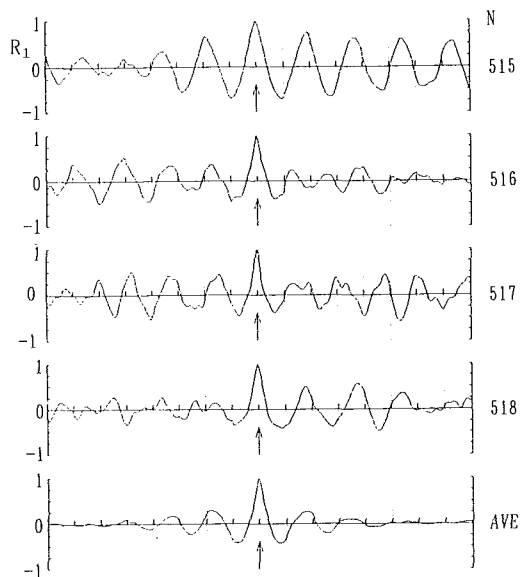
The cross correlation R_2 of two sensors 36 deg apart from each other is also examined. Just before the stall inception, appreciable correlation was hardly seen over each revolution, and there was no correlation in the average of 20 revolutions as shown in Fig. 10(a). Figure 10(b) is only one case tested where a coherent structure appears in R_2 for the small tip clearance. There are only two revolutions before the stall trigger pulse. In this case, a stall inception cell smaller than the trigger threshold was observed in the low pass filtered signal of the pressure sensor.

There seems to be no coherent disturbance before the stall inception in the case of small tip clearance. The stall inception cell appears without any forerunner and grows rapidly. If the periodicity of correlation with blade spacing disappears, it is likely that a small stall cell will appear.

Rotor With Moderate Tip Clearance. In the case of moderate tip clearance ($\tau = 2.0$ mm), the phase-locked correlations RP_1 and RP_2 are periodic over the whole relative circumference at the design flow rate (figures are omitted). As the flow rate decreases, the periodicity of RP_1 and RP_2 degenerates and collapses at the maximum pressure rise point as shown in Figs. 11(a) and 12(a). This behavior is similar to that just before



(a) the maximum pressure-rise point ($\phi = 0.373$)



(b) just before rotating stall ($\phi = 0.351$)

Fig. 13 Time autocorrelations for moderate tip clearance (rotor B, $\tau = 2.0$ mm)

the stall inception in the small tip clearance. In the RP_2 correlation, however, a considerably higher value appears near a location of 2 on the abscissa. If the disturbance at the position of sensor f had moved with the blade, RP_2 would become high at the location of 0 in Fig. 12(a). The high values at the location of 2 suggest the existence of disturbances rotating at 44 percent speed of the rotor speed in the circumferential direction.

A clearer coherent structure of the disturbances is found in the RP_1 correlation just before the stall inception (Fig. 11(b)). This structure makes the two point cross correlation R_2 negative as shown in Fig. 6. The comparison of the RP_1 and RP_2 correlation indicates that the disturbances rotate in the circumferential direction at 46 percent of the rotor speed.

This phenomenon can be observed in shorter time scale (order of a rotor revolution) by means of the time correlation R_1 and R_2 . Figures 13(a) and 13(b) are the variation of the autocorrelation R_1 with the rotor revolution at the maximum

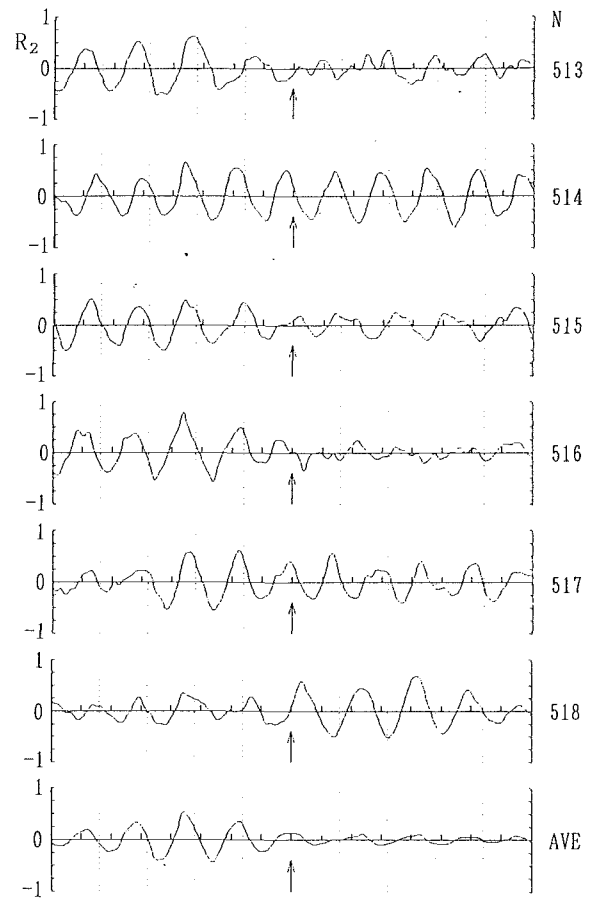


Fig. 14 Time cross correlations just before stall inception for moderate tip clearance (rotor B, $\tau = 2.0$ mm)

pressure-rise point and just before the stall inception. At the maximum pressure rise point, various types of the R_1 correlation are observed depending on the number of rotor revolutions: periodic nature with blade spacing ($N = 265$), random nature of small disturbance ($N = 264, 266$), and coherent nature of larger scaled disturbance ($N = 263$). Averaging these distributions, the resultant correlation is similar to the phase-locked autocorrelation in Fig. 11. Near the stall condition, the R_1 correlation indicates the nature of larger scaled disturbances in comparison with the blade spacing for almost all revolutions. If the disturbance rotates in the circumferential direction, its speed is about a half of the rotor speed judging from the number of the peaks. As the interval of the R_1 peaks differs a little depending on rotor revolution, the averaged correlation becomes weaker with the relative distance from the reference point, and is similar to the phase-locked autocorrelation in Fig. 12(b).

Figure 14 is the variation of the cross correlation R_2 just before the stall inception. The distributions are similar to those of the R_1 correlation. In each revolution, the rotating speed of the disturbance cannot be estimated because it is difficult to find which peaks correspond to each other between R_1 and R_2 . However, averaging the R_2 correlation, the peaks of R_2 indicates the existence of dominant rotating speed, which coincides with the speed estimated by the phase-locked correlations. At the maximum pressure rise point, both the random mode in Fig. 10 and the coherent mode in Fig. 14 appear depending on rotor revolution (the figure is omitted). The averaged R_2 correlation was similar to the phase-locked cross correlation in Fig. 12(b).

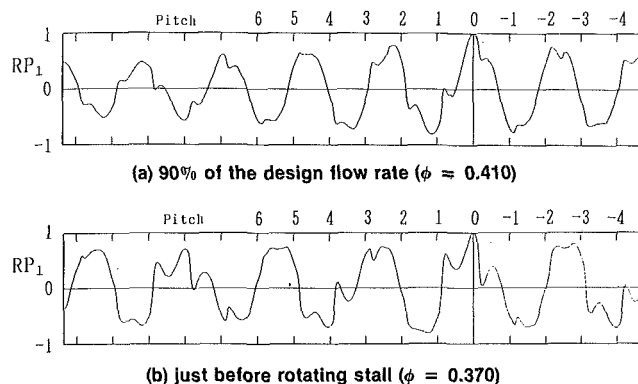


Fig. 15 Phase-locked autocorrelation for large tip clearance (rotor B, $\tau = 5.0$ mm)

Rotor With Large Tip Clearance. In the case of the largest tip clearance, the performance deteriorates noticeably because the clearance is 4.3 percent of chord length and 5.1 percent of blade span. The measurements for these rotors were made not for practical purpose but for physical interest. At the design point, the periodicity with blade spacing is appreciable in the phase-locked correlation. But it collapses at flow rates considerably higher than that for the maximum pressure-rise point. Instead, the large scaled disturbances appear in the RP_1 correlation as shown in Fig. 15(a). As a result, the two-point correlation R_s becomes negative at considerably high flow rate as shown in Fig. 6. The scale of disturbances changes little as the flow rate is reduced to the stall point value as shown in Fig. 15(b), and is 2 ~ 2.3 times the blade spacing. The time correlation R_1 is similar to the phase-locked correlation RP_1 for each revolution as shown in Fig. 16(a). The rotating speed of the disturbances is estimated to be 40 ~ 50 percent. This nature of the disturbances exists about 100 revolutions before the stall inception (the figure is omitted). However, the new type of disturbance appears about 20 revolutions before the stall. As shown in Fig. 16(b), it turns into a long wave mode length, which is of the order of the circumferential length of the annulus.

Additional Discussions. The phase-locked patterns of the statistical characteristics of pressure fluctuation presumed the occurrence of intermittent local separation at the leading edge near the stall condition (Inoue et al., 1990, 1991). There is experimental evidence to support this presumption. In order to examine a fluctuating condition in each blade flow passage, the blade fluctuation moment (BFM) and the blade pressure variance (BPV) are defined as

$$BFM = \overline{p'(\theta - s/2)} / (\rho u_t^2 s/2) \quad (4)$$

$$BPV = \overline{(p')^2} / (\rho u_t^2/2)^2 \quad (5)$$

where p' is the pressure fluctuation component shown in Fig. 4 and a bar indicates the average from suction side to pressure side in a blade flow passage at a fixed axial location. When the instantaneous circulation (proportional to lift force) is higher (or lower) than the average, the pressure is higher (or lower) on the pressure side and/or lower (or higher) on the suction side, then the BFM is positive (or negative). The BPV value is high in a blade flow passage with large disturbances. Figure 17 shows the variation of BFM and BPV just before the stall inception in the case of moderate tip clearance. Near stall, the flow passages with high negative BFM appear intermittently due to the leading edge separation. It is found from Fig. 17 that BPV becomes high in the same flow passage with negative BFM. That is, the large disturbance is caused by the intermittent local separation of the blade. Occurrence of the local separation is quite irregular. The frequency of the oc-

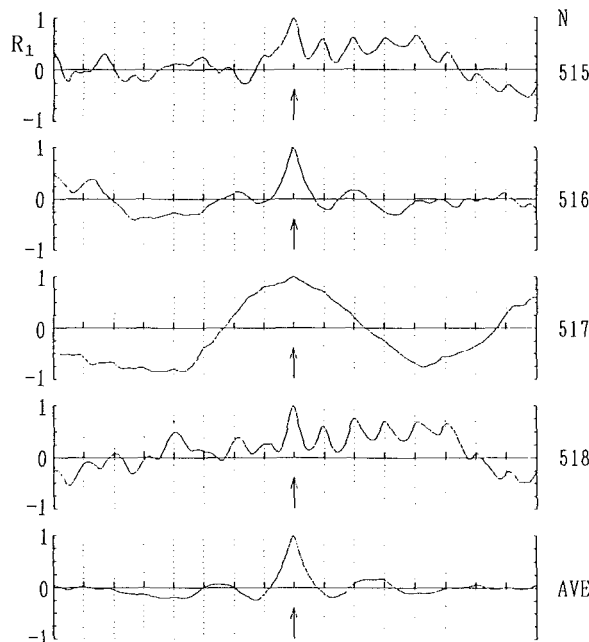
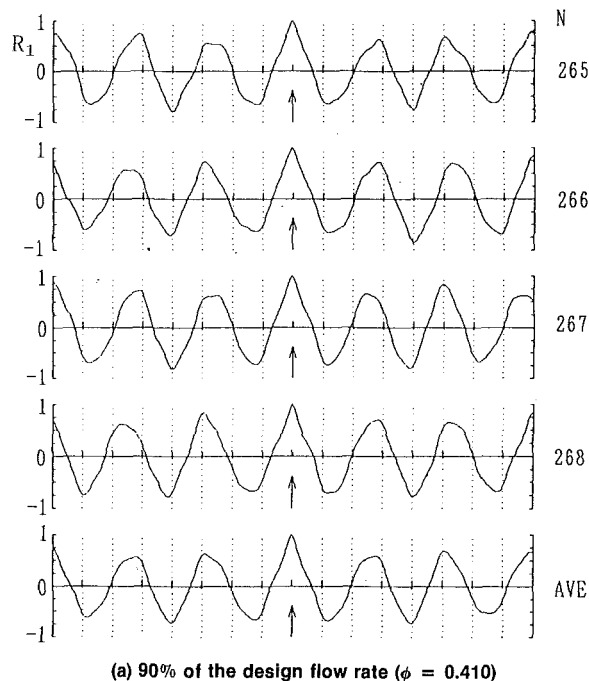


Fig. 16 Time autocorrelation for large tip clearance (rotor B, $\tau = 5.0$ mm)

currence increases as stall inception is approached. A small stall cell develops abruptly from one of them.

There seem to be two types of disturbances that collapse the periodic nature with blade spacing at low flow rate. One is a small scaled random disturbance, which appears mainly in the case of small tip clearance. Another is a larger scaled coherent-structured disturbance appearing even at considerably higher flow rates in the case of large tip clearance. In the case of moderate tip clearance, both types of disturbances coexist. The frequency with which the coherent-structured disturbances appear increases as the tip clearance becomes large. It increases also as the solidity is increased. This is probably related to accumulation of low-energy fluid in the tip region. The low-

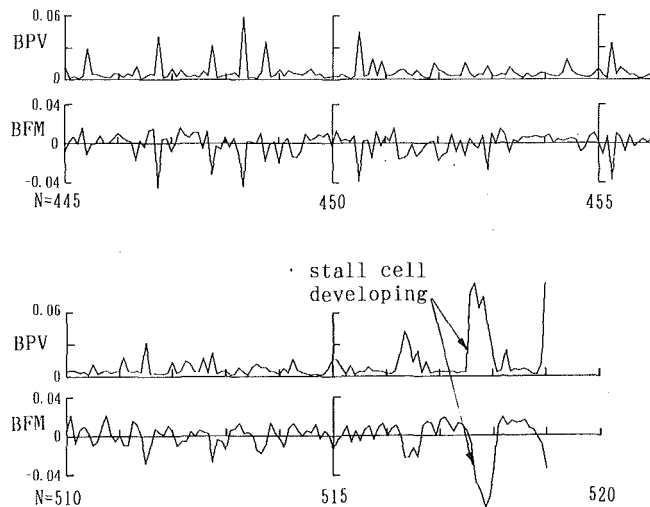


Fig. 17 Variation of blade fluctuation moment and blade pressure variance with rotor revolution (rotor A, $\tau = 0.5$ mm)

energy fluid blocks the blade flow passages near the tip. The accumulation is severe for large tip clearances and low flow rates. A rotor with high blade solidity is likely to be blocked by the low energy fluid. It makes the casing wall boundary layer thick and tends to change the thickness along the circumference of casing wall (McDougall et al., 1990). Does the coherent-structured disturbance form in this condition? If so, the tip clearance may not be the only parameter. The inlet boundary layer thickness may be an important parameter as well. Blade loading distribution also affects this behavior because the intermittent local separation near the leading edge brings about the accumulation of low-energy fluid due to the centrifugal force. The effects of these parameters should be investigated in the future.

The estimated rotating speed of the coherent-structured disturbance was 40 to 50 percent of the rotor speed in this experiment. On the other hand, the rotating speed of the stall cell was 64 to 68 percent in all the cases tested.

An attempt was made to find a long prestall wave, which was found upstream of the rotor investigated by McDougall et al. (1990) and Garnier et al. (1991). In the present study, the signals from two pressure sensors 36 deg apart from each other were examined through a numerical low pass filter. In some cases for short time length, the disturbances rotating near 50 percent of rotor speed were appreciable. However, the low pass filtered signals were too noisy to obtain sufficient evidence of the wave. In the present stage, it is not clear that the coherent-structured disturbance in this experiment is directly related to the long prestall wave. However, it is probable that the coherent-structured disturbance affects the fluctuation upstream of the rotor.

Conclusions

The casing wall pressure fluctuation of two axial flow compressor rotors with various tip clearance has been investigated. The regular saw-toothed pressure fluctuation due to blade passing is removed by subtracting the phase-locked ensemble average of pressure. The fluctuation component excluding the blade passing wave has been analyzed by the use of two kinds of correlation functions. One is the statistical function in the reference frame relative to rotating blades, and designated as "phase-locked correlation function," which is obtained by

phase-locked multisampling data acquisition during several hundred revolutions of rotor. Another is a common time correlation function which is obtained in each rotor revolution. The results are summarized as follows:

1 A pattern of the phase-locked correlation function varies depending on flow rate, tip clearance, and solidity. This is closely related to the nature of the disturbances.

2 There are two types of disturbance at low flow rate. One is of random disturbances appearing in the case of small tip clearance, and another is of coherent-structured disturbances appearing even at considerably higher flow rates in the case of large tip clearance.

3 In the case of moderate tip clearance, both types of disturbances coexist at low flow rate. The frequency with which the coherent-structured disturbances appear increases as the tip clearance becomes large and the solidity is increased.

4 For small and moderate tip clearances, the periodicity of the correlation function with blade spacing decreases noticeably as the flow rate is reduced to the stall point value. This is due to the random disturbances with large amplitude produced by intermittent local separation at blade leading edge.

5 The coherent-structured disturbances rotate in the circumferential direction. In this experiment, the rotating speed was 40 ~ 50 percent of the rotor speed, which was different from the rotating speed of the stall cell.

Acknowledgments

The authors appreciate the assistance of Messrs. S. Higuchi and H. Ugajin during the experimental work. They also gratefully acknowledge the financial support of Grant in Aid for Scientific Research (B) of The Ministry of Education, Science and Culture, and of Harada Memorial Foundation.

The first author is extremely grateful to Dr. I. J. Day for useful discussions in his short stay in Cambridge, and to Prof. N. A. Cumpsty for inviting him to Cambridge. He is also appreciative of the useful information from Prof. E. M. Greitzer.

References

- Day, I. J., 1993a, "Stall Inception in Axial Flow Compressors," *ASME JOURNAL OF TURBOMACHINERY*, Vol. 115, this issue, pp. 1-9.
- Day, I. J., 1993b, "Active Suppression of Stall and Surge in Axial Flow Compressors," *ASME JOURNAL OF TURBOMACHINERY*, Vol. 115, this issue, pp. 40-47.
- Epstein, A. H., Ffowcs, Williams, J. E., and Greitzer, E. M., 1989, "Active Suppression of Aerodynamic Instabilities in Turbomachinery," *Journal of Propulsion and Power*, Vol. 5, No. 2, pp. 204-211.
- Garnier, V. H., Epstein, A. H., and Greitzer, E. M., 1991, "Rotating Waves as a Stall Inception Indication in Axial Compressors," *ASME JOURNAL OF TURBOMACHINERY*, Vol. 113, pp. 290-301.
- Inoue, M., and Kuroumaru, M., 1989, "Structure of Tip Clearance Flow in an Isolated Axial Compressor Rotor," *ASME JOURNAL OF TURBOMACHINERY*, Vol. 111, pp. 250-256.
- Inoue, M., Kuroumaru, M., and Ando, Y., 1990, "Behavior of Tip Clearance Flow in an Axial Flow Impeller at Low Flow Rate," *Proceedings of the 3rd China-Japan Joint Conference of Fluid Machinery*, Vol. 2, pp. 179-186.
- Inoue, M., Kuroumaru, M., Iwamoto, T., and Ando, Y., 1991, "Detection of Rotating Stall Precursor in Isolated Axial Flow Compressor Rotors," *ASME JOURNAL OF TURBOMACHINERY*, Vol. 113, pp. 281-287.
- Jackson, A. D., 1987, "Stall Cell Development in an Axial Compressor," *ASME JOURNAL OF TURBOMACHINERY*, Vol. 109, pp. 492-498.
- Mathioudakis, K., and Breugelmans, F. A. E., 1985, "Development of Small Rotating Stall in a Single Stage Axial Compressor," *ASME Paper No. 85-GT-227*.
- McDougall, N. M., Cumpsty, N. A., and Hynes, T. P., 1990, "Stall Inception in Axial Compressors," *ASME JOURNAL OF TURBOMACHINERY*, Vol. 112, pp. 116-125.
- Paduano, J., Epstein, A. H., Valavani, L., Longlei, J. P., Greitzer, E. M., and Guenette, G. R., 1993, "Active Control of Rotating Stall in a Low Speed Axial Compressor," *ASME JOURNAL OF TURBOMACHINERY*, Vol. 115, this issue, pp. 48-56.

DISCUSSION

Y. N. Chen¹

The authors show a very interesting measurement about the pressure fluctuations across the blade channel on the casing wall. They attribute the appearance of the second peak of the pressure fluctuation within the blade channel as the second harmonic for the inception of the rotating stall. The respective pressure traces are given in Fig. 18. The second peak is shown in blade channel k . The discussor would interpret the phenomenon in channel k as a sharp negative pressure pulse, the development of which can be followed from the previous channels $a-j$. This sharp negative pulse represents a sharp vortex sink

¹Sulzer Brothers Ltd., 8401 Winterthur, Switzerland.

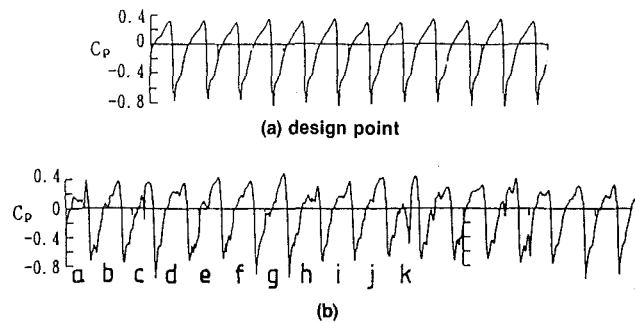


Fig. 18 Time traces of pressure measured on the casing wall at design point (a) and just before stall inception (b)

caused by the vortex-filament-natured reverse flow, as described by Chen et al. (1989, 1992). Such a very sharp negative velocity pulse from special blade channel was also found by Day (1992) in the frontal region of the rotors as the initiating factor for the inception of the rotating stall.

References

Chen, Y. N., Haupt, U., and Rautenberg, M., 1989, "The Vortex Filament Nature of the Reverse Flow on the Verge of Rotating Stall," *ASME JOURNAL OF TURBOMACHINERY*, Vol. 111, pp. 450-561.

Chen, Y. N., Haupt, U., Seidel, U., and Rautenberg, M., 1992, "Rotating Stall Cell and von Karman Vortex Street, a Meteorological Theory," von Karman Institute for Fluid Dynamics, Lecture Series 1992-02, Axial Flow Compressors.

Authors' Closure

The authors thank Dr. Chen for his comment. After reading his comment, they re-examined all the time traces of the casing wall pressure that they have. The sharp negative pulse appears at random within the rotor blade passage ($IZ \geq 12$ in Fig. 2) as well as upstream of the rotor leading edge ($IZ = 10$). It appears more frequently at the intrarotor than upstream of it. The pulses appearing upstream have to show the existence of reverse flow. But as this phenomenon occurs irregularly and instantaneously, it seems to be improper to explain it by a steady flow consideration. Furthermore, any propagation of the pulse from one blade passage to another has not been observed so far. At the present, therefore, the authors believe this is due to stall vortex caused by intermittent separation at the blade leading edge. Most of the stall vortices flow downstream, but they are occasionally disgorged forward of the rotor leading edge.

J. J. Adamczyk

NASA Lewis Research Center,
Cleveland, OH 44135

M. L. Celestina

Sverdrup Technology, Inc.,
Lewis Research Center Group,
Cleveland, OH 44135

E. M. Greitzer

Massachusetts Institute of Technology,
Cambridge, MA 02139

The Role of Tip Clearance in High-Speed Fan Stall

A numerical experiment has been carried out to define the near-stall casing endwall flow field of a high-speed fan rotor. The experiment used a simulation code incorporating a simple clearance model, whose calibration is presented. The results of the simulation show that the interaction of the tip leakage vortex and the in-passage shock plays a major role in determining the fan flow range. More specifically, the computations imply that it is the area increase of this vortex as it passes through the in-passage shock that is the source of the blockage associated with stall. In addition, for fans of this type, it is the clearance over the forward portion of the fan blade that controls the flow processes leading to stall.

Introduction

A characteristic feature of high-speed, high pressure ratio axial compressor rotors is the limited range of stable operation at design speed, often as little as 10 percent of the design flow. To use these high performance rotors to best advantage in an aeropropulsion system, it is thus desirable to develop methods for increasing this flow range. Understanding the underlying phenomena that control fan stall and stability is an important part of this problem.

In the last decade, there has been considerable progress in understanding and modeling of stall and surge of axial flow compression systems. See, for example, the work of Moore (1984), Moore and Greitzer, Greitzer and Moore (1986). Existing stability models, however, take as input the pressure characteristic map of the compressor. None of the models advanced in the open literature describe the detailed flow phenomena occurring within the blade row passage that give the characteristic its shape at stall. This is an important piece of the problem because it determines not only the base flow from which an instability evolves but also the nature of the instability.

The objective of the present work is to identify, using numerical simulation, the base flow from which an instability can develop in the tip region of a high-speed fan rotor, for it is well known that stall of modern fan rotors often originates in this region. Put another way, what is aimed at here is an answer to the fluid dynamic question of what are the dominant phenomena that are involved in the fan stall process? A principal component of the answer to this will be shown to be the strong interaction between the tip leakage vortex and the in-passage shock system.

Background: Tip Clearance Flows and Effects on Compressor Stability

Many researchers have documented the importance of tip

clearance on the stability boundary of axial flow compressors. Smith (1970) showed that increasing the clearance between the tips of rotors and the casing of a low-speed compressor caused the point of stall inception to move to a higher flow rate. Similar results were reported by Moore (1982), Freeman (1985), and Wisler (1985) for high-speed machinery. The role of tip clearance is also brought out in the correlation of Koch (1981), and Schweitzer and Garberoglio (1983).

An early attempt at examining the in-passage shock system at the tip of a transonic rotor was made by Miller and Bailey (1971), who measured the shroud pressure distribution over the tip of several rotors. We show these distributions to illustrate the general features of the problem that is addressed. Figure 1, taken from their report, shows two plots, at choke and near-stall condition. The location of the in-passage shocks, and the leakage vortex inferred from the contours, have been added by the authors. At choke flow the contours suggest that the shock system consists of a series of oblique waves, which propagate across the blade channel without noticeable distortion. There is no clear evidence of a leakage vortex. At the near-stall point the contour plot shows the shock system is a single nearly normal wave standing in front of the entrance to the blade channel. The low-pressure trough that forms near the leading edge of the suction surface is the signature of the leakage vortex, which forms as a result of the encounter between the clearance flow and the flow entering the blade channel from upstream. Where the vortex intersects the in-passage shock, there is a local distortion of the contours, which implies a strong interaction between the shock and the vortex.

Another perspective on the rotor endwall flow field is provided by the laser holograms of Nicholas and Freeman (1982). Figure 2, a photographic reproduction of one of their holographic images, shows the shape of the in-passage shock as well as the leakage vortex. Their report, like those noted previously, points to the importance of clearance in determining the stall limit.

The studies cited show that tip clearance effects play a major role in setting the stall limit, but they do not draw any clear, causal connections between endwall flow structure and instability onset. A main reason for this is the inherent complexity

Contributed by the International Gas Turbine Institute and presented at the 36th International Gas Turbine and Aeroengine Congress and Exposition, Orlando, Florida, June 3-6, 1991. Manuscript received at ASME Headquarters February 19, 1991. Paper No. 91-GT-83. Associate Technical Editor: L. A. Riekert.

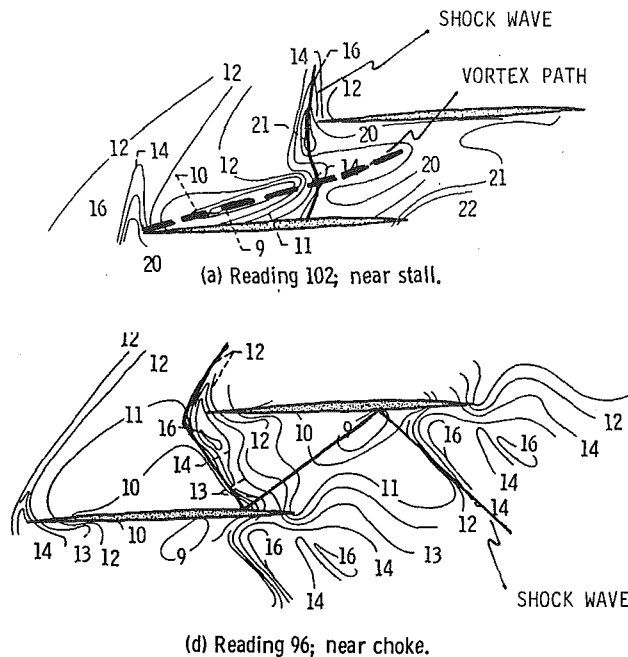


Fig. 1 Pressure contours of a high-speed rotor, from Miller and Bailey (1971)

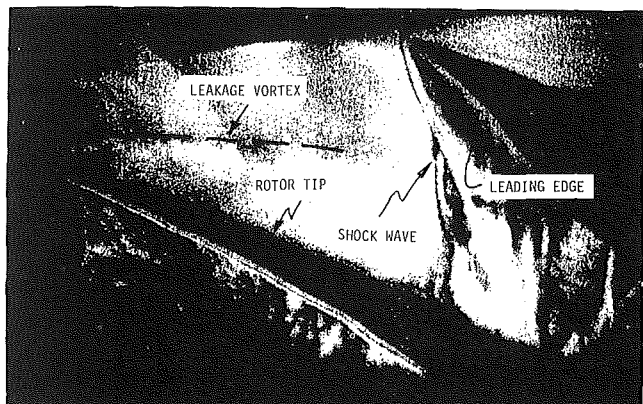


Fig. 2 Photographic reproduction of a laser hologram of the tip flow field of a high-speed fan, from Nicholas and Freeman (1982)

of the former. For example, features of the endwall region that can be significant are: clearance flow, associated leakage vortex and its behavior in an adverse pressure gradient, incoming casing boundary layer, and, for high-speed machines, passage shock system. The central point is that the behavior of interest is the resultant of an interaction among the various items and it is only in recent years that the capability to examine the interaction via numerical simulation has been developed.

In this context, a useful resolution of at least part of the question was provided by Crook (1989) who executed a series of numerical simulations of the endwall flow in a low-speed machine. Crook examined the flow with and without casing treatment, although we only discuss the smooth wall situation here. In the simulation, the flow from the clearance was seen to evolve into a vortex, which grew in cross section as it encountered the adverse pressure gradient in the passage. The region of high loss at the rear of the passage was essentially the core of the vortex. The result, taken with the data reported by Miller and Bailey (1971) and Nicholas and Freeman (1982) suggests that similar phenomena arise as a result of the interaction between the leakage vortex and the in-passage shock

system. Later in this paper, we will present the results of several simulations that suggest that, under certain operating conditions, the low-energy fluid generated by this interaction spills forward, raising the blockage in the forward portion of the blade passage and causing the flow system to become unstable.

Flow spillage forward of the blade passage has been previously suggested as triggering the onset of stall (McDougall et al., 1990). The connection between spillage and stall inferred from the computations reported herein, however, is only that they occur as parts of the same process. Whether the spillage is a cause or a result of the stall onset is an aspect of the stall transient that is beyond the scope of this paper; the goal here is rather to elucidate those features of the (pre)stall flow that can be directly linked to the breakdown of steady-state conditions.

The remaining portion of this paper is divided into three parts. The first presents an overview of the numerical solution procedure and a description of the clearance flow model. It also contains comparisons between simulations and measurements, which serve to calibrate the simulation code. The second part focuses on the casing end-wall flow at a near stall condition. The last part presents a series of simulations designed to substantiate the inferences drawn from the second section.

Calibration of the Numerical Simulation Code

The code used in the present study is based on a finite volume discretization of the Reynolds-averaged form of the Navier-Stokes equations. The temporal integration procedure is a four-stage Runge-Kutta scheme. The details of the simulation code, including a description of the artificial damping operator, the turbulence model, and the boundary conditions can be found from Adamczyk et al. (1989). The flow in the clearance gap was simulated using a model suggested by Kirtley et al. (1990). The flow is taken to be transported tangentially through the gap with no loss in mass, momentum, or energy. The effect of the vena contracta is accounted for by choosing the clearance to be smaller than the actual clearance. The model leads to the formation of a wall jet, which interacts with the oncoming flow in the passage.

At the solid boundaries, the simulation code used wall functions to estimate the wall shear stress when the value of y^+ at the center of the first mesh cell away from the wall boundary exceeded 30. (y^+ is the distance normal to a solid surface nondimensionalized by the square root of the ratio of the wall shear stress to the fluid density at the surface and the kinematic viscosity.) For values of y^+ less than 30, the wall shear stress was evaluated from the gradient of the velocity vector at the wall. The eddy viscosity at the cell adjacent to the wall was estimated consistent with the procedure used to estimate the wall shear stress.

The simulations were of the NASA Lewis Rotor 67, whose measured performance is reported by Strazisar et al. (1989). The rotor is a 1.56 aspect ratio transonic design with a tip relative Mach number of 1.38. The measured efficiency is over 90 percent at design speed.

The grid used in the simulations had 31 cells in the radial and circumferential directions. One hundred five cells were placed between the inlet and exit boundaries, of which 41 were along the blade chord line. The clearance gap was spanned by two cells in the radial direction. The grid in the clearance gap region above the rotor tip is constructed by simply extending the grid below the tip to the shroud while maintaining the tangential distance across the blade passage fixed to its value at the rotor tip. The number of grid points spanning the gap in the radial direction would be too few if one were interested in resolving the details of the flow entering and exiting the gap (see Crook, 1989, for a description of these regions). In the present study however, we are interested mainly in clearance

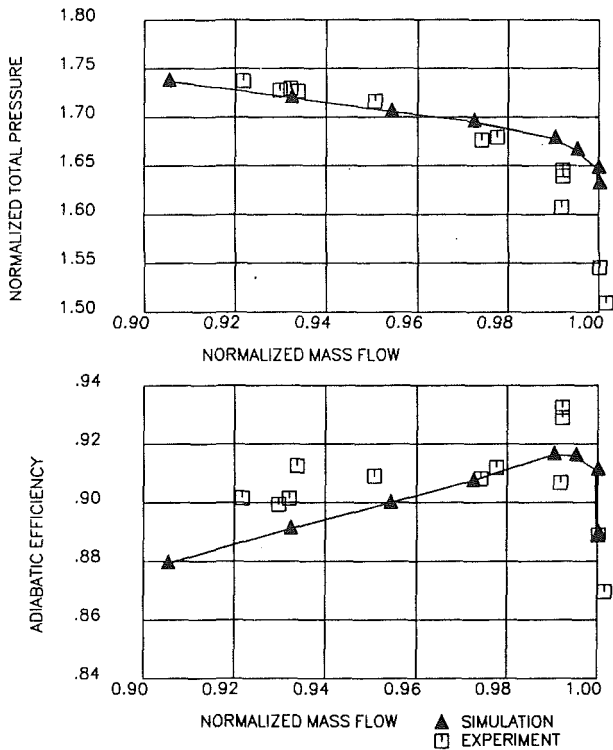


Fig. 3 Comparison of predicted and measured pressure rise characteristic and adiabatic efficiency map of Rotor 67, tip clearance/tip chord = 0.25 percent

flow as it interacts with the primary stream out in the blade passage. Several studies have shown that reasonable estimates of this interaction can be obtained without a detailed description of the flow exiting the gap if one has a good estimate of the gap mass flow. This can be accomplished in a numerical simulation with as few as one grid cell spanning the radial direction if one accounts for the blockage introduced by the vena contracta.

To show the ability of the simulation code to capture the correct trends, computed and measured adiabatic efficiency and pressure ratio at design speed are presented in Fig. 3. The abscissa for both curves is the ratio of the mass flow rate to the mass flow rate at choke. The exit total pressure is a mass-averaged value normalized by the inlet mass-averaged value. Agreement between computation and experiment is good. Further, the shape of the predicted efficiency curve is consistent with the reported curve, the predicted flow rate at peak efficiency being nearly equal to the measured value. The only apparent discrepancies are a slight overestimate of the pressure rise near max flow and the underprediction of the efficiency.

The predicted pressure level and the flow rate at stall also agree reasonably well with the measured values. Note that in the present paper, the stall point in the simulation is defined as the flow rate corresponding to the maximum pressure ratio for which the numerical simulation would converge (i.e., stall onset is taken as the flow rate below which the simulation will not converge). All attempts to find a steady solution for mass flows less than this value produced a transient response where the mass flow at the inlet steadily decreases as the solution was marched forward in iteration cycle, terminating in a reversed flow region at the inlet and divergence.

Figure 4 shows the radial distribution of the computed and measured mass-averaged total pressure and total temperature profiles downstream of the rotor for peak efficiency and near-stall operation. Again agreement between the simulation and the measured values is good, the only disagreement being a slight overprediction of the pressure at peak efficiency. How-

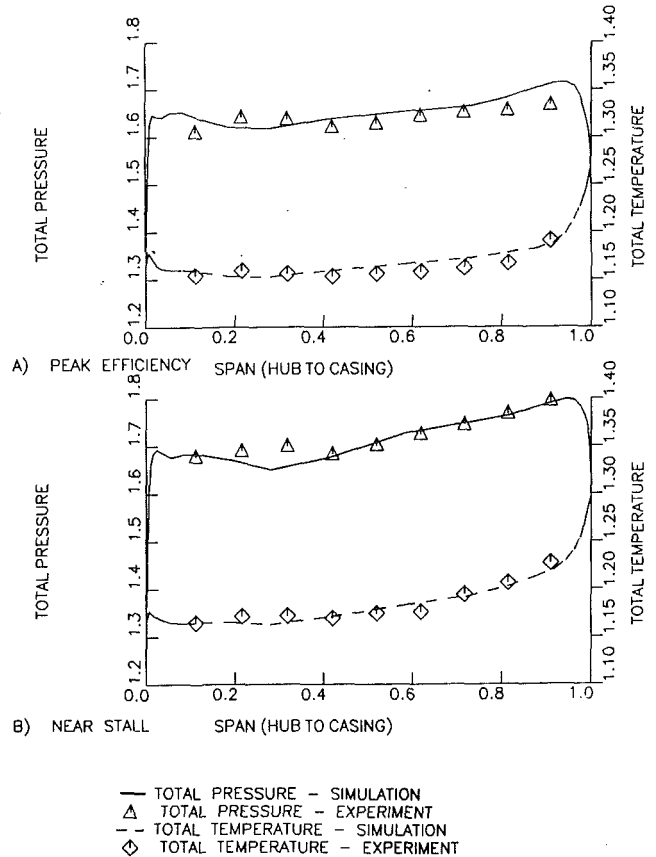


Fig. 4 Comparison of predicted and measured axisymmetric-averaged and mass-averaged total pressure and total temperature profiles, tip clearance/tip chord = 0.25 percent

ever, and this is the main point of Figs. 3 and 4 (as well as the more detailed comparisons in Figs. 5 and 6), the parametric dependence is well captured so that there is confidence in the use of the code for numerical experimentation.

A third assessment of the simulation is given in Figs. 5 and 6, which show intrablade Mach number distributions. The experimental results were estimated from LDV measurements of the velocity field. The plots are for 90 and 70 percent of span as measured from the hub. The contours from the simulation and those estimated from the measured velocity field are in good agreement, as is the location of the in-passage shock implied by the contours. The latter is important because the shock plays a key role in forcing the clearance flow through the gap.

As stated, the results confirm the suitability of the simulation code for a qualitative study of the shroud end-wall flow. They indicate that the code is capable of predicting loading level, and shock position. Discrepancies between prediction and measurement are judged to be sufficiently minor so as not to affect the conclusions concerning physical mechanisms that are drawn from the simulations that follow.

Prediction of Clearance Effects on Rotor Performance and Endwall Flow Structure

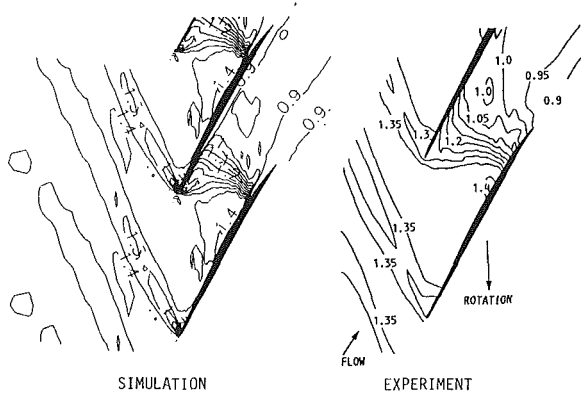
Overall Behavior. A series of simulations of Rotor 67 were executed at clearance to tip chord ratios of zero, 0.25, 0.75, and 1.25 percent. These span the range found in modern high-speed fans. For each clearance, pressure and efficiency maps were computed along a line of constant corrected speed. The speed lines include the point of stall onset, which (as stated) is defined to be the point of operation at which any increase

in the exit static pressure results in a steady decrease in the mass flow at the inlet as the solution iteration cycle count is advanced. (One might interpret this behavior as an indication that the pressure characteristic has reached its maximum so the slope of the characteristic is either zero or possibly discontinuous.) The endwall flow field will be analyzed near this point to define the flow field from which the instability evolves.

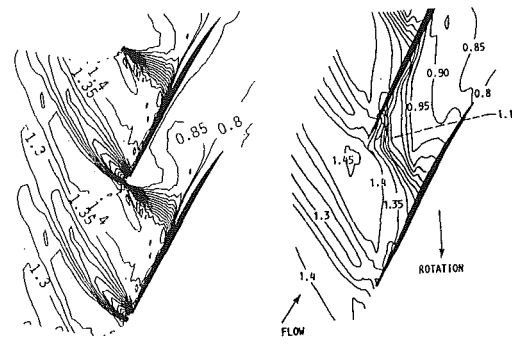
The computed pressure rise and efficiency are shown in Fig. 7 for the four clearances. Increasing the clearance from zero results in a decrease in rotor pressure rise capability and a

reduction in operating range. On the other hand, the efficiency has a maximum at a nonzero clearance. Although no direct comparison is made, these trends are consistent with those reported in the experimental studies of Freeman (1985) and Wennerstrom (1984).

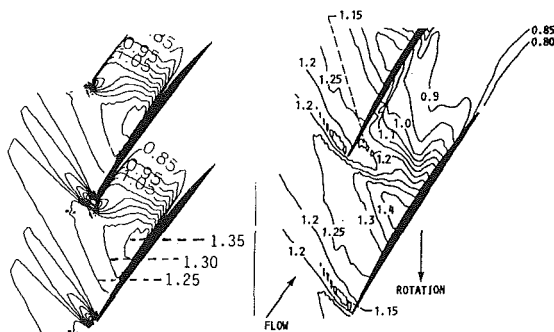
Endwall Flow Field. In this section we will examine in some detail the results from simulations done at three different clearances. The first is the nominal clearance of 0.25 percent of tip chord, which might be a tight clearance in a modern fan. This



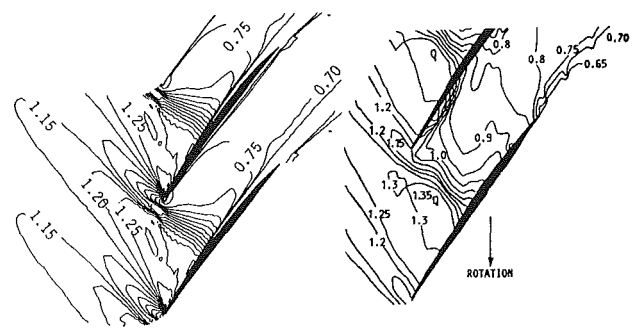
A) NINETY PERCENT SPAN FROM HUB



A) NINETY PERCENT SPAN FROM HUB



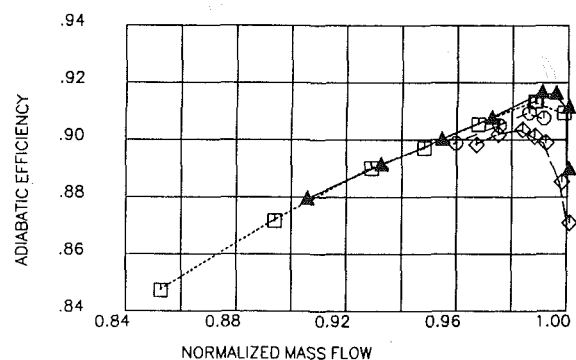
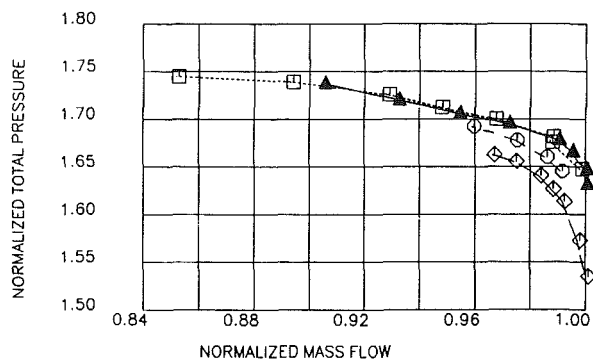
B) SEVENTY PERCENT SPAN FROM HUB



B) SEVENTY PERCENT SPAN FROM HUB

Fig. 5 Comparison of predicted and measured intrablade Mach number contours at 90 and 70 percent span at near peak efficiency, tip clearance/tip chord = 0.25 percent (contour increments 0.05)

Fig. 6 Comparison of predicted and measured intrablade Mach number contours at 90 and 70 percent span at near stall, tip clearance/tip chord = 0.25 percent (contour increments 0.05)



□ ZERO CLEARANCE
 ▲ 0.25% TIP CLEARANCE / TIP CHORD
 ◇ 0.75% TIP CLEARANCE / TIP CHORD
 ○ 1.25% TIP CLEARANCE / TIP CHORD

Fig. 7 Comparison of predicted pressure rise characteristics and adiabatic efficiency maps of Rotor 67 for tip clearance/tip chord ratios of 0, 0.25, 0.75, and 1.25 percent

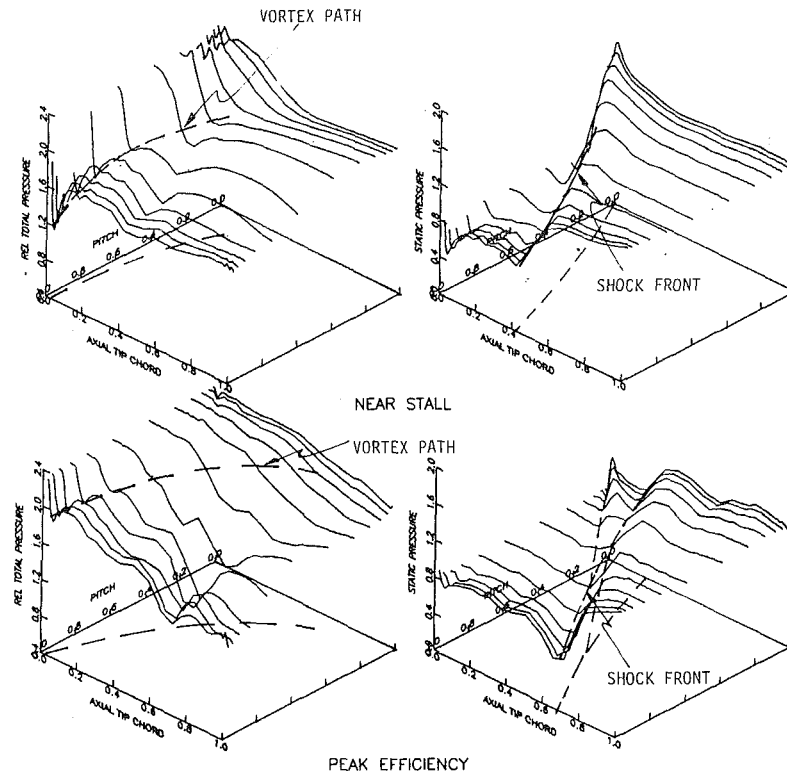


Fig. 8 Relative total and static pressure in the clearance region, tip clearance/tip chord = 0.25 percent

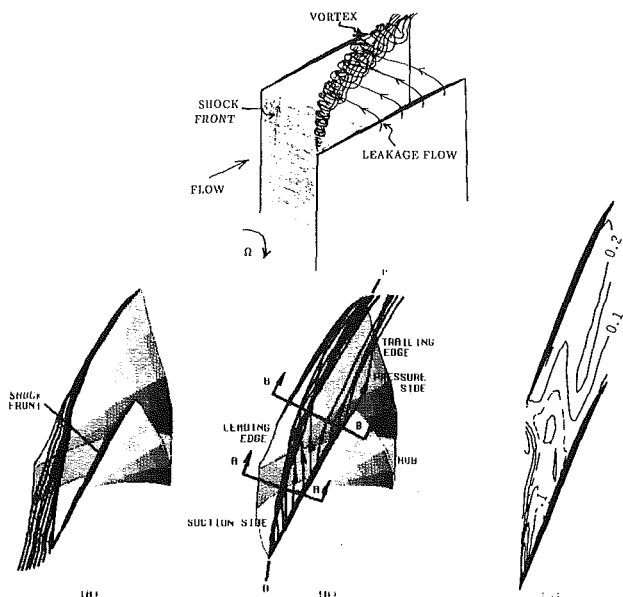


Fig. 9 Illustration of the flow field in the tip clearance region at near stall by particle traces and contours of axial velocity at tip clearance/tip chord = 0.25 percent: (A) particles released upstream of the leading edge and restricted to blade-to-blade surface adjacent to the casing; (B) particles released near the suction surface; and (C) contours of axial velocity nondimensionalized by tip wheel speed (dashed contour denotes zero contour level)

will show the effects that are to be expected from vortex-shock interaction in such a situation. A larger clearance, 1.25 percent of tip chord, will then be considered. Although the behavior is qualitatively the same, because of the larger clearance (and hence larger leakage vortex), this set of computations illustrates in a more evident manner, the influence of the shock vortex

interaction. Finally we consider the situation with zero clearance, which will be seen to be qualitatively different from either of the first two cases, because of the absence of the leakage vortex.

Nominal Clearance (0.25 Percent Tip Chord) Flow Field. Figure 8 shows the relative total pressure and static pressure distributions on a surface of revolution at 99.85 percent of span as a function of nondimensional axial tip chord and pitch. The clearance to tip chord ratio is 0.25 percent, and the operating conditions are peak efficiency, and near stall. The nondimensional pitch and axial tip chord each vary from zero to one with zero pitch corresponding to the pressure surface and zero axial chord corresponding to the rotor inlet plane. The line plots in this figure as well as those in similar figures that follow are drawn at 3, 5, 10, 15, 20, 25, 40, 60, 75, 85, 90, 95, and 97 percent of pitch.

The structure of the in-passage shock system at the rotor tip can be seen from the pressure plots. At peak efficiency the shock structure is a lambda pattern with both legs originating from the pressure surface, while near stall the pattern is that of a strong oblique wave, which stands off of the leading edge.

The leakage vortex can be tracked in the static pressure plots by the low-pressure depression that forms near the leading edge of the suction surface, but it is more evident in the relative total pressure plots. In the latter its signature appears as a low-pressure trough originating near the leading edge of the suction surface. As the rotor is throttled toward stall the relative total pressure in the core of the vortex decreases and the trajectory of the vortex across the blade passage becomes more tangential.

Slightly upstream of the impingement of the in-passage shock on the suction surface (i.e., near 0.70 axial tip chord at peak efficiency and 0.40 axial tip chord for the near-stall point), there is a second region of low relative total pressure created by the interaction of the shock with the suction surface boundary layer and the fluid particles that have come through the

gap from the adjoining blade passage. At the near-stall point this total pressure fluid is transported upstream by the fluid exiting the gap and entrained in the leakage vortex near 0.40 pitch and 0.25 axial tip chord. The total pressure in the core of the vortex is decreased by this process. This transport mechanism will be made evident by means of plots that show the path of fluid particles in the end-wall region. Upon encountering the shock, the size of the vortex cross section is increased, causing the low relative total pressure within the core to be spread laterally across the blade passage.

Figure 9 shows the flow structures that control the flow field at the tip of a rotor at the near-stall operating condition. The upper portion of the figure shows an illustration that identifies these structures. The two key structures are the leakage vortex and the leakage flow from which it was formed, and the in-passage shock. The blade geometry is also shown to give a perspective of the relationship between these structures and the geometry. The lower portion of the figure contains three plots in which the view is from the shroud looking in toward the hub. These plots quantify the structures identified in the illustration. The plot on the lower left shows, in the relative frame of reference, the paths of the fluid particles released upstream of the rotor inlet plane between the rotor tip and the shroud (99.85 percent of span) and restricted to an axisymmetric surface of revolution at 99.85 percent of span. This surface is between the shroud and the rotor tip. The middle plot shows the paths, in the relative frame of reference, of fluid particles released between the rotor tip and the shroud (99.85 percent of span) above the suction surface. The plot on the right shows contour levels of the axial velocity as viewed in the relative frame of reference on an axisymmetric surface of revolution at 99.85 percent of span. The location of the in-passage shock at the tip is shown in the plot on the bottom left, while the trace of the leakage vortex is noted by the line O-P on the lower middle plot.

The plot on the lower left shows that, near the shroud, the majority of the fluid particles approaching the rotor do not directly enter the blade passage. They appear to be blocked from doing so by a flow obstruction.

The formation of the leakage vortex is illustrated in the lower middle plot. These particles were released above the suction surface in the clearance region. These traces outline the leakage vortex (line O-P). A curve drawn through the furthestmost upstream position of the paths of the particles released between the leading edge and midchord corresponds very nearly to the fluid particle path in the lower left plot originating from the suction surface leading edge. This result suggests the leakage vortex is acting as a flow obstruction, which causes the flow entering the blade passage to pass around it rather than through it.

Contour levels of the axial velocity normalized by the wheel speed on a surface of revolution at 99.85 percent of span are shown in the lower right plot. The dashed contour is zero axial velocity. All the contours within the zero contour have a negative value, while those outside the zero contour have positive values. In the negative contour region, the fluid particles, in the relative frame of reference, travel upstream as they move across the passage. This motion, which can also be seen in the lower middle plot, is responsible for transporting the region of low relative total pressure originating near midchord in Fig. 8 toward the leading edge vortex.

Figure 10 shows the relative total pressure distribution at near stall on cross-sectional planes A-A and B-B as shown in Fig. 9. These planes are nearly orthogonal to the vortex axis so the representation of the cross-sectional dimension of the vortex structure is to scale. The abscissa in the plots is physical distance measured from the left edge of the sectional cut while the ordinate is the radius. The location of the suction surface relative to the sectional plane A-A is 1 percent of span and is noted on the figure. The location of the pressure surface rel-

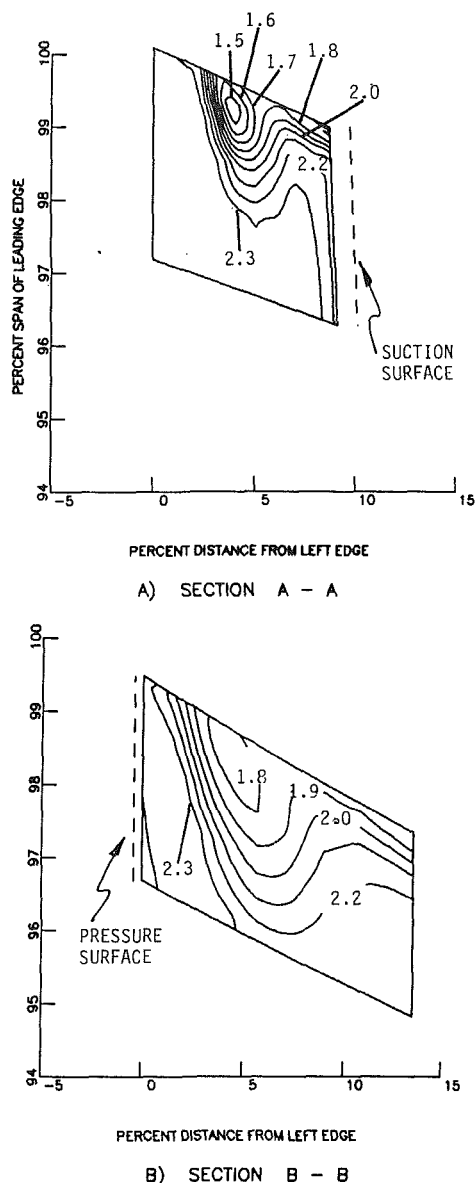


Fig. 10 Sectional cuts of relative total pressure at near stall in the tip clearance region, tip clearance/tip chord = 0.25 percent

ative to the sectional plane B-B is 0.4 percent of span and is also noted in the figure. All dimensions on this figure are nondimensionalized with respect to the span of the rotor at the leading edge. A-A is upstream of the in-passage shock and the cut at B-B is downstream of the shock as drawn in Fig. 9. (The upper edge of the contour plots is not straight because the intersection of the shroud and the plane is not a line of constant radius. The shape of the lower edge is the result of the graphics routines used in the generation of these plots, which draws the lower edge parallel to the upper edge.)

In both plots the contour level 2.3 represents the relative total pressure of the primary stream. By comparing contour level 2.1 in both plots, one can see the growth of the vortex as it passes through the shock. (For reference, in these units the relative inlet dynamic pressure is roughly unity.) In agreement with Crook's (1989) observations, the region of low relative total pressure within the core of the vortex causes large growth of the vortex when it encounters a pressure rise. Most of the pressure rise in the present case is produced by the shock, while Crook (1989) based his observations on analyzing low-speed machinery. The interaction he observed between the

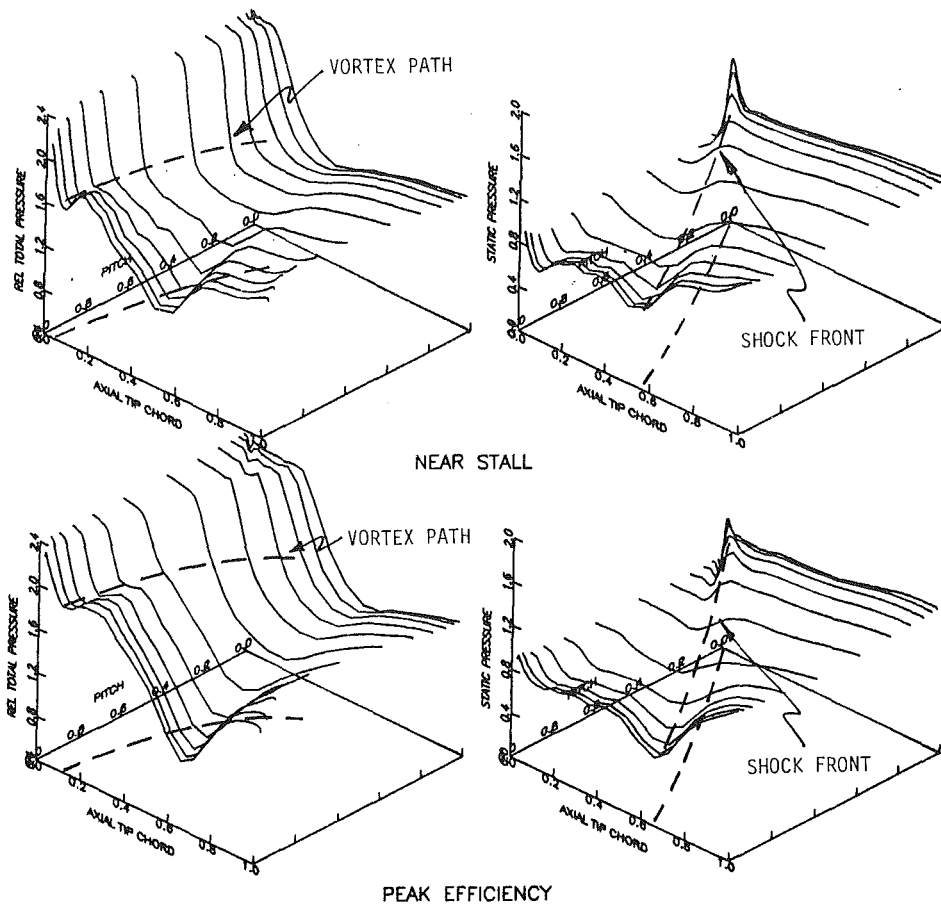


Fig. 11 Relative total and static pressure in the clearance region, tip clearance/ tip chord = 1.25 percent

leakage vortex and the blade passage pressure field, however, also takes place in high-speed machinery, with the shock the generator of the adverse pressure gradient. It will be shown that suppression of this interaction can lead to an increase in the stable operating range of a rotor.

As the flow is reduced, the leakage vortex inclines more toward the tangential direction and the shock moves forward. As a result, the large blockage generated by the interaction of the vortex and the shock also moves forward. This produces a region of low relative total pressure along the shroud near the pressure surface, which spills forward, initiating numerical stall. The spillage of low-energy flow drives the bow shock at the leading edge of the tip blade section forward, altering the upstream wave pattern, reducing the mass flow rate, and increasing the blade incidence. This increased incidence raises the blade loading, which, in turn, increases the leakage flow, driving the bow shock farther forward. This series of events leads to a steady reduction of the mass flow as the simulation iteration cycle count is advanced and results in the simulation undergoing a rapid divergence when the region of low relative total pressure reaches the inlet plane of the computational domain. The mass flow rate just prior to the onset of this rapid divergence has dropped far below a level that is reasonable to expect stable operation of a high-speed machine. We, therefore, feel that there is physical significance to this point of instability. Furthermore, this point of operation coincides with the peak in the predicted pressure characteristic curve and, because of this, we suggest that the flow field at mass flows just above the predicted peak in the pressure characteristic curve may form the base flow from which rotating stall develops in an isolated fan rotor.

Increased Tip Clearance (1.25 Percent Tip Chord) Flow Field. The behavior just illustrated can be seen more clearly if we examine a rotor with larger tip clearance. This is done in Figs. 11 to 13, which are derived from computations carried out with a tip clearance of 1.25 percent of tip chord. Figure 11 presents plots of the relative total pressure and the static pressure on a surface of revolution just inboard of the tip (99 percent of span). Both peak pressure and near-stall conditions are shown. The format is the same as that in Fig. 8, with zero values of pitch and axial chord corresponding to pressure side and leading edge plane, respectively.

If we compare the pressure distribution at near stall to that with the smaller tip clearance (Fig. 8) we find the shock structure is qualitatively similar. There is, however, a lower pressure rise through the shock, and thus a reduction in pressure difference across the blade over the outer 10 percent of blade span.

The leakage vortex is indicated by the trough in relative total pressure observed originating from the suction surface slightly aft of the leading edge. Its trajectory is shown by the dashed line. Farther aft along the suction surface there is another region of low relative total pressure (as with the 0.25 percent clearance) due to the shock interacting with the suction surface boundary layer and the flow that has come through the gap from the adjoining blade passage. At near stall the minimum relative total pressure, along the suction surface, is lower than that for 0.25 percent clearance. At peak efficiency the low total pressure is transported tangentially into the blade passage by the clearance flow while at the near-stall point the transport is not only tangentially but toward the rotor inlet plane. The transport process at the near-stall condition will be illustrated

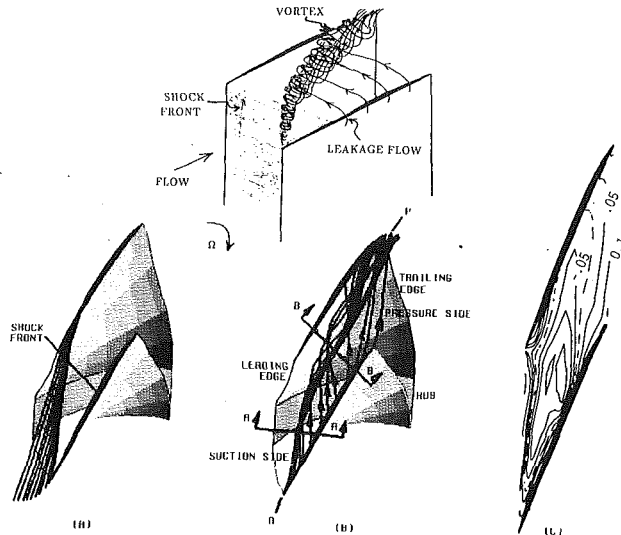


Fig. 12 Illustration of the flow field in the tip clearance region at near stall by particle traces and contours of axial velocity at tip clearance/ tip chord = 1.25 percent: (A) particles released upstream of the leading edge and restricted to blade-to-blade surface adjacent to the casing; (B) particle released near the suction surface; and (C) contours of axial velocity nondimensionalized by tip wheel speed (dashed contour denotes zero contour level)

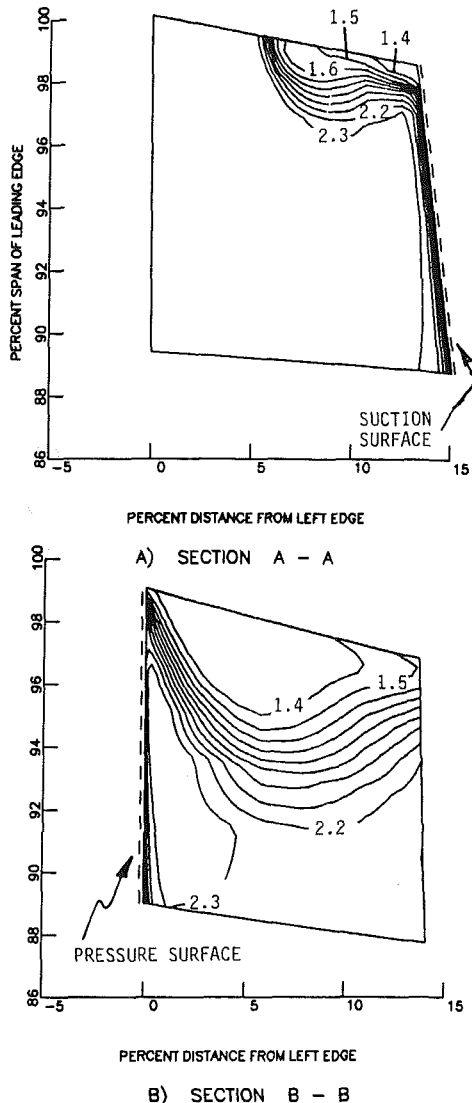


Fig. 13 Sectional cuts of relative total pressure at near stall in the tip clearance region, tip clearance/tip chord = 1.25 percent

below by means of a series of plots of fluid particle paths in Fig. 12.

The upper portion of Fig. 12 shows an illustration of the formation of the leakage vortex and its encounter with the in-passage shock at the near-stall operating condition.

The purpose of this illustration, as it was in Fig. 9, is to aid the interpretation of the plots that appear in the lower portion of the figure. The view for Figs. 12(A), 12(B), and 12(C) is from the shroud looking in toward the hub. The format for these figures is identical to that for Figs. 9(A), 9(B), and 9(C). Figure 9(A) shows the streamlines of the relative flow field on an axisymmetric surface of revolution located at 99 percent of span as defined by particle paths originating upstream of the rotor. This surface lies between the shroud and the rotor tip. The streamline originating from the leading edge divides the upstream flow from that which came through the clearance. This line is an indication of the forward edge of the leakage flow across the passage and the geometry near stall is similar to the corresponding streamline in Fig. 9(A). Figure 12(C) shows the paths of fluid particles released in the clearance region over the suction surface. The line O-P shows the trajectory of the vortex across the passage. The shock front at the shroud is shown in Fig. 12(A). The formation of the leakage vortex from the clearance flow is evident. Figure 12(A) is a contour plot of the axial velocity normalized with respect to the tip wheel speed on an axisymmetric surface of revolution at 99 percent of span. The dashed contour corresponds to zero axial velocity. The contours within the region bounded by the zero contour are negative while those that are outside are positive. In comparing Fig. 12(C) with Fig. 9(C), it is clear that the larger clearance has resulted in a larger region of negative axial velocity. In fact, this region extends across the entire passage in Fig. 12(C) while in Fig. 9(C) it ends before it reaches the pressure surface. Within the region of negative axial velocity in Fig. 12(C) the low relative total pressure found between 20 and 50 percent of axial chord in Fig. 11 is transported toward the vortex and becomes entrained in the vortex prior to the in-passage shock. This is also evident in Fig. 12(B). As the flow is further reduced toward stall, the low-energy flow associated with the clearance flow spills forward of the rotor inlet plane.

Figure 13 illustrates the vortex cross section at the near-stall point using contour plots of the relative total pressure on sectional planes A-A and B-B. The planes are located on either

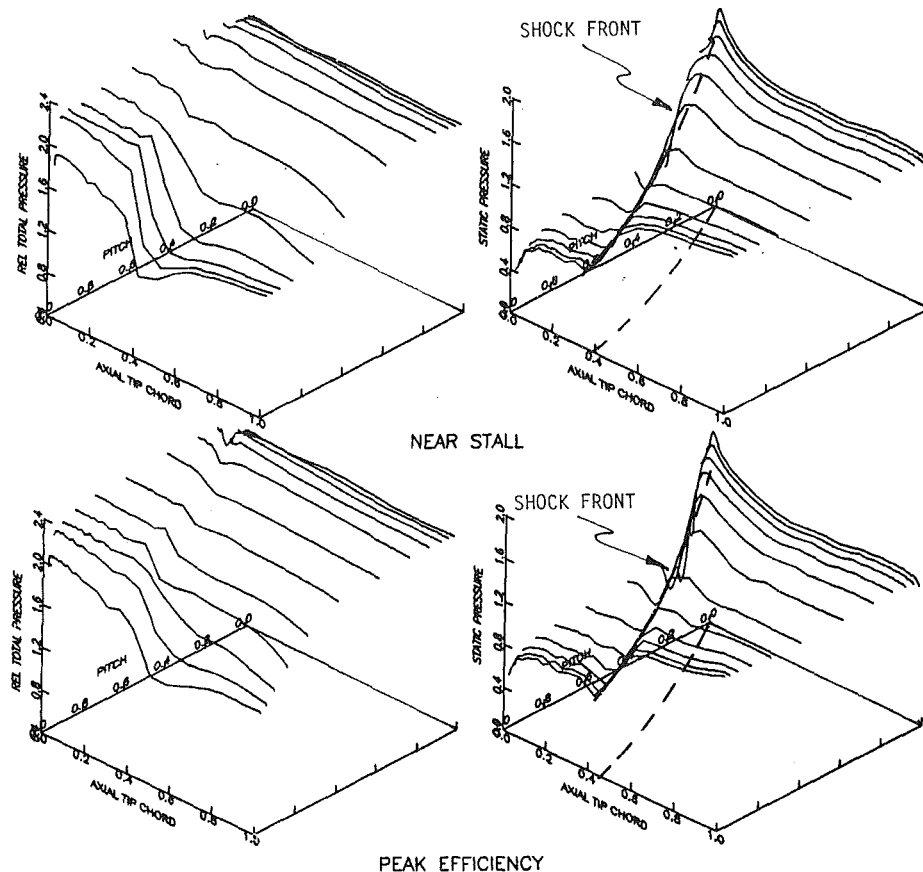


Fig. 14 Relative total and static pressure in the clearance region, zero tip clearance

side of the shock and are nearly orthogonal to the vortex trajectory. The format for the plots is identical to that for Fig. 10. The location of sectional plane A-A relative to the suction surface is 0.18 percent of span, while the sectional plane at B-B is located at 0.21 percent of span relative to the pressure surface. These locations are noted in the figure. The contour plots in Figs. 10 and 13 for section A-A show that the larger clearance produces a larger vortex as is expected. (The vortex size should roughly scale on clearance (Chen et al., 1991).) The vortex cross section increases markedly in size upon passing through the shock, as can be seen by comparing contour level 2.1 on plane A-A in Fig. 13 with the corresponding contour on plane B-B. This vortex growth is responsible for the sharp increase in endwall blockage as stall is approached. At numerical stall, this blockage increase forces the bow shock at the tip section forward causing a steady reduction in mass flow through the rotor as the simulation iteration cycle is advanced.

Zero Clearance Flow Field. It is instructive to compare the flow fields in the two above cases with that for zero tip clearance, where the structure is qualitatively different. Figure 14 shows the relative total pressure and the pressure distribution near the casing for zero clearance as a function of nondimensional pitch and axial tip chord at peak efficiency and near-stall throttle setting. The scale is identical to Fig. 8 and the mass flow rates for corresponding plots are nearly the same.

The shock structure for the near-stall operating point is close to that in Fig. 8. There is, however, a difference between the relative total pressure (in Figs. 8 and 14) forward of 0.30 axial tip chord. The comparison illustrates the loss in relative total pressure that occurs as a result of the formation of the leakage

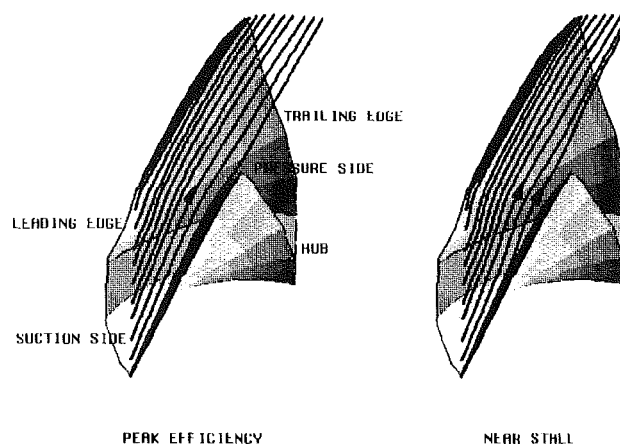


Fig. 15 Particle traces injected upstream of the leading edge and restricted to blade-to-blade surface adjacent to the casing, zero clearance

vortex and the influence this loss generation mechanism has on the blockage in the forward portion of the blade passage. It is apparent at peak efficiency and especially so for the near-stall operating point. However, even at peak efficiency, the clearance flow and the blockage it generates appear to have an impact on the shock structure. The relative total pressure plot in Fig. 14 also shows a region of low pressure developing along the suction surface (pitch ratio of unity) near 0.50 axial tip chord. The low pressure results from the interaction of the in-passage shock with the suction surface boundary layer and grows in size as the rotor is throttled toward stall.

Figure 15 shows the paths of fluid particles released at the

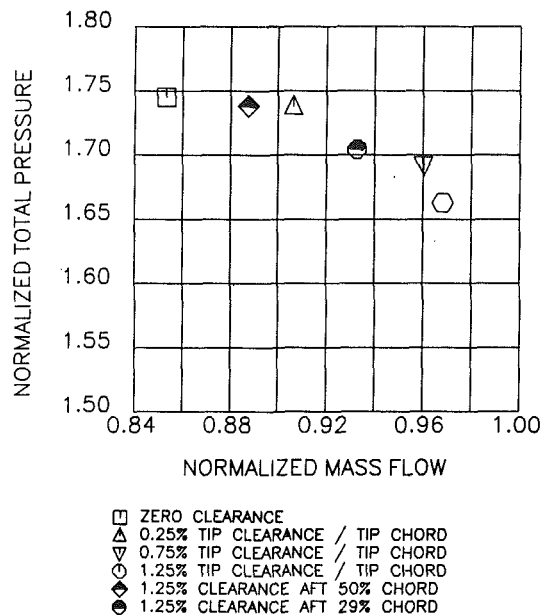


Fig. 16 Predicted pressure ratio at near-stall points for tip clearance/tip chord ratios of 0, 0.25, 0.75, 1.25 percent and clearance of 1.25 percent aft of 29 percent and 50 percent chord

inlet plane to the rotor and restricted to an axisymmetric surface of revolution at 99 percent of span. The intent is to portray the streamlines near the shroud. Note the differences with Figs. 9 and 12. In Fig. 12 there is little deflection of the streamlines because there is no leakage vortex. The blockage generated by the vortex deflects the incoming stream in the tangential direction.

Relation Between Low-Energy Flow in Vortex and Stall Onset. The simulations discussed in the previous section showed a strong correlation between the onset of stall and the forward movement of low-energy fluid, which is connected with the clearance vortex. To examine this further, two sets of simulations were executed in which the growth of the blockage in the end-wall region was controlled by reducing the clearance to zero over the forward portion of the rotor only. For the first set, the clearance to tip chord ratio was 0 to midchord, and 1.25 percent from there to the trailing edge. For the second set of results, the clearance ratio was 0 to 29 percent of chord, and 1.25 percent from there to the trailing edge. These configurations yielded varying degrees of interaction between the clearance flow and the in-passage shock system.

The flow range associated with each of the partial clearance configurations as well as that of all the previously examined configurations is shown in Fig. 16. The most significant result contained in this figure is the flow range that is obtained with the partial clearance. The two partial clearances are shown as the half solid symbols. The large change due to sealing the front part of the blade is evident. Specifically, the partial clearance with 50 percent of the blade sealed could be throttled to a lower flow than the 0.25 percent configuration. Even sealing the blade over the front 29 percent of blade yields a flow range near that of the 0.25 percent configuration.

The reason for this improvement can be seen in Fig. 17, which presents near-stall relative total pressure plots on an axisymmetric surface at 99 percent of span. Four different configurations are shown, the nominal clearance (0.25 percent), the large clearance (1.25 percent), zero clearance, and the 50 percent partial clearance. The first two of these can be seen to be at least qualitatively similar to each other, as are the latter two, but there is a substantial difference between the two pairs. With the partial clearance (as with the zero clearance), there is no leakage vortex in the front part of the blade

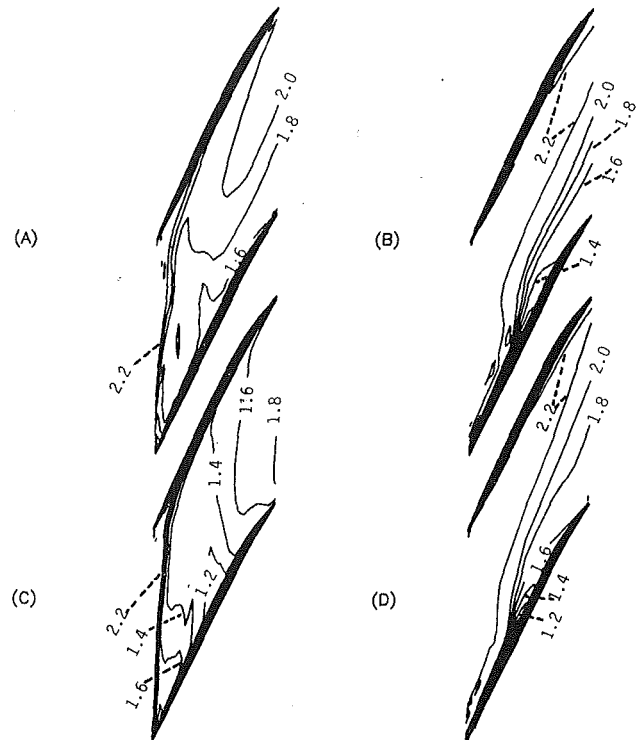


Fig. 17 Blade-to-blade cut of relative total pressure at near-stall flow at tip clearance/tip chord of: (A) 0.25 percent; (B) zero; (C) 1.25 percent and (D) 1.25 percent aft of 50 percent

passage. We associate the absence of the leakage vortex in the front part of the passage with the shift in the stall onset point.

An alternative presentation of the tip region flow field for the partial clearance configuration is given in Fig. 18, which shows relative total pressure and static pressure at the near-stall point on an axisymmetric surface of revolution at 99 percent of span. The format of this figure is identical to that introduced in Figs. 8 and 11, and the plots themselves are similar in appearance to those for zero clearance presented previously in Fig. 15. The region of low relative total pressure found along the suction surface with zero clearance is also found in the present configuration, although the loss in relative total pressure is less than that for zero clearance because of the high-energy fluid, which has come through the gap at the rear portion of the blade.

With the partial clearance, the interaction of the clearance flow with the primary passage flow is confined to the region aft of the shock. The end-wall flow in the middle of the passage approaching the shock has high relative total pressure. Suppression of the interaction of the shock with the low relative total pressure fluid associated with the leakage vortex has led to a reduction in end-wall loss and blockage in the forward portion of the blade passage, producing the increases in stability shown in Fig. 16. These results substantiate the important role played by the tip vortex in initiating the onset of stall and show the sensitivity of the stall point to the clearance over the forward portion of the fan blade.

Summary and Conclusions

1 A numerical experiment was performed to document the structure of the near-stall end-wall flow field in a high-speed rotor. Tip clearance was varied from zero over a range representative of modern fans so the influence on the structure of the end-wall flow could be seen.

2 Analysis of the runs with clearance showed a build-up

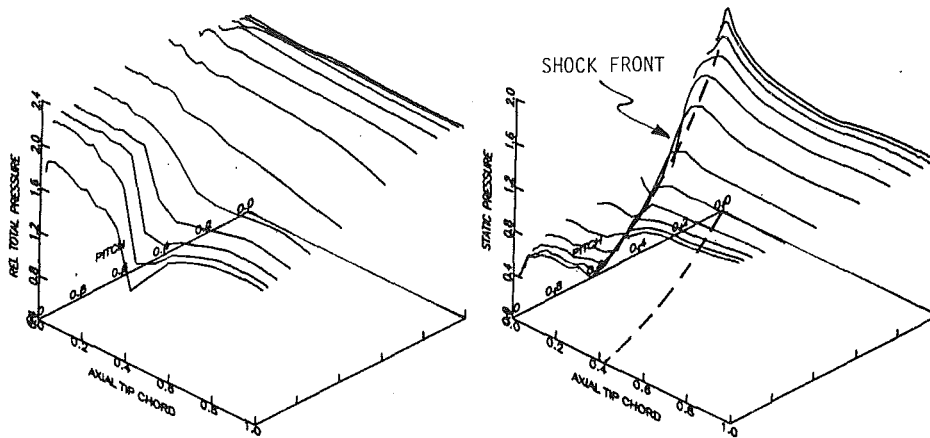


Fig. 18 Relative total and static pressure in the clearance region at near stall, tip clearance/tip chord = 1.25 percent aft of 50 percent chord

of low-energy fluid along the casing due to the interaction of the clearance vortex and the in-passage shock. This region of low-energy fluid grew and moved forward as the flow rate was decreased. At a critical value of the flow rate, the region of low-energy fluid rapidly moved forward with corresponding increases in loss and blockage. The numerical simulation would stall at this point, being unable to converge to a solution.

3 The zero clearance computation showed an increased flow range compared to results with clearance, due to the absence of vortex-shock interaction.

4 Simulations were also carried out with zero clearance over the forward portion of the fan rotor but a large clearance over the aft part. The rotor exhibited a large stable operating range, again because of the reduction in vortex-shock interaction. These results show the strong dependence of the flow range on the clearance over the forward portion of the blade.

5 From the present study it appears that injection of high-energy fluid in the forward part of the casing end-wall region to reduce or eliminate the growth of low regions of relative total pressure would have a beneficial effect on flow range. As noted by Crook (1989), axial groove casing treatment appears to provide such an injection mechanism.

6 It would be worthwhile to examine the end-wall flow structure in a multistage axial flow compressor to see whether the findings of the present study are relevant to multistage machinery.

Acknowledgments

The authors wish to acknowledge the extent to which this work was stimulated by the initial numerical experiments and their analysis by Mr. A. Crook of Allison Gas Turbine Division. Mr. Crook's work provided much useful insight into the importance of the clearance vortex for the end-wall flow. We are also grateful to Professor N. A. Cumpsty of Cambridge University for helpful comments as well as to Mr. D. J. Nicholas and Mr. C. Freeman of Rolls-Royce Derby for providing reproductions of their holographic photographs and a copy of their very informative paper. The comments of Dr. I. J. Day concerning his measurements are also appreciated. We would further like to thank Dr. K. Dugas for her invaluable help with the manuscript. Support for E. M. Greitzer in this work is from NASA Lewis Research Center under Grant NSG-3208,

Mr. F. A. Newman, Contract Monitor. This support is gratefully acknowledged.

References

- Adamczyk, J. J., Celestina, M. L., Beach, T. A., and Barnett, M., 1989, "Simulation of Three-Dimensional Viscous Flow Within a Multi-stage Turbine," *ASME JOURNAL OF TURBOMACHINERY*, Vol. 112, No. 3, pp. 370-376.
- Chen, G. T., Greitzer, E. M., Ton, C. S., and Marble, F. W., 1991, "Similarity Analysis of Compressor Tip Clearance Flow Structure," *ASME JOURNAL OF TURBOMACHINERY*, Vol. 113, pp. 260-271.
- Crook, A., 1989, "Numerical Investigation of Endwall/Casing Treatment Flow Phenomena," M. S. Thesis, MIT, Cambridge, MA.
- Freeman, C., 1985, "Tip Clearance Effects in Axial Turbomachines," VKI Lecture Series 1985-05, Apr., pp. 15-19.
- Kirtley, K. R., Beach, T. A., and Adamczyk, J. J., 1990, "Numerical Analysis of Secondary Flow in a Two-Stage Turbine," Paper No. AIAA-90-2356.
- Koch, C. C., 1981, "Stalling Pressure Rise Capability of Axial Compressor Stages," *ASME Journal of Engineering for Power*, Vol. 103, pp. 645-656.
- McDougall, N. M., 1990, "A Comparison Between the Design Point and Near-Stall Performance of an Axial Compressor," *ASME JOURNAL OF TURBOMACHINERY*, Vol. 112, pp. 109-115.
- McDougall, N. M., Cumpsty, N. A., and Hynes, T. P., 1990, "Stall Inception in Axial Compressors," *ASME JOURNAL OF TURBOMACHINERY*, Vol. 112, pp. 116-125.
- Miller, G. R., and Bailey, E. E., 1971, "Static-Pressure Contours in the Blade Passage at the Tip of Several High Mach Number Rotors," NASA TM X-2170.
- Moore, F. K., 1984, "A Theory of Rotating Stall of Multi-stage Compressors," Parts I-III, *ASME Journal of Engineering for Gas Turbine and Power*, Vol. 106, pp. 313-336.
- Moore, F. K., and Greitzer, E. M., also Greitzer, E. M., and Moore, F. K., 1986, "A Theory of Post-Stall Transients in Axial Compression Systems," Parts I and II, *ASME Journal of Engineering for Gas Turbines and Power*, Vol. 108, pp. 231-239.
- Moore, R. D., 1982, "Rotor Tip Clearance Effects on Overall and Blade-Element Performance of Axial-Flow Transonic Fan Stage," NASA TP 2049.
- Nicholas, D. J., and Freeman, C., 1982, "Recent Advances in the Performance of High Bypass Ratio Fans," presented at the 13th Congress of the International Council of Aeronautics (ICAS)/AIAA Aircraft System and Technology Conference, held in Seattle, WA, Aug. 22-27.
- Schweitzer, J. K., and Garberoglio, J. E., 1984, "Maximum Loading Capability of Axial Flow Compressors," *J. Aircraft*, Vol. 21, No. 8, pp. 593-600.
- Smith, L. H., 1970, "Casing Boundary Layers in Multi-stage Compressors," *Proceedings of the Symposium on Flow Research on Blading*, Elsevier Publishing Company.
- Strazisar, A. J., Wood, J. R., Hathaway, M. D., and Suder, K. L., 1989, "Laser Anemometer Measurements in a Transonic Axial-Flow Fan Rotor," NASA TP 2879.
- Wennerstrom, A. J., 1984, "Experimental Study of a High Through-Flow Transonic Axial Compressor Stage," *ASME Journal of Engineering for Gas Turbines and Power*, Vol. 106, pp. 552-560.
- Wisler, D. C., 1985, "Loss Reduction in Axial-Flow Compressors Through Low-Speed Model Testing," *ASME Journal of Engineering for Gas Turbines and Power*, Vol. 107, pp. 354-363.

L. H. Smith¹

In Fig. 7 it is seen that the calculated peak pressure rise is reduced from 0.74 to 0.66 (11 percent) as the tip clearance/chord ratio is increased by 1 percent from 0.25 to 1.25. This is a rather large effect; some time ago this discussor correlated mostly subsonic test data and concluded that the slope should be more like 5 percent for 1 percent clearance/chord ratio. Could the authors clarify how the tip clearance flow was modeled in their calculations?

N. A. Cumpsty²

This is a very useful contribution to our understanding of the difficult problem of tip clearance flow. I think that our understanding could be further helped if the authors would complete the test cases given in Fig. 16 and show the effect of having clearance near the front of the blade but zero clearance near the rear.

It is in a multistage compressor where the hub-casing radius ratio is relatively high that the effect of tip clearance flow is often experienced most acutely. I would like to encourage the authors to continue this work to look at stages more typical of a multistage compressor, in particular looking at the numerical instability when the flow is largely or entirely subsonic.

Authors' Closure

The authors thank Dr. Smith and Professor Cumpsty for their interest in the results given in the paper. We regret that we were not more explicit in describing the clearance model used in the numerical simulations. As modeled, the full clearance height is the height of the leakage jet; this is a consequence of the simple description that was adopted for the jet flow. The clearance that would exist in an actual rotor are therefore larger than the values quoted in the paper. The proportionality between actual and quoted clearance, which is associated with the occurrence of a vena contracta, is not certain. The value for this ratio obtained from "classical" free streamline theory is $\pi/(\pi+2)$, or 0.611, but Storer and Cumpsty (1991) used a higher value (0.8) to match data in their cascade, and computations of Chen et al. (1991) imply a contraction coefficient of roughly 0.7.

For the present rotor, the value of 0.5 is judged to be the most appropriate. This value was found to give best agreement with measurements of the peak pressure rise at one value of clearance. Based on that study, the magnitude of clearance used in the calculations (and specified in the paper) would be viewed as one-half the actual clearance. The sensitivity of peak pressure rise to clearance would therefore be only half as great as for an actual rotor, i.e., the sensitivity obtained from the computations should be multiplied by a factor of one-half for

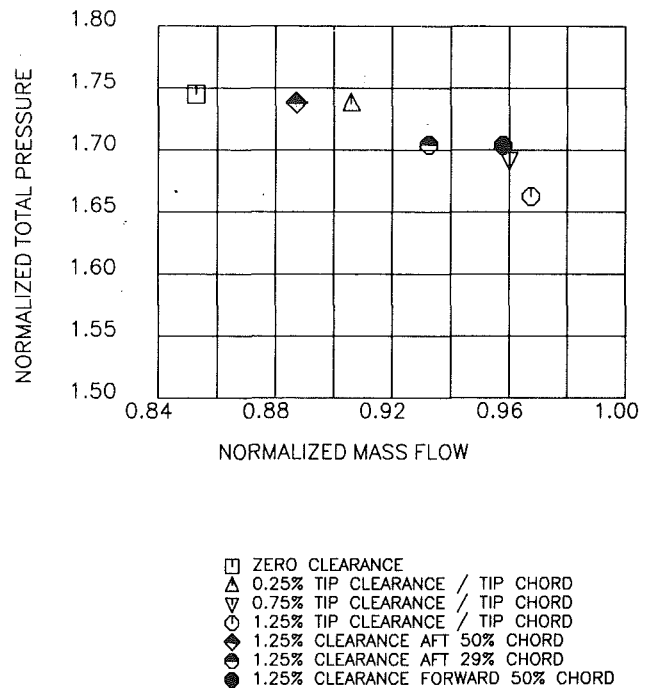


Fig. 19 Predicted pressure ratio at near-stall points for tip clearance/tip chord ratios of zero, 0.25 percent, 0.75 percent, and clearance of 1.25 percent aft of 29 percent and 50 percent chord and forward of 50 chord

comparison with rotor data. Doing this yields results for the change of peak pressure rise with clearance that are closely in accord with the results of the experiments described by Dr. Smith.

Based on Professor Cumpsty's suggestion, we have executed a simulation in which the clearance from the leading edge to midchord was set at 1.25 percent of blade chord, while aft of midchord the clearance was set to zero. The predicted peak pressure ratio and corresponding mass flow are indicated by the solid octagon in the accompanying figure, along with the results previously presented in Fig. 16. By opening the clearance over the forward 50 percent of chord, the peak pressure and corresponding mass flow are nearly those for the same clearance over the entire blade chord. However, as previously shown, for clearance over the aft 50 percent of chord, zero clearance over the forward 50 percent chord, the peak pressure and corresponding mass flow lie closer to those for zero clearance.

The computations show that the clearance over the forward portion of a fan blade is far more important than that over the aft portion of a blade in establishing the peak pressure rise of a fan. Further, by reducing the clearance to zero over the forward portion of a fan blade, the interaction between the in-passage shock and the clearance vortex is reduced, leading to an increase in the operating range.

References

- Chen, G.-T., Greitzer, E. M., Tan, C. S., and Marble, F. E., 1991, "Similarity Analysis of Tip Clearance Flow Structure," *ASME JOURNAL OF TURBOMACHINERY*, Vol. 113, pp. 260-271.
- Storer, A. J., and Cumpsty, N. A., 1991, "Tip Leakage Flow in Axial Compressors," *ASME JOURNAL OF TURBOMACHINERY*, Vol. 113, pp. 252-259.

¹GE Aircraft Engines, One Neumann Way, M/D A322, Cincinnati, OH 45215.

²Whittle Laboratory, Cambridge University, Madingley Rd., Cambridge, CB3 0DY, United Kingdom.

Active Suppression of Rotating Stall and Surge in Axial Compressors

I. J. Day

Whittle Laboratory,
Cambridge University Engineering
Department,
Cambridge, United Kingdom

This paper reports on an experimental program in which active control was successfully applied to both rotating stall and surge in a multistage compressor. Two distinctly different methods were used to delay the onset of rotating stall in a four-stage compressor using fast-acting air injection valves. The amount of air injected was small compared to the machine mass flow, the maximum being less than 1.0 percent. In some compressor configurations modal perturbations were observed prior to stall. By using the air injection valves to damp out these perturbations, an improvement of about 4.0 percent in stall margin was achieved. The second method of stall suppression was to remove emerging stall cells by injecting air in their immediate vicinity. Doing this repeatedly delayed the onset of stall, giving a stall margin improvement of about 6.0 percent. Further studies were conducted using a large plenum downstream of the compressor to induce the system to surge rather than stall. The resulting surge cycles were all found to be initiated by rotating stall and therefore the stall suppression systems mentioned above could also be used to suppress surge. In addition, it was possible to arrest the cyclical pulsing of a compressor already in surge.

Introduction

Compressor performance at the peak of the pressure rise characteristic is limited by aerodynamic instabilities, which lead to rotating stall and surge. Rotating stall is a localized disturbance affecting the compressor only and leads to excessive blade vibration. Surge, on the other hand, is a system oscillation associated with reversed flow transients, and these cause unusual stresses in the compressor. The accepted way of avoiding these dangers is to restrict the compressor to an operating point safely removed from the stability boundary. The stability boundary, however, is often ill defined, being affected by engine acceleration, inlet distortion, and deterioration with age, and therefore the safety margins allowed are generous. To decrease the need for wasteful safety margins, and thus increase the useful operating range of the compressor, Epstein et al. (1986) first suggested in the open literature that active control techniques might be employed to delay the onset of stall or surge.

In the context of the proposals put forward by Epstein et al., stall and surge are seen as limit cycles whose final strength is set by nonlinear effects. In origin, however, these disturbances start out as small perturbations and, if treated early enough, can be modeled by linear theory. Active control as envisaged by Epstein et al. would be applied at this linear stage of development and would require the feedback of additional disturbances into the flow field. These disturbances would have the effect of increasing the damping in the system and would

thus restrict the growth of the original perturbation. The additional disturbances would be created by a system of actuators driven by a controller using real-time measurements from inside the compressor. A control system such as this would require minimal input effort and would allow the compressor to operate safely at flow rates that would otherwise have been unobtainable.

Alternative stall suppression systems have been proposed in the past, using controllers that sensed the approach of stall and took remedial action fast enough to prevent the disturbances from developing. Ludwig and Nenni (1980) suggested using fast blow-off valves and Reis and Blocker (1987) proposed a system using rapid rescheduling of the stator vanes. This type of control is achieved simply by unloading the compressor and is termed avoidance control. In practice neither of these approaches falls into the category of true active control, as defined herein, since neither interferes with the unsteady aerodynamic damping in the compressor.

The conceptual difference between active control and stall avoidance control is illustrated in Fig. 1. In this comparison the avoidance control makes use of a fast blow-off valve, while the active control system is based on continuous stabilizing feedback. Both systems allow the compressor to deliver at a lower than usual mass flow rate while avoiding stall, but in each case the true operating point of the machine is very different. With active control the blade loading is pushed to higher values without the basic fluid mechanic processes, by which the pressure rise is produced, being altered. In the case of the blow-off valve, the effective operating point of the machine is kept on the stable side of the characteristic by dumping excess air. The bleed valve approach is less efficient and, unlike

Contributed by the International Gas Turbine Institute and presented at the 36th International Gas Turbine and Aeroengine Congress and Exposition, Orlando, Florida, June 3-6, 1991. Manuscript received at ASME Headquarters February 19, 1991. Paper No. 91-GT-87. Associate Technical Editor: L. A. Riekert.

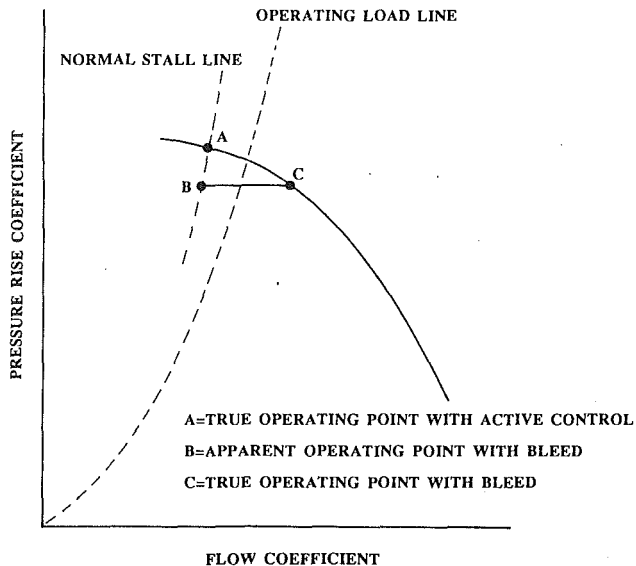


Fig. 1 Schematic of compressor characteristic emphasizing the difference between active control and control using a bleed valve

active control, the pressure rise will be lower if a safety margin is to be maintained.

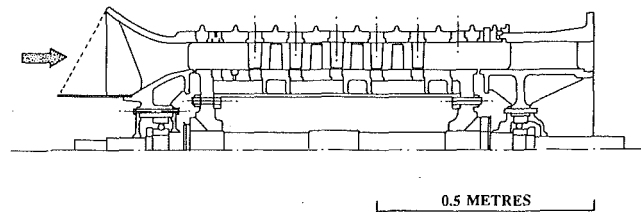
In the approach to active control suggested in the literature, the initial phase of stall development is modeled in terms of long length scale disturbances of small amplitude. Stall inception measurements by McDougall et al. (1990) and Garnier et al. (1991) have shown that in some instances stall cells do develop from such beginnings, but this is not always the case. It has been shown by Day (1993) that emerging stall cells, representing short length scale disturbances, can originate without any detectable precursive build-up. This means that linear modeling will not cover the whole range of stall inception possibilities, and that active control will be more complex to apply than originally envisaged.

Disturbance of long length scale, i.e., modes, can be damped out through the feedback of counteracting disturbances. Stall cells emerging without precursive build-up cannot be treated in this way. It will be shown below, however, that these cells are limited in circumferential and radial extent and, as such, are amenable to localized corrective action. Stabilization in this case does not depend on increasing the damping in the system, but rather on energizing the flow in the vicinity of the blade tips and thus making it more disturbance tolerant. This approach, like that applied to longer length scale disturbances, requires minimal input effort and therefore can be included in a broad definition of the term "active control."

The details of stall inception in the C106 compressor will be considered below, showing why two different approaches to stall suppression are necessary. The experimental results covering the damping of modal waves, and the elimination of unannounced stall cells, will then be considered. Finally it will be shown that surge inception is initiated by rotating stall, and the use of stall suppression to avert surge will be demonstrated.

Stall Inception Measurements in a Four-Stage Compressor

The four-stage compressor chosen for these experiments is one of those used in a wider study of stall inception by Day (1992). The machine is a low-speed research compressor with four identical stages preceded by a lightly loaded set of inlet guide vanes. The hub-casing radius ratio is 0.75. The blading is of modern controlled diffusion design and is intended to be representative of current high-pressure compressor practice. A



THE C106 FOUR STAGE COMPRESSOR
Mid-Height Blading Details and Other Parameters

	Rotor	Stator
Solidity	1.47	1.56
Aspect Ratio	1.75	1.75
Chord (mm)	35.5	36.0
Stagger (deg.)	44.2	23.2
Camber (deg.)	20.0	40.6
No. of aerofoils	58	60
No. of IGVs		60
Axial Spacing (mm)		13.0
Tip diameter (mm)		508
Hub/Tip ratio		0.75
Speed of Rot. (rpm)		3000
Reynolds Number		1.7×10^5

Fig. 2 Cross-sectional view of the C106 compressor with table of basic design details

concentric throttle was used, either close coupled to the compressor for rotating stall studies, or mounted downstream of a large plenum for the study of surge. A schematic diagram is shown in Fig. 2 along with some basic design values.

To map out the stalling behavior of the compressor, a number of hot wires equally spaced about the circumference of the machine were used. The wires could be positioned at almost any axial location throughout the compressor and several axial stations could be examined simultaneously. It was found that the stall cells always originated near the tips of the first-stage rotor blades and then spread in both the radial and axial directions. A stall cell could be detected at the back of the machine roughly one full revolution after being seen in the front; this was also about the time needed for the cell to spread from the casing to the hub on the first stage.

In terms of the way the compressor goes into stall, the pattern of finite cell formation is always the same, regardless of whether modal (long wavelength) perturbations are present or not. A small sharply defined stall cell, four or five blade pitches wide, forms abruptly near the first-stage rotor tips and rotates around the annulus at about 70 percent of rotor speed. As the cell grows radially and circumferentially, the speed of rotation slows down until after about four complete revolutions the cell is fully formed and moving at about 38 percent of rotor speed. A typical example of cell formation, without a modal perturbation being present, is given in Fig. 3. The outputs from four hot wires equally figure a stall cell appears abruptly at about rotor revolution 16. No form of precursive build-up to the cell can be detected, even when the data are spatially and temporally decomposed.

In some experiments, where the tip clearance over the first rotor was increased from 1.2 to 1.5 percent chord, modal waves appeared in the compressor prior to stall. These waves represent a small amplitude velocity perturbation and may be thought of as the linear phase of the approach to rotating stall. The perturbation is detectable right throughout the compressor and in the incoming flow. An example of cell formation accompanied by these waves is given in Fig. 4. Besides the waves, the point to note is that when the stall cell appears (at time $t = 17$) its dimensions, speed of rotation, and rate of growth are the same as in Fig. 3. In other words the stall cell does not appear to be a continuous development of the modal wave,

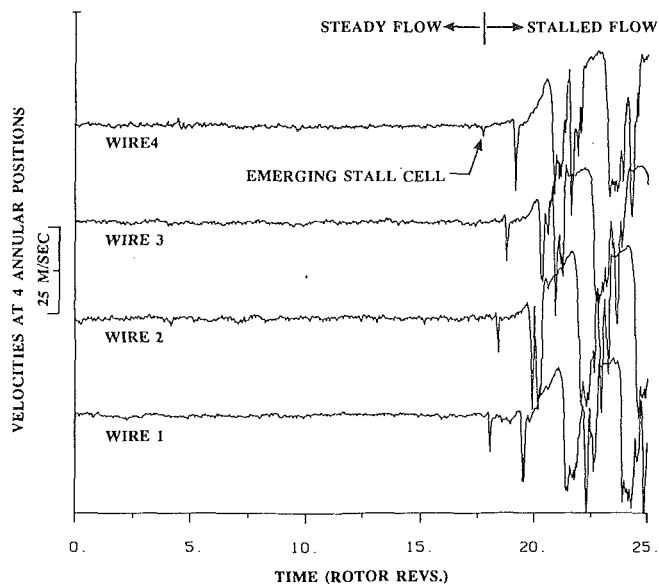


Fig. 3 Hot-wire measurements showing a small finite stall cell emerging from a steady flow field (mean axial velocity prior to stall ~ 30 m/s)

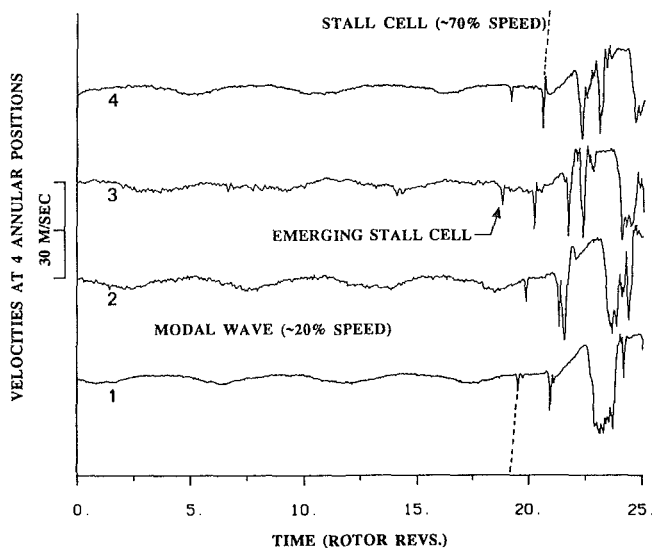


Fig. 4 Hot-wire measurements showing a small finite stall cell emerging from a flow field perturbed by a clear modal wave

but rather a separate disturbance, which appears despite the presence of the modal wave. Repeated measurements show, however, that the two phenomena are not totally unrelated. The trough of the modal wave represents a deficit in the throughflow velocity and this often provides a natural starting place for the stall cell. (The details of stall inception in this compressor are discussed in greater detail in a companion paper by Day, 1993.)

The experiments from the C106 therefore imply that, although modal perturbations are sometimes present, they do not appear to be the cause of stall. Fully developed stall only occurs after the formation of a short length scale stall cell, so that limited scope exists for a linear interpretation of stall build-up in this compressor. Recent experiments on a real engine confirm, however, that the C106 is a representative machine and as such provides an appropriate vehicle on which to examine stall suppression. In the work described below two approaches to stall suppression have been investigated. The first is based on suppression of the modal wave (when the modal wave exists) and the second introduces a new technique of flow energizing applied directly to the emerging stall cell. The latter

approach is applicable whether the modal wave is present or not.

The Control System

To implement stall suppression, a system of actuators was necessary to interact with the flow field in the compressor. Numerous ideas, including tip clearance control and actuated inlet guide vanes, were considered but in the end an air injection system was selected. (Use of actuated inlet guide vanes is described by Paduano et al., 1993.) An array of twelve individually controllable valves was designed and built. These valves were to be positioned near the tips of the first rotor as this is where the stall cells were known to first appear. (An alternative to the 12-valve system was also developed for use in some of the early experiments. This system, described more fully below, consisted of a ring of 60 small air injection slots, fed by a single valve.)

To make room for the air injection valves (and the ring of slots) the inlet guide vanes were moved upstream by one chord length. These vanes are lightly loaded and tests showed that this move did not affect the stalling pattern in any way. The 12 trapdoor-type valves were then interposed between the inlet guide vanes and the first rotor. The valves were equally spaced around the circumference. The valve flaps were about 25 mm square, hinged along one side, and were flush with the outer casing of the annulus when closed. When open, about 3 mm, air was emitted into the mainstream of the compressor near the outer casing wall. Each valve was housed in a cylindrical housing and could be rotated about its axis so that the direction of the air injection could be varied. A schematic of the valves is shown in Fig. 5.

The injected air was supplied by an outside source. When all 12 valves were open at the same time, a total of 1 percent of the compressor flow rate at stall was consumed, i.e., each valve passed a flow equal to about 1/12th of 1 percent. This satisfies the basic requirement that the control effort expended should be minimal in comparison with the power of the compressor. The maximum velocity of the air leaving the valves, when measured just downstream of the valve opening, was about 1.5 times the mean axial velocity in the compressor. To drive the valves, an on-off signal was supplied, either by an analog controller, or by a minicomputer. Testing with a square wave signal generator gave a maximum frequency response of about 140 cycles per second, i.e., about three times rotor frequency or seven times stall cell frequency.

Experimental Results

1 Suppression of Modal Waves. The air injection valves could be used in a variety of different ways to delay the onset of stall. We consider first the case where modal waves appear in the compressor prior to cell formation. As pointed out earlier, the modes in this compressor do not appear to turn into stall cells themselves, but rather generate a localized dip in the throughflow velocity where stall cells tend to start. By reducing the amplitude of the modal waves, and so removing the localized velocity deficit, the average flow rate through the machine can be lowered slightly without causing stall. As the axial velocity dips associated with the modal waves do not usually grow to more than a few percent of the mean axial velocity, it may be conjectured that the decrease in mass flow at stall onset would only be of the same order.

With sufficient hot wires around the circumference, the velocity distribution at any time can be treated with a discrete Fourier transform to obtain a measure of the amplitude and phase angle of any modal perturbation. Repeating this process at each sampling interval, the growth and position of the modal wave can be tracked from well before stall until the stall cells are essentially fully developed. An example is given in Fig. 6

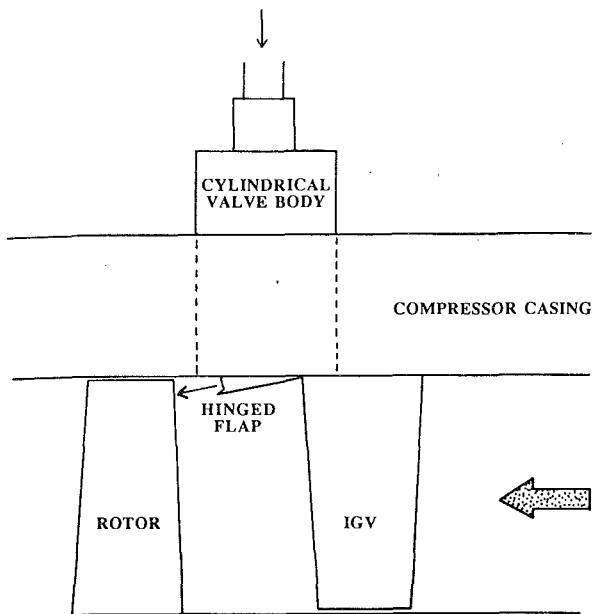


Fig. 5 Schematic picture of trapdoor-type air injection valve

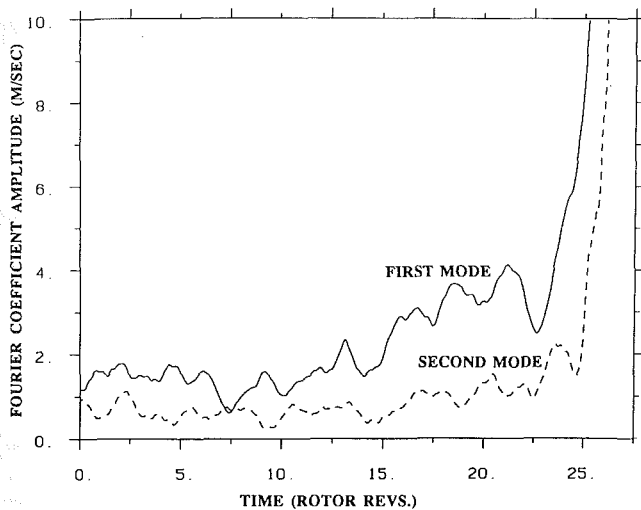


Fig. 6 Amplitude of first and second circumferential modes measured as the compressor goes into stall

where the amplitudes of the first and second-order modes are plotted for the compressor approaching stall. The first mode is clearly dominant in this case. The amplitude of this mode rises progressively until, at revolution 26, a finite stall cell is formed. The point of finite cell formation can be seen quite clearly at revolution 26 in the original data from which this figure was obtained. Furthermore, the phase angle plots of this data show that the first-order mode is well defined and rotates steadily around the annulus. The second-order mode is ill defined and the phase angles show a total lack of coherence.

The 12 air injection valves could be used to damp the modal oscillation shown in Fig. 6. To achieve this, the outputs from six hot wires were used in conjunction with an analogue computer to open and close the valves. Full proportional control was obviously not possible using a discrete number of valves that are not amplitude controlled, i.e., the valves were either open or closed, but could not be held at an intermediate position. Effective damping could, however, be achieved by judicious adjustment of the number of valves in use at any time

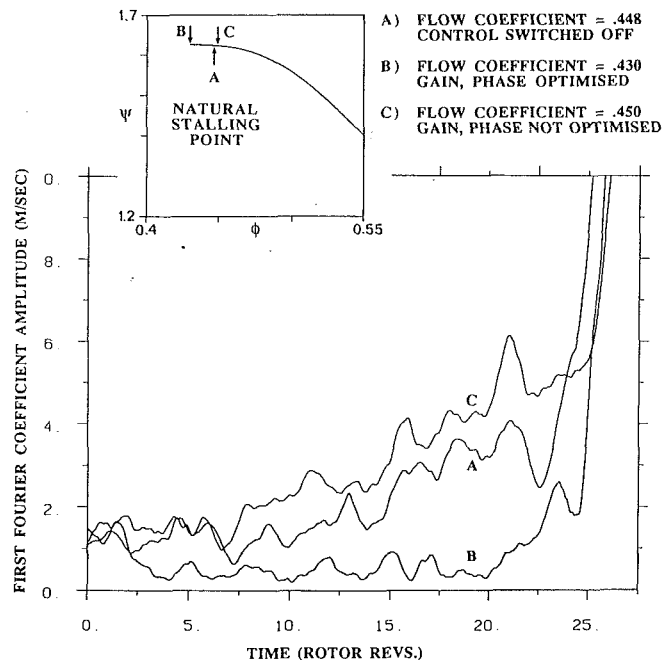


Fig. 7 Amplitude of first circumferential mode going into stall for different control options: Note that each complete data trace was recorded at a different throttle setting

and by varying the opening times and the supply pressure to the valves. The results using this scheme are shown in Fig. 7.

Figure 7 is actually a composite picture made up of Fig. 6, trace A, plus two other sets of measurements using the air injection valves. Only the first-order modal amplitudes are displayed in this case. The trace marked "B" shows how, with control system in operation, the velocity perturbations can be kept to a relatively low value right up to the point at which the compressor stalls. The inset diagram shows that in this case the compressor characteristic was extended beyond the natural stalling limit; the benefit achieved represents about 4 percent reduction in stalling flow rate. The third trace in Fig. 7, trace C, shows the effect of deliberately offsetting the phase shift in the controller so that the action of the valves exacerbates the modal perturbations. When this is done the compressor stalls prematurely. In interpreting Fig. 7 it should be emphasized that the three sets of results each show a snapshot of what happens during the last half second as the compressor goes into stall and it should be emphasized that the results were obtained at very different throttle settings. In other words, the data traces have been overlaid on a common time axis for comparative purposes only.

When the compressor goes unstable with the control system working effectively (trace B) it is interesting to note that stall does not occur because the controller loses authority over the long length scale modes. It is rather that a short length scale disturbance, a stall cell, appears in the flow field and grows within about four revolutions to become a fully developed cell. The original data from which trace B was derived are shown in Fig. 8 to emphasize that this compressor stalls through the formation of a small fast-moving stall and not through the exponential growth of a modal perturbation. (It should be stressed that the hot-wire signals shown in Fig. 8 were more severely filtered than in Figs. 3 and 4, and were AC coupled for compatibility with the control system. The emerging stall cell therefore appears less sharply defined than in the previous figures.)

2 The Suppression of Finite Stall Cells. Whether modal perturbations are present or not, the C106 compressor always ends up in rotating stall shortly after the appearance of a small

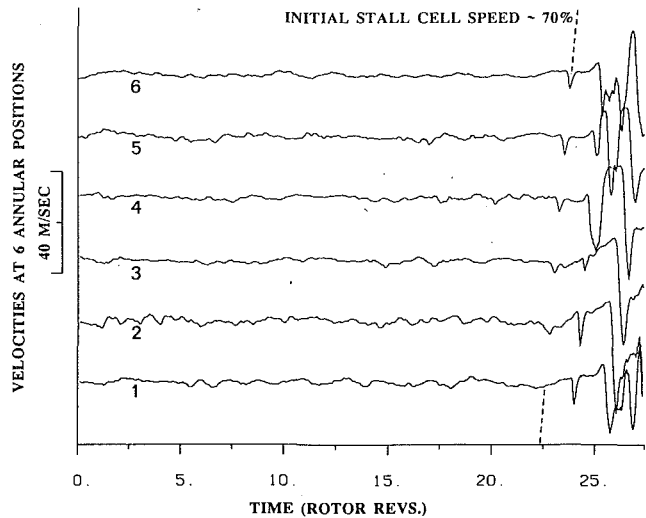
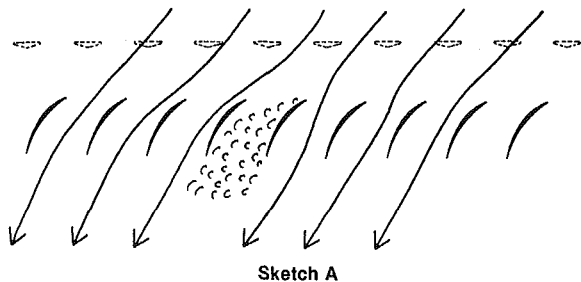


Fig. 8 Hot-wire measurements recorded while control system in operation; a coherent modal pattern is not detectable prior to the formation of a small finite stall cell

sharply defined stall cell. Direct interference with the stall cell itself may therefore be an effective method of extending the compressor operating range. A useful way of visualizing these small stall cells is to use a flow picture first suggested by Emmons et al. (1955). In Sketch A the separated flow in one of the blade passages is shown diverting the incoming streamlines to either side of the affected area. Emmons suggested that the resulting increase in incidence on one side of the separation, and the decrease on the other, provides a mechanism for the disturbance to propagate from blade to blade around the machine. While this picture may not be accurate in all respects, it provides a useful means of visualizing how air injection might be used to energize the flow field and remove the blockage. The direction in which the air is injected plays an important part in the process. As drawn, Sketch A also emphasizes the fact that the stall cell is a localized disturbance and therefore localized corrective action may be appropriate.



To test the idea initially of using injected air to correct the flow in a localized disturbance, it was decided to use a very simple injection system consisting of one fast-acting valve, a manifold, and a row of small directional slots. The relative size and position of these slots is indicated in Sketch A. The principle is the same as in the case of the trap-door valves, i.e., to inject air near the casing wall at the rotor tips where the stall cells are known to appear first. Using a manifold arrangement means that there is an inherent delay in the response time of the system, but this was kept to a minimum. The quantity of the air injected through the slots was limited to a total of 1 percent of the compressor flow rate. An array of eight probes was used to detect the emerging stall cell anywhere in the annulus and the central valve was opened immediately thereafter. The use of continuous air injection to delay the onset of stall is not a new concept. However, the use of air injection to remove a stall cell that has already become

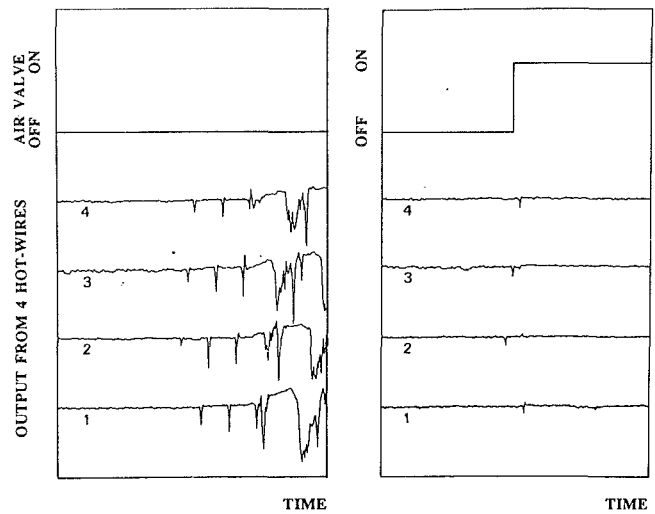


Fig. 9 Hot-wire measurements showing stall cell developing without air injection (LHS), and truncation of cell development with air injection (RHS)

a finite amplitude disturbance has not been tried before. The results are important because they show that stall control *after* cell formation is a viable proposition.

Figure 9 illustrates the operation of the system. The left-hand side of the figure shows the compressor going into stall naturally (without the control system being used). The right-hand side shows that opening the air injection valve as soon as the cell is detected will suppress the cell. The delay in the response of the system meant that the stall cell executed one complete revolution before the injected air could affect it. This delay in response was acceptable in this case because the stall cell developed relatively slowly. Increasing the delay time in the detection system by just a half cell revolution more meant that the cell had time to grow bigger and the air injection system became ineffective.

In the right-hand half of Fig. 9, the air supply was maintained after the stall cell had disappeared. If the supply were removed at some stage, a new stall cell would appear and the air supply would again be required. This on/off approach was tried by allowing the central valve to close again after a set number of milliseconds if no cells were detected. Figure 10 shows the result of such a test where air is injected only when required; it also shows that if the detection system is switched off the compressor goes into stall. (It is interesting to note that after the cell is suppressed a new cell does not appear instantly. There is usually a delay of erratic duration, anything between 2 and 8 rotor revolutions.) When the throttle is moved toward the point where the control system becomes ineffective, the stall cells still form in the normal way, but their intensity deepens more quickly. Eventually a point is reached where the injected air only reaches the cells once they have already grown too big to be suppressed.

The decrease in stalling mass flow obtained with this type of on/off suppression system was about 6.0 percent, as illustrated in Fig. 11. The characteristic shown was measured by sampling and averaging the output from the pressure rise and mass flow transducers as the throttle was being closed. No filtering was used and the jagged nature of the line is due to normal unsteadiness in the pressure rise and mass flow readings. While a 6.0 percent stall margin improvement is not particularly useful, it is an encouraging start, especially for a system that has not been optimized in any way and only has control applied to the first of four stages. The control system does not appear to affect the overall trend of the characteristic, which is extended horizontally. This shows that the action of the air jets is primarily to suppress cell formation rather than to change the basic flow pattern in the machine.

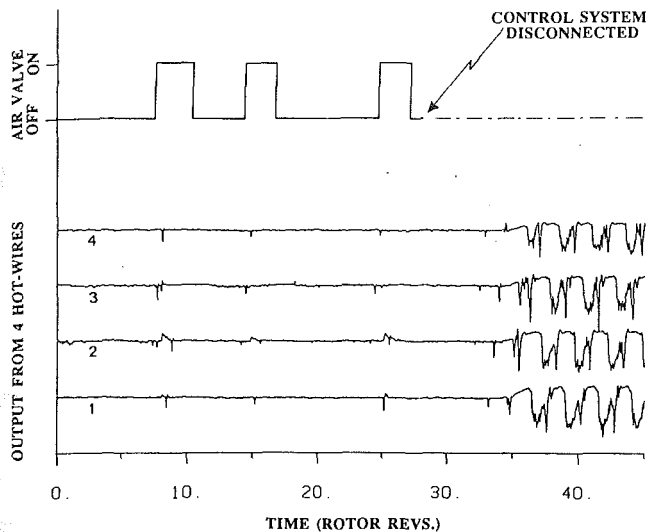


Fig. 10 Measurements showing air injection being switched on only when necessary (LHS); at time $t = 29$ the control system is disconnected and the compressor stalls

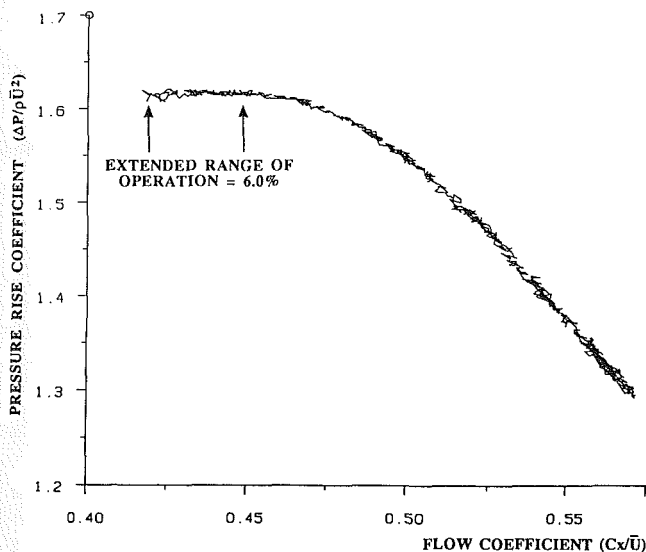


Fig. 11 Automatically recorded compressor characteristic showing the extended range of operation achieved with active stall suppression

Because the stall cells in the C106 compressor appear as localized disturbances, it was hypothesized that the action needed to remove them could also be localized. Using the 12 independently controlled valves and 12 detection probes, a system was configured so that only the valves nearest the stall cell need open at any time. Knowing the typical speed of rotation of the cell, a suitable phase shift was introduced so that no matter where the stall cell first appeared, a valve could be opened in time to coincide with its passing. As before, each valve was automatically closed after a short time if no further disturbance was detected.

Figure 12 shows the opening and closing sequence of 6 of the 12 valves (each alternative valve) when operating in this way. It can be seen that in some cases the action of just one valve was needed to remove a cell, whereas in other cases additional valves were brought into play. This localized approach to cell suppression worked well, especially when two valves were opened at a time, 180 deg apart. (This strategy was employed because it balanced out the one-sided effect of using just one valve.) The stall margin improvement was only 5.0 percent less than in the previous experiment; but this is

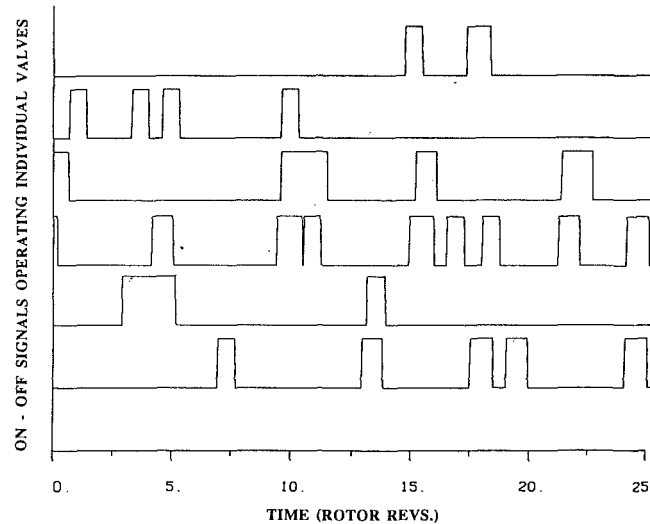


Fig. 12 The on-off signals driving 6 of the 12 air injection valves during operation beyond the natural stall limit

not surprising given that there were only 12 discrete injection points as opposed to 60 in the previous case. The localized approach has the advantage of using much less air, there seldom being more than two valves open at any time.

3 The Suppression of Surge. The compressor could be made to exhibit surge rather than pure rotating stall by using a large plenum between the compressor and the exit throttle. Surge is basically the interaction between stall and recovery in the compressor, and the dynamics of the gas stored in the plenum chamber. Two types of surge cycles have been observed, labeled as “classic surge” and “deep surge” by Greitzer (1976). Classic surge does not involve any significant reversed flow in the compressor, while deep surge does. The C106 system only exhibited deep surge, and therefore no experiments were possible on classic surge. It should be mentioned, however, that deep surge is the more prevalent type, occurring at the high speeds and pressure ratios used in aero-engines.

Measurements from a typical surge sequence are shown in Fig. 13 where the plenum pressure and the output from a single hot wire at the front of the compressor are plotted. At the left of this figure the compressor is operating unstalled and the throttle is slowly being closed, thus moving the operating point toward the surge line. At time $t = 25$ the compressor goes into rotating stall. In doing so it loses its ability to support pressure rise and the plenum air blows back through the compressor. This process eliminates the stall cell and sets up a (temporary) regime of axisymmetric reversed flow. The plenum pressure then drops rapidly until a point is reached at which the compressor can re-establish forward flow and start filling the plenum again. The pressure in the plenum then rises back to peak value, where the compressor again stalls and the same sequence of events re-occurs.

In Fig. 13 the compressor momentarily exhibits rotating stall on two occasions, the first after a period of steady operation ($t = 25$), and the second after refilling of the plenum ($t = 145$). The number of stall cells that form on these two occasions may differ noticeably, but in each case the cells are of the type described previously, i.e., small, sharply defined, and initially rotating at about 70 percent of rotor speed. A single stall cell is most likely to form at the start of the first cycle while groups of multiple cells are more likely thereafter. In each case, however, the surge cycle is initiated by this burst of rotating stall. An example is given in Fig. 14 where the stalling and recovery phase of a typical first cycle is presented. Six hot wires were used here to illustrate how, at the start of the surge cycle, a

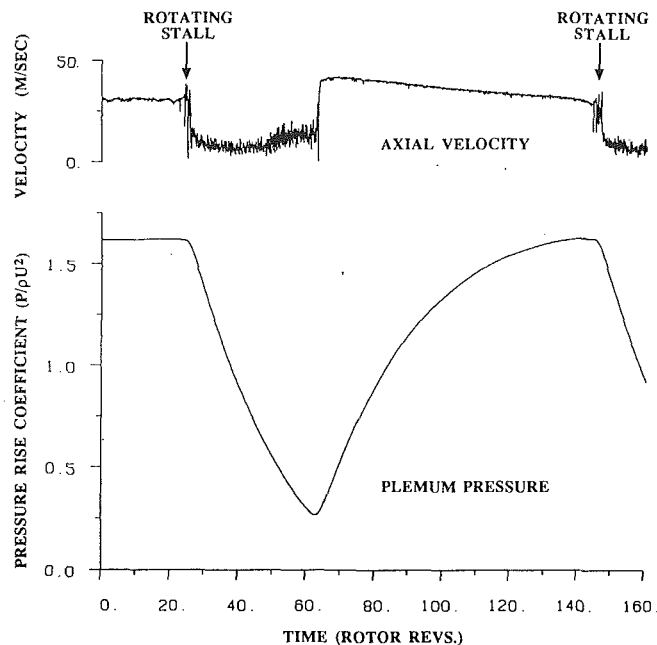


Fig. 13 Measurements of axial velocity and plenum pressure during a typical surge cycle

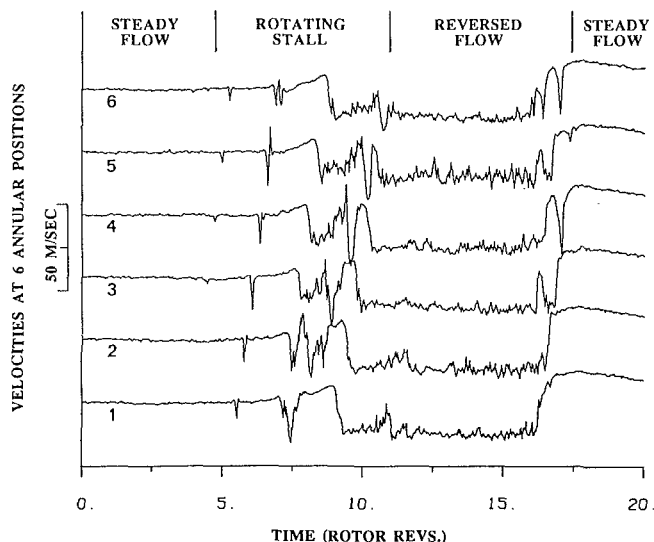


Fig. 14 Hot-wire measurements showing stall cell development and reversed flow during a typical surge cycle

single stall cell forms and grows and then decays as the annulus becomes engulfed in reversed flow.

The above description of surge inception shows that rotating stall is always the precursor of a surge cycle. Any active suppression technique that delays the onset of stall will therefore also be effective in delaying surge. Experiments carried out with the same stall cell detection and elimination procedures described above showed a mass flow decrease at instability of 5 or 6 percent, just as with pure rotating stall. If the compressor is allowed to surge without control, and the throttle position is unchanged, repeated surge cycles will occur, each one being triggered afresh by rotating stall. Switching on the rotating stall suppression system while the compressor is in such a repeating surge sequence will therefore arrest the next surge cycle and hold the compressor in a stable condition.

The results of an experiment to demonstrate this point are shown in Fig. 15, where the output from a single hot wire is displayed on a compressed time scale. The system can be seen

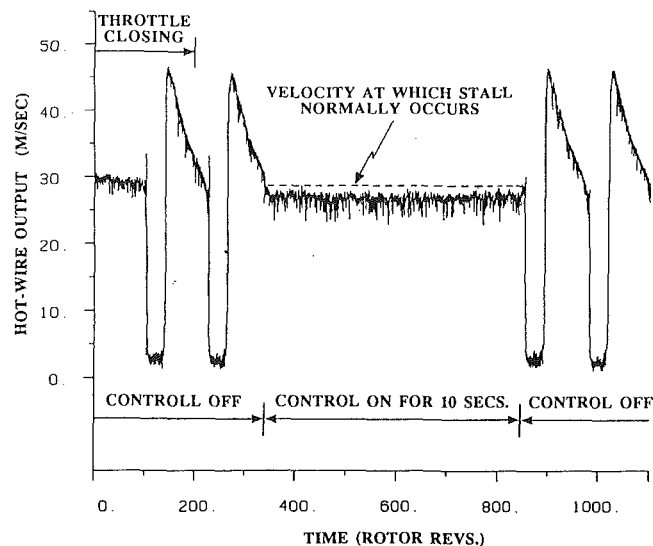


Fig. 15 Example of the use of stall suppression to stabilize a surging compressor (control system switched on 10 s only)

to go through two surge cycles before the controller is switched on. In this case, the 12 trapdoor valves were used, and after being triggered to open by cell formation in the compressor, all the valves were held continuously open for 10 s before being closed. The reason for doing this was to be sure that the action of the valves is purely to hold off the formation of stall cells rather than to interfere with the dynamics of the surging process. Using the control system in the stall suppression mode to open and close the valves automatically, either all at once or one at a time, also worked successfully. To highlight the effectiveness of the control system, a horizontal line has been drawn in Fig. 15 to indicate the throughflow velocity at which the compressor first started to surge. During the first cycle the throttle was closed a bit further to show that the system could be stabilized at a flow rate lower than is normally possible. The surge sequence was therefore arrested even though the compressor operating point was to the left of the usual surge boundary. After a period of 10 s the controller was switched off and the surging sequence began again.

(In Figs. 13 and 15, the hot-wire velocity traces do not go below zero even though other measurements confirm that reversed flow does occur during part of the surge cycle. This is because the hot-wire system sees only the modulus of the velocity and so the negative velocity component is returned as a positive value. The changeover from forward to reversed flow occurs during the period of rotating stall and therefore no clear zero velocity point is seen.)

Discussion

The work presented here was started without formal ideas of how active suppression of stall should be implemented. The C106 compressor was chosen as the test vehicle and the subsequent experiments were based solely on the observed stalling behavior of the machine. At the start it was unknown whether the C106 compressor might be unique in the way that it stalled. Additional work on stall inception by Day (1993) on other compressors, and recent measurements from a real engine have, however, shown that the behavior of the C106 is representative and that the stall suppression techniques developed here can be applied in other situations as well.

In terms of stall inception, flow breakdown in the C106 compressor is always initiated by the abrupt appearance of a small localized disturbance, which at first rotates at about 70 percent of rotor speed. The disturbance usually covers just the tip region of four or five blade passages on the first rotor. In some instances, prior to the formation of this kind of dis-

turbance, a more global perturbation of the flow through the compressor is detected. This perturbation, usually referred to as a mode, rotates at a comparatively low speed (20 percent of rotor speed) and does not itself grow to become a finite stall cell. Instead the trough of the perturbation wave appears to provide a starting point for the formation of a localized disturbance. It is this localized disturbance, and not the modal perturbation itself, which is responsible for the collapse of the pressure rise.

In response to this picture of stall inception, two basic experiments were performed; the first to damp the modal perturbation so as to remove its promotional effect on cell formation, and the second to remove the emerging stall cell itself. When modal perturbations occur, damping of these disturbances delays the onset of stall by allowing the average throughflow velocity to decrease without anywhere falling low enough to trigger the formation of a localized stall cell. Whether modal perturbations are present or not, repeated elimination of the stall cells themselves also improves the stall margin by removing disturbances that would otherwise lead immediately to a complete collapse of the pressure rise. Ideally these two approaches to stall suppression should be applied simultaneously to obtain maximum benefit. In the current experiment the existing valve configuration, which only has twelve valves, is not versatile enough to operate in both the global and localized mode at the same time. The stall margin improvements achieved are nonetheless encouraging.

In discussing the approach adopted here, it should be emphasized that while a large number of compressors stall in the same way as the C106, there are others that do not. Measurements in the Deverson rig in Cambridge by McDougall et al. (1990) and Day (1992), and at M.I.T. by Garnier et al. (1991) suggest that in some instances modal perturbations can grow progressively into stall cells, i.e., stall cells may originate on a global rather than a localized scale. The work presented here, although focused mainly on stall cells of small dimension, suggests that air injection as a means of active control would also be applicable in machines that stall progressively. Air injection has the added advantage that in an aero-engine application high-pressure air can easily be ducted from the rear of the compressor to suppress any stalling tendency originating at the front of the machine.

Conclusions

1 The suppression of stalling disturbances using fast-acting air injection valves has been shown to be both practical and effective in two different stall onset processes.

2 Modal perturbations of long length scale have been detected in a four-stage compressor and have been suppressed using feedback of controlled disturbances. In the compressor used here, the modes do not appear to be the primary cause of stall, but rather promote the formation of finite stall cells by producing a localized deficit in the velocity distribution. Suppressing the modal waves produced a 4.0 percent mass flow rate improvement in stall margin.

3 Short length scale stall cells, emerging without precursive build-up, are of localized extent and can therefore be removed by local, rather than global, action. Elimination of these stall cells has been proved possible and stall margin improvements of 5 or 6 percent have been achieved in a multistage compressor.

4 The need to control long *and* short length scale disturbances has been demonstrated by this work. The effective application of active control will therefore present a greater challenge than originally thought.

5 The control effort needed to suppress both types of disturbance has been shown to be minimal in comparison with the power of the compressor.

6 Measurements presented here have shown that in the case of surge, each cycle is preceded by a brief period of rotating stall. *Stall* suppression techniques have therefore been used for the first time to delay the onset of surge, and to suppress surge once a repeating cycle has been established.

Acknowledgments

I am extremely grateful to Rolls Royce plc. for their financial support of the project and of myself through a Rolls Royce Fellowship at Wolfson College. Significant financial support in the form of a cooperative grant was also provided by the SERC and this is gratefully acknowledged. Messrs C. Freeman, A. Cargill, and S. Morgan of Rolls Royce Derby are to be thankful for their informative assistance. In Cambridge I would like to thank Prof. J. Ffowcs Williams and Prof. N. Cumpsty, for their support and guidance. I am also appreciative of the help and useful comments received from my colleague, Dr. J. Longley. I would like to thank Prof. E. Greitzer for his interest and encouragement, J. Paduano for useful discussions, and Dr. D. Wisler for recent confirmation of some of my ideas.

References

- Day, I. J., 1993, "Stall Inception in Axial Flow Compressors," *ASME JOURNAL OF TURBOMACHINERY*, Vol. 115, this issue, pp. 1-9.
- Emmons, H. W., Pearson, C. F., and Grant, H. P., 1955, "Compressor Surge and Stall Propagation," *Transactions of the ASME*, Vol. 77, pp. xx-00.
- Epstein, A. H., Ffowcs Williams, J. E., and Greitzer, E. M., 1986, "Active Suppression of Aerodynamic Instabilities in Turbomachines," *AIAA Journal of Propulsion and Power*, Vol. 5, No. 2, pp. 204-211.
- Garnier, V. H., Epstein, A. H., and Greitzer, E. M., 1991, "Rotating Waves as a Stall Inception Indication in Axial Compressors," *ASME JOURNAL OF TURBOMACHINERY*, Vol. 113, pp. 290-302.
- Greitzer, E. M., 1976, "Surge and Rotating Stall in Axial Flow Compressors, Part II: Experimental Results and Comparison With Theory," *ASME Journal of Engineering for Power*, Vol. 98, pp. 199-217.
- Ludwig, G. R., and Nenni, J. P., 1980, "Tests of an Improved Rotating Stall Control System on a J-85 Turbojet Engine," *ASME Journal of Engineering for Power*, Vol. 102, pp. 903-911.
- McDougall, N. M., Cumpsty, N. A., and Hynes, T. P., 1990, "Stall Inception in Axial Compressors," *ASME JOURNAL OF TURBOMACHINERY*, Vol. 112, pp. 116-125.
- Paduano, J., Epstein, A. H., Longley, J. P., Valavani, L., Greitzer, E. M., and Guenette, G. R., 1993, "Active Control of Rotating Stall in a Low Speed Axial Compressor," *ASME JOURNAL OF TURBOMACHINERY*, Vol. 115, this issue, pp. 48-56.
- Reis, W., and Blocker, U., 1987, "Possibilities for On-Line Surge Suppression by Fast Guide Vane Adjustment in Axial Compressors," AGARD-CP-421.

J. D. Paduano

A. H. Epstein

L. Valavani

J. P. Longley¹

E. M. Greitzer

G. R. Guenette

Gas Turbine Laboratory,
Massachusetts Institute of Technology,
Cambridge, MA 02139

Active Control of Rotating Stall in a Low-Speed Axial Compressor

The onset of rotating stall has been delayed in a low-speed, single-stage, axial research compressor using active feedback control. Control was implemented using a circumferential array of hot wires to sense propagating waves of axial velocity upstream of the compressor. Using this information, additional circumferentially traveling waves were then generated with appropriate phase and amplitude by "wiggling" inlet guide vanes driven by individual actuators. The control scheme considered the wave pattern in terms of the individual spatial Fourier components. A simple proportional control law was implemented for each harmonic. Control of the first spatial harmonic yielded an 11 percent decrease in the stalling mass flow, while control of the first, second, and third harmonics together reduced the stalling mass flow by 23 percent. The control system was also used to measure the sine wave response of the compressor, which exhibited behavior similar to that of a second-order system.

Introduction

Axial compressors are subject to two distinct aerodynamic instabilities, rotating stall and surge, which can severely limit compressor performance. Rotating stall is characterized by a wave traveling about the circumference of the machine, surge by a basically one-dimensional fluctuation in mass flow through the machine. Whether these phenomena are viewed as distinct (rotating stall is local to the blade rows and dependent only on the compressor, while surge involves the entire pumping system—compressor, ducting, plenums, and throttle) or as related (both are natural modes of the compression system with surge corresponding to the zeroth order mode), they generally cannot be tolerated during compressor operation. Both rotating stall and surge reduce the pressure rise in the machine, cause rapid heating of the blades, and can induce severe mechanical distress.

The traditional approach to the problem of compressor flow field instabilities has been to incorporate various features in the aerodynamic design of the compressor to increase the stable operating range. Balanced stage loading and casing treatment are examples of design features that fall into this category. More recently, techniques have been developed that are based on moving the operating point close to the surge line when surge does not threaten, and then quickly increasing the margin when required, either in an open or closed-loop manner. The open-loop techniques are based on observation, supported by many years of experience, that compressor stability is strongly influenced by inlet distortions and by pressure transients caused

by augmentor ignition and, in turn, that inlet distortion can be correlated with aircraft angle of attack and yaw angle. Thus, significant gains have been realized by coupling the aircraft flight control and engine fuel control so that engine operating point is continually adjusted to yield the minimum stall margin required at each instantaneous flight condition (Yonke et al., 1987).

Closed-loop *stall avoidance* has also been investigated. In these studies, sensors in the compressor were used to determine the onset of rotating stall by measuring the level of unsteadiness. When stall onset was detected, the control system moved the operating point to higher mass flow, away from the stall line (Ludwig and Nenni, 1980). While showing some effectiveness at low operating speeds, this effort was constrained by limited warning time from the sensors and limited control authority available to move the compressor operating point.

This paper presents the initial results of an alternative and fundamentally different means for attacking the problem posed by rotating stall. Here, we *increase the stable flow range* of an axial compressor by using closed-loop control to damp the unsteady perturbations that lead to rotating stall. In contrast to previous work, this dynamic stabilization concept improves the stable operating range of the compressor by moving the stall point to lower mass flows, as illustrated conceptually in Fig. 1. There appear to be at least two advantages of this new technique. One is that engine power always remains high with dynamic stabilization while power must be cut back with stall avoidance (often at critical points in the flight envelope). A second advantage is that the gain in operating range can be potentially greater. In the following sections, we briefly describe those elements in the theory of compressor stability that are relevant to active stability enhancement, discuss the design of the experimental apparatus, and present the experimental results.

¹Current address: Whittle Laboratory, Cambridge University, Cambridge, United Kingdom.

Contributed by the International Gas Turbine Institute and presented at the 36th International Gas Turbine and Aeroengine Congress and Exposition, Orlando, Florida, June 3–6, 1991. Manuscript received at ASME Headquarters February 19, 1991. Paper No. 91-GT-88. Associate Technical Editor: L. A. Riekert.

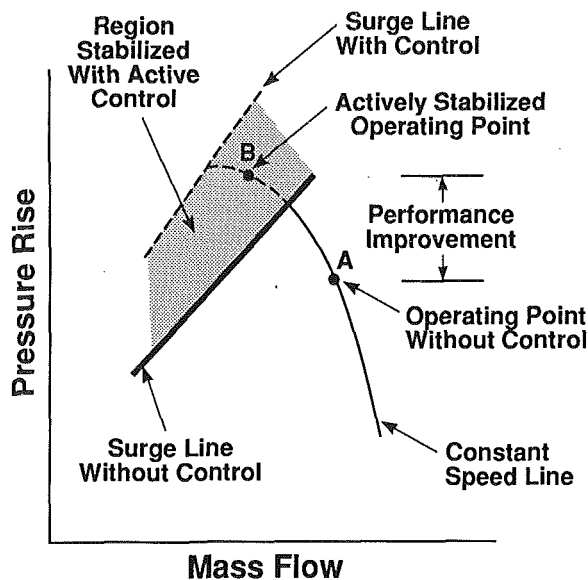


Fig. 1 The intent of active compressor stabilization is to move the surge line to lower mass flow

Conceptual View of Compressor Stability and Active Stall Control. We consider rotating stall to be one of the class of natural instabilities of the compression system, as analyzed for example by Moore and Greitzer (1986) for low-speed machines of high hub-to-tip radius ratio. Their model predicts that the stability of the compressor is tied to the growth of an (initially small amplitude) wave of axial velocity, which travels about the circumference of the compressor. If the wave decays (i.e., its damping is greater than zero), then the flow in the compressor is stable. If the wave grows (wave damping negative), the flow in the compressor is unstable. Thus, wave growth and compressor flow stability are equivalent in this view.

One prediction of this model that is useful for present purposes is that rotating waves should be present at low amplitude prior to stall. McDougall (1988) and McDougall et al. (1990) identified these waves in a low-speed, single-stage compressor, and Garnier et al. (1991) observed them in both a single and a three-stage low-speed compressor, and in a three-stage high-speed compressor. The waves were often evident long (ten to one hundred rotor revolutions) before stall. It was found that the waves grew smoothly into rotating stall, without sharp changes in phase or amplitude, and that the wave growth rate agreed with the theory of Moore and Greitzer (1986). Further, the measurements showed how the wave damping, and thus the instantaneous compressor stability, could be extracted from real time measurements of the rotating waves.

In 1989, Epstein et al. suggested that active control could be used to damp these rotating waves artificially when at low

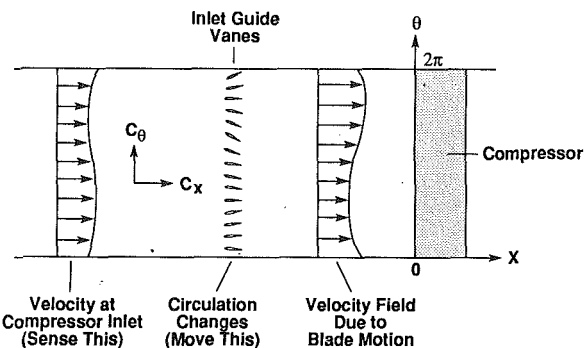


Fig. 2 Conceptual control scheme using "wiggly" inlet guide vanes to generate circumferential traveling waves

amplitude. If, as the theory implies, rotating stall can be viewed as the mature form of the rotating disturbance, damping of the waves would prevent rotating stall from developing, thus moving the point of instability onset as in Fig. 1. It was proposed that the compressor stability could be augmented by creating a traveling disturbance with phase and amplitude based on real time measurement of the incipient instability waves. This paper presents an experimental investigation of this idea.

The overall concept is to measure the wave pattern in a compressor and generate a circumferentially propagating disturbance based on those measurements, so as to damp the growth of the naturally occurring waves. In the particular implementation described herein, shown schematically in Fig. 2, individual vanes in an upstream blade row are "wiggled" to create the traveling wave velocity disturbance. The flow that the upstream sensors and the downstream blade rows see is a combination of the naturally occurring instability waves and the imposed control disturbances. As such, the combination of compressor and controller is a different machine than the original compressor—with different dynamic behavior and different stability.

At this point, it is appropriate to present the rotating stall model and connect it with the idea of control. Here, it is the structure of the model that is most important rather than the fluid mechanic details. Since the structure provides a framework for design of the control system, the quantitative details can be derived by fitting experimental data to the model.

The existing models for rotating stall inception in multirow axial compressors are typified by an equation for the velocity and pressure perturbations of the form

$$\frac{\delta P_{\text{compressor exit}} - \delta P_{T_{\text{compressor inlet}}}}{\rho U^2} = \left(\frac{d\psi}{d\phi} \right) \delta\phi - \lambda \frac{\partial \delta\phi}{\partial \theta} - \mu \frac{\partial \delta\phi}{\partial \bar{t}} \quad (1)$$

Here, δP and δP_T are the static and total pressure perturbations, respectively, $\delta\phi$ is the nondimensional axial velocity perturbation,

Nomenclature

C_n = complex spatial Fourier coefficient (Eq. (5))
 IGV = inlet guide vane
 n = mode number
 P = static pressure
 P_T = total pressure
 R_n = controller gain = $|Z_n|$
 r = mean compressor radius
 \bar{t} = nondimensional time = Ut/r
 U = mean compressor blade speed
 V_k = axial velocity measurement (Eq. (5))

Z_n = controller complex gain and phase
 β_n = controller phase for n th mode = $\angle Z_n$
 γ = IGV stagger angle
 $\delta(\)$ = perturbed quantity
 θ = circumferential coordinate
 λ = rotor inertia parameter
 μ = rotor + stator + IGV inertia parameter
 μ_{IGV} = IGV inertia parameter
 ρ = density

ϕ = local flow coefficient = axial velocity/ U
 $\bar{\phi}$ = area-averaged flow coefficient
 ψ = compressor pressure rise = $(P - P_T)/(\rho U^2)$

Subscripts

I = imaginary part of complex quantity
 n = n th circumferential Fourier mode.
 R = real part of complex quantity

bation at the compressor, λ and μ are nondimensional parameters reflecting the fluid inertia in rotor and rotor + stator + IGV, respectively, $(d\psi/d\phi)$ is the slope of the nondimensional compressor characteristic, and \tilde{t} is a nondimensional time, $\tilde{t} = tU/r$. Equation (1) has been shown in several publications (e.g., Hynes and Greitzer, 1987; Longley, 1988) and we will not present its development here. The equation is an expression of the matching conditions (across the compressor) for flowfields upstream and downstream of the compressor and, as such, upstream and downstream flowfield descriptions are needed to be able to find a solution.

Using these, Longley (1990) has shown that one can put Eq. (1) in a wave operator form. For the n th spatial Fourier coefficient, this is

$$\left\{ \left(\frac{2}{|n|} + \mu \right) \frac{\partial}{\partial \tilde{t}} + \lambda \frac{\partial}{\partial \theta} \right\} \delta\phi = \left(\frac{d\psi}{d\phi} \right) \delta\phi \quad (2)$$

The left-hand side of Eq. (2) is a convective operator corresponding to circumferential propagation with velocity $(\lambda/(2/|n| + \mu)) \cdot$ (rotor speed). The growth rate of the wave is dependent on the slope of the compressor characteristic. If $(d\psi/d\phi)$ is positive the waves grow; if negative they decay. Neutral stability (waves traveling with constant amplitude) occurs at $(d\psi/d\phi) = 0$.

We can cast Eq. (2) in a form that is more useful for control by considering a purely propagating disturbance. The first Fourier mode will be of the form $e^{i\theta}$, so Eq. (2) can be written as

$$(2 + \mu) \frac{\partial \delta\phi}{\partial \tilde{t}} + \left[i\lambda - \left(\frac{d\psi}{d\phi} \right) \right] \delta\phi = 0 \quad (3)$$

Thus far, the equations presented have been for flow associated with uncontrolled compressor dynamics. If, in addition, we model the control as due to perturbations in IGV stagger, $\delta\gamma$, we obtain the following equation for the first Fourier mode:

$$(2 + \mu) \frac{\partial \delta\phi}{\partial \tilde{t}} + \left[i\lambda - \left(\frac{\partial\psi}{\partial\phi} \right) \right] \delta\phi + \left[i\bar{\phi}\mu_{IGV} \left(\frac{\partial\psi}{\partial\phi} \right) - \left(\frac{\partial\psi}{\partial\gamma} - \bar{\phi}\mu_{IGV}\lambda \right) \right] \delta\gamma - i\bar{\phi}\mu_{IGV} \left(1 + \mu - \frac{\mu_{IGV}}{2} \right) \frac{\partial\delta\gamma}{\partial\tilde{t}} = 0 \quad (4)$$

where $\bar{\phi}$ is the axisymmetric (annulus-averaged) flow coefficient, μ_{IGV} is the fluid inertia parameter for the IGVs, and $(\partial\psi/\partial\gamma)$ represents the incremental pressure rise obtainable from a change in IGV stagger, γ .

This is formally a first-order equation for $\delta\phi$; however, it must be remembered that the quantity of interest is the real part of $\delta\phi$. If we express $\delta\phi$ in terms of its real and imaginary parts, $\delta\phi = \delta\phi_R + i\delta\phi_I$, then Eq. (4), which is a coupled pair of first-order equations for $\delta\phi_R$ and $i\delta\phi_I$, becomes mathematically equivalent to a second-order equation for $\delta\phi_R$. The form used in the system identification discussed below is thus second order. Another way to state this is that a first-order equation with a complex (or pure imaginary) pole is equivalent to a second-order system in the appropriate real-valued states.

The second-order model of compressor behavior is useful for two reasons. First, it can be tested experimentally in a straightforward manner. Second, it provides both a conceptual qualitative framework about which to design a control system (i.e., the stabilization of a second-order system) and, given the results of the experimental test, the quantitative inputs required to do the control system design.

Experimental Apparatus

A 0.52-m-dia, single-stage low-speed research compressor was selected as a test vehicle due to its relative simplicity. The general mechanical construction of the machine was described by Lee and Greitzer (1988), and the geometry of the build

Table 1 Single-stage compressor geometry

Tip Diameter	0.597 m		
Hub-to-Tip Ratio	0.75		
Axial Mach No.	0.10		
Operating Speed	2700 RPM		
	IGV	Rotor	Stator
Mean Line Stagger	0	35°	22.5°
Chamber Angle	0	25°	25°
Solidity	0.6	1	1
Aspect Ratio	0.9	2.0	1.9

studied here is given in Table 1. The apparatus can be considered to consist of four sections: the compressor (described above), instrumentation for wave sensing, actuators for wave launching, and a signal processor (controller). The design of the last three components is discussed below.

The sensors used in the present investigation are eight hot wires evenly spaced about the circumference of the compressor, 0.5 compressor radii upstream of the rotor leading edge. The wires were positioned at midspan and oriented so as to measure axial velocity. Hot wires were chosen because their high sensitivity and frequency response are well suited to low-speed compressors. The sensors were positioned relatively far upstream so that the higher harmonic components of the disturbances generated by the compressor would be filtered (the decay rate is like $e^{-n|x|/r}$, where n is the harmonic number). This reduced the likelihood of spatial aliasing of the signal. With eight sensors, the phase and amplitude of the first three disturbance harmonics may be obtained. The outputs of the anemometers were filtered with four pole Bessel filters with a cutoff frequency of 22 times rotor rotation. The axial location of the sensors is important in determining the signal-to-noise ratio (SNR) of the rotating wave measurements; this question was studied by Garnier et al. (1991), who showed the SNR to be greatest upstream of the stage.

There are many ways to generate the required traveling waves in an axial compressor. Techniques involving oscillating the inlet guide vanes (IGVs), vanes with oscillating flaps, jet flaps, peripheral arrays of jets or suction ports, tip bleed above the rotor, whirling the entire rotor, and acoustic arrays were all considered on the basis of effectiveness, complexity, cost, and technical risk. For this initial demonstration in a low-speed compressor, oscillating the IGVs was chosen on the basis of minimum technical risk.

Considerable care was taken in design of the actuation system to maximize effectiveness and minimize complexity and cost. An unsteady singularity method calculation of the potential flow about a cascade was carried out first to evaluate tradeoffs between blade angle of attack and flow turning angles versus cascade solidity, fraction of the cascade actuated, and airfoil aspect ratio (Silkowski, 1990). The unsteady flow was examined since, although the reduced frequency of the IGV airfoil relative to rotating stall is about 0.3 for the first harmonic, several harmonics may be of interest. Calculations were also performed to evaluate the relative effectiveness of bang-bang actuation versus continuous airfoil positioning. As an example of these actuation studies, the tradeoff between the peak airfoil angle of attack excursion and the fraction of the cascade actuated is shown in Fig. 3. As the fraction of the airfoils actuated is increased, the angle of attack requirements on individual blades are reduced.

The limits to blade motion are set by both mechanical constraints (i.e., actuator torque limits) and airfoil boundary layer separation at large angles of attack. A NACA 65-0009 airfoil section was chosen due to its good off-angle performance and relatively low moment. The airfoils were cast from low-density epoxy to reduce their moment of inertia. A coupled inviscid-

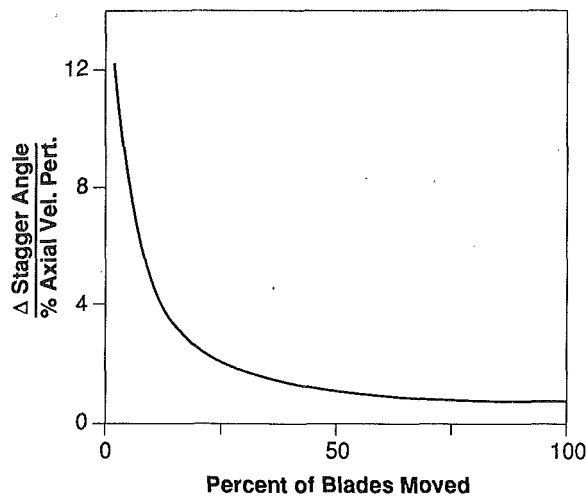


Fig. 3 Calculated blade stagger angle change required to generate a given first harmonic axial velocity perturbation as a function of the fraction of the blade row actuated

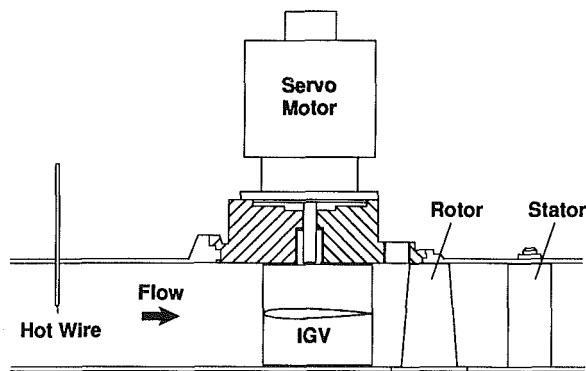


Fig. 4 Compressor flow path

viscous solution of the flow over the blades indicated that the boundary layers would stay attached at angles of attack up to 15 deg (Drela, 1988).

In this experiment, blade actuation torque requirements are set by the airfoil inertia since the aerodynamic forces are small. Both hydraulic and electric actuators are commercially available with sufficient torque and frequency response. Hollow core d-c servomotors were selected because they were considerably less expensive than the equivalent hydraulic servos. The blades and motors have roughly equal moments of inertia.

For a given IGV solidity, the number of actuators required can be reduced by increasing the blade chord, but this is constrained by actuator torque and geometric packaging. The final IGV design consists of 12 untwisted oscillating airfoils with an aspect ratio of 0.9 and a solidity of 0.6 (Fig. 4). The complete actuation system has a bandwidth of 80 Hz (approximately eight times the fundamental rotating stall frequency) at plus or minus 10 deg of airfoil yaw. The flow angle distribution measured at the rotor leading edge station (with the rotor removed) for a stationary 10 deg cosine stagger pattern of the IGVs is compared in Fig. 5 to a prediction of the same flow made by Silkowski (1990).

The control law implemented for the tests described here is a simple proportionality; at each instant in time, the n th spatial mode of the IGV stagger angle perturbation is set to be directly proportional to the n th mode of the measured local velocity perturbation. The complete control loop consisted of the following steps. First, the sensor signals are digitized. Then, a discrete Fourier transform is taken of the eight sensor readings. The first and/or second discrete Fourier coefficients are then

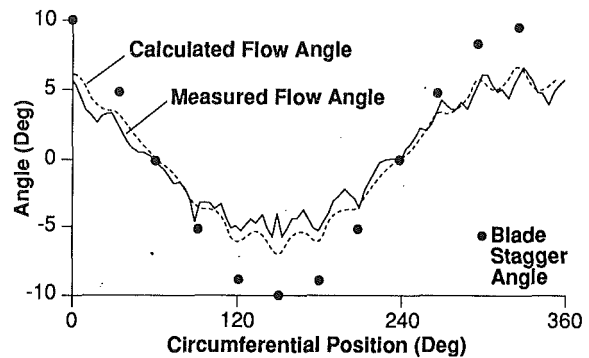


Fig. 5 A comparison of the measured and calculated flow angle generated 0.3 chords downstream by a 10 deg cosine stagger pattern distribution of 12 inlet guide vanes

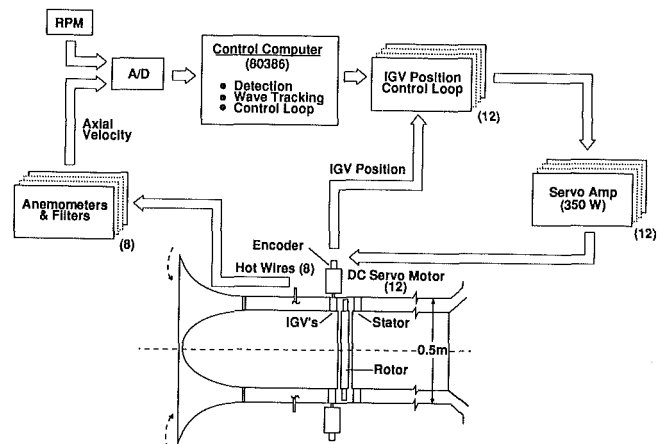


Fig. 6 Hardware components of actively stabilized axial flow compressor

multiplied by the (predetermined) complex feedback gains for that mode. Next, an inverse Fourier transform is taken that converts the modal feedback signals into individual blade commands. These, in turn, are then sent to the individual digital motor controllers. Additional housekeeping is also performed to store information for post-test analysis, limit the motor currents and excursions (for mechanical protection), and correct for any accumulated digital errors.

The controller hardware selection is set by CPU speed requirements (main rotating stall control loop and individual blade position control loops), I/O bandwidth (sensor signals in, blade positions out, storage for post-test analysis), operating system overhead, and cost. The final selection was a commercial 20 MHz 80386 PC with coprocessor. A multiplexed, twelve-bit analog to-digital converter digitized the filtered hot-wire outputs. The d-c servomotors were controlled individually by commercial digital motion control boards. Using position feedback from optical encoders on the motors, each motor controller consisted of a digital proportional, integral, derivative (PID) controller operating at 2000 Hz. The entire control loop was run at a 500 Hz repetition rate. Motor power was provided by 350-W d-c servo amplifiers. The complete hardware arrangement is shown in Fig. 6.

Open-Loop Compressor Response

The inputs and outputs that characterize the fluid system of interest (the compressor and associated flow in the annular region) are the inlet guide vane angles (inputs) and the axial velocity distribution (outputs). In the present configuration this consists of twelve inputs (twelve inlet guide vanes) and

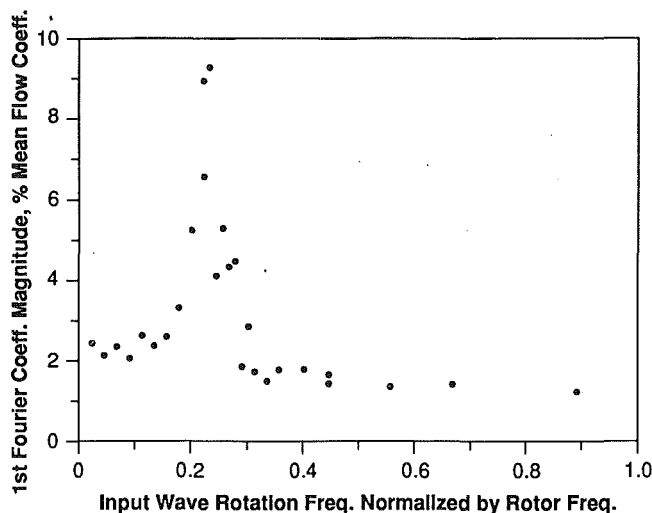


Fig. 7 Measured open-loop response of the first spatial mode of the compressor to a 10 deg IGV stagger rotating sine wave excitation

eight outputs (eight hot wires) so that the system is multiple input-multiple output. Because the disturbances of interest are of small amplitude, the system behavior can be taken as linear and we can express the spatial distribution of the input and output perturbations (or indeed of any other flow perturbations) as a sum of spatial Fourier components, each with its own phase velocity and damping. This representation, which is consistent with Eq. (2), allows us to treat the disturbances on a harmonic-by-harmonic basis, and reduces the input-output relationship to single input-single output terms for each spatial mode, an enormous practical simplification.

The complex spatial Fourier coefficient for each mode n is given by

$$C_n = \frac{1}{K} \sum_{k=0}^{K-1} V_k \exp \left[-\frac{2ink\pi}{K} \right] \quad (5)$$

where K is the number of sensors about the circumference (eight in this case), and V_k is the axial velocity measured at angular position k . The magnitude of C_1 is thus the amplitude of the first harmonic at any time; its phase is the instantaneous angular position of the spatial wave Fourier component.

An important concept in the present approach is the connection between rotating stall and traveling wave type of disturbances in the compressor annulus. In this view, the wave damping and the compressor damping are equivalent and determine whether the flow is stable. At the neutral stability point, the damping of disturbances is zero, and close to this point, the damping should be small. (The measurements given by Garnier et al. (1991) show this.) Thus, for a compressor operating point near stall, the flow in the annulus should behave like a lightly damped system, i.e., should exhibit a resonance peak when driven by an external disturbance. As with any second-order system, the width of the peak is a measure of the damping.

The present apparatus is well suited to establishing the forced response of the compressor, since the individual inlet guide vanes can be actuated independently to generate variable frequency traveling waves. The sine wave response of the compressor was measured by rotating the ± 10 deg sinusoidal IGV angle distribution shown in Fig. 5 about the circumference at speeds ranging from 0.05 to 1.75 of rotor rotational speed. Figure 7 shows the magnitude of the first spatial Fourier coefficient (as a percentage of the mean flow coefficient) as a function of input wave rotation frequency, i.e., the transfer function for the first spatial mode.

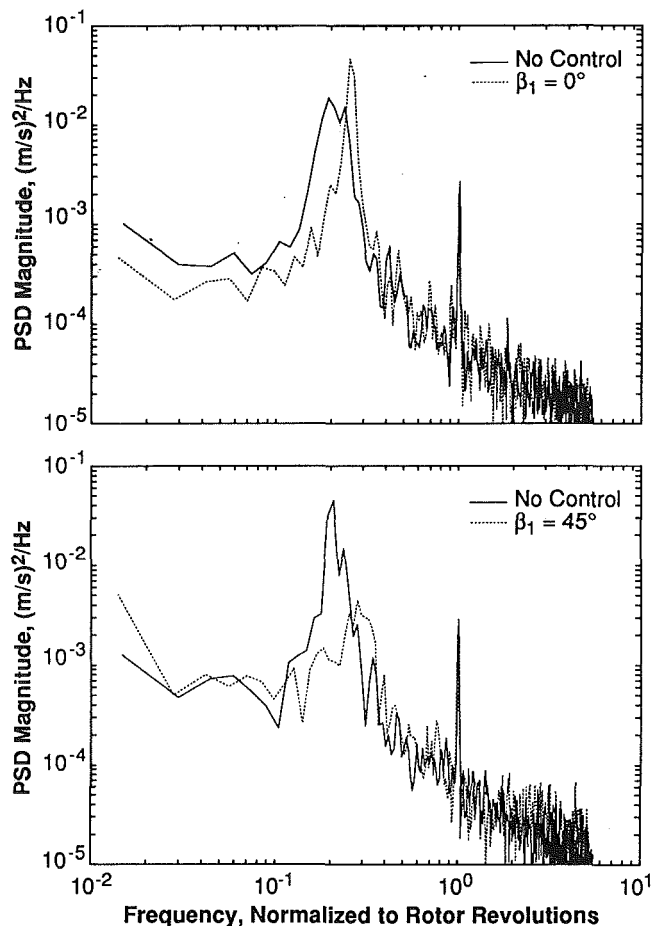


Fig. 8 The influence of proportional feedback control on the power spectral density (PSD) of the first spatial mode of the compressor at two feedback phase angles (β_1) versus the behavior with fixed IGVs

The peak response to the forcing sine wave is seen in Fig. 7 to be at 23 percent of the rotor rotation frequency. This is close to the frequency observed for the small amplitude waves without forcing (20 percent) and for the fully developed rotating stall (19 percent). This behavior supports the view stated previously that the compressor behaves as a second-order system.

Closed-Loop Experiments—Rotating Stall Stabilization of the First Fourier Mode

While the open-loop experiments described above are of interest in elucidating the basic structure of the disturbance field in the compressor annulus, this work is principally aimed at suppressing rotating stall using closed-loop control. To assess this, experiments were performed using a control scheme of the form

$$[\delta\gamma_{IGV}]_{nth \text{ mode}} = Z_n C_n \quad (6)$$

where

$$Z_n \equiv R_n e^{i\beta_n} \quad (7)$$

In Eqs. (6) and (7), $\delta\gamma_{IGV}$ is the change in inlet guide vane stagger angle. The quantity Z_n is the complex feedback gain for the n th Fourier mode (n th spatial harmonic component of the disturbance), with R_n the amplitude and β_n the phase angle between the measured axial velocity spatial harmonic (0.5 radii upstream of the rotor) and the input inlet guide vane angular position spatial harmonic. The influence of feedback amplitude (R_n) and phase (β_n) were established with a set of para-

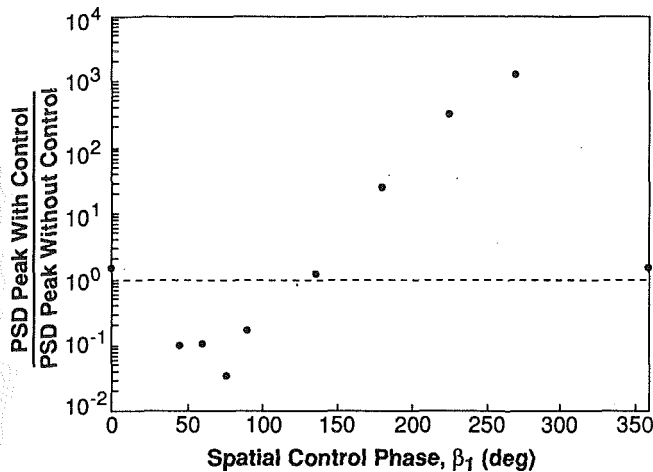


Fig. 9 Influence of feedback control phase angle (β_1) on the strength of the first spatial mode of the flow in the compressor at $\phi = 0.475$

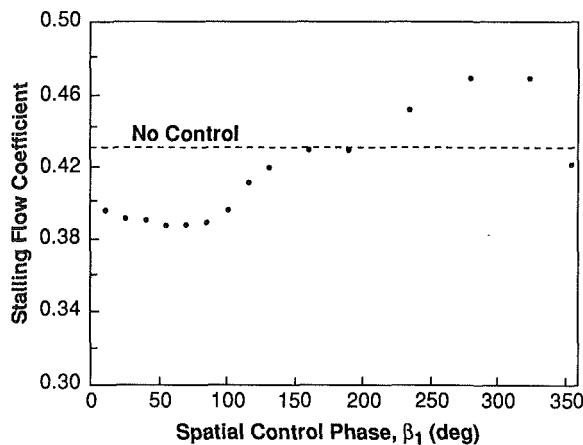


Fig. 10 Influence of feedback control phase angle (β_1) on the flow coefficient at which the compressor goes into rotating stall

metric experiments carried on at a flow coefficient (ϕ) close to stall, in a region of marginal flow stability.

Data are shown in Fig. 8 in the form of the power spectral density (PSD) of the first spatial mode axial velocity disturbance (C_1) at two control phase angles (β_1), 0 and 45 deg. The operating point is fixed at a normally stable flow coefficient of $\phi = 0.475$ (stall without control occurs at $\phi = 0.430$). For each phase, spectra are shown with feedback control and with no control (vanes stationary at zero flow angle). The rotating disturbance is evident in the strong peaks at 23 percent of rotor rotation frequency. The height of the peaks is a measure of the strength of the rotating waves. The scales are dimensional but all plots are to the same scale so they can be compared directly. The difference between the peak heights with no control in the two cases is due to finite sampling time, i.e., to differences in the ambient disturbance levels during the sampling period.

At 0 deg phase angle, the peak at 0.23 frequency is higher with active control than with fixed vanes, implying that the feedback control at this phase is amplifying the rotating disturbance waves (i.e., making them less stable). At 45 deg phase angle, however, the peak with control is lower than that with fixed vanes, implying that control is attenuating the waves in this case. Thus, the ratio of the height of the peak in the PSD with and without control (i.e., the wave amplification) is a measure of the effectiveness of the feedback in influencing the traveling wave's stability. The influence of controller phase (β_1), at fixed gain, on the wave amplitude ratio was experi-

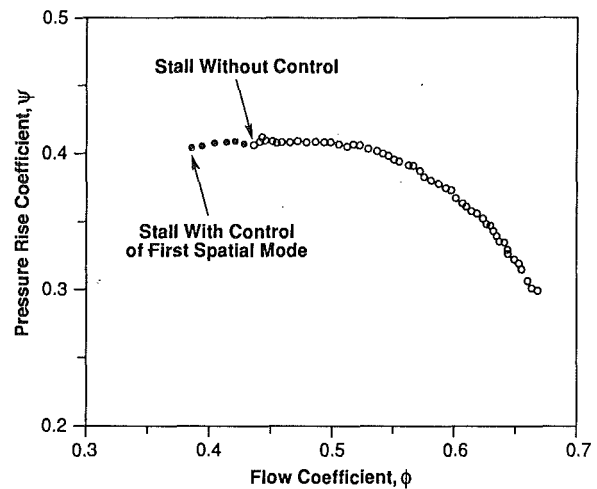


Fig. 11 Nondimensional pressure rise (ψ) versus mass flow (ϕ) characteristic showing the measured influence of feedback control of the first spatial mode on compressor operating range

mentally evaluated for phase shifts between 0 and 360 deg, as shown in Fig. 9. For phases between 0 and 150 deg, the waves are attenuated, while the waves are amplified for phase angles between 160 and 350 deg. The maximum attenuation found was roughly 30 at $\beta_1 = 75$ deg, and the maximum measured amplification of a factor of 1300 occurs at $\beta_1 = 275$ deg. Between $\beta_1 = 290$ and $\beta_1 = 345$, the system is unstable (i.e., goes into rotating stall).

If wave stability is equivalent to compressor stability, then compressor stability should be enhanced for control phases at which the waves are attenuated and should be decreased when the waves are amplified. This is indeed the case as illustrated in Fig. 10. Here, the flow coefficient (ϕ) at which the compressor goes into rotating stall as the compressor throttle is very slowly closed ($d\phi/dt = 2 \times 10^{-5}$ /rotor revolution) is shown as a function of controller phase angle (β_1). Depending upon the phase, the control changes the stalling flow coefficient by as much as ± 11 percent. Comparison of Figs. 9 and 10 makes clear the connection between wave damping and rotating stall. Rotating stall is suppressed when the waves are damped and is promoted when the waves are amplified.

Figure 11 shows the influence of control of the first spatial harmonic wave in a more familiar form of nondimensional pressure rise (ψ) versus nondimensional mass flow (flow coefficient, ϕ) at constant corrected compressor speed. With fixed inlet guide vanes (no control), the compressor stalls at $\phi = 0.43$. With feedback control at the most effective phase found ($\beta_1 = 60$ deg), the stalling flow coefficient is $\phi = 0.38$, 11 percent lower. At the phase producing the highest measured wave amplification ($\beta_1 = 275$ deg), the stalling flow coefficient is 0.475.

Time-Resolved System Behavior. Much can be learned from examining the time-resolved behavior of the controlled compressor as the throttle is slowly closed at a controller phase (β_1) of 60 deg. The overall system behavior is shown in Fig. 12. Here, the onset of stall occurs at a nondimensional time of 0. Prior to that time, the sensor output is small relative to the rotating stall amplitude. The actuators, however, are clearly producing a traveling wave. (The actuator response to the rotating stall after stall onset is due to the light damping of the blade servos.)

The time evolution measured by a single sensor is shown in Fig. 13. For this compressor with no control (Fig. 13a), the rotating stall grows quite slowly. With control of the first spatial mode (Fig. 13b), the growth is much faster. (Note that this occurs at a lower flow coefficient than Fig. 13a.) Further, the disturbances with control have twice the frequency as in

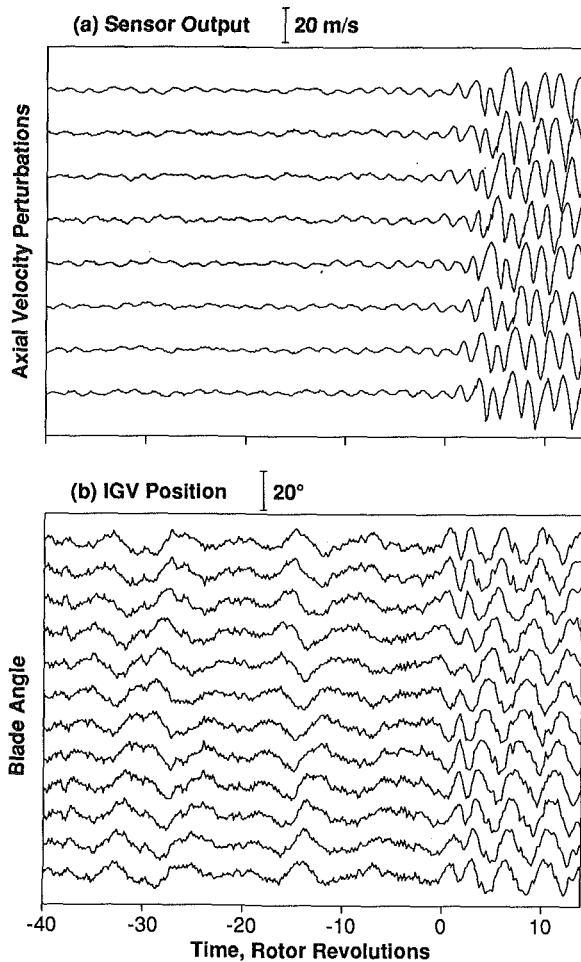


Fig. 12 Time history of compressor sensor output (a) and actuator response (b) with first spatial mode control as the throttle is very slowly closed. Rotating stall onset is at a time of 0.

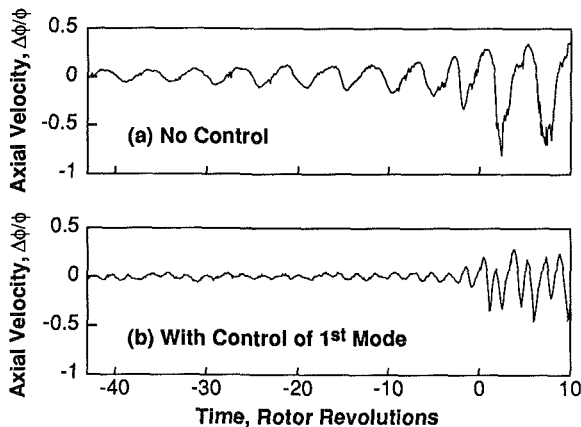


Fig. 13 The influence of control on the time history of a single sensor as the throttle is slowly closed to stall the compressor

the no-control case. This is due to the primary disturbance now being a two-cell rotating stall, i.e., the second spatial mode.

The influence of first mode control on the disturbance modal structure is illustrated in Figs. 14 and 15, which show disturbance phase and amplitude versus time. A linear variation of phase with time indicates that the disturbance is propagating at constant speed. Without control (Fig. 14), both the first and second spatial modes are evident in both magnitude and phase for 40 rotor revolutions before stall. The first mode is clearly the strongest everywhere and the fully developed stall is an

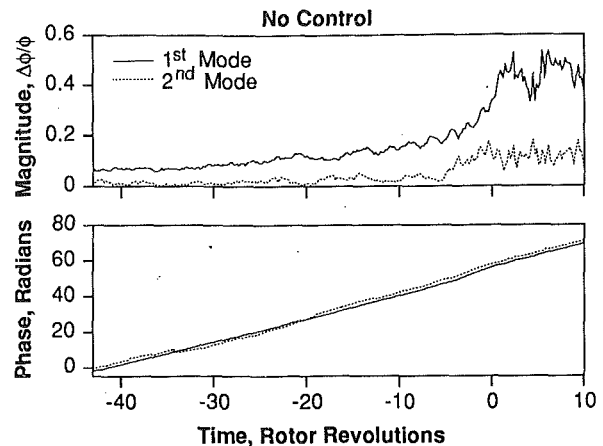


Fig. 14 Time history without control of the first two Fourier coefficients as the throttle is slowly closed to stall the compressor at $t=0$ revs

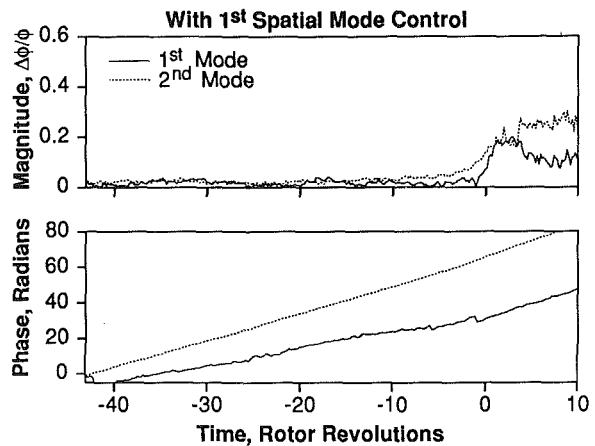


Fig. 15 Same as Fig. 14, but with control of the first spatial mode

admixture of both modes. When the first spatial mode is controlled (Fig. 15), it is the second that is stronger prior to stall, and predominates in the fully developed rotating stall.

Control of the Second and Third Spatial Modes. Since the second spatial mode appears predominant when the first mode is under control, it makes sense to control the second mode as well. The effect of simultaneous control of the first two spatial modes on compressor stalling pressure rise is shown in Fig. 16. With both modes under the control, the compressor does not stall until a flow coefficient of $\phi = 0.35$, an 18 percent increase in operating range over the no-control case. Examination of the time behavior of the Fourier coefficients, as the compressor throttle is slowly closed (Fig. 17), shows that, prior to stall, the first and second modes are of about equal strength. At the stall point, the second-mode growth is initially more rapid but fully developed stall is predominantly the first mode. This suggests that (nonlinear) mode coupling is important as the wave matures. Nevertheless, controlling the third spatial mode extends the stable flow range down to $\phi = 0.33$, a 23 percent improvement over the no-control case. Control of the fourth spatial mode was not attempted due to poor signal-to-noise ratio.

System Identification

The measurements presented have been for a compressor with a simple proportional control law, one whose rationale is based on a linear theory as summarized by Eq. (4). There are many analytical tools now available to design more sophisticated control schemes with, it is hoped, improved per-

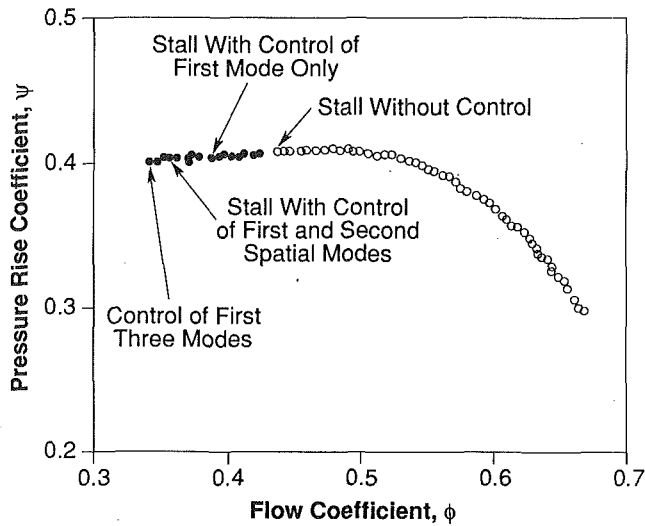


Fig. 16 Compressor characteristic as in Fig. 11, but with active control of the first and second, and of the first, second, and third modes

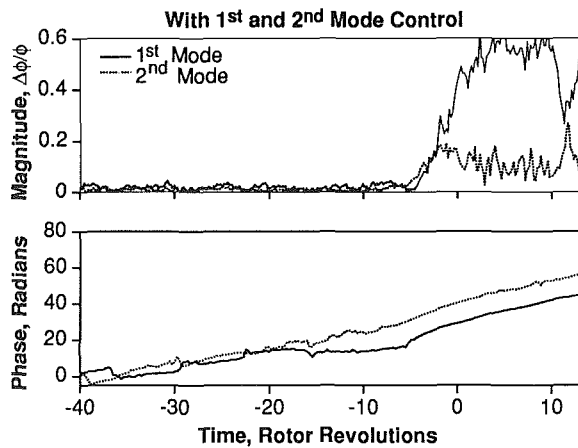


Fig. 17 Same as Figs. 14 and 15, but with control of the first and second spatial modes

formance. The success of the control design, however, will be based in no small part on the fidelity of the system model assumed for the compressor. Also, we are interested in understanding more about the compressor fluid mechanics. The apparatus assembled for the active control experiment is well suited to quantitatively establishing the dynamic response of the compressor by directly measuring its transfer function.

The magnitude behavior of the compressor response to IGV motion was given in Fig. 7. This behavior can be put into a more complete form, and compared to at least the structure of the fluid dynamic model, by plotting the phase and magnitude (Bode diagram) of the transfer function between the first Fourier coefficient of IGV motion and the first Fourier coefficient of the resulting axial velocity perturbations. This transfer function has both a magnitude and a phase, which results from both spatial and time lags between the input and output. We expect the behavior of this system based on the modeling described earlier to be that of a second-order system. This should be easily identifiable from experiments such as a rotating sine wave response, for example.

We can express the fluid model of Eq. (4) in more convenient transfer function form as

$$\frac{\delta\phi}{\delta\gamma}(s) = K \frac{s + (A + Bi)}{s + (C + Di)} \quad (8)$$

where s is the Laplace transform variable. The complex form of this transfer function gives rise to second-order behavior in

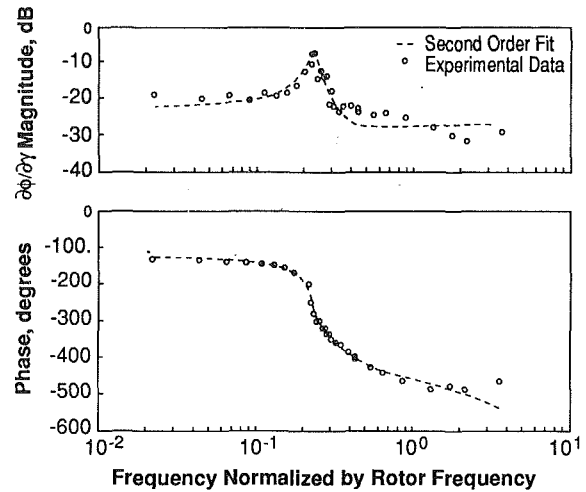


Fig. 18 Bode plot showing response of the compressor to a sine wave forcing excitation at $\phi = 0.475$

the measured variables, as mentioned previously. The advantage of this form is that it uses the minimum number of parameters to completely specify the transfer characteristics of the system. A linear regression type fit (Lamaire, 1987) can be done for the parameters K , A , B , C , and D . This gives rise to the results shown in Fig. 18, where it can be seen that the response characteristics in the experiment are mimicked by the model. We have obtained this type of fit using various types of IGV inputs: rotating waves, stationary waves with oscillating amplitudes, and stationary waves with random amplitudes. As would be expected in a linear system, the input-output behavior is unaffected by such variations in the character of the input. It should be noted, however, that the shape of the compressor response *does* change with operating point; thus the numerical values of K , A , B , C , and D are functions of flow coefficient. More details on this system identification can be found from Paduano et al. (1992). Overall, the fit of the second-order model to the measurements is very good.

In summary, the fidelity of the model fit to the data in Fig. 18 indicates that the structure of the fluid model of Eq. (4) is appropriate for this compressor at the flow conditions examined.

Discussion

The most important point of this paper is that these experiments demonstrate that it is physically possible to control rotating stall actively in an axial flow compressor and, by doing so, obtain a useful extension in compressor operating range. A second point is that these experiments more firmly establish a clear link between low amplitude circumferentially propagating disturbances prior to stall and fully developed rotating stall—when the disturbances are suppressed, rotating stall is prevented. This initial attempt to control rotating stall is encouraging. As is often the case, however, these results raise many more questions than they answer. These questions thus suggest future research directions.

The control law used in the experiments reported herein is quite simple. Considerable effort is being spent on the design of more sophisticated, and it is hoped more effective, controllers. The controllers can be useful in two ways: first, in extending compressor performance and, second, in elucidating the details of the dynamic behavior of the compression system.

At the moment, we do not have a quantitative explanation for the experimentally observed limit to control effectiveness on this compressor (i.e., why is there a 23 percent flow range improvement rather than a 10 or 30 percent improvement). Preliminary investigations show that, insofar as the linear sys-

tem analysis exemplified by Eq. (8) is concerned, the bandwidth and actuator authority limits of the current system have not yet been reached. Another possibility is that higher order modes may drive the instability. Various other nonlinearities can be important. Also, at some flow coefficients, the assumptions that underlie the wave model (Eq. (4)) and the actuation scheme chosen may cease to be valid (i.e., two-dimensional flow). Work is ongoing to address these questions.

There are also more general issues raised that go beyond the behavior of this particular compressor. We have no basis on which to extrapolate rotating stall control quantitatively beyond the machine tested. We note, however, that the wave behavior exploited in this control scheme has been observed of other low and high-speed compressors by McDougall and Garnier. Thus, we might expect that those machines could be controlled in a similar fashion to a greater or lesser degree. This question can only be addressed in substance by experimental investigation of other builds of this compressor and of other compressors. A second approach is to reconcile the system behavior quantitatively such as observed experimentally in Fig. 18 with a first principles fluid mechanic model related to compressor geometry as exemplified by Eq. (4). This would facilitate more accurate predictions of compressor behavior with control. Work is ongoing in both areas.

Another concern is the generality of the rotating stall model. Certainly such assumptions as two-dimensionality and incompressible flow are of limited applicability. These models can and are being made more elaborate as fidelity with experimental data requires. It is important to emphasize here that the concept of active control of compressor instabilities is not dependent on the accuracy of any particular mathematical model or conceptual view of the flow in a compressor. The model is there to provide a framework about which to design a control system. Any model would do (assuming it was an accurate representation of the fluid mechanics), although certainly some formulations are much more tractable for control design than others.

Actuation schemes are also important since they influence both the effectiveness of control and the complexity and difficulty of implementation. The approach adopted here was chosen mainly on the basis of minimum technical risk. Many other techniques can be considered and each must be quantitatively evaluated in terms of control authority and implementation difficulty for a particular installation. Research efforts in this area may be fruitful.

As a final point, we would like to comment on the interdisciplinary nature of this research. The effort to date has been successful due to the work of both compressor and controls engineers and it has been challenging for both specialties. In the past several years, we have spent considerable time learning how to talk with each other and can report that the effort appears so far to be rewarding.

Conclusions

Rotating stall in a low-speed axial compressor has been suppressed using active feedback control. To date, a 23 percent gain in compressor mass flow range has been achieved. The

measured dynamic behavior of the compressor has followed trends outlined by a two-dimensional compressor stability model. These results reinforce the view that the compressor stability is equivalent to the stability of low-amplitude waves, which travel about the machine circumferentially.

This is a progress report on an ongoing effort. The results so far indicate that active control of large-scale fluid mechanic instabilities such as rotating stall in axial compressors is very promising. Much work still needs to be done to assess the practical applicability of these results.

Acknowledgments

The authors wish to acknowledge the contributions of Mr. P. Silkowski in the calculation of the oscillating airfoil fluid mechanics. They thank Dr. I. J. Day for his thought-provoking discussions. This work was supported by the US Air Force Office of Scientific Research, Dr. J. McMichael, Technical Monitor, and by the Office of Naval Research, Dr. R. J. Hansen, Technical Monitor.

References

- Drela, M., 1988, Private Communication.
- Epstein, A. H., Ffowcs Williams, J. E., and Greitzer, E. M., 1989, "Active Suppression of Aerodynamic Instabilities in Turbomachines," *J. of Prop. and Power*, Vol. 5, No. 2, pp. 204-211.
- Garnier, V. H., Epstein, A. H., and Greitzer, E. M., 1991, "Rotating Waves as a Stall Inception Indication in Axial Compressors," *ASME JOURNAL OF TURBOMACHINERY*, Vol. 113, pp. 290-302.
- Hynes, T. P., and Greitzer, E. M., 1987, "A Method for Assessing Effects of Inlet Flow Distortion on Compressor Stability," *ASME JOURNAL OF TURBOMACHINERY*, Vol. 109, pp. 371-379.
- Lamaire, R. O., 1987, "Robust Time and Frequency Domain Estimation Methods in Adaptive Control," PhD thesis, Department of Electrical Engineering and Computer Science, MIT, Cambridge, MA.
- Lee, N. K. W., and Greitzer, E. M., 1990, "Effects of Endwall Suction and Blowing on Compressor Stability Enhancement," *ASME JOURNAL OF TURBOMACHINERY*, Vol. 112, pp. 133-144.
- Longley, J. P., 1988, "Inlet Distortion and Compressor Stability," PhD thesis, Cambridge University Engineering Dept., Cambridge, United Kingdom.
- Longley, J. P., 1990, Unpublished MIT Gas Turbine Laboratory Technical Note.
- Ludwig, G. R., and Nenni, J. P., 1980, "Tests of an Improved Rotating Stall Control System on a J-85 Turbojet Engine," *ASME Journal of Engineering for Power*, Vol. 102, pp. 903-911.
- McDougall, N. M., 1988, "Stall Inception in Axial Compressors," PhD thesis, Cambridge University, United Kingdom.
- McDougall, N. M., Cumpsty, N. A., and Hynes, T. P., 1990, "Stall Inception in Axial Compressors," *ASME JOURNAL OF TURBOMACHINERY*, Vol. 112, pp. 116-125.
- Moore, F. K., and Greitzer, E. M., 1986, "A Theory of Post-Stall Transients in Axial Compressors: Part I—Development of the Equations," *ASME Journal of Engineering for Gas Turbines and Power*, Vol. 108, pp. 68-76.
- Paduano, J., Valavani, L., Epstein, A. H., Greitzer, E. M., and Guenette, G. R., 1990, "Modelling for Control of Rotating Stall," presented at 29th IEEE Conference on Decision and Control, IEEE Control System Society, Honolulu, HI.
- Paduano, J. D., 1992, "Active Control of Rotating Stall in Axial Compressors," *GTL Report No. 208*, Gas Turbine Laboratory, MIT.
- Silkowski, P. D., 1990, "Aerodynamic Design of Moveable Inlet Guide Vanes for Active Control of Rotating Stall," M.S. thesis, Department of Aeronautics and Astronautics, MIT, Cambridge, MA.
- Yonke, W. A., Landy, R. J., and Stewart, J. F., 1987, "HIDEC Adaptive Engine Control System Flight Evaluation Results," *ASME Paper No. 87-GT-257*.

Evaluation of Approaches to Active Compressor Surge Stabilization

J. S. Simon

L. Valavani

A. H. Epstein

E. M. Greitzer

Gas Turbine Laboratory,
Massachusetts Institute of Technology,
Cambridge, MA 02139

Recent work has shown that compression systems can be actively stabilized against the instability known as surge, thereby realizing a significant gain in system mass flow range. Ideally, this surge stabilization requires only a single sensor and a single actuator connected by a suitable control law. Almost all research to date has been aimed at proof of concept studies of this technique, using various actuators and sensor combinations. In contrast, the work reported here can be regarded as a step toward developing active control into a practical technique. In this context, the paper presents the first systematic definition of the influence of sensor and actuator selection on increasing the range of stabilized compressor performance. The results show that proper choice of sensor as well as actuator crucially affects the ability to stabilize these systems, and that, overall, those actuators most closely coupled to the compressor (as opposed to the plenum or throttle) appear most effective. In addition, the source of the disturbances driving the system (for example, unsteady compressor pressure rise or unsteady combustor heat release) has a strong influence on control effectiveness, as would be expected for a controls problem of this type. This paper both delineates general methodologies for the evaluation of active compressor stabilization strategies and quantifies the performance of several approaches that might be implemented in gas turbine engines.

Introduction

The stable operating regime of a compressor installed in a jet engine (or any pumping system) is often limited by the onset of large-amplitude fluctuations in mass flow and pressure rise known as surge. Due to the loss of performance and thrust, as well as possible mechanical and thermal loads, surge is an important factor in compressor design and operation.

Surge is understood to be the lowest order natural oscillatory mode of the compression system (Greitzer, 1981) and experiments show that small-amplitude, linear disturbances can quickly grow into large amplitude, fully developed surge (Fink, 1992). Epstein et al. (1989) proposed that surge could be prevented by actively damping these disturbances while their amplitude was low. In this approach, the unsteady perturbations are directly influenced and the mean operating parameters are virtually unaltered. Epstein et al. gave some discussion of the mechanism of this stabilization and commented that various feedback schemes actually differ in how the instability is suppressed.

Active stabilization has now been demonstrated experimentally for centrifugal compressors by several investigators, for example, Ffowcs Williams and Huang (1989) and Pinsley et al. (1991). Gysling et al. (1991) also showed that significant gains in mass flow range can be realized using a tailored structure to provide the feedback path. These studies also showed that a lumped parameter model of the pumping system cap-

tured the essential dynamics of the surge process in the machines investigated, and this will be the approach taken here.

For example, Fig. 1 shows experimental and analytical results taken from Pinsley et al. (1991) and Gysling et al. (1991), compared to the results for no control. All the results are for a centrifugal turbocharger at a pressure ratio of roughly two. The surge point without control as well as with feedback is also indicated. An active compressor stabilization system conceptually consists of sensors to detect fluid disturbances within the compression system, actuators to introduce desired perturbations, and a suitable control law connecting the two. Theoretically, surge requires only a single sensor and actuator,

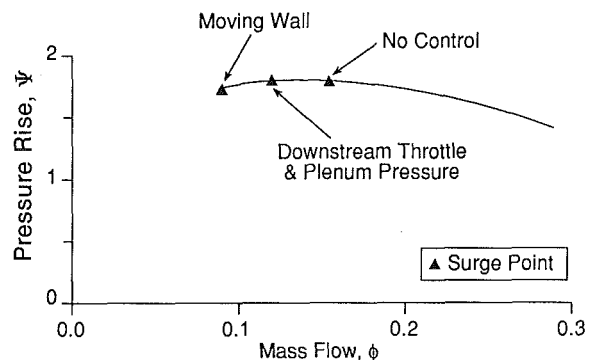


Fig. 1 Centrifugal compressor flow range using different control schemes (data of Pinsley et al. (1991), Gysling et al. (1991), and Simon (1992))

Contributed by the International Gas Turbine Institute and presented at the 37th International Gas Turbine and Aeroengine Congress and Exposition, Cologne, Germany, June 1-4, 1992. Manuscript received by the International Gas Turbine Institute February 11, 1992. Paper No. 92-GT-182. Associate Technical Editor: L. S. Langston.

Table 1 Sensing and actuation options considered

Actuation	Sensing
Injection in compressor duct	Inlet mass flow
Valve close-coupled to compressor	Plenum pressure
Plenum bleed valve	Compressor face P_{total}
Plenum heat addition	Compressor face P_{static}
Variable plenum volume	Plenum temperature
Variable inlet geometry	
Fast inlet guide vanes	
Tangential inlet injection	
Auxilliary compressor stage	
Plenum mass injection	
Inlet duct bleed	

with many choices available for their type and location. Sensors may measure pressure, mass flow, velocity, or temperature within the compressor duct upstream or downstream of the compressor, in the plenum, or at the throttle. Similarly, there are many methods to introduce unsteady fluid perturbations: varying throttle area, moving a plenum or duct wall, introducing or bleeding off mass flow, varying the heat addition in the plenum (when it is a combustor), as well as introducing a variable throttle between the compressor and plenum, to name a few. A representative list of sensing and actuation options in Table 1.

The purpose of this paper is to show that selection of sensor and actuator type and location is a critical factor in determining the effectiveness and practicality of an active stabilization system. Because of the practical interest in this question, the paper presents a methodology to compare different implementation alternatives and carries out this comparison for a number of candidate strategies. Comparing the performance of active compressor surge stabilization systems is difficult in that there are many sensor-actuator pairs conceivable. When coupled to the compressor, each forms a different physical system, with differing dynamic behavior, physical limitations, and overall performance. The steps included in the comparison of different control strategies are thus as follows:

Analytical models of specific systems are developed to elu-

cidate the relative performance sensitivities to nondimensional system parameters.

Numerical calculations are carried out to quantify the limits to control of various sensor-actuator pairs when connected by a simple proportional control law.

Optimal control theory is used to evaluate the physical limits to control given perfect measurements of the system state.

It may be useful to mention two factors that bear on the overall viewpoint and scope of the present work. First, we note that the general problem of actuator/sensor selection has been considered by a number of researchers in other applications (see, for example, Norris and Skelton, 1989; Schmitendorf, 1984; Muller and Weber, 1972), and these approaches should certainly be considered in future investigations of this type. For the present purposes, it was thought useful to obtain quantitative comparisons in a manner more closely related to the concepts and thinking of the turbomachinery community. The methodology followed here was developed to this end.

Second, the goals of this work are to make clear the large influence that implementation (sensor-actuator selection) has on the effectiveness of active compressor control and to elucidate physical limitations on active control. We thus do not consider all possible active control systems but select those that may be most readily implemented in various gas turbine systems.

Compressor System Modeling for Control

We use a standard lumped parameter model of compression system dynamics (Greitzer, 1981) following the geometry of Fig. 2(a). This model incorporates the following assumptions: one-dimensional, incompressible flow in the compressor duct; compressor considered as a quasi-steady actuator disk; pressure in the plenum is spatially uniform but varying in time and flow velocity is negligible; throttle behavior is quasi-steady. The temporal (τ) behavior of the nondimensional plenum pressure rise (ψ) and nondimensional mass flow (or flow coefficient) (ϕ) can then be described as:

$$\frac{d\phi}{d\tau} = B(\Psi_c(\phi) - \psi) \tag{1a}$$

$$\frac{d\psi}{d\tau} = \frac{1}{B}(\phi - \Phi_T(\psi)) \tag{1b}$$

for the system without active control. Equation (1a) expresses

Nomenclature

- a = speed of sound
- A_c = compressor flow through area
- A_w = area of movable plenum wall
- B = compressor stability parameter = $(U_T/2a) \sqrt{V/(A_c \mathcal{L}_c)}$
- C_p = specific heat at constant pressure
- C_v = specific heat at constant volume
- E = energy of gas in plenum
- E^* = dimensionless energy of gas in plenum = $C_v T_p / \rho_a \bar{V}_p C_v T_a$
- K = proportional gain
- \mathcal{L} = equivalent length = $\int_0^x A_c / A(x) dx$
- m = mass of gas in plenum
- m^* = dimensionless mass of gas in plenum = $\rho_p \bar{V}_p / \rho_a \bar{V}_p$
- m_C = dimensionless slope of compressor speed line = $\partial \Psi_c / \partial \phi$
- m_{Ce} = dimensionless slope of equiv-

- alent compressor speed line formed by compressor in series with close-coupled valve = $\partial / \partial \phi (\Psi_c - \Psi_{cc})$
- m_T = dimensionless slope of throttle pressure drop versus flow characteristic = $1 / (\partial \Phi_T / \partial \Psi)$
- m_{Te} = dimensionless slope of equivalent throttle characteristic for parallel combination of throttle and plenum bleed valve = $1 / (\partial (\Phi_T + \Phi_b) / \partial \Psi)$
- M_T = impeller tip Mach number = U_T / a_a
- p = absolute pressure
- p_p^* = plenum pressure ratio = p_p / p_a
- Q = heat release rate
- Q^* = dimensionless heat release rate = $Q / \rho_a U_T A_c C_p T_a$

- R = gas constant for ideal gas = $C_p - C_v$
- S = Laplace transform variable
- ΔT_{oc} = total temperature rise across compressor
- ΔT_{oc}^* = dimensionless total temperature rise across compressor $\Delta T_{oc}^* = \Delta T_{oc} / T_a$
- t = time
- t_w = first-order constant for movable plenum wall
- t_w^* = dimensionless first-order lag time constant for movable plenum wall = $t_w \omega_H$
- u = control input signal
- U_T = impeller tip speed
- v_w = velocity of movable wall
- V = slope of valve characteristic = $\partial \Phi / \partial \alpha$
- V^* = dimensionless plenum volume = \bar{V} / \bar{V}

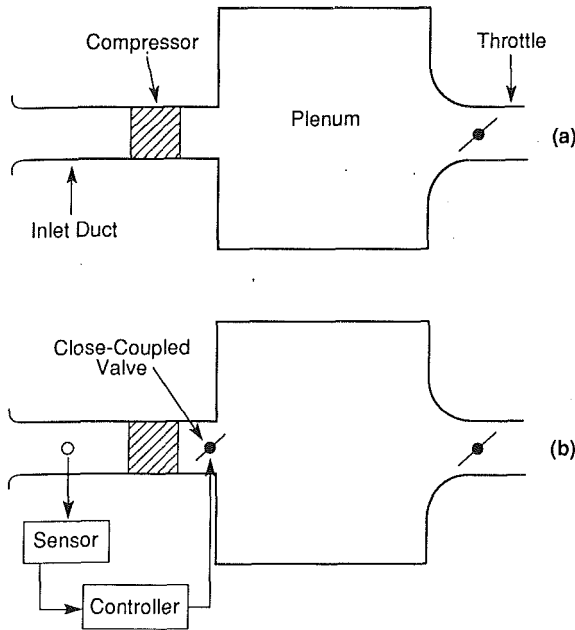


Fig. 2 Lumped parameter compression system: (a) no control; (b) with sensor in inlet and close-coupled valve actuator control system

a one-dimensional momentum balance in the compressor duct. Equation (1b) represents the mass balance for the plenum. The compressor characteristic, $\Psi_c(\phi)$, gives the nondimensional compressor pressure rise as a function of the flow coefficient, ϕ , and the throttle characteristic, $\Phi_T(\psi)$, represents the throttle pressure drop. The nondimensional quantity B , defined as $(U_T/2a) \sqrt{V/(A_c \mathcal{L}_c)}$, can be regarded as a measure of the ratio of plenum compliance to duct inertia. B will be seen to be of importance in determining control effectiveness.

To describe actively controlled systems, we must account for the influence of actuators on system performance, represent sensor measurements, and incorporate a feedback law. Each choice of sensor-actuator pair results in a distinct system with different dynamics. Because the detailed derivation of the system equations is fairly lengthy, we shall derive the characteristic equations for one particular system to illustrate the idea, and present only results for the other systems.

Suppose a total pressure probe at the compressor inlet is used as the sensor, and a valve that modulates the compressor exit area is selected for the actuator. This actuator will be referred to as the *close-coupled valve* (Fig. 2b). The basic model of Fig. 2(a) must be modified to include the valve pressure drop in the compressor duct momentum balance. Because the instantaneous mass flow through the compressor is the same as the flow through the close-coupled valve, the equations that describe the system are now:

$$\frac{d\phi}{d\tau} = B(\Psi_c(\phi) - \psi - \Psi_{cc}(\phi, \alpha_{cc})) \quad (2a)$$

$$\frac{d\psi}{d\tau} = \frac{1}{B}(\phi - \Phi_T(\psi)) \quad (2b)$$

Comparison with Eqs. (1) shows that the original system has been modified by the introduction of a *control term*, $\Psi_{cc}(\phi, \alpha_{cc})$, which represents the pressure drop through the close-coupled valve as a function of flow through the valve, ϕ , and valve fraction open, α_{cc} . To include the sensor measurement in the model, the following *output equation* is formed:

$$\psi_{02} = \Psi_{cc}(\phi, \alpha_{cc}) - \Psi_c(\phi) + \psi,$$

which expresses the total pressure, ψ_{02} , at the compressor face, as a function of the *state variables*, ϕ , ψ , and the *input variable* α_{cc} .

For small perturbations from equilibrium, which we denote as $\hat{\phi}$ and $\hat{\psi}$, the system dynamics and measurement equation can be approximated by the linear system

$$\frac{d}{d\tau} \begin{bmatrix} \hat{\phi} \\ \hat{\psi} \end{bmatrix} = \begin{bmatrix} B \left(\frac{\partial \Psi_c}{\partial \phi} - \frac{\partial \Psi_{cc}}{\partial \psi} \right) & -B \\ \frac{1}{B} & -\frac{1}{B} \left(\frac{\partial \Phi_T}{\partial \psi} + \frac{\partial \Phi_b}{\partial \psi} \right) \end{bmatrix} \begin{bmatrix} \hat{\phi} \\ \hat{\psi} \end{bmatrix} + \begin{bmatrix} -B \frac{\partial \Psi_{cc}}{\partial \alpha_{cc}} \\ 0 \end{bmatrix} \hat{\alpha}_{cc} \quad (3a)$$

$$\hat{\psi}_{02} = \left[\left(\frac{\partial \Psi_{cc}}{\partial \phi} - \frac{\partial \Psi_c}{\partial \phi} \right) 1 \right] \begin{bmatrix} \hat{\phi} \\ \hat{\psi} \end{bmatrix} + \left[\frac{\partial \Psi_{cc}}{\partial \alpha_{cc}} \right] \hat{\alpha}_{cc} \quad (3b)$$

Nomenclature (cont.)

\dot{V}_c^* = dimensionless commanded rate of change of plenum volume
 W = dimensionless term relating changes in plenum volume to plenum pressure = $2p_p/M_T^2 p_a$
 x = vector of system states
 α_b = bleed valve fraction open
 α_{cc} = close-coupled valve fraction open
 α_d = desired (commanded) valve fraction open
 γ = ratio of specific heats
 ζ = damping ratio
 ξ = dimensionless rate of change of plenum volume = $A_w v_w / U_T A_c$
 ρ = density
 τ = dimensionless time = $t\omega_H$
 ϕ = flow coefficient = $\dot{m} / \rho_a U_T A_c$
 Φ = function giving dimensionless

flow through valve as function of pressure and valve area
 ψ = plenum pressure coefficient = $(p_p - p_a) / (1/2 \rho_a U_T^2)$
 Ψ_{oj} = mass injector supply pressure coefficient = $(p_{oj} - p_a) / (1/2 \rho_a U_T^2)$
 Ψ_{cc} = dimensionless total pressure drop across close-coupled valve = $\Psi_{cc}(\phi, \alpha_{cc})$
 Ψ_c = dimensionless pressure rise versus flow characteristic of compressor, $\Psi_c(\phi)$
 $\Delta\Psi_d$ = downstream injector characteristic; $\Psi_d = \Psi_{02} - \Psi_{oj}$
 $\Delta\Psi_u$ = upstream injector characteristic; $\Psi_u = \Psi_{01} - \Psi_{oj}$
 ω_H = Helmholtz frequency
 ω_c = filter cut-off frequency

Superscripts

$\hat{}$ = perturbation quantity
 $\dot{}$ = first derivative with respect to time
 $\ddot{}$ = second derivative with respect to time
 $\bar{}$ = time mean quantity

Subscripts

a = ambient
 b = bleed valve
 c = compressor
 cc = close-coupled valve
 j = injector jet
 p = plenum
 T = throttle or impeller tip
 1 = compressor duct inlet
 2 = compressor duct downstream of injector
 0 = total

which results from retaining only first-order terms in a standard Taylor series expansion about equilibrium. In a similar fashion, linear time domain models may be obtained for other sensor-actuator pairs.

The behaviors of systems with different sensor-actuator pairing are most clearly revealed from their *transfer functions*, which are defined as the ratio of the Laplace transformed system output (sensor signal, ψ_{o2}) to input (actuator motion, α_{cc}). For the present example, the transfer function, $G(s)$, is

$$G(s) \triangleq \frac{\psi_{o2}(s)}{\alpha_{cc}(s)} = \frac{m_{Ce}BT \left(s + \frac{1}{Bm_T} \right)}{s^2 + \left(\frac{1}{Bm_T} - Bm_{Ce} \right) s + \left(1 - \frac{m_{Ce}}{m_T} \right)} \quad (4)$$

In Eq. (4), s is the Laplace transform variable, $m_{Ce} = \partial(\Psi_c - \Psi_{cc})/\partial\phi$ is defined as the equivalent compressor slope for the combined valve and compressor; $m_T = 1/(\partial\Phi_T/\partial\psi)$ is the slope of the throttle pressure drop versus flow characteristic, and $T = -\partial\Psi_{cc}/\partial\alpha_{cc}$ relates changes in valve area to valve pressure drop.

Open loop transfer functions for three different actuators and four different sensors illustrated in Fig. 3 are presented in Table 2. The transfer functions for all the sensor-actuator pairs in Table 2 have the same denominator polynomial (de-

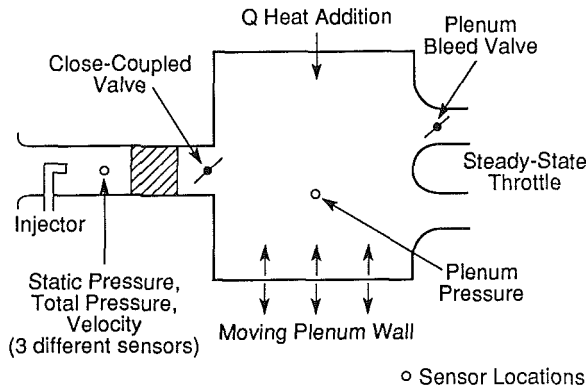


Fig. 3 Actuators and sensors selected for evaluation

noted as $D(s)$ and given below the table), but the numerator polynomials differ. The inherent differences are thus captured by the latter. For generality, the expressions given in Table 2 use the equivalent throttle slope m_{Te} of a throttle in parallel with a bleed valve. If no bleed valve is used, $m_T = m_{Te}$.

Feedback Stabilization. For feedback stabilization, one measures the system output, compares it with some desired reference level, determines the error and computes an input signal (command to the actuator) based upon this error to drive the error towards zero. If this can be successfully accomplished, the system output will be maintained close to the desired value, which normally implies that the system is stable.¹ The relationship between the system error signal and the actuator command is called the *control law*, and may be dynamic (involving differential equations) or static (using only algebraic relationships). In this section, we will use the simplest control law, a proportional relationship between input and output, to elucidate effects of actuator and sensor selection, but in a subsequent section, we will examine the impact of the form of the control law.

Stability Modification Using Proportional Control. System stability under the influence of a proportional control law is determined from the roots of the *closed loop characteristic equation* (this is derived in many texts: see, for example, Ogata, 1970; Di Stefano et al., 1990; Van de Vegte, 1990):

$$G_D(s) + KG_N(s) = 0 \quad (5)$$

In Eq. (5), $G_N(s)$ and $G_D(s)$ are the numerator and denominator polynomials, respectively, of the transfer function given in Table 2 and the gain, K , is a real constant of proportionality in the control law. The system will be stable if and only if all the roots of the characteristic equation have strictly negative real parts. For the present case, where the characteristic equation is a second-order polynomial, that is equivalent to requiring all the coefficients in the equation to be strictly positive.

Equation (5) is the sum of two terms, $G_D(s)$ and $KG_N(s)$. When the control is off (K set to zero), stability is determined

¹It is possible, in special cases, for a system to have an instability that cannot be seen in a particular sensor's output. However, if a system is *detectable* (Kwakernaak and Sivan, 1972), as is almost invariably the case, this type of pathological behavior cannot occur.

Table 2 Open loop transfer functions (numerator shown in table; denominator, $D(s)$, given below)

Actuator	Close-Coupled Valve	Plenum Bleed Valve	Moveable Wall
Sensor			
Compressor Mass Flow	$\frac{BT \left(s + \frac{1}{Bm_{Te}} \right)}{D(s)}$	$\frac{V}{D(s)}$	$\frac{WB}{D(s)}$
Plenum Pressure	$\frac{T}{D(s)}$	$\frac{-\frac{V}{B} (s - Bm_{Ce})}{D(s)}$	$\frac{-W (s - Bm_{Ce})}{D(s)}$
Compressor Face Total Pressure	$\frac{-Ts \left(s + \frac{1}{Bm_{Te}} \right)}{D(s)}$	$\frac{-\frac{V}{B} s}{D(s)}$	$\frac{-Ws}{D(s)}$
Compressor Face Static Pressure	$\frac{-T \left(s^2 + \left(2\phi B + \frac{1}{Bm_{Te}} \right) s + \frac{2\phi}{m_{Te}} \right)}{D(s)}$	$\frac{-\frac{V}{B} (s + 2\phi B)}{D(s)}$	$\frac{-W (s + 2\phi B)}{D(s)}$

$$D(s) = s^2 + \left(\frac{1}{Bm_{Te}} - Bm_{Ce} \right) s + \left(1 - \frac{m_{Ce}}{m_{Te}} \right)$$

from the roots of $G_D(s)$ only, and is the same whatever the actuator-sensor pair. As gain K is increased from zero, system stability becomes increasingly modified by the $KG_N(s)$ term, and because the various actuator-sensor pairs have different numerator polynomials, $G_N(s)$, the effect of feedback also varies. This is best illustrated by several specific examples. The first two examples show the effect of sensor type, whereas the first two examples show the effect of sensor type, whereas comparison between behavior in the second and third illustrates the impact of the actuator.

Example 1: Close-Coupled Control Valve With Mass Flow Measurement. Using the appropriate transfer function from Table 2, substituting into the characteristic Eq. (5), and rearranging results in a characteristic equation of the form

$$s^2 + \left(\frac{1}{Bm_{Te}} - Bm_{Ce} + KBT \right) s + \left(1 - \frac{m_{Ce}}{m_{Te}} + \frac{KT}{m_{Te}} \right) = 0 \quad (6)$$

For stability we require

$$\left(\frac{1}{Bm_{Te}} - Bm_{Ce} + KBT \right) > 0 \quad (7a)$$

and

$$\left(1 - \frac{m_{Ce}}{m_{Te}} + \frac{KT}{m_{Te}} \right) > 0. \quad (7b)$$

All the parameters in these two inequalities are positive numbers except for the compressor slope, m_{Ce} . If $m_{Ce} < 0$, as it typically is for high flow rates, the system will be stable with no feedback, that is with K set equal to zero. As the flow rate becomes lower, m_{Ce} will become less negative, reaching zero at the peak of the compressor characteristic, and then moving to a large enough positive value so that the system will be unstable without feedback. For sufficiently large values of the gain K , however, both the inequalities expressed in Eqs. (7a) and (7b) can be simultaneously satisfied and the system can always be stabilized.

Example 2: Close-Coupled Valve With Plenum Pressure Measurement. In this case, as given in Table 2, the numerator polynomial of the transfer function contains only a constant term. The characteristic equation is:

$$0 = s^2 + \left(\frac{1}{Bm_{Te}} - Bm_{Ce} \right) s + \left(1 - \frac{m_{Ce}}{m_{Te}} + KT \right), \quad (8)$$

The system can now only be stabilized if the equivalent compressor slope is small enough so that the term $(1/Bm_{Te} - Bm_{Ce})$ is positive; in other words, the equivalent compressor slope obeys the inequality $m_{Ce} < 1/B^2 m_{Te}$. The ability of proportional feedback to stabilize this system is thus limited to a certain range of parameters. For many applications, B is unity or larger and the throttle slope, m_{Te} , is on the order of ten to one hundred, so the useful range can be quite small.

Example 3: Plenum Bleed Valve With Measurement of Plenum Pressure. From Table 2, the numerator polynomial for this case is

$$G_N(s) = -\frac{V}{B} (s - Bm_{Ce}) \quad (9)$$

and the characteristic equation is given by

$$0 = s^2 + \left(\frac{1}{Bm_{Te}} - Bm_{Ce} - \frac{KV}{B} \right) s + \left(1 - \frac{m_{Ce}}{m_{Te}} + KVm_{Ce} \right) \quad (10)$$

Whether the gain K is chosen to be positive or negative, it will have the desired effect on only one of the two coefficients of the characteristic equation. As a result, stabilization is limited to cases where $m_{Ce} < 1/B$. The limitation is associated with the sign change between the leading and the constant coefficient of $G_N(s)$ (Eq. (9)), which implies that $G_N(s)$ has a zero in the right half of the complex plane. Systems whose transfer functions have numerators with zeros in the right half of the complex plane are called nonminimum phase systems. The ability to control nonminimum phase systems is known to be subject to certain fundamental limitations (see Freudenberg and Looze, 1985) and this is just one manifestation of the generally poor behavior encountered in such systems.

The remaining actuator-sensor pairs whose transfer functions appear in Table 2 have also been analyzed, and the results are summarized in Tables 3 and 4. Table 3 gives the characteristic equation (the roots of which define the stability of the closed loop system) for all the sensor-actuator pairs. For stability, all coefficients in the characteristic equation must be

Table 3 Closed loop characteristic equations with proportional gain K

Actuator Sensor	Close-Coupled Valve	Plenum Bleed Valve	Moveable Wall
Compressor Mass Flow	$s^2 + \left(\frac{1}{Bm_{Te}} - Bm_{Ce} + KBT \right) s + \left(1 - \frac{m_{Ce}}{m_{Te}} + \frac{KT}{m_{Te}} \right)$	$s^2 + \left(\frac{1}{Bm_{Te}} - Bm_{Ce} \right) s + \left(1 - \frac{m_{Ce}}{m_{Te}} + KV \right)$	$s^2 + \left(\frac{1}{Bm_{Te}} - Bm_{Ce} \right) s + \left(1 - \frac{m_{Ce}}{m_{Te}} + KWB \right)$
Plenum Pressure	$s^2 + \left(\frac{1}{Bm_{Te}} - Bm_{Ce} \right) s + \left(1 - \frac{m_{Ce}}{m_{Te}} + KT \right)$	$s^2 + \left(\frac{1}{Bm_{Te}} - Bm_{Ce} + \frac{KV}{B} \right) s + \left(1 - \frac{m_{Ce}}{m_{Te}} - Km_{Ce}V \right)$	$s^2 + \left(\frac{1}{Bm_{Te}} - Bm_{Ce} + KW \right) s + \left(1 - \frac{m_{Ce}}{m_{Te}} - KWBm_{Ce} \right)$
Compressor Face Total Pressure	$(1+KT)s^2 + \left(-Bm_{Ce} + \frac{1}{Bm_{Te}} + \frac{KT}{m_{Te}} \right) s + \left(1 - \frac{m_{Ce}}{m_{Te}} \right)$	$s^2 + \left(\frac{1}{Bm_{Te}} - Bm_{Ce} + \frac{KV}{B} \right) s + \left(1 - \frac{m_{Ce}}{m_{Te}} \right)$	$s^2 + \left(\frac{1}{Bm_{Te}} - Bm_{Ce} + KW \right) s + \left(1 - \frac{m_{Ce}}{m_{Te}} \right)$
Compressor Face Static Pressure	$(1+KT)s^2 + \left(-Bm_{Ce} + \frac{1}{Bm_{Te}} + KT2\phi B + \frac{KT}{m_{Te}} \right) s + \left(1 - \frac{m_{Ce}}{m_{Te}} + \frac{KT2\phi}{m_{Te}} \right)$	$s^2 + \left(\frac{1}{Bm_{Te}} - Bm_{Ce} + \frac{KV}{B} \right) s + \left(1 - \frac{m_{Ce}}{m_{Te}} + 2KV\phi \right)$	$s^2 + \left(\frac{1}{Bm_{Te}} - Bm_{Ce} + KW \right) s + \left(1 - \frac{m_{Ce}}{m_{Te}} + 2KW\phi B \right)$

Table 4 Limitations on compressor flow range increase with proportional control

Actuator Sensor	Close-Coupled Valve	Plenum Bleed Valve	Moveable Wall
Compressor Mass Flow	Unlimited Range Increase $K \sim \frac{m_{Ce}}{T}$ as $m_{Ce} \rightarrow \infty$ $K \sim \frac{m_{Ce}}{T}$ as $B \rightarrow \infty$	Limited Range Increase $m_{Ce} < \frac{1}{B^2 m_{Te}}$	Limited Range Increase $m_{Ce} < \frac{1}{B^2 m_{Te}}$
Plenum Pressure	Limited Range Increase $m_{Ce} < \frac{1}{B^2 m_{Te}}$	Limited Range Increase $m_{Ce} < \frac{1}{B}$	Limited Range Increase $m_{Ce} < \frac{1}{B}$
Compressor Face Total Pressure	Limited Range Increase $m_{Ce} < m_{Te}$	Limited Range Increase $m_{Ce} < m_{Te}$	Limited Range Increase $m_{Ce} < m_{Te}$
Compressor Face Static Pressure	Unlimited Range Increase $K \sim \frac{m_{Ce}}{2T\phi}$ as $m_{Ce} \rightarrow \infty$ $K \sim \frac{m_{Ce}}{2T\phi}$ as $B \rightarrow \infty$	Unlimited Range Increase $K \sim \begin{cases} \frac{m_{Ce}B^2}{V} \text{ when } \frac{1}{2\phi B^2 m_{Te}} < 1 \\ \frac{m_{Ce}}{2V\phi m_{Te}} \text{ otherwise as } m_{Ce} \rightarrow \infty \end{cases}$ $K \sim \frac{B^2 m_{Ce}}{V}$ as $B \rightarrow \infty$	Unlimited Range Increase $K \sim \begin{cases} \frac{m_{Ce}B}{W} \text{ when } \frac{1}{2\phi B^2 m_{Te}} < 1 \\ \frac{m_{Ce}}{2m_{Te}W\phi B} \text{ otherwise as } m_{Ce} \rightarrow \infty \end{cases}$ $K \sim \frac{Bm_{Ce}}{W}$ as $B \rightarrow \infty$

positive; from this requirement, the capability of each scheme to extend the flow range to high values of compressor slope can be determined.

The behavior of the different pairs is shown more explicitly in Table 4, which summarizes the limitations of each pair. In some instances, for example sensing compressor mass flow and actuating with a close-coupled valve, the range of parameters over which stabilization may be achieved is unlimited, although large values of gain may be required with a large compressor slope or large value of the B parameter. In these cases, therefore, the asymptotic behavior of the required gain is given for large B and compressor slope, in order to show the trends to be expected in these regimes. As will be discussed in more detail subsequently, excessive gain must be avoided in practical situations; however, as shown in Table 4, the gain increases either linearly or quadratically with compressor slope and B . Thus, there will be a practical limitation on maximum slope or maximum B at which the system can be stabilized.

An additional point to note is that the limitations on stability can, in some cases, be relaxed or removed by using a dynamic control law. Thus, the limitations expressed in this section reflect the combined properties of actuator, sensor, and control law taken together, and not necessarily the individual elements. Within the restriction to a fixed control law maintained here, however, the comparison of different sensor-actuator pairs is both valid and useful.

Practical Limits to Control

The analytical results so far indicate that the ability to stabilize the system with proportional control depends strongly on proper pairing of actuator and sensor, as well as on the values of the system parameters, particularly the compressor slope (m_C) and B .

In the above examples, however, we have considered ideal, linear systems in which only the dynamics of the pumping system are modeled. To address the issue of implementation, it is also necessary to include bandwidth limitations and actuator constraints (for example, servo dynamics and stops), which are encountered in any physical realization. As a matter of definition, by actuator we refer here to the entire actuation system including the flow train element (e.g., the valve), the motor that drives it, and any included feedback elements.

The bandwidth limitations may be imposed by the sensors, processor, actuator, or some combination of the three. System bandwidth may also need to be constrained to maintain stability if unmodeled dynamics are present. Unless the bandwidth of the actuator is much greater than that of the compression system, there is a nonnegligible time lag between the command output of the control law and the response of the flow train element. The lags introduced by the actuator generally result in reduced control effectiveness, although to some degree, they can be compensated for by use of a control law more sophisticated than proportional control.

Another constraint on control effectiveness is introduced by bounds on actuator influence. For example, valve areas can only be modulated between 0 and 100 percent (i.e., the valve must be somewhere between full open and full closed).

Sensor and Actuator Pairs and Fluid Model. In this section, we numerically examine the limitations imposed by effects such as those described in the preceding. Five actuators and four sensors are studied as representative of a diverse set of implementation options. The selected actuators were:

- 1 injection in the compressor duct
- 2 close-coupled control valve
- 3 plenum bleed valve
- 4 plenum heat addition
- 5 a movable plenum wall

The selected sensors were:

- 1 compressor duct mass flow
- 2 plenum pressure
- 3 compressor face static pressure
- 4 compressor face total pressure

These actuators and sensors are shown schematically in Fig. 3. At the level of idealization used here, the close-coupled valve could be either at compressor inlet or exit without changing the results.

The linear lumped parameter models of the previous section were extended as required, because the various actuators require additional system states. The following assumptions were made in modeling the actuator behavior:

- 1 The injector flow is incompressible and fully mixed out.
- 2 The injector is quasi-steady; inertial effects are lumped into upstream and downstream ducts.

- 3 The close-coupled valve flow is incompressible and quasi-steady.
- 4 The plenum is well mixed, has uniform pressure, temperature, negligible velocities, and follows ideal gas laws with constant specific heat.
- 5 The mass of fuel is neglected and heat release is instantaneous.
- 6 The throttle and bleed valve are quasi-steady.

The differential equations that describe the system dynamics are obtained by performing balances on momentum in the ducts and mass and energy in the plenum (Simon, 1992). They are:

$$\frac{d\phi_1}{d\tau} = \frac{-B}{(\mathcal{L}_1/\mathcal{L}_c)} (\Delta\Psi_u + \psi_{oj}) \quad (11a)$$

$$\frac{d\phi_2}{d\tau} = \frac{B}{(\mathcal{L}_2/\mathcal{L}_c)} ((\Delta\Psi_d + \psi_{oj}) + \Psi_c - \Psi_{cc} - \psi) \quad (11b)$$

$$\frac{dm^*}{d\tau} = \frac{M_T^2}{2BT_p^*} (\phi_2 - (\Phi_T + \Phi_b)) \quad (11c)$$

$$\frac{dE^*}{d\tau} = \frac{M_T^2\gamma}{2BT_p^*} \left(\phi_2(1 + \Delta T_{oc}^*) - (\phi_T + \phi_b)T_p^* + Q^* - P_p^* \left(\frac{\gamma-1}{\gamma} \right) \xi \right) \quad (11d)$$

$$\frac{dV^*}{d\tau} = -\frac{1}{t_w^*} V^* + \dot{V}_c^* \quad (11e)$$

There are five states needed. The mass flow rates in the portion of the duct upstream and downstream of the injector are given by ϕ_1 and ϕ_2 , the nondimensional mass and energy of the gas in the plenum are given by m^* and E^* , and the nondimensional plenum volume is given by V^* . The effects of the various actuators are given by the functions $\Delta\Psi_u$ and $\Delta\Psi_d$, representing the injector, Ψ_{cc} , representing the close coupled valve, Φ_b , representing the plenum bleed, Q^* , representing the plenum heat addition, and ξ , representing the plenum wall motion.

The general description is nonlinear, but it is small perturbations that are of primary interest here, and Eqs. (11) can be linearized to yield an equation set of the form:

$$\dot{\mathbf{x}} = \mathbf{Ax} + \mathbf{Bu} \quad (12)$$

with the output vector \mathbf{y} defined as

$$\mathbf{y} = \mathbf{Cx} + \mathbf{Du} \quad (13)$$

In Eqs. (12) and (13), the linearized state variables \mathbf{x} , the inputs \mathbf{u} , and the outputs \mathbf{y} are perturbations from the corresponding equilibrium values, and \mathbf{A} , \mathbf{B} , \mathbf{C} , and \mathbf{D} are appropriately dimensioned constant matrices. The state variables have been normalized as detailed in Table 5, so that unity magnitude for any of these perturbation variables has roughly the same physical significance.

All twenty pairings of the five actuators and four sensors have been evaluated with a proportional control law. Such a comparison provides two useful results. One is the identification of actuator-sensor pairs, which may be stabilized over a significant range of system parameters using the simplest possible control law. In addition, for those pairs with significant stabilization, the required gain gives a measure of the combined effectiveness of this choice of sensing and actuating locations.

As was discussed, it is useful to weed out those systems that could mathematically be stabilized but stand little chance of succeeding in an actual implementation. To this end, two constraints were imposed. First, the allowable magnitude of the normalized proportional gain was limited to be not more than 20. For example, at the maximum allowable gain, a 5 percent change in compressor mass flow would yield a 100 percent

Table 5 Normalization factors

Perturbation Variable	Normalized By
Flow	Time mean flow through compressor
Pressure	Time mean compressor pressure rise
Thermal input	Mean compressor work
Moving wall work input	Mean compressor work
Plenum bleed valve area	Area to fully close valve
Close-coupled valve area	Area to fully open or close (whichever is smaller)

change in plenum bleed valve area; that is, the valve would be fully closed. Second, the bandwidth of the feedback loop was limited by modeling a two-pole, low pass Butterworth filter in the feedback path. This filter can be given various physical interpretations such as probe dynamics, amplifier dynamics, actuator dynamics, or unmodeled dynamics in the compression system itself. Whatever the interpretation, the insertion of the filter insures that the feedback path has finite bandwidth, a constraint that will always exist in practice. The study was carried out with the cutoff frequency of this filter maintained at ten times the Helmholtz frequency of the system formed by the plenum and compressor ducts. Sensitivity to this assumption will be examined subsequently.

The figure of merit used to assess the actuator-sensor pairs was to examine the stability boundaries in a compressor slope versus B parameter plane. Preliminary studies showed that these two parameters have a dominant effect on system stability. It is thus more relevant, for example, to quantify the amount of stabilization that can be achieved in terms of the compressor slope, which enters into the stability in an explicit manner, rather than the change in mass flow at stall. The relative extent of the stabilized region in this compressor slope B -parameter plane thus provides an appropriate and useful basis for comparison. The boundaries were computed by first performing an incremental search over the three-dimensional (slope, B parameter gain) parameter space. For each fixed B , the value of gain that maximized the slope at instability, as well as the corresponding slope, was then found, again using an incremental search. The stability boundaries in the B parameter versus slope plane thus represent the maximum slope that could be stabilized using any gain less than 20.

Results of the Control Scheme Evaluations

The results of the calculations are summarized in Fig. 4, which shows the stability boundaries for 20 actuator-sensor pairs. The figure is broken into four plots, one for each sensor. Within each plot, the five curves indicate the different actuators. The region below and to the left of any given line is the region in which stabilization can be achieved. In the upper left-hand plot, for example, all the region to the left of the dash-dot line represents the range of compressor slope and B in which the combination of compressor mass flow sensor and close-coupled valve is capable of suppressing the instability.

Several general conclusions can be drawn from the results in Fig. 4:

- 1 The overall trend is that control becomes more difficult as the compressor slope and B parameter increase, with the maximum stable slope decreasing with increasing B .
- 2 Only the actuators located in the compressor duct, which act upon the compressor duct momentum (injector and close-coupled control valve), are capable of stabilization at steep slopes over the full range of B .
- 3 Plenum heat addition gives little or no stability.
- 4 In general, there is no best sensor independent of the actuator.

For reference, the range of B parameters that might be associated with large axial gas turbine engines is roughly 0.2

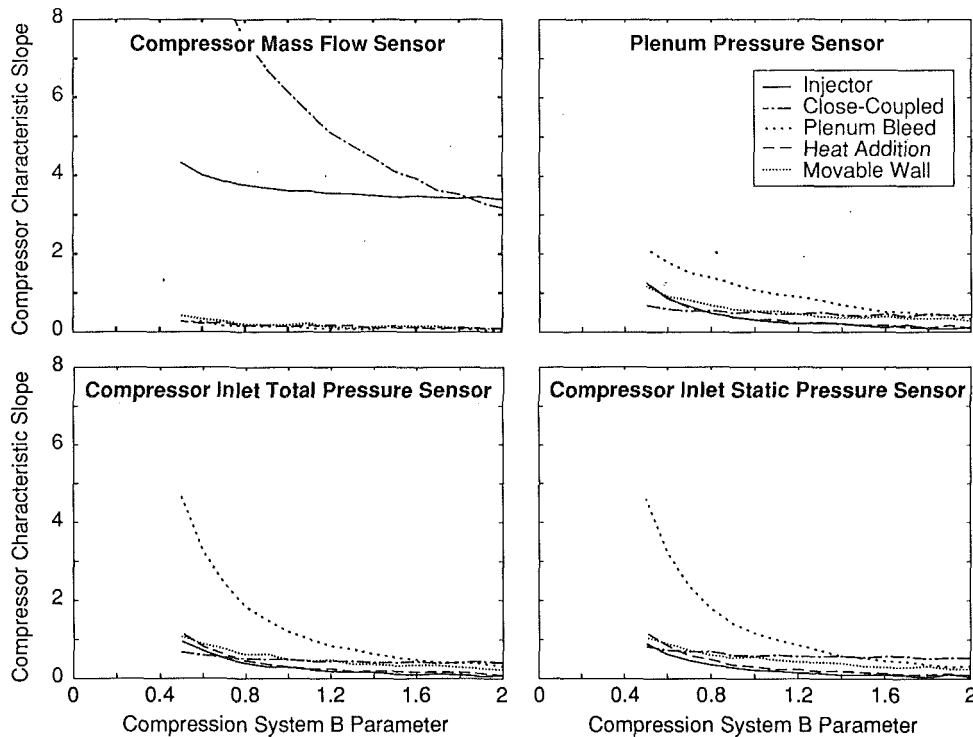


Fig. 4 Influence of sensor and actuator selection on maximum stabilized compressor characteristic slope for a bandwidth and gain-limited system

to 0.4, with that for small centrifugal machines approximately 0.5 to 2.

A more specific conclusion is given by the comparison of the results with the mass flow sensor to the other sensor locations. As B reaches a value of roughly unity, the ability of all the pairs to stabilize the system becomes quite small, except for the close-coupled valve and the injector, which use mass flow sensing. This points out clearly that not only is actuator position important, but so is sensor position as well.

The conclusion about the effect of actuator position is one that is in general accord with intuitive ideas of system behavior, but that having to do with sensors is somewhat less familiar. It is therefore worthwhile to give some physical motivation for the impact of sensor position.

The different dynamics brought about by the various sensors can be understood with reference to the nondimensional characteristic equation for the unsteady system behavior with no feedback:

$$s^2 + \left(\frac{1}{Bm_{Te}} - Bm_{Ce} \right) s + \left(1 - \frac{m_{Ce}}{m_{Te}} \right) = 0 \quad (14)$$

For stability the coefficients of the second and third terms must be positive, so that

$$m_{Ce} < \frac{1}{B^2 m_{Te}} \quad (15a)$$

$$m_{Ce} < m_{Te} \quad (15b)$$

As described by Greitzer (1981) the mechanism of instability can either be static, corresponding to the inequality in Eq. (15b) being violated, or dynamic, corresponding to the violation of that in Eq. (15a). Whichever of these events occurs (it is the second that is generally more important), the cause for this is a positive slope of the compressor pressure rise characteristic. Therefore, let us examine how the destabilizing effect of positive slope is ameliorated when different sensing schemes are used. As a case of high practical interest, we consider the close-coupled valve with two different sensors,

one measuring compressor mass flow and the other measuring the total pressure at the compressor inlet face.

In the first of these, the valve position, and hence the valve pressure drop, is proportional to the sensed perturbations in compressor mass flow. The pressure perturbations across the compressor and the across valve are both proportional to the mass flow perturbations. Because the valve is just downstream of the compressor, the two act in series, creating an effective compressor slope that is the sum of the (positive) slope across the compressor and the (negative) slope across the valve. It is this combined characteristic the system "sees."

Suppose the constant of proportionality between sensed mass flow and valve opening angle is K , and the rate of change of valve pressure drop per increment in opening angle is T . For a given mass flow perturbation, the effective slope of the compressor will change from m_{Ce} , with no feedback, to $m_{Ce} - KT$ when feedback is applied. Sensing the compressor mass flow and feeding the signal back to the valve actuator thus works directly on the cause of the instability, the positive compressor slope. (Insertion of the slope $m_{Ce} - KT$ in Eq. (14) in fact gives just the characteristic equation in Table 3.)

A different situation prevails for the inlet total pressure sensor. The inlet total pressure perturbation is related to the derivative of the inlet mass flow, i.e., the fluid acceleration in the compressor duct, through the unsteady Bernoulli equation

$$P_{t0} - P_{t1} = \rho \int_0^1 \frac{\partial C_x}{\partial t} dx$$

Nondimensionalizing and linearizing gives

$$-\delta\psi_{t1} = \frac{1}{B} \frac{d\phi}{d\tau}$$

where $\delta\psi_{t1}$ is the total pressure perturbation at the compressor face in nondimensional form. If the valve angle perturbation is proportional to the compressor inlet total pressure, the result is to create a pressure change across the valve proportional to the *acceleration*, which is the derivative of the state variable ϕ . In other words the effect of feedback in this case is to alter

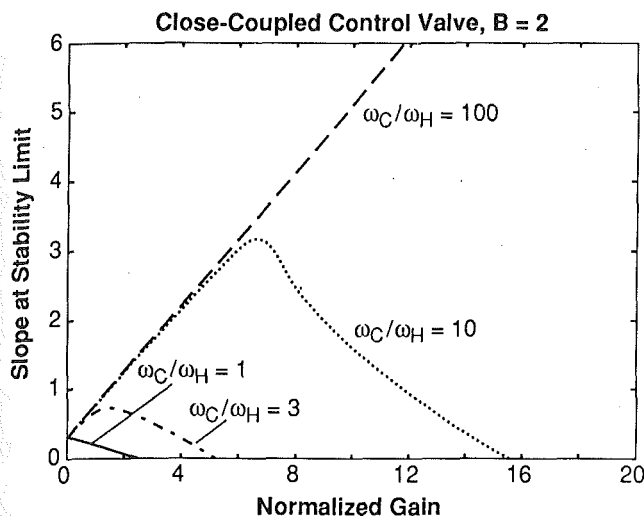


Fig. 5 Influence of normalized control system bandwidth (ω_c/ω_H) on the feedback gain required and flow coefficient at instability onset; close-coupled control valve

the overall pressure difference from duct inlet to exit for a given fluid acceleration rate. As far as the system is concerned, this is seen as a change in compressor duct length, since the longer the duct, the larger will be the instantaneous pressure change that results from a given fluid acceleration.

An increase in effective length of the duct does several things to the system. It drops the natural frequency, which scales as $1/\sqrt{\mathcal{L}_c}$. More importantly, it changes the effective value of the B parameter, which also scales as $1/\sqrt{\mathcal{L}_c}$. Both these changes can be seen in the characteristic equation in Table 3, in which the critical value of B for instability is increased by $\sqrt{1+KT}$, $1+KT$ being just the factor by which the effective length is increased. In the case of total pressure sensing, however, only the dynamic instability is influenced, because the increase in effective inertia does nothing to alter the static stability. The instability limit is thus still $m_{Ce} \geq m_{Te}$.

Somewhat similar arguments can be made for other sensor-actuator pairs, but the main point is that the use of different sensors for the feedback gives the system quite different properties. For the feedback on mass flow, one of the resistive elements in the system is altered directly, whereas for the feedback on inlet total pressure, it is the effective inertia that is changed, and different dynamic behavior thus results.

Effect of Control System Bandwidth. As mentioned previously, the study of the sensor-actuator pairs was carried out using a value of control system bandwidth (ω_c) ten times the compression system Helmholtz frequency (ω_H). We can also examine the influence of this parameter, in other words, of controller bandwidth, on the stabilization process. Figure 5 thus shows the changes in instability onset that occur with different controller bandwidths for conditions corresponding to the close-coupled control valve, with feedback on mass flow, and a B parameter of 2. In the figure, the horizontal axis is the controller gain, and the vertical axis is the compressor characteristic slope at instability. Curves are shown for values of ω_c/ω_H from 1.0 to 100, representing extremes of this ratio, and it is evident that controller bandwidth strongly influences the range of stabilization that can be achieved.

Several trends are exhibited in Fig. 5. First, for a controller bandwidth such that $\omega_c/\omega_H = 1$, use of the control actually degrades the stability: the more gain the less steep the compressor slope that can be achieved. In this regime, control system effectiveness is adversely affected by the controller system dynamics. Second, increasing the controller bandwidth increases the compressor slope that can be attained. Third, for

a given level of bandwidth, increasing gain increases stability only up to a point; beyond this point the stabilization decreases as gain increases. (This is true even for $\omega_c/\omega_H = 100$, although it cannot be seen over the range of values plotted here.)

The necessity to go to higher bandwidth at higher slope arises because, as the slope increases, the system dynamics become faster relative to the undamped natural frequency (Helmholtz frequency). There can thus be coupling between oscillations in the controller and in the aerodynamic system that lead to instabilities, so actuator dynamics play a role in setting the range of stability (as they clearly do at $\omega_c/\omega_H = 1$). This point is an important one since, in many cases, it is difficult to engineer actuators with bandwidths many times that of the Helmholtz frequency. The analysis suggests that actuator bandwidth will be a prime determinant of practical system performance and that research and development on this topic is useful to pursue.

Limits to Control With an Ideal Controller

With the four sensors studied, and proportional control, the close-coupled valve and injector emerge as the most promising actuators. A further question to address, however, is whether the type of compensation or choice of sensors would affect this conclusion. In this section, optimal control theory is used to provide a definite answer to this question. To motivate the approach taken, some basic aspects of linear dynamic system stabilization are first presented. For small disturbances, the compression system, actuators, and disturbances are described by the linear differential equation set:

$$\dot{\mathbf{x}} = \mathbf{A}\mathbf{x} + \mathbf{B}u + \mathbf{L}w$$

where \mathbf{x} is a five-dimensional vector of system states, u is a scalar representing a particular actuated variable, w is a p -dimensional vector of external disturbances, and \mathbf{A} , \mathbf{B} , and \mathbf{L} are constant matrices of appropriate dimensions. This is just Eq. (12) modified to include the effect of external disturbances. It is known (see, for example, Kwakernaak and Sivan, 1972) that systems of this type can be stabilized for all conditions using the control law $u = -K\mathbf{x}$, where K is now a one-by-five constant gain matrix, provided only that the pair A, B is controllable.² Such a control law is known as *full state feedback* and requires that the state of the system, \mathbf{x} , be known perfectly. For a system with n states, this would require n properly placed sensors. For the situation of interest here, over the range of parameters analyzed, the requirement of controllability is met. Thus, with enough properly placed sensors, stabilization of the idealized linear system is not a problem.

All actuators are not equally suitable for this; some have excessive amplitude requirements. In the analysis, therefore, the actuators are compared based upon their minimal required rms (root mean square) response to a persistent broadband disturbance, while maintaining system stability. This comparison is independent of choice of sensor, because it is assumed that the state of the system is known at all times. Further, the comparison is based upon the minimal possible rms amplitude, and hence there is no question as to whether a particular actuator would perform better if another control law were used. In this sense, the comparison is also independent of the control law.

Specific details of the computations performed are given by Simon (1992), and a more general treatment can be found from Kwakernaak and Sivan (1972). The central concept to be used is that, if the disturbance can be described as a stationary, Gaussian, white noise process, a particular gain matrix K can

²A linear time invariant system $\dot{\mathbf{x}} = \mathbf{A}\mathbf{x} + \mathbf{B}u$ is controllable if and only if there exists a piecewise continuous function $u(t)$, which will transfer the system from any initial state $x_0(t_0)$ to a final state $x_1(t_1)$ in a finite time interval $t_1 - t_0$ (see Kwakernaak and Sivan, 1972).

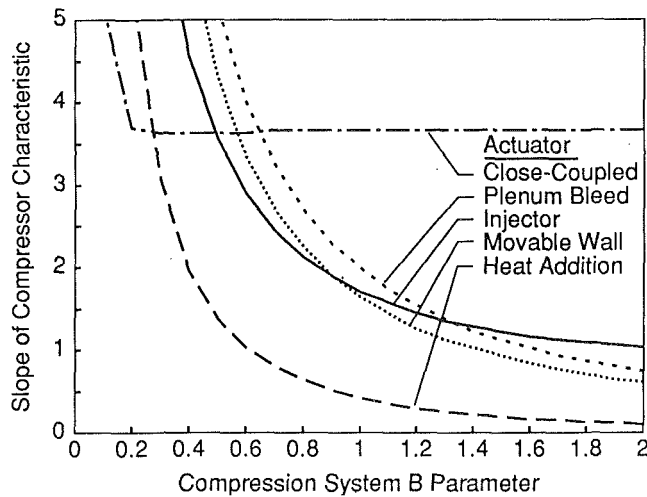


Fig. 6 Maximum slope at which the rms actuation will be no greater than 25 percent of the maximum actuator authority; ideal controller and perfect knowledge of the system state

be found that will minimize the root mean square value of the actuated variable u . The gain matrix K and the rms value of u will depend upon the matrix L , which determines how the disturbance enters the system and upon the statistical properties of the disturbance.

For this analysis, the disturbances driving the system must be chosen. Three disturbances were studied: (1) a compressor with an unsteady pressure rise; (2) an unsteady heat release in the plenum chamber; and (3) an unsteady outflow through the throttle. In each case, the input disturbance amplitude (white noise intensity) was normalized to that required to produce a 1 percent rms fluctuation in compressor mass flow at a fixed, stable operating point.

The results of this analysis are illustrated in Fig. 6. In the figure, the maximum allowable slope that can be attained is plotted as a function of B for five different actuators, based on the restriction that the normalized rms actuation is no greater than 0.25 for the most deleterious type of disturbance. The choice of this level of maximum rms actuation is somewhat arbitrary, but it is taken to be one that can be achieved in practice. In addition, computations have been carried out at other levels, and the results show similar trends.

For all the actuators, the maximum slope that can be attained decreases as the B parameter increases. However, the sensitivity of the slope to B varies markedly between different actuators. As with the proportional control, those actuators that are most closely coupled to the compressor (the injection and the close-coupled valve) are the most effective. The figure shows that, for B greater than unity, the maximum compressor slope at which the restriction on rms actuation can be maintained is quite limited. (For reference, the characteristic of the turbo-charger used in the experiments described previously has a maximum slope of approximately six, i.e., $m_c \geq 6$). In addition, except for the close-coupled valve, whose performance becomes independent of B , the maximum slope decreases monotonically with the B parameter. In particular, heat addition, which might seem attractive because of ease of implementation through fuel injection, shows little potential for stabilization at values of B larger than unity.

Another result is that the behavior of the plenum bleed, the injector, and the moving wall are roughly comparable, although the injector has some advantage for larger values of B (greater than two, say). At these high values of the B parameter, however, the close-coupled valve has a clear advantage, over all of the other schemes examined, in stabilizing the system.

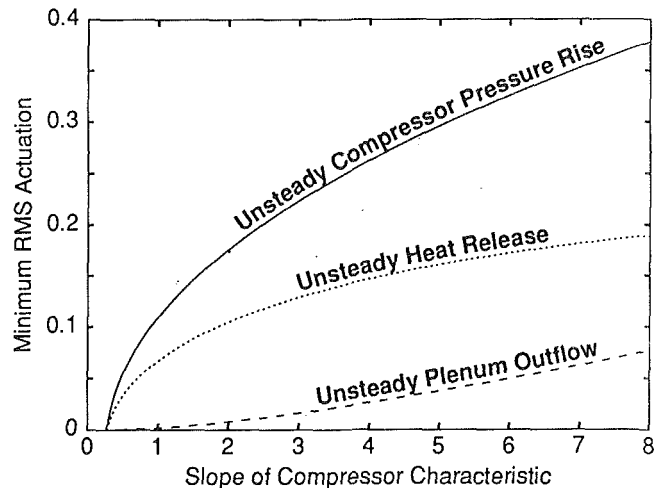


Fig. 7 Influence of compression system disturbance type on actuator motion required to stabilize the system; close-coupled valve actuator, $B = 2$

Effect of Disturbance Type on System Behavior

The influence of the disturbance type on controlled compressor performance is shown in Fig. 7 for the close-coupled valve, the actuator shown to be most effective in enhancing flow range for large values of B . The horizontal axis is the slope of the compressor characteristic, and the vertical axis is the normalized rms actuation level. The difference between the three curves indicates the impact of disturbance type on the ability to control the system. Compressor pressure rise disturbances, such as might arise from local unsteady flow in the rotor or diffuser, create a situation that is more difficult to control than disturbances due to combustor heat release or throttle mass flow fluctuation.

The implication of Fig. 7 is that the nature of the disturbances driving the system is an important factor in setting the requirements for stabilization. There is little known at present about the detailed disturbance structure within turbomachinery and engines, and it appears that characterization of these unsteady phenomena is a research item of considerable practical concern.

Summary and Conclusions

An evaluation of strategies for the active control of compression system surge has been carried out as a first step toward developing rational design procedures for active surge stabilization. A basic result is that actuators and sensors that measure and act upon the momentum of the fluid in the compressor duct are the most effective for geometries and compressor slopes of interest for gas turbine applications. Although this result was qualitatively known, the analysis has quantified the severity of these trends, showing them to be extremely important over the parameter range of interest. The following specific conclusions can be made:

- Proper choice of actuator and sensor is an important part of the overall design of a surge stabilization system.
- Mass flow measurement with either a close-coupled valve or an injector for actuation are the most promising approaches of those evaluated.
- Fuel modulation is not a promising candidate for practical ranges of system parameters.
- Characterization of compression system disturbance sources is important for determining the requirements for active control schemes.
- Steep slopes and large B parameters make control more difficult.

- Actuator bandwidth can be an important constraint in many practical implementations.

Acknowledgments

The authors would like to thank Dr. J. Paduano, Dr. G. R. Guenette, and Mr. D. L. Gysling for many useful discussions, and Ms. D. I. Park for her forbearance during preparation of this manuscript. This work was supported by the US Army Propulsion Directorate, Aviation Research and Technology Activity, Aviation Systems Command, Dr. L. F. Schumann, Technical Monitor, and the Air Force Office of Scientific Research, Major D. Fant, Technical Monitor.

References

- Di Stefano, J. J., Stubberud, A. R., and Williams, I. J., 1989, *Feedback and Control Systems*, 2nd ed., Schaum's Outline Series, McGraw-Hill, New York.
- Epstein, A. H., Ffowcs Williams, J. E., and Greitzer, E. M., 1989, "Active Suppression of Compressor Instabilities," *Journal of Propulsion and Power*, Vol. 5, pp. 204-211.
- Ffowcs Williams, J. E., and Huang, X., 1989, "Active Stabilization of Compressor Surge," *Journal of Fluid Mech.*, Vol. 204, pp. 245-262.
- Fink, D. A., Cumpsty, N. A., and Greitzer, E. M., 1992, "Surge Dynamics in a Free-Spool Centrifugal Compressor System," *ASME JOURNAL OF TURBOMACHINERY*, Vol. 114, pp. 321-332.
- Freudenberg, J. S., and Looze, D. P., 1985, "Right Half Plane Poles and Zeros and Design Tradeoffs in Feedback Systems," *IEEE Transactions on Automatic Control*, AC-30, pp. 555-565.
- Greitzer, E. M., 1981, "The Stability of Pumping Systems—The 1980 Freeman Scholar Lecture," *ASME Journal of Fluids Engineering*, Vol. 103, pp. 193-242.
- Gysling, D. L., Dugundji, J., Greitzer, E. M., and Epstein, A. H., 1991, "Dynamic Control of Centrifugal Compressor Surge Using Tailored Structures," *ASME JOURNAL OF TURBOMACHINERY*, Vol. 113, No. 4, pp. 710-722.
- Kwakernaak, H., and Sivan, R., 1972, *Linear Optimal Control Systems*, Wiley, New York.
- Muller, P. C., and Weber, H. I., 1972, "Analysis and Optimization of Certain Qualities of Controllability and Observability for Linear Dynamical Systems," *Automatica*, Vol. 8, No. 3, pp. 237-246.
- Norris, G. A., and Skelton, R. E., 1989, "Selection of Dynamic Sensors and Actuators in the Control of Linear Systems," *ASME Journal of Dynamic Systems, Measurement and Control*, Vol. 111, pp. 389-397.
- Ogata, K., 1970, *Modern Control Engineering*, Prentice-Hall, Englewood Cliffs, NJ.
- Pinsley, J. E., Guenette, G. R., Epstein, A. H., and Greitzer, E. M., 1991, "Active Stabilization of Centrifugal Compressor Surge," *ASME JOURNAL OF TURBOMACHINERY*, Vol. 113, pp. 723-732.
- Schmitendorf, W. E., 1984, "An Exact Expression for Computing the Degree of Controllability," *Journal of Guidance*, Vol. 7, No. 4, pp. 502-504.
- Simon, J. S., 1992, "Feedback Stabilization of Compression and Pumping Systems," Ph.D. Thesis, Department of Mechanical Engineering, Massachusetts Institute of Technology, Cambridge, MA.
- Van de Vegte, J., 1990, *Feedback Control Systems*, 2nd ed., Prentice-Hall, Englewood Cliffs, NJ.

J. E. Ffowcs Williams

Department of Engineering,
University of Cambridge,
Cambridge, United Kingdom

M. F. L. Harper

D. J. Allwright

Topexpress Limited,
Cambridge, United Kingdom

Active Stabilization of Compressor Instability and Surge in a Working Engine

We have applied feedback control to the compressor of a 45 kW auxiliary power unit. Using this, the engine is able to deliver more than 10 percent extra shaft power before surge occurs. We achieve control by suppressing a nonaxisymmetric flow phenomenon in the diffuser of the centrifugal compressor. Control is effected by modulating a small extra air flow into the impeller. We present results of modeling and analysis suggesting that linear feedback control will be sufficient to stabilize a compression system, even when both axisymmetric surge and rotating stall are present as possible instabilities.

1 Introduction

In 1986 Epstein et al. [1] suggested that the phenomena of surge and rotating stall could be controlled using low-power active feedback systems. Since then, the approach has been proved on a series of laboratory models [3, 5, 17].

Control of axisymmetric surge alone has also been demonstrated on a working gas turbine engine with a centrifugal compressor [2, 9]. It was found that although surge inception could not be prevented, surge could be suppressed within a single period of the limit cycle. The method used appeared to be closely analogous to that shown to be effective in suppressing limit-cycle behavior in the firing of neurons [16, 9].

We believe that surge inception could not be prevented because the test engine was undergoing "classic surge" [7] in which surge is initiated by nonlinear interaction with a non-axisymmetric, periodic flow phenomenon, analogous to rotating stall, in the compressor. In this paper we consider the use of independent linear controllers to suppress rotating stall and axisymmetric ("deep") surge separately. We put forward reasons for expecting such a scheme to be capable of rendering the engine stable against any disturbance. Lastly, we present experimental results on the suppression of "classic" surge in the test engine by feedback control of nonaxisymmetric disturbances in the compressor.

2 Theory

Our aim is to develop the strategy and theoretical details of an active control system that will, in the absence of noise, maintain a compressor-plenum system in its steady operating condition with axisymmetric flow through the compressor, even though its uncontrolled behavior may be rotating stall, deep surge, or classic surge.

We shall assume that the compressor is satisfactorily mod-

eled by Moore's theory of finite amplitude disturbances in a multistage axial compressor [13]. This theory has been further developed in the joint work of Moore and Greitzer [14, 15], and in the work of McCaughan [10-12]. It is a nonlinear theory that appears to account successfully for many of the observed features of compressor behavior, as described by Greitzer [8]. In particular, the model predicts the existence (depending on parameter values) of steady nonaxisymmetric flow, unsteady axisymmetric limit cycles, and unsteady nonaxisymmetric limit cycles, which are the observed features of rotating stall, deep surge, and classic surge, respectively.

On the basis of this theory we know that the compressor-plenum system has two instabilities that need to be controlled, and that although these two are distinct, they are coupled together at finite amplitudes by the nonlinearity of the system. Apart from this coupling, the two instabilities are:

(a) As the flow through the compressor is reduced, the axisymmetric flow becomes unstable to small nonaxisymmetric disturbances. If the total flow is then held constant, the non-axisymmetric disturbances develop into steadily rotating stall, and the pressure rise generated is different from the characteristic assumed for steady axisymmetric flow. This instability is confined to the compressor and ducting.

(b) Even if the flow through the compressor could be maintained axisymmetric, as the flow is reduced the steady state becomes unstable to small fluctuations in total mass flow. These fluctuations develop into a limit cycle where the flow accelerates and decelerates through the compressor, with corresponding fluctuations in plenum pressure. This instability is not confined to the compressor: It works through the compressor-plenum interaction.

The uncontrolled effects of (a) and (b) alone are rotating stall and deep surge, respectively. As already mentioned, the two instabilities do interact with one another. An axisymmetric cycle as described in (b) may itself be unstable to small non-axisymmetric disturbances. Typically a limit cycle of non-axisymmetric flow develops, which is called classic surge. Looking at this the other way round, we may say that rotating stall

Contributed by the International Gas Turbine Institute and presented at the 37th International Gas Turbine and Aeroengine Congress and Exposition, Cologne, Germany, June 1-4, 1992. Manuscript received by the International Gas Turbine Institute February 4, 1992. Paper No. 92-GT-88. Associate Technical Editor: L. S. Langston.

affects the net characteristic of the compressor in a way that can trigger instability (*b*).

The existence of these two distinct types of instability naturally suggests that we consider a control strategy involving two distinct control systems:

- (A) A controller on the compressor alone that measures and controls any nonaxisymmetric disturbances to the flow.
- (B) A controller on the compressor-plenum system that measures and controls any disturbances to total mass flow and plenum pressure.

Each of these controllers should stabilize the required operating point to both small and large disturbances. So a linear controller, designed to stabilize the linearized system, has to be further checked out in its effect on and interaction with the full nonlinear model. To spell out these requirements in detail:

Controller A is required to eliminate nonaxisymmetric disturbances to the compressor flow, even in the presence of fluctuating total mass flow. This point is essential to the strategy: It means that controller A has to eliminate instability (*a*) not only when it occurs alone but also when it occurs in connection with instability (*b*). In terms of the observed types of behavior, the effect of controller A has to be to convert both rotating stall and classic surge into some kind of axisymmetric behavior, either the required steady equilibrium, or a deep surge cycle. Controller A alone may of course stabilize a deep surge cycle that was previously unstable. This does not matter, because *Controller B* is required to stabilize the axisymmetric equilibrium point, and to eliminate any axisymmetric limit cycles. This includes not only "naturally occurring" deep surge cycles, but also deep surge that occurs only because it has been artificially stabilized by controller A.

3 Theoretical Details

Controller A. Our main result here is that in the absence of inlet guide vane losses, a linear controller generating a pressure proportional to the local departure of velocity from axisymmetry can meet the requirements of controller A. Provided that the gain of the controller exceeds the maximum positive slope of the assumed steady axisymmetric characteristic, a simple energy argument shows that the requirements are met.

Let $V_a(\theta, t)$ be the axial velocity through the compressor at position θ around the circumference at time t . We write its Fourier series as

$$V_a(\theta, t) = V(t) + \sum_{-\infty}^{\infty} v_n(t) e^{in\theta} \quad (1)$$

where the prime on the summation indicates that the term $n = 0$ is omitted. Then we include our controller term $k(V_a - V)$ into Moore's equation for the pressure rise from ambient (p_T) to plenum (p_s):

$$p_s - p_T = P_{sa}(V_a) - a_0 \frac{dV}{dt} - \sum_{-\infty}^{\infty} a_n \frac{dv_n}{dt} e^{in\theta} - b \frac{\partial V_a}{\partial \theta} - k(V_a - V) \quad (2)$$

Here P_{sa} is the assumed steady axisymmetric characteristic, and a_0 , a_n , and b are constants depending on the physical parameters of the compressor and ducts. When we multiply this equation by $V_a - V$ and integrate over θ from 0 to 2π , the axisymmetric terms produce 0 because V is the mean flow. Also

$$\int_0^{2\pi} \frac{\partial V_a}{\partial \theta} (V_a - V) d\theta = \left[\frac{1}{2} (V_a - V)^2 \right]_{\theta=0}^{\theta=2\pi} = 0. \quad (3)$$

So we are left with

$$0 = \int_0^{2\pi} P_{sa}(V_a) (V_a - V) d\theta - 2\pi \sum_{-\infty}^{\infty} a_n \frac{dv_n}{dt} \bar{v}_n - k \int_0^{2\pi} (V_a - V)^2 d\theta \quad (4)$$

We write this in the form

$$\frac{dT}{dt} = R_2 - R_1 \quad (5)$$

where

$$T = \sum_{-\infty}^{\infty} \pi a_n |v_n|^2 \quad (6)$$

measures the kinetic energy of the nonaxisymmetric flow,

$$R_2 = \int_0^{2\pi} P_{sa}(V_a) (V_a - V) d\theta \quad (7)$$

measures the rate at which the compressor is working on the nonaxisymmetric flow, and

$$R_1 = k \int_0^{2\pi} (V_a - V)^2 d\theta \quad (8)$$

measures the rate at which controller A is reducing the kinetic energy of the nonaxisymmetric flow.

Now since $V_a - V$ integrates over θ to zero, and V is independent of θ ,

$$R_2 = \int_0^{2\pi} (P_{sa}(V_a) - P_{sa}(V)) (V_a - V) d\theta = \int_0^{2\pi} \frac{P_{sa}(V_a) - P_{sa}(V)}{V_a - V} (V_a - V)^2 d\theta. \quad (9)$$

Nomenclature

A = matrix modeling compressor dynamics	$P_{sa}(V_a)$ = compressor characteristic	$V_a(\theta, t)$ = axial flow velocity
a = const	p, p_s = plenum pressure	V_E = equilibrium value of V
b = const	p_E = equilibrium value of p	$V_i(p)$ = exit velocity from plenum
\mathbf{b} = vector relating z to \mathbf{x}	p_T = ambient pressure	v_n = magnitude of n th angular harmonic of flow velocity
\dot{E} = rate at which controller extracts energy from unsteady flow	R_1 = rate at which controller extracts energy from unsteady flow	\mathbf{v}_j = j th eigenvector of A
$k_{1,2,3}$ = design constants in axisymmetric controller	R_2 = rate at which compressor works on unsteady flow	w = auxiliary variable in controller design
K = controller	T = kinetic energy of unsteady flow	\mathbf{x} = compressor state
M = maximum slope of P	t = time	z = input to compressor
n = angular order of flow harmonic	$V(t)$ = mean axial flow velocity	λ_j = j th eigenvalue of A
		ρ = desired new eigenvalue

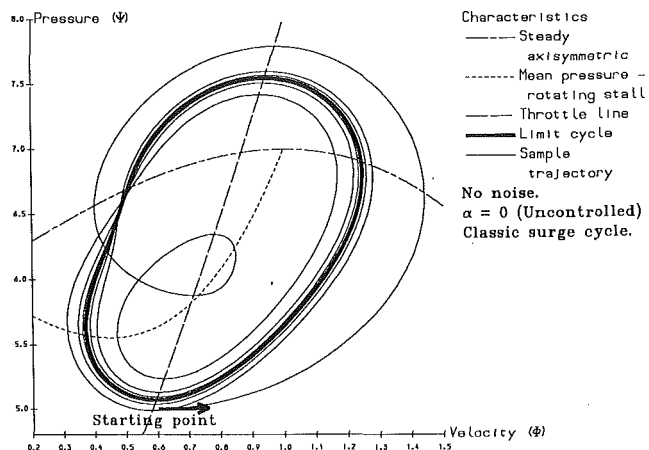


Fig. 1

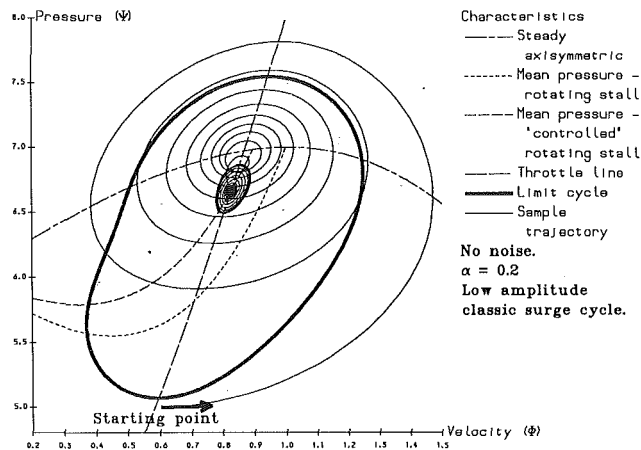


Fig. 3

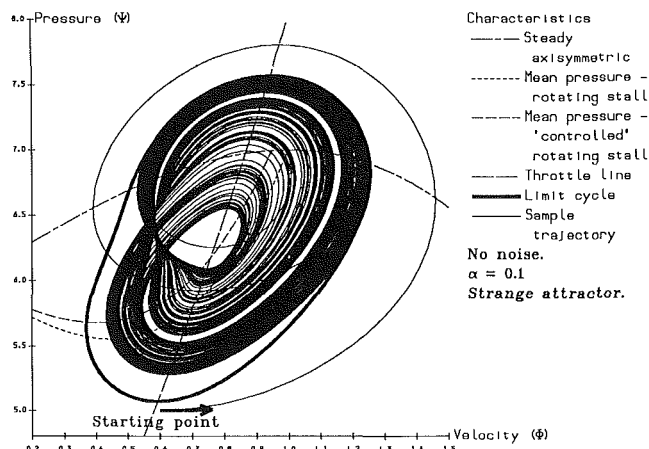


Fig. 2

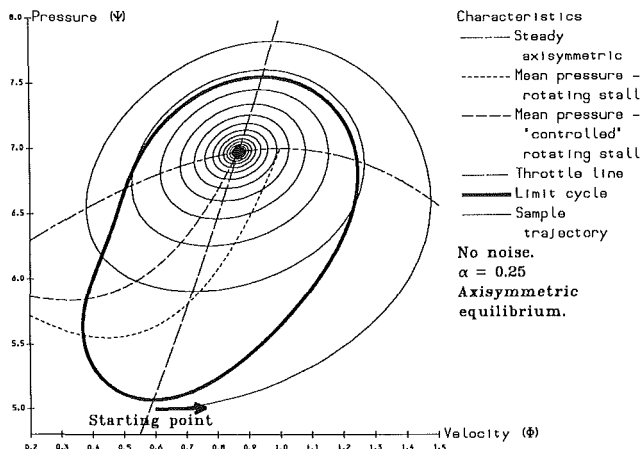


Fig. 4

If M is the maximum positive slope of P_{sa} , then the difference quotient in this last form of R_2 is always at most M , so

$$R_2 \leq M \int_0^{2\pi} (V_a - V)^2 d\theta \quad (10)$$

So if the controller gain k exceeds M then we have $R_2 \leq R_1$ and so the controller is always reducing the energy in the nonaxisymmetric part of the flow faster than the compressor is increasing it (except, of course, when $V_a \equiv V$, i.e., when the flow is axisymmetric). This argument is perfectly valid with a time-varying V and so does cover exactly the requirement for controller A: The departure of the flow from axisymmetry is steadily reduced to zero, whatever the mean flow is doing.

We should make several observations about this:

1 The result may be affected to some extent when inlet guide vane losses are taken into account, because although they act so as to reduce the total energy, they do not necessarily reduce the part of the energy in the nonaxisymmetric flow.

2 This is a purely theoretical result; we are not proposing any actual control system by which this result could be achieved, but are simply pointing it out as an ideal that would certainly have the required effect. As such, we are suggesting it as a useful guideline to bear in mind when designing an actual control system.

3 The theoretical stability result does not depend on only one angular order being present in the velocity disturbance, nor does it depend on assuming that the assumed steady axisymmetric characteristic is a cubic function. It is a general stability result covering cases in which all angular orders are present, all interacting nonlinearly with each other through an

arbitrary assumed characteristic. The fact that the theoretical result is fairly robust in this way indicates that it is not a particularly thin or sensitive guideline that we are suggesting here. It is a guideline with a sound physical basis in the energetics of the system, so a controller designed as a sensible approximation to the ideal may well be expected to go a substantial way toward achieving the required goal.

If the gain k is required to stabilize a particular operating point in the positively sloped region of the steady axisymmetric characteristic, rather than to stabilize all possible operating points, then a value smaller than M may be sufficient. To illustrate this, we present some phase space plots of the system as studied by McCaughan [10, 11], when controller A is included with a gain that is some fraction α of the maximum slope of the characteristic, $k = \alpha M$. In Fig. 1, the uncontrolled system ($\alpha = 0$) is represented: The axisymmetric operating point, where the throttle line cuts the steady axisymmetric characteristic, is unstable to nonaxisymmetric disturbances. The steady rotating stall point, where the throttle line cuts the rotating stall characteristic, is also unstable. The stable behavior of the uncontrolled system is classic surge: The heavy line on Fig. 1 represents this classic surge cycle, and a sample trajectory converging to it is also shown. Figures 2, 3, and 4 show what happens as α is increased to 0.1, 0.2, and 0.25 respectively. For values of $\alpha > 0$, the rotating stall characteristic is modified: The figures show both the original uncontrolled characteristic (as in Fig. 1) and the new controlled rotating stall characteristic. At $\alpha = 0.1$ the classic surge cycle has become unstable and the new stable behavior is a strange attractor. At $\alpha = 0.2$ the stable behavior is a classic surge cycle of much smaller amplitude than the uncontrolled one.

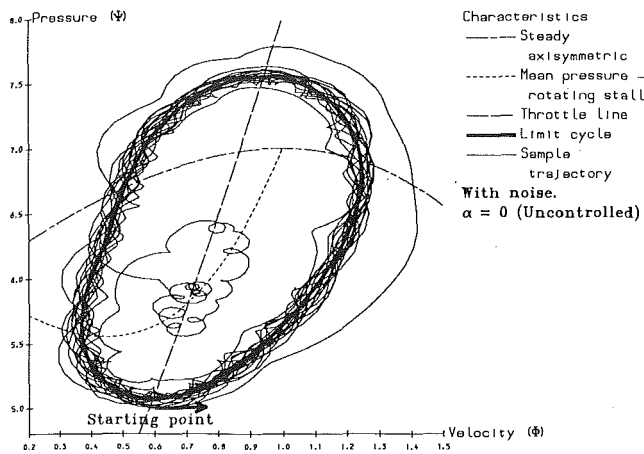


Fig. 5

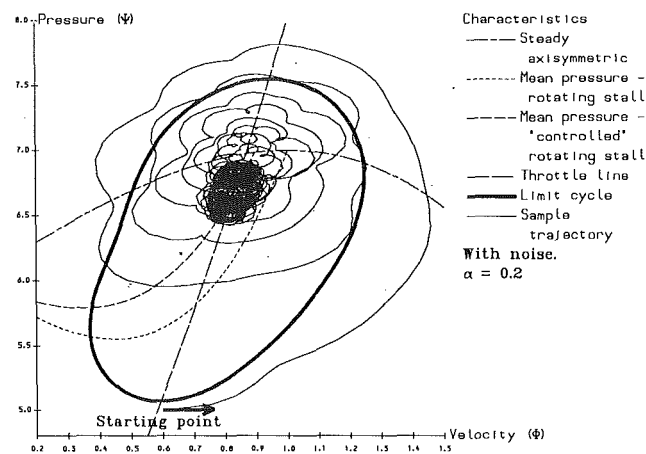


Fig. 7

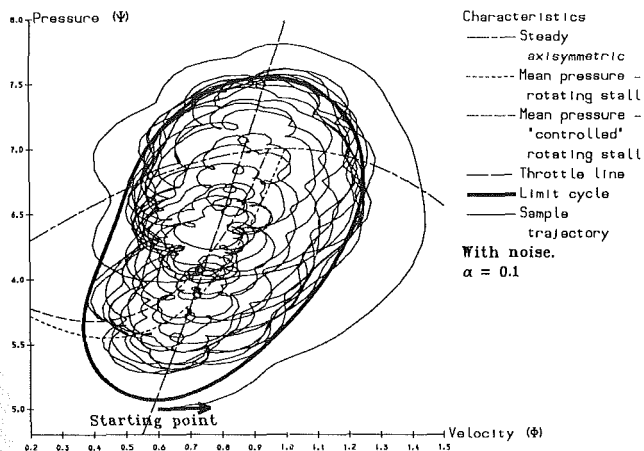


Fig. 6

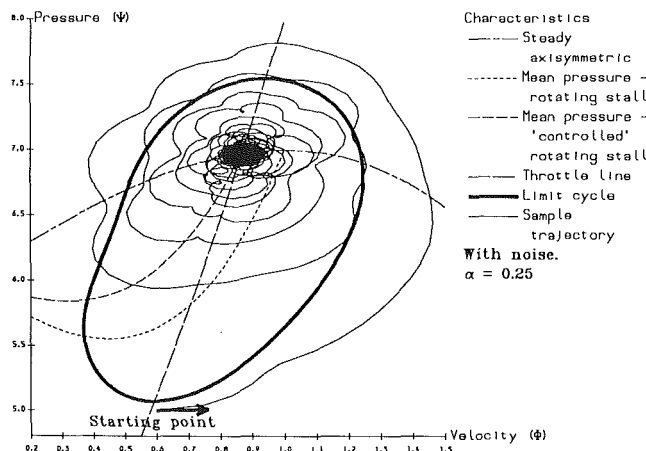


Fig. 8

Finally, at $\alpha = 0.25$, the required axisymmetric operating point has been stabilized and nonaxisymmetric behavior eliminated; the sample trajectory converges to the steady axisymmetric operating point. Figures 5–8 show corresponding plots when a fixed level of noise is added into the mass flow equation. They are much as one would expect: Fig. 5 is essentially a noisy classic surge cycle, Fig. 6 a noisy strange attractor, and so on.

Controller B. Following Moore's theory again, the uncontrolled equations for the plenum pressure p and flow velocity V will be

$$\frac{dV}{dt} = a(P_{sa}(V) - p) \quad (11)$$

$$\frac{dp}{dt} = b(V - V_i(p)) \quad (12)$$

for some positive constants a and b , with $V_i(p)$ being proportional to the steady exit velocity from the plenum when the pressure is p . At the required steady equilibrium point, the values p_E and V_E of p and V satisfy

$$p_E = P_{sa}(V_E) \quad (13)$$

$$V_E = V_i(p_E) \quad (14)$$

The matrix of the linearized equations about equilibrium is

$$\begin{pmatrix} aP'_{sa}(V_E) & -a \\ b & -bV'_i(p_E) \end{pmatrix} \quad (15)$$

A controller using direct proportional feedback on plenum pressure would replace the pressure equation by

$$\frac{dp}{dt} = b(V - V_i(p)) + k_1(p - p_E) \quad (16)$$

However, this has the disadvantage that the controlled system has two eigenvalues and the choice of only one control parameter k_1 does not allow us the full freedom to place these eigenvalues arbitrarily. The remedy for this suggested by classical linear control theory is to use a dynamic controller. In fact, the theory of pole shifting by dynamic compensation given, for instance, by Wonham [19, Section 3.8] shows that for this problem it will suffice to have a single auxiliary variable w in the controller. It is governed by

$$\frac{dw}{dt} = k_1 w + (p - p_E) \quad (17)$$

and the control into the pressure equation depends on both $p - p_E$ and w :

$$\frac{dp}{dt} = b(V - V_i(p)) + k_2(p - p_E) + k_3 w. \quad (18)$$

The theory of dynamic compensators now ensures that the three eigenvalues of the resulting controlled system can be placed arbitrarily by choice of k_1 , k_2 , and k_3 . This suggests investigating the following approach:

1 Choose values of k_1 , k_2 , k_3 , dependent on the required operating point, to position the eigenvalues of the linearized system sufficiently far to the left in the complex plane, so as to make small disturbances decay as rapidly as desired.

2 With these values of k_1, k_2, k_3 investigate the nonlinear behavior of the system numerically.

The investigations carried out so far along these lines indicate that a control system designed in this way is capable of not only stabilizing the equilibrium point to small disturbances, but also eliminating the possibility of unsteady axisymmetric behavior of finite amplitude. Thus it appears that there is no fundamental reason why the requirements for controller B should not be met in this way.

The effects of noise on a system like this will be to set up typical levels of departure from the required operating point, and therefore to set up typical levels of the required control signals, and typical power levels needed to produce the required controls. These aspects of the theory are under current investigation.

4 Experiment

We have reported elsewhere in detail [4] on the occurrence of a nonaxisymmetric resonance in the compressor of our test engine. The resonance grows out of a background of broadband noise as engine load is increased. As surge load is approached the Q of the resonance increases rapidly and its center frequency gradually increases toward 200 Hz compared to a shaft rate of approximately 800 Hz. A typical high-load static pressure spectrum, observed with a sensor in a channel of the vaned diffuser of the one-stage centrifugal compressor, is shown in Fig. 9. The phase of the resonance varies spatially at an average rate of two degrees of phase per degree of position around the diffuser. The resonance is always observed growing rapidly as the engine goes into surge.

The resonance thus has many of the properties of one of the angular harmonics of rotating stall, used by Garnier et al. [6] as stall inception indicators in axial compressors. In our compressor, however, we have so far observed only the second harmonic. The question has therefore naturally arisen as to whether this resonance in a centrifugal compressor plays the same rôle as rotating stall is thought to do in classic surge of axial compression systems [8]. If so, controlling it should at least postpone the onset of surge to higher engine loads and lower mass flows.

The objectives of our experiments were therefore twofold. Firstly, to discover whether this phenomenon was controllable. Secondly, to test whether controlling it would suppress "classic surge" in the manner suggested in the previous section. It has not yet been possible to implement both "controller A" and "controller B" of Section 2 simultaneously. We have thus not yet tested whether the predictions made for axial compressor systems carry over qualitatively to the (centrifugal compressor) test engine in full. However, any delay in the onset of surge resulting from the use of a "controller A" alone will demonstrate a close analogy between surge in our test engine and "classic surge," and provide strong motivation for the implementation of the full strategy suggested in Section 2.

4.1 Approach to Control. We treat the potentially unstable compressor as a "black box." Its input is the modulated air flow from our actuator; its outputs are the unsteady components of the static pressures observed in the diffuser channels. For the purpose of designing a linear controller, we assume that the system is linear. Although this will obviously not be true once the compressor has stalled, we expect it to be a reasonable approximation when the compressor is operating normally. We also assume that the system's state can always be deduced from its outputs, i.e., that it is fully observable.

Under these conditions, we are able to make use of existing results from the extensive literature of linear control theory. We write the equation of state of the system as

$$\dot{\mathbf{x}} = \mathbf{A} \mathbf{x} + \mathbf{b} \mathbf{z} \quad (19)$$

where \mathbf{x} is the state of the system, \mathbf{z} is the single control input

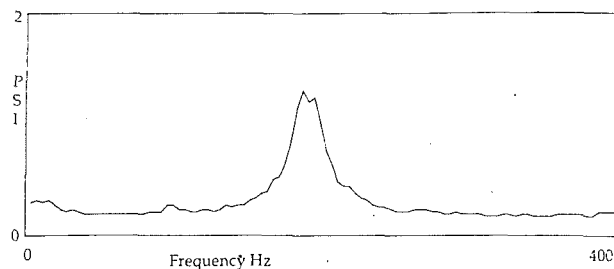


Fig. 9 Typical near-surge spectrum of diffuser channel static pressure

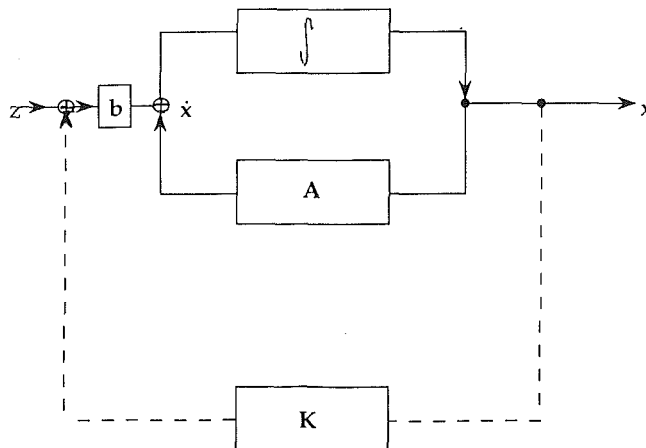


Fig. 10 System model

to it, and \mathbf{A} is a square matrix representing its internal dynamics. The vector \mathbf{b} is assumed real. This is represented in block diagram form in Fig. 10. The poles of the system response are the eigenvalues of \mathbf{A} . The transition of the real part of a complex conjugate pair of eigenvalues from negative to positive initiates instability in the system.

To prevent instability occurring, we apply feedback control via the controller \mathbf{K} in Fig. 10. An accessible account of how this can be used to modify chosen eigenvalues of \mathbf{A} appears in Chapter 5 of [18]; essentially, the outputs are combined to obtain signals proportional to the amplitudes of the modes to be controlled. Negative scalar gains, proportional to the desired decrease in the real parts of the corresponding eigenvalues, are applied; the signals are then summed and fed back to the input (i.e., the actuator).

For control of a complex pair of eigenvalues (λ_j, λ_j^*) with left eigenvectors ($\mathbf{v}_j, \mathbf{v}_j^*$) the controller \mathbf{K} in Fig. 10 is given by

$$\mathbf{K} = 2\text{Re} \left[\frac{(\rho - \lambda_j)(\rho^* - \lambda_j^*) \mathbf{v}_j^T}{\mathbf{v}_j^T \mathbf{b} (\lambda_j^* - \lambda_j)} \right] \quad (20)$$

where ρ is the desired new eigenvalue. A more general account of single-input control appears in [21].

The feedback operates to extract energy from the potentially unstable mode at a rate given by

$$\dot{E} \propto \text{Re}(\rho - \lambda) [\text{Re}(\mathbf{v}_j^T \mathbf{x})]^2 \quad (21)$$

i.e., the rate of energy extraction depends on feedback gain and on the square of the modal amplitude. This control law may be expected to be robust against nonlinearity of the system at finite amplitudes of the unstable mode. As long as the mode shape remains substantially the same, feedback control may be expected to extract energy from it. Sufficiently large, and negative feedback gain may therefore be expected to maintain the stability of the system against finite disturbances. Thus we

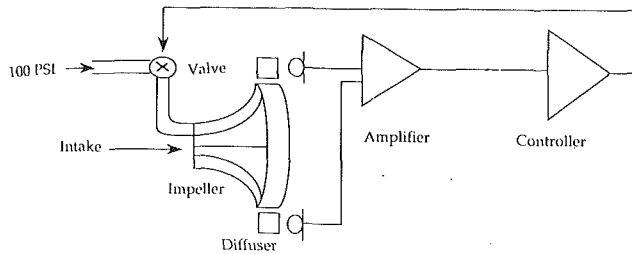


Fig. 11 Control system

expect our controller to play precisely the same rôle as “controller A” in the previous section.

4.2 Control System. The control system is shown in outline in Fig. 11. A number of pressure sensors are positioned flush in the walls of diffuser channels around the compressor. Their signals are conditioned and routed to a many-input, single-output controller. This provides a control signal to a high-speed actuator, which modulates a flow of compressed air. The modulated flow is fed to a point at the outer edge of the impeller eye, where it is injected parallel to the impeller axis. The injection tube has an i.d. of 21 mm, compared to the eye diameter of about 97 mm. It terminates about 5 mm short of the impeller blades. The mean injected flow is 1.4 percent of the engine total mass flow; the area ratio of the injection tube to the impeller eye is 5.7 percent.

The controller is essentially a multichannel digital FIR filter implemented using an Analog Devices ADSP2100 DSP chip on a proprietary PC plug-in board. Coefficients for the filter were calculated off-line and downloaded via the host computer, an 80386-based IBM compatible PC. Input and output signals are obtained using ADC and DAC cards also mounted on plug-in boards in the PC. The controller is capable of providing a four-in one-out filter matrix with 64 coefficients per channel at a sampling rate of 20 kHz. The boards are obtainable via [20].

The actuator is shown in outline in Fig. 12. It is essentially a lightweight sleeve valve driven by a loudspeaker coil and has a useful bandwidth well in excess of the required figure of 200 Hz. The slider is connected to the push-rod via an open spider, to avoid a large pressure differential displacing the driver coil. The slider can move sufficiently to allow ± 100 percent modulation of the mean injected flow. The actual modulation is highly dependent on engine state as well as on feedback gain; in typical control experiments, with the engine at the uncontrolled surge line, its rms level would be very roughly 10 percent of the mean flow.

The practical implementation of control required signals in the feedback loop to be band-limited to reduce noise. They also had to be phase-shifted: Individual sensor signals had to be treated to produce an efficient mode-observer; the output signal had to be treated to compensate for the effect on phase of delays in the actuation system. The chosen method was to incorporate further delays, which avoided distortion of signal power spectra and allowed easy and rapid adaptation of the controller response. However, control systems incorporating delays are known to be limited in the stability margin ($Re(\rho - \lambda)$) they can produce [22]. Subsequent modeling has suggested this was probably a serious limitation in this case.

4.3 Control Trials. Trials consisted of testing whether control had moved the engine’s surge point, using three different techniques. Our most commonly used measure of performance was the engine power delivery to the dynamometer just before surge. The engine governor was mechanical, and maintained a constant pressure ratio over the range of (stable) operating conditions used.

Test 1: The engine’s surge point would be established without control by slowly increasing load via a waterbrake dyna-

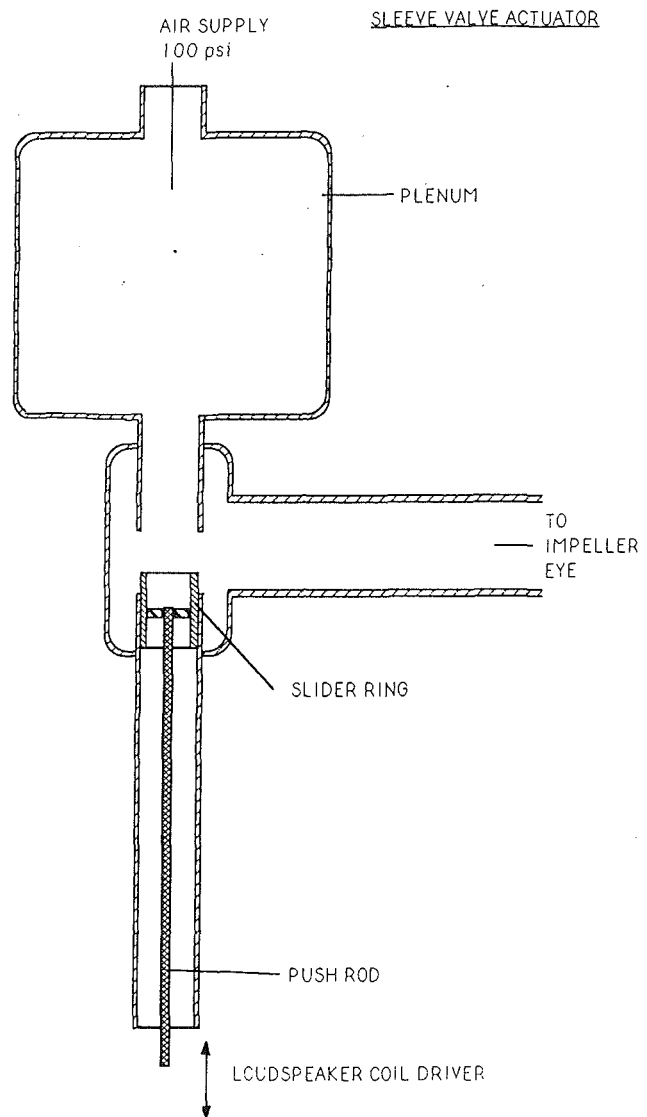


Fig. 12

meter. The controller would then be switched on and the surge point remeasured using the same procedure. In practice the surge point tended to drift: It could differ by 1 percent in engine load between 2 measurements in rapid succession, and by 3–4 percent over the course of a day’s testing. Our tests were therefore done in as rapid succession as possible, but occasionally there would be a delay of up to 20 minutes. In view of this we suggest there is an uncertainty of ± 2 percent in any measurement of power at surge (measured as being proportional to dynamometer load times shaft speed). Table 1 shows results from a succession of control filter settings. In filter one, a first-order filter function was used to shape the frequency response, while in set 2 a second-order filter function was used. Phase was optimized by adding or subtracting delays; letter subscripts denote different delays. The precise phase shifts required for optimum control had to be approached by trial and error. An initial set of values would be calculated using the transfer functions from actuator drive to pressure sensor signals measured with the engine at a stable operating point. The transfer functions were known to change with the operating point, and hence these values would not be optimal when the engine was taken up to and beyond the normal surge line. Changes of up to 40 deg were required to obtain the best performance.

The variability of power at surge is clear from the results

Table 1 Surge margin achieved by control: test 1

Filter Set Number	Power Increase %
1a	4
1b	6
1c	5
1d	4, 1.5
1e	6
1f	8.5, 9, 5.5
1g	11.5, 7
2a	6
2b	3.5

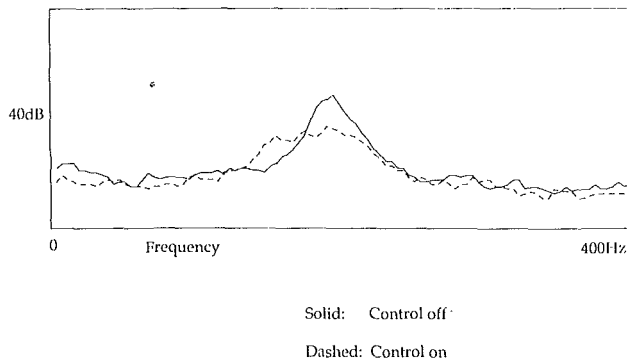


Fig. 13 Effect of control on diffuser channel pressure spectrum

of repeated trials with filters 1d, 1f, and 1g in Table 1. Corrected mass flow through the compressor at surge appeared to vary much less than delivered power and could be deduced from static pressure measured in the throat of a bellmouth on the air intake. This was occasionally recorded on tape. For trials with filter set 1g, corrected mass flow was 2.6 percent lower at surge with control on than with control off.

Test 2: The engine surge point without control would be determined; control would be switched on and engine load increased to about 5 percent above this point. Control would then be switched off. This was tried four times. On three occasions the engine surged immediately after control was removed; on one, it surged while control was still on.

Test 3: The engine would be surged without control. Control would then be turned on to see whether surge was then suppressed. This was tried twice without success. The reason became obvious on analyzing recordings of the actuator's displacement: The control system responded to some extent to the pressure variations produced by the very large changes in axisymmetric flow during surge. These saturated the control system and prevented it responding properly.

4.4 Response Before Surge. The effect of feedback on the spectrum of a diffuser pressure signal is shown in Fig. 13. The spectrum was recorded during normal operation, with engine load too low to precipitate surge. The developing instability in the absence of control (solid line) produces the broad peak centered at 190 Hz. On applying feedback control (dashed line) the peak is reduced, is broader, and has moved towards lower frequency; the resonance has become more heavily damped.

The effect of control on the behavior of diffuser static pressure in time is indicated by Fig. 14. All three traces are to the same vertical scale (± 2.5 psi). The center trace is a 45-second sequence covering a period during which control was turned off with the engine condition held constant at a normally unstable load; the engine surged, as indicated by the large increase in variance for the last 3/4 second. The upper trace

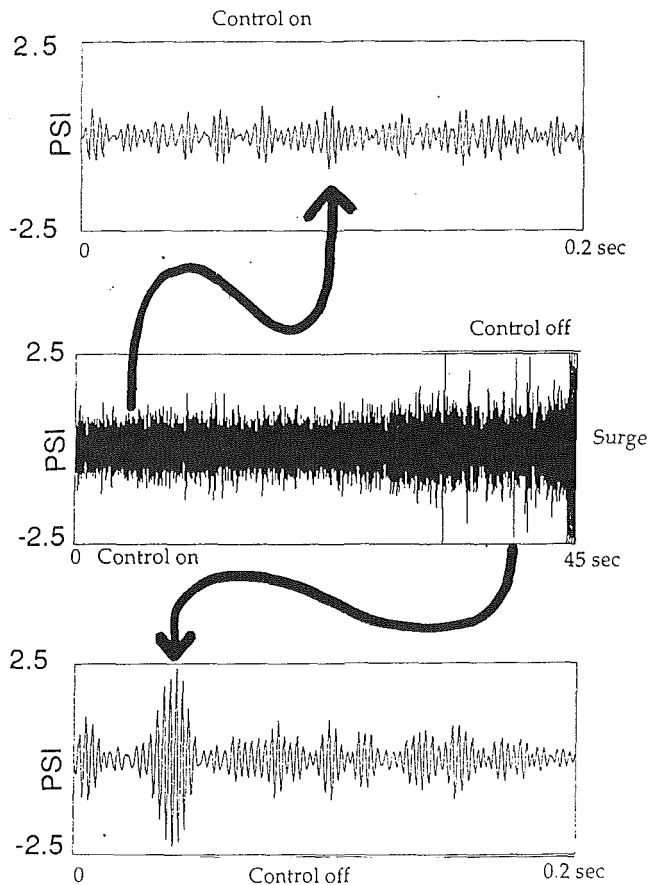


Fig. 14 Effect of control on diffuser channel pressure

is an expanded section, 0.2 seconds long, with control on. The lower, similarly expanded, is with control off. Evidently, the effect of control is to suppress large bursts of oscillation, one of which eventually triggers surge. It is an interesting feature of engine behavior that the oscillations do occur in bursts: We believe this is because of the large levels of fluctuating pressure in the engine. Fluctuations in combustion chamber static pressure exceed 1 psi about a mean of 3 bar; we attribute this to the combustion process. This is sufficient to affect the engine's operating condition: When its time-average condition is close to marginal stability, its instantaneous state switches rapidly between stability and instability. This causes oscillations alternately to grow and decay, until one burst grows large enough to trigger surge.

4.5 Effect of Control on the Surge Mechanism. Figure 15 shows a diffuser pressure trace during surge onset, with and without control. The time window is 0.4 seconds.

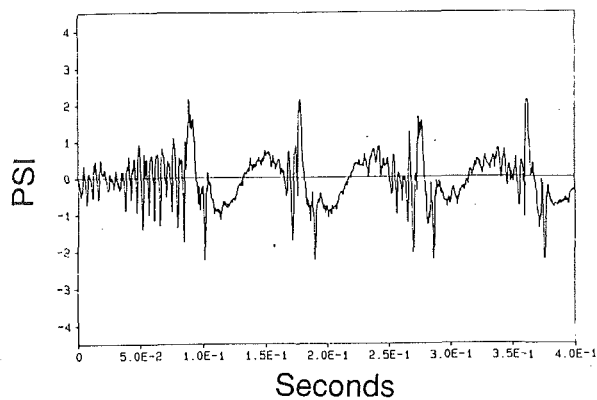
It is evident that in both cases, surge starts with a strong burst of oscillation. The surge cycle with no control involves an episode of rapidly growing oscillation in a manner typical of "classic surge"; this seems to be still present with control on. The surge cycle period is somewhat smaller with control on.

5 Discussion

Our results demonstrate that the nonaxisymmetric oscillation in the diffuser is controllable and that controlling it can move the surge point to higher loads and lower mass flows. We believe that this behavior is in close analogy with that theoretically expected of an axial compression system in which rotating stall only is controlled.

However, we interpret the results of section 4.5 as showing that, when the engine surges with control on, it is still doing

Control on:



Control off:

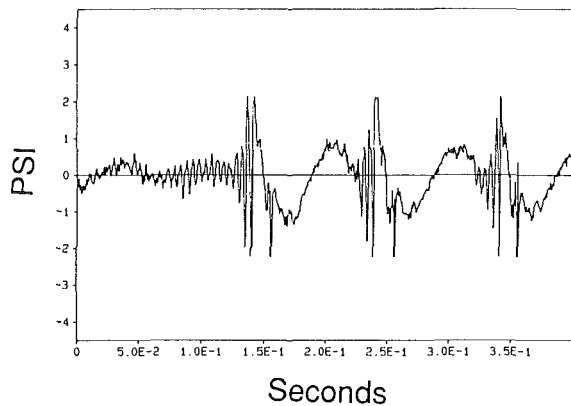


Fig. 15 Effect of control on surge mechanism: diffuser channel static pressure around surge onset

so via an interaction of the compressor instability with axisymmetric surge: "classic surge." Our control system has introduced only a finite stability margin, and has not therefore eliminated this route to surge.

We believe that this is due, not to any limitation on feedback gain, but to the significant approximations made in the design of the control system. It is for example typical of control loops containing delays that the extra stability margin achievable should be limited.

In order to test the control strategy outlined in section 2, the system described should be improved and combined with the type of axisymmetric control system described for example in [3]. When the route to instability is "classic surge" rather than "deep surge," axisymmetric control does not appear to increase stability margin [9]. In order for the combined system to show any further benefit, therefore, the nonaxisymmetric controller must produce a sufficient stability margin that "deep surge" becomes the first mode of instability.

6 Conclusions

We have shown that it is theoretically possible for a linear control system to stabilize nonaxisymmetric modes of a compressor. Numerical modeling results suggest that by using this together with a second linear controller for axisymmetric modes, a compression system may be rendered absolutely stable to all disturbances.

We have shown by experiment that a linear controller can indeed stabilize a nonaxisymmetric mode. In our test engine,

a Rover IS/60 45 kW power unit, a relatively crude control system produced an increase of more than 10 percent in delivered power before surge, with a corresponding decrease of 2.6 percent in corrected mass flow.

Acknowledgments

The authors would like to acknowledge the help of D. Williams, W. Hodson, M. Myers, and M. Gulliver of Topexpress during engine tests. Mr. Williams also programmed the DSP hardware to implement the digital filters. We should also like to thank staff at Noel Penny Turbines Ltd., in particular F. Dumbleton (Manager, R&D), R. Oliver (Workshop Manager), and M. Dredge (fitter).

The support of the Office of Naval Research of the US Government is gratefully acknowledged.

References

- 1 Epstein, A. H., Ffowcs Williams, J. E., and Greitzer, E. M., "Active Suppression of Compressor Instabilities," Paper No. AIAA-86-1994.
- 2 Ffowcs Williams, J. E., and Graham, W. R., "An Engine Demonstration of Active Surge Control," ASME Paper No. 90-GT-224.
- 3 Ffowcs Williams, J. E., and Huang, E. Y., "Active Stabilization of Compressor Surge," *J. Fluid Mech.*, Vol. 204, 1989, pp. 245-262.
- 4 Ffowcs Williams, J. E., Harper, M., and Allwright, D. J., "The Active Control of Surge in a Gas Turbine Engine," Report No. TOP/ONR-N00014-87-5-1214/90/1 to the Office of Naval Research (Code 1512), USA, Aug. 1990.
- 5 Ffowcs Williams, J. E., Graham, W. R., Harper, M., and Jeffries, B., "Active Control of Surge in Gas Turbines: Phase II," Report to ONR. Topexpress report number TOP/N0014-87-J-1214/89/1, 1989.
- 6 Garnier, V. H., Epstein, A. H., and Greitzer, E. M., "Rotating Waves as a Stall Inception Indication in Axial Compressors," *ASME JOURNAL OF TURBOMACHINERY*, Vol. 113, 1991, pp. 290-302.
- 7 Greitzer, E. M., "Surge and Rotating Stall in Axial Flow Compressors: Part I: Theoretical Compression System Model," *ASME Journal of Engineering for Power*, Vol. 98, 1976, pp. 190-198.
- 8 Greitzer, E. M., "Surge and Rotating Stall in Axial Flow Compressors: Part II: Experimental Results and Comparison With Theory," *ASME Journal of Engineering for Power*, Vol. 98, 1976, pp. 199-217.
- 9 Harper, M., "Active Control of Surge in a Gas Turbine Engine," presented at the Conference on Recent Advances in Active Control of Sound and Vibration, Virginia State University, Blacksburg, VA, Apr. 15-17, 1991.
- 10 McCaughan, F. E., "Application of Bifurcation Theory to Axial Flow Compressor Instability," *ASME JOURNAL OF TURBOMACHINERY*, Vol. 111, 1989, pp. 426-433.
- 11 McCaughan, F. E., "Bifurcation Analysis of Axial Flow Compressor Stability," *SIAM Journal of Applied Mathematics*, Vol. 50, Oct. 1990, pp. 1232-1253.
- 12 McCaughan, F. E., "Numerical Results for Axial Flow Compressor Instability," *ASME JOURNAL OF TURBOMACHINERY*, Vol. 111, 1989, pp. 434-441.
- 13 Moore, F. K., "A Theory of Rotating Stall of Multistage Axial Compressors: Part I—Small Disturbances, Part II—Finite Disturbances, Part III—Limit Cycles," *ASME Journal of Engineering for Gas Turbines and Power*, Vol. 106, 1984, pp. 313-336.
- 14 Moore, F. K., and Greitzer, E. M., "A Theory of Post-Stall Transients in Axial Compression Systems: Part I—Development of Equations," *ASME Journal of Engineering for Gas Turbines and Power*, Vol. 108, 1986, pp. 68-76.
- 15 Greitzer, E. M., and Moore, F. K., "A Theory of Post-Stall Transients in Axial Compression Systems: Part II—Application," *ASME Journal of Engineering for Gas Turbines and Power*, Vol. 108, 1986, pp. 231-239.
- 16 Murray, J. D., *Mathematical Biology*, Springer-Verlag, Berlin, 1989, Chap. 8.
- 17 Pinsley, J. E., Guenette, G. R., Epstein, A. H., and Greitzer, E. M., "Active Stabilization of Centrifugal Compressor Surge," *ASME JOURNAL OF TURBOMACHINERY*, Vol. 113, 1991, pp. 723-732.
- 18 Porter, B., and Crossley, R., *Modal Control—Theory and Applications*, Taylor & Francis, London, 1972.
- 19 Wonham, W. M., *Linear Multivariable Control: a Geometric Approach*, 2nd ed., Springer-Verlag, New York, 1979.
- 20 Loughborough Sound Images Ltd., "DSP Devices Catalogue," obtainable from LSI Ltd at The Technology Centre, Epinal Way, Loughborough, Leicestershire, LE11 0QE, United Kingdom.
- 21 Owens, D. H., *Multivariable and Optimal Systems*, Academic Press, London, 1981.
- 22 Marshall, J. E., "Control of Time-Delay Systems," *IEEE Control Engineering Series*, Vol. 10, 1979.

Unsteady Aerodynamic Response of a Cascade to Nonuniform Inflow

J. E. Caruthers

Associate Professor of Engineering
Science and Mechanics,
University of Tennessee Space Institute,
Tullahoma, TN 37388

W. N. Dalton

Development Engineer,
Allison Gas Turbine Division,
General Motors Corporation,
Indianapolis, IN 46206

A solution method is developed for the small perturbation approximation to the inviscid, unsteady fluid equations for a two-dimensional cascade of airfoils. By introducing the unsteady field as a locally small perturbation from a nonuniform steady field, a first-order coupling between the unsteady fluid properties and the gradients of the steady field properties results. Results of this analysis procedure are compared with the experimentally determined unsteady pressure distribution on the vane of a low-speed research compressor produced by the wakes from the upstream rotor. Correlation between experimental and analytical results is good. Similar comparisons of the data with an analysis method that approximates the vane as a two-dimensional cascade of flat plates at zero mean incidence did not exhibit acceptable correlation. The lack of correlation was particularly evident for the chordwise phase angle distribution.

Introduction

Aerodynamically induced vibration has continuously plagued designers of turbomachine blading since the earliest days. While aeroelastic instability (flutter) has received much of the published effort, resonant vibration driven by nonuniform inflow or outflow accounts for the great majority of development and operational problems. Within this context, the excitation of a trailing blade row by the viscous wake from its upstream neighbors represents one of the major sources of fatigue failures in gas turbine blading.

A key element in reducing the occurrence of vibration-induced failures in blading is the development of a method for predicting resonant vibration levels. Accurate prediction of the unsteady aerodynamic excitation forces is a crucial factor in developing such a predictive tool. Many investigators have contributed to the understanding of this problem. Until recently, such efforts have reduced the complicated three-dimensional geometry of an actual turbomachine blade passage to a two-dimensional cascade of flat plates at negligible angle of attack. As a result of this simplification, both the time mean and time dependent departures from free-stream conditions can be regarded as small and of equal order. The unsteady fluid properties then become formally independent of the local steady flow. A less restrictive approach—as developed by Verdon and Caspar (1981) for unsteadiness produced by airfoil vibration, Atassi and Akai (1979) for incompressible flow, and Caruthers (1980) for subsonic flows including unsteadiness resulting from nonuniform inflow or outflow conditions—assumes the unsteady field to be a small local perturbation about a spatially varying steady field. The resulting boundary value problem remains linear. However, new terms appear in both the field equations and the boundary conditions reflecting

a first-order modification to the unsteady flow resulting from spatial gradients in the steady flow. This paper describes the current state of development of an analysis procedure based on this local linearization concept. A comparison is presented between the measured unsteady pressure field on the vane of a low-speed research compressor produced by the wakes from the upstream rotor blades and theoretical predictions. It is shown that coupling between the steady and unsteady flows must be considered, even at low levels of steady loading.

Analytical/Numerical Method. The method used to provide the numerical results presented here is an improved version of that presented in great detail in the paper by Caruthers (1980). The primary differences are threefold. First, as indicated in the reference, the vortical part of the flow may be calculated more efficiently by using Goldstein's splitting procedure (Goldstein, 1979). This procedure was incorporated into the method and reported originally in an unpublished contract report (Caruthers and Scott, 1981). Second, the semi-intrinsic coordinate system used previously, where one set of coordinate lines was taken as the mean flow streamlines, gave difficulties whenever there existed an axial mean flow reversal, which is often encountered near the leading edge of turbine stators. For this reason the numerical discretization was modified for compatibility with a more arbitrary grid system, as reported in a second unpublished contract report (Caruthers, 1984). Since the work contained in these two documents was not published in the open literature, the most relevant portions of them are presented as appendices to this paper. Third and finally, the exit radiation boundary conditions for the velocity potential are somewhat complicated due to the presence of the distorted vortical flow and inhomogeneity of the potential equation at the exit. This unnecessary complication has been eliminated by recasting the exit radiation condition in terms of the perturbation pressure. The method, as it currently stands, is outlined below.

It is assumed from the beginning that the flow is two di-

Contributed by the International Gas Turbine Institute and presented at the 36th International Gas Turbine and Aeroengine Congress and Exposition, Orlando, Florida, June 3-6, 1991. Manuscript received at ASME headquarters February 20, 1991. Paper No. 91-GT-174. Associate Technical Editor: L. A. Riekert.

mensional and adiabatic, inviscid, and that the fluid is a perfect gas. It is also assumed that the temporal variations of all flow and thermodynamic properties are small compared to mean values of their reference quantities. In particular,

$$\bar{V}(x, y, t) = \bar{V}_o(x, y) + \bar{v}(x, y, t); \quad |\bar{v}| \ll c_o \quad (1)$$

$$P(x, y, t) = P_o(x, y) + p(x, y, t); \quad |p| \ll P_o \quad (2)$$

$$S(x, y, t) = S_o(x, y) + s(x, y, t); \quad |s| \ll c_p \quad (3)$$

$$\rho(x, y, t) = \rho_o(x, y) + \rho'(x, y, t); \quad |\rho'| \ll \rho_o \quad (4)$$

Using this assumption, the continuity, momentum, and energy equations may be split as follows:

Steady mean flow:

$$\nabla \cdot (\rho_o \bar{V}_o) = 0 \quad (5)$$

$$\rho_o \bar{V}_o \cdot \nabla \bar{V}_o = -\nabla P_o \quad (6)$$

$$\bar{V}_o \cdot \nabla S_o = 0 \quad (7)$$

thereby allowing independent solution for the mean flow quantities.

Unsteady flow (to first order):

$$\frac{D_o \rho'}{Dt} + \rho' (\nabla \cdot \bar{V}_o) + \nabla \cdot (\rho_o \bar{v}) = 0 \quad (8)$$

$$\rho_o \left(\frac{D_o \bar{v}}{Dt} + \bar{v} \cdot \nabla \bar{V}_o \right) + \rho' \bar{V}_o \cdot \nabla \bar{V}_o = -\nabla p \quad (9)$$

$$\frac{D_o s}{Dt} + \bar{v} \cdot \nabla S_o = 0 \quad (10)$$

where

$$\frac{D_o}{Dt} = \frac{\partial}{\partial t} + \bar{V}_o \cdot \nabla \quad (11)$$

It is assumed that the mean flow field is homentropic ($S_o = \text{const}$), reducing Eq. (10) to

$$\frac{D_o s}{Dt} = 0 \quad (12)$$

so that the perturbation entropy field may be solved independently of other perturbation quantities. Its solution is simple, given in terms of mean flow variables as

$$s = s(\psi_o, \tau) \quad (13)$$

$$\tau = t - \psi_o \int_o^L dl / V_o \quad (14)$$

where

ψ_o = mean flow stream function

l = distance along a streamline

Eliminating ρ' from Eqs. (8) and (9) gives

$$\frac{D_o}{Dt} \left(\frac{p'}{\rho_o c_o^2} \right) + \frac{1}{\rho_o} \nabla \cdot (\rho_o \bar{v}) = 0 \quad (15)$$

$$\frac{D_o \bar{v}}{Dt} + \bar{v} \cdot \nabla \bar{V}_o - \frac{s}{c_p} \bar{V}_o \cdot \nabla \bar{V}_o = -\nabla \left(\frac{p}{\rho_o} \right) \quad (16)$$

The perturbation velocity is now split into potential and vortical parts as

$$\bar{v} = \nabla \phi + \bar{w} \quad (17)$$

The addition of another variable by the above splitting naturally leaves an indeterminacy in the problem formulation. The indeterminacy may be removed in a variety of ways as noted in Caruthers (1980). Goldstein's (1979) procedure is, however, most elegant. The procedure begins by substitution of Eq. (17) into Eq. (16). Letting

$$\bar{w}' = \bar{w} - s \bar{V}_o / 2c_p \quad (18)$$

this yields

$$\nabla \frac{D_o \phi}{Dt} + \frac{D_o \bar{w}'}{Dt} + \bar{w}' \cdot \nabla \bar{V}_o = -\nabla (p / \rho_o) \quad (19)$$

By choosing to set

$$\frac{D_o \bar{w}'}{Dt} + \bar{w}' \cdot \nabla \bar{V}_o = 0 \quad (20)$$

a simple relation between the perturbation potential and pressure may be recovered as

$$\frac{D_o \phi}{Dt} = -p / \rho_o \quad (21)$$

where an arbitrary function of time has been absorbed into ϕ . Goldstein gives a simple general solution of Eq. (20) when $\nabla \times V_o = 0$ (an assumption which is now invoked).

Nomenclature

c = airfoil chord
 c_o = speed of sound
 c_p = constant pressure specific heat
 i = imaginary number = $\sqrt{-1}$
 k = reduced frequency
 l = dummy integration variable along steady-state streamline
 L = reference location on steady-state streamline (Eq. (14))
 n = unit normal vector to airfoil surface
 P = pressure
 p = perturbation pressure
 S = entropy
 s = perturbation entropy
 t = time
 \bar{V} = velocity vector
 \bar{v} = perturbation velocity vector
 \bar{w} = rotational component of perturbation velocity field
 \bar{w}' = auxiliary variable of Goldstein defining rotational velocity field (Eq. (18))

\hat{w} = vector amplitude of rotational velocity for harmonic time dependence
 x = axial coordinate
 y = tangential coordinate
 α = characteristic tangential wave number associated with general solution for potential equation in far field
 β = interblade phase angle
 $\xi_{1,2}$ = local nonorthogonal coordinate axes in computational mesh
 $\left. \begin{matrix} \bar{\eta} \\ \bar{\xi} \end{matrix} \right\}$ = vector functions defining solution for \hat{w}
 λ = characteristic axial wave number associated with general solution for potential equation in far field
 ρ = fluid density
 ρ' = perturbation fluid density
 σ = cascade solidity

τ = Lighthill's drift function (Eq. (14))
 ϕ = perturbation velocity potential
 $\tilde{\phi}$ = amplitude of perturbation potential for harmonic time dependence
 ψ = stream function
 ω = circular frequency

Subscripts

o = time mean quantity
 $-\infty$ = refers to upstream reference plane, where mean properties assumed uniform
 $+\infty$ = refers to downstream reference plane, where mean properties have returned to uniform state

Superscripts

n = order of characteristic wave numbers associated with far field solution
 $*$ = complex conjugate

$$\bar{w}' = \nabla \bar{\eta} \cdot \bar{\xi} \quad (22)$$

where in two dimensions the rectangular Cartesian components of η are

$$\eta_1 = \psi_o \int_0^L dl/V_o; \quad \eta_2 = \psi_o \quad (23)$$

where ψ_o is the steady mean flow stream function. The function $\bar{\xi}$ is an arbitrary vector function of the arguments $\eta_1 - t$ and η_2 . That is,

$$\bar{\xi} = \bar{\xi}(\eta_1 - t, \eta_2) \quad (24)$$

The solution is rendered unique by applying initial conditions to \bar{w}' at an upstream reference location, thereby determining the particular form of $\bar{\xi}$. The details of the procedure, originally reported by Caruthers and Scott (1981), are given in Appendix A.

A slight problem arises with regard to this method on the airfoil and wake surfaces. This occurs because η_1 and $\nabla \eta_1$ are singular aft of a stagnation point where $V_o = 0$. Consequently, \bar{w}' becomes singular as well so that the method apparently fails along the airfoil and wake surfaces. If it were possible to continue on with the solution for ϕ at this point, $\nabla \phi$ would develop a singularity, which would just cancel the singularity in \bar{w}' . Goldstein (1981) and Atassi (1985) have suggested a method for removing the singularity explicitly. The method proceeds on the basis that the gradient of any scalar function, ψ , which is a solution of $D_o \psi / Dt = 0$, is a solution of Eq. (20). Therefore, $\nabla \psi(\eta_1 - t, \eta_2)$ is a solution of Eq. (20) and may be adjusted so that

$$\nabla \psi(\eta_1 - t, \eta_2) = -\bar{w}' \quad (25)$$

all along the airfoil and wake surfaces. Thus, adding $\nabla \psi$ to \bar{w}' while subtracting the same from $\nabla \phi$ removes the troublesome singularity.

An early attempt by the authors to use this device to remove the singularity totally was only partially successful in that a phase singularity in the streamwise component of \bar{w}' could not be removed. Since this negated some of the advantage originally sought by employing the method and since use of this method incurs a considerable increase in the complexity of the procedure (for example, the remaining potential part of the unsteady flow no longer satisfies radiation conditions at infinity), it was not employed in producing the current numerical results. It was observed during the early stages of development that the numerically evaluated steady mean velocity field, which is used in the numerical evaluation of the integral in Eq. (22) was never quite zero in the grid cell containing the stagnation point, although it approaches zero as the grid is refined. The value of η_1 grows correspondingly larger as the grid is refined but is never numerically singular. While this caused some concern initially, numerical experimentation has shown the results to be relatively insensitive to grid refinement in the leading edge region. This observation, illustrated by Fig. 7, which is discussed in detail later in this paper, has served to dispel this concern. It may also be argued that the result obtained in this manner is indistinguishable from that obtained by the physical addition of a small, subgrid scale, forward cusp to the airfoil. However, if one is willing to cope with the additional complexity, Hall and Verdon (1989) have reported a full singularity removal process following the procedure outlined above.

Equations (15) and (21) combine to yield the equation for the perturbation potential:

$$1/\rho_o \nabla \cdot (\rho_o \nabla \phi) - \frac{D_o}{Dt} \left(\frac{D_o \phi}{Dt} / c_o^2 \right) = -1/\rho_o \nabla \cdot (\rho_o \bar{w}) \quad (26)$$

Simple harmonic solutions of the above are sought. Letting $\phi = \bar{\phi} e^{ikt}$ and $\bar{w} = \bar{w} e^{ikt}$ then

$$1/\rho_o \nabla \cdot (\rho_o \nabla \bar{\phi}) - L \{ L \{ \bar{\phi} \} / c_o^2 \} = -1/\rho_o \nabla \cdot (\rho_o \bar{w}) \quad (27)$$

where $L = ik + \bar{V}_o \cdot \nabla$ and $k = c\omega / V_{o-\infty}$.

Since \bar{w} is known already from the previous calculation, Eq. (27) may be solved once the boundary conditions are established. For convenience sake, all variables are taken as appropriately nondimensionalized by $\rho_{-\infty}$, $V_{o-\infty}$, and chord length, where $-\infty$ refers to conditions at the upstream reference plane.

Boundary Conditions. At all blade surfaces and in the absence of blade motion

$$(\nabla \bar{\phi} + \bar{w}) \cdot \hat{n} = 0 \quad (28)$$

Throughout the geometrically periodic region of the cascade the so-called quasi-periodic condition is enforced.

$$\bar{\phi}(x, y) = \bar{\phi} \left(x, y + \frac{1}{\sigma} \right) e^{i\beta} \quad (29)$$

where β is the phasing imposed by the wake gust velocity, \hat{w} , and σ is the cascade solidity. The mean flow is assumed to be uniform upstream of the computational domain boundary and an outward radiation condition is enforced on ϕ . This may be expressed as

$$\bar{\phi} = \sum_{n=-\infty}^{\infty} b_n e^{i\lambda^n x} e^{i\alpha^n y} \quad (30)$$

where $\alpha^n = \sigma(2n\pi - \beta)$ and

$$\begin{aligned} -\lambda^n &= [-b + (b^2 - 4ac)^{1/2}]^* / 2a \\ a &= 1 - M_{-\infty}^2 \cos^2 \theta_{-\infty} \\ b &= -2 \cos \theta_{-\infty} M_{-\infty}^2 (\alpha^n \sin \theta_{-\infty} + k) \\ c &= (\alpha^n)^2 - M_{-\infty}^2 (\alpha^n \sin \theta_{-\infty} + k)^2 \end{aligned} \quad (31)$$

and the b_n are determined by matching ϕ from Eq. (30) to the interior numerical solution along the inlet boundary. The details of the matching procedure are too lengthy to include here but may be found from Caruthers (1980).

Downstream of the cascade, the computational boundaries are set to lie approximately along the mean wake streamlines. Continuity of pressure and displacement (normal velocity in this case) are applied. Continuity of pressure across the wake, along with Eq. (29) yields

$$\bar{\phi}_L - e^{i\beta} \bar{\phi}_u = (\bar{\phi}_L - e^{i\beta} \bar{\phi}_u)_{t.e.} e^{-ik\eta_1} \quad (32)$$

where the subscripts indicate the upper and lower wake boundaries, while continuity of normal velocity yields

$$(\nabla \bar{\phi} + \bar{w})_L \cdot \hat{n} = e^{i\beta} (\nabla \bar{\phi} + \bar{w})_u \cdot \hat{n} \quad (33)$$

It is noted that since Atassi's (1985, private communication) singularity removal method was not used, $\hat{w} \cdot \hat{n}$ is discontinuous across the wake surfaces, which forces a cancelling discontinuity in $\nabla \phi \cdot \hat{n}$.

Far downstream the flow once again becomes uniform so that ϕ satisfies

$$\nabla^2 \bar{\phi} - L^2 \bar{\phi} / c_o^2 = -\nabla \cdot \bar{w} \quad (34)$$

Applying the L operator to Eq. (34) gives

$$\nabla^2 (L \bar{\phi}) - L^2 (L \bar{\phi}) / c_o^2 = 0 \quad (35)$$

or

$$\nabla^2 p - L^2 (p) / c_o^2 = 0 \quad (36)$$

since $L(\nabla \cdot \hat{w}) = 0$ in the downstream field. Taking the mean flow as uniform beyond the downstream computational boundary, the outgoing radiation condition is applied by setting

$$L \bar{\phi} = \sum_{n=-\infty}^{+\infty} a_n e^{i^+ \lambda^n x} e^{i\alpha^n y} \quad (37)$$

where $i^+ \lambda^n$ is given by Eq. (31), but with the sign of the radical

Table 1 Airfoil mean section characteristics and compressor design point condition

	Rotor	Stator
Type of airfoil	65 Series	65 Series
Number	42	40
Chord, in. (cm)	4.589 (11.66)	5.089 (12.93)
Solidity, $s = C/S$	1.435	1.516
Camber, 0 - deg.	20.42	48.57
Aspect ratio, $AR = S/C$	1.046	0.943
Leading edge radius/C	0.0044	0.0049
Trailing edge radius/C	0.0028	0.0030
Inlet air angle, B_1 - deg.	59.38	37.84
Exit air angle, B_2 - deg.	42.41	0.00
Loss coefficient	0.043	0.056
Diffusion factor	0.449	0.410
Rotor-stator axial spacing-in. (cm)	1.485 (3.772)	
Flow rate	31.02 lb/sec (14.07 kg/sec)	
Tip speed	183.5 ft/sec (5593.1 cm/sec)	
Rotational speed	876.3 rpm	
Stage pressure ratio	1.0125	
Inlet tip diameter	48.01 in. (121.95 cm)	
Hub/tip radius ratio	0.80	
Stage efficiency, percent	88.1	

set negative and the constants a , b , c referred to $+\infty$. The a_n are again determined by matching to the interior numerical solution. An imposed potential disturbance originating from downstream can easily be added by adding a single term of known amplitude from the opposite (upstream moving) wave family to Eq. (37).

This procedure for applying the exit boundary condition is much simpler than previous methods, which were cast in terms of the velocity potential and thus had to contend with discontinuous wake potentials and particular solutions of the non-homogeneous Eq. (34). It therefore represents a substantial improvement.

Numerical Solution. The discretized field equations and boundary conditions (see Appendix B) can be arranged in the block tridiagonal form

$$A^I \Phi_{I-1} + B^I \Phi_I + C^I \Phi_{I+1} = F^I \quad (38)$$

where Φ^I and F^I are column vectors and A^I , B^I and C^I are square matrices for each value of the discrete coordinate index, $I=2, 3, \dots, M-1$. The system is completed by discretizing the inlet and exit radiation boundary conditions.

These may be put in the forms

$$\Phi_1 + C^1 \Phi_2 = F^1 = 0 \quad (39)$$

for the inlet and

$$A^M \Phi_{M-1} + \Phi_M = F^M = 0 \quad (40)$$

for the exit, where to retain the block tridiagonal form, the field equations at coordinate index M have been used to eliminate Φ_{M+1} .

The block tridiagonal system of Eq. (38) is solved by

$$\Phi_{I+1} = a'_I + b'_I \Phi_I \quad (41)$$

where the b'_I and a'_I are matrices and vectors, respectively, given by the recursion relations

$$b'_{I-1} = -(B^I + C^I b'_I)^{-1} (A^I) \quad (42)$$

and

$$a'_{I-1} = (B^I + C^I b'_I)^{-1} (F^I - C^I a'_I) \quad (43)$$

and where

$$b'_{M-1} = -A^M \quad (44)$$

$$a'_{M-1} = F^M \quad (45)$$

$$\Phi_1 = -(b'_1 + [C^1]^{-1})^{-1} (a'_1 + [C^1]^{-1} F^1) \quad (46)$$

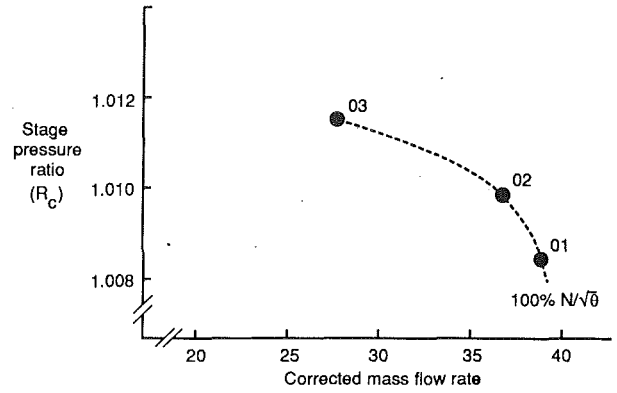


Fig. 1 Allison low-speed research compressor operating conditions

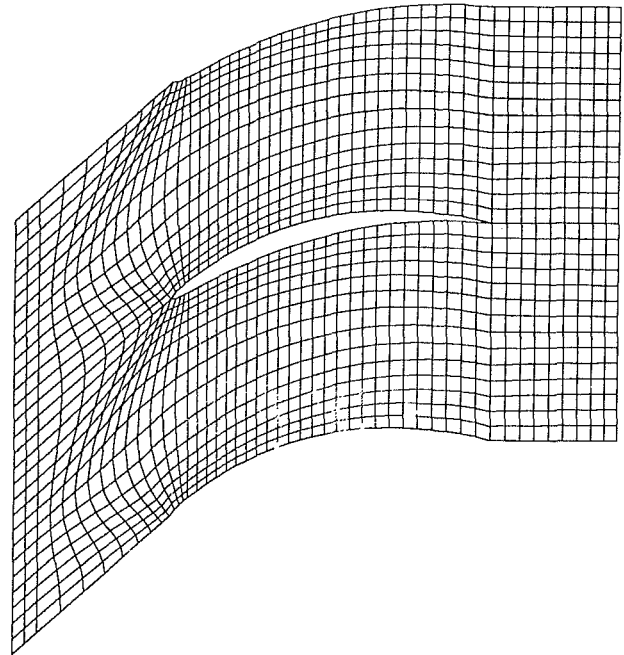


Fig. 2 Computational mesh for low-speed rig vane

Comparison of Theoretical Predictions and Experimental Data

All unsteady data presented for comparison were acquired in a single-stage, low-speed research compressor by Fleeter et al. (1980). A detailed description of both the rig and the experiment may be found there. For reference, Table 1 presents the midannulus section properties of the two airfoil rows. The data were obtained at the three steady-state flow conditions shown in Fig. 1. These conditions correspond to incidence angles to the vane mean camber line, which vary from highly negative at the lowest pressure ratio to nearly zero at the highest pressure ratio. Since the unsteady flow problem is posed as a small perturbation about a spatially nonuniform steady flow, accurate modeling of the mean flow field is a necessary first step. Predictions of the steady flow properties were derived from a numerical solution of the equation for the stream function in an irrotational fluid. Due to the negligible flow path convergence through the vane and the low Mach numbers inherent in this rig, the effects of spanwise streamline curvature and convergence were neglected. The numerical procedure was implemented on a body-fitted grid system obtained using an algebraic generation method. Both the steady and unsteady results presented in this paper were obtained on a mesh with 20 points in the tangential direction and 60 points in the axial

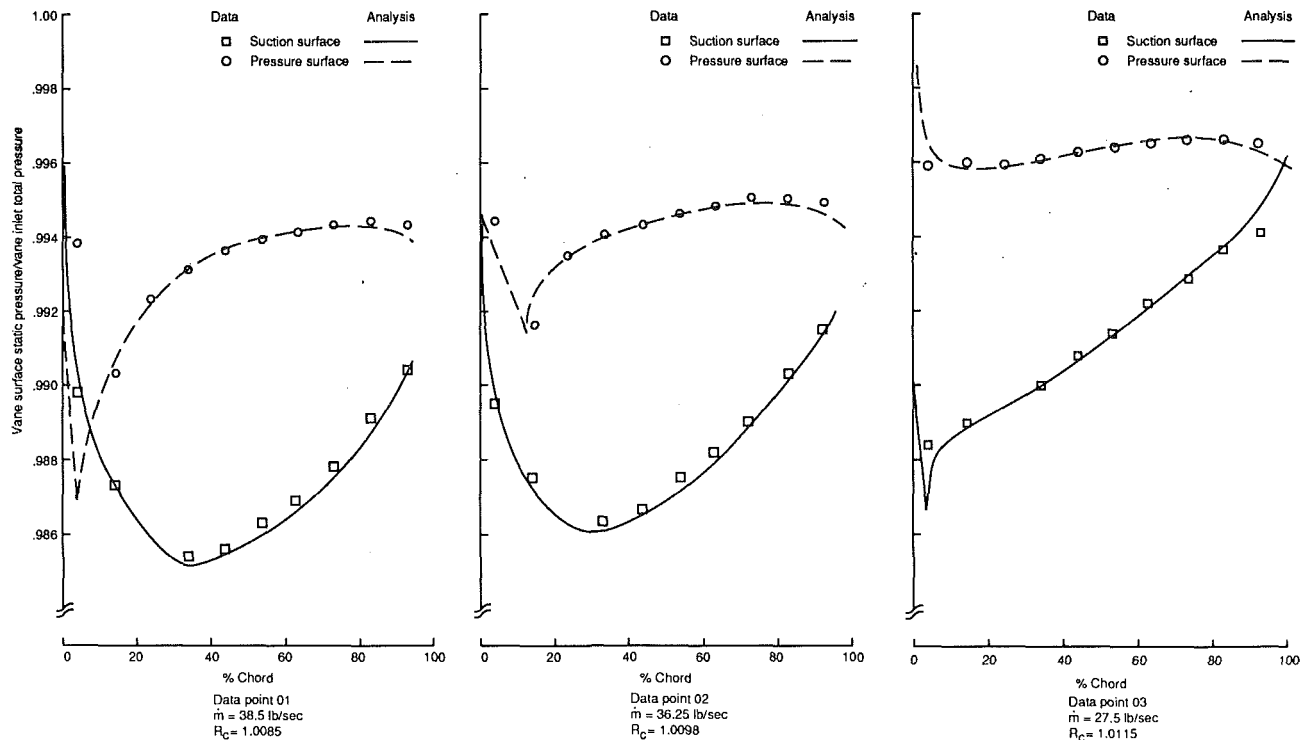


Fig. 3 Time mean pressure distribution on vane surface for three operating conditions

Table 2 Nondimensional parameters describing rig operating conditions

Pt.	Inlet Mn.	Inlet air angle	Reduced freq. ($c\omega/V_{0-\infty}$)	Interblade phase	$w/V_{0-\infty}$
1	0.115	26 deg	12.96	-18 deg	.036
2	0.115	32 deg	13.3	-18 deg	.0355
3	0.105	42 deg	13.9	-18 deg	.135

direction. A slightly coarser version of the grid for the subject airfoil is shown in Fig. 2. Since the procedure is actually implemented across a flow channel, Fig. 2 is composed of two grid systems matched at a periodic boundary. This is done to illustrate clearly the leading edge mesh packing that is produced. A comparison of the static pressure distribution on the vane surface resulting from the theoretical model with experimental measurements is shown in Fig. 3 for each of the three operating points. Inlet conditions were determined approximately from mean velocity and angle measurements from a hot-wire anemometer. The assumed inlet angle for the analysis was then varied to obtain a best fit to the measured surface pressures. Using this technique, it was possible to obtain a good match between experimental and computational results for the two lower pressure rise conditions. At the highest pressure ratio, the experimental results exhibit a significantly lower level of over speeding in the leading edge region and a reduced static pressure rise near the trailing edge on the suction surface than do the computational predictions. While no data were obtained during the investigation that would prove the conclusion, it is believed that the discrepancy may be the result of the presence of regions of locally separated flow. In spite of this area of disagreement, the computational results are believed to be an adequate approximation to the steady flow field.

The unsteady pressure data are presented in terms of the nondimensional pressure jump between the suction and pres-

sure surfaces and a phase angle. As can be seen from the theoretical development, the amplitude of the unsteady pressure response produced by the rotor wake should scale with the level of the velocity defect associated with the wake. This fact was used in defining the appropriate nondimensionalization of the pressure. The time domain output of both the pressure transducers and hot-wire anemometer were converted to a series of integer multiples of the rotor blade passing frequency using standard Fourier analysis procedures. The harmonics of the pressure signal were then made nondimensional by dividing them by the vane inlet dynamic head and scaling the resultant levels by the ratio of the free-stream velocity ($V_{0-\infty}$) to the same harmonic of the wake velocity (w). The phase angles of the pressure response harmonics were also established with respect to the harmonics of the wake velocity. As was previously mentioned, the unsteady pressure data were obtained on the adjacent surfaces of a channel formed by two of the vanes. By phase shifting the data from one surface through the known interblade phase lag associated with the difference in the numbers of the rotor blades and stator vanes, the equivalent unsteady response of the two surfaces of a single vane were obtained, thereby allowing determination of the equivalent unsteady response on the two surfaces of a single vane. This format was selected to facilitate comparisons with theoretical predictions.

The experimental data are presented in Figs. 4-6. In addition, Table 2 lists the value of important nondimensional parameters associated with each of the data points. The figures also present the results of two theoretical methods. The first method is the one described earlier in this paper and by Caruthers (1980). The second method is that of Smith (1971), which approximates the vane airfoils as a two-dimensional cascade of flat plates oriented at zero incidence to the mean flow vector. This method is presented as a baseline and to illustrate the importance of coupling between the unsteady flow and gradients in the mean flow. Examination of Figs. 4-6 shows that the correlation between the amplitude and the pressure coefficient predicted by the current method and the measured values is good. The flat plate theory of Smith is in general

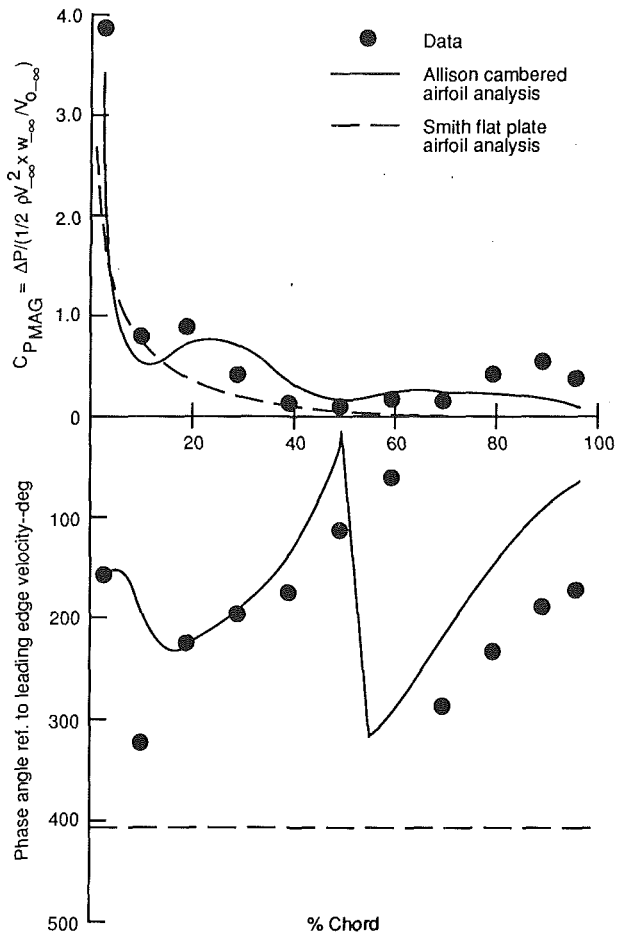


Fig. 4 Unsteady pressure jump due to first harmonic of rotor passage—operating point 01

agreement with the data, but is unable to reproduce certain characteristic features of the regions between 20 and 40 percent of chord and 80 and 100 percent of chord. This variance is most pronounced for point 01, which corresponds to the largest negative values of incidence to the vane. Referring to the time mean data in Fig. 3, it can be seen that the region between 20 and 40 percent chord contains strong gradients in the steady flow field on both the suction and pressure surfaces, as the pressure goes through its minimum value on both surfaces and then begins to diffuse. The middle portion of the airfoil is well described by both theoretical methods, even though the steady flow continues to decelerate at a fairly high but nearly constant rate. As the trailing edge is approached and the steady flow attempts to adjust to the presence of an edge, the unsteady pressure amplitude again increases. Neither analysis method follows the trend near the trailing edge particularly well, and it may be that viscous phenomena are a dominant feature in this region.

Turning now to the phase portion of Figs. 4–6, it is quickly evident that the flat plate approximation yields a chordwise phase distribution that is totally different from the experimental data. The current method is very reasonable match to the data for data points 01 and 02, except for one isolated location. At the 10 percent chord location for point 01, the phase data and predictions disagree by approximately 180 deg. In the original data reduction program, it was necessary for the analyst to determine the quadrant in which the phase lay in the Argand diagram and to add a 180 deg correction to all angles lying in the second and third quadrants. While the raw data are no longer available to prove the supposition, it seems likely that this location is improperly corrected. If this sup-

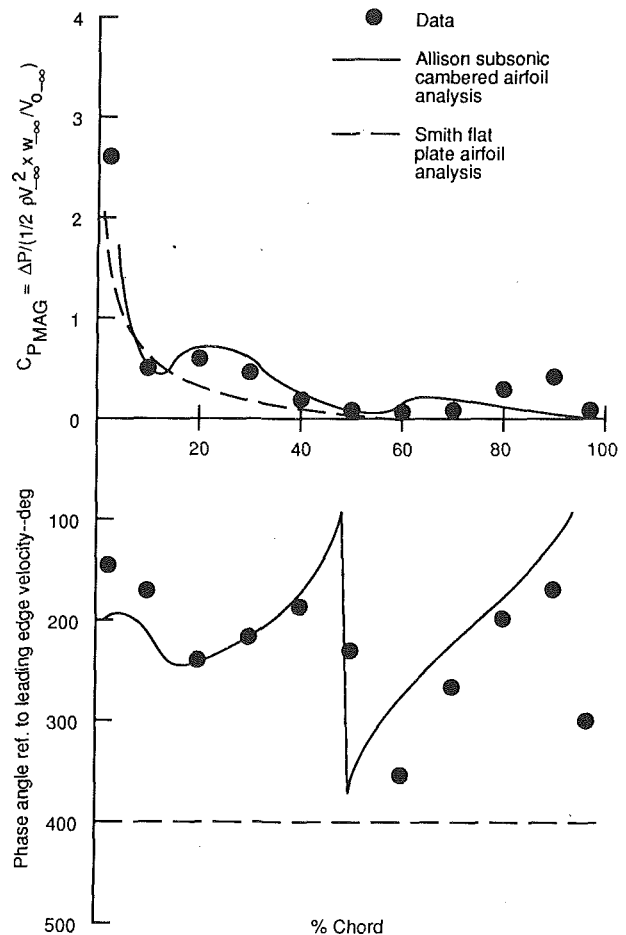


Fig. 5 Unsteady pressure jump due to first harmonic of rotor passage—operating point 02

position is correct, then the theoretical method is found to reproduce the trends of the data at negative incidence quite well.

The theoretical values for chordwise phase shift for data point 03 follow the basic trends of the experimental data, but are not as good a qualitative match as the two previous data points. This was at first somewhat surprising, since the steady-state incidence was approaching zero and the chordwise distribution of pressure magnitude was well predicted. Initially, it was thought the phase discrepancy might be related to the approximate treatment of the stagnation point singularity of the rotational velocity field. As a result of the grid compaction in the leading edge region produced by the generation method, modifying the axial grid density substantially alters the resulting leading edge grid distribution. If in fact the results were being influenced by a singular term, a small variation in the mesh point locations should produce substantial changes in the final results. A second set of results were produced for point 03 on a grid with 15 tangential points and 48 axial points (this is the grid system shown in Fig. 2). The resulting pressure amplitude distribution could not be distinguished from the results on the refined grid, and therefore is not presented here. A small change in the phase distribution was noted in the region between 0 and 20 percent of the chord, with the maximum difference between the two predictions being approximately 15 deg, as shown in Fig. 7. We believe these results indicate that the discrepancy between experiment and analysis is not related to any residual singular component in the velocity field. During the data reduction process, it was necessary to introduce fairly substantial phase corrections into the results, which varied between the data channels as a result of phase shifts in-

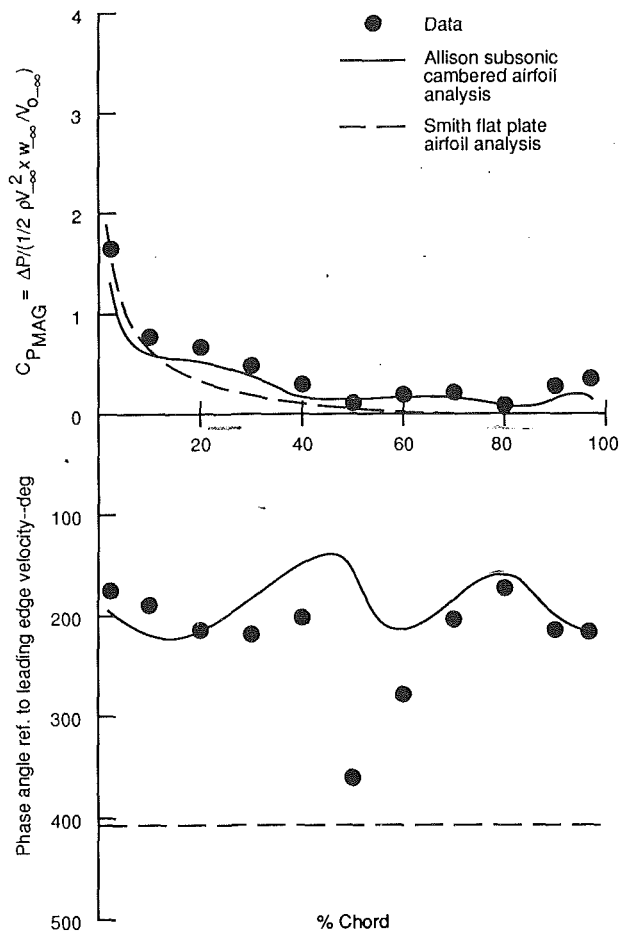


Fig. 6 Unsteady pressure jump due to first harmonic of rotor passage—operating point 03

produced by the instrumentation amplifiers and multiplexing of the analog to digital converter. Thus, it becomes tempting to ascribe the discrepancy to an accumulation of error in the data reduction process. However, referring to Table 2, it seems a more fundamental process may be at work. For data points 01 and 02, the first harmonic of the inlet velocity profile is found to be approximately 3.6 percent of the mean velocity. However, for data point 03, the first harmonic of the velocity profile has increased to 13.5 percent of the mean velocity. A similar increase was observed in the second harmonic of the inlet velocity profile, suggesting that the overall strength of the rotor wake has substantially increased. The velocity perturbation levels associated with this last data point are of sufficient size to raise questions concerning the validity of the small perturbation assumption.

The dramatic difference in phase response between the idealized unloaded flat plate cascade and an actual airfoil can be traced to the convection process associated with transporting the wake through the blade row. As a rotor wake is pulled across the face of the downstream vane, it establishes a phase front with a particular orientation, which then convects through the downstream blade row. When no steady flow gradients are present, this phase front maintains a fixed orientation in space. However, in the presence of gradients in the convecting velocity field, this phase front is deformed. This will produce a particularly strong effect at the airfoil surfaces where induced velocities must cancel the imposed wake velocity distribution. While the current analysis method is in good qualitative agreement with the experiment data, quantitative discrepancies do exist. Referring again to Figs. 4–6, it can be seen that the slope of the phase distribution along the chord, which is related to

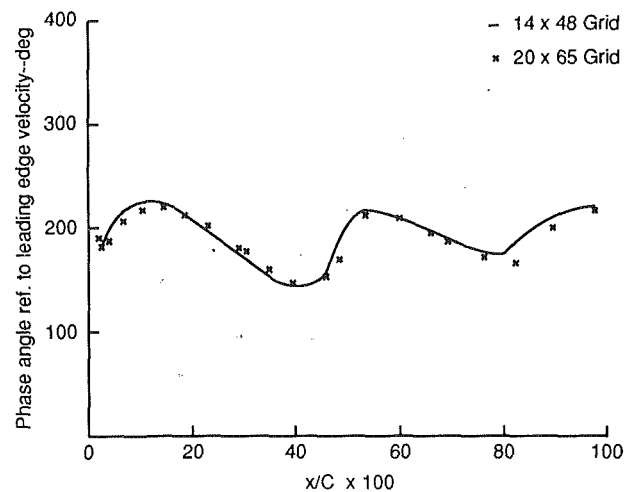


Fig. 7 Effect of grid refinement on phase results for data point 03

the phase velocity, is different for the experimental data and the theoretical predictions of our method. A likely source of the phase discrepancy noted here can be traced to the assumptions of two-dimensional, inviscid flow on which the steady flow solution method is based. As previously noted, the transport of the wake through the cascade is a convective process. The presence of gradients in the steady field deforms the wake surfaces during this transport process. Variations in steady flow conditions will alter the distribution of the wake field along the chord. For small changes in steady flow parameters, the most pronounced effect on the unsteady flow will be the phase distribution. For the high levels of reduced frequency associated with these data, the corresponding wave lengths of the velocity disturbance field are short. Thus, small changes in the convection rate will produce large changes in phase. As detailed earlier, the inflow conditions for the steady flow analysis were varied to produce the best correspondence between theoretical and experimental surface pressure distributions. It is to be expected that the velocity distribution associated with a particular static pressure field will be different for a two-dimensional, inviscid flow field and a three-dimensional viscous flow. In addition, for point 03, the velocity perturbations associated with the wake were found to be a much larger percentage of the mean flow velocity than for the other two conditions. As the primary assumption of small perturbations becomes marginal, the secondary assumption that the unsteady vorticity and entropy are transported at a rate equal to the local mean flow velocity will also become marginal. For high reduced frequency, the phase angle results will be the first to be affected. This is the result of the additional distortion of the phase surfaces of the harmonic decomposition of the velocity profile, which occurs when the velocity increment associated with passage of the wake can no longer be neglected relative to the mean velocity.

The change in phase distribution of the unsteady surface pressures in the presence of steady flow gradients has significant implications on efforts to predict forced response of compressor blading resulting from wake passage. In general, the vibration modes of compressor blading excited by wake passage are complex, high-order chordwise bending modes. These modes occur as standing waves along the chord of the airfoil, with all points along the chord either in or directly out of phase. The ability of an imposed loading distribution to drive these modes will change drastically with changes in the phase distribution of the loading pattern. Thus, while the differences in pressure amplitude along the chord between the two theoretical methods presented here are not sufficient to produce significantly different predictions for vibratory stress levels, the differences in their phase distributions are. There-

fore, any aeroelastic forced response predictive methodology must employ unsteady aerodynamic models, such as the one presented here, which include the effects of steady flow gradients on the unsteady flow field.

Summary

In summary, a method based on a linearization of the unsteady Euler approximation to the fluid equations about a spatially nonuniform mean flow has been developed for two-dimensional cascades. This method is applicable to unsteady flows resulting from nonuniform, unsteady inflow and outflow conditions. Theoretical predictions were compared with experimental measurements of the unsteady pressure response on the surface of a compressor vane produced by the rotor wakes. Good correlation between predicted and measured levels was obtained. Theoretical predictions based on approximations to the fluid equations that neglect the effects of steady flow gradients do not match the experimental data well. This deviation is particularly evident in the chordwise phase distribution. Since chordwise phasing strongly affects the energy absorbed by a natural mode of a structure, aeroelastic forced response predictions based on the method described in this paper will be more accurate than those employing unsteady flow models, which neglect the interaction of the unsteady pressure field with steady flow gradients.

Acknowledgments

The authors gratefully acknowledge the support of Allison Gas Turbine Division of General Motors for this work.

References

- Atassi, H., and Akai, T. J., 1979, "Aerodynamic and Aeroelastic Characteristics of Oscillating Loaded Cascades at Low Mach Number," ASME Paper No. 79-GT-111.
- Atassi, H. M., 1985, University of Notre Dame, private communication.
- Caruthers, J. E., 1980, "Aerodynamic Analysis of Cascaded Airfoils in Unsteady Rotational Flow," *Second Symposium on Aeroelasticity in Turbomachines*, Lausanne, Switzerland, Paper No. 1-2.
- Caruthers, J. E., and Scott, M. G., 1981, "Wake Excitation of Cascades," Contract final report, Detroit Diesel Allison Division of General Motors Corporation.
- Caruthers, J. E., 1984, "An Automatic Body-Fitted Grid Generation Method for Turbine Cascades," Final report, Allison Gas Turbine contract No. H262399.
- Fleeter, S., Bennett, W. A., and Jay, R. L., 1980, "The Time-Variant Aerodynamic Response of a Stator Row Including the Effects of Airfoil Camber," ASME *Journal of Engineering for Power*, Vol. 102, pp. 334-343.
- Goldstein, M. E., 1979, "Turbulence Generated by the Interaction of Entropy Fluctuations With Nonuniform Mean Flows," *Journal of Fluid Mechanics*, Vol. 93, Part 2, pp. 209-224.
- Goldstein, M. E., 1981, NASA LeRC, Cleveland, OH, private communication.
- Hall, K. C., and Verdon, J. M., 1989, "Gust Response Analysis for Cascades Operating in Nonuniform Mean Flows," presented at AGARD specialist meeting on Unsteady Aerodynamic Phenomena in Turbomachines, Luxembourg.
- Smith, S. N., 1971, "Discrete Frequency Sound Generation in Axial Flow Turbomachines," Report and Memoranda 3709, British Aeronautical Research Council, London, United Kingdom.
- Verdon, J. M., and Casper, J. R., 1981, "Development of an Unsteady Aerodynamic Analysis for Finite Deflection Cascades," NASA-CR-3455.

APPENDIX A

Determining $\bar{\xi}$ From Initial Conditions on \bar{w}

Given $\bar{w} = \bar{w}_{-\infty}$ and $s = s_{-\infty}$ at the inlet plane, $x = 0$, $\bar{\xi}$ is determined as follows:

$$\bar{w}'(\eta_1 - t, \eta_2) = \bar{w}_{-\infty}(-t, \eta_2) - s_{-\infty}(-t, \eta_2) \bar{V}_{o-\infty} / 2c_p \quad (A1)$$

$$= \nabla \bar{\eta} \cdot \bar{\xi} |_{x=0} = [\xi_1 \nabla \eta_1 + \xi_2 \nabla \eta_2]_{x=0} \quad (A2)$$

but

$$\nabla \eta_1 |_{x=0} = \hat{i} / V_{ox-\infty} \quad (A3)$$

and

$$\nabla \eta_2 |_{x=0} = \nabla \psi_o |_{x=0} = \sigma(-\tan \theta_{-\infty} \hat{i} + \hat{j}) \quad (A4)$$

where ψ_o has been normalized by the cascade passage mass flow rate. Equating components gives

$$\xi_2(-t, \eta_2) = [w_{y-\infty} - s_{-\infty} V_{oy-\infty} / 2c_p] / \sigma \quad (A5)$$

and

$$\xi_1(-t, \eta_2) = V_{x0-\infty} [\tan \theta_{-\infty} (w_{y-\infty} - s_{-\infty} V_{oy-\infty} / 2c_p + w_{x-\infty} - s_{-\infty} V_{ox-\infty} / 2c_p)] \quad (A6)$$

To obtain $\xi(\eta_1 - t, \eta_2)$ simply substitute $\eta_1 - t$ in the component Eqs. (A5) and (A6). Finally $\bar{w}(\eta_1 - t, \eta_2)$ is obtained as

$$\bar{w} = \nabla \bar{\eta} \cdot \bar{\xi} + s_{-\infty}(\eta_1 - t, \eta_2) \bar{V}_o / 2c_p \quad (A7)$$

APPENDIX B

Discretization Process

The numerical solution of the governing equation for the perturbation potential (Eq. (27)) requires the development of discrete approximations to the divergence of two terms and the operator L , which represents the linearized approximation to the substantial derivative for harmonic time dependence. The discrete form of these equations for node (I, J) is not obtained by a direct application of finite differencing to the adjacent grid nodes, but instead involves a finite volume approximation on the auxiliary node system shown in Fig. 8. The required variables on the auxiliary node system are obtained by suitable averaging of the values from the primary grid system. This process allows high-order accuracy to be retained even when substantial grid shear is present. The details of the averaging process for the derivative operators follow.

The term $L\{L\{\phi\}/c_o^2\}$ appearing in Eq. (27) may be expanded as

$$L\{L\{\phi\}/c_o^2\} = L\{\phi\}/c_o^2(ik - \nabla \cdot \bar{V}_o) + \nabla \cdot (\bar{V}_o L\{\phi\}/c_o^2) \quad (B1)$$

By applying the divergence theorem in numerically approximate form to the last term and using an average of the four auxiliary nodes for the first term, Eq. (B1) is evaluated on the small volume V of Fig. 8 as:

$$L\{L\{\phi\}/c_o^2\} = \sum_{k=A}^D \beta_k L\{\phi\}_k \quad (B2)$$

where

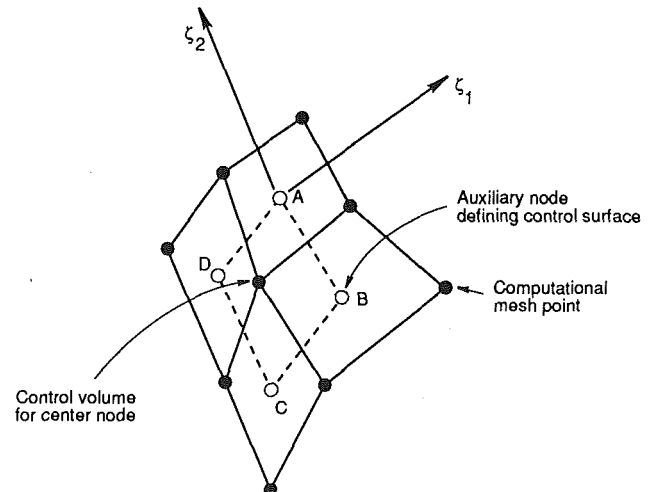


Fig. 8 Computational molecule for field point

$$\beta_A = \left[\frac{1}{2Vc_o^2} (\Delta y_{DB} V_{x_o} - \Delta x_{DB} V_{y_o}) + (ik - \nabla \cdot \bar{V}_o) / 4c_o^2 \right]_A$$

$$\beta_B = \left[\frac{1}{2Vc_o^2} (\Delta y_{AC} V_{x_o} - \Delta x_{AC} V_{y_o}) + (ik - \nabla \cdot \bar{V}_o) / 4c_o^2 \right]_B$$

$$\beta_C = \left[\frac{-1}{2Vc_o^2} (\Delta y_{DB} V_{x_o} - \Delta x_{DB} V_{y_o}) + (ik - \nabla \cdot \bar{V}_o) / 4c_o^2 \right]_C$$

$$\beta_D = \left[\frac{-1}{2Vc_o^2} (\Delta y_{AC} V_{x_o} - \Delta x_{AC} V_{y_o}) + (ik - \nabla \cdot \bar{V}_o) / 4c_o^2 \right]_D$$

Likewise, applying the divergence theorem to the first term of Eq. (27) yields:

$$\frac{1}{2\rho_o V} \left\{ \left(\rho_o \frac{\partial \tilde{\phi}}{\partial x} \Big|_A - \rho_o \frac{\partial \tilde{\phi}}{\partial x} \Big|_C \right) \Delta y_{DB} - \left(\rho_o \frac{\partial \tilde{\phi}}{\partial y} \Big|_A - \rho_o \frac{\partial \tilde{\phi}}{\partial y} \Big|_C \right) \Delta x_{DB} + \left(\rho_o \frac{\partial \tilde{\phi}}{\partial x} \Big|_B - \rho_o \frac{\partial \tilde{\phi}}{\partial x} \Big|_D \right) \Delta y_{AC} - \left(\rho_o \frac{\partial \tilde{\phi}}{\partial y} \Big|_B - \rho_o \frac{\partial \tilde{\phi}}{\partial y} \Big|_D \right) \Delta x_{AC} \right\} \quad (B3)$$

The entire equation is now approximated by the expression

$$\sum_{k=A}^D \alpha_k \frac{\partial \tilde{\phi}}{\partial x} \Big|_k + \gamma_k \frac{\partial \tilde{\phi}}{\partial y} \Big|_k - ik\beta_k \tilde{\phi}_k \quad (B4)$$

where

$$\alpha_k = \rho_{ok} \Delta Z_k / 2\rho_o V - \beta_k V_{x_{ok}}; \quad \Delta Z_k = \begin{cases} \Delta y_{DB} \\ \Delta y_{AC} \\ -\Delta y_{DB} \\ -\Delta y_{AC} \end{cases} \quad (B5)$$

and

$$\gamma_k = -\rho_{ok} \Delta W_k / 2\rho_o V - \beta_k V_{y_{ok}}; \quad \Delta W_k = \begin{cases} \Delta x_{DB} \\ \Delta x_{AC} \\ -\Delta x_{DB} \\ -\Delta x_{AC} \end{cases} \quad (B6)$$

The above derivatives are expressed in terms of local grid coordinates by

$$\frac{\partial \tilde{\phi}}{\partial x_i} \Big|_k = J_{ij}^k \frac{\partial \tilde{\phi}}{\partial \xi_j} \Big|_k \quad (\text{no sum on } k) \quad (B7)$$

where $x_1 = x$; $x_2 = y$, ξ_i are local grid-oriented coordinates, and J_{ij}^k are transposed Jacobian matrices

$$J_{i,j}^k = \frac{\partial \xi_j}{\partial x_i} \Big|_k \quad (B8)$$

The derivatives in the grid coordinates are directly approximated at the auxiliary nodes by

$$\frac{\partial \tilde{\phi}}{\partial \xi_1} \Big|_k = \frac{1}{2} (\phi_{I_{k+1}, J_k} + \phi_{I_{k+1}, J_{k+1}} - \phi_{I_k, J_k} - \phi_{I_k, J_{k+1}}) \quad (B9)$$

$$\frac{\partial \tilde{\phi}}{\partial \xi_2} \Big|_k = \frac{1}{2} (\phi_{I_k, J_{k+1}} + \phi_{I_{k+1}, J_{k+1}} - \phi_{I_k, J_k} - \phi_{I_{k+1}, J_k}) \quad (B10)$$

where

$$I_k = \begin{Bmatrix} I \\ I \\ I-1 \\ I-1 \end{Bmatrix} \quad J_k = \begin{Bmatrix} J \\ J-1 \\ J-1 \\ J \end{Bmatrix} \quad (B11)$$

The final system of equations can be summarized in block tri-diagonal form as

$$A^I \phi_{I-1} + B^I \phi_I + C^I \phi_{I+1} = F^I \quad (B12)$$

where ϕ_I and F^I are vectors, and A^I , B^I , and C^I are matrices. The first and last elements of F^I embody the boundary conditions.

Letting $b_{i,j}$ be the elements of B^I (superscript I dropped with the understanding that $b_{i,j}$ represents a different set of components for each I) then

$$b_{j,j} = -\alpha_A (J_{1,1}^A + J_{1,2}^A) / 2 - \gamma_A (J_{2,1}^A + J_{2,2}^A) / 2 + \alpha_B (-J_{1,1}^B + J_{1,2}^B) / 2 + \gamma_B (-J_{2,1}^B + J_{2,2}^B) / 2 + \alpha_C (J_{1,1}^C + J_{1,2}^C) / 2 + \gamma_C (J_{2,1}^C + J_{2,2}^C) / 2 + \alpha_D (J_{1,1}^D - J_{1,2}^D) / 2 + \gamma_D (J_{2,1}^D + J_{2,2}^D) / 2 - ik / 4 (\beta_A + \beta_B + \beta_C + \beta_D) \quad (\text{no sum on } j)$$

$$b_{j,j-1} = -\alpha_B (J_{1,1}^B + J_{1,2}^B) / 2 - \gamma_B (J_{2,1}^B + J_{2,2}^B) / 2 + \alpha_C (J_{1,1}^C - J_{1,2}^C) / 2 + \gamma_C (J_{2,1}^C - J_{2,2}^C) / 2 - ik / 4 (\beta_B + \beta_C)$$

$$b_{j,j+1} = \alpha_A (-J_{1,1}^A + J_{1,2}^A) / 2 + \gamma_A (-J_{2,1}^A + J_{2,2}^A) / 2 + \alpha_D (J_{1,1}^D + J_{1,2}^D) / 2 + \gamma_D (J_{2,1}^D + J_{2,2}^D) / 2 - ik / 4 (\beta_A + \beta_D) \quad (B13)$$

All other components of B^I are zero, except the first and last rows, which express the boundary conditions along the upper and lower boundaries of the cascade channel.

The elements of A^I are

$$a_{j,j} = \alpha_C (-J_{1,1}^C + J_{1,2}^C) / 2 + \gamma_C (-J_{2,1}^C + J_{2,2}^C) / 2 + \alpha_D (-J_{1,1}^D - J_{1,2}^D) / 2 + \gamma_D (-J_{2,1}^D - J_{2,2}^D) / 2 - ik / 4 (\beta_C + \beta_D)$$

$$a_{j,j-1} = \alpha_C (-J_{1,1}^C - J_{1,2}^C) / 2 + \gamma_C (-J_{2,1}^C - J_{2,2}^C) / 2 - ik\beta_C / 4$$

$$a_{j,j+1} = \alpha_D (-J_{1,1}^D + J_{1,2}^D) / 2 + \gamma_D (-J_{2,1}^D + J_{2,2}^D) / 2 - ik\beta_D / 4 \quad (B14)$$

All other components of A^I are zero, except for the first and last rows as with B^I above. The elements of C^I are given by

$$c_{j,j} = \alpha_A (J_{1,1}^A - J_{1,2}^A) / 2 + \gamma_A (J_{2,1}^A - J_{2,2}^A) / 2 + \alpha_B (J_{1,1}^B + J_{1,2}^B) / 2 + \gamma_B (J_{2,1}^B + J_{2,2}^B) / 2 - ik / 4 (\beta_A + \beta_B)$$

$$c_{j,j-1} = \alpha_B (J_{1,1}^B - J_{1,2}^B) / 2 + \gamma_B (J_{2,1}^B - J_{2,2}^B) / 2 - ik\beta_B / 4$$

$$c_{j,j+1} = \alpha_A (J_{1,1}^A + J_{1,2}^A) / 2 + \gamma_A (J_{2,1}^A + J_{2,2}^A) / 2 - ik\beta_A / 4 \quad (B15)$$

All other components of C^I are zero except the first and last rows as with A^I and B^I above.

The discretized blade surface boundary condition, occupying the first and last rows of A^I , B^I , and C^I within the blade region and the continuity of normal velocity in the wake region, are obtained using

$$\nabla \tilde{\phi} \cdot \hat{n} = n_j J_{ji} \frac{\partial \tilde{\phi}}{\partial \xi_i}$$

where the summation convention is invoked. The n_j are the direction cosines of the unit normal to the wall and $\partial \tilde{\phi} / \partial \xi_i$ is discretized at the wall nodes and is biased forward or backward depending on the orientation of the unit normal. The remainder of the boundary conditions in the periodic and wake region (Eq. (29), (30), and (31)) are applied directly as stated.

The radiation boundary conditions given by Eq. (30) and (37) are discretized by evaluating the Fourier coefficients b_n and a_n at the inlet and exit planes. Numerical integration across these planes yields the coefficients in terms of $\tilde{\phi}$. Equations (30) and (37) may then be used to relate adjacent rows of nodes at the inlet and exit. All details of the radiation discretization procedure may be found from Caruthers (1980) and so are only briefly summarized above.

Unsteady Rotor Dynamics in Cascade

Y. T. Lee

T. W. Bein

David Taylor Research Center,
Bethesda, MD 20084

J. Feng

C. L. Merkle

The Pennsylvania State University,
University Park, PA 16802

A time-accurate potential-flow calculation method has been developed for unsteady incompressible flows through two-dimensional multi-blade-row linear cascades. The method represents the boundary surfaces by distributing piecewise linear-vortex and constant-source singularities on discrete panels. A local coordinate is assigned to each independently moving object. Blade-shed vorticity is traced at each time step. The unsteady Kutta condition applied is nonlinear and requires zero blade trailing-edge loading at each time. Its influence on the solutions depends on the blade trailing-edge shapes. Steady biplane and cascade solutions are presented and compared to exact solutions and experimental data. Unsteady solutions are validated with the Wagner function for an airfoil moving impulsively from rest and the Theodorsen function for an oscillating airfoil. The shed vortex motion and its interaction with blades are calculated and compared to an analytic solution. For a multi-blade-row cascade, the potential effect between blade rows is predicted using steady and quasi-unsteady calculations. The accuracy of the predictions is demonstrated using experimental results for a one-stage turbine stator-rotor.

Introduction

Unsteady flow analyses for turbomachinery can be categorized as linear or nonlinear. The linear method uses either the linear potential approach (Verdon and Caspar, 1984) or the linear Euler approach (Hall and Crawley, 1987). The nonlinear method includes both the nonlinear Euler and the Reynolds-averaged Navier-Stokes (Rai, 1987; Giles, 1988) methods. Linear methods use the isentropic and irrotational assumptions. Quandt (1989) has shown that the solution obtained from the unsteady linear potential-flow method gives correct fluid enthalpy, pressure, and velocity changes obtained from the traditional nonlinear Euler turbomachine energy equation. The disadvantage of using the linear potential analysis is that the method does not allow for incoming vorticity. Engineering experience (Lee et al., 1990) shows that linear potential methods are the simplest models that give accurate predictions of the very large changes in lift and moment for shock-free subsonic flows. Computational efforts increase sharply when Reynolds-averaged Navier-Stokes methods are used. However, more complete physics of fluid flow, e.g., flow separation, nonlinear vortex interaction, and turbulence, can be predicted. Due to the greater completeness of the nonlinear methods, these methods can be used to supplement the simplified linear approaches during a design process when experimental data are not available.

In this paper, a time-accurate two-dimensional linear potential-flow calculation method is developed. Viscosity effects are partially accounted for in the analysis by using a nonlinear Kutta condition at the airfoil trailing edge. In applying the

Kutta condition, the wake of the airfoil is represented by discrete vortices (Kim and Mook, 1986; Yao et al., 1989). The method developed is capable of providing flow predictions for various combinations of steady and unsteady body motions. The emphasis of the present paper is on cascade flows, particularly unsteady cascade flows. Although the numerical method developed is general, cascade flows require special analyses. When calculating unsteady flows between two blade rows, the vortex/blade interaction requires detailed treatment. The unsteady cascade predictions are possible only when the building blocks of steady cascade flow calculations and some basic unsteady single airfoil calculations are predicted correctly. This paper compares calculated results for single airfoils and cascades under similar conditions. It concludes with a quasi-unsteady solution for a two-blade-row cascade (Dring et al., 1982).

Mathematical Model

Consider a two-dimensional system configuration consisting of multiple airfoils and/or nonlifting bodies, or a linear multi-blade-row cascade, which execute arbitrary relative motions between airfoils/bodies or between cascades in an incompressible potential flow. Let the surface of the solid boundaries be denoted by $\Lambda(\mathbf{R}, t)$, where \mathbf{R} is a distance vector in a global ground-fixed coordinate system (x, y) and t is time. The shear layer next to the surface Λ and the shed vorticity in the wake are assumed to consist of thin layers modeled as vortex sheets. The vortex sheets in the wake are symbolized by $W(\mathbf{R}, t)$. They are allowed to move with the local fluid particles. The flow field can be represented by a total scalar velocity potential Φ as follows:

$$\mathbf{V} = \nabla \Phi = \nabla \phi_{\infty} + \nabla \phi = \mathbf{v}_{\infty} + \mathbf{v}, \quad (1)$$

where ϕ_{∞} and \mathbf{v}_{∞} represent the inflow velocity potential and

Contributed by the International Gas Turbine Institute and presented at the 36th International Gas Turbine and Aeroengine Congress and Exposition, Orlando, Florida, June 3-6, 1991. Manuscript received at ASME Headquarters February 20, 1991. Paper No. 91-GT-147. Associate Technical Editor: L. A. Riekert.

velocity at infinity, including any incoming onset flow and induced flow due to a near-field disturbance. ϕ and \mathbf{v} represent the disturbance velocity potential and velocity due to airfoils/bodies and the wake vorticity. Both the total and disturbance velocity potentials satisfy Laplace's equation

$$\nabla^2 \Phi = \nabla^2 \phi = 0. \quad (2)$$

The problem posed is to find the velocity potential ϕ and the free wake vortex structure. To ensure a unique solution to the problem, the disturbance velocity potential is subjected to: (1) a kinematic condition applied at the surface Λ where fluid particles maintain the same normal velocity as the moving surface; (2) the Kutta-Joukowski condition of equal pressure between the upper and lower airfoil surfaces applied at the trailing edge; (3) total circulation is conserved at any time, i.e., Kelvin's theorem; and (4) a dynamic condition of continuous pressure applied at free wake vortex sheets.

Using the classic Green's function approach and Morino's formulation (Morino and Tseng, 1978) in the global coordinate system, Eqs. (1) and (2) are transformed into an integral equation

$$\phi(p) = \frac{1}{2\pi} \int_w \phi_w(q) \frac{\partial G(p, q)}{\partial n_w} ds_q + \frac{1}{2\pi} \int_\Lambda \left[\phi(q) \frac{\partial G(p, q)}{\partial n} - G(p, q) \frac{\partial \phi(q)}{\partial n} \right] ds_q. \quad (3)$$

Here p represents the field point on Λ while q is the running index over all panels. The symbol ϕ_w represents the velocity potential due to shed wake vortices and $\mathbf{n} = n_x \mathbf{i} + n_y \mathbf{j}$ and \mathbf{n}_w are the unit outward surface normal vectors to Λ and the upper side of W . The Green's function is given by $G = \ln(1/r)$, where r is the distance between p and q . This formulation allows $|\mathbf{v}(p)|$ to be equal to the vortex sheet strength $\gamma(p)$ on Λ . $\partial\phi/\partial n$ is given from the normal boundary condition

$$\nabla \Phi \cdot \mathbf{n} = \mathbf{V}_B \cdot \mathbf{n} \quad (4a)$$

or

$$\frac{\partial \phi}{\partial n} = \mathbf{V}_B \cdot \mathbf{n} - \frac{\partial \phi_\infty}{\partial n}, \quad (4b)$$

where \mathbf{V}_B is the velocity, including translational and rotational speeds, of the surface Λ . For a finite number of airfoils/bodies,

$\partial\phi_\infty/\partial n$ is prescribed as an onset flow \mathbf{V}_o . Equation (3) is a Fredholm integral equation of the second kind for the unknown ϕ .

The calculation of unsteady force and moment on each moving body/airfoil is reduced to an integration using the unsteady Bernoulli's equation in the global coordinate system as

$$\frac{\partial \Phi}{\partial t} + \frac{V^2}{2} + \frac{p}{\rho} = \frac{p_\infty}{\rho} + \frac{V_o^2}{2}. \quad (5)$$

Equation (5) can also be nondimensionalized by a reference velocity U . If one uses the original symbols for nondimensional variables, the following formula in a body-fixed coordinate is obtained:

$$C_p = \frac{p - p_\infty}{\rho U^2 / 2} = -2 \frac{\partial \phi}{\partial t} - \mathbf{V} \cdot (2\mathbf{V}_B + \mathbf{V}) + V_o^2. \quad (6)$$

Here the velocity potential of the onset flow is assumed to be steady.

Numerical Method

Singularity Distributions. The surface Λ is discretized into small line segments. The control point for each segment is located at the center of the segment. The normal to the surface is approximated by the perpendicular to the straight segment. The distributions of the vortices and the sources on each segment are assumed to be linear and constant, respectively. The velocity potential at a field point p due to a line segment q of length S with a constant unit-strength source, i.e., $\sigma(\xi) = 1$, in a local line-segment coordinate (ξ, η) as shown in Fig. 1 is

$$\begin{aligned} 2\pi\phi_\sigma(p, q) &= \int_{-\frac{S}{2}}^{\frac{S}{2}} \sigma(\xi) \ln \frac{1}{r(p, \xi)} d\xi \\ &= S - \eta_p F_1 - \xi_p F_3 - \frac{S}{2} F_4. \end{aligned} \quad (7)$$

The velocity potential at the point p due to a constant unit-strength vortex, i.e., $\gamma(\xi) = 1$, is

Nomenclature

C_L = lift coefficient
 C_p = pressure coefficient
 c = chord of the airfoil
 CDU = velocity potential due to uniformly distributed vortex
 CDL = velocity potential due to linearly distributed vortex
 CD1 = coefficient defined in Eq. (12)
 CD2 = coefficient defined in Eq. (12)
 CS = coefficient defined in Eq. (12)
 ds = small surface element
 E = numerical error
 F = functions defined in Eq. (10)
 G = Green's function
 H = cascade spacing or pitch
 h = spacing between two flat plates
 N = total number of panel
 \mathbf{n} = surface normal

p = field point or local static pressure
 q = running index over surface integration
 \mathbf{R} = distance vector in (x, y) coordinate
 \mathbf{r} = distance vector in (ξ, η) coordinate
 S = panel length
 t = time
 U = reference velocity
 \mathbf{V} = total velocity
 \mathbf{V}_B = surface moving velocity
 \mathbf{V}_o = onset flow velocity
 \mathbf{v} = disturbance velocity
 \mathbf{v}_∞ = incoming flow velocity
 W = vortex-sheet surface in the wake
 x, y = global ground-fixed coordinate
 α = angles defined in Eq. (10) or angle of attack

Γ = circulation around an airfoil
 γ = vortex strength
 Θ = blade stagger angle
 κ = ratio of panel lengths
 Λ = boundary surfaces
 λ = a constant defined in Eq. (10)
 ξ, η = local panel coordinates
 ρ = fluid density
 σ = source strength
 Φ = total scalar velocity potential
 ϕ = disturbance velocity potential
 ϕ_∞ = inflow velocity potential
 ω = angular rotational speed

Subscripts and Superscripts

e = exact solution
 l = lower surface
 m = cascade modification
 s = tangent to the surface
 sa = single airfoil
 u = upper surface
 v = vortex

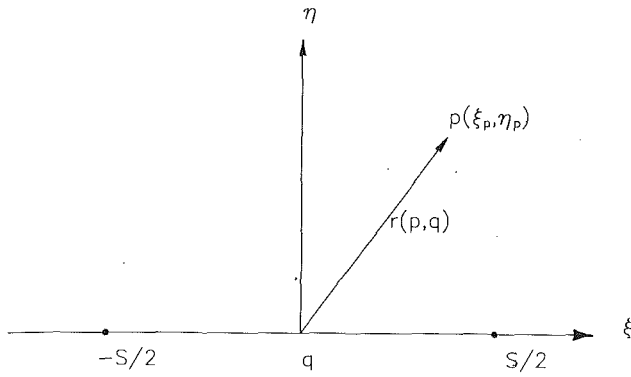


Fig. 1 Schematics for a line segment

$$2\pi\phi_{\gamma U}(p, q) = \int_{-S/2}^{S/2} \gamma(\xi) \arctan \frac{\xi - \xi_p}{\eta_p} d\xi$$

$$= \frac{\xi_p}{2} F_1 - F_2 - \frac{\eta}{4} F_3. \quad (8)$$

The velocity potential corresponding to a linearly distributed vortex sheet, i.e., $\gamma(\xi) = 2\xi/S$, is

$$2\pi\phi_{\gamma L}(p, q) = \int_{-S/2}^{S/2} \gamma(\xi) \arctan \frac{\xi - \xi_p}{\eta_p} d\xi$$

$$= \frac{\eta_p}{2} + \frac{1}{2S} \left(\xi_p^2 - \eta_p^2 - \frac{S^2}{4} \right) F_1 - \frac{1}{2S} \xi_p \eta_p F_3, \quad (9)$$

In Eqs. (7)–(9) we have

$$F_1 = \alpha_1 - \alpha_2$$

$$F_2 = \pi - \alpha_1 - \alpha_2 + 2\pi\lambda$$

$$F_3 = \ln(R_1/R_2)$$

$$F_4 = \ln(R_1 R_2) \quad (10)$$

$$R_1 = \left[\left(\frac{S}{2} + \xi_p \right)^2 + \eta_p^2 \right]^{1/2}$$

$$R_2 = \left[\left(\frac{S}{2} - \xi_p \right)^2 + \eta_p^2 \right]^{1/2}$$

$$\alpha_1 = \arctan \frac{\xi_p + S/2}{\eta_p}$$

$$\alpha_2 = \arctan \frac{\xi_p - S/2}{\eta_p}$$

The function F_2 is multiple valued when $\xi_p > 0$ and $|\eta_p|$ approaches zero, i.e., $\lambda = 1$ when η_p crosses the positive real axis from positive η_p , $\lambda = -1$ when η_p crosses the positive real axis from negative η_p , and $\lambda = 0$ for all other cases. Thus the velocity potential at an i th segment due to a j th segment, which contains uniformly and linearly distributed vortices, i.e., $\gamma(\xi) = (\gamma_j + \gamma_{j+1})/2 + (\gamma_{j+1} - \gamma_j)\xi/2S_j$ as shown in Fig. 2, and a constant source is given by

$$\phi_{ij} = CD1_{ij}\gamma_j + CD2_{ij}\gamma_{j+1} + CS_{ij}\sigma_j, \quad (11)$$

where

$$CD1_{ij} = \frac{1}{2}(CDU_{ij} - CDL_{ij})$$

$$CD2_{ij} = \frac{1}{2}(CDU_{ij} + CDL_{ij}), \quad (12)$$

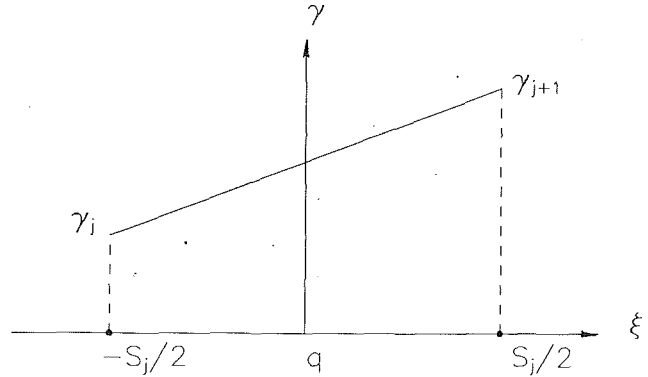


Fig. 2 Linearly distributed vortex on a line segment

and CDU_{ij} and CDL_{ij} represent the velocity potentials due to the uniformly and the linearly distributed vortices from Eqs. (8) and (9), and CS_{ij} is due to the uniformly distributed source from Eq. (7). The velocity potential at p due to a discrete shed vortex in the wake is

$$2\pi\phi_w(p, q) = \gamma_w(q) \arctan \frac{y_p - y_q}{x_p - x_q} \quad (13)$$

Matrix Equation for Bound Vortex γ . For a unique solution outside of the surface Λ described by Eq. (3), the flow inside the surface Λ can be assumed at rest. If each body/airfoil surface Λ is divided into N segments, the interior flow-quiet condition requires

$$\nabla\phi = \phi_{i+1} - \phi_i = 0 \quad i = 1, 2, \dots, N-1. \quad (14)$$

The no-penetration boundary condition, Eq. (4), is imposed at the control point of each line segment. By substituting Eqs. (3), (4), (11), and (12) into Eq. (14), a set of linear algebraic equations for the bound vortex γ is formed:

$$(CD1_{i,1} - CD1_{i-1,1})\gamma_1 + CD2_{i,N} - CD2_{i-1,N})\gamma_{N+1}$$

$$+ \sum_{j=1}^{N-1} (CD1_{i,j+1} - CD1_{i-1,j+1} + CD2_{ij} - CD2_{i-1,j})\gamma_{j+1}$$

$$= \sum_{j=1}^N (CS_{ij} - CS_{i-1,j}) \frac{\partial\phi}{\partial n_j} - \sum_{j=1}^{ITS-1} \gamma_{wj} \phi_{wj}$$

$$i = 1, 2, \dots, N-1. \quad (15)$$

Here ITS represents the total time steps. Equation (15) forms $N-1$ equations for $N+1$ unknown values of γ . Hence two extra equations are required for obtaining a unique solution.

Extra Conditions for Nonlifting Body. An unsteady potential flow past a nonlifting body generally does not shed vorticity in the wake. Hence an extra condition can be obtained by requiring

$$\gamma_1 = \gamma_{N+1} \quad (16)$$

for a closed body, where γ_1 and γ_{N+1} are the first and the last vortex strengths as defined in Eq. (15). Since no lift will be generated, a zero net circulation around the body can be used, i.e.,

$$\sum_{j=1}^N S_j(\gamma_j + \gamma_{j+1}) = 0. \quad (17)$$

Equations (15), (16), and (17) form a set of linear equations for determining γ on a nonlifting configuration.

Nonlinear Kutta Condition for Lifting Body. The Kutta-Joukowski condition was originally applied to two-dimensional steady flow in order to obtain a finite velocity at the trailing edge, and as a consequence, the flow is uniquely de-

terminated. This hypothesis implicitly accounts for viscous effects otherwise neglected in the potential-flow theory. Instead of requiring a velocity condition at the trailing edge, a pressure condition is used in the present numerical model. Since the trailing edge does not account for any loading, the pressures there on the upper surface (sub- or superscript u) and the lower surface (sub- or superscript l) are required to be the same. It is worth noting that this condition does not restrain the trailing edge from having a variation of pressure in the time domain. Using Eq. (6), one obtains

$$2 \frac{\partial}{\partial t} (\phi_u - \phi_l) + [(\mathbf{V} + \mathbf{V}_B)_u \cdot (\mathbf{V} + \mathbf{V}_B)_u - (\mathbf{V} + \mathbf{V}_B)_l \cdot (\mathbf{V} + \mathbf{V}_B)_l] = 0. \quad (18)$$

Since the impermeable boundary condition is applied at Λ , the flow on the upper and lower surfaces is along the tangents (sub- or superscript s) to both surfaces. Use Eq. (1) and the following relations

$$\phi_u - \phi_l \equiv \Gamma = \sum_{j=1}^N \frac{1}{2} (\gamma_j + \gamma_{j+1}) S_j$$

$$\bar{v}_t \equiv \frac{1}{2} (v_\infty^{su} - v_\infty^{sl} + v^{su} - v^{sl} + v_B^{su} - v_B^{sl}), \quad (19)$$

Equation (18) is cast as

$$\left(1 + \frac{S_1}{2VT}\right) \gamma_1 + \sum_{j=1}^{N-1} \frac{S_j + S_{j+1}}{2VT} \gamma_{j+1} + \left(1 + \frac{S_N}{2VT}\right) \gamma_{N+1} = \frac{-\Gamma(t - \Delta t)}{VT} - v_\infty^{su} - v_\infty^{sl}. \quad (20)$$

where $VT = 2(\Delta t)\bar{v}_t$ and Γ is the circulation of the airfoil and defined as positive in a clockwise direction. Equation (20) is linear in γ if VT is considered to be a constant. In the present study, Eq. (20) is solved iteratively to account for the nonlinearity of VT . Both Yao et al. (1989) and Kim and Mook (1986) applied a more restricted Kutta condition at the trailing edge by requiring $\gamma_1 = \gamma_{N+1} = 0$ and placing a wake vortex of unknown strength there. This implies that their algebraic equations are linear and require an optimization technique to produce a deterministic system.

For the present scheme, according to Eq. (15) one more equation is needed in order to obtain a unique γ -distribution for a lifting body. This condition is provided by requiring the velocity gradients along the tangents at the trailing edge from both the upper and lower surfaces to be the same, i.e.,

$$\left(\frac{\partial \gamma}{\partial s}\right)_u = \left(\frac{\partial \gamma}{\partial s}\right)_l. \quad (21)$$

Allowing the equality of velocity gradients from the upper and the lower surfaces at the trailing edge further ensures the smooth merge of two jet flows. Experience also indicates that this condition offers stable and accurate predictions. When a second-order backward differencing scheme is used, Eq. (21) is transformed to

$$\gamma_{N+1} = \frac{\kappa[\kappa_1(2 + \kappa_1)\gamma_1 - (1 + \kappa_1)^2\gamma_2 + \gamma_3] + (1 + \kappa_u)^2\gamma_N - \gamma_{N-1}}{\kappa_u(2 + \kappa_u)} \quad (22)$$

where $\kappa_u = S_{N-1}/S_N$, $\kappa_l = S_2/S_1$ and $\kappa = S_{N-1}(1 + \kappa_u)/S_2(1 + \kappa_l)$. Hence Eqs. (15), (20), and (22) form a determinate system of nonlinear equations for determining γ for a lifting configuration. They are solved using an iterative scheme.

Determination of Shed Vorticity. Kelvin's theorem states that the total circulation of the fluid at any instant is conserved. This condition provides a mechanism to shed vorticity into the wake. At each time step, a uniformly distributed vortex segment with strength γ_w is generated in the wake adjacent to the airfoil trailing edge. The length S_w of the vortex segment is

the distance the trailing edge moves between $t - \Delta t$ and t . At a subsequent time step this uniform line vortex is replaced by a discrete concentrated vorticity of equivalent strength located at the center of the segment. The generated trailing-edge vortex segment relates to the airfoil circulation Γ as follows:

$$\frac{\Gamma(t) - \Gamma(t - \Delta t)}{\Delta t} + \frac{S_w(t)\gamma_w(t)}{\Delta t} = 0. \quad (23)$$

The model depicted in Eq. (23) yields stable solutions, which are independent of the time-step used. However, for the present calculations, the solutions were found to be dependent on the time step used if a concentrated vorticity model was adopted for modeling the trailing-edge vortex generation. The latter model was used in Kim and Mook's model (1986). Since the time step used by Kim and Mook was extremely small, they may not be aware of the time dependency of the discrete vortex generating mechanism at the trailing edge.

The wake vortices are convected downstream and develop a vorticity field. In the present numerical scheme, these vortices are tracked through the flow field using Lagrangian techniques. The convection of these discrete vortices is modeled by a predictor-corrector scheme as

$$\mathbf{r}_w^{(1)}(t + \Delta t) = \mathbf{r}_w(t) + \mathbf{v}_w[\mathbf{r}_w(t), t]\Delta t \quad (24a)$$

$$\mathbf{r}_w^{(2)}(t + \Delta t) = \mathbf{r}_w^{(1)}(t + \Delta t)$$

$$+ \frac{1}{2}(\mathbf{v}_w[\mathbf{r}_w^{(1)}(t + \Delta t), t] - \mathbf{v}_w[\mathbf{r}_w(t), t])\Delta t \quad (24b)$$

$$\mathbf{r}_w(t + \Delta t) = \mathbf{r}_w^{(2)}(t + \Delta t). \quad (24c)$$

The superscripts in parentheses represent the iteration number within each time step. The corrector in Eq. (24b) is particularly important for a body oscillating at low frequency. For such a flow, $\partial\Gamma/\partial t$ is relatively small in Eqs. (18) and (19). Both equations imply that the nonlinear effect in the Kutta condition is strong and the velocity prediction within each time step plays a dominant role in obtaining a converged solution. Giesing (1969) also used a predictor-corrector scheme to convect the vortices in the wake, but treated the intermediate iteration step as a complete separate "time step." The present calculation only uses the corrector to locate the new vortex positions without performing the rest of the calculations at the next time step. Hence the calculation time only increases slightly. Kim and Mook (1986) used only Eq. (24a) for vortex convection, but their time step is rather small.

Special Considerations for a Cascade. For a cascade of blades with pitch H , each blade generates a circulation. If the cascade runs along the y axis, there exists an upwash at upstream infinity of the cascade and a downwash at downstream infinity. In conjunction with a specified inflow onset condition as shown in Eq. (4), an extra term is needed to ensure a unique upstream inflow condition, i.e.,

$$\frac{\partial \phi_\infty}{\partial n} = n_y \sum_{mj=1}^{MJ} \frac{\Gamma_{mj}}{2H_{mj}} \quad (25)$$

for a multi-blade-row cascade flow, where MJ is the total number of blade rows, H_{mj} is the mj -th cascade spacing or pitch, and Γ_{mj} is the blade circulation from the mj -th cascade.

In a cascade configuration, the velocity potentials at a field point p due to a point source and a point vortex on a blade surface q can be written as

$$\phi_s(p, q) = -\frac{1}{2\pi} \ln[\sinh^2 \bar{H}(x_p - x_q) \cos^2 \bar{H}(y_p - y_q) + \cosh^2 \bar{H}(x_p - x_q) \sin^2 \bar{H}(y_p - y_q)]^{1/2} \quad (26a)$$

$$\phi_v(p, q) = \frac{1}{2\pi} \arctan \frac{\sin \bar{H}(y_p - y_q)}{\sinh \bar{H}(x_p - x_q)}, \quad (26b)$$

where $\bar{H} = \pi/H$. Equation (11) is therefore modified to

$$\begin{aligned} \phi_i &= \sum_j (\sigma_j \phi_{\sigma ij} + \gamma_j \phi_{\gamma ij}) \\ &= \sum_j (\sigma_j \phi_{\sigma ij}^{sa} + \gamma_j \phi_{\gamma ij}^{sa}) + \sum_j [\sigma_j (\phi_{\sigma ij} - \phi_{\sigma ij}^{sa}) + \gamma_j (\phi_{\gamma ij} - \phi_{\gamma ij}^{sa})] \\ &= \phi_i^{sa} + \phi_i^m \end{aligned} \quad (27)$$

where the superscripts *sa* and *m* represent the corresponding single airfoil and its cascade modification. ϕ^{sa} is defined as

$$\phi_{\sigma ij}^{sa} = -\frac{1}{2\pi} \ln \sqrt{x_i^2 + y_i^2} \quad (28a)$$

$$\phi_{\gamma ij}^{sa} = \frac{1}{2\pi} \arctan \frac{y_i}{x_i} \quad (28b)$$

and the cascade modification is

$$\phi_{\sigma ij} - \phi_{\sigma ij}^{sa} = -\frac{1}{2\pi} \ln \left[\frac{\sinh^2 \bar{H}x_i + \sin^2 \bar{H}y_i}{(\bar{H}x_i)^2 + (\bar{H}y_i)^2} \right]^{1/2} \quad (29a)$$

$$\phi_{\gamma ij} - \phi_{\gamma ij}^{sa} = \frac{1}{2\pi} \arctan \frac{x_i \sin \bar{H}y_i - y_i \sinh \bar{H}x_i}{x_i \sinh \bar{H}x_i + y_i \sin \bar{H}y_i} \quad (29b)$$

A complete integration of the velocity potentials for the source and the vortex distributions on each segment was performed numerically for the cascade modification term ϕ_i^m in Eq. (27).

Applications

The present calculation method was first validated by comparison to known steady flows. Steady-flow comparisons are presented for two cases. The first case is for flow past a biplane, which has an exact conformal mapping solution (Robinson and Laurmann, 1956). The second steady flow calculation is for flows past a NACA 65-1210 cascade for which the solutions compared to measured values (Herrig et al., 1957). For unsteady flows, four cases calculated using the present method are presented. They include the following three basic blade motions: an airfoil moving impulsively from rest, an oscillating airfoil, and a vortex interacting with an airfoil. Calculations were made for both a single airfoil and a cascade under each of the specified blade motions. The last case presented is a quasi-unsteady calculation for a two-blade-row stator-rotor configuration.

Steady Flows. The main purpose of investigating flows past a biplane, i.e., two flat plates, is threefold: to examine the accuracy of the prediction when compared to an exact solution; to explore the limits of the prediction scheme numerically; and to understand the prediction capability of the nonlinear Kutta condition.

Figure 3(a) shows a schematic of the biplane geometry and inflow description. The comparisons between the present calculated results and the exact conformal mapping solutions in Fig. 3(b) correspond to a constant inflow angle $\alpha = 20$ deg, and various spacings between two plates. When the spacing is large, pressure distributions are identical on the two plates. As the spacing is reduced, a stronger interaction between the two plates is observed. The pressure of the lower surface of the upper plate approaches that of the upper surface of the lower plate. Figures 3(c) and 3(d) show the effect of varying the inflow angle under the condition of strong plate interaction. As α varies from 20 to 90 deg, the pressure on the lower surface of the upper plate stays nearly the same as that on the upper surface of the lower plate. However, the lift generated by the lower plate is reduced as α increases. The zero-lift α for the lower plate at $h/c = 0.228$ is between 50 and 65 deg. For α

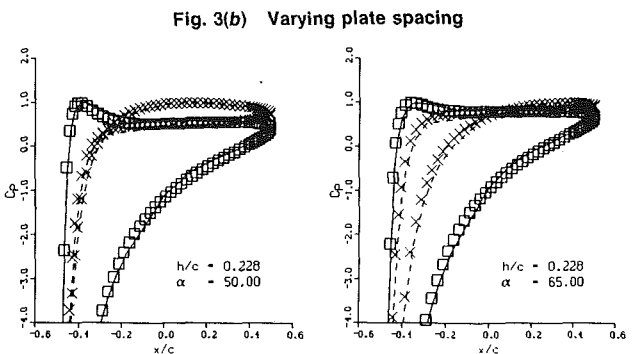
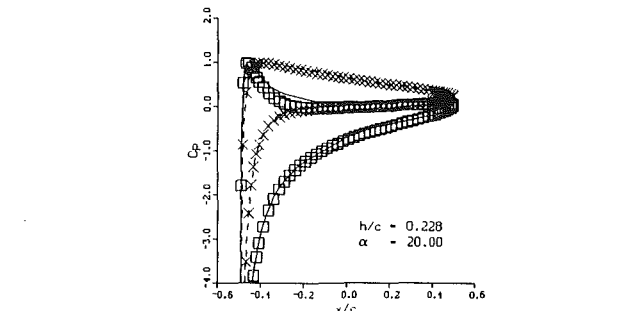
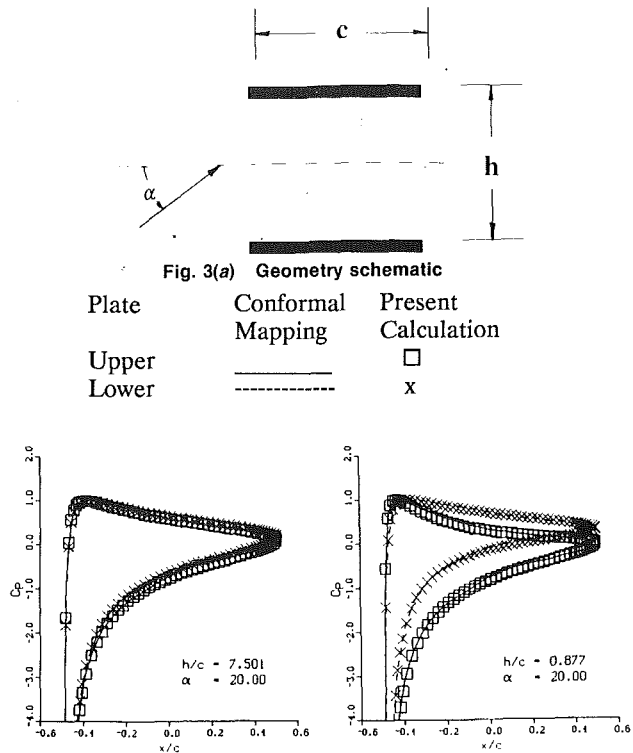


Fig. 3 Pressure distributions on a biplane

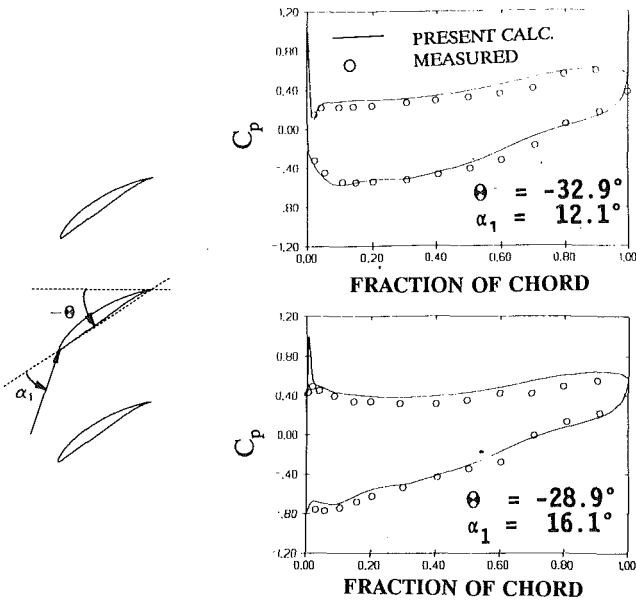


Fig. 4(a) Predicted pressure distributions

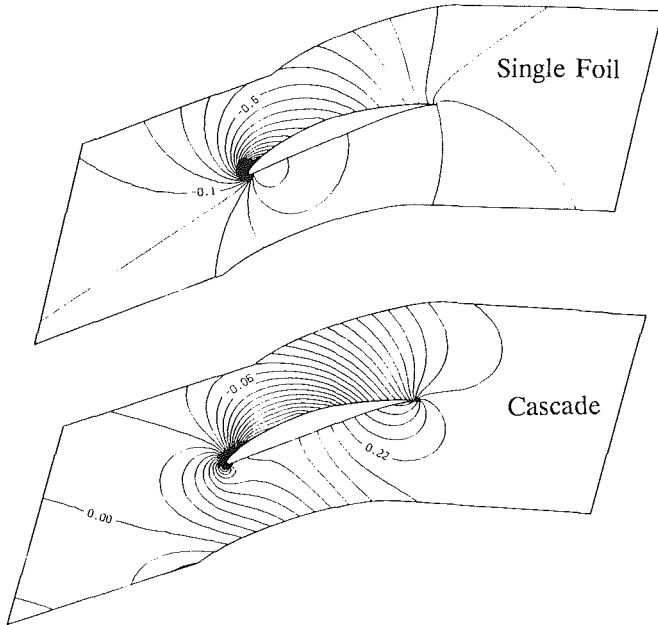


Fig. 4(b) Blade-to-blade pressure contours
Fig. 4 Calculation for NACA 65-1210 cascade

larger than the zero-lift value, the lower plate actually begins to generate negative lift. When α approaches 90 deg as shown in Fig. 3(d), the pressure curve for the upper surface of the upper plate matches that for the lower surface of the lower plate, and similarly for the other surfaces of both plates. The total lift of the two-plate system is zero. When the spacing between the two plates increases at $\alpha = 90$ deg, the pressures on the lower surface of the upper plate and on the upper surface of the lower plate approach those of the other surfaces. At $h/c = 9.708$, as shown in Fig. 3(d), the pressures on all the surfaces coincide and the interaction between the two plates is minimum. Although in reality flow separates at high values of α , the present numerical calculations serve the purpose of validating the implemented numerical procedures under extremely severe flow conditions by comparing with the conformal-mapping solutions. For all the cases predicted, the present results agree well with the exact solutions and show

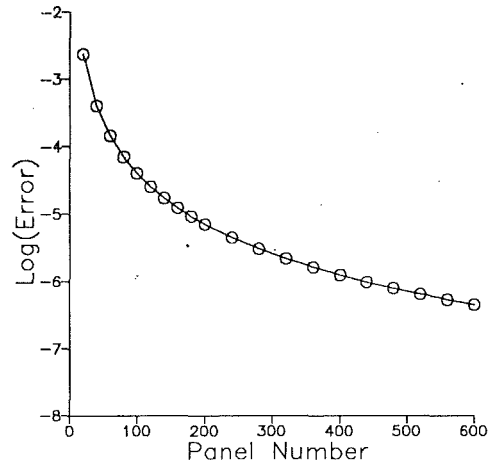


Fig. 5(a) For a circular cylinder

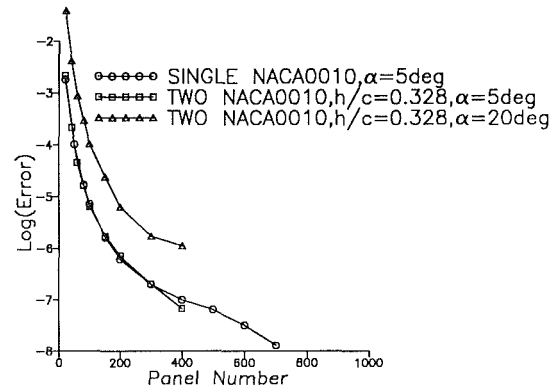


Fig. 5(b) For one and two NACA 0010 airfoils
Fig. 5 Numerical convergence versus panel numbers

extremely "clean" predictions at both the leading and the trailing edges.

Steady flows through a cascade of NACA65-1210 blades were also examined. Figure 4(a) shows the calculated blade pressure distributions compared to measurements (Herrig et al., 1957) at two different inlet flow angles ($\alpha_1 = 12.1$ and 16.1 deg) and blade stagger angles ($\Theta = -32.9$ and -28.9 deg). Flow is at the design condition for the first case. The predicted blade loading agrees well with the measurements. The computed blade-to-blade pressure contours for flows past a single airfoil and a cascade are depicted in Fig. 4(b). The results indicate that the pressure gradient for the cascade due to blockage is larger than that of the single foil, particularly in the leading and trailing edge areas. The computed flow turning angles through the cascade for both cases are 21.98 and 26.13 deg versus the measured values of 19.6 and 23.3 deg. If an estimated boundary-layer displacement thickness of 0.4 percent of the chord, obtained based on a flat-plate boundary layer, at the trailing edge is added to the airfoil ordinates, the calculated turning angles become 19.99 and 23.8 deg. This modification in the calculation procedure indicates that the cascade exit flow angle depends also on the viscous effect in the trailing-edge area.

The numerical error E of the present calculations was evaluated based on

$$E = \frac{1}{N} \left[\sum_{i=1}^N (C_p - C_{pe})^2 \right]^{1/2} \quad (30)$$

where C_{pe} represents the exact pressure distribution. There are two cases in Fig. 5 to show the numerical convergence versus the panel numbers used. The first case shown in Fig. 5(a) is for nonlifting flows past a circular cylinder. The panel numbers used range from 20 to 600. The second case shown in Fig. 5(b)

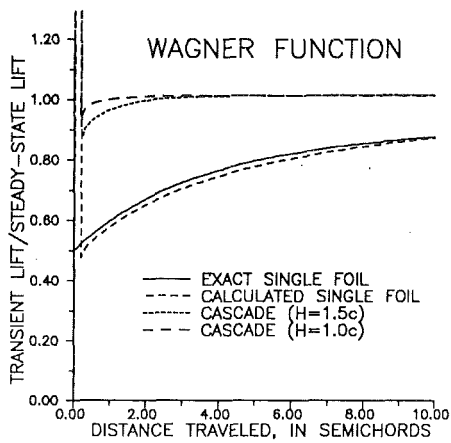


Fig. 6(a) Instantaneous lift



Fig. 6(b) Wake pattern for a single airfoil

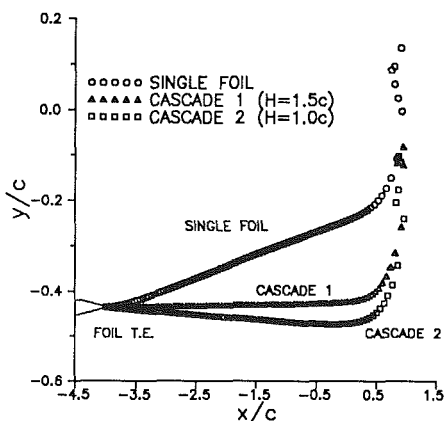


Fig. 6(c) Wake vortex locations

Fig. 6 Predictions for impulsively starting airfoils

is for lifting flows past either a single NACA 0010 airfoil or two NACA 0010 airfoils. The exact pressure distributions used for calculating errors are the numerical solutions of 1000 panels for the single airfoil and 500 panels for the bi-foil. The numerical convergence rate shown in Fig. 5(b) is independent of the number of the airfoil, but it decreases as the angle of attack increases. Since the coarse grid points do not usually match with the finest grid points used as the exact solution, the convergence dependency on the angle of attack relates to the inaccurate interpolated exact C_p -distribution in the leading-edge area when the slope becomes steep for large angles of attack. Nevertheless, based on this analysis using 100 panels for a closed body indicates that the error of the solution is under 10^{-4} .

Unsteady Flows. Figure 6(a) shows the calculated transient lift coefficients as a function of the airfoil traveling distance for an impulsively moving NACA 0012 airfoil of 4 percent thickness at an angle of attack of 5 deg and two cascades with different spacings (H) as compared to the exact Wagner function (Fung, 1969) for a single airfoil. The wake pattern of the calculated single airfoil case is depicted in Fig. 6(b). Figure 6(c) shows the calculated vortex locations for the three cases. The results indicate that the period of the transient phenomenon becomes shorter for the cascade flow.

Figure 7 shows a similar comparison for oscillating NACA

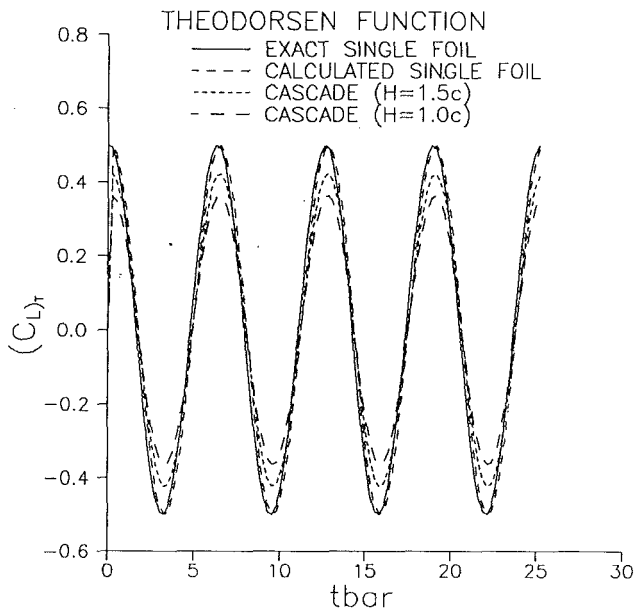


Fig. 7(a) Instantaneous lift



Fig. 7(b) Flow visualization of Bratt for a NACA 0015 airfoil

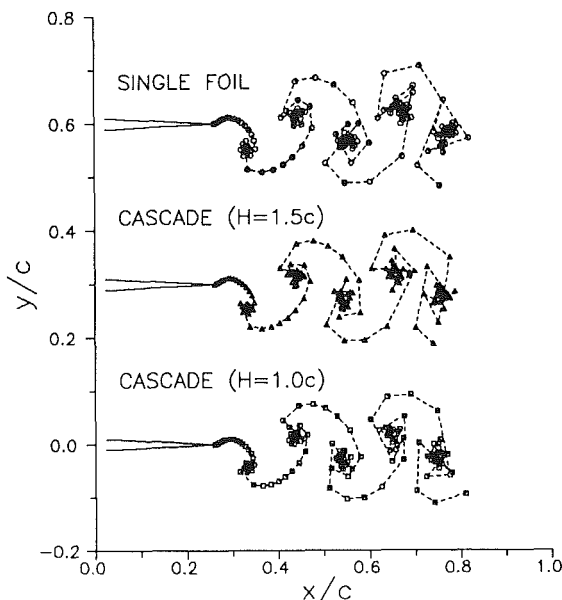


Fig. 7(c) Wake vortex locations

Fig. 7 Predictions for oscillating NACA 0012 airfoils at a reduced frequency of 17

0012 blades. The exact solution plotted is the Theodorsen function (Fung, 1969) at a reduced frequency $\omega c/U$ of 17. The time step chosen is to cover one period of the oscillating motion with minimum 25 points. The amplitude of the calculated lift coefficients using the present method, referring to $(C_L)_r$ versus $t(=\omega t)$ in Fig. 7(a), is smaller for the cascade data. The shed vortex patterns, shown in Fig. 7(c), of the single foil and the cascades are compared to the flow visualization of Bratt (1950), shown in Fig. 7(b), for a single NACA 0015 airfoil. The width of the cascade vortex wakes in Fig. 7(c) is predicted to be slightly smaller than that of the single foil. This result dem-

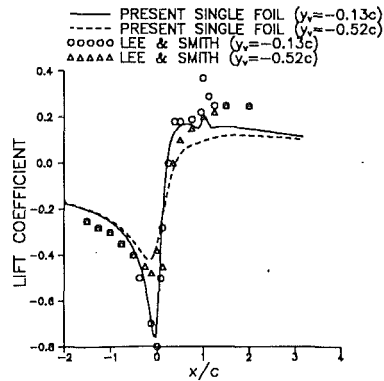


Fig. 8(a) Instantaneous lift for single airfoil

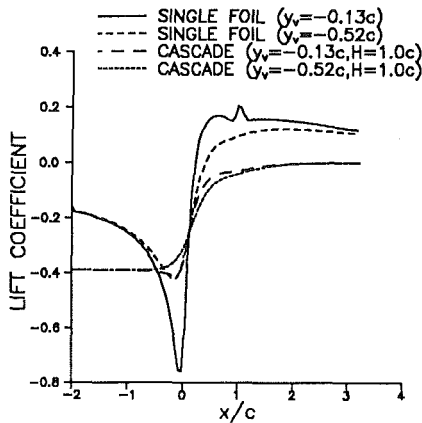


Fig. 8(b) Calculated instantaneous lift for cascades

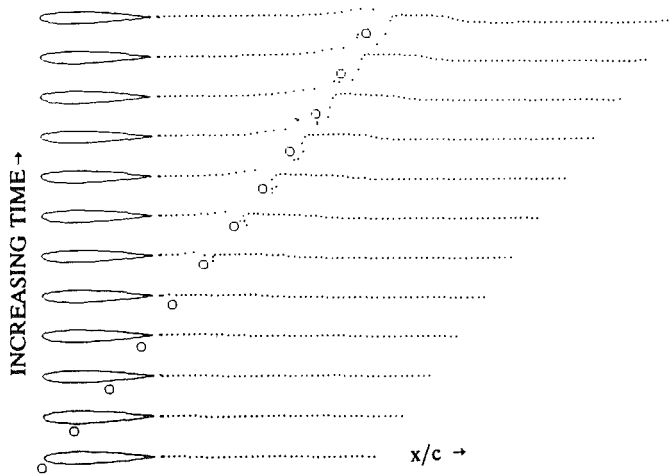


Fig. 8(c) Incoming vortex at $\gamma_v/c = -0.13$ interacts with wake vortices

Fig. 8 Incoming vortex interacting with airfoil

onstrates that the cascade effect is more important than the wake vortex structure for predicting the blade loading.

Figure 8(c) shows the time history of the shed vortices for a NACA 0012 section at zero angle of attack interacting with an incoming vortex initially located upstream of the airfoil at $\gamma_v/c = -0.13$. The calculated instantaneous lifts versus vortex locations (the airfoil is located between 0 and 1) for the single foil are shown in Fig. 8(a) as compared with Lee and Smith's (1987) solutions. The lift decreases first to a negative value, recovers quickly to a positive value, and drops slowly to near zero when the vortex passes through the airfoil. Two curves for different vertical separation distances between the airfoil and the vortex are depicted. When the vortex is placed closer

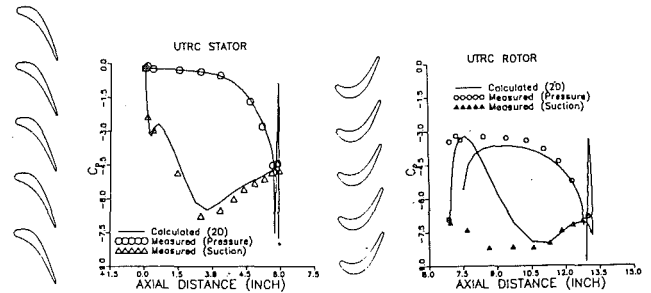


Fig. 9(a) Considering stator and rotor separately under uniform flows at zero angle of attack

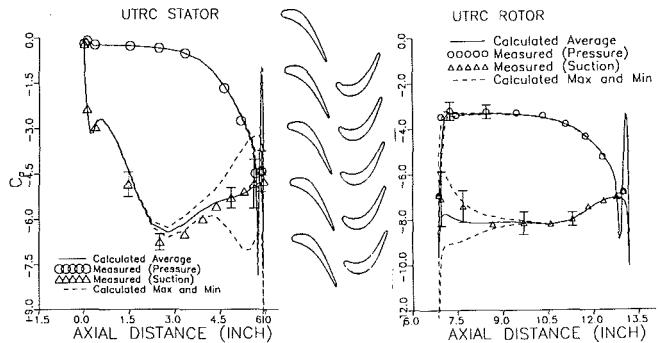


Fig. 9(b) Considering stator and rotor as one single unit

Fig. 9 Quasi-unsteady blade-loading predictions for UTRC stator and rotor

to the airfoil, the effect of producing a fluctuating lift is more pronounced. Figure 8(b) shows the calculated lifts for both single foils and cascades. For the cascade results, the fluctuation in lifts when the vortex passing through the leading edge and the trailing edge of the airfoil is suppressed significantly. This may suggest that vortical flows through turbomachinery blade passages are distributed much more orderly than one can conceive based on a single airfoil motion.

Figure 9 presents calculated two-dimensional quasi-unsteady two-blade-row cascade results and corresponding three-dimensional measurements (Dring et al., 1982). The turbine consists of a 22-blade stator with pitch $H = 0.854c$ and a 28-blade rotor with pitch $H = 0.813c$. Both the stator and the rotor have round trailing edges. The gap between the two blade rows is 15 percent of the stator chord. The calculated steady solutions under uniform flows of zero angles of attack for each separate blade row are shown in Fig. 9(a). Since the unknown inlet flow angle for the rotor blade row was specified incorrectly as an input parameter, the pressure prediction in the rotor leading edge area does not agree with the measured data at all. The pressure prediction in the rotor trailing edge area is, however, independent of the inlet flow angle and relates to the viscous effect and the application of the Kutta condition. Since the rotor operates at a reduced passing frequency of 2.8 (based on the turbine diameter), both the stator trailing edge and the rotor leading edge sense a variation of pressure. Figure 9(b) shows the "time-averaged" maximum and minimum pressure distributions of the steady calculations for both stator-rotor blade rows at 10 different relative blade locations, which represent a full cycle of the stator-rotor blade interaction. The measured values shown in Fig. 9(b) are also the time-averaged pressures and the range of the unsteady fluctuating pressures (represented by the uncertainty symbols centered at the time-averaged value). The calculated quasi-unsteady pressure ranges are larger at the stator trailing edge and the rotor leading edge than the measured ranges. They become smaller elsewhere. The predicted large fluctuations near the stator and rotor trailing edges are associated with the round shapes when the Kutta

condition is enforced at the centers of the trailing-edge circular arcs. Since small trailing-edge separation bubbles are expected for both the rotor and the stator, a more realistic location for applying the Kutta condition would be some point outside the circular arcs. However, this influence will be very localized. These results clearly demonstrate a strong potential effect of the stator flow on the rotor flow. It also shows the capability and accuracy of the two-dimensional potential-flow calculations.

Conclusions

A time-dependent potential-flow method is described to calculate the vortex shedding and blade-vortex interaction for cascades and for single airfoils. Without a separation, the steady potential-flow calculation has the capability of accurately predicting the cascade blade loading. A simple inclusion of the boundary-layer displacement effect enables the present calculation to predict the cascade exit flow conditions reliably. The unsteady interaction phenomena between the incoming vortex field or the wake shedding vorticity field and the airfoil are found to be similar for the single airfoil and cascade flows. The predicted periodic blade lifts have smaller amplitude for the cascade flows. For the transient calculations, i.e., the Wagner function prediction, the cascade flow approaches steady state much faster than the single airfoil flow. The present calculation method has been shown to be effective in predicting steady and unsteady flows through a multi-blade-row cascade.

Acknowledgments

This work is supported by the Independent Exploratory Development Program administered at the David Taylor Research Center and the Submarine Auxiliary Systems Exploratory Development Project, Program Element 62323N, Block ND3A, Project RB23P11. The work is also sponsored by the Office of Naval Research under Grant No. N14-89-J-1363. The com-

puting time is provided by the Numerical Aerodynamic Simulation Program of the NASA Ames Research Center.

References

- Bratt, J. B., 1950, "Patterns in the Wake of an Oscillating Aerofoil," *Royal Aeronautical Establishment*, R&M 2773, pp. 269-295.
- Dring, R. P., Joslyn, H. D., Hardin, L. W., and Wagner, J. H., 1982, "Turbine Rotor-Stator Interaction," *ASME Journal of Engineering for Power*, Vol. 104, pp. 729-742.
- Fung, Y. C., 1969, *An Introduction to the Theory of Aeroelasticity*, Dover, New York, pp. 207, 401-407.
- Giesing, J. P., 1969, "Vorticity and Kutta Condition for Unsteady Multi-energy Flows," *ASME Journal of Applied Mechanics*, Vol. 36, pp. 608-613.
- Giles, M. B., 1988, "Calculation of Unsteady Wake Rotor Interaction," *AIAA Journal of Propulsion and Power*, Vol. 4.
- Hall, K. C., and Crawley, E. F., 1987, "Calculation of Unsteady Flows in Turbomachinery Using the Linearized Euler Equations," *Proceedings of 4th Symposium on Unsteady Aerodynamics and Aeroelasticity of Turbomachines and Propellers*.
- Herrig, L. J., Emery, J. C., and Erwin, J. R., 1957, "Systematic Two-Dimensional Cascade Tests of NACA 65-Series Compressor Blades at Low Speeds," NACA Technical Note 3916.
- Kim, M. J., and Mook, D. T., 1986, "Application of Continuous Vorticity Panels to General Unsteady Incompressible Two-Dimensional Lifting Flows," *Journal of Aircraft*, Vol. 23, No. 6, pp. 464-471.
- Lee, D. J., and Smith, C. A., 1987, "Distortion of the Vortex Core During Blade/Vortex Interaction," AIAA Paper No. 87-1243.
- Lee, Y. T., Jiang, C. W., and Bein, T. W., 1990, "Rotor/Stator Flow Coupling in Turbomachines," *Proceedings of 3rd International Symposium on Transport Phenomena and Dynamics of Rotating Machinery*, J. H. Kim and W.-J. Yang, eds., Honolulu, HI.
- Morino, L., and Tseng, K., 1978, "Time-Domain Green's Function Method for Three-Dimensional Nonlinear Subsonic Flows," presented at the AIAA 11th Fluid and Plasma Dynamics Conference, Seattle, WA, Paper No. 78-1204.
- Quandt, E., 1989, "The Acoustic Radiation From Unsteady 3-D Potential Flow Vortex System Produced by Turbomachine Blade Motions," ASME Paper No. 89-WA/NCA-10.
- Rai, M. M., 1987, "Unsteady Three-Dimensional Navier-Stokes Simulations of Turbine Rotor-Stator Interaction," AIAA Paper No. 87-2058.
- Robinson, A., and Laurmann, J. A., 1956, *Wing Theory*, Cambridge University Press, pp. 137-142.
- Verdon, J. M., and Caspar, J. R., 1984, "A Linearized Unsteady Aerodynamic Analysis for Transonic Cascades," *Journal of Fluid Mechanics*, Vol. 149, pp. 403-429.
- Yao, Z. X., Garcia-Fogeda, P., Liu, D. D., and Shen, G., 1989, "Vortex/Wake Flow Studies for Airfoils in Unsteady Motions," AIAA Paper No. 89-2225.

Inviscid-Viscous Coupled Solution for Unsteady Flows Through Vibrating Blades: Part 1—Description of the Method

L. He

J. D. Denton

Whittle Laboratory,
Cambridge University,
Cambridge, United Kingdom

An efficient coupled approach between inviscid Euler and integral boundary layer solutions has been developed for quasi-3-D unsteady flows induced by vibrating blades. For unsteady laminar and turbulent boundary layers, steady correlations are adopted in a quasi-steady way to close the integral boundary layer model. This quasi-steady adoption of the correlations is assessed by numerical test results using a direct solution of the unsteady momentum integral equation. To conduct the coupling between the inviscid and viscous solutions for strongly interactive flows, the unsteady Euler and integral boundary layer equations are simultaneously time-marched using a multistep Runge-Kutta scheme, and the boundary layer displacement effect is accounted for by a first order transpiration model. This time-resolved coupling method converges at conditions with considerable boundary layer separation.

1 Introduction

In order further to enhance predictions of the aerodynamic and aeroelastic performance of turbomachinery blades, unsteady viscous flow effects need to be modeled. Recently several time-marching solutions for the unsteady Reynolds-averaged Navier-Stokes equations have been developed, e.g., by Rai (1987), Krothén and Giles (1988) for blade row interactive flows and by Huff (1987) for oscillating cascade flows. The Reynolds-averaged Navier-Stokes solvers can provide detailed insights into the nature of unsteady viscous flows in turbomachinery if one can be confident in the turbulence model adopted. One of the major concerns, however, is the computing cost of such solutions.

For the extensively developed explicit schemes, the computing efficiency is severely restricted by the CFL condition to guarantee numerical stability. When the resolution of the thin viscous layers in the vicinity of solid surfaces or in wakes is required, the time step allowed has to be very small, much smaller than that required for timewise resolution. As a result the CPU time consumed is greatly increased. For steady flow calculations this limitation can be effectively relieved by using the pseudotimewise acceleration techniques, such as the multigrid and nonuniform local time-stepping which have been successfully used in time-marching Euler solvers (e.g., Denton, 1983; Ni, 1981). However, these measures, because of the loss of the time accuracy, cannot be used for computations of unsteady flows. Timewise implicit schemes, on the other hand,

are able to overcome the time step limitation and seem suitable for unsteady viscous computations. But at every time step, the solution involves a large amount of computing work for matrix inversion. So although a large time step can be used, the overall computation efficiency is still low. A considerable improvement of the efficiency has been achieved by using the Approximate Factorization (AF) scheme (Beam and Warming, 1978). However the factorization error in a time-dependence form would cause both the time-accuracy and convergence characteristics to deteriorate if a much larger time step is used.

At a high Reynolds number, it is usually adequate to use a boundary layer model. A well-known example of steady and unsteady boundary layer solvers is the Keller-Box finite difference method developed by Cebeci (e.g., Cebeci and Smith, 1974; Cebeci, 1977). He and Zhou (1987) adopted Cebeci's method to analyze unsteady boundary layer behaviors in blade passage under inlet perturbations, where the unsteady inviscid flow field was obtained by an Euler solver using Denton's scheme, but no coupling between the inviscid and viscous parts was carried out. Jang et al. (1991) developed a strong inviscid-viscous coupling approach between a panel method and the Cebeci's method for incompressible unsteady airfoil flows. On the other hand, adoption of an integral form of boundary layer equations leads to a more efficient way of including viscous effects in numerical solutions. This has been well demonstrated for steady flow calculations. As just mentioned, the time step for unsteady Navier-Stokes solutions in the highly developed explicit schemes is severely restricted by the fine spatial mesh size needed for viscous layer resolution. Hence, an inviscid-integral viscous coupled approach seems particularly attractive for the unsteady flow calculations of present interest.

Contributed by the International Gas Turbine Institute and presented at the 36th International Gas Turbine and Aeroengine Congress and Exposition, Orlando, Florida, June 3-6, 1991. Manuscript received at ASME Headquarters February 20, 1991. Paper No. 91-GT-125. Associate Technical Editor: L. A. Riekert.

In an integral boundary layer solution, empirical correlations must be involved. At present it is fair to say that there is no correlation specifically established for unsteady flows. However, for turbulent boundary layers subject to free-stream oscillations, experiments have shown that the velocity profile inside the unsteady boundary layer changes approximately in a quasi-steady way (e.g., Cousteix et al., 1981; Parikh et al., 1981). Some computations of unsteady boundary layers using the integral models have also shown that the adoption of the steady correlations in a quasi-steady way can give fairly good predictions (e.g., Lyrio and Ferziger, 1983; Cousteix and Houdeville, 1988).

As far as the coupling methodology is concerned, the iterative direct mode has been widely used for attached boundary layers. But the direct coupling fails if boundary layer separation occurs where inviscid-viscous interaction is strong. In the past a number of different methods have been developed to carry out the strong inviscid-viscous coupling. They are mainly applied to steady separated flow calculations, e.g., full inverse mode coupling (Calvert, 1982), semi-inverse coupling (e.g., Carter, 1979), quasisimultaneous coupling (e.g., Veldman, 1981), and time-marching coupling (Freeman, 1984). For unsteady flows, computations using an inviscid-viscous coupling model are less developed. Desopper (1981) used Green's entrainment method for the boundary layer solution and an unsteady small perturbation potential method for the inviscid flow. Similar viscous and inviscid models were used by Rizzetta (1982) to study transonic unsteady flows induced by oscillating airfoils. In these approaches the coupling was performed in the direct mode, so the applications were restricted to attached boundary layers. For unsteady separated flow computations a successful example of coupling methods is the work by Houwink and Veldman (1984). In their method the unsteady small-perturbation-potential model and the entrainment boundary layer model were again adopted. But the coupling was conducted in a fully implicit way. Their computations for transonic unsteady separated flow around an oscillating airfoil showed encouraging results. However, attempts to apply the inviscid-viscous coupled approach to unsteady turbomachinery flows due to either oscillating blades or blade row interactions have rarely been reported.

In this paper, an efficient inviscid-viscous coupled solution for quasi-three-dimensional unsteady flows around oscillating blades is presented. In Part 1, the direct unsteady Euler and integral boundary layer solutions, the simultaneous coupling method and some validations of the boundary layer solution are described. The computational results by the coupled solution will be presented in Part 2.

2 Inviscid Euler Solution

Inviscid flow for a given blade geometry (or a modified

geometry due the boundary layer displacement effect) is governed by the unsteady Euler equations. To deal with a moving grid due to blade oscillation, an integral conservation form of the equations is taken over a dynamic (temporally moving) finite volume:

$$\frac{\partial}{\partial t} \iint U dx dy + \int \left[\left(F - U \frac{\partial x}{\partial t} \right) dy - \left(G - U \frac{\partial y}{\partial t} \right) dx \right] = 0 \quad (1)$$

where

$$U = \begin{pmatrix} \rho \\ \rho u \\ \rho v \\ \rho e \end{pmatrix} \quad F = \begin{pmatrix} \rho u \\ \rho u u + p \\ \rho u v \\ (\rho e + p) u \end{pmatrix} \quad G = \begin{pmatrix} \rho v \\ \rho u v \\ \rho v v + p \\ (\rho e + p) v \end{pmatrix}$$

and $\partial x/\partial t$, $\partial y/\partial t$ are the velocity components of the corresponding mesh point.

Equation 1 is solved using a time-marching method. The basic numerical scheme consists of a cell-vertex finite volume spatial discretization (Denton, 1983; Ni, 1981) and a multistep Runge-Kutta temporal integration (Jameson et al., 1981). The two-step and four-step Runge-Kutta integration schemes are used. The present work was started with the two-step scheme. But the four-step scheme was found to be computationally more efficient, especially for calculations of low-frequency flows. In order to enhance computing efficiency, the basic numerical scheme is combined with a zonal moving-grid technique and a novel implementation method for the phase-shifted periodic condition. A description of this unsteady Euler solver has been given in detail by He (1990a), and will not be repeated here.

3 Integral Unsteady Boundary Layer Solution

Firstly, a direct boundary layer solution with specified free-stream parameters is developed and validated. It is started with a two-dimensional incompressible flow model. The compressibility and quasi-three-dimensional effects will be introduced later.

3-1 Direct Solution of Boundary Layer Momentum Integral Equation. If the amplitude of blade vibration is of the same order as the thickness of boundary layer, it is not easy to define the boundary layer in an absolute system. A convenient way is to look at the situation in a relative system fixed with the vibrating blade. It has been shown (He, 1990b) that for the situation of present interest, the boundary layer problem with relative parameters and corresponding boundary conditions can be solved in exactly the same way as for a conventional boundary layer solution.

Nomenclature

A_m = amplitude
 C_f = skin friction coefficient
 C = length of blade chord
 E_T = turbulent entrainment coefficient
 f = frequency
 H = shape factor
 M = Mach number
 P = pressure
 R_θ = Reynolds number based on momentum thickness
 ΔS = area of computational cell
 T_k = streamtube height

u = axial velocity for Euler solver; streamwise velocity for boundary layer solver
 v = pitchwise velocity for Euler solution; normal velocity for boundary layer solution
 x = axial coordinate for Euler solver; streamwise coordinate for boundary layer solver
 δ = boundary layer thickness
 δ^* = displacement thickness
 θ = momentum thickness
 σ = interblade phase angle
 τ_w = wall shear stress

ω = angular frequency

Subscripts

0 = time-averaged value
 1 = first harmonics; inlet boundary
 2 = outlet boundary
 e = Euler solution
 j = streamwise station
 st = starting point
 w = parameters on wall

Superscripts

i = number of iteration
 n = number of time step

The unsteady momentum integral equation for an incompressible boundary layer is:

$$\frac{1}{u_e^2} \frac{\partial}{\partial t} (\delta^* u_e) + \frac{\partial \theta}{\partial x} + \frac{\partial u_e}{\partial x} \frac{\theta}{u_e} (2+H) = \frac{C_f}{2} \quad (2)$$

To solve Eq. (2), some auxiliary relations must be used. In the present work, correlations for steady laminar and turbulent boundary layers are adopted in a quasi-steady way for unsteady boundary layer calculations, similar to the work by Lyrio and Ferziger (1983) and Cousteix and Houdeville (1988).

Solution for Laminar Flow. Thwaites' method for steady laminar boundary layers is modified for calculations of unsteady laminar boundary layers. In the original method, a nondimensional parameter is defined as:

$$\lambda = \frac{\partial u_e}{\partial x} \frac{\theta^2}{\nu} \quad (3)$$

which reflects the external flow condition and the dynamic nature of the boundary layer. The solution is assumed to be dependent on this parameter. For the present unsteady boundary layer calculations, based on the consideration that the external unsteady perturbations should be included in the parameter λ in a manner consistent with that for steady flows, the parameter is redefined as:

$$\lambda = \left(\frac{1}{u_e} \frac{\partial u_e}{\partial t} + \frac{\partial u_e}{\partial x} \right) \frac{\theta^2}{\nu} \quad (4)$$

When the other correlations for steady flows are retained, the integral equation (Eq. (2)) can be reduced to:

$$\frac{\partial}{\partial x} (\theta^2 u_e^6) = \left[0.45 - \frac{2\theta}{\nu u_e} \left(u_e \frac{\partial \delta^*}{\partial t} + \theta \frac{\partial u_e}{\partial t} \right) \right] \nu u_e^5 \quad (5)$$

A simple relaxation-iteration method is adopted to solve Eq. (5). In the iteration process, the time derivative terms lag the current solution by one iteration step, so that we can still integrate Eq. (5) along the streamwise direction at a given time level, i.e.:

$$(\theta^2)_j^{i-1/2} = \frac{1}{u_e^6} \int \left[0.45 - \frac{2\theta^{i-1}}{\nu u_e} \left(u_e \left(\frac{\partial \delta^*}{\partial t} \right)^{i-1} + \theta^{i-1} \frac{\partial u_e}{\partial t} \right) \right] \nu u_e^5 dx \quad (6)$$

At each streamwise station j , the integration is performed using Simpson's rule. The current solution of the momentum thickness is obtained by:

$$\theta_j^i = (1-r)\theta_j^{i-1} + r\theta_j^{i-1/2} \quad (7)$$

The test cases showed that for convergence of the iteration the best value for the relaxation factor is $r=0.1$.

Solution for Turbulent Flow. For turbulent boundary layers, an entrainment correlation is usually introduced, which controls the growth of boundary layer. The entrainment coefficient is defined as a nondimensional rate at which mainstream flow enters the boundary layer:

$$E_T = \frac{1}{\rho_e u_e} \frac{\partial}{\partial x} \left(\int_0^{\delta} \rho u dy \right) = \frac{1}{u_e} \frac{\partial}{\partial x} [u_e (\delta - \delta^*)] \quad (8)$$

Lyrio and Ferziger (1983) adopted a very simple entrainment correlation for unsteady boundary layers under an adverse pressure gradient and their computations agreed well with the corresponding experiments. In the present method the same correlation is used:

$$E_T = 0.0083 (1-\Delta)^{-2.5} \quad (9)$$

where

$$\Delta = \frac{\delta^*}{\delta} \quad (10)$$

A shape factor correlation, derived from Cole's velocity profile by Bardina et al. (1981) and followed by Lyrio and Ferziger (1983), is also used here.

$$h = 1.5\Delta + 0.179V_T + 0.321V_T^2/\Delta \quad (11)$$

where

$$h = \frac{H-1}{H} \quad (12a)$$

$$V_T = 2.439 \left(\frac{|\tau_w|}{\rho u_e^2} \right)^{1/2} \text{sgn}(\tau_w) \quad (12b)$$

For the skin friction, the Ludwig-Tillman correlation (e.g., Cousteix, 1980) is used:

$$C_f = 0.245 R_\theta^{-0.268} 10^{-0.678 H} \quad (13)$$

The solution procedure is similar to that used for laminar boundary layers. Now the entrainment equation (Eq. (8)) is also integrated along the streamwise direction:

$$\Delta_j^{i-1/2} = \int \left[\frac{(1-\Delta)\Delta}{\delta^*} \left(\frac{\partial \delta^*}{\partial x} - \frac{\Delta}{1-\Delta} E_T + \frac{\delta^*}{u_e} \frac{\partial u_e}{\partial x} \right) \right]^{i-1} dx \quad (14)$$

It is updated using relaxation in the same way as the momentum thickness.

3-2 Numerical Examples of Boundary Layer Solution. Validation of the direct boundary layer solution for steady flow conditions was carried out by calculating a laminar boundary layer and turbulent boundary layer under adverse pressure gradients. The calculated results compared well with the corresponding analytical solution and experimental data (He, 1990b). Here, some unsteady boundary layer calculations are presented, with the main emphasis on checking the quasi-steady adoption of the laminar and turbulent correlations.

Laminar Flow. We consider an unsteady laminar boundary layer over a flat plate under a free stream perturbation with a traveling wave form:

$$u_e = u_o \left[1 + A_m \sin \left(\omega t - \frac{\omega x}{u_c} \right) \right] \quad (15)$$

where u_c is a constant convection speed of the perturbation. An extreme case is that when the convection speed is infinite, we can have a purely time-dependent free-stream perturbation:

$$u_e = u_o(1 + A_m \sin \omega t) \quad (16)$$

Lighthill (1954) obtained a time-linearized solution for unsteady boundary layers under the purely time-dependent free-stream velocity perturbation given by Eq. (16). This method was later extended to the situations with a finite convection speed of the velocity perturbation (Eq. (15)), by Patel (1975).

The present calculations are carried out under two flow conditions corresponding to those given in Eqs. (15) and (16).

- (i) $u_c = \infty$, $u_o = 10$ m/s, $A_m = 0.05$,
- (ii) $u_c = 7.7$ m/s, $u_o = 10$ m/s, $A_m = 0.025$,

Figure 1 shows calculated phase-lead of the wall friction with respect to the reduced frequency in the purely time-dependent condition Eq. (16), compared with the results by Lighthill's linear theory (two solid lines correspond to low-frequency and high-frequency solutions) and a finite difference method by Telionis (1981). The present calculation predicts higher phase lead than the other solutions, especially at high-frequency conditions.

In Fig. 2, the calculated wall friction phase lag with respect to the reduced frequency for the traveling wave case (Eq. (15)) is compared with Patel's low-frequency solution and with his experimental data (Patel, 1975). A qualitative agreement between the present calculation and Patel's solution and experiment is obtained. In this case less phase lag is predicted.

Turbulent Flow. An unsteady turbulent boundary layer

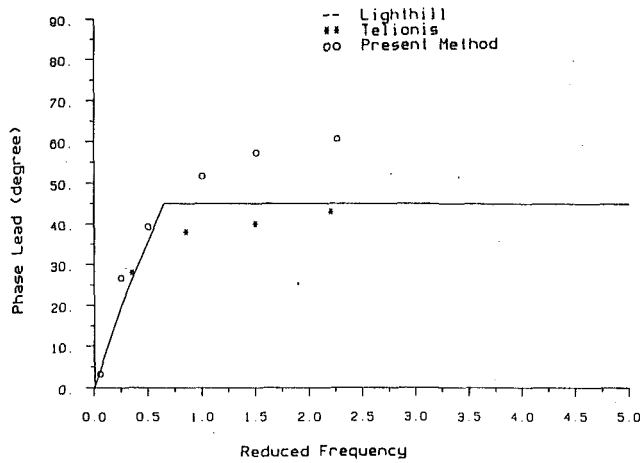


Fig. 1 Phase lead of wall friction with respect to reduced frequency under purely time-dependent free-stream perturbation

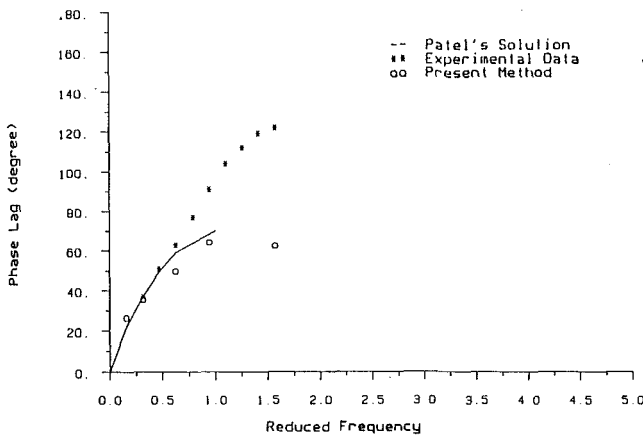


Fig. 2 Phase lag of wall friction with respect to reduced frequency under traveling wave free-stream perturbation

measured by Parikh et al. (1981) is calculated. At the test condition, the boundary layer is subject to an unsteady external velocity distribution:

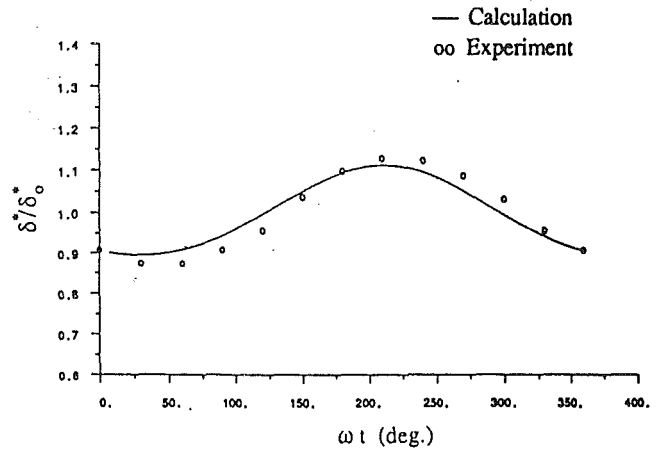
$$u_e(x, t) = u_o - \frac{A_m(x - x_o)}{L} (1 - \cos \omega t) \quad (x_o \leq x \leq x_o + L) \quad (17)$$

where $u_o = 0.73$ m/s; $A_m = 0.05$, $L = 0.6$ m. Hence the external flow is decelerated in a time-averaged sense and oscillated with an increased amplitude in the streamwise direction.

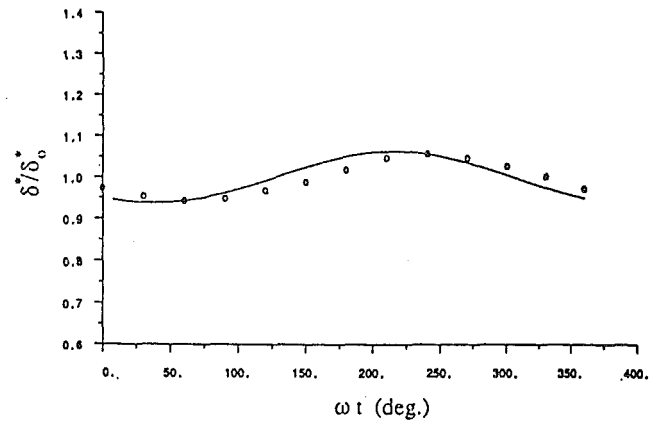
Figure 3 shows the comparisons between the calculated and measured timewise variations of the relative displacement thickness δ^*/δ_o^* in one period of oscillation at three different frequencies. The calculations agree well with the experimental results for all three frequency conditions. One point to note is that the comparison for the highest frequency condition, shown in Fig. 3 (c) (where $f = 2$ Hz, $K = \omega(x - x_o)/u_o = 9.78$), is better than that at the medium frequency condition (Fig. 3b). It seems surprising because one would expect that the steady correlations could work better under a lower frequency. To understand this, a simple analysis on the boundary layer momentum equation may be helpful. Assume that the effect of turbulence is effectively expressed by the viscosity coefficient, then we have:

$$\frac{\partial u}{\partial t} + u \frac{\partial u}{\partial x} + v \frac{\partial u}{\partial y} = \frac{\partial u_e}{\partial t} + u_e \frac{\partial u_e}{\partial x} + v \frac{\partial^2 u}{\partial y^2}$$

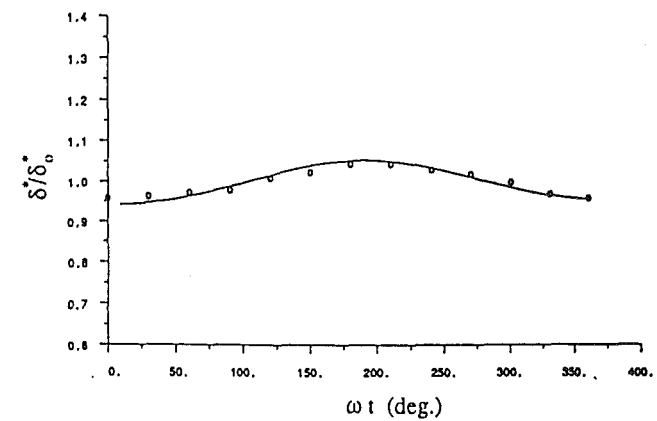
linear inertia
nonlinear inertia
driving force
viscous



(a) $f = 0.25$ Hz ($k = 1.22$)



(b) $f = 0.5$ Hz ($k = 2.45$)



(c) $f = 2$ Hz ($k = 9.78$)

Fig. 3 Displacement thickness variation in one period

At low-frequency conditions, the nonlinear inertia term may be quite significant. However, because the boundary layer has sufficient time to develop, all the unsteady behavior can be traced in a quasi-steady way. When the frequency is high, the driving force and linear inertial terms become dominant. Then the local flows tend to behave more or less in the same way throughout the whole boundary layer except for the near the wall where the oscillation amplitude is forced to approach zero. The boundary layer is now mainly controlled by a linear equation:

$$\frac{\partial u}{\partial t} = \frac{\partial u_e}{\partial t} + v \frac{\partial^2 u}{\partial y^2} \quad (18)$$

The solution for the amplitude of the flow velocity can be expressed in a form as (Lighthill, 1954):

$$\frac{u_1}{u_{e1}} = f\left(y \sqrt{\frac{\omega}{2\nu}}\right) \quad (19)$$

The above solution can be interpreted in a simple way. A scaling analysis on the linear equation (Eq. (18)) gives:

$$\delta_w \sim \sqrt{\frac{\nu}{\omega}} \quad (20)$$

δ_w can be considered as a thickness of a layer across which the velocity amplitude drops from the external value u_{e1} to zero on the wall. The higher the frequency, the thinner the layer. This means that at high frequencies the velocity profile through the boundary layer (except within the layer of thickness δ_w) oscillates almost in the same amplitude and phase as the external perturbation. Therefore under high frequencies the velocity profile is "frozen" simultaneously with the external unsteady velocity. So the steady velocity profile correlations, if adopted in a quasi-steady manner for unsteady boundary layer calculations, should work well at high frequencies.

The outcome of the above analysis implies that more attention should be paid to the situation at medium frequencies. We should note the role of the unsteady behavior of the skin friction in controlling the whole unsteady velocity profile, which is important for the unsteady inviscid-viscous coupling. Because the near-wall region, in which the local velocity does change its phase, is confined to a smaller part of the whole boundary layer as the frequency is increased, the unsteady variation of the skin friction may not be a sensible parameter to look at. In other words, there might be no close correlation between the skin friction and the velocity profile integral parameters (e.g., δ^* , θ) at high frequencies. This point should also be taken into account for the laminar cases just presented.

On the whole, the above comparisons between the calculations and the experimental results or other analytical solutions can be considered as a justification for the adoption of the steady correlations in a quasi-steady manner for the computations of unsteady boundary layers of current interest. It is expected that further improvements may be obtained by introducing frequency corrections to the previous steady correlations.

4 Inviscid-Viscous Coupled Solution

It is suggested (Veldman, 1981) that the failure of the direct coupling at the boundary layer separation is due to the clearly defined hierarchy between the inviscid and viscous flow parts when solving the boundary layer equation in a direct mode. A more natural mode for inviscid-viscous coupling follows from the consideration of simultaneous coupling. The boundary layer equation is solved in a time-marching manner. It is temporally integrated with the time-marching Euler solution, and the effect of the boundary layer blockage is accounted for by transpiring extra mass flow from the solid wall. This method has been applied to steady turbomachinery flow calculations by Freeman (1984), where the timewise accuracy is not of concern. In the present work, both the Euler and boundary layer equations are simultaneously integrated in time using the same discretization scheme so that the time accuracy can be maintained for unsteady flow calculations.

4-1 Transpiration Coupling Model. Let us consider the inviscid-viscous coupling model in a more general way. It is assumed that the whole flow field is subject to the solution of the thin-layer Navier-Stokes equations. The quasi-three-dimensional effect is included by the streamtube height varying along the streamwise distance. Outside the viscous layer, viscous effects are negligible and the governing equations reduce to the Euler equations. Inside the viscous layer, an equivalent

inviscid flow is assumed, which is also governed by the Euler equations. To guarantee that both the thin-layer Navier-Stokes and the Euler solutions give the same answers at the edge of the viscous layer, extra mass, momentum, and energy sources must be added to the equivalent inviscid solution.

By using the defect form of the Euler and the thin-layer Navier-Stokes equations in terms of the continuity and the streamwise momentum, the integral momentum equation for the quasi-three-dimensional thin-layer viscous flow can be derived (He, 1990b):

$$\begin{aligned} \frac{\partial}{\partial t}(\rho_{ew} u_{ew} \delta^*) + \rho_{ew} u_{ew}^2 \left[\frac{\partial u_{ew}}{\partial x} \frac{1}{u_{ew}} (2\theta + \delta^*) + \frac{1}{\rho_{ew}} \frac{\partial \rho_{ew} \theta}{\partial x} \right. \\ \left. + \frac{\theta}{T_k} \frac{\partial T_k}{\partial x} - \frac{C_f}{2} \right] + \frac{\partial}{\partial x} \int_0^\infty (p_e - p) dy \\ - u_{ew} \frac{\partial}{\partial t} \int_0^\infty (\rho_e - \rho) dy = 0 \quad (21) \end{aligned}$$

and the source mass term on the wall for equivalent inviscid Euler solution is

$$\rho_{ew} v_{ew} = \frac{1}{T_k} \rho \frac{\partial}{\partial x} (T_k \rho_{ew} u_{ew} \delta^*) + \frac{\partial}{\partial t} \int_0^\infty (\rho_e - \rho) dy \quad (22)$$

In the present work, the conventional first-order boundary layer model is still adopted for simplicity. That is, the pressure and velocity in the equivalent inviscid flow are assumed to be constant across the boundary layer. Then the boundary layer blockage effect on the inviscid flow can be easily accounted for. For a computational cell adjacent to the wall, if the timewise integration of the Euler equations is performed using the two-step Runge-Kutta scheme, we have:

$$U^{n+1/2} = U^n \frac{\Delta S^n}{\Delta S^{n+1/2}} - \frac{1}{2} \frac{\Delta t}{\Delta S^{n+1/2}} R^n \quad (23a)$$

$$U^{n+1} = U^n \frac{\Delta S^n}{\Delta S^{n+1}} \frac{\Delta t}{\Delta S^n} R^{n+1/2} \quad (23b)$$

where

$$R = \sum_j \left[\left(F - U \frac{\partial x}{\partial t} \right)_i \Delta y_i - \left(G - U \frac{\partial y}{\partial t} \right)_j \Delta x_j \right] + S_b \Delta L_b \quad (23c)$$

ΔL_b is the length of the boundary of the cell along the wall. The source terms on the boundary face for mass, momentum, and energy due to the boundary layer blockage are:

$$S_b = \begin{pmatrix} \rho_{ew} v_{ew} \\ u_e (\rho_{ew} v_{ew}) \\ v_e (\rho_{ew} v_{ew}) \\ H (\rho_{ew} v_{ew}) \end{pmatrix} \quad (24)$$

The mass source $\rho_{ew} v_{ew}$ is determined from Eq. (22).

4-2. Time-Marching Integration of Boundary Layer Equation. Under the first-order boundary layer approximation, the quasi-three-dimensional unsteady compressible momentum integral equation for the viscous thin layer becomes:

$$\begin{aligned} \frac{1}{\rho_e u_e^2} \frac{\partial}{\partial t} (\rho_e u_e \delta^*) + \frac{\partial \theta}{\partial x} + \frac{\partial u_e}{\partial x} \frac{1}{u_e} (2\theta + \delta^*) + \frac{\theta}{\rho_e} \frac{\partial \rho_e}{\partial x} \\ + \frac{\theta}{T_k} \frac{\partial T_k}{\partial x} - \frac{1}{\rho_e u_e} \frac{\partial}{\partial t} \int (\rho_e - \rho) dy = \frac{C_f}{2} \quad (25) \end{aligned}$$

Equation (25) is integrated in time in the same multistep Runge-Kutta scheme as is used for the time-marching Euler solution (e.g., for the two-step scheme):

$$(\rho_e u_e \delta^*)^{n+1/2} = (\rho_e u_e \delta^*)^n + \frac{\Delta t}{2} R_b^n \quad (26a)$$

$$(\rho_e u_e \delta^*)^{n+1} = (\rho_e u_e \delta^*)^n + \Delta t R_b^{n+1/2} \quad (26b)$$

where

$$R_b = \rho_e u_e^2 \left[\frac{C_f}{2} - \frac{\theta}{T_k} \frac{\partial T_k}{\partial x} - \frac{\partial \theta}{\partial x} - \frac{\theta}{u_e} (2 + H) \frac{\partial u_e}{\partial x} - \frac{\theta}{\rho_e} \frac{\partial \rho_e}{\partial x} + \frac{1}{\rho_e u_e} \frac{\partial}{\partial t} \int (\rho_e - \rho) dy \right] \quad (26c)$$

An approximate evaluation of the term involving the density defect integration is given by a simple quasi-steady model (He, 1990b):

$$\frac{\partial}{\partial t} \int (\rho_e - \rho) dy = 0.5 \frac{\partial}{\partial t} \left[\rho_e \delta \left(1 - \frac{1}{1 + \frac{\gamma - 1}{2} M_e^2} \right) \right] \quad (27)$$

This term is updated with one time step delay in the multistep Runge-Kutta time-marching process. Then, once the flow field at a current time level n is known, the solution for both the inviscid and the viscous parts of the flow can be simultaneously stepped forward to a new time level $n + 1/2$, $n + 1$, etc., without a hierarchy being defined between them. This feature is essentially required for strong inviscid-viscous coupling calculations.

For turbulent flows, the entrainment equation is also solved in a time-marching way for convenience. By analogy with the steady flow, an unsteady entrainment coefficient is defined as:

$$E_T = \frac{1}{\rho_e u_e} \left[\frac{1}{u_e} \frac{\partial}{\partial t} \left(\int_0^{\delta} \rho u dy \right) + \frac{\partial}{\partial x} \left(\int_0^{\delta} \rho u dy \right) \right] \quad (28)$$

which can be written as:

$$\frac{\partial}{\partial t} \left[\rho_e u_e \delta^* \left(\frac{1}{\Delta} - 1 \right) \right] = u_e \left\{ \rho_e u_e E_T - \frac{\partial}{\partial x} \left(\rho_e u_e \delta^* \left(\frac{1 - \Delta}{\Delta} \right) \right) \right\} \quad (29)$$

Equation (29) is integrated in time using the same multistep Runge-Kutta scheme as Eq. (26).

The inviscid-viscous coupling starts from the blade leading edge and ends at the outlet of the computation domain. As the integral equation has to be started with a finite boundary layer thickness, the starting displacement thickness is specified. It is intended that the specified starting thickness should not affect the downstream boundary layer solution. Based on numerical tests, it is specified that:

$$\delta_{st}^* = 0.0001 C$$

Additionally, for boundary layers starting with a laminar state, the starting shape factor is specified:

$$H_{st} = 2.6$$

For those starting with a turbulent state, based on the 1/7th power velocity profile, the starting shape parameter is defined:

$$\Delta_{st} = 0.125$$

All other parameters are determined by the correlations.

In the wake region the skin-friction coefficient is specified to be zero. To carry out the boundary layer calculation along one mesh line in the wake region, the computational grids in this region are allowed to move adaptively in order to ensure that there is no loading on the wake. The time-dependent mesh is accounted for by the fully conserved discretization on a moving grid so that the wake movement is time solved (He, 1990b).

It is recognized that the transition from a laminar state to

a turbulent one is a complicated problem, especially under unsteady flow conditions. In the present work, for simplicity, the transition point is either specified as input or determined by using the Horton's laminar separation bubble model (Horton, 1969) in a quasi-steady way.

5 Summary

A Euler/integral boundary layer coupling approach has been developed for calculations of unsteady flows induced by oscillating blades. The steady correlations used to close the integral boundary layer equation for both laminar and turbulent flows are adopted in a quasi-steady way. Assessments of these assumptions have been made by calculating unsteady attached boundary layers and comparing the results with the corresponding experimental data or other well-documented solutions. A simple analysis shows that care should be taken mainly for situations with a medium range of frequency. Under high-frequency conditions, the whole velocity profile inside the boundary layer is "frozen" instantaneously with the external unsteady velocity.

In order to perform coupling calculations for strongly inviscid-viscous interactive flows (i.e., with boundary layer separation), a simultaneous coupling strategy is adopted. The unsteady Euler and the unsteady integral boundary layer equations are time-marched simultaneously using the same multistep Runge-Kutta scheme. The boundary layer displacement effect on the inviscid flow is accounted for by using the first-order transpiration model. This simultaneous time-marching coupling approach not only overcomes the singularity around the separation point associated with the direct solution, but also guarantees timewise resolution, which is essential for unsteady flow calculations.

The numerical results by the coupling solution will be presented in Part 2.

References

- Bardina, J., Lyrio, A., Kline, S. J., Ferziger, J. H., and Johnston, J. P., 1981, "A Prediction Method for Planar Diffusor Flows," *ASME Journal of Fluids Engineering*, Vol. 103, pp. 315-321.
- Beam, R. M., and Warming, R. F., 1978, "Implicit Factored Scheme for the Compressible Navier-Stokes Equation," *AIAA J.*, Vol. 14, No. 4.
- Calvert, W. J., 1982, "An Inviscid-Viscous Interaction Treatment to Predict the Blade-to-Blade Performance of Axial Compressors With Leading-Edge Normal Shock Waves," ASME Paper No. 82-GT-135.
- Carter, J. E., 1979, "A New Boundary-Layer Iteration Technique for Separated Flow," AIAA Paper No. 79-1450.
- Cebeci, T., and Smith, A. M. O., 1974, *Analysis of Turbulent Boundary Layers*, Academic Press, New York.
- Cebeci, T., 1977, "Calculations of Unsteady Two-Dimensional Laminar and Turbulent Boundary Layers With Fluctuations in External Velocity," *Proc. Roy. Soc. Lon.*, Vol. A355.
- Cousteix, 1980, "Integral Techniques," in: *Proceedings of the AFOSR-HTTM Stanford Conference on Complex Turbulent Flows*.
- Cousteix, J., Houdeville, R., and Javelle, J., 1981, "Response of a Turbulent Boundary Layer to a Pulsation of the External Flow With and Without Adverse Pressure Gradient," in: *Unsteady Turbulent Shear Flows*, R. Michel et al., eds., Springer-Verlag, New York.
- Cousteix, J., and Houdeville, R., 1988, "Effects of Unsteadiness on Turbulent Boundary Layers," in: *Unsteady Aerodynamics*, V. K. I. Lecture Series, 1988-07.
- Denton, J. D., 1983, "An Improved Time Marching Method for Turbomachinery Flow Calculations," *ASME Journal of Engineering for Power*, Vol. 105, pp. 514-524.
- Desopper, A., 1981, "Influence of the Laminar and Turbulent Boundary Layer in Unsteady Two-Dimensional Viscous-Inviscid Coupled Calculations," in: *Unsteady Turbulent Shear Flows*, R. Michel et al., eds., Springer-Verlag, New York.
- Freeman, C., 1984, "A Viscous Inviscid Interaction Method for Calculating the Flow in Transonic Fan Blade Passages by the Use of a Time Dependent Free Stream Calculation and a Time Dependent Boundary Layer Calculation," *IMECH E* 1984-3, Paper No. c71/84.
- He, L., and Zhou, S., 1987, "Computation of Unsteady Compressible Turbulent Boundary Layer in Cascade Flows With Inlet Forcing," in: *Proceedings of the 4th Symposium on Unsteady Aerodynamics and Aeroelasticity of Turbomachines and Propellers*, Aachen, Federal Republic of Germany.
- He, L., 1990a, "An Euler Solution for Unsteady Flows Around Oscillating Blades," *ASME JOURNAL OF TURBOMACHINERY*, Vol. 112, pp. 714-722.

- He, L., 1990b, "Unsteady Flows Around Oscillating Turbomachinery Blades," Ph.D. Thesis, Cambridge Univ. Engineering Dept., United Kingdom, Sept.
- Horton, H. P., 1969, "A Semi-empirical Theory for the Growth and Bursting of Laminar Separation Bubble," A. R. C. CP-1073.
- Houwink, R., and Veldman, A. E. P., 1984, "Steady and Unsteady Separated Flow Computations for Transonic Airfoils," AIAA 84-1618.
- Huff, D. L., 1987, "Numerical Simulations of Unsteady, Viscous, Transonic Flow Over Isolated and Cascaded Airfoils Using a Deformed Grid," AIAA Paper No. 87-1316.
- Jameson, A., Schmidt, W., and Turkel, E., 1981, "Numerical Solutions of the Euler Equation by Finite Volume Method Using Runge-Kutta Time-Stepping Scheme," AIAA Paper No. 81-1259.
- Jang, H. M., Ekiaterinaris, J. A., Platzer, M. F., and Cebeci, T., "Essential Ingredients for the Computation of Steady and Unsteady Blade Boundary Layers," ASME JOURNAL OF TURBOMACHINERY, Vol. 113, pp. 608-616.
- Krouthen, B., and Giles, M. B., 1988, "Numerical Investigation of Hot Streaks in Turbines," AIAA Paper No. 88-3015.
- Lighthill, M. J., 1954, "The Response of Laminar Skin Friction and Heat Transfer to Fluctuations in the Freestream Velocity," *Proc. Roy. Soc. Lond.*, Vol. 224a, pp. 1-23.
- Lyrio, A. A., and Ferziger, J. H., 1983, "A Method of Predicting Unsteady Turbulent Flows and Its Applications to Diffusers With Unsteady Inlet Conditions," *AIAA J.*, Vol. 21, No. 4.
- Ni, R. H., 1981, "A Multiple Grid Scheme for Solving the Euler Equation," AIAA Paper No. 81-1025.
- Parikh, P. G., Reynolds, W. C., Jayaraman, R., and Carr, L. W., 1981, "Dynamic Behavior of an Unsteady Turbulent Boundary Layer," in: *Unsteady Turbulent Shear Flow*, IUTAM Symposium, Toulouse, France.
- Patel, M. H., 1975, "On Laminar Boundary Layer in Oscillatory Flows," *Proc. R. Soc. Lond.*, Vol. A347, pp. 99-123.
- Rai, M. M., 1987, "Unsteady Three-Dimensional Navier-Stokes Simulation of Turbine Rotor-Stator Interaction," AIAA Paper No. 87-2058.
- Rizzetta, D. P., 1982, "Procedure for the Computation of Unsteady Transonic Flows Including Viscous Effects," NASA CR-166249.
- Telionis, D. P., 1981, *Unsteady Viscous Flows*, Springer-Verlag, New York.
- Veldman, A. E. P., 1981, "New Quasi-simultaneous Method to Calculate Interacting Boundary Layers," *AIAA J.*, Vol. 19, No. 1.

Inviscid-Viscous Coupled Solution for Unsteady Flows Through Vibrating Blades: Part 2—Computational Results

L. He

J. D. Denton

Whittle Laboratory,
Cambridge University
Cambridge, United Kingdom

A quasi-three-dimensional inviscid-viscous coupled approach has been developed for unsteady flows around oscillating blades, as described in Part 1. To validate this method, calculations for several steady and unsteady flow cases with strong inviscid-viscous interactions are performed, and the results are compared with the corresponding experiments. Calculated results for unsteady flows around a biconvex cascade and a fan tip section highlight the necessity of including viscous effects in predictions of turbomachinery blade flutter at transonic flow conditions.

1 Introduction

As described in Part 1 of this paper (He and Denton, 1993), in order to efficiently include viscous flow effects in blade flutter predictions, an Euler-integral boundary layer coupled solution for quasi-three-dimensional unsteady flows around oscillating blades has been developed. For unsteady laminar and turbulent boundary layers, steady correlations are adopted in a quasi-steady way to close the integral boundary layer model. This quasi-steady adoption of the correlations is assessed by numerical test results using a direct solution of the unsteady momentum integral equation with specified free-stream pressure distributions. To conduct the coupling between the inviscid and viscous solutions for strongly interactive flows (i.e., with boundary layer separation), the unsteady Euler and integral boundary layer equations are simultaneously time-marched using the multistep Runge-Kutta scheme. The boundary layer displacement effect is accounted for by the first-order transpiration model. This coupling method overcomes the singular behavior around the separation point in the direct boundary layer solution, and guarantees timewise accuracy, which is essential for unsteady flow calculations.

To validate the inviscid-viscous coupled solution, calculations for steady and unsteady flow cases with significant viscous effects are performed. The calculated results are presented as follows.

2 Steady Flow Results

2.1 Low-Speed Supercritical Compressor Cascade. Steady flow through a supercritical compressor cascade, which was measured as "Case-2" by Dong (1988) in the Whittle Laboratory, is calculated. The calculated surface static

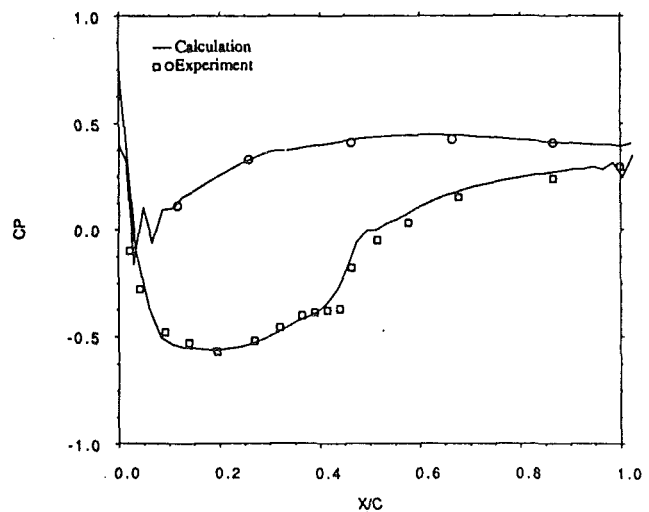
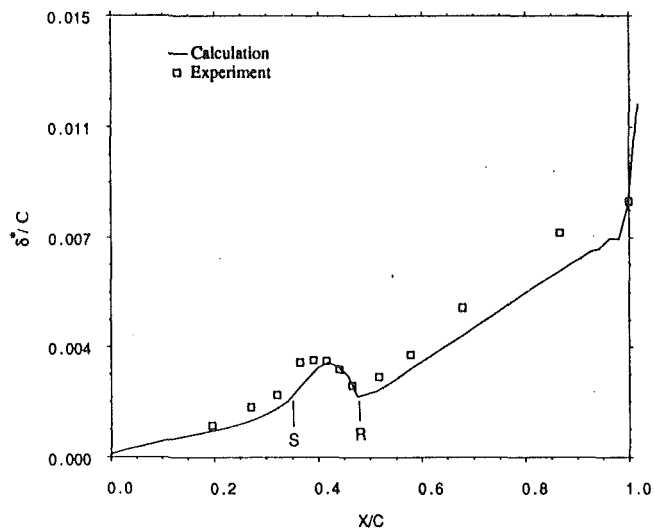


Fig. 1 Static pressure coefficient along chord

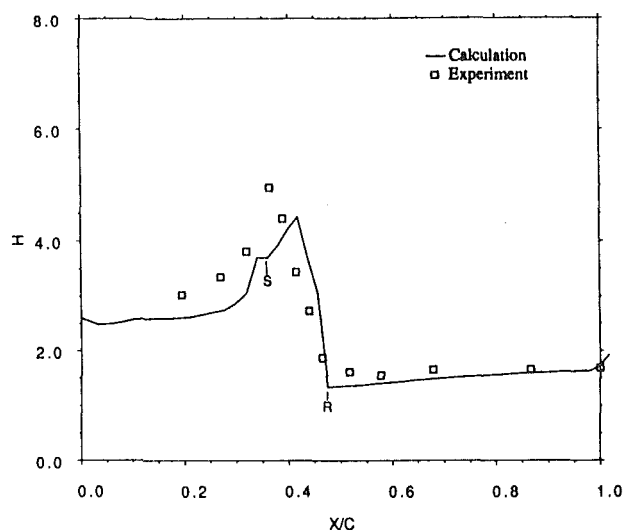
pressure coefficient distribution is given in Fig. 1, compared with the measured data. The measurement showed a suction surface laminar separation bubble at 35~45 percent chord. The laminar separation position is well predicted by the present calculation. Figure 2 shows the displacement thickness and shape factor distributions of the suction surface boundary layer, in which "S" and "R" indicate the predicted separation and reattachment points. It is noted that both the displacement thickness and the shape factor in this region are underpredicted. A better prediction is expected if a more sophisticated separation bubble-transition model is adopted.

2.2 Transonic Compressor Cascade. A transonic cascade flow of compressor blades, for which the experimental data

Contributed by the International Gas Turbine Institute and presented at the 36th International Gas Turbine and Aeroengine Congress and Exposition, Orlando, Florida, June 3-6, 1991. Manuscript received at ASME Headquarters February 20, 1991. Paper No. 91-GT-126. Associate Technical Editor: L. A. Riekert.



(a) Displacement Thickness



(b) Shape Factor

Fig. 2 Suction surface boundary layer parameter distributions

are available (Stow, 1989), is calculated. The inlet flow conditions are:

$$i=0, \quad M_1=0.8$$

Under these conditions, there are small laminar separation bubbles in the very close vicinity of the leading edge, which

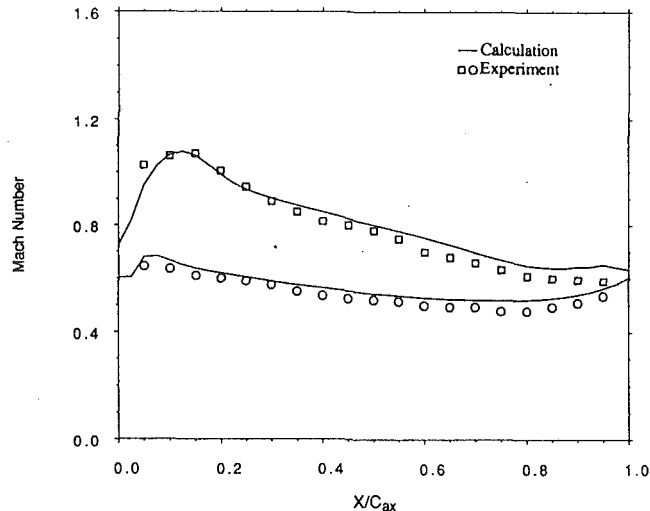


Fig. 3 Mach Number distribution along axial chord

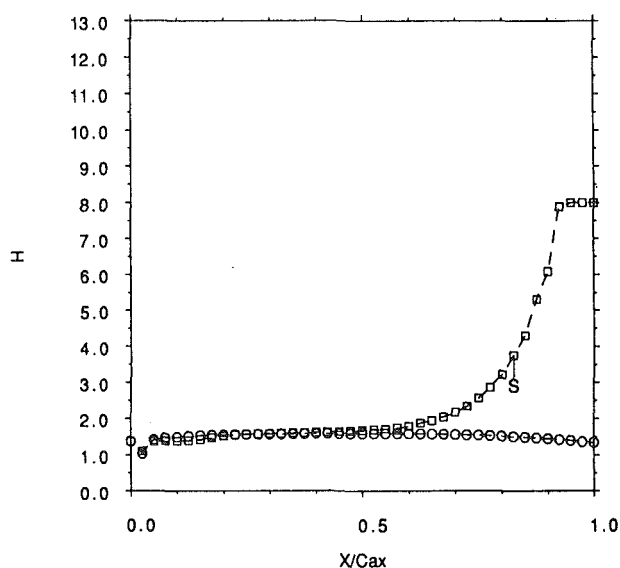


Fig. 4 Calculated boundary layer shape factor

effectively trigger transition on both the suction and the pressure surface (Stow et al., 1989). To capture these leading-edge bubbles correctly, high resolution of the flow around the stagnation point is necessary, which needs a very fine mesh. In the present calculation, the boundary layers on both the surfaces are simply assumed to be turbulent from the leading edge. Figure 3 shows the surface isentropic Mach number distri-

Nomenclature

A_m = amplitude
 a_0 = stagnation speed of sound
 c = blade chord length
 C_f = skin friction coefficient
 C_p = pressure coefficient
 i = incidence
 f = frequency
 H = shape factor
 k = reduced frequency = $\omega c/U_1$,
 unless otherwise defined

M = Mach number
 P = static pressure
 P_0 = stagnation pressure
 T_k = streamtube height
 U = absolute velocity
 γ = specific heat ratio
 δ = boundary layer thickness
 δ^* = displacement thickness
 θ = momentum thickness

σ = interblade phase angle
 ω = angular frequency

Subscripts

1 = first harmonics; inlet boundary
 2 = outlet boundary
 av = time-averaged
 p = pressure
 sh = shock
 t = torsion

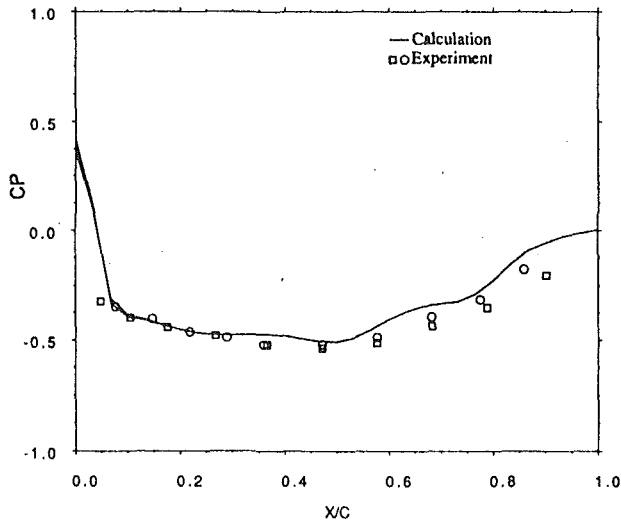
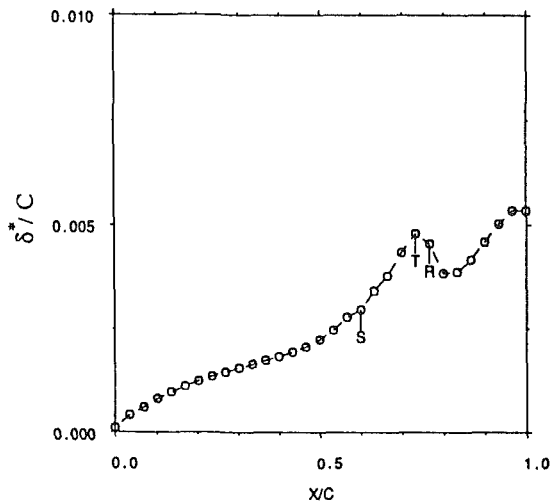
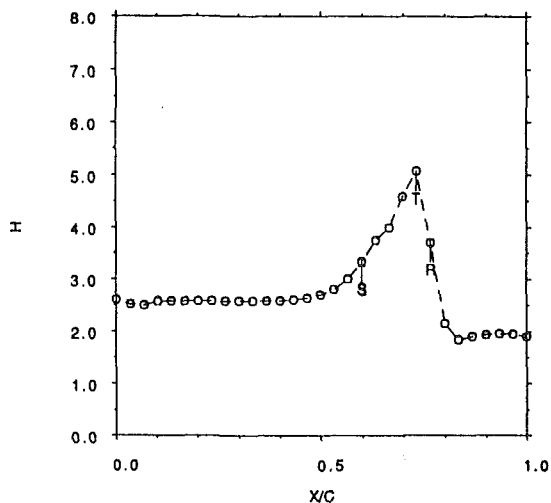


Fig. 5 Steady pressure coefficient along chord ($i=0$ deg)



(a) Displacement Thickness



(b) Shape Factor

Fig. 6 Calculated boundary layer parameters ($i=0$ deg)

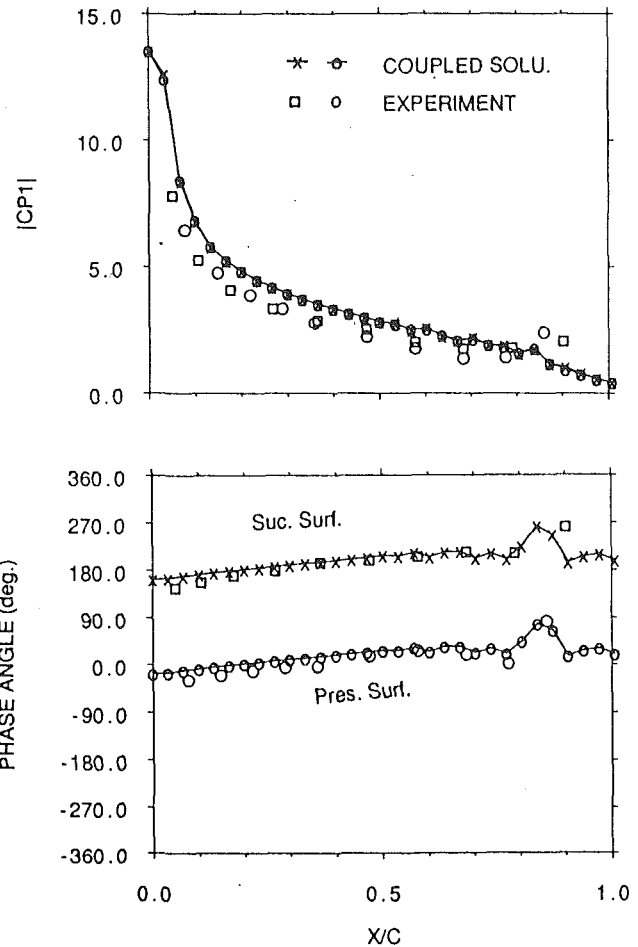


Fig. 7 Amplitude and phase angle of first harmonics of unsteady pressure coefficient ($i_{av}=0$ deg)

tribution along the axial chord from the present calculation and the experimental data. In the vicinity of the leading edge on the suction surface, the displacement thickness effect due to the leading-edge bubble may account for the discrepancy between the measurement and the calculation. Figure 4 shows the calculated boundary layer shape factor distribution against axial chord. A turbulent separation is observed around 80 percent chord on the suction surface. This is also indicated by the flattened pressure distributions of both the calculated and experimental results.

3 Unsteady Flow Results

3.1 Oscillating NACA-65 Airfoil. The first check on the unsteady inviscid-viscous coupling solution is made by calculating unsteady flows around a single airfoil oscillating with a torsion amplitude of 2 deg and a frequency of 20 Hz ($k=0.686$), for which the experimental data are available (He, 1990b; He and Denton, 1991). The calculated results for two mean incidence conditions, $i_{av}=0$ deg, $i_{av}=7.5$ deg, will be presented. Based on the experimental observations, at 0 deg mean incidence, the unsteady transition on both suction and pressure surfaces is controlled by a laminar separation bubble. But at 7.5 deg mean incidence, only on the pressure surface is the transition subject to the laminar separation bubble; the suction surface boundary layer is found to be entirely turbulent.

Case 1 (0 deg Time-Mean Incidence). Figure 5 shows the calculated steady pressure coefficient distribution along the

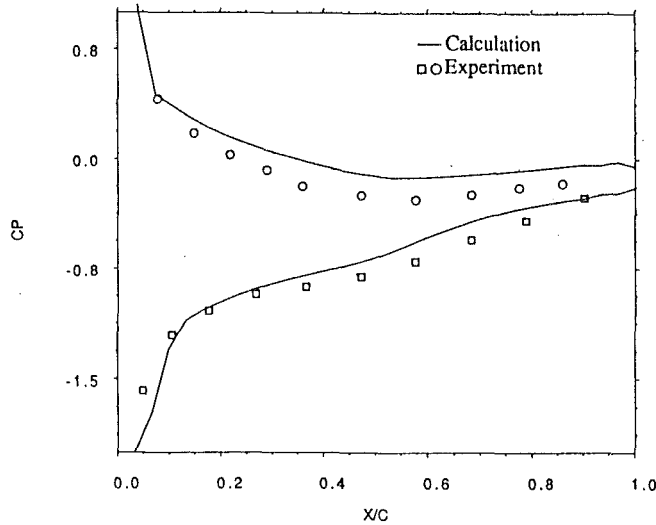
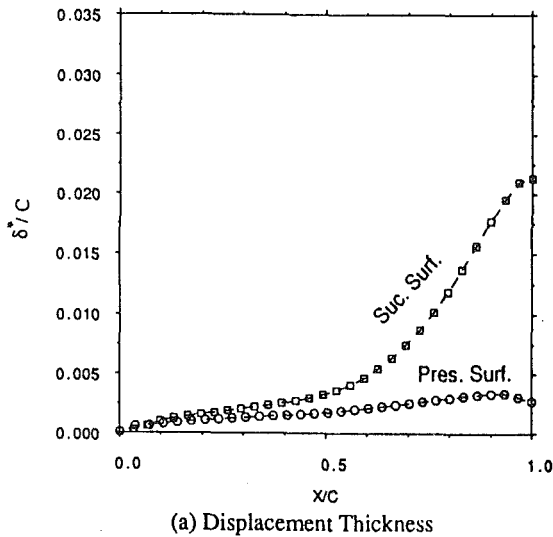
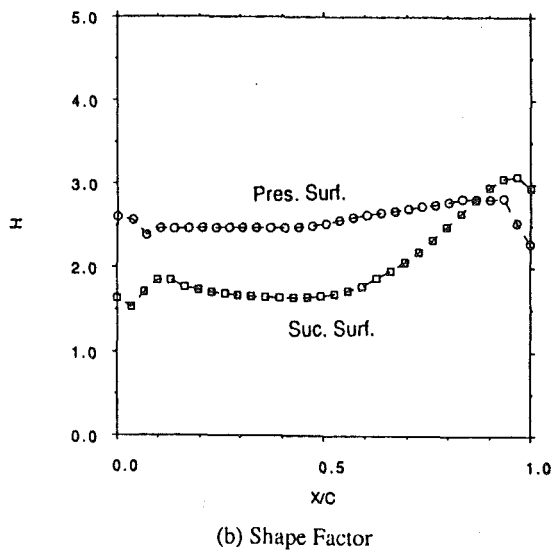


Fig. 8 Steady pressure coefficient along chord ($i = 7.5$ deg)



(a) Displacement Thickness



(b) Shape Factor

Fig. 9 Calculated boundary layer parameters ($i = 7.5$ deg)

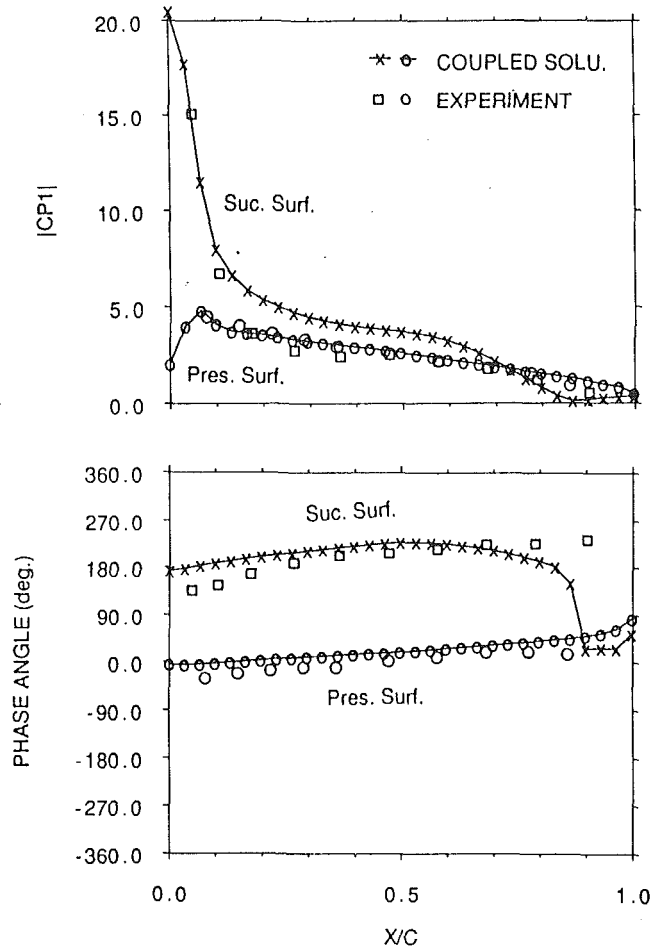


Fig. 10 Amplitude and phase angle of first harmonics of unsteady pressure coefficient ($i_{av} = 7.5$ deg)

chord compared with the measured data. The calculated boundary layer displacement thickness and shape factor distributions are presented in Fig. 6. A laminar separation bubble is predicted at about 60–80 percent chord position, which is also indicated in the measurement (He and Denton, 1991).

The calculated amplitude and phase distributions of the first harmonics of the unsteady pressure coefficient by the coupled solution are compared with the experimental data in Fig. 7, which shows a quite good agreement. In the separation bubble region the amplitude is underpredicted. From the phase distribution, the influence of the separation bubble is clearly demonstrated by about a 90 deg local phase-lead in the rear part of the bubble. This phase variation could not be predicted by the purely inviscid solution (He, 1990b).

Case 2 (7.5 deg Time-Mean Incidence). Figure 8 shows the steady pressure coefficient distributions from the coupled solution and the experiment. It is noted that the agreement between these two is only fair. A possible reason for the discrepancy between the calculation and the experiment may be that the modeling of the quasi-three-dimensional effect, which is expected to be more influential at a higher loading condition, is inaccurate. The calculated boundary layer parameter distributions are presented in Fig. 9. The rapid growth of the suction surface boundary layer approaching the trailing edge separation is clearly shown by both δ^* and H variations. A trend toward the leading edge bubble-type turbulent separation on the suction surface is indicated by the shape factor distribution. On the pressure surface the boundary layer remains fully laminar.

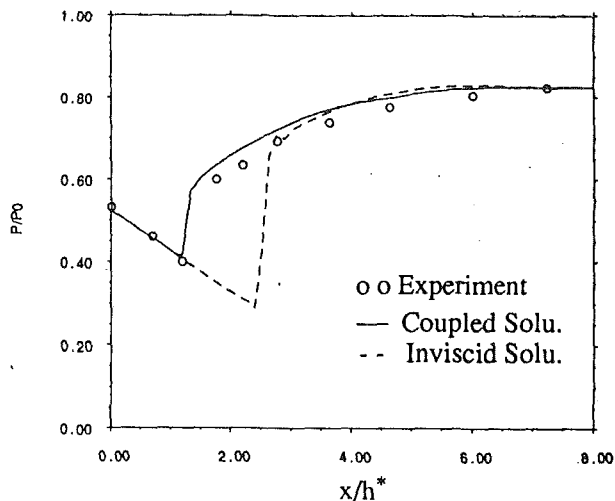


Fig. 11 Steady relative pressure on top wall of duct

Figure 10 shows the amplitude and phase distributions of the first harmonics of the unsteady pressure coefficient from the coupled approach and the experiment. For the phase there is a marked discrepancy around 70~90 percent chord on the suction surface. This may be because both the measured and calculated unsteady pressure amplitudes in this region are very small, so that a large uncertainty is involved in determining the corresponding phase angles. The discrepancy of the phase angle of the unsteady pressure around the leading edge of the suction surface may be attributed to low resolution of the leading-edge flow.

3.2 Transonic Duct Flow. A transonic diffuser flow with both steady and unsteady measurements, tested by McDonnell-Douglas (Bogar et al., 1983; Salmon et al., 1983; Sajben et al., 1984) is calculated to check the present coupled solution at a high-speed flow condition.

The steady calculation is performed at a constant back pressure condition:

$$P_2/P_0 = 0.826$$

Under this condition the experimental results show that the shock wave with $M_{sh} = 1.24$ is positioned at $x/h^* = 1.4$, where h^* is the diffuser throat height and x is measured from the location of the throat. The computational domain is taken from $x/h^* = -4$ to $x/h^* = 8$. To get a better resolution of the shock, the computational mesh is gradually refined around $x/h^* = 1.4$, with the minimum mesh length $\Delta x/h^* = 0.0625$.

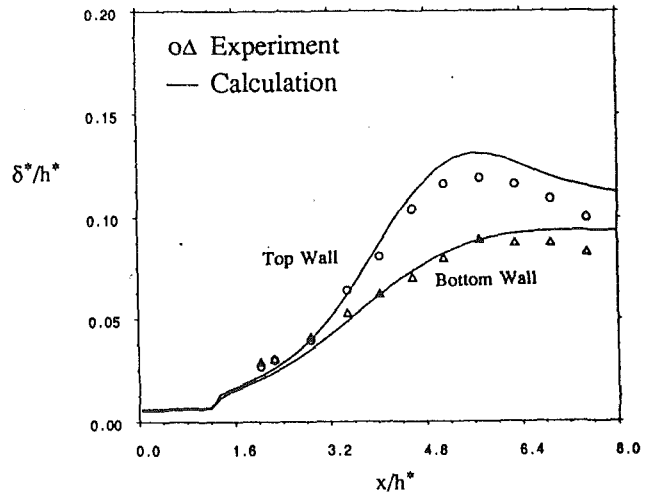
The boundary layers on both the top and bottom walls are assumed to be turbulent. The same inlet boundary layer thickness is specified as that used by Hsieh et al. (1984), who adopted a full Navier-Stokes solver, and Allmaras (1989) who adopted a coupled Navier-Stokes/Euler solver for this case:

$$\text{Top wall: } \delta = 0.090 h^*$$

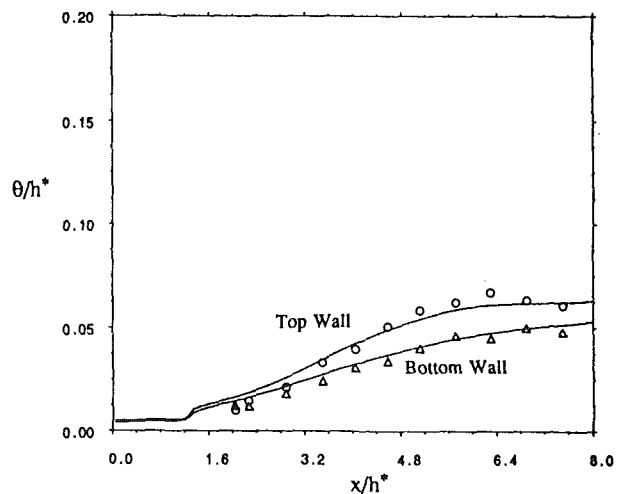
$$\text{Bottom wall: } \delta = 0.0045 h^*$$

Figure 11 shows the calculated steady pressure distribution along the top wall compared with the experimental data. The comparison between the calculation and the experiment for the displacement thickness and momentum thickness distributions of the boundary layers on both walls is given in Fig. 12. The predicted shock wave position is about $x/h^* = 1.35$, slightly upstream of the experimental one. An inviscid solution under the same conditions (also shown in Fig. 11), however, predicts the shock wave position at about $x/h^* = 2.7$, illustrating the significant effect of boundary layer blockage.

The unsteady calculation is performed for the flows with



(a). Displacement Thickness



(b). Momentum Thickness

Fig. 12 Comparison of boundary layer parameters

forced outlet pressure oscillation. The unsteady pressure distributions in the region downstream of the shock wave position were measured by Sajben et al. (1984). The experimental unsteady pressure data reveal a fairly harmonic pattern at the exit. Hence in the present calculation, the static pressure variation in time at the exit is approximated by a sinusoidal form:

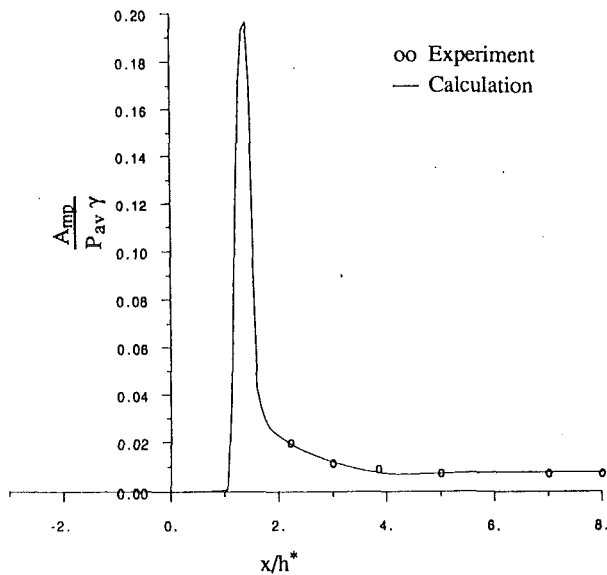
$$P_2 = P_{2av}(1 + Am_p \sin \omega t) \quad (1)$$

Figure 13 shows the amplitude and phase distributions of the first harmonics of unsteady pressure under the conditions:

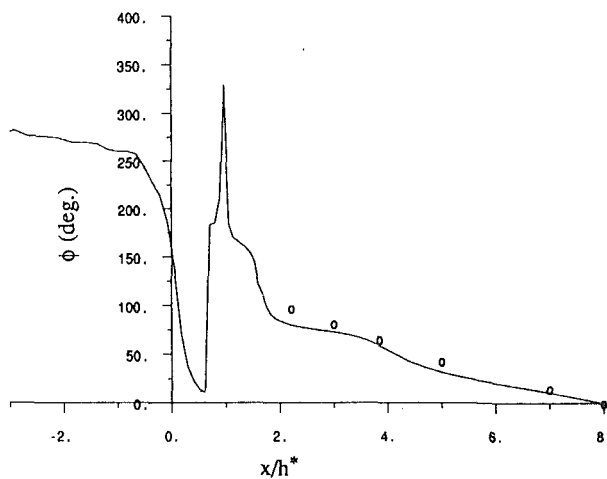
$$f = 150 \text{ Hz}, \quad Am_p = 0.011, \quad k = \frac{\omega h^*}{a_0} = 0.117,$$

The comparison of the amplitude of the shock wave movement between the calculation and the experiment for three frequency conditions is given in Fig. 14. The frequency dependence of the forced shock wave oscillation is well predicted.

3.3 Transonic Biconvex Cascade. The unsteady transonic flows around a biconvex cascade have been calculated using the inviscid Euler solver by He (1990a). There are two distinctively different types of shock wave motion, the sinusoidal type and the propagating type. The latter is of a very nonlinear nature. Here, in order to demonstrate the unsteady viscous



(a). Amplitude



(b). Phase Angle

Fig. 13 First harmonics of unsteady pressure on top wall

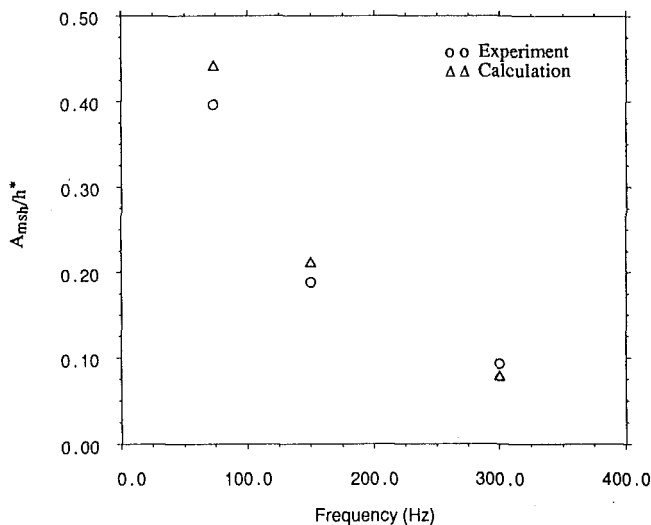


Fig. 14 Amplitude of shock motion at different frequencies

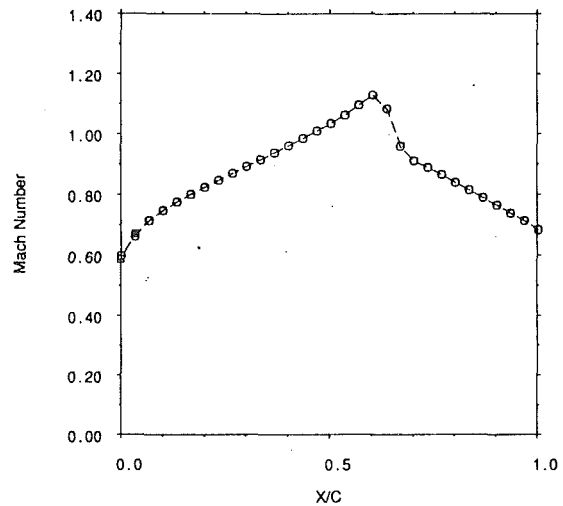


Fig. 15 Steady Mach number distribution ($P_2/P_0 = 0.708$)

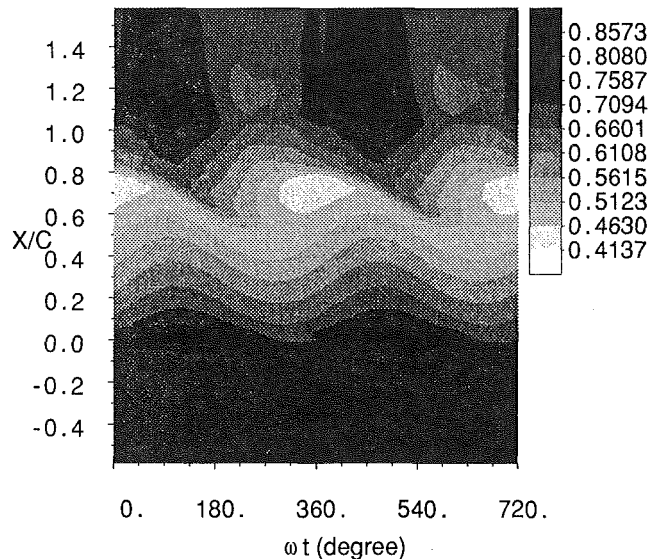


Fig. 16 S-T contour of surface static pressure (P/P_0)

effects in a situation of transonic cascade flow, a test case with the same geometry and under the same steady and unsteady conditions is calculated. The outlet back pressure condition is:

$$P_2/P_0 = 0.708$$

The inviscid Euler solution for the oscillating cascade at this back pressure condition predicted a sinusoidal shock motion, which is confined in a small region near the trailing edge (He, 1990a).

In the present calculation, the boundary layers are assumed to be turbulent from the leading edge. Figure 15 shows the calculated steady Mach number distribution. It should be mentioned that the inviscid solution at the same back pressure condition gives a strong shock wave at around 85 percent chord position (He, 1990a), while the present coupled solution gives a much weaker shock at about 60 percent chord. Figure 16 shows the S-T contour of the relative static pressure on the upper surface in two periods, calculated under the same unsteady conditions as those in the inviscid calculation. It can be seen that the shock wave movement calculated by the present coupled method is very different from its counterpart by the inviscid Euler solver (He, 1990a). Actually it is more like a

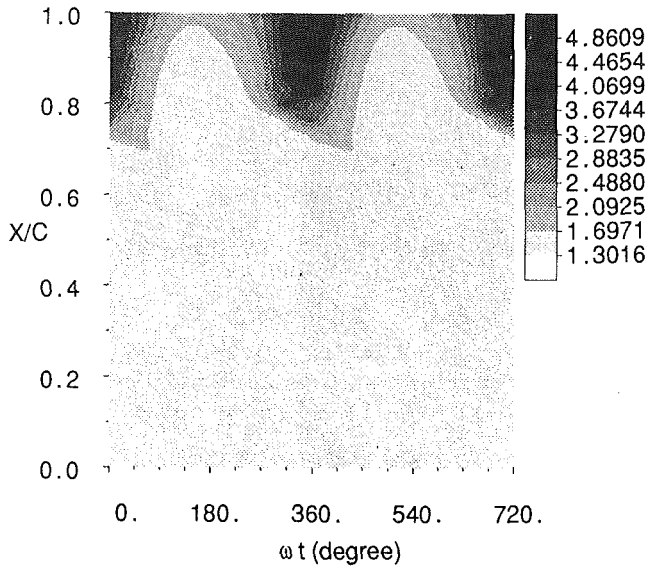


Fig. 17 S-T contour of boundary layer shape factor

periodic upstream propagating shock wave, which is dominated by a strong nonlinear mechanism. This marked viscous effect may result from two aspects. First, the steady (time-mean) boundary layer blockage results in a farther upstream time-mean shock wave position. As indicated by the inviscid calculation, a shock near the throat is moving in a quite nonlinear way once the cascade is oscillating. Second, the strong unsteady inviscid-viscous interaction affects the unsteady boundary layer behavior. Figure 17 shows the S-T contour of the boundary layer shape factor on the upper surface. Comparing this S-T plot with that for the static pressure (Fig. 16), we can see that when the symmetrically oscillating cascade reaches its maximum divergent shape at $\omega t = 270$ deg, a passage shock begins to form around 80 percent chord. A trailing-edge turbulent separation is then induced with about a 45 deg phase lag. Hence when the cascade passage is getting less and less divergent, the passage shock wave is pushed upstream not only owing to a changed geometry, but also owing to enhanced instantaneous viscous blockage.

3.4 Transonic Fan Tip Section. The final case of the present calculation is for a transonic tip section cascade of a low-pressure fan, for which a fully three-dimensional steady viscous solution was available. The tip section is subject to a supersonic inlet flow. The present calculation is carried out at the design condition for this tip section:

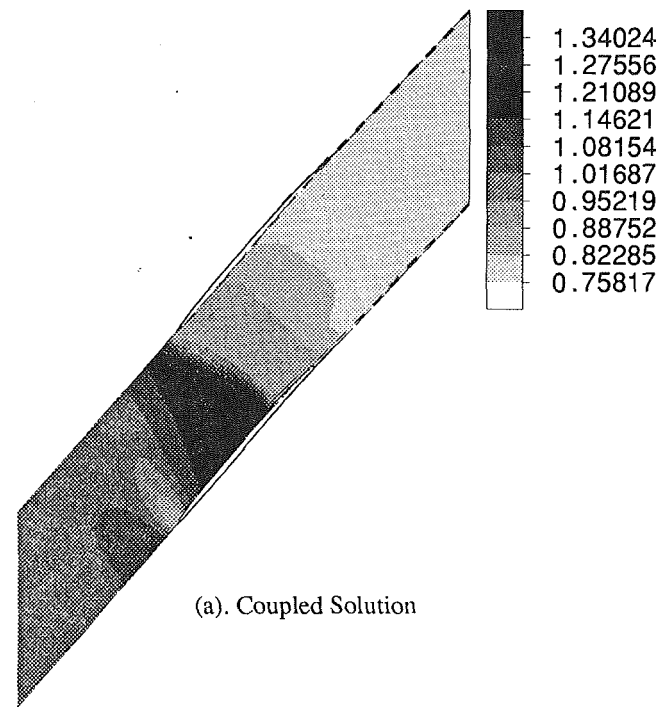
$$M_1 = 1.06$$

$$P_2/P_0 = 0.644$$

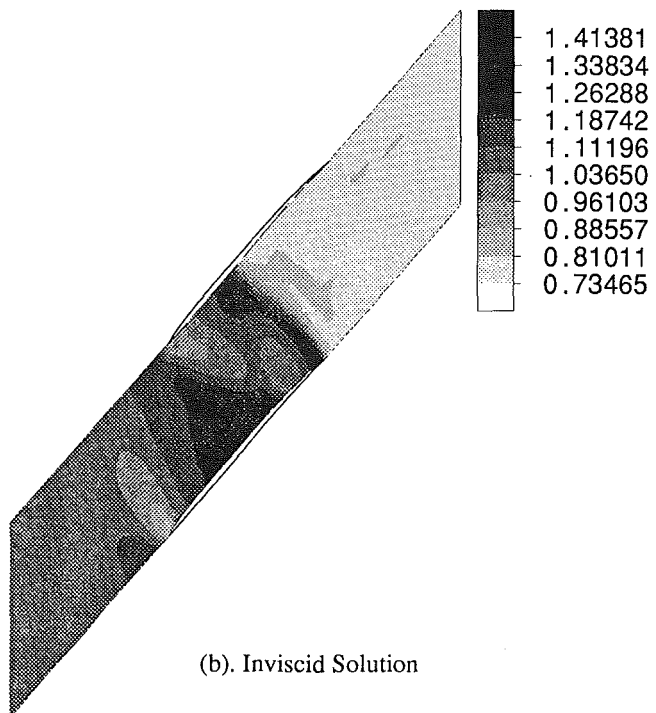
The surface boundary layers are assumed to be turbulent from the leading edge.

The calculated steady Mach number contours by both the coupled solution and the pure inviscid solution are shown in Fig. 18. In the results from the coupled solution (Fig. 18a), the passage shock is slightly detached from the leading edge with its foot being on the suction surface around 55 percent chord. The whole flow pattern agrees well with that designed by the fully three-dimensional viscous flow calculation. The inviscid Euler solution (Fig. 18b), however, predicts a very different flow pattern. In the inviscid result, there is a strong and normal passage shock near the suction surface trailing edge. The front part of the passage seems subject to a reflecting oblique shock wave system.

Unsteady calculations using both the inviscid and coupled methods are performed at the following conditions:



(a). Coupled Solution



(b). Inviscid Solution

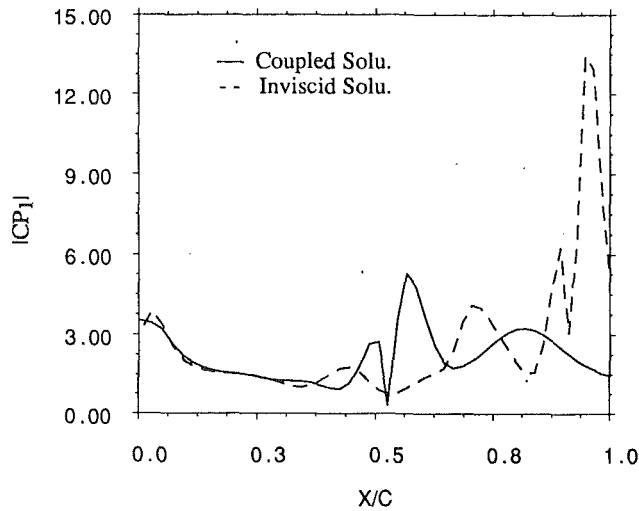
Fig. 18 Calculated steady Mach number contours

$$A_{mt} = 1 \text{ deg (torsion around the leading edge)}$$

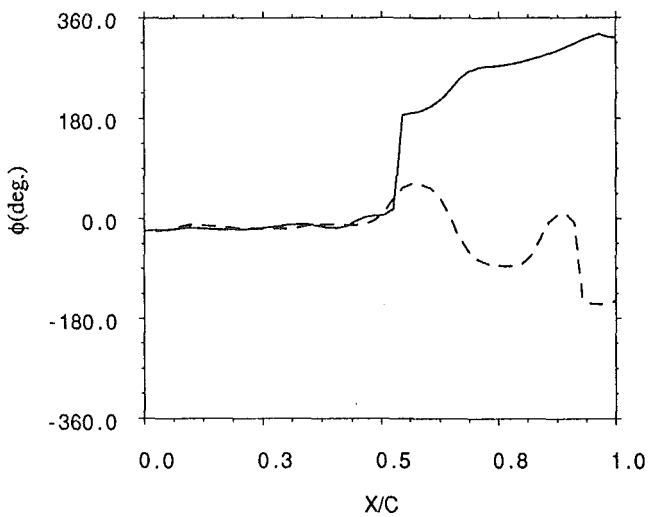
$$f = 425 \text{ Hz } (k = 1)$$

$$\sigma = 180 \text{ deg}$$

The calculated first harmonic pressure distributions on the suction surface are shown in Fig. 19, and those on the pressure surface are shown in Fig. 20. It is not surprising that the inviscid-viscous coupled solution and the pure inviscid solution produce substantially different results, considering the difference in the steady flow features predicted by the two methods. For instance, on the pressure surface, the inviscid solution is mainly subject to a shock-induced local pressure fluctuation

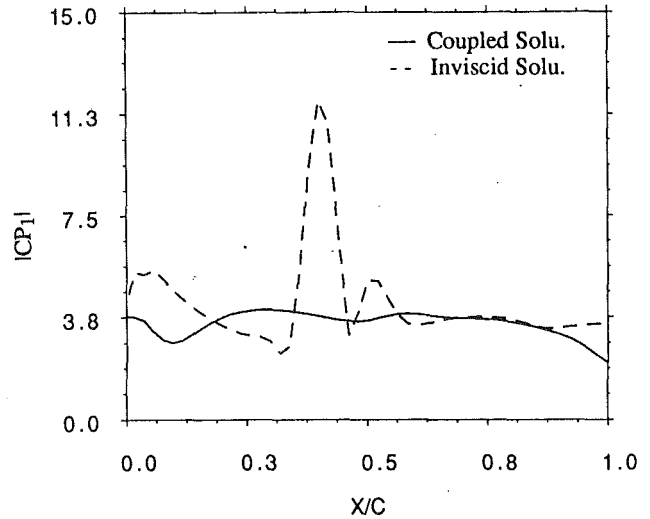


(a) Amplitude

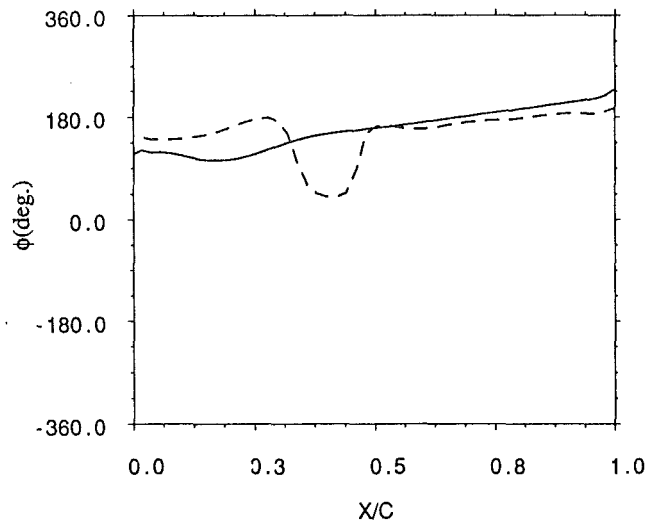


(b) Phase Angle

Fig. 19 Unsteady pressure on suction surface



(a) Amplitude



(b) Phase Angle

Fig. 20 Unsteady pressure on pressure surface

around 40 percent chord, while in the results of the coupled solution, the unsteady surface pressure has a smooth distribution because the passage shock is slightly detached from the upper blade leading edge. The results shown in Figs. 19 and 20 demonstrate the significant viscous blockage effect on the unsteady blade loading at transonic flow conditions, and therefore highlight the importance of including viscous effects in predictions of compressor blade flutter.

4 Concluding Remarks

To include viscous flow effects efficiently in the blade flutter calculations, a time-marching Euler/integral boundary layer coupling approach has been developed (He and Denton, 1993). Calculations for the following steady and unsteady flow cases with strong inviscid-viscous interactions are carried out for validation of the method and the computer code:

- Steady flow over a low-speed supercritical compressor cascade with laminar separation bubble.

- Steady flow over a transonic compressor cascade with trailing-edge separation.
- Unsteady flow around a low-speed oscillating airfoil with laminar separation bubble and trailing-edge turbulent separation.
- Unsteady transonic duct flow with shock/boundary layer interaction subject to back pressure oscillation.

The calculated results are compared with the corresponding experimental data

A calculation for transonic unsteady flows around the bi-convex oscillating cascade reveals that the inclusion of unsteady viscous effects changes the pattern of unsteady shock wave movement. It is shown by calculated results for a transonic fan tip section that the passage viscous blockage significantly affects both steady and unsteady loadings, which highlights the necessity of including viscous flow effects in predictions of practical blade flutter.

Finally, it should be mentioned that for a typical quasi-three-dimensional oscillating cascade flow, the present inviscid-vis-

coupled solution requires about 30~40 percent more CPU time than does the previous purely inviscid Euler solver.

Acknowledgments

This work has been financially sponsored by Rolls-Royce plc. The authors wish to thank Drs. P. Stow, A. Cargill, and A. Suddhoo (Theoretical Science Group, Rolls-Royce, Derby) for their continuous interest and technical support. During his study at Cambridge University, L. He has been in receipt of the O.R.S. Award and the Edward Boyle Memorial Scholarship, in addition to a sponsorship from Rolls-Royce.

References

Allmaras, S. R., 1989, "A Coupled Euler/Navier-Stokes Algorithm for 2-D Unsteady Transonic Shock/Boundary Layer Interaction," GTL Report #196, Massachusetts Institute of Technology, Cambridge, MA.
Bogar, T. J., Sajben, M., and Kroutil, J. C., 1983, "Characteristic Frequencies of Transonic Diffuser Flow Oscillations," *AIAA J.*, Vol. 21, No. 8.

Dong, Y., 1988, "Boundary Layers on Compressor Blades," Ph.D. Thesis, Cambridge University Engineering Dept., Cambridge, United Kingdom.
He, L., 1990a, "An Euler Solution for Unsteady Flows Around Oscillating Blades," *ASME JOURNAL OF TURBOMACHINERY*, Vol. 112, pp. 714-722.
He, L., 1990b, "Unsteady Flows Around Oscillating Turbomachinery Blades," Ph.D. Thesis, Cambridge University Engineering Dept., Cambridge, United Kingdom.
He, L., and Denton, J. D., 1993, "Inviscid-Viscous Coupled Solution for Unsteady Flows Through Vibrating Blades—Part I. Description of the Method," *ASME JOURNAL OF TURBOMACHINERY*, Vol. 115, this issue, pp. 94-100.
He, L., and Denton, J. D., 1991, "An Experiment on Unsteady Flow Over an Oscillating Airfoil," *ASME Paper No. 91-GT-181*.
Hsieh, T., Wardlaw, A. B., Jr., Collins, P., and Coakley, T. J., 1984, "Numerical Investigation of Unsteady Inlet Flow Fields," *AIAA Paper No. 84-0031*.
Sajben, M., Bogar, T. J., and Kroutil, J. C., 1984, "Forced Oscillation Experiments in Supercritical Diffuser Flows," *AIAA J.*, Vol. 22, No. 4.
Salmon, J. T., Bogar, T. J., and Sajben, M., 1983, "Laser Doppler Velocimeter Measurements in Unsteady, Separated Transonic Diffuser Flows," *AIAA J.*, Vol. 21, No. 12.
Stow, P., 1989, "Blading Design for Multi-stage HP Compressors," in: *Blading Design for Axial Turbomachines*, AGARD-LS-167.
Stow, P., Cargill, A., and Suddhoo, A., 1989, Rolls-Royce, Private Communication.

Validation of a Numerical Method for Unsteady Flow Calculations

M. Giles

R. Haimes

Department of Aeronautics and Astronautics,
Massachusetts Institute of Technology,
Cambridge, MA 02139

This paper describes and validates a numerical method for the calculation of unsteady inviscid and viscous flows. A companion paper compares experimental measurements of unsteady heat transfer on a transonic rotor with the corresponding computational results. The mathematical model is the Reynolds-averaged unsteady Navier-Stokes equations for a compressible ideal gas. Quasi-three-dimensionality is included through the use of a variable streamtube thickness. The numerical algorithm is unusual in two respects: (a) For reasons of efficiency and flexibility, it uses a hybrid Navier-Stokes/Euler method, and (b) to allow for the computation of stator/rotor combinations with arbitrary pitch ratio, a novel space-time coordinate transformation is used. Several test cases are presented to validate the performance of the computer program, UNSFLO. These include: (a) unsteady, inviscid flat plate cascade flows (b) steady and unsteady, viscous flat plate cascade flows, (c) steady turbine heat transfer and loss prediction. In the first two sets of cases comparisons are made with theory, and in the third the comparison is with experimental data.

Introduction

In the last seven years there have been several research groups working on the development of methods for the calculation of unsteady flows in turbomachinery (Hodson, 1985; Koya and Kotake, 1985; Rai, 1987a, 1987b; Fourmaux, 1986; Lewis et al., 1987; Gibeling et al., 1988). At MIT we have also been working on unsteady flow calculation methods for the last five years, starting initially with an inviscid wake/rotor interaction program (Giles, 1988a). Later, additional capabilities were added including a shearing interface treatment for the analysis of stator/rotor interaction. Results have been presented (Giles, 1990) of a calculation of the strongly unsteady flow in a transonic turbine, with oblique shocks extending from the stator trailing edge reflecting off the downstream rotor. Visualization of the unsteady flow field revealed a great amount of detail about the shock propagation, which led to improved understanding and interpretation of experimental data at Oxford University (Johnson et al., 1990).

The current version of the program UNSFLO has been extended to include viscous flow analysis, and a companion paper (Abhari et al., 1992) presents a viscous analysis of the same transonic turbine, and compares the unsteady heat transfer to experiments performed at MIT in the Gas Turbine Laboratory Blowdown Turbine Facility. One purpose of this paper is to present an overview of the numerical methods used by UNSFLO, concentrating on the three most unusual features, the hybrid viscous/inviscid algorithm, the technique for analyzing stator/rotor interactions with arbitrary pitch ratios, and the variety of different unsteady boundary condition options. The second purpose of this paper is to present test cases that thor-

oughly validate the program. This is not an easy thing to do, and many papers have been published showing unsteady flow calculations but with very limited attempts at validation. This paper shows the variety of analytic test cases that exist for different unsteady flows and shows the good level of agreement that can be obtained.

Numerical Method

Basic Inviscid and Viscous Algorithms. In viscous flow computations the computational grid has two parts. As shown in Fig. 4 one part is a structured O-type mesh around each blade. This mesh, which will be referred to as the viscous grid, is at least as wide as the boundary layer thickness and has the necessary grid resolution to resolve the details in the boundary layer. The other part of the grid, which will be referred to as the inviscid grid, is an unstructured finite-element type of mesh composed of an arbitrary mix of quadrilateral and triangular cells.

On the viscous grid the equations of motion that are solved are the unsteady Reynolds-averaged Navier-Stokes equations. The Reynolds averaging gives the mean effect due to the turbulence averaged over the short turbulent time scales, while leaving alone the longer time-scale unsteadiness due to wake-passing, stator/rotor interaction, etc. The Reynolds stresses due to the turbulence are modeled using the simple Cebeci-Smith algebraic turbulence model (Cebeci and Smith, 1974). Quasi-three-dimensional effects are included through the specification of a streamtube thickness in the third dimension. Using the structured nature of the viscous grid, the numerical method is an ADI (alternating-direction-implicit) method with Roe's flux-difference splitting (Roe, 1986) giving third-order upwinding for the residual operator and first-order upwinding for the implicit operator. This is similar to the method used

Contributed by the International Gas Turbine Institute and presented at the 36th International Gas Turbine and Aeroengine Congress and Exposition, Orlando, Florida, June 3-6, 1991. Manuscript received at ASME Headquarters March 4, 1991. Paper No. 91-GT-271. Associate Technical Editor: L. A. Riekert.

by Rai (1987b). A sonic line treatment based on the recent ideas of van Leer et al. (1989) is used to prevent expansion shocks through the use of a minimal level of numerical smoothing. Full details on the viscous algorithm will be available soon in a technical report (Giles, 1991).

On the inviscid grid, the equations that are solved are the Euler equations, again with a streamtube thickness specified in the third dimension. The numerical method is a generalization of Ni's Lax-Wendroff algorithm (Ni, 1981), and is also similar to the Euler-Taylor-Galerkin finite element method of Löhner et al. (1985). Full second-order accuracy is achieved on irregular meshes through the use of a carefully constructed fourth difference smoothing, which does not corrupt linear solutions, and a second difference shock smoothing using an adaptive coefficient based on the flow divergence. Full details of the inviscid algorithm are given in a technical report (Giles, 1988b).

Both the Navier-Stokes equations and the Euler equations are solved in their conservative formulation, in which the unknown variables are $U = (\rho, \rho u, \rho v, \rho E)T$, the density, momentum components, and total internal energy. The corresponding equations are based upon a control volume formulation of the mass, momentum, and energy equations and thus correctly capture steady and moving shocks. At the interface between the viscous and inviscid grids, the viscous and inviscid algorithms are linked in a manner that uses a consistent definition of the fluxes across the interface, and thus maintains absolute conservation; i.e., no mass, momentum, or energy is lost at the interface. In addition, the smoothing operators are carefully constructed to keep the solution smooth through the interface. For purely inviscid flow computations, no viscous grid is used and the boundary of the inviscid grid is the blade surface. At this surface the boundary treatment is a slip condition that allows a tangential velocity but no normal velocity.

The hybrid viscous/inviscid scheme outlined above is unusual. It is certainly more complicated to implement than most other schemes for turbomachinery, but there are a number of advantages. First, the choice of an implicit ADI method to calculate the viscous flow region was motivated by the desire to do time-accurate unsteady flow computations. An explicit Navier-Stokes method with sufficient grid resolution to resolve leading edge boundary layers properly would need an extremely small time step due to the CFL stability limit, and so would be excessively expensive for unsteady computations. The selection of an implicit method meant that a structured grid was required since there are at present no well-established implicit methods for unstructured grids.

Having decided on a structured grid around each blade for the viscous computation, there were several options for the rest of the domain. One was to extend the viscous grid to cover the whole blade passage, either as a C-mesh or an O-mesh. In both cases this would cause problems in the upstream far field where the mesh would inevitably be rather coarse. This would lead to excessive numerical diffusion of incoming wakes in wake/rotor interaction. It also would not give the flexibility to perform complex pylon/OGV (outlet guide vane) calculations. The second option was to use the type of multiblock grid system used by Rai (1987b). This would solve the problem of inadequate grid resolution upstream, but would involve significant complications in grid generation and the flow algorithm, and would still not give the flexibility to analyze pylon/OGV configurations efficiently.

The third option that was adopted in this work, an outer unstructured grid and an explicit flow algorithm, gives the flexibility to form a grid around any size and shape of bodies using a triangular cell advancing front grid generator based on the work of Lo (1985) and Peraire et al. (1988). A description of the grid generator and examples of its usefulness for pylon/OGV calculations are given in a paper by Lindquist and Giles (1990). For more standard cascade configurations a modified

H-mesh grid generator is used to produce an unstructured grid of rectangular cells, with a line of triangular cells at the inflow and outflow. The purpose of the triangular cells is to reduce the shearing of the quadrilateral cells by making the grid more orthogonal. An additional advantage of the unstructured grid approach is that the grid can be adapted later by subdividing triangular cells to give enhanced resolution of high-gradient flow features such as shocks or separated shear layers. This capability has been added recently but is not used in this paper.

There are two weaknesses of the current algorithm. The first is the turbulence model, which is the standard Cebeci-Smith model. Being an algebraic model, it bases the local turbulent viscosity on the instantaneous local velocity profile, and does not take into account any "history" effects due to the temporal or spatial development of the flow field. In addition, transition is currently specified by the user, based on experimental data, or at the leading edge for flows with high free-stream turbulence levels. At present work is under way to replace this turbulence model with a one-equation kinetic energy model combined with an algebraic length scale. This model will also allow for the calculation of the effect of a turbulent wake on the transition of the boundary layer on a downstream blade.

The second weakness is that the wake is treated inviscidly since the viscous grid is limited to the boundary layer region. This is believed to be a relatively minor error, since the reduced decay of the wake due to the absence of the physical viscosity is probably offset largely by the additional decay due to the inevitable presence of numerical smoothing. Also, the unsteady forces on a downstream blade row due to wake/blade interaction are largely dependent on the integrated momentum defect in the wake and this is independent of the rate of decay of the wake.

Unsteady Boundary Conditions. The utility of this program for the calculation of unsteady flows is greatly increased by being able to analyze a wide variety of different unsteady phenomena. The capabilities can be split into four categories. The first is unsteadiness in a single blade row due to unsteady inflow or outflow boundary conditions. This category includes: (a) wake/blade interaction in which the user can specify the velocity and temperature profile of the wake or hot streak coming into the blade row, (b) potential/blade interaction in which the user specifies a potential disturbance of fixed spatial form that travels across the inflow or outflow boundary, corresponding to the pressure field of a neighboring blade row, and (c) an outflow static pressure, which varies sinusoidally in time. In each of these cases there is a model for the far-field behavior of the flow, based on linear characteristic theory, and the boundary conditions are formulated in a nonreflecting manner that ensures that outgoing pressure and vorticity waves do not produce artificial reflections at the inflow and outflow boundaries (Giles, 1989b).

The second category is stator/rotor calculations in which the unsteadiness is due to the relative motion of the two blade rows. There are several different possible methods for treating the stator/rotor interface. The approach used here is to analyze the unsteady flow using grid-relative flow variables on two grids, one fixed to the stator and one to the rotor, and to combine the two by placing between the stator and rotor grids a line of cells for which a special form of the inviscid flow algorithm is required (Giles, 1990). This approach is conservative and produces acceptably well-behaved solutions at the interface. Overall, however, it is probably no better or worse than Rai's conservative sliding interface treatment (Rai, 1987a).

The third category is a single blade row with unsteadiness due to blade vibration. This has been implemented as an option only for viscous flow calculations. The viscous grid nodes on the blade surface move with the blade, and the nodes at the interface with the inviscid grid, as well as the entire inviscid grid, remain stationary. The grid nodes in the interior of the

viscous grid move appropriately, maintaining a straight line with fixed proportional spacing from blade to the inviscid interface. The viscous algorithm is modified to take account of the grid motion and the extra flux terms it produces (Giles, 1991).

The final category is natural unsteadiness, such as vortex shedding, which is due to flow instabilities and not to any unsteady boundary condition.

Periodic Boundary Condition. When the number of stators and rotors is equal, the periodic boundary condition is simple. The flow along one periodic surface is defined to be identical to the flow along the other periodic surface, which is displaced by one blade pitch. Mathematically, this is equivalent to enforcing the condition

$$U(x, y, t) = U(x, y + P, t), \quad (1)$$

where P is the blade pitch. Numerically this is achieved by enforcing the condition that the computational grid is periodic with values on one periodic surface being identical to those on the other.

When the number of stators and rotors is not equal, the flow does not have a simple spatial periodicity in the circumferential direction. Instead, the periodic boundary condition for a stator is now

$$U(x, y, t) = U(x, y + P_s, t + \Delta T), \quad (2)$$

where ΔT is equal to the difference between the stator pitch P_s and the rotor pitch P_r , divided by the rotor wheel speed V (Giles, 1988a):

$$\Delta T = (P_s - P_r) / V. \quad (3)$$

This time delay in the periodic boundary condition is equivalent to an interblade phase angle when one considers a single frequency of unsteadiness.

The numerical difficulty is how to implement the lagged periodic boundary condition that arises from the unequal pitches. Erdos et al. (1977) were the first to develop a method, and it has subsequently been used by Koya and Kotake (1985), Hodson (1985), and Lewis et al. (1987). The technique assumes that the flow field is periodic in time and involves the storage of a complete blade-passing period of unsteady flow data on both periodic surfaces, and the creation of boundary values by the interpolation of data at earlier times on the opposing periodic surface.

There are several drawbacks to Erdos' technique. One is that it requires a large amount of computer memory to store an entire period of information on each periodic surface. Another is that the use of boundary data, from (on average) half a period earlier on the opposite periodic surface, delays the convergence of the unsteady flow solution to the assumed final periodic state. Lewis et al. (1987) found that 15–20 blade-passing periods can be required for convergence to the periodic state, whereas calculations for unity pitch ratios require 5–7 periods.

For viscous calculations, the primary problem with the Erdos technique is the assumption of a final periodic state. This is incorrect in cases in which there is a second unrelated frequency of oscillation. The simplest example of this is vortex shedding at the trailing edge of a turbine. There is no reason to expect that the shedding frequency will be a multiple of the blade-passing frequency and so there will be no final periodic state and calculations with the Erdos boundary condition will fail to arrive at a self-consistent solution. Another more important example is the calculation of rotating stall in a single stage. The spatial extent of the rotating stall cell could be captured by performing a calculation with multiple stators and rotors, but there is again no final periodic state.

An alternative approach to the problem of the lagged periodic boundary condition was developed by Giles (1988a). It can be interpreted in two ways: From a computational per-

spective it can be viewed as a time-inclined computational plane (Giles, 1987), while from a mathematical viewpoint it is a space-time coordinate transformation:

$$\begin{aligned} x' &= x \\ y' &= y \\ t' &= t - \lambda y. \end{aligned} \quad (4)$$

The parameter λ is defined as

$$\lambda = \frac{\Delta T}{P}. \quad (5)$$

With this coordinate transformation, the lagged periodic boundary condition for the stator becomes

$$U(x', y', t') = U(x', y' + P_s, t'), \quad (6)$$

which is once again easily implemented numerically by making the discrete flow variables identically equal on the upper and lower periodic surfaces.

The simplicity in the periodic boundary condition is achieved at the expense of modifying the basic partial differential equations in the interior of the computational domain. When one transforms the two-dimensional Euler equations, written in the standard conservative vector form as

$$\frac{\partial U}{\partial t} + \frac{\partial F}{\partial x} + \frac{\partial G}{\partial y} = 0, \quad (7)$$

into the new computational coordinate system, the resultant equations are

$$\frac{\partial}{\partial t'} (U - \lambda G) + \frac{\partial F}{\partial x'} + \frac{\partial G}{\partial y'} = 0. \quad (8)$$

Thus the conservation state variables have changed from U to $Q = U - \lambda G$. For an inviscid flow of an ideal gas, this change in the conservation variables requires just minor changes to the basic numerical algorithm because one can calculate U from Q in closed form (Giles, 1987, 1988a). In stator/rotor calculations, the stator and rotor grids require different values of λ , since ΔT is the same for both and the pitches are different. In addition the time steps are different on the two grids because the blade passing period is different in the two frames of reference and the calculation requires matching numbers of timesteps per period. As a result, the interface treatment becomes more complicated (Giles, 1988b).

For a viscous flow calculation, there is a problem that at first sight is quite significant. The new conservation variables, $Q = U - \lambda G$, include viscous stress terms that involve spatial derivatives of flow variables. Therefore, it is impossible to deduce the local value of U from the local value of Q . This problem is solved by neglecting the viscous terms in Q . The justification for this is that the largest of the neglected terms are of the form $\partial^2 u / \partial n \partial t$, where $\partial / \partial n$ denotes a derivative normal to the blade surface across the boundary layer. For high Reynolds number flows these terms are a factor \sqrt{Re} smaller than the dominant normal derivative terms such as $\partial^2 u / \partial n^2$, and so can be safely neglected in the same manner that one neglects streamwise diffusion terms and spatial cross-derivatives terms (Giles, 1989a).

This space-time coordinate transformation method has its limitations. Due to domain-of-dependence restrictions, there are constraints on the magnitude of λ that can be used (Giles, 1987, 1988b). In stator/rotor interactions, depending on the true pitch ratio, it may be necessary to perform calculations with more than one stator or rotor. However, due to the faster convergence rate relative to the use of Erdos' technique, it will be more efficient for calculations in which the Mach number is not very small. For very small Mach numbers, and for flutter and forced response problems at very low reduced frequencies, and limitations on λ are such that many blade passages must

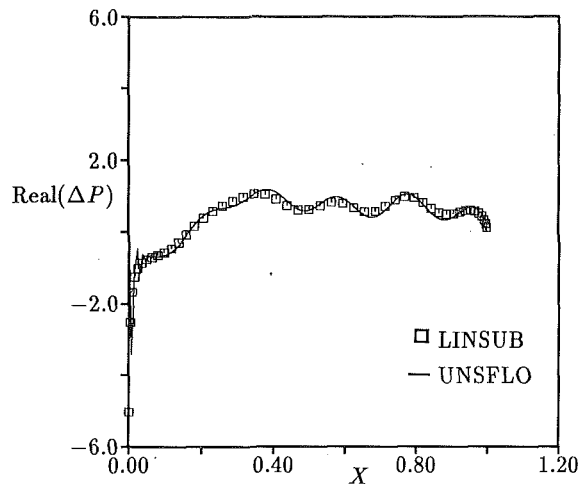


Fig. 1 Complex amplitude of pressure jump on flat plate due to wake interaction

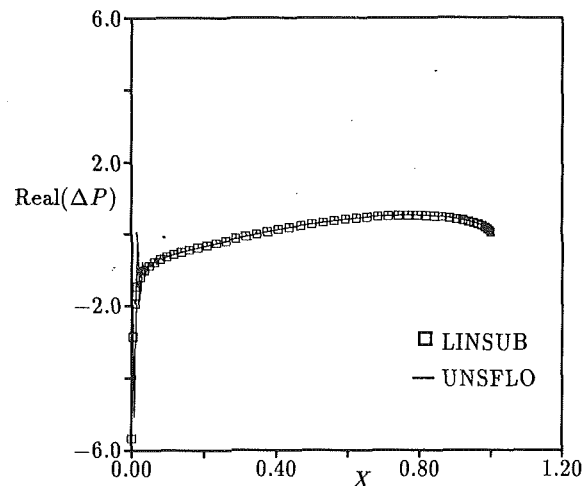
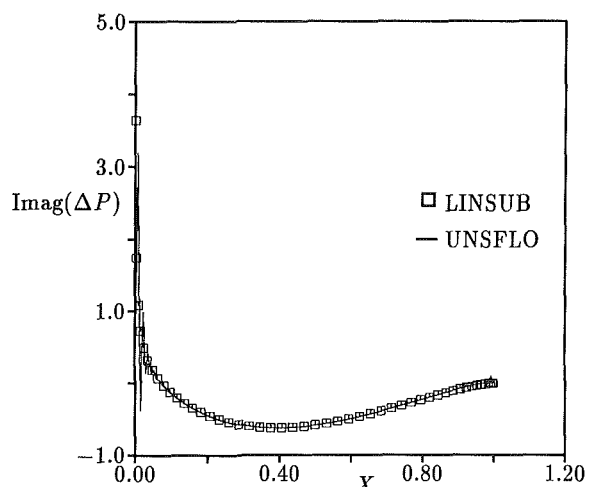
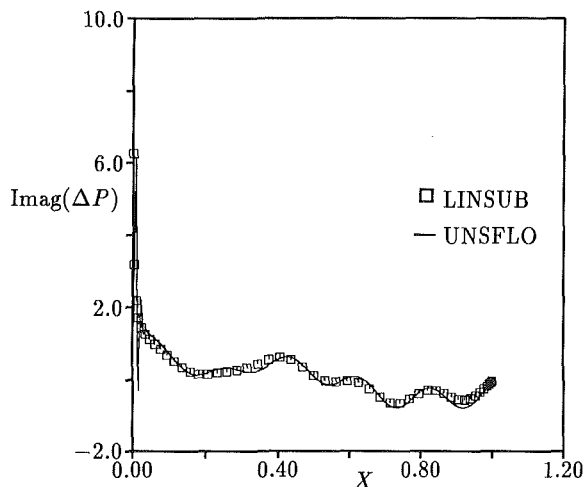


Fig. 2 Complex amplitude of pressure jump on flat plate due to oscillating back pressure



be calculated. For these calculations Erdos' technique is therefore preferable if one is sure that there is a consistent periodic final state.

A final observation is that both the space-time coordinate transformation and the Erdos technique are restricted in general to calculations in a single stage, with just two blade rows. If one considers three blade rows, then in typical real geometries the first and third row will have different numbers of blades, and therefore different blade pitches. Correspondingly, the middle blade row will experience two different blade passing frequencies. In this case it is not possible to perform an unsteady calculation with just one blade passage in each row. The minimum size of calculation that would be mathematically correct would include multiple blades in the first and third row in a ratio exactly matching the real geometry; this might often require the full annulus.

Results

Inviscid Flat Plate. The first set of test cases is for small amplitude, unsteady disturbances of a uniform inviscid steady flow past an unloaded flat plate cascade. The advantage of this configuration is that results can be compared to the linear inviscid analysis of Smith (1971). This analysis is based upon the distribution of a vorticity sheet along the flat plate cascade in a manner that satisfies the inviscid boundary condition that there is no relative flow normal to the flat plate. The formulation leads to an integral equation, which must be ap-

proximately solved computationally using the program LINSUB written by D. Whitehead (1987), but the solution can be obtained so accurately that for test purposes it may be considered to be an exact analytic solution. An attraction of the linear analysis as a test case is that it can be used in a variety of applications, for wake/blade interaction, potential/blade interaction, and bending or torsion of the blade, all with an arbitrary pitch ratio or interblade phase angle.

For all three test cases in this section, the flat plate cascade has a pitch/chord ratio of 0.5, a stagger angle of 30 deg, and a mean flow Mach number of 0.7. In each case the unsteadiness has a single frequency component and is of a sufficiently low amplitude that second-order nonlinear effects are negligible. The computational grid is extremely fine, 400×50 , to provide resolution of the leading and trailing edge singularities, as well as the waves in the high reduced frequency cases. Comparison with the linear theory is made by plotting the real and imaginary components of the nondimensional complex amplitude of the unsteady pressure difference across the plate.

The first test case is a wake/blade interaction, in which the incoming wake has a sinusoidal form, producing a single frequency response. The wake has a pitch that is a factor 0.9 smaller than the blade, and the flow angle in the wake frame of reference is -30 deg. This results in a high reduced frequency (based on axial velocity and axial chord) of 13.96, and so the unsteady pressure waves produced by the interaction have a wavelength that is a small fraction of the chord. Figure 1 shows the comparison between the unsteady pressure jump

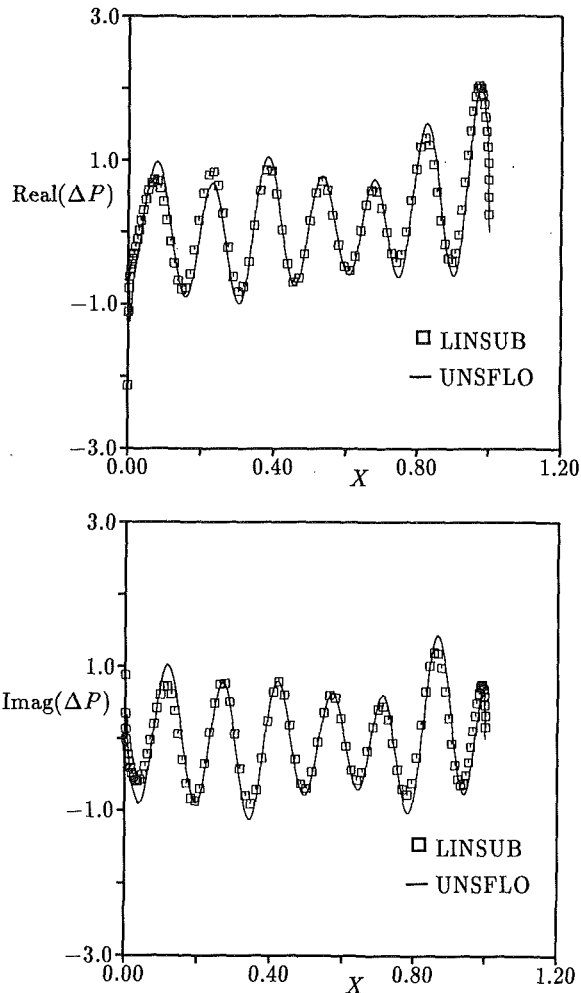


Fig. 3 Complex amplitude of pressure jump on flat plate due to outflow potential disturbance

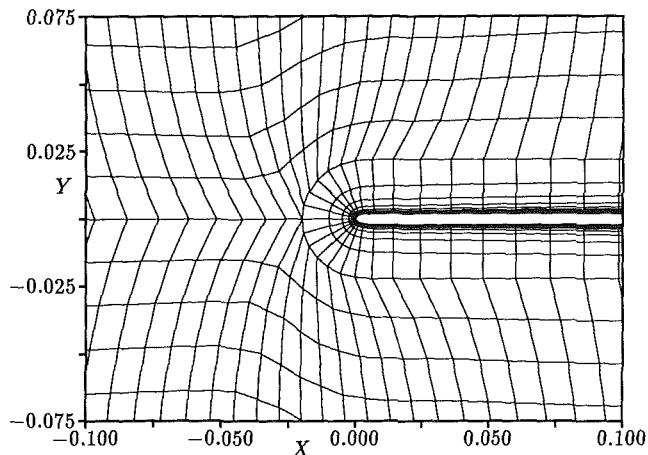


Fig. 4 Leading edge region of a viscous flat plate grid

distributions from UNSFLO (nonlinear, time-marching analysis) and LINSUB (linear theory).

In the second test case the exit static pressure is varied sinusoidally with a reduced frequency of 1.086. Figure 2 shows the comparison between the nonlinear and linear results. This low frequency case gives almost perfect agreement.

The final inviscid test case is a potential/blade interaction, in which the exit static pressure varies spatially across the outflow, with a sinusoidal form and a pitch that is a factor 0.667 smaller than the blade pitch. The mean flow angle in

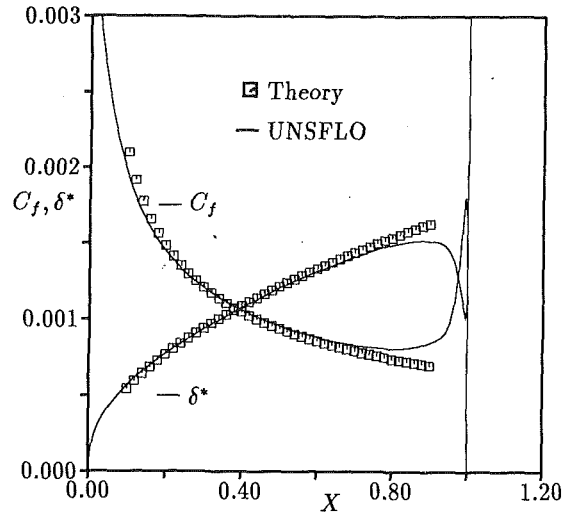


Fig. 5 Flat plate skin friction coefficient and displacement thickness

the frame of reference of the potential disturbance is -30 deg, giving a very high reduced frequency of 18.85. Figure 3 shows the comparison between the nonlinear and linear results. The very high reduced frequency makes this an extremely tough test case, since LINSUB and UNSFLO are both trying to resolve a single wavelength in no more than ten grid points.

In addition to validating the different inflow and outflow boundary conditions the first and third test cases are also a validation of the time-included computational plane procedure adopted to treat the problem of unequal pitches. Both calculations were performed with a single blade passage and a single incoming disturbance.

Viscous Flat Plate. This set of test cases begins with a steady calculation of a low Mach number flow over an unstaggered flat plate cascade. The blades have a 0.2 percent thickness and the leading edge is rounded carefully to avoid a leading edge separation. The pitch/chord ratio is unity so that the flow is as closely as possible equal to the flow over an isolated flat plate. Similarly, for comparison to Blasius boundary layer theory, the flow is chosen to be laminar with a Reynolds number of 10^6 , and the free-stream Mach number is 0.2.

Figure 4 shows the computational grid near the leading edge. The inviscid grid density is 150×60 , and the viscous grid density is 200×20 . Figure 5 compares the skin friction coefficient and displacement thickness with incompressible Blasius theory. In both cases the agreement is very good until the pressure gradient becomes nonzero near the trailing edge.

Using this steady flow as a base, three unsteady flow calculations were performed. In the first two, the blade was displaced in bending and torsion modes, with a zero interblade phase angle and a reduced frequency of 15.80. The unsteady flow in response to these motions is primarily inviscid, since in the absence of any unsteady flow the motion of the blades violates the inviscid boundary condition of zero relative flow normal to the blade surface. Therefore, for small amplitude unsteadiness the unsteady pressure distribution produced should correspond to that predicted by LINSUB using linear inviscid theory. Figures 6 and 7 show that this is indeed true. There is good agreement on the amplitude of the disturbance, and just a small shift in the phase. A particular implication of the agreement is that the viscous flow at the trailing edge agrees well with the Kutta condition imposed in the linear theory. This is of interest since the theoretical validity of the Kutta condition at high reduced frequencies is questionable, at best. In this application, however, the very thin trailing edge gives a reduced frequency based on diameter of 0.06 and so the flow in the neighborhood of the trailing edge is in a low-

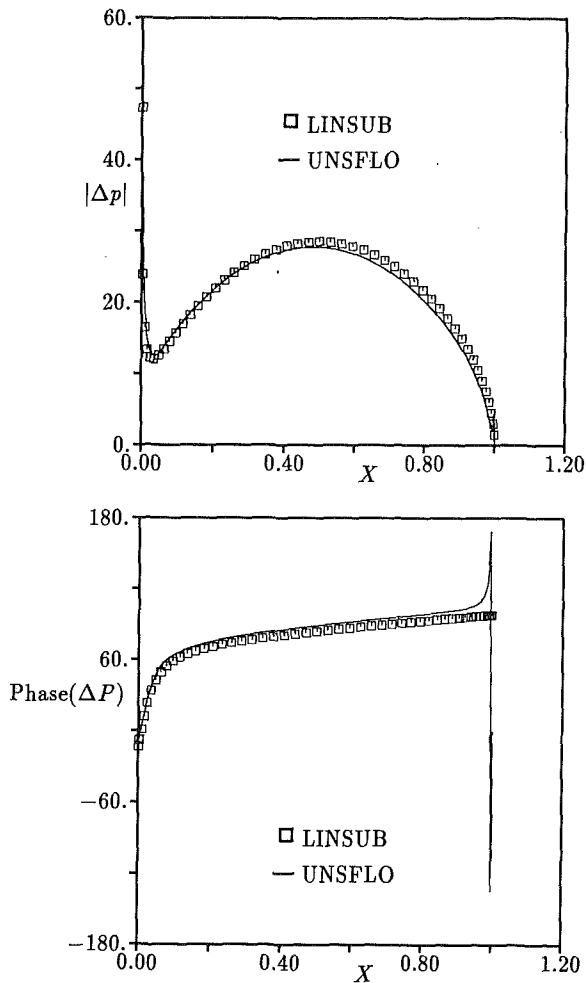


Fig. 6 Complex amplitude of unsteady loading on a flat plate cascade in bending

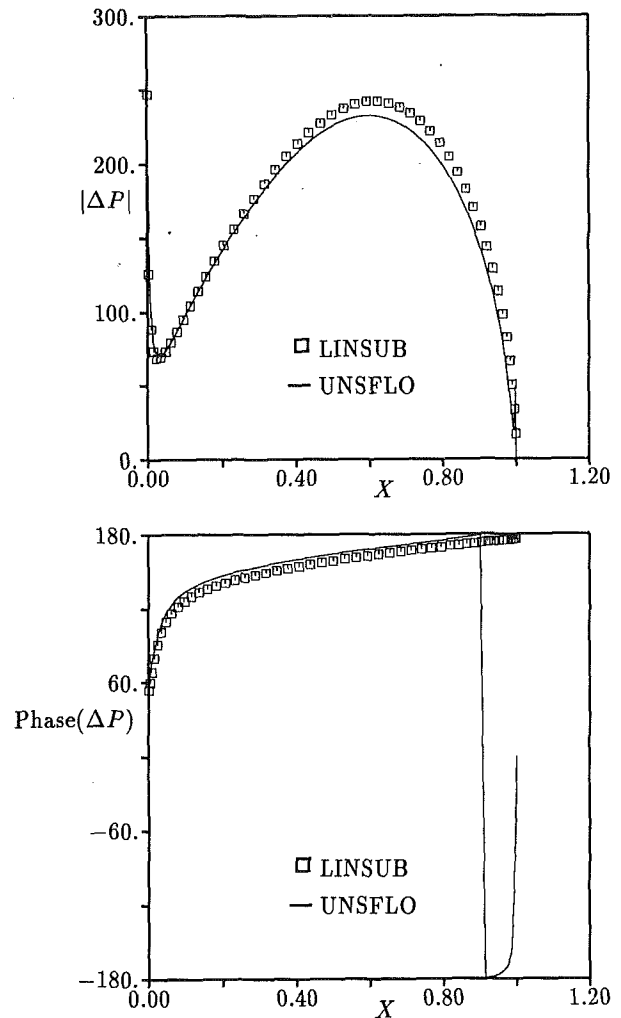


Fig. 7 Complex amplitude of unsteady loading on a flat plate cascade in torsion

frequency regime in which the Kutta condition should be an appropriate approximation to the true flow.

The third unsteady case imposes an oscillatory lateral motion of the flat plate along its own length. The lack of any normal velocity component, except at the leading and trailing edges, means that no significant unsteady inviscid flow is generated, and the unsteadiness is confined to the boundary layer as a consequence of the no-slip condition at the blade surface.

At very low reduced frequencies this would produce a quasi-steady flat plate boundary layer in the frame of reference of the moving plate, and would effectively reproduce the steady test case. Instead, the test case is computed for a very high reduced frequency. In this limit, the unsteady vorticity does not have sufficient time in one period to diffuse across the entire boundary layer, and is instead confined to a thin layer next to the surface. This layer is referred to as the Stokes layer since it corresponds to the classic Stokes problem of the flow generated by the oscillation of an infinite flat plate in a semi-infinite domain with stagnant conditions at infinity (Batchelor, 1967; Schlichting, 1979). The unsteady part of the velocity field on the upper surface of the blade is

$$u(x, y, t) = \Re \{ \hat{u}_w e^{-i\Omega t - \kappa y} \}, \quad (9)$$

where

$$\kappa = (1 - i) \sqrt{\frac{\Omega}{2\nu}}, \quad (10)$$

and the corresponding unsteady surface vorticity is

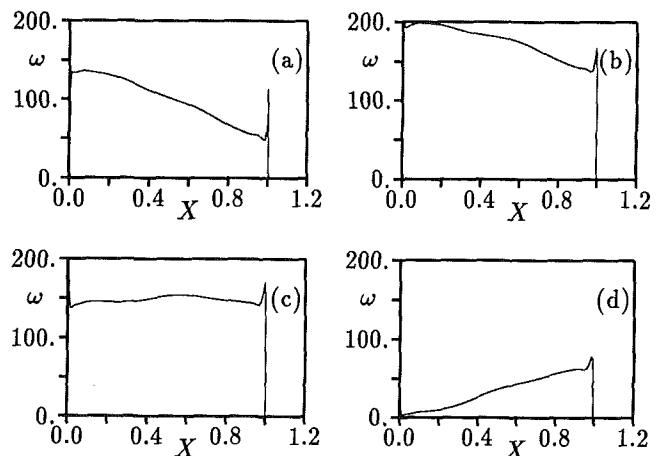


Fig. 8 Unsteady component of computed surface vorticity. Analytic values: (a) $t = 0.0$, $\omega = 141.0$; (b) $t = 0.125$, $\omega = 200.0$; (c) $t = 0.25$, $\omega = 141.0$; (d) $t = 0.375$, $\omega = 0.0$

$$\omega(x, 0, t) = -\frac{\partial u}{\partial y} = \Re \{ \kappa \hat{u}_w e^{-i\Omega t} \}. \quad (11)$$

This test case has also been used recently by Power et al. (1991) for the validation of an unsteady compressible boundary layer code.

Figure 8 plots the surface vorticity along the plate at four

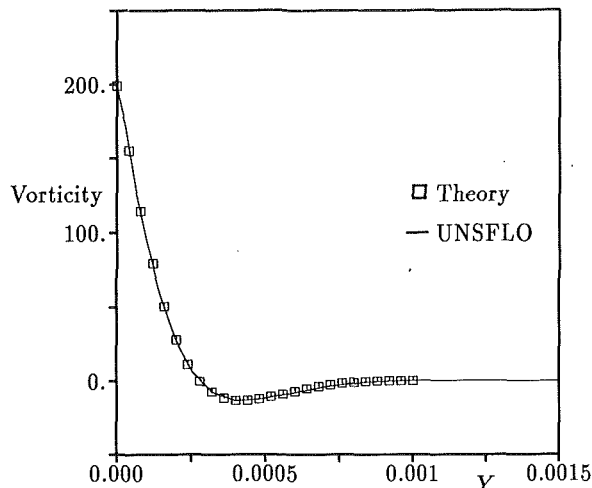


Fig. 9 Unsteady component of vorticity across oscillating plate boundary layer

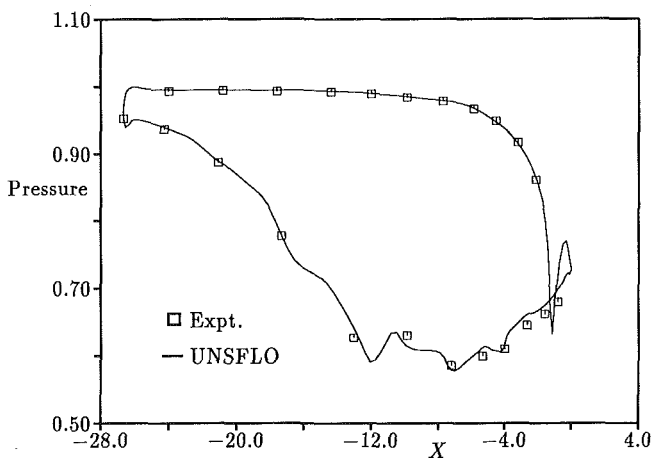


Fig. 10 Pressure distribution on turbine cascade

equally spaced times during one half period, and lists the corresponding analytic values, which do not depend on location. Clearly, the figures show that the numerical results do depend on location. For $0 < x < 0.4$ the agreement with analytic theory is quite good, both in magnitude and phase. Figure 9 shows the excellent agreement in the distribution of unsteady vorticity across the boundary layer at location $x = 0.2$ and time $t = 0.125$. However, toward the rear of the flat plate the predicted amplitude of unsteady vorticity is low by approximately 20 percent, and there is a phase lag of approximately 25 deg.

This spatial variation in the quality of the computed results is due to variations in the boundary layer grid resolution. The Stokes layer has a constant thickness of approximately 0.5×10^{-3} , while the steady boundary layer displacement thickness is approximately $2 \times 10^{-3} \times \sqrt{x}$. To resolve both the Stokes layer and the steady boundary layer in this case there are only 15 grid points. These points are distributed across the boundary layer with the outermost point lying just outside the steady boundary layer. A calculation was performed with the remaining points being equally spaced across the boundary layer. This gave much poorer results than those shown here, because at the rear of the blade it put only three points across the Stokes layer, which was woefully inadequate. In the calculation shown here, the grid points were stretched exponentially across the boundary layer, with a stretching ratio of 1.15, so that the normal grid spacing for the cell next to the blade is a factor $1.15^{14} \approx 7$ smaller than the outermost cell. Despite this im-

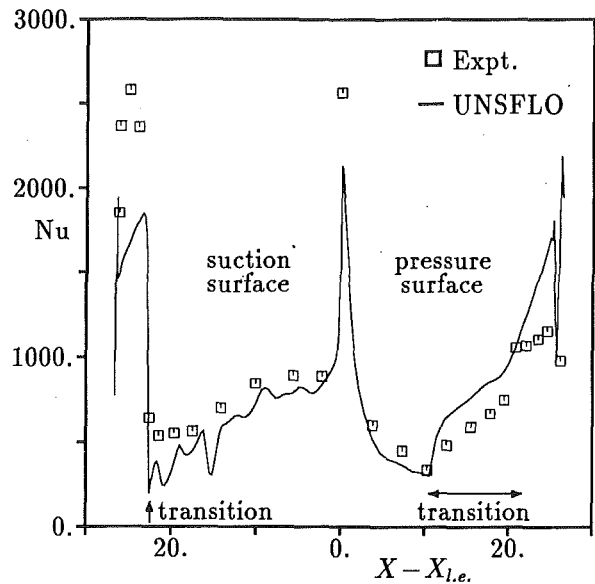


Fig. 11 Nusselt number distribution on turbine cascade

provement in the grid, there are still several more grid points across the Stokes layer at $x = 0.2$ than at $x = 0.9$, and this is what produces the better results at $x = 0.2$.

In the boundary layer calculations of Power et al. (1991), 101 points were used across the boundary layer and very good agreement with theory was achieved along the full length of the flat plate. This level of grid resolution can be achieved with efficient boundary layer methods, but for Navier-Stokes calculations the number of grid points used in the present calculation is quite typical. This suggests that most Navier-Stokes calculations of unsteady flows will be barely resolving the details of the unsteady viscous flow in the lower part of the boundary layer. It is likely that this will lead to some underprediction of transient responses, such as the heat transfer transient produced by a passing shock (Abhari et al., 1992).

Steady, Viscous Flow in a Turbine. A companion paper presents the use of the program UNSFLO to calculate the unsteady heat transfer in a transonic stator/rotor interaction. Therefore, this final test case is not unsteady, but is instead a steady, viscous flow in a turbine with an isothermal wall boundary condition. Experimental heat transfer measurements for this turbine were made at Oxford University by Doorly et al. (1985), and heat transfer calculations have been performed previously by Birch (1987).

Figure 10 shows the surface pressure distribution compared to the experimental data, for an isentropic exit Mach number of 0.735 and Reynolds number of 1.11×10^6 . Figure 11 shows the calculated Nusselt number distribution compared to the experimental data. The transition locations are indicated on the figure, and were specified from experimental data. As stated in the algorithm description earlier, the principal weakness of the current program is its lack of a predictive transition model. Aside from this deficiency, the agreement in heat transfer is reasonable. Finally, the computed loss, nondimensionalized by the outflow dynamic pressure, was computed to be 2.9 percent, compared to an experimental value in the range 2.7–3.0 percent.

Conclusions

This paper has presented a numerical method for the computation of two-dimensional, unsteady, inviscid, and viscous flows in turbomachinery. Options include the analysis of unsteadiness due to wake/rotor, potential/rotor or stator/rotor interactions, unsteady exit static pressure, or specified blade

vibration. A particular feature of the method is the ability to analyze stator/rotor geometries with arbitrary pitch ratios.

An extensive set of test cases is presented to validate the range of unsteady options. Steady boundary layer parameters, heat transfer, and loss predictions compare well against theoretical and experimental data.

Acknowledgments

The authors are grateful to Rolls-Royce plc for their financial support, and Drs. P. Stow and A. Suddhoo for their technical collaboration in the development of the computational method.

References

- Abhari, R. S., Guenette, G. R., Epstein, A. H., and Giles, M. B., 1992, "Comparison of Time-Resolved Turbine Rotor Blade Heat Transfer Measurements and Numerical Calculations," *ASME JOURNAL OF TURBOMACHINERY*, Vol. 114, pp. 818-827.
- Batchelor, G. K., 1967, *An Introduction to Fluid Dynamics*, Cambridge University Press, United Kingdom.
- Birch, N. T., 1987, "Navier-Stokes Predictions of Transition Loss and Heat Transfer in a Turbine Cascade," *ASME Paper No. 87-GT-22*.
- Chen, Y. S., 1988, "3-D Stator-Rotor Interaction of the SSME," *AIAA Paper No. 88-3095*.
- Cebeci, T., and Smith, A. M. O., 1974, *Analysis of Turbulent Boundary Layers*, Academic Press, New York.
- Doorly, D. J., Oldfield, M. L. G., and Scrivener, C. T. J., 1985, "Wake-Passing in a Turbine Rotor Cascade," presented at the AGARD Symposium on Heat Transfer and Cooling in Gas Turbines, AGARD PEP CP-390.
- Erdos, J. I., Alzner, E., and McNally, W., 1977, "Numerical Solution of Periodic Transonic Flow Through a Fan Stage," *AIAA Journal*, Vol. 15, pp. 1559-1568.
- Fourmaux, A., 1986, "Unsteady Flow Calculation in Cascades," *ASME Paper No. 86-GT-178*.
- Gibeling, H. J., Buggeln, R. C., Chen, S. Y., and McConnaughey, H. V., 1988, "An Implicit Navier-Stokes Analysis of Turbine Rotor-Stator Interaction," *AIAA Paper No. 88-3090*.
- Giles, M. B., 1987, "Generalized Conservation Cells for Finite Volume Calculations," *AIAA Paper No. 87-1118-CP*.
- Giles, M. B., 1988a, "Calculation of Unsteady Wake Rotor Interaction," *AIAA Journal of Propulsion and Power*, Vol. 4, pp. 356-362.
- Giles, M. B., 1988b, "UNSFLO: A Numerical Method for Unsteady Inviscid Flow in Turbomachinery," Technical Report 195, MIT Gas Turbine Laboratory.
- Giles, M. B., 1989a, "Non-reflecting Boundary Conditions for Euler Equation Calculations," *AIAA Paper No. 89-1942-CP*.
- Giles, M. B., 1989b, "Numerical Methods for Unsteady Turbomachinery Flow (VKI Lecture Series Notes)," Technical Report TR-89-3, MIT Computational Fluid Dynamics Laboratory, Cambridge, MA.
- Giles, M. B., 1990, "Stator/Rotor Interaction in a Transonic Turbine," *AIAA Journal of Propulsion and Power*, Vol. 6, pp. 621-627.
- Giles, M. B., 1991, "UNSFLO: A Numerical Method for Unsteady Flow in Turbomachinery," Technical Report currently under preparation, MIT Gas Turbine Laboratory, Cambridge, MA.
- Hodson, H. P., 1985, "An Inviscid Blade-to-Blade Prediction of a Wake-Generated Unsteady Flow," *ASME JOURNAL OF TURBOMACHINERY*, Vol. 107, pp. 337-344.
- Johnson, A. B., Rigby, M. J., Oldfield, M. L. G., and Giles, M. B., 1990, "Nozzle Guide Vane Shock Wave Propagation and Bifurcation in a Transonic Turbine Rotor," *ASME Paper No. 90-GT-310*.
- Koya, M., and Kotake, S., 1985, "Numerical Analysis of Fully Three-Dimensional Periodic Flows Through a Turbine Stage," *ASME Journal of Engineering for Gas Turbines and Power*, Vol. 107, pp. 945-952.
- Lewis, J. P., Delaney, R. A., and Hall, E. J., 1987, "Numerical Prediction of Turbine Vane-Blade Interaction," *AIAA Paper No. 87-2149*.
- Lindquist, D. R., and Giles, M. B., 1990, "Generation and Use of Unstructured Grids for Turbomachinery," *Proceedings of Computational Fluid Dynamics Symposium on Aeropropulsion*, NASA CP-10045.
- Lo, S. H., 1985, "A New Mesh Generation Scheme for Arbitrary Planar Domains," *International Journal for Numerical Methods in Engineering*, Vol. 21, pp. 1403-1426.
- Löhner, R., Morgan, K., Peraire, J., and Zienkiewicz, O. C., 1985, "Finite Element Methods for High Speed Flows," *AIAA Paper No. 85-1531*.
- Ni, R.-H., 1981, "A Multiple Grid Scheme for Solving the Euler Equations," *AIAA Journal*, Vol. 20, pp. 1565-1571.
- Peraire, J., Peiro, J., Formaggia, L., Morgan, K., and Zienkiewicz, O., 1988, "Finite Element Euler Computations in Three Dimensions," *International Journal for Numerical Methods in Engineering*, Vol. 26, pp. 2135-2159.
- Power, G. D., Verdon, J. M., and Kousen, K. A., 1991, "Analysis of Unsteady Compressible Viscous Layers," *ASME JOURNAL OF TURBOMACHINERY*, Vol. 113, pp. 644-653.
- Rai, M. M., 1987a, "Navier-Stokes Simulations of Rotor-Stator Interaction Using Patched and Overlaid Grids," *AIAA Journal of Propulsion and Power*, Vol. 3, pp. 387-396.
- Rai, M. M., 1987b, "Unsteady Three-Dimensional Navier-Stokes Simulations of Turbine Rotor-Stator Interaction," *AIAA Paper No. 87-2058*.
- Roe, P., 1986, "Characteristic-Based Schemes for the Euler Equations," *Ann. Rev. Fluid Mech.*, Vol. 18, pp. 337-365.
- Schlichting, H., 1979, *Boundary Layer Theory*, McGraw-Hill, New York.
- Smith, S. N., 1971, "Discrete Frequency Sound Generation in Axial Flow Turbomachines," University of Cambridge, Department of Engineering Report CUED/A-Turbo/TR 29.
- van Leer, B., Lee, W., and Powell, K., 1989, "Sonic-Point Capturing," *AIAA Paper No. 89-1945*.
- Whitehead, D. S., 1987, "Classic Two-Dimensional Methods," in: *Aeroelasticity in Axial-Flow Turbomachines*, AGARD-AG-298, Vol. 1, M. Platzer and F. O. Carta, eds.

On the Propagation of Viscous Wakes and Potential Flow in Axial-Turbine Cascades

T. Korakianitis

Assistant Professor of Mechanical Engineering,
Washington University,
St. Louis, MO 63130

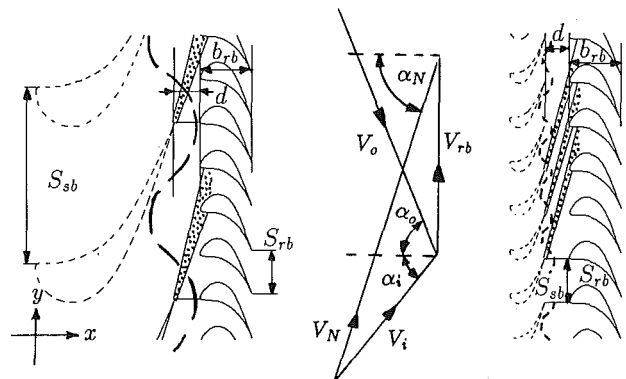
This paper investigates the propagation of pressure disturbances due to potential-flow interaction and viscous-wake interaction from upstream blade rows in axial-turbine-blade rotor cascades. Results are obtained by modeling the effects of the upstream stator viscous wake and potential-flow fields as incoming disturbances on the downstream rotor flow field, where the computations are performed. A computer program is used to calculate the unsteady rotor flow fields. The amplitudes for the rotor inlet distortions due to the two types of interaction are based on a review of available experimental and computational data. We study the propagation of the isolated potential-flow interaction (no viscous-wake interaction), of the isolated viscous wake interaction (no potential-flow interaction), and of the combination of interactions. The discussion uses as example a lightly loaded cascade for a stator-to-rotor-pitch ratio $R = 2$. We examine the relative magnitudes of the unsteady forces for two different stator-exit angles. We also explain the expected differences when the stator-to-rotor pitch ratio is decreased (to $R = 1$) and increased (to $R = 4$). We offer new and previously unpublished explanations of the mechanisms of generation of unsteady forces on the rotor blades. The potential flow field of the rotor cuts into the potential flow field of the stator. After the potential-flow disturbance from the stator is cut into a rotor cascade, it propagates into the relative flow field of the rotor passage as a potential-flow disturbance superimposed on the rotor-relative flow. The potential flow field of the rotor near the leading edge and the leading edge itself cut into the wake and generate two counterrotating vortical patterns flanking the wake centerline in the passage. The vortical pattern upstream of the wake centerline generates an increase in the local pressure (and in the forces acting on the sides of the passage). The vortical pattern downstream of the wake centerline generates a decrease in the local pressure (and in the forces acting on the sides of the passage). The resulting unsteady forces on the blades are generated by the combined (additive) interaction of the two disturbances.

Introduction

In the preliminary design of turbines, one starts for two dimensional stator and rotor velocity diagrams at one or more radii across the blade span and proceeds to design the shape of the two-dimensional cascades of the rotor and the stator. There is a lot of freedom on the choice of the ratio of the number of rotor blades to the number of stator blades, which affects the pitches S_{rb} and S_{sb} and is equal to the stator-to-rotor-pitch ratio R , defined by:

$$R = \frac{S_{sb}}{S_{rb}} = \frac{N_{rb}}{N_{sb}} \quad (1)$$

The effect of R on geometry is illustrated in Fig. 1, where the geometry of the downstream rotor is kept constant, the non-



$$R = S_{sb}/S_{rb} = 4.0$$

$$R = S_{sb}/S_{rb} = 1.0$$

Fig. 1 The effect of R on the stage geometry. The rotor velocity diagrams and the downstream rotors (flow from left to right) are identical.

Contributed by the International Gas Turbine Institute and presented at the 36th International Gas Turbine and Aeroengine Congress and Exposition, Orlando, Florida, June 3-6, 1991. Manuscript received at ASME Headquarters March 4, 1991. Paper No. 91-GT-373. Associate Technical Editor: L. A. Riekert.

dimensional geometry of the upstream stator is identical, but R is varied by changing the value of S_{sb} . The two-dimensional flow unsteadiness between the rotor and the stator is due to: viscous velocity wakes shed from the trailing edge of the stator, generated by the boundary layer along the stator surfaces; inviscid potential-flow interaction because of the relative motion of the lifting surfaces of the rotor and the stator; vortices shed at the stator trailing edge; flutter of both cascades; and the effect of flow changes due to cooling flows in high-pressure high-temperature turbine stages. In Fig. 1 the velocity wake is illustrated in the dotted region starting at the stator trailing edges; the potential-flow interaction is illustrated as a sinusoidal static-pressure variation with a maximum at the stator trailing edge. As R increases, the potential-flow interaction relative to the rotor increases, and its frequency and decay rate decrease. As R increases, the amplitude of the velocity defect in the wake remains about constant, and one may observe a modest increase in the width of the wake because of the increased Reynolds numbers and larger lengths over which the boundary layers develop on the larger stators.

Engine designers try to "detune" the forced response of the cascades by choosing unequal numbers of blades in stators and rotors N_{sb} and N_{rb} . Economic considerations force designs to higher values of R , but this results in larger disturbances entering the rotor cascade and it will probably lead to larger unsteady forces acting on the rotor. For a given rotor size and velocity diagrams R is inversely proportional to the reduced frequency parameter, defined by:

$$\tilde{\omega} \equiv \frac{\omega \cdot b_{rb}}{c_x} = \frac{2\pi V_{rb} b_{rb}}{S_{rb} c_x} \cdot \frac{1}{R} \quad (2)$$

The purpose of this paper is to provide some insights on the magnitude and shape of the unsteady forcing function acting on the blade structure, and to examine some of the mechanisms by which these forces are generated in the rotor passages.

Background

In past investigations (Korakianitis, 1987a, 1988a, 1988b, 1988c, 1992a, 1992b) we computed the amplitude of the harmonics of the spatially analyzed unsteady forces on rotor blades as a function of R for a series of typical turbine cascades. For

a first approximation we considered the effect of the viscous wake interaction (generated by the boundary layers along the blade surfaces and propagating downstream only) and of the potential flow interaction (a static-pressure variation due to the presence of the lifting surfaces in the cascades and propagating upstream as well as downstream). We neglected the effect of vortex shedding and assumed infinitely rigid blades without cooling slots that expel lower-enthalpy jets of cooling air. For these studies (past and the present one) we have used Giles' (1988a) computer program UNSFLO (which models the two-dimensional, unsteady, compressible, inviscid flow around rotor blades) to compute the flow field and the forces for different stator-exit (nozzle) angles α_N . This program was chosen because it can handle arbitrary values of R with reasonable CPU and storage requirements due to a novel "tilting" of the time domain. In the computational field the problem has been simplified by considering the effects of the stator disturbances on the rotor blades in the rotor-relative frame.

The accuracy of the computations has been checked in the past by Giles (1988a) and Korakianitis (1987a, 1988b, 1992a). These checks involved comparisons of the results of calculations using UNSFLO with the results of four steady and unsteady-flow cases of known theoretical or experimental output. For steady flows we used a comparison of computed results with the closed-form analytic solution obtain by conformal transformation for the incompressible potential flow past Gostelow's (1984) compressor cascade (Korakianitis, 1987a, 1988b, 1992a). For unsteady flows three checks have been published. Giles (1988a) published comparisons with the theoretical results of a sinusoidal wake acting on a flat-plate compressor cascade, and comparisons with measurements and computations performed on a turbine cascade by Hodson (1983, 1985a, 1985b). Korakianitis (1987a, 1988b, 1992a) also compared computational results with the experimental data obtained with laser two-focus velocimeter measurements in a rotor cascade operating behind a stator at the DLR (Binder et al., 1987).

This paper examines the propagation of the same disturbances, of the viscous wake and the potential-flow interaction, as a typical rotor cascade moves past one stator pitch by examining details of the flow fields at six relative positions of rotors and stator disturbances. At the same time we match

Nomenclature

a = acoustic velocity (Eq. (4))
 B = amplitude of potential variation (Eq. (6))
 b = axial chord
 C_L = tangential-lift coefficient (Eq. (10))
 c = rotor-inlet total sonic velocity (Eq. (11))
 D = wake amplitude, fraction of V_N (Eq. (3))
 d = stator-rotor axial gap (fraction of b_{rb})
 F', F = force (Eq. (11))
 $j \equiv \sqrt{-1}$ (Eq. (5))
 M = Mach number
 N = number of blades (Eq. (1))
 $R \equiv S_{sb}/S_{rb}$ = stator-to-rotor-pitch ratio
 S = pitch of a cascade
 T'_z, T_z = moment (in the z direction) (Eq. (11))

t = time (nondimensionalized by y/S_{sb})
 u = velocity component in the x direction
 V = velocity
 V_{ip} = velocity perturbation due to potential, fraction of c (Eq. (7))
 v = velocity component in the y direction
 W = characteristic width of the wake, expressed as fraction of S_{sb} (Eq. (3))
 (x, y, z) = Cartesian coordinates (in subscripts also)
 α = flow angle
 $\Delta\epsilon, \epsilon$ = angles locating the potential (Eqs. (7), (8))
 δ = perturbation operator (on u and v)
 ξ = parameter for the x decay of Φ (Eq. (6))

ρ = relative total density at rotor inlet
 Φ = velocity potential defined by Eq. (5)
 ω = rotor passing frequency (Eq. (2))
 $\tilde{\omega}$ = reduced frequency parameter (Eq. (2))

Subscripts

i, o = rotor-relative inlet, outlet, respectively
 ip = flow property for potential-flow model
 iw = flow property in the wake
 N = stator-exit (nozzle, in absolute frame)
 p = pressure side
 q = suction (s) or pressure (p) side (Eq. (3))
 rb = rotor blade row
 s = suction side
 sb = stator blade row
 ss = steady flow

observations of details of the flow fields with the shape of the forcing function.

The Rotor-Inlet Boundary

Results have been obtained by considering the two disturbances from the upstream stator (viscous wake and potential-flow interaction) as inputs to the computational rotor-inlet boundary. The rotor-relative flow is computed; the stator disturbances are modeled and input as inlet distortions moving across the computational rotor-inlet boundary. This simplification provides accurate computational results only if one is extremely careful to specify the correct boundary conditions to the problem. Details of the following derivations have been published by Korakianitis (1987a, 1992) and Giles (1988b). A few important equations have been included here for clarity and completeness because they are essential to understanding the model of the rotor-inlet boundary, and the following results and discussion.

The axial gap between blade rows in modern engines is between 0.2 and 0.5 of the axial chord. Narrower gaps result in shorter engines but increase the unsteadiness to which the next blade row is subjected. Throughout these investigations we have used $d=0.3$, nondimensionalized with the rotor axial chord b_{rb} .

The velocity disturbance is characterized by the maximum amplitude of the velocity defect D , expressed as a fraction of the undisturbed velocity, and by the "width" W of the velocity defect (see Eq. (3)). Most velocity wakes observed in experimental data have velocity distributions which resemble Gaussian distributions. The width of the velocity defect is characterized by the corresponding characteristic width of the Gaussian distribution that would best fit the velocity data. In the following this width is expressed as a fraction of the pitch of the blade cascade that generates the wake. In most cases the pressure side of the velocity wake is narrower than the suction side, especially for small axial distances downstream of the cascade that generates the wake. The reason for this is that the boundary layer of the pressure side is thinner than the boundary layer of the suction side. Two "characteristic widths" are used: the suction-side characteristic width, and the pressure-side characteristic width. For the wake model we assumed that in the stator frame the flow vectors in the wake are parallel to the undisturbed flow (a velocity deficit with no angle variation), that the static pressure is constant across the wake, that the total enthalpy is constant across the wake, and that the velocity defect is an asymmetric Gaussian distribution. The above are modeled by:

$$\begin{aligned} u_{iw,q} &= V_N \left[1 - D \cdot \exp \frac{1}{2} \left(-\frac{y - \tan(\alpha_N)}{S_{sb} W_q} \right)^2 \right] \cos(\alpha_N) \\ v_{iw,q} &= V_N \left[1 - D \cdot \exp \frac{1}{2} \left(-\frac{y - \tan(\alpha_N)}{S_{sb} W_q} \right)^2 \right] \sin(\alpha_N) \end{aligned} \quad (3)$$

where q is either s (for the suction surface) or p (for the pressure surface). The way this wake function varies from one computational rotor passage to the next, and a literature review of experimental data on wake amplitudes and widths has been published (Korakianitis, 1988a, 1992a). Based on these data we chose as a representative wake amplitude $D=0.10$ of V_N , and characteristic widths $W_p=0.14$ and $W_s=0.16$ of the rotor pitch S_{rb} for the axial gap $d=0.30$.

The model for the potential-flow disturbance was developed by observing the experimentally measured and computed static pressure fields of various turbine-blade cascades. These indicate that across the line of the trailing edges of the cascades there is a variation of static pressure with maxima at (or very near) the trailing edges and minima at (or very near) the middle of the passage. The exact location and shape of the pressure

variation depends on the geometric shape of the passage. The pressure variation is nearly sinusoidal and the amplitude of the pressure disturbance decays very fast with distance downstream. Numerous examples of this static pressure variation can be seen in the experimental wake sources (Korakianitis, 1987a, 1988a, 1992a). For example, measured cascade data such as those shown in Fig. 6 of Sieverding et al. (1984), Fig. 7 of Boletis and Sieverding (1984), Fig. 6 of Sonoda, (1985), and Fig. 4 of Yamamoto and Yanagi (1985), show the shape and the rapid decay of the potential-flow interaction.

The potential-flow model (in the stator frame) is derived as a two-dimensional, linear, isentropic, irrotational perturbation to uniform flow (see page 198 of the text by Liepmann and Roshko, 1957):

$$(u^2 - a^2) \frac{\partial u}{\partial x} + (v^2 - a^2) \frac{\partial v}{\partial y} + uv \left(\frac{\partial u}{\partial y} + \frac{\partial v}{\partial x} \right) = 0 \quad (4)$$

The velocity potential is defined by:

$$\frac{\partial \Phi}{\partial x} = u \quad \frac{\partial \Phi}{\partial y} = v \quad (5)$$

For subsonic flows of interest to this study one expects that the potential-flow interaction is periodic in the y direction and that it decays exponentially in the x direction. Thus the general solution of Eq. (4) is of the form:

$$\Phi(x,y) = B \cdot \exp \left[j \frac{2\pi}{S_{sb}} y + \xi x \right] \quad (6)$$

where B is the amplitude, ξ governs the decay and $2\pi/S_{sb}$ dictates the periodicity of the potential Φ . Substituting these in Eq. 4 we derive solutions of the form:

$$\delta v = -V_{ip} \cdot \exp \left[-\frac{2\pi}{S_{sb}} \frac{\sqrt{1-M^2}}{1-M_x^2} (x-x_{inl}) \right] \cdot \sin [2\pi(\epsilon + \Delta\epsilon)] \quad (7)$$

$$\begin{aligned} \delta u &= -\tan(\alpha_{ip}) \delta v - \frac{\sqrt{1-M^2}}{1-M_x^2} V_{ip} \\ &\cdot \exp \left[-\frac{2\pi}{S_{sb}} \frac{\sqrt{1-M^2}}{1-M_x^2} (x-x_{inl}) \right] \cdot \cos [2\pi(\epsilon + \Delta\epsilon)] \end{aligned}$$

where M is given by $M = \sqrt{M_x^2 + M_y^2}$, the phase ϵ at any location is given by

$$\epsilon = \frac{y - \tan(\alpha_{ip})x}{S_{sb}}, \quad (8)$$

$\tan(\alpha_{ip})$ is the direction of propagation of the potential field given by

$$\tan(\alpha_{ip}) = -\frac{M_x M_y}{1 - M_x^2}, \quad (9)$$

and V_{ip} is the maximum perturbation in v at the stator trailing edge (rotor-inlet) boundary (a fraction of c). Then the velocity perturbations are a function of the axial distance from the inlet boundary ($x-x_{inl}$), where x_{inl} denotes the axial location of the computational rotor-inlet boundary and $\Delta\epsilon$ is a phase-shifting constant used to ensure that the maximum amplitude in the pressure disturbance due to the potential-flow field of the stator coincides with the centerlines of the velocity wakes at the (x_{inl}, y) locations that model the stator trailing edges.

The amplitude of V_{ip} was chosen by investigating the pressure and velocity fluctuations from experimental measurements and from published computations across the line joining the trailing edges of numerous typical turbine-stator cascades, and across other lines a little downstream (5 and 10 percent of the axial chord) parallel to the line across the trailing edges. These measurements indicated that across the line of the trailing edges the

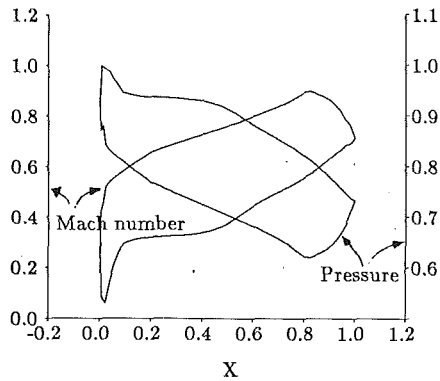


Fig. 2(a) Surface Mach number and pressure distributions

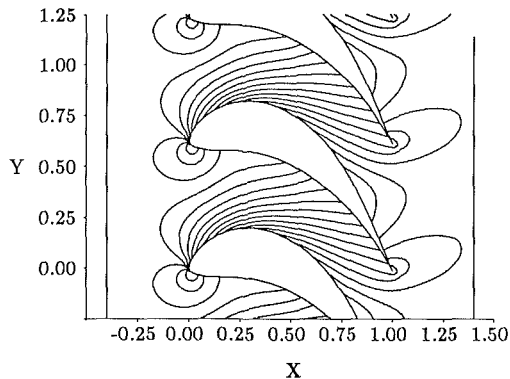


Fig. 2(b) Passage pressure distribution (increment 0.02)

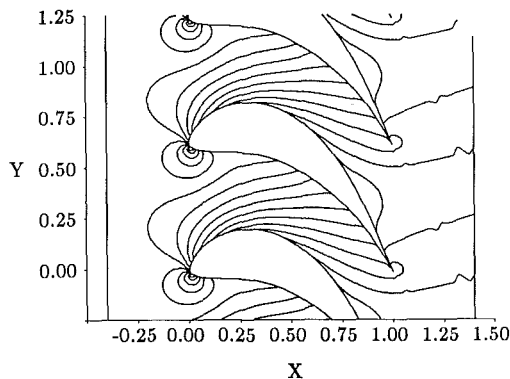


Fig. 2(c) Passage Mach number distribution (increment 0.05)

Fig. 2 Steady-flow performance of the sample rotor cascade with $\alpha_i = 40$ deg; $\alpha_o = -60$ deg; $M_i = 0.334$; and $M_o = 0.800$

static pressure fluctuations were typically between 4 and 4.5 percent of the average pressure. The corresponding values of V_{ip} for various values of V_{rb} were between 4.52 and 5.31 percent of c . For the results presented below we used $V_{ip} = 0.05 c$. The following unsteady flow-field figures show that the potential-flow-interaction model inputs a sinusoidal static-pressure variation at the stator-exit/rotor-inlet computational boundary typical of that downstream of turbine cascades of various solidities, with a maximum value at the modeled stator trailing edge and a minimum value near the middle of the modeled line across the stator trailing edges.

The combined disturbance of the potential-flow and wake interactions are input as rotor-inlet distortions at the rotor-inlet computational boundary. This is done by adding the values of the two disturbances at that boundary, and by a coordinate transformation to the rotor-relative frame. These models include the effects of the stator potential-flow and wake

Table 1 Some information on the sample cascade

inlet flow angle α_i	40.00°
outlet flow angle α_o	-60.00°
stagger angle	-32.00°
loading coefficient C_L	0.80
cascade solidity S_{rb}/b_{rb}	0.6223
inlet Mach number M_i	0.334
outlet Mach number M_o	0.800
steady-flow x-force $F'_{x,ss}$	0.1140
steady-flow y-force $F'_{y,ss}$	0.1361
steady-flow z-moment $T'_{z,ss}$	0.0869
high nozzle angle α_N	74.49°
V_{rb} for high α_N	0.7026
$\tilde{\omega}$ for high α_N and $R = 2$	13.863
low nozzle angle α_N	66.75°
V_{rb} for low α_N	0.3783
$\tilde{\omega}$ for low α_N and $R = 2$	7.464

interactions on the rotor, and via the Euler solution in the rotor relative frame the effect of the rotor potential-flow field propagating upstream from the rotor leading-edge region to modify the potential-flow field in the axial gap between stator and rotor. They do not include the cross-coupling effect of the rotor potential-flow field modifying the (initial) stator potential-flow field.

Results

Wilson (1984) shows that a measure of cascade loading is the incompressible tangential-lift coefficient, given by:

$$C_L = 2 \frac{S}{b} \cos^2 \alpha_o [\tan(\alpha_i) - \tan(\alpha_o)] \quad (10)$$

For lightly, intermediately, and highly loaded cascades C_L is approximately 0.8, 1.0, and 1.2, respectively. Results have been obtained for numerous rotor cascades of various values of C_L and inlet and outlet flow angles. For discussion purposes we use a lightly loaded cascade designed with continuous-slope-of-curvature surfaces using the airfoil-design method (Korakianitis; 1987b, 1989). The sample cascade used in this study has incompressible tangential-lift coefficient $C_L = 0.80$. Its steady-flow performance is shown in Fig. 2. Additional information about this cascade is shown in Table 1. The relative amplitudes of the rotor-inlet flow distortions due to the potential-flow and wake interactions in each case are functions of the nozzle angle α_N and the corresponding rotor velocity V_{rb} . They can be computed using the information supplied in Table 1 to reconstruct the velocity diagram at the rotor-inlet boundary. The values for the forces $F'_{x,ss}$, $F'_{y,ss}$, and $T'_{z,ss}$ in Table 1 have been evaluated by running the unsteady-flow program with $D = 0.0$ and $V_{ip} = 0.0$ (the resulting "unsteady" performance is identical to the steady-flow performance shown in Fig. 2).

The wake and potential-flow were modeled at the rotor-inlet boundary as described above. The forces and moments were calculated under these conditions for two nozzle angles (corresponding to two identical rotor-velocity triangles, but different stator velocity triangles). As the rotor moves past a series of stator pitches, the forces and moment exhibit a periodic pattern. To investigate these patterns, we chose to

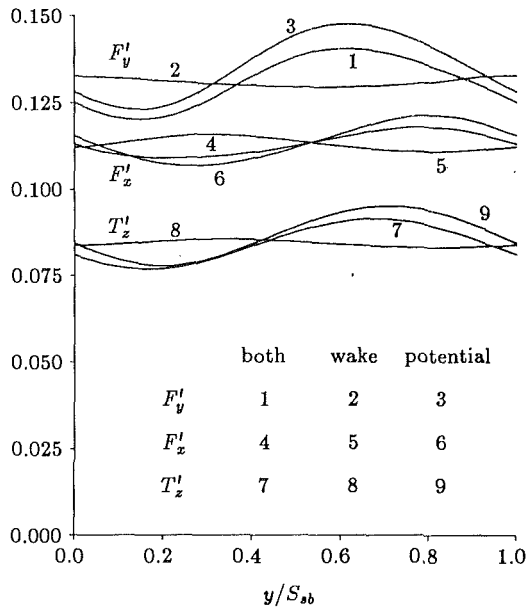


Fig. 3 Time evolution of the forces and moment over a full stator pitch for the high nozzle angle ($\alpha_N = 74.49$ deg)

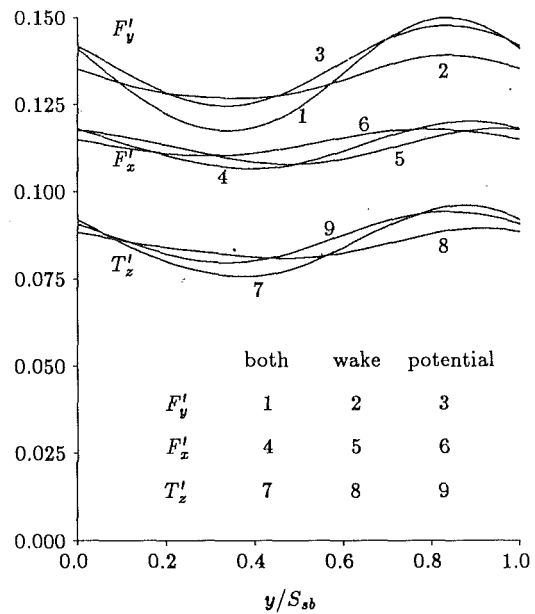


Fig. 4 Time evolution of the forces and moment over a full stator pitch for the low nozzle angle ($\alpha_N = 66.75$ deg)

study the effects of the wake and potential-flow interactions on the sample cascade moving past a stator that has double the pitch of the rotor ($R = 2$). In production engines designers would normally try to choose unequal integers for all blade rows, and R would not be an integer. This unlikely geometry is useful for the purposes of this paper because it provides a symmetry that facilitates the discussion (see later figures), because it is in a range where both types of interaction are of comparable magnitude (so that neither one dominates the generation of the unsteady part of the force (Korakianitis, 1987a, 1992a, 1992b)), and because it is close to the value of R of many turbine stages in production engines.

The origin ($t = y/S_{sb} = 0.0$) of the period of the unsteadiness in each case (Figs. 3, 4, 5, 6) corresponds to the y location at which a stator velocity wake touches the leading edge of a rotor blade (numbered blade 0 in the following figures). The end of the period ($t = y/S_{sb} = 1.0$) corresponds to the velocity wake from the next stator blade touching the leading edge of the same rotor blade. In each case we considered the interaction of the rotor blade row under three different conditions: (a) with the isolated potential-flow interaction (the wake amplitude D was set equal to zero); (b) with the isolated viscous-wake interaction (the potential amplitude V_{ip} was set equal to zero); and (c) with the combined interaction of the viscous-wake and potential-flow interactions. These studies can only be performed on a computer because in experimental or production turbine stages both types of interaction are always present.

The dimensional forces per unit length of blade span (such as F_x in the x direction) are related to the nondimensional forces (F'_x) by:

$$F'_x \equiv \frac{F_x/z}{\rho b_{rb} c^2} \quad (11)$$

(the moment T'_z is taken about the leading edge, and it is divided by b_{rb}^2).

Figures 3 and 4 show the unsteady part of the forces and moment for blade 0 over one stator pitch. To understand how these forces vary from the average value, we considered the propagation of the unsteady part of the pressure in the passages. The unsteady pressure at a point is defined as the instantaneous pressure at any time t minus the steady-flow

pressure at that point. Because $R = 2$ the flow is repeating every other passage, and at $t = 0$ the next wake impinges at the leading edge of blade 2. This means that what occurs between blades 0 and 1 at $t = 0.50$ occurs between blades 1 and 2 at time $t = 0.00$. Thus for every figure shown at time $t = \tau$, we can also deduce the flow at time $t = \tau + 0.50$. (This was one of the reasons for which we chose $R = 2$ for discussion.) The unsteady pressure contours with increment 0.002 for the high nozzle angle and for times $t = 0.000$, [0.167], 0.333, [0.500], 0.667, and [0.833], for isolated potential-flow interaction, for the isolated wake interaction, and for the combined interaction are shown in Fig. 5. The square brackets indicate that one should consider the blades with numbers in square brackets in the appropriate plot. The corresponding unsteady pressure contours for the low nozzle angle are shown in Fig. 6. Entropy contours are superimposed to show the location of the velocity wake. The rotor is always shown at the same location; as time increases the wake and the potential-flow interaction of the stator are shown moving at the rotor-inlet boundary toward the negative Y values. The regions in which the unsteady pressure is positive are dotted. In the remaining regions the unsteady pressures are negative. Following the dotted or the not-dotted regions from their edge inward or outward, one can derive the values of the corresponding unsteady pressures anywhere in the flow field. In Figs. 5 and 6 the increment of the unsteady pressure contours is 1/10th of the increment of the steady-flow pressure contours shown in Fig. 2. The blades are numbered starting from blade 0, which is the blade at the leading edge of which the centerline of a wake impinges at time $t = 0$.

Discussion

The shape of F'_x , F'_y , and T'_z in Figs. 3 and 4 indicates that the spatially analyzed Fourier harmonics of the unsteady forces is dominated by the first harmonic amplitude, and that the amplitude of the second harmonic is an order of magnitude smaller than the first harmonic for $R = 2$. These agree with the conclusions from our past work. Higher values of wake defect D , velocity disturbances due to the potential V_{ip} or stator-to-rotor-pitch ratio R result in forcing functions with higher amplitudes for the second and third harmonics (Korakianitis, 1987a, 1988a, 1992b). The stator-outlet flow velocities V_N are

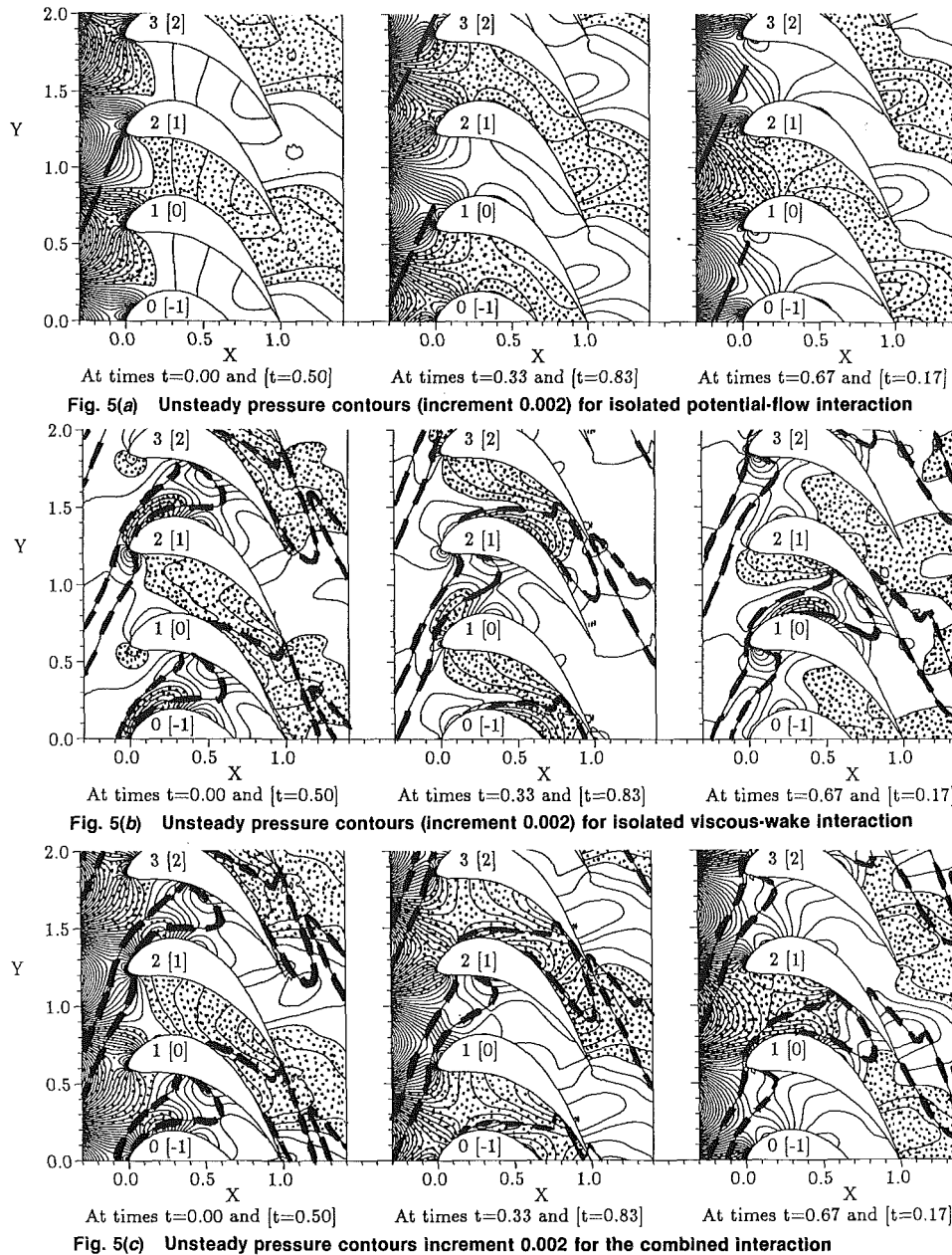


Fig. 5(a) Unsteady pressure contours (increment 0.002) for isolated potential-flow interaction

Fig. 5(b) Unsteady pressure contours (increment 0.002) for isolated viscous-wake interaction

Fig. 5(c) Unsteady pressure contours increment 0.002 for the combined interaction

Fig. 5 Unsteady pressure contours of increment 0.002 showing the propagation of disturbances in cascade 4060c08 for high nozzle angle. Left, time $t=0$ and $[t=0.50]$. Middle $t=0.33$ and $[t=0.83]$. Right, $t=0.67$ and $[t=0.17]$.

in the high subsonic regime in this paper. Higher velocities may induce shocks in the passages that will result in forcing functions with even higher harmonics (see the flow fields of Giles, 1990).

Potential-Flow Interaction. The explanation of the potential-flow interaction in this paper extends our previous interpretations, where we considered two limiting cases of rotor velocity (first infinitely small V_{rb} , and second a higher V_{rb} resulting in just subsonic flow fields) to show that the potential interaction originates at the rotor-inlet boundary and it is affected by the rotor velocity. Here we show some additional details of the temporal variation of the potential-flow interaction.

The effect of the potential-flow field of the stator on the potential-flow field of the rotor can be seen by the distortion (existence) of the unsteady pressure lines in Figs. 5(a) and 6(a). The effect of the potential-flow field of the rotor on the flow can be seen where the wake centerlines are bent near the leading

edge of the rotors in Figs. 5(b) and 6(b). The initial directions of the wake centerlines are shown as dashed lines in Figs. 5(a) and 6(a) to indicate the location of the stators. The weaker potential flow field of the rotor blades cuts into the stronger and stationary potential flow field of the stators. Figures 5(a) and 6(a) show the positive unsteady pressure at the trailing edges of the stator, the negative unsteady pressure between the trailing edges of the stator, and the rapid decay of the potential-flow interaction downstream of the stator trailing edge. As the rotor passage moves it cuts the potential flow field of the stator into two regions: one upstream region, still attached to the stator; and one downstream region which is now traversing with the rotor. The latter propagates downstream superimposed on the rotor flow field according to potential-flow theory while continuously decaying. This can be seen in Fig. 5(a) between blades 0 and 1 (also corresponding to the passage between blades 2 and 3). At time $t=0$ the relative position of rotor and stator is such that a positive portion of the potential (called PPP) has moved into the rotor passage almost to the

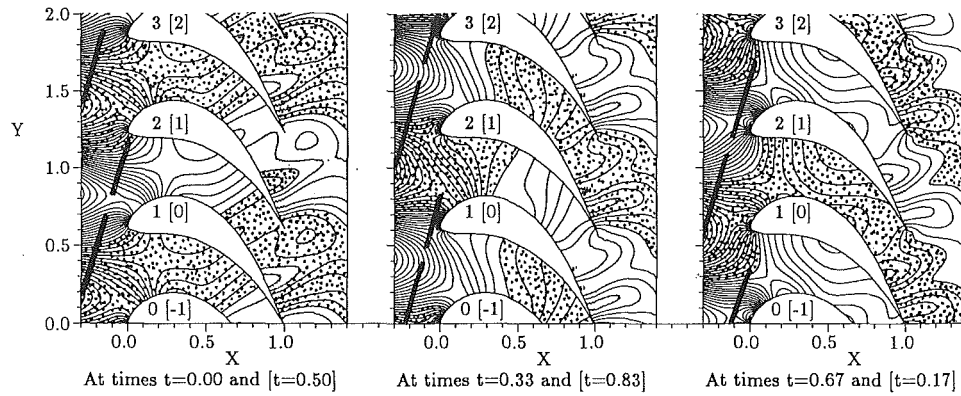


Fig. 6(a) Unsteady pressure contours (increment 0.002) for isolated potential-flow interaction

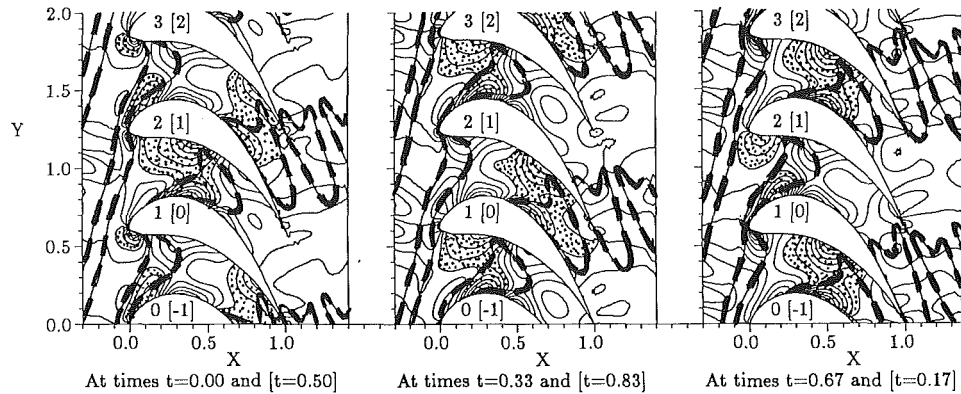


Fig. 6(b) Unsteady pressure contours (increment 0.002) for isolated viscous-wake interaction

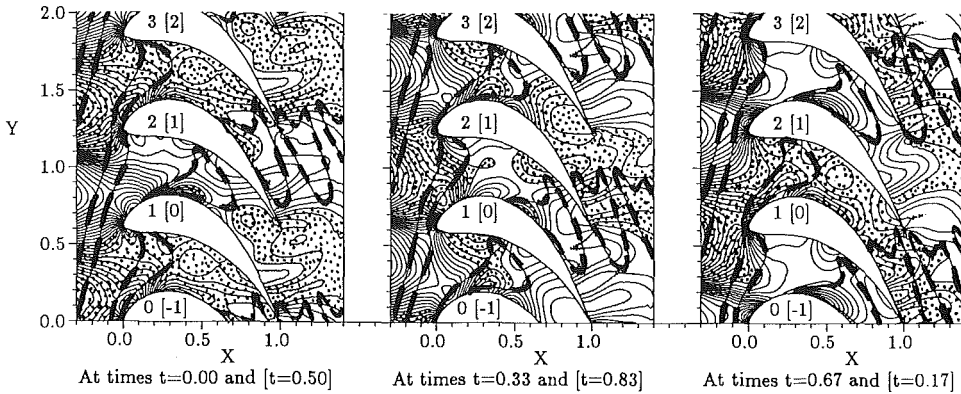


Fig. 6(c) Unsteady pressure contours (increment 0.002) for the combined interaction

Fig. 6 Unsteady pressure contours of increment 0.002 showing the propagation of disturbances in cascade 4060c08 for low nozzle angle. Left, time $t=0$ and $[t=0.50]$. Middle, $t=0.33$ and $[t=0.83]$. Right, $t=0.67$ and $[t=0.17]$.

rotor throat. The shape and velocity of the rotor cascade passage distorts the potential-flow field. A similar negative portion of the potential (called NPP) has moved into the next passage between blades 1 and 2. At $[t=0.17]$ the rotor leading edge has cut half of the PPP off, while the rotor-passage portion of the PPP has almost been separated from the inflow-boundary portion of the PPP, and part of it has moved into the rotor-outflow region. At time $t=0.33$ the PPP has moved past $X=0.5$ in the passage and even more of it is in the rotor-outflow region. At $[t=0.50]$ it has reached the rotor throat. At times $t=0.67$ and $[t=0.83]$ the first PPP is into the rotor outflow region and it has merged with the next portion of positive potential from the next stator trailing edge. Similar observations can be made for the low nozzle angle in Fig. 6(a). One can observe a direct correspondence between the space and time location of the maxima and minima in the unsteady pressure fields in Figs. 5(a) and 6(a), and the increases or decreases from the average forces in Figs. 3 and 4, respectively.

The potential-flow interaction from the stator extends into the rotor cascade passages and large portions of it enter the cascade when the direction of propagation of the potential is aimed near the center of the rotor passage (best illustrated at $t=0.67$ in Fig. 6a). The potential flow field of the stator is cut by the advancing potential flow field of the rotor (best illustrated at $t=0.00$ in Fig. 6a). After it is cut it moves downstream according to Eq. (7) as a potential-flow disturbance superimposed in the rotor flow field (best illustrated at all values of t in Fig. 5a).

Wake Interaction. The explanation of the wake interaction in this paper extends previous interpretations. Meyer (1958) and Lefcort (1965) considered the cutting of wakes by the rotor, and Smith (1966) introduced the idea of distinct wake segments in the rotor passages. Hodson (1985a) discussed the rotation of the cut wake segments and the effects of the lower momentum fluid in the wake region, and Korakianitis (1987a,

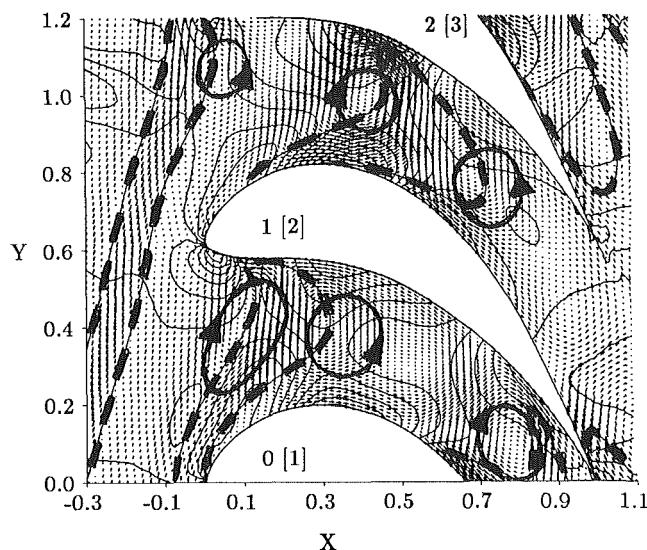


Fig. 7 Unsteady flow vectors of magnitude 0.45 superimposed on unsteady pressure contours of increment 0.002 and on entropy contours for the high nozzle angle at $t=0$

1988c, 1992b) used the idea of recirculating flows to show how they resulted in “suction” and “impingement” of unsteady-flow (low-momentum) jets that generate suction and pressure regions in the turbine passages. In Korakianitis (1992b) we stated that “. . . the temporal variation of these instantaneous pressure maxima and minima, which act in addition to the local pressure in steady flow, generate the unsteady forces on the blade . . .”. Here we show and explain some new and additional details of the temporal variation of the wake interaction.

The wake centerlines are shown as superimposed entropy contours in Figs. 5(b) and 6(b), respectively. We concentrate on a small region of Fig. 5b at time $t=0$, for $1.2 > Y > 0.0$. The unsteady flow vectors superimposed on entropy contours and unsteady pressure contours for that region are shown in Fig. 7. The unsteady flow vectors are defined as the instantaneous local velocity minus the local steady-flow velocity. The entropy contours locate the wake centerlines, and the positive and negative values of unsteady pressure can be found by comparing Figs. 5(b) and 7.

The wakes are first bent by the potential flow field of the rotor as shown in the region $(X, Y) = (-0.2, 0.7)$ in Fig. 7. As the leading edge in the rotor stagnation region interacts with the lower-momentum fluid in the wake (for example near points $(X, Y) = (0.0, 0.0)$ and $(X, Y) = (0.0, 1.2)$), recirculating-flow patterns are established in the stagnation region of the leading edge of the rotor as shown in the region $(X, Y) = (0.0, 1.1)$ in Fig. 7. These recirculating flow patterns are generated as the wake is being cut; once generated they result in a counterclockwise rotating unsteady-flow pattern downstream of the wake centerline, and a clockwise rotating unsteady-flow pattern upstream of the wake centerline. The wakes are cut by the passing rotor into individual segments that are acting in each passage. After the stator wake is cut to produce a segment of a wake in the rotor passage, the two ends of the wake segment travel at the local speeds: the portion attached to the pressure side moves downstream into the passage much slower than the portion attached to the suction side, because the local flow velocities are higher on the suction side of the cascade. At the same time lower momentum fluid moves from the wake end near the pressure side to the wake end near the suction side. The last two phenomena cause a thinner wake on the pressure side, a thicker wake on the suction side, and

a counterclockwise rotation of the centerline of the wake as it moves through the passage. The initial vorticity is conserved; before the wake is cut, for example near $(X, Y) = (-0.3, 0.4)$ and $(X, Y) = (-0.2, 0.4)$, there is no unsteady pressure on either side of the wake; after the wake is cut, for example near $(X, Y) = (0.4, 1.0)$ and $(X, Y) = (0.7, 0.8)$ there is substantial positive unsteady pressure on the upstream side of the wake and negative unsteady pressure on the downstream side of the wake. These vortices start to form as the leading edge of the rotor shears into the downstream side of the wake, generating the positive unsteady pressures upstream of the wake centerline (for example near $(X, Y) = (0.05, 0.1)$ and $(X, Y) = (0.05, 0.6)$) and the negative unsteady pressures downstream of the wake centerline (for example near $(X, Y) = (0.05, 0.7)$ and $(X, Y) = (0.05, 1.2)$). The two counterrotating vortices that flank the wake centerline must be equal and opposite. The two vortex patterns act in opposite directions. The upstream clockwise-rotating vortical flow pattern causes a local increase in pressure, and the downstream counterclockwise-rotating vortical flow pattern causes a local decrease in pressure. As the vortices move downstream and out of the rotor cascade, the wake is sheared, distorted, and enlarged, while the amplitude of the unsteady pressure maximum or minimum is decreased and its region of influence increased. One can observe a direct correspondence between the space and time location of the maxima and minima in the unsteady pressure fields in Figs. 5(b) and 6(b), and the increases or decreases from the average forces in Figs. 3 and 4, respectively.

The cutting of the wake by the rotor generates two recirculating regions of low-momentum fluid, one upstream and the other downstream of the wake centerline. The unsteady forces from the wake interaction are due to the positive unsteady pressure (generated in the vortical pattern upstream of the wake centerline) and due to the negative unsteady pressure (generated in the vortical pattern downstream of the wake centerline).

Figures 5(b) and 6(b) indicate that the wakes from lower stator exit angles act for a shorter part of the period (actually of a triple period from blade 0 to blade 4 or 5) in the rotor cascade. The residence times of the wakes inside the rotor cascade are longer for the higher nozzle angles, but there are also better opportunities for unsteady pressure maxima (or minima) to align themselves at opposite sides of the blades and thus reduce the resultant unsteady force. The residence times inside the rotor cascade are shorter for the lower nozzle angles, but there are fewer opportunities for unsteady pressure maxima (or minima) to align themselves at opposite sides of the blades because their wakes also spread more in the axial direction of the cascade. It is more likely for an unsteady pressure maximum on one side to align with a minimum on the other side of the blade and maximize the unsteady force. The unsteady forces for the isolated wake interaction from lower values of nozzle angle are likely to be higher than those from higher values of nozzle angle. The forces in Figs. 3 and 4 and the unsteady pressure contours in Figs. 5(b) and 6(b) indicate that indeed this is the case for the sample cascade. Although many parameters affect the results (loading also plays an important role on the propagation of disturbances), this result is confirmed by observing the results from most similar loaded cascades associated with this and our past studies.

Combined Potential-Flow and Wake Interactions. The combination of both interactions is shown in Figs. 5(c) and 6(c). It is easier to study the effects of the combined interaction by first looking at Figs. 5(a) and 6(a), and at Figs. 5(b) and 6(b), and then considering Figs. 5(c) and 6(c). The corresponding unsteady pressure maxima and minima due to the combined interaction are easily interpreted as the combined (additive) effect of the two interactions described above. The

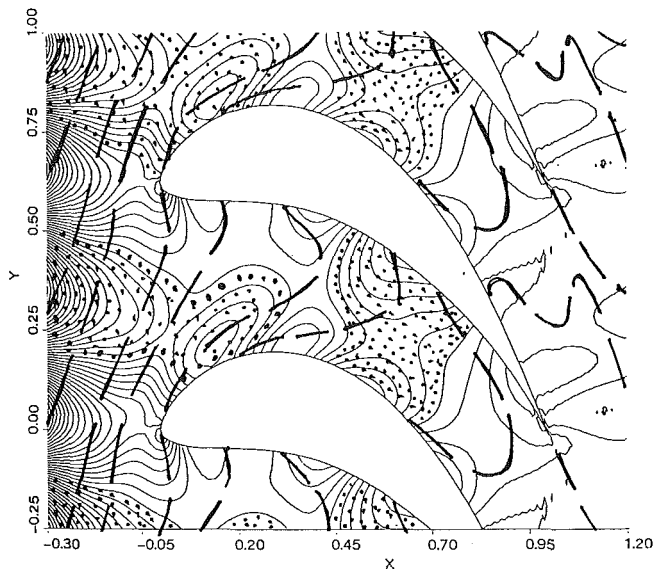


Fig. 8 Unsteady pressure contours of increment 0.002 from the combined interaction for $R=1$

magnitude of the unsteadiness of the force is increasing or decreasing accordingly at different times in Figs. 3 and 4. In general the unsteadiness in F'_y is lower for the high nozzle angle because of counteraction of the two disturbances (see Figs. 3 and 5), and higher for the low nozzle angle because of reinforcement of the two disturbances (see Figs. 4 and 6).

The value of R has a significant effect on which type of interaction dominates the unsteady flow field. Figure 8 shows the unsteady pressure contours and the entropy contours from the combined interaction for the same cascade and for a ratio $R=1$ at $t=0$. In this case the potential-flow interaction decays very fast downstream so that it hardly affects the flow in the rotor cascade. The unsteady pressure contours inside the cascade passage are due to the wake interaction only, and they agree with the explanation of the wake interaction discussed above. Figure 9 shows the unsteady pressure contours and the entropy contours from the combined interaction for the same cascade and for a ratio $R=4$ at $t=0$. In this case the potential flow interaction decays very slowly downstream and it dominates the flow in the rotor cascade. The unsteady pressure contours due to the wake interaction are visible only above blade 0. The region of positive unsteady pressure downstream of blade 2 is also due to the potential-flow interaction.

Conclusions

The unsteady forces on two-dimensional gas-turbine rotors due to potential-flow and viscous-wake interactions from upstream blade rows are computed using a compressible, two-dimensional, inviscid rotor/stator-disturbance interaction program. The viscous wake and the potential-flow interactions from the upstream stator are modeled as inlet distortions at the rotor-inlet boundary. New explanations of the mechanism of generation of unsteady forces on turbine blades are offered by observing unsteady pressure contours in the rotor passages. The results used in this paper to facilitate the discussion have been compared with the results from numerous other cascades of a variety of loading distributions and geometries. The conclusions presented in this paper have been confirmed by all cases we have studied to date.

We conclude the following:

1 The potential flow field of the rotor cuts into the potential flow field of the stator and vice versa. After the potential flow disturbance from the stator is cut into a rotor cascade, it

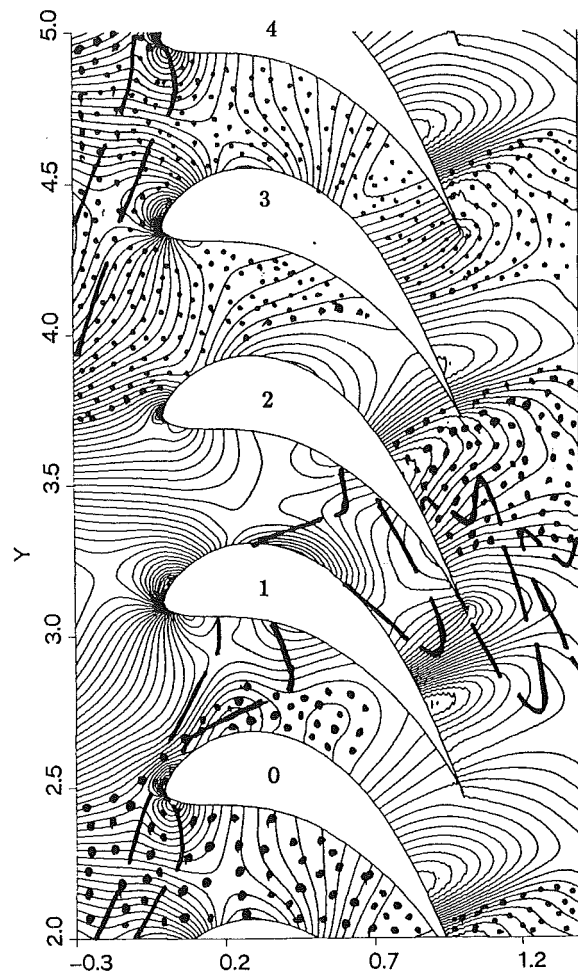


Fig. 9 Unsteady pressure contours of increment 0.002 from the combined interaction for $R=4$

propagates into the relative flow field of the rotor passage as a potential-flow disturbance superimposed on the rotor flow field. Due to the relative size of rotor and stator, the unsteadiness from the potential flow field dominates the rotor flow field only at high values of R .

2 The potential flow field of the rotor near the leading edge and the leading edge itself cut into the wake. The cutting action generates two counterrotating vortical patterns flanking the wake-segment centerline in the passage. The vortical pattern upstream of the wake centerline generates an increase in local pressure (and forces acting on the sides of the passage). The vortical pattern downstream of the wake centerline generates a decrease in local pressure (and forces acting on the sides of the passage). The wake-segment ends attached to the sides of the passage travel at the local flow velocities; the wake-segment end near the suction surface moves downstream faster than the wake-segment end near the pressure surface; and the centerline of the wake segment rotates counterclockwise as it propagates downstream. Due to the relative size of rotor and stator, the unsteadiness from the vortex patterns generated by the wake dominate the rotor flow field at low values of R .

3 The unsteady forces on the blades due to the potential-flow and wake interactions acting simultaneously are generated by the combined (additive) interaction of the two disturbances. The unsteady pressure fields due to the combined interaction can be explained by considering the influence of each type of interaction in different regions of the flow.

4 For low values of stator-to-rotor-pitch ratio ($R \approx 1$) the

unsteady forces are dominated by the wake interaction. For high values of stator-to-rotor-pitch ratio ($R > 3$) the unsteady forces are dominated by the potential-flow interaction. For intermediate values of stator-to-rotor-pitch ratio ($R \approx 2$) the unsteady forces are affected by both wake interaction and potential-flow interaction.

Acknowledgments

The author thanks Professor Michael B. Giles and Rolls Royce plc. for their permission to use UNSFLO in this investigation, and the Department of Mechanical Engineering at Washington University in St. Louis for supporting his work on this research program.

References

- Binder, A., Forster, W., Mach, K., and Rogge, H., 1987, "Unsteady Flow Interaction Caused by Stator Secondary Vortices in a Turbine Rotor," *ASME JOURNAL OF TURBOMACHINERY*, Vol. 109, pp. 251-257.
- Boletis, E., and Sieverding, C. H., 1984, "Experimental Study of the Flow Field Behind an Annular Turbine Nozzle Guide Vane With and Without Downstream Rotor," ASME Paper No. 84-GT-15.
- Giles, M. B., 1988a, "Calculation of Unsteady Wake/Rotor-Interactions," *AIAA Journal of Propulsion and Power*, Vol. 4, pp. 356-362.
- Giles, M. B., 1988b, "UNSFLO: A Numerical Method for Unsteady Inviscid Flow in Turbomachinery," MIT Gas Turbine Laboratory Report No. 195, Oct.
- Giles, M. B., 1990, "Stator/Rotor Interaction in a Transonic Turbine," *AIAA Journal of Propulsion and Power*, Vol. 6, pp. 621-627.
- Gostelow, J. P., 1984, *Cascade Aerodynamics*, Pergamon Press, New York.
- Hodson, H. P., 1983, "Unsteady Boundary-Layers on Axial-Flow Turbine Rotor Blades," PhD thesis, University of Cambridge, United Kingdom.
- Hodson, H. P., 1985a, "An Inviscid Blade-to-Blade Prediction of a Wake-Generated Unsteady Flow," *ASME Journal of Engineering for Gas Turbines and Power*, Vol. 107, pp. 337-344.
- Hodson, H. P., 1985b, "Measurements of Wake-Generated Unsteadiness in the Rotor Passages of Axial Flow Turbines," *ASME Journal of Engineering for Gas Turbines and Power*, Vol. 107, pp. 467-476.
- Korakianitis, T., 1987a, "A Design Method for the Prediction of Unsteady Forces on Subsonic, Axial Gas-Turbine Blades," Doctoral thesis (Sc.D.) in Mechanical Engineering, Massachusetts Institute of Technology, Cambridge, MA.
- Korakianitis, T., 1987b, "A Parametric Method for Direct Gas-Turbine-Blade Design," AIAA Paper No. 87-2171.
- Korakianitis, T., and Wilson, D. G., 1988a, "The Effect of the Magnitude of the Inlet-Boundary Disturbance on the Unsteady Forces on Axial Gas-Turbine Blades," *Proceedings of the Fourth International Symposium on Unsteady Aerodynamics and Aeroelasticity of Turbomachines and Propellers*, Aachen, Sept. 6-10, 1987, H. E. Gallus and S. Servaty, eds., published by RWTH Aachen, Feb. 1988, pp. 109-124.
- Korakianitis, T., 1988b, "On the Prediction of Unsteady Forces on Gas Turbine Blades. Part 1: Typical Results and Potential-Flow-Interaction Effects," ASME Paper No. 88-GT-89.
- Korakianitis, T., 1988c, "On the Prediction of Unsteady Forces on Gas Turbine Blades. Part 2: Viscous-Wake-Interaction and Axial-Gap Effects," ASME Paper No. 88-GT-90.
- Korakianitis, T., 1989, "Design of Airfoils and Cascades of Airfoils," *AIAA Journal*, Vol. 27, No. 4, pp. 455-461.
- Korakianitis, T., 1992a, "On the Prediction of Unsteady Forces on Gas Turbine Blades. Part 1: Description of the Approach," *ASME JOURNAL OF TURBOMACHINERY*, Vol. 114, pp. 114-122.
- Korakianitis, T., 1992b, "On the Prediction of Unsteady Forces on Gas Turbine Blades. Part 2: Analysis of the Results," *ASME JOURNAL OF TURBOMACHINERY*, Vol. 114, pp. 123-131.
- Lefcort, M. D., 1965, "An Investigation of Unsteady Blade Forces in Turbomachines," *ASME Journal of Engineering for Power*, Vol. 87, pp. 345-354.
- Liepmann, H. W., and Roshko, A., 1957, *Elements of Gasdynamics*, Wiley, New York.
- Meyer, R. X., 1958, "The Effect of Wakes on the Transient Pressure and Velocity Distributions in Turbomachines," *Trans. ASME*, Vol. 80, pp. 1544-1552.
- Sieverding, C. H., Van Hove, W., and Boletis, E., 1984, "Experimental Study of the Three-Dimensional Flow Field in an Annular Turbine Nozzle Guide Vane," *ASME Journal of Engineering for Gas Turbines and Power*, Vol. 106, pp. 437-448.
- Smith, L. H., 1966, "Wake Dispersion in Turbomachines," *ASME Journal of Basic Engineering*, Vol. 88, pp. 688-690.
- Sonoda, T., 1985, "Experimental Investigation of Spatial Development of Streamwise Vortices in a Turbine Inlet Guide Vane Cascade," ASME Paper No. 85-GT-20.
- Wilson, D. G., 1984, *The Design of High-Efficiency Turbomachinery and Gas Turbines*, The MIT Press, Cambridge, MA.
- Yamamoto, A., and Yanagi, R., 1985, "Production and Development of Secondary Flows and Losses Within a Three Dimensional Turbine," ASME Paper No. 85-GT-217.

Effects of Stator Wakes and Spanwise Nonuniform Inlet Conditions on the Rotor Flow of an Axial Turbine Stage

J. Zeschky

H. E. Gallus

Institut für Strahlantriebe und
Turboarbeitsmaschinen,
RWTH Aachen,
Federal Republic of Germany

Detailed measurements have been performed in a subsonic, axial-flow turbine stage to investigate the structure of the secondary flow field and the loss generation. The data include the static pressure distribution on the rotor blade passage surfaces and radial-circumferential measurements of the rotor exit flow field using three-dimensional hot-wire and pneumatic probes. The flow field at the rotor outlet is derived from unsteady hot-wire measurements with high temporal and spatial resolution. The paper presents the formation of the tip clearance vortex and the passage vortices, which are strongly influenced by the spanwise nonuniform stator outlet flow. Taking the experimental values for the unsteady flow velocities and turbulence properties, the effect of the periodic stator wakes on the rotor flow is discussed.

Introduction

The efficiency of modern turbine stages is strongly affected by the generation of secondary flows and the development of the profile boundary layers. The first models for cascade flows were presented by Hawthorne (1955) and Klein (1966) and later by Langston et al. (1977) and Marchal and Sieverding (1977). The turbulence and loss generation in cascades were investigated in detail by Gregory-Smith et al. (1989) and Zunino et al. (1987). Based on these and many other investigations, great progress on the development of numerical methods for aerodynamic calculations has been made, so that the prediction of the steady flow through an isolated blade row is possible with impressive accuracy.

However, the flow in a real turbomachine is unsteady as a result of the relative motion of the blade rows. Potential field interactions between stationary and rotating airfoils and unsteadiness due to the cutting of wakes and secondary vortices shed from upstream blade rows have a profound effect upon the turbine performance. This is amplified by small axial gaps in modern turbomachines. The stator-rotor interaction is known to affect aerodynamic efficiency, heat transfer, structural loading, and noise generation of turbine stages. Improvements of high-response measurement techniques provided means for the experimental investigation of the unsteady rotor flow.

Joslyn et al. (1983) demonstrated that the rotor outlet flow at midspan of a turbine changes markedly as the rotor interacts periodically with the stator wakes. The three-dimensional flow

through a large-scale turbine was measured by Hunter (1982), Sharma et al. (1985), and Joslyn and Dring (1992). They detected considerable variations of flow angles, velocity, and pressure distribution for different rotor-stator positions.

Besides the potential interaction, the cutting and transport of wakes through a downstream blade row is a major source for the unsteadiness. Meyer (1958) presented an early model of the wake convection, Fig. 1, representing the wake as a negative jet in the downstream blade row. Kerrebrock and Mikolajczak (1970) used the model to explain the temperature redistribution by compressor rotor wakes passing through a stator. The very detailed measurements of Adachi and Murakami (1979) in a cascade with an upstream wake generator confirmed the model further. Additionally, the incoming stator wakes have a strong impact on the rotor profile boundary

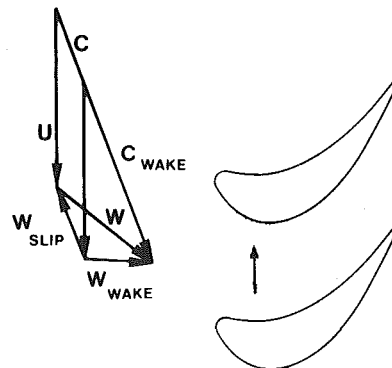
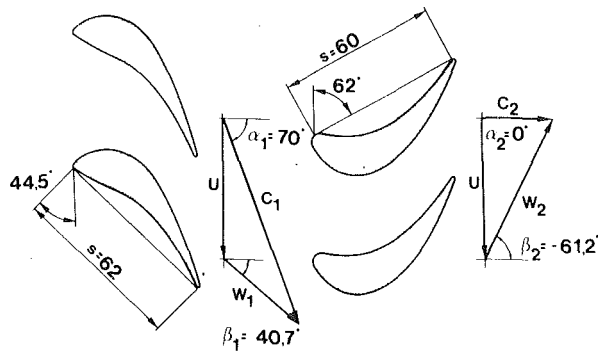


Fig. 1 Stator wake as negative jet in the rotor passage (Meyer, 1958)

Contributed by the International Gas Turbine Institute and presented at the 36th International Gas Turbine and Aeroengine Congress and Exposition, Orlando, Florida, June 3-6, 1991. Manuscript received at ASME Headquarters February 19, 1991. Paper No. 91-GT-93. Associate Technical Editor: L. A. Riekert.



	stator	rotor
Aspect ratio h/s	0.887	0.917
Pitch (midspan) t	47.6 mm	41.8 mm
Blade number	36	41
Tip clearance δ_r	-	0.4 mm
Reynolds number, based on chord and exit velocity	6.8×10^5	4.9×10^5
Rotational speed	-	3500 rpm
Tip diameter	600 mm	600 mm
Axial vane/blade spacing	-	15 mm
Inlet velocity	45 m/s	-

Fig. 2 Turbine design data

layers. Hodson (1983) reported a 50 percent increase of the profile losses compared to a cascade with steady inflow. This is explained by the early transition of the suction side boundary layer, which is likely to occur when the turbulent wake impinges on the blade surface. Unsteady transition and the oscillation of the boundary layer between turbulent and laminar state were also found by Evans (1978) for a compressor and by Dring et al. (1982) for an axial turbine rotor. Many other investigators studied the unsteady wake boundary layer interaction with respect to heat transfer, but this is beyond the scope of this paper.

Another effect causing unsteadiness in the rotor is the cutting of stator secondary vortices. This was examined by Binder (1985), who measured a sudden increase of turbulence energy when the rotor intercepted the passage vortices of the upstream stator row. By using the laser technique he was able to detect the stator wakes by increased turbulence and to show the convection of the wakes through the rotor passage (Binder et al., 1985a).

The objective of the present study is to investigate the flow in a turbine rotor as it is influenced by an upstream stator, including the effects spanwise nonuniform inlet conditions have on the rotor secondary flow and periodically unsteady stator wakes have on the rotor exit velocity and turbulence distribution. The results are of interest for designers using steady-state solutions to estimate the significance of the unsteady effects. On the other hand, the data can be used for a comparison with advanced numerical flow calculations, like the three-dimensional Navier-Stokes solvers presented by Dawes (1992) and Rao and Delaney (1990), which are capable of performing full-stage calculations by coupling the grids of stator vanes and moving rotor blades.

Experimental Facility and Instrumentation

The experimental work was carried out in a single-stage axial turbine with untwisted blades (Fig. 2). In the stator, the Traupel

profile described by Utz (1972) was used; the rotor consists of modified VKI profiles. The application of hot-wire probes limited the investigations to subsonic flows. Although some results may be specific to this turbine, the data can improve the understanding of the more complex flow in modern, multistage turbines. A cross section of the stage with midspan velocity triangles is shown in Fig. 2.

A turbocompressor set provided a continuous airflow to the test rig. The total temperature at turbine inlet was set to $308 \text{ K} \pm 0.5$ by cooling the air at the compressor outlet; the total pressure could be adjusted by bypassing part of the compressor mass flow. With a shaft speed variation of less than ± 0.2 percent during the run, the tests could be repeated with a flow coefficient variation of less than ± 0.7 percent. The Reynolds numbers were constant with an accuracy of ± 1.0 percent.

The flow in the rotor exit plane was surveyed with pneumatic five-hole probes and three-or hot-wire probes, with the probes mounted in the absolute frame. Close to the endwalls, X-hot-wire and pneumatic boundary layer probes were used. The probes were traversed from hub to tip and circumferentially over two blade pitches. In the stator exit plane, only pneumatic probes were located 18 and 12 percent axial chord downstream of stator and rotor, respectively. The measurement of the static pressure distribution on the rotor blades was accomplished with a rotating scanivalve. Using 10 pressure taps on the suction side and 6 on the pressure side, the distributions were obtained at five radial locations. The measurements were corrected to take into account centrifugal effects on the column of air in the rotating piping, and thus could be repeated with an accuracy of ± 2 percent. In order to obtain the unsteady static pressure field at the casing above the rotor, miniature high response pressure transducers were mounted at 25 axial locations in the casing. To improve the accuracy of the measurements, only the unsteady pressure amplitude of the transducers was recorded and superimposed on the time-mean static pressure measured by steady-state instrumentation. The data acquisition and reduction scheme was essentially the same as described in the following section for the hot-wire probes.

Nomenclature

b_p = axial chord
 C = velocity, absolute frame
 h = span
 n = shaft speed
 p = static pressure
 p_t = total pressure
 s = chord
 t = pitch
 u = circumferential speed
 u' = random axial velocity fluctuation

v' = random radial velocity fluctuation
 w = velocity, relative frame
 w' = random circumferential velocity fluctuation
 Z = blade number
 α = flow angle in circumferential direction, absolute frame
 β = flow angle in circumferential direction, relative frame
 δ_r = tip clearance
 ω_r = reduced frequency

Subscripts

r = radial direction
 x = axial direction
 Φ = circumferential direction
 0 = stator inlet plane
 1 = rotor inlet plane
 2 = rotor exit plane

Superscripts

\sim = periodic value
 $\bar{\quad}$ = averaged value

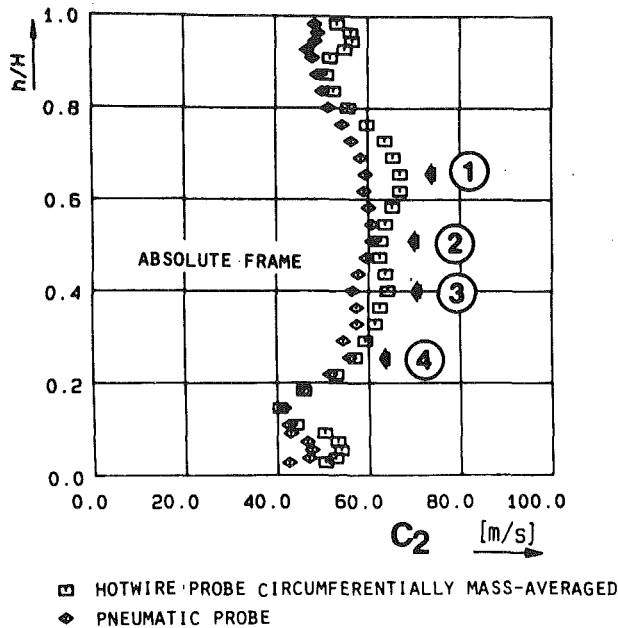


Fig. 3(a) Comparison of hot-wire and pneumatic probe measurements: flow velocity at rotor exit

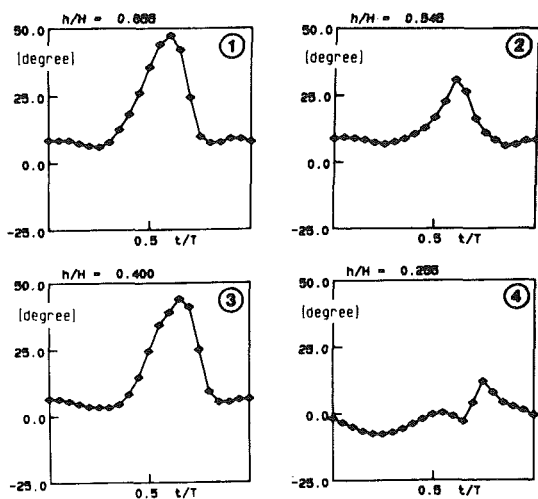


Fig. 3(b) Flow angle fluctuation in the rotor exit plane over the blade passing period

All experimental data are normalized with respect to the International Standard Atmosphere at stator inlet and refer to the design operation point of the turbine.

Real Time Data Acquisition and Reduction

Since the hot-wire probes are a key feature of this investigation, the calibration and data acquisition are described shortly. A more detailed description was presented by Poengen and Gallus (1991).

The unsteady voltages from the hot-wire bridges were logged with a high-speed (up to 10 MHz) multichannel data acquisition system. In these experiments, 256 real-time samples were recorded over roughly four blade passing periods and averaged over 256 revolutions. For each of the 65,000 data points, the velocity vector was calculated based on a polynomial least-square fit method. Input for this were the results from a free-jet calibration of the probes, where an accuracy in velocity of 0.5 m/s and in pitch and yaw angle of less than 0.2 deg was

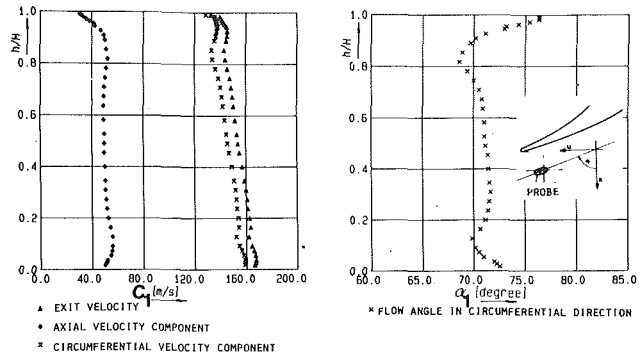


Fig. 4 Circumferential mass-averaged flow angle and velocity in the stator exit plane

achieved. Phase-locked averaging (Gostelow, 1977) has been used for the data reduction. The results of the velocity measurements, for example, are presented in the form of the ensemble mean values,

$$\bar{c}(i) = \frac{1}{N} \sum_{n=1}^N c(i, n) \quad (1)$$

and the ensemble root mean square of the random fluctuations,

$$\sqrt{\bar{c}'^2(i)} = \sqrt{\frac{1}{N} \sum_{n=1}^N [c(i, n) - \bar{c}(i)]^2} \quad (2)$$

where N denotes the number of revolutions and i the index for the circumferential direction. Using a square wave signal, the corner frequency of the hot wires was found to be greater than 20 kHz, which is a conservative estimate. At 50 kHz, the ratio between signal amplitude and probe response is still greater than 0.8, while the blade passing frequency is only 2.4 kHz. The recorded real-time signals were filtered by a digital low-pass Blackman filter to eliminate high-frequency noise. The Channon factor, which describes the relation between cut-off frequency of the filter process and the sampling frequency, is about 0.3.

During the measurements, the probes having a sensitive cone of ± 25 deg yaw and pitch angle were always aligned to the mean flow direction. It was found, however, that at some measurement stations the pitch angle fluctuation exceeded the acceptance cone when a rotor wake passed the probe.

Therefore, it was necessary to record additional data after rotating the probe. Data were only accepted if the ensemble mean pitch angle was smaller than 15 deg, thus allowing for turbulent fluctuations, and they had to be derived from two measurements with different probe orientations. Figure 3 compares the circumferentially averaged flow velocity at rotor outlet as detected by hot-wire and pneumatic probes. At locations (2) and (4), where the pitch angle variation is relatively small, good agreement is reached, whereas at locations (1) and (3) with a pitch angle variation of more than 40 deg during the passing wake, the differences between steady and unsteady measurements amount to more than 10 percent. Based on this, the authors felt that the hot-wire technique yields reliable results, confirmed by the good agreement with the five-hole probe, and that the steady-state pneumatic probe readings were not reliable in regions of large unsteady fluctuations.

Experimental Results

Stator Flow. Flow measurements downstream of the stator are presented briefly to document the rotor inlet conditions. The circumferentially mass-averaged exit velocity measured at 20 percent of axial chord downstream of the stator, Fig. 4,

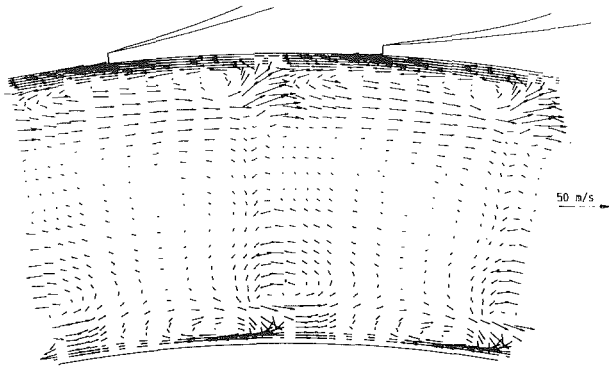


Fig. 5 Secondary flow field at stator exit

indicates the higher acceleration at the hub. The reason for this is the high exit swirl and the resulting higher static pressure at the tip. The overall averaged outlet Mach number M_1 is 0.45. The plot of the exit flow angle, Fig. 4, exhibits a pattern familiar in secondary flow studies, with overturning at the endwalls and the corresponding underturning at a short distance away from the endwalls. In spite of the lower acceleration, the overturning is stronger at the tip. This is explained by the thicker inlet boundary layer, with an estimated 99 percent thickness of 11.8 and 5.5 percent span at tip and hub, respectively. At both end walls, the boundary layers are naturally turbulent. The secondary flow field, Fig. 5, demonstrates the circumferential extension of the passage vortices. At the tip, the overturning occurs over the whole cross sections, whereas at the hub only a smaller passage vortex is observed. In the wake area, the imbalance between centrifugal and pressure forces causes inward directed radial components. In the total pressure loss contour plot, Fig. 6, significant losses are found only in the wake of the profile and in the corner between suction side and tip. Two loss cores can be seen at about 15 and 85 percent span. At these locations, a third vortex at the hub and a somewhat distorted flow region at the tip are observed in Fig. 5. Flow visualization at the passage surfaces with a Ti_2O -oil mixture and the results from other authors, as for example Gregory-Smith et al. (1988), indicate that, forced by the passage vortices, low-momentum fluid from the inlet endwall boundary layers is transported toward the suction side and accumulated in the loss cores. Again, the higher losses and the larger extension of the wake at the tip are due to the thicker inlet boundary layer.

In Fig. 7, the time-averaged rotor inlet flow in the relative frame obtained from the absolute values and a vector addition of the circumferential speed is presented. The incidence angle increases toward the hub because of the higher stator exit velocity and the lower circumferential speed. At the radial locations of 15 and 85 percent span, a local turning of the inlet flow vector of about 10 deg toward the suction side occurs, which is caused by stator underturning, Fig. 4. The velocity increases nearly linearly from tip to hub, with almost no detectable reduction at the hub, whereas the higher losses at the tip lead to a reduced velocity between casing and 90 percent span.

The shaded areas in Fig. 7 mark the velocity and incidence fluctuations as the rotor passes the stator wakes. At midspan, the incidence is reduced by 8.5 deg and the velocity by 10 percent. The highest incidence fluctuations occur at about 85 and 15 percent span. When the rotor blade passes the loss cores in the stator wake, the incidence at these locations decreases 22 deg and 15 deg, respectively. At the tip, the incidence fluctuations are generally high, caused by the large extension of the wake. The velocity fluctuations are nearly of the same magnitude across the whole span, showing higher fluctuations only at the locations of the loss cores. The steady-state meas-

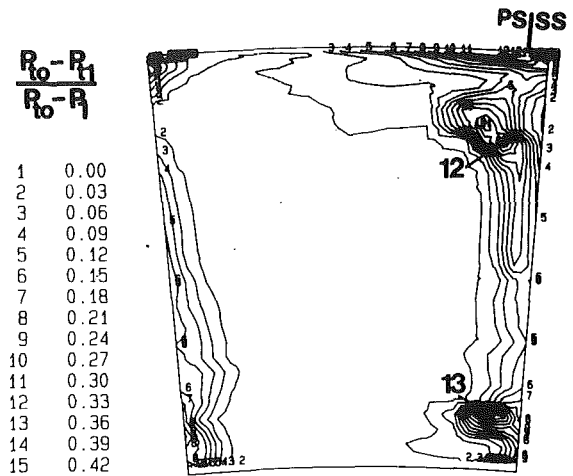


Fig. 6 Total pressure loss contours at stator exit

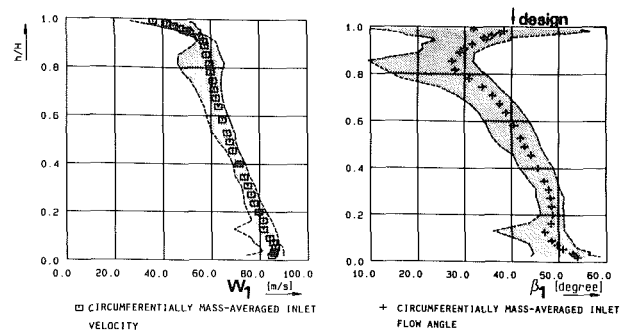


Fig. 7 Rotor inlet velocity and flow angle, fluctuation shaded

urements in the stator exit flow could not detect the potential flow field interaction. However, the upstream influence of the rotor potential field on the steady-state stator flow is only weak, as stated by Dring et al. (1982) and Dunn et al. (1990), who varied the rotor-stator axial spacing between 10 to 65 percent of blade pitch. They also found that the fluctuations in the rotor were of much larger amplitude than could be explained by the stator potential flow field alone and that the decay with increased axial gap was similar to the wake decay. Therefore, the authors believe, the influence of the stator wakes on the rotor flow is considerably stronger than that of the potential flow field of the thin trailing part of the stator vanes.

Rotor Flow. The time-mean static pressure distribution on the rotor blades was measured at five radial locations, Fig. 8. With increasing loading toward the hub, see Fig. 7, the stagnation point moves to the pressure side. From tip to midspan, the suction side flow accelerates smoothly up to the throat at about 60 percent chord and decelerates toward the trailing edge. At lower radii, the high positive incidence angle causes a strong acceleration around the leading edge and merely a weak deceleration over nearly the whole suction side. At the pressure side, the flow is only slightly affected by the spanwise varying incidence. The static pressure is nearly constant up to 40 percent axial chord, followed by an acceleration in the last part of the passage. Figure 9 shows the time-mean static pressure distribution at the casing for a certain rotor position. As expected for an inlet flow with nearly zero incidence, see Fig. 7, the stagnation point at design point is located at the leading edge. If the direction of the local velocity is assumed to be perpendicular to the lines of constant static pressure, Fig. 9 indicates between the blades an underturning of the flow at the casing from pressure to suction side. The effect of the tip

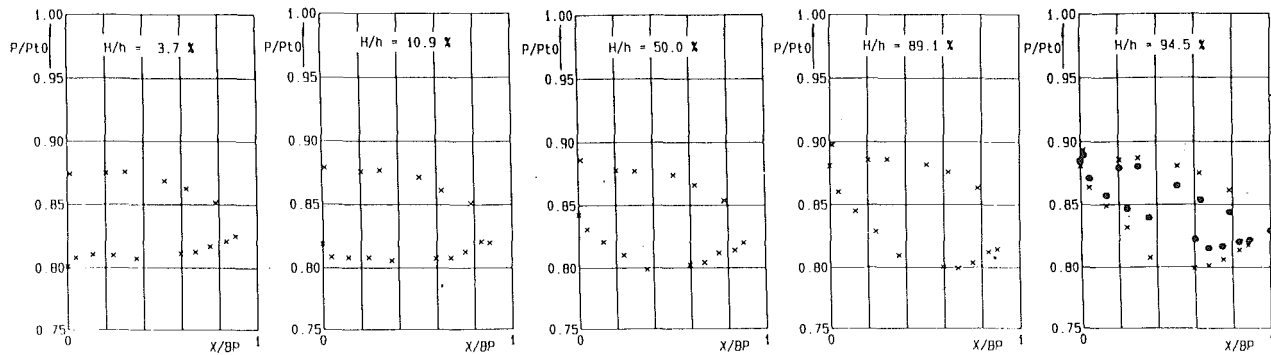


Fig. 8 Profile pressure distribution on the rotor blades

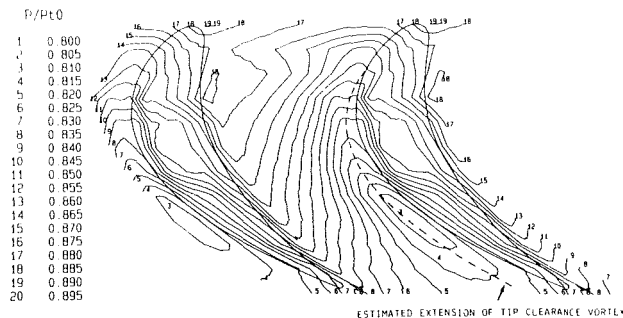


Fig. 9 Ensemble-averaged static pressure field at the casing above the rotor

clearance flow is also visible. The crossflow starts at the leading edge and seems to emerge at the suction side at about 25 percent axial chord. The highest crossflow intensity, indicated by the close spacing of the isolines, is noted between 50 and 90 percent chord. In this part of the passage, the blade thickness is continuously reduced while the pressure difference between pressure and suction side is very large. The extension of the tip clearance vortex is estimated by connecting the locations of lowest static pressures and is shown as a dashed line in Fig. 9. At the trailing edge, it extends over 20 to 25 percent of the passage.

To identify the effect of the tip clearance flow on the blade pressure distribution, the static pressure at the casing was plotted together with the blade pressures at 94.5 percent span in Fig. 8. Both distributions agree well at the leading and the trailing edge, thus confirming the measurement techniques. Starting at about 25 percent axial chord, where the tip clearance flow begins to emerge from the gap, the pressures at the suction side are considerably increased. The corresponding pressure decrease on the pressure side starts at about 50 percent chord, where the intensity of the crossflow through the radial gap is amplified. This leads to clearly reduced blade forces in the tip region. Another interesting fact is that even at the casing downstream of the trailing edge the static pressure at the suction side is considerably lower than at the pressure side, see Fig. 9. As is evident in Fig. 10, this causes intense mixing in the wake downstream of the rotor.

At 12 percent axial chord downstream of the rotor, hot-wire measurements were carried out. The measurements were recorded at 32 radial and 9 circumferential locations. From these measurements, a stop-action sequence was computed, which can be understood as "photographs" of the rotor exit flow. All data presented in this chapter refer to the same position relative to the upstream stator, while the rotor blades pass the stationary observer. The four rotor positions referenced here are equally spaced, i.e., between each position the rotor passes 20 percent of the stator pitch.

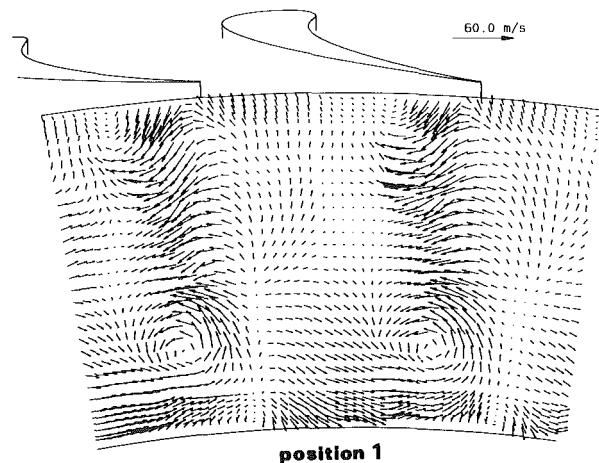


Fig. 10 Secondary flow field at rotor exit, stationary frame

Prior to the effects of stator wakes on the rotor flow, the basic flow pattern at rotor exit is discussed. The secondary flow field in the stationary frame is depicted in Fig. 10 for a specific rotor-stator position. The arrows represent the local velocity vectors viewed from the downstream direction. This direction is defined by the overall mass-averaged pitch angle α and a zero yaw angle. Between 2.7 and 9 percent and 92 and 98 percent span only two-dimensional hot-wire probes could be used. To obtain the radial velocity components in these locations, the Euler equations were solved under the assumptions of steady-state flow and negligible pressure gradients in axial direction. Figure 10 reveals strong crossflow components from the pressure side into the wake area, as expected from pressure measurements, Fig. 9. In the tip region, the clearance causes outward-directed flow at the pressure side and strong inward-directed components at the suction side. Stator passage vortices persisting throughout the rotor as mentioned by Sharma et al. (1985) could not be detected. At the hub, the exit swirl is directed against the sense of rotation, due to the lower circumferential speed.

A possible explanation for the wavy flow pattern at the hub might be the combination of small measurement errors and the simplifications used for the calculation of the radial components. However, since the computed flow pattern at the tip is very smooth, the hub flow may be influenced by the small gap between the rotor and the downstream stationary hub. The gap, which is sealed by a labyrinth seal, is located right under the measurement plane.

The secondary flow fields in the relative frame, Fig. 11, show two intense passage vortices and a tip clearance vortex. At rotor position 1, which corresponds to Fig. 10, the tip clearance vortex extends to about 20 percent of the blade-to-

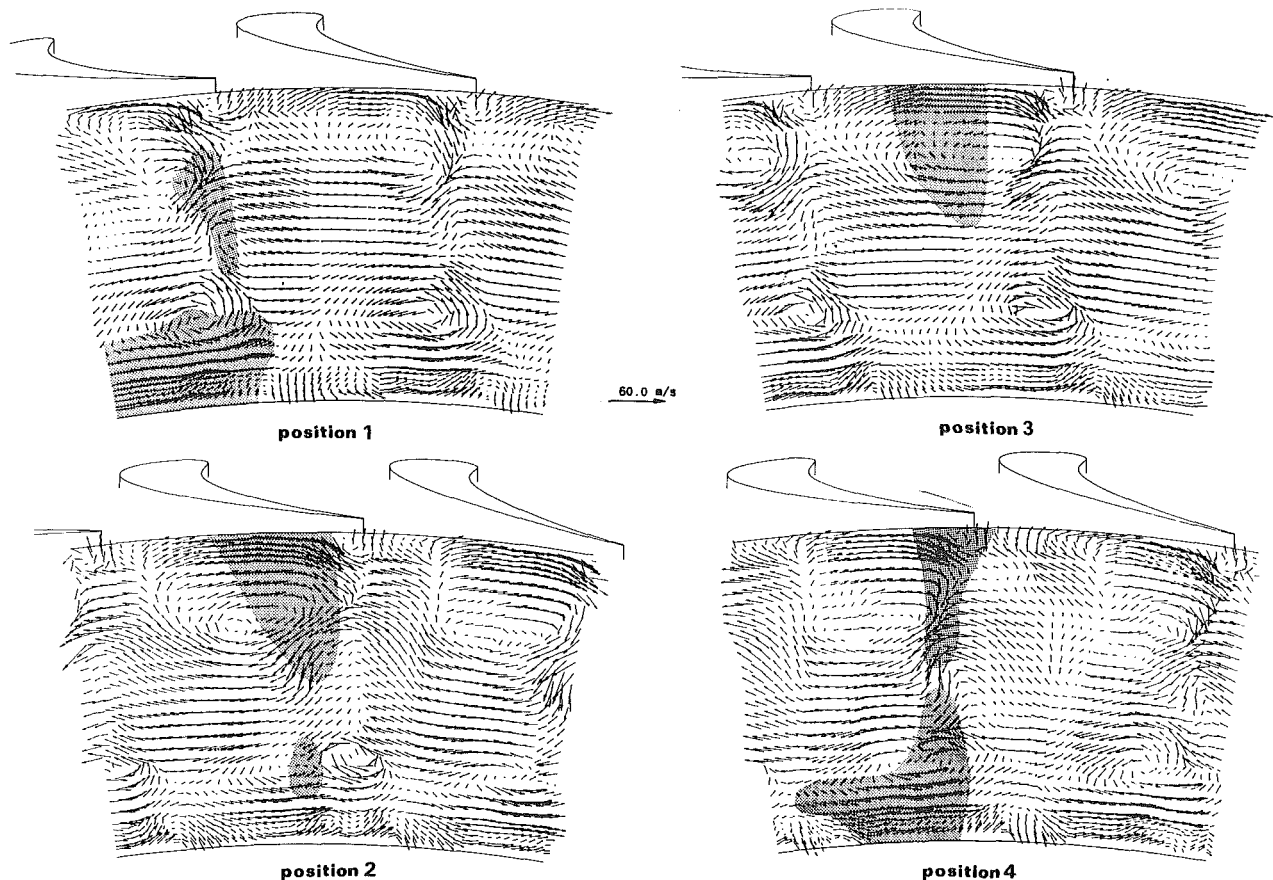


Fig. 11 Secondary flow field at rotor exit for four different rotor/stator positions, relative frame; areas with increased turbulence shaded

blade cross section. This is in good agreement with the casing static pressures, Fig. 9. The relatively small tip clearance vortex with a radial extension of only 10 percent span is due to the small radial gap of 0.6 percent span.

The passage vortex in the tip region is generated by the action of the blade-to-blade pressure gradient on the low-momentum fluid at the casing as it enters the rotor passage. The overturning, also observed in Fig. 9, is further amplified by the relative movement of the casing. Close to the suction side, the interaction between passage vortex and tip clearance vortex leads to strong inward-directed radial components.

At the hub, the maximum overturning occurs at about 15 percent span and not, as expected, close to the endwall. A similar effect was observed by Binder et al. (1985b) in a transonic turbine stage and by Hunter (1982) in a large-scale turbine test rig, but presented without detailed explanation. Hunter found that the hub boundary layer was extremely thin and that overturning occurred only in the first part of the rotor passage. The measured stator exit flow, Figs. 6 and 7, also shows very thin boundary layers at rotor inlet. It is unlikely that these thin boundary layers cause such strong crossflow. The separation of the passage vortex from the hub is also unlikely, since low-momentum fluid tends to migrate toward the hub due to the radial pressure gradient. Therefore, it was assumed that the distorted rotor inlet flow strongly influences the flow through the rotor passage. As already mentioned, in Fig. 7 the incidence angle at rotor inlet increases toward the hub with a local decrease of about 10 deg at 15 percent span. The circumferentially mass-averaged outlet flow angle in the relative frame, Fig. 12, shows the highest overturning at the same location. Without remarkable reduction, the distortions of the stator outlet are visible in the rotor outlet flow. The profile pressure distributions, Fig. 8, measured at 3.7 and 10.9 percent

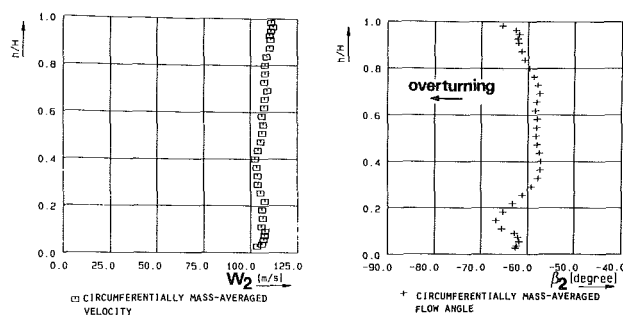


Fig. 12 Flow angle and velocity in the rotor exit plane, relative frame

span, remain basically the same; only the blade pressures at the leading edge are influenced by the local displacement of the stagnation point to the suction side. In spite of the reduced incidence angle at 10.9 percent span, the low pressures at the leading part of the suction side indicate a strong acceleration and increased circumferential velocity components toward the suction side. This could be explained by the fact that the profile pressure distribution in the three-dimensional flow cannot respond to the local change of incidence as expected from the two-dimensional theory. It seems as if the pressures from higher and lower radial locations are superimposed on the local unloading of the blade, thus causing the observed overturning in the hub region at 15 percent span.

The measured exit velocity distribution in the relative frame is shown in Fig. 13. The wake can be clearly distinguished, with sharp gradients at the pressure side edge. The favorable pressure gradient on the pressure side leads to the development of a thin profile boundary layer. On the suction side, the wake

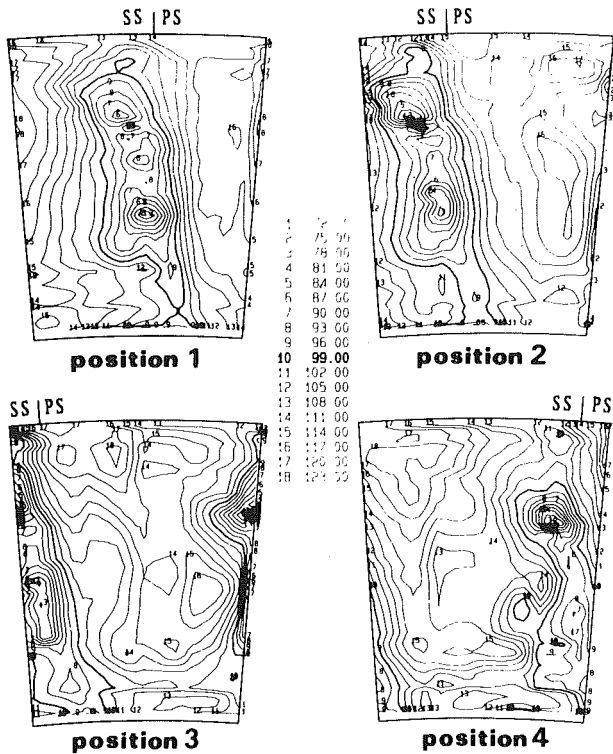


Fig. 13 Contour plots of rotor exit velocity, relative frame

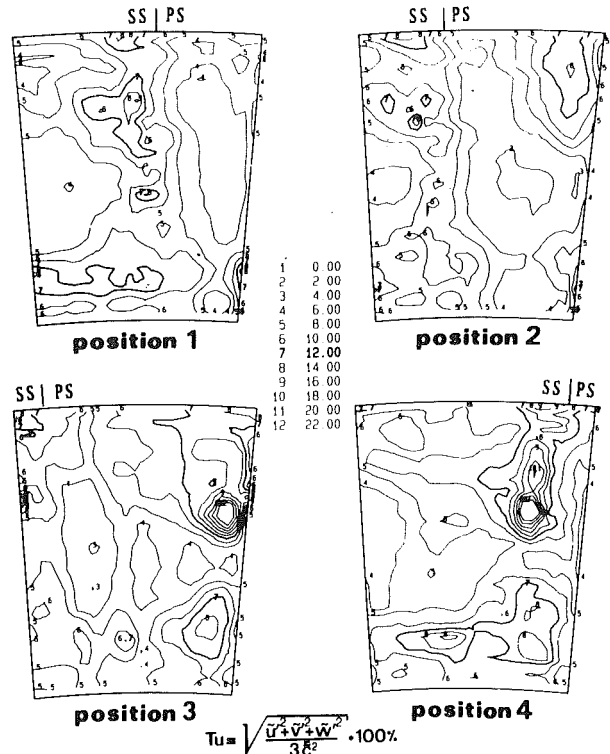


Fig. 14 Contour plots of turbulence intensity in the rotor exit plane

is more extended. At the present stage of the investigation, no measurements of the rotor boundary layers were made. Hodson and Addison (1989) found that the transition of the profile boundary layer in their turbine rotor occurred shortly before the peak suction point. This point is located at about 60 percent chord at the tip, 40 percent chord at midspan, and close to the leading edge at the hub, see Fig. 8. The transitional and turbulent nature of the suction side boundary layer accounts for the thicker wake at the suction side, which is even more extended at the hub than at the tip. The two minima in the velocity distribution at about 60 and 40 percent span seem to be accumulations of low-energy fluid, which is transported to these locations by the passage vortices from higher and lower locations, respectively. This leads to a small rotor wake close to the endwalls, where the wake is energized by the passage vortices.

As a consequence of the different number of airfoils in stator and rotor, the flow field in two adjacent rotor passages is slightly different. For the sake of clarity, only the flow of the left rotor blade passage in Fig. 11, which corresponds to the contour plot of Figs. 13 and 14, is discussed here. The wakes are characterized by increased turbulence and velocity defects. Figure 14 shows the turbulence intensity measured downstream of the rotor. Close to the endwalls, where only two-dimensional measurements were carried out, the radial turbulence intensity was assumed to be of the same order as two other components. This seemed to be justified from the analysis of the three-dimensional measurements close to the endwalls.

To explain the flow behavior, the convection of the stator wakes through the rotor passage was calculated using a simplified, nonviscous, two-dimensional flow model. The modeling effort concentrated on predicting the path of the stator wake centerline as it encounters the blade row and progresses through the passage. The data did not allow the accurate prediction of leading and trailing edge propagation rates of the stator wakes. The results agreed well with locations of increased turbulence in the rotor exit flow. These areas, showing a turbulence level of more than 10 percent outside or 15 percent

inside of the rotor wake, are shaded in Fig. 11. The positions of the stator wakes remain nearly unchanged in the stationary frame. Because of the higher axial velocity and the negative swirl at the hub, the leading edge of the stator wake is detected first at the hub (rotor position 3), then at midspan (position 1), and later in the tip region (position 3). According to a reduced frequency of

$$\omega_R = \frac{n * z_V * b_{P,B}}{c_X} = 2.06 \quad (3)$$

(n = shaft speed, z = number of stator vanes, c_x = axial velocity, b_p = axial chord of rotor blades), about two stator wakes are simultaneously present in each rotor passage.

The flow at midspan is only little affected by the stator wakes. The average free-stream velocity decreases from 115 m/s to 90 m/s at the rotor wake centerline; the turbulence intensity increases from 6 percent to 10 percent. The highest turbulence of 12 percent at midspan is detected at rotor position 1, with a velocity defect of 20 percent in the wake. At positions 2 and 3, the turbulence in the rotor wake is reduced to 8 percent, with a velocity defect of 26 percent. At position 4 the turbulence level is low, i.e., 8 percent, and the velocity defect amounts to 20 percent. The higher turbulence and the higher velocity in the wake are caused by the early transition of the suction side boundary layer, which is likely to occur when the stator wake impinges on the blade surface (Hodson and Addison, 1989). At positions 2 and 3, the lower turbulence and higher velocity defects in the rotor wake indicate an undisturbed suction side boundary layer, being laminar over the first part of the passage. At position 4, shortly before the leading edge of a stator wake is visible, the turbulence intensity is still rather low, but the velocity defect in the rotor wakes is already reduced.

The width of the rotor wake is not only affected by the state of the profile boundary layer, but mainly by complex secondary flow and mixing phenomena. Comparing the flow over the whole passage for the 4 rotor positions, the rotor wake can be clearly distinguished for all positions by reduced velocity, Fig.

13, and increased turbulence, Fig. 14. The highest changes of the flow properties were noted at the locations of the passage vortices, Fig. 11, between 10–40 percent and 60–90 percent span. This agrees with the high losses and incidence fluctuations in the rotor inlet flow at these radii. While the basic flow pattern remains the same for all rotor-stator positions, the intensity and size of the vortices change significantly.

In the literature, the stator wake passing through the rotor passage is mostly understood as a negative jet, Fig. 1, which is induced by the slip velocity between free stream and wake fluid at rotor inlet. Hodson (1983) and Adachi and Murakami (1979) confirmed the model by measuring the flow in the cross section at midspan of an axial turbine and an axial compressor. They showed that the negative jet persists within the rotor passage, even if it has been chopped by the rotor blades. Within the negative jet, the stator wake fluid is transported relative to the main flow toward the suction side of the rotor blades. The transport is interrupted by the blade surface, with the result that turbulent low-energy fluid tends to accumulate at the suction side.

In Fig. 10, the negative jet can be identified by increased crossflow components toward the suction side. At rotor positions 4 and 1 the stator wake is visible in the hub region. The crossflow between 10 and 20 percent span is intensified; the same effect can be noted in the tip region at positions 3 and 4.

With no stator wake visible at the hub, position 2, the intensity of the passage vortex is clearly reduced. At position 3, the leading edge of a stator wake intercepts the lower passage vortex, which coincides with increased turbulence. A similar interception was observed by Hebert and Tiederman (1990) in a linear cascade with an upstream wake generator. In the upper part of the channel the turbulence level is generally higher than at the hub. One explanation for the high turbulence is the high losses and incidence fluctuations, which arise as the rotor passes the stator wake area. Another explanation was suggested by Binder (1985), who found that the cutting of the stator secondary vortices by the rotor blade was associated with high turbulence energy of about the same magnitude as measured here. The cutting of the passage vortex occurs shortly after the rotor blade has passed the centerline of the stator wake. Since intensity and size of the stator passage vortex at the casing fairly exceed that of the hub passage vortex, Fig. 5, the turbulence in the outer region is considerably higher. It is further amplified by the interaction between passage and tip clearance vortex.

Because of the strong radial components, the region with the highest turbulence and lowest velocity has a moved toward midspan.

The analysis of the data showed that the tip clearance vortex is only slightly affected by the passing stator wakes, which was also observed by Sharma et al. (1985). Its size, velocity, and turbulence were not significantly different at the various rotor positions, although the intensity seemed to be reduced at positions 3 and 4, when the stator wake was visible in the tip region.

Summary and Concluding Remarks

The measurements of the unsteady, three-dimensional rotor flow field have demonstrated that the development of the rotor secondary flow, the rotor wake, and the outlet flow angles are mainly influenced by the circumferentially averaged, nonuniform stator exit flow. But, as observed by several other investigators, the periodically unsteady rotor inlet flow caused by the upstream stator also influences the rotor flow significantly. The present results can be summarized as follows:

- 1 The passage vortices in the rotor are strongly influenced

by the nonuniform stator outlet flow and cause the accumulation of low-energy fluid in the rotor wake close to midspan.

- 2 The stator wakes are discernible in the rotor outlet. Data of fast-response hot-wire probes traversed circumferentially relative to the stator show a variation of the time-averaged rotor exit velocity of 5 percent at midspan and more than 9 percent in the regions of the passage vortices. The time-averaged outlet flow angle varies between 3 deg at midspan and 7 deg in the outer regions. This emphasizes the need to traverse probes circumferentially, if the probes are mounted at a short axial distance downstream of the rotor, even if only steady-state values will be recorded.

- 3 The stator wakes act as “negative jets” in the rotor passages and amplify the crossflow components of the passage vortices toward the suction side.

- 4 The stator wakes impinging on the rotor blade surface have a significant effect on the rotor wake at midspan. The early boundary layer transition increases the turbulence intensity in the wake and causes a lower free-stream velocity at the edge of the wake, thus leading to higher profile losses.

- 5 The highest fluctuations of the velocity, the flow angle, and the turbulence intensity are detected in the hub and tip region. Here the deep stator wakes and the cutting of stator secondary vortices lead to periodically high turbulence levels and intensified crossflow components toward the suction side.

These results suggest that the radial distribution of the flow properties has to be included into the design process. Although no correlation for a quantitative assessment of the unsteady effects has been derived from the data, the results can be very useful for estimating the importance of these effects, if a steady-state design method is applied.

References

- Adachi, T., and Murakami, Y., 1979, “Three-Dimensional Velocity Distribution Between Stator Blades and Unsteady Force on a Blade Due to Passing Wakes,” *Trans. JSME*, Vol. 22, No. 170, pp. 1074–1082.
- Addison, J. S., and Hodson, H. P., 1990, “Unsteady Transition in an Axial-Flow Turbine: Part 2—Cascade Measurements and Modeling,” *ASME JOURNAL OF TURBOMACHINERY*, Vol. 112, pp. 215–221.
- Binder, A., Förster, W., Kruse, H., and Rogge, H., 1985a, “An Experimental Investigation Into the Effect of Wakes on the Unsteady Turbine Rotor Flow,” *ASME Journal of Engineering for Gas Turbines and Power*, Vol. 107, pp. 458–466.
- Binder, A., Rogge, H., and Kauratschke, W., 1985b, “Sekundärströmungen im Laufrad einer Turbine,” *VDI-Berichte* 527.2.
- Binder, A., 1985, “Turbulence Production Due to Secondary Vortex Cutting in a Turbine Rotor,” *ASME Journal of Engineering for Gas Turbines and Power*, Vol. 107, pp. 1039–1046.
- Dawes, W. N., 1992, “Toward Improved Throughflow Capability: The Use of Three-Dimensional Viscous Flow Solvers in a Multistage Environment,” *ASME JOURNAL OF TURBOMACHINERY*, Vol. 114, pp. 8–17.
- Dring, R. P., Joslyn, H. D., Hardin, L. W., and Wagner, J. H., 1982, “Turbine Rotor-Stator Interaction,” *ASME Journal of Engineering for Power*, Vol. 104, pp. 729–742.
- Dunn, M., Senett, W., Delaney, R., and Rao, K., 1990, “Investigation of Unsteady Flow a Transonic Turbine Stage: Part I—Data/Prediction Comparison for Time-Averaged and Phase-Resolved Pressure Data,” *AIAA Paper No. 90-2409*.
- Evans, R. L., 1978, “Boundary Layer Development on an Axial-Flow Compressor Stator Blade,” *ASME Journal of Engineering for Power*, Vol. 100, pp. 287–293.
- Gostelow, J. P., 1977, “A New Approach to the Experimental Study of Turbomachinery Flow Phenomena,” *ASME Journal of Engineering for Power*, Vol. 99, pp. 97–105.
- Gregory-Smith, D. C., Graves, C. P., and Walsh, J. A., 1988, “Turbulence Measurements and Secondary Flows in a Turbine Rotor Cascade,” *ASME JOURNAL OF TURBOMACHINERY*, Vol. 110.
- Hawthorne, W. R., 1955, “Rotational Flow Through Cascades,” *J. Mech. Appl. Math.*, Vol. 3.
- Hebert, G. J., and Tiederman, W. G., 1990, “Comparison of Steady and Unsteady Secondary Flows in a Turbine Stator Cascade,” *ASME JOURNAL OF TURBOMACHINERY*, Vol. 112, pp. 625–632.
- Hodson, H. P., 1983, “The Development of Unsteady Boundary Layers on the Rotor of an Axial-Flow Turbine,” *AGARD CP-351*, Copenhagen.
- Hodson, H. P., 1985, “Measurements of Wake-Generated Unsteadiness in the Rotor Passages of Axial Flow Turbines,” *ASME Journal of Engineering for Gas Turbines and Power*, Vol. 107, pp. 467–477.
- Hodson, H. P., and Addison, J. S., 1989, “Wake-Boundary Layer Inter-

- actions in an Axial Flow Turbine Rotor at Off-Design Conditions," *ASME JOURNAL OF TURBOMACHINERY*, Vol. 111, pp. 181-192.
- Hunter, I. H., 1982, "Endwall Boundary Layer Flows and Losses in an Axial Turbine Stage," *ASME Journal of Engineering for Power*, Vol. 104, pp. 184-193.
- Joslyn, H. D., Dring, R. P., and Sharma, O. P., 1983, "Unsteady Three-Dimensional Turbine Aerodynamics," *ASME Journal of Engineering for Power*, Vol. 105, pp. 322-331.
- Joslyn, H. D., Caspar, J. R., and Dring, R. P., 1986, "Inviscid Modelling of Turbomachinery Wake Transport," *J. Propulsion*, Vol. 2, No. 2, Mar.
- Joslyn, D., and Dring, R., 1992, "Three-Dimensional Flow in an Axial Turbine: Part 1—Aerodynamic Mechanisms; Part 2—Profile Attenuation," *ASME JOURNAL OF TURBOMACHINERY*, Vol. 114, pp. 61-78.
- Kerrebrock, J. L., and Mikolajczak, A. A., 1970, "Intra-stator Transport of Rotor Wakes and Its Effect on Compressor Performance," *ASME Journal of Engineering for Power*, Vol. 92, pp. 359-368.
- Klein, A., 1966, "Untersuchungen über den Einfluß der Zuström Grenzschicht auf die Sekundärströmung in den Beschaufelungen von Axialturbinen," *Forschung Ing.*, Vol. 32, No. 6.
- LaGraff, J. E., Ashworth, D. A., and Schultz, D. L., 1989, "Measurement and Modeling of the Gas Turbine Blade Transition Process as Disturbed by Wakes," *ASME JOURNAL OF TURBOMACHINERY*, Vol. 111, pp. 315-322.
- Langston, L. S., Nice, M. L., and Hooper, R. M., 1977, "Three-Dimensional Flow Within a Turbine Blade Passage," *ASME Journal of Engineering for Power*, Vol. 99, pp. 21-28.
- Lefcort, M. D., 1965, "An Investigation Into Unsteady Blade Forces in Turbomachines," *ASME Journal of Engineering for Power*, Vol. 87, pp. 345-354.
- Marchal, P., and Sieverding, C. H., 1977, "Secondary Flows Within Turbomachinery Blades," *Secondary Flows in Turbomachinery*, AGARD CP-214.
- Meyer, R. X., 1958, "The Effect of Wakes on the Transient Pressure and Velocity Distributions in Turbomachines," *ASME Journal of Basic Engineering*, Vol. 80, pp. 1544-1552.
- Poensgen, C., and Gallus, H. E., 1991, "Three-Dimensional Wake Decay Inside of a Compressor Cascade and Its Influence on the Downstream Unsteady Flow Field: Part I—Wake Decay Characteristics in the Flow Passage," *ASME JOURNAL OF TURBOMACHINERY*, Vol. 113, pp. 180-189.
- Rao, K., and Delaney, R., 1990, "Investigation of Unsteady Flow Through a Transonic Turbine Stage, Part I: Analysis," AIAA Paper No. 90-2408.
- Sharma, O. P., Butler, T. L., Joslyn, H. D., and Dring, R. P., 1985, "Three-Dimensional Unsteady Flow in an Axial Flow Turbine," *Jet Propulsion*, Vol. 1, No. 1, pp. 29-38.
- Utz, C., 1972, "Experimentelle Untersuchung der Strömungsverluste in einer mehrstufigen Axialturbinen," Thesis ETH Zürich, Switzerland.
- Zunino, P., Ubaldi, M., and Satta, A., 1987, "Measurements of Secondary Flows and Turbulence in a Turbine Cascade," ASME Paper No. 87-GT-132.

Blade Row Interaction in a Multistage Low-Pressure Turbine

N. Arndt

MTU München,
Munich, Federal Republic of Germany

The objective of this work was to enhance the understanding of unsteady flow phenomena in multistage low-pressure turbines. For this purpose, hot-film probe measurements were made downstream of every rotor blade row of a five-stage low-pressure turbine. Rotor-rotor interaction and stator-rotor interaction were observed to have a profound influence on the flow through the low-pressure turbine. Interaction of rotors of different turbine stages occurred owing to the influence of the wakes shed by one rotor blade row upon the flow through the next downstream rotor blade row. This wake-induced rotor-rotor interaction resulted in strongly amplitude-modulated periodic and turbulent velocity fluctuations downstream of every rotor blade row with the exception of the most upstream one. Significantly different wake depths and turbulence levels measured downstream of every rotor blade row at different circumferential positions evidenced the effect of the circumferentially nonuniform stator exit flow upon the next downstream rotor blade row. Stator-rotor interaction also strongly influenced the overturning and the underturning of the rotor wakes, caused by the rotor secondary flows, in the rotor endwall regions. Low rotor wake overturning and underturning, i.e., reduced rotor secondary flow influence, were observed to correlate well with low rotor wake turbulence levels.

Introduction

The unsteady flow in a turbomachine resulting from the relative motion of neighboring blade rows causes various interactions between the blade rows that may influence both the aerodynamic and the structural behavior as well as the noise emission of the rotor blades and the stator vanes of the turbomachine. The potential flow interaction between two blade rows moving relative to each other arises because of the circulation about the blades and because of the potential fields, other than circulation, about the blades that are due to the finite thickness of the blades (Lefcort, 1965). The potential flow fields about a blade extend both upstream and downstream of the blade, and decay exponentially with a length scale of the order of the chord. The wake interaction refers to the unsteadiness induced at a blade row by the wakes shed by the blades of an upstream blade row and thence convected downstream (e.g., Binder et al., 1985). Owing to the slow decay of wakes, the wake interaction persists significantly farther downstream than the potential flow interaction. In the endwall regions, the unsteadiness caused by secondary flows and associated vortices also contributes to the blade row interactions (e.g., Binder et al., 1987; Sharma et al., 1988). In transonic turbomachines, further interactions arise from the impingement of the trailing edge shock wave of one blade row upon the immediate downstream blade row (e.g., Guenette et al., 1989; Doorly and Oldfield, 1985).

The turbine investigated herein, the low-pressure turbine of an aircraft engine, is a multistage, subsonic, moderately high-

aspect-ratio turbine. Therefore, with the exceptions of the end-wall regions, interactions between different blade rows are due to wake interaction and possibly also potential flow interaction. Wake-induced transition has been observed to have a profound effect upon the boundary layer behavior of blade rows operating under conditions typical to those found in low-pressure turbines (e.g., Schröder, 1989; Hodson and Addison, 1989). It is thus of great importance to assess correctly the perturbations to which a blade row is subjected owing to oncoming wakes. In this investigation unsteady velocity measurements were made using hot-film probes at two circumferential positions, referred to as Position A and Position B, downstream of every rotor blade row of the low-pressure turbine. The measurements were carried out at design pressure ratio and corrected speeds at Re numbers of 120,000 (corresponding to high altitude cruise), 170,000 (corresponding to cruise), and 220,000, with the rig Re number based on the chord length and on the exit flow conditions of the first-stage stator vane. The distance in the circumferential direction between any of the two measurement positions downstream of a rotor blade row equalled a multiple plus one half of the spacing of the immediate upstream stator vanes. Hence, the analysis of the measurements permits the assessment of the influence of the nonuniform stator exit flow on the flow through the immediate downstream rotor blade row and also permits the assessment of the effects on the flow through the turbine that are due to interaction of different rotor blade rows. By regarding turbulence levels and wake depths downstream of the individual rotor blade rows, the hot-film probe measurements also help evaluate the performance of the individual rotor blade rows and help detect operating conditions for which flow separation occurs.

Contributed by the International Gas Turbine Institute and presented at the 36th International Gas Turbine and Aeroengine Congress and Exposition, Orlando, Florida, June 3-6, 1991. Manuscript received at ASME Headquarters March 4, 1991. Paper No. 91-GT-283. Associate Technical Editor: L. A. Riekert.

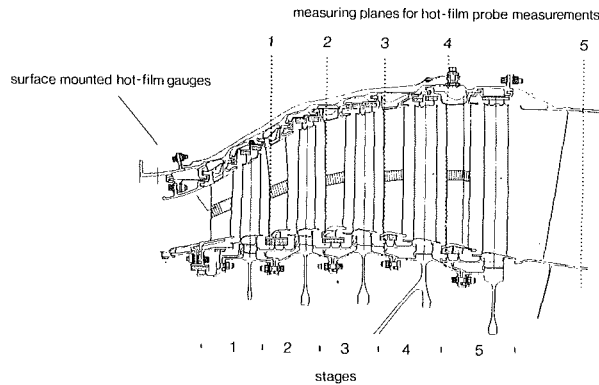


Fig. 1 Five-stage low-pressure turbine

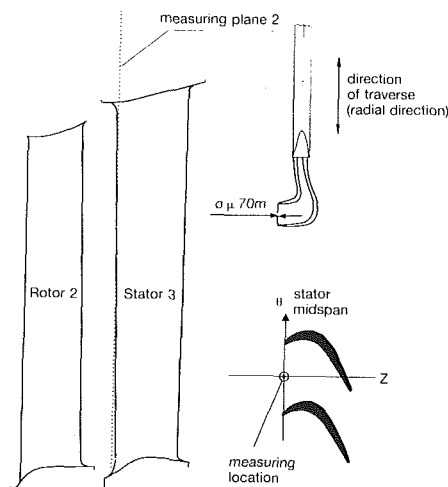


Fig. 2 Location of the measuring plane downstream of Rotor 2

Test Facility and Instrumentation

The experiment was carried out in the five-stage low-pressure turbine shown in Fig. 1, installed in the high-altitude test facility at Stuttgart University. Unsteady velocity measurements were made by radially traversing hot-film probes at two circumferential positions downstream of all five turbine rotors, Figs. 1 and 2. Downstream of Rotors 1-4 the distances in relative flow direction between the respective hot-film probes and the respective rotor blade trailing edges were slightly less than one chord, Table 1. Owing to mechanical design constraints, the measurements downstream of Rotor 5 had to be made at a significantly larger distance away from the rotor blade trailing edge. Thus, the fluctuations measured downstream of Rotor 5 could not be compared to those measured downstream of the other four rotors and will therefore not be discussed in this paper.

DANTEC 55 R03 hot-film probes were used for this inves-

Table 1 Location of measurement positions

Measuring Plane	Distance between Hot-Film Probe and Rotor Blade Trailing Edge (in relative flow direction at midspan)
1	0.85 chord
2	0.88 chord
3	0.73 chord
4	0.63 chord
5	4.37 chord

tigation. The probes were arranged so that they were sensitive to the axial and circumferential velocity components of the flow, Fig. 2. Hence, the magnitude of the component of the velocity vector in the plane spanned by vectors in the circumferential and in the axial direction was measured in this investigation. The probes were connected to a TSI Model 1050 anemometer operating in constant-temperature mode. The probe signals were linearized prior to recording. (For a detailed description of the data recording and the data reduction procedure, see Schröder, 1989.)

The setting parameters of the linearizer, i.e., the coefficients for the polynomial used for linearizing, were determined in a calibration procedure at constant density. Since the density in a turbine decreases in flow direction from one rotor to the next, using identical coefficients for linearizing signals of hot-film probes in a multistage turbine may result in measurement errors. In this investigation only fluctuating signals normalized by the time mean signal are presented. Data from a hot-wire calibration made at different densities were used to estimate the magnitude of the measurement error on the thus normalized fluctuating signals. It was found that the amplitudes of the fluctuations were underestimated for low densities when the linearization was carried out with the linearization coefficients determined at significantly higher densities. Under the assumption that the density dependence of the calibration is similar for hot wires and for hot films, the amplitudes of the fluctuations presented in this investigation are thus underestimated by up to 20 percent, with the largest error occurring for the lowest density observed in the experiment, i.e., downstream of the last turbine stage for the lowest rig Re number. Although a measurement error of this size would not be acceptable if a quantitative analysis of the flow through the

Nomenclature

c = absolute flow velocity	\bar{c} = time-averaged absolute velocity	
\bar{c} = ensemble-averaged periodic fluctuations of the absolute velocity	$\overline{c'}$ = time average of the ensemble-averaged turbulent fluctuations of the absolute velocity	PS = pressure side
\bar{c}' = ensemble-averaged turbulent fluctuations (ensemble-averaged root-mean-square of the random fluctuations) of the absolute velocity	c_i = magnitude of the i th Fourier coefficient	Re = Reynolds number
	f_i = blade passing frequency of the i th rotor	SS = suction side
		T_R, T_B = rotor revolution, rotor blade passing period
		z = axial direction (axis of rotation)
		θ = circumferential direction

Position

A

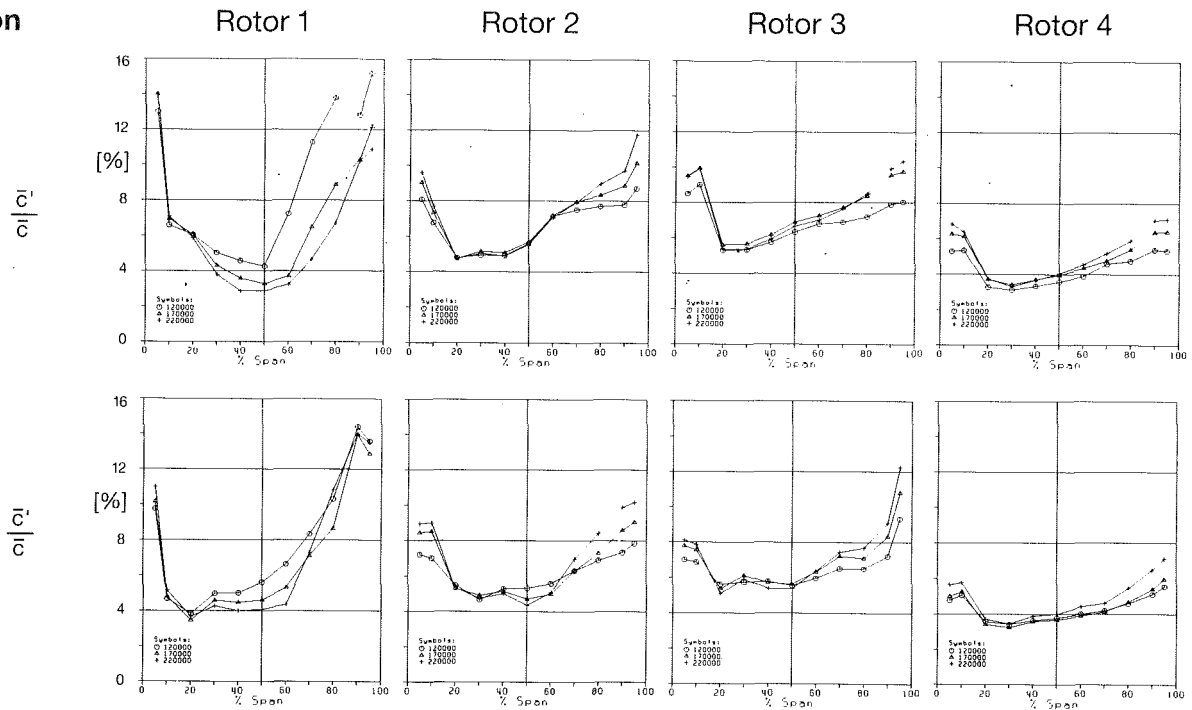


Fig. 3 Time-averaged turbulent fluctuations downstream of Rotors 1-4 ($Re = 120,000, 170,000, \text{ and } 220,000$, Positions A and B)

turbine was attempted, the quality of the measurements was considered sufficient for the purpose of this investigation, namely, to enhance the understanding of unsteady flow phenomena in multistage turbines, in particular of the effects of rotor-rotor interaction and of stator-rotor interaction on the flow through the turbine.

Data Reduction

Owing to the superposition of periodic and random fluctuations, a direct analysis of the linearized hot-film probe signals would have been extremely difficult to perform. To separate the periodic and random fluctuations in the signals, the unsteady data were ensemble averaged. The ensemble-averaged periodic fluctuations and the ensemble-averaged root-mean-square of the random fluctuations, in the following referred to as the ensemble-averaged turbulent fluctuations, were obtained by:

$$\bar{c}_j(t) = \frac{1}{N} \sum_{k=1}^N c_{k,j}(t) \quad \text{and} \quad \bar{c}'_j(t) = \sqrt{\frac{1}{N-1} \sum_{k=1}^N \{c_{k,j}(t) - \bar{c}_j(t)\}^2}$$

where N is the number of averaging periods, k denotes the k th averaging period, and j denotes the j th data point in any of the N averaging periods. As averaging period two rotor revolutions were chosen. About 1600 data points were taken per rotor revolution. A total of 500 averaging periods were found to be sufficient for the ensemble-averaging process. The time-averaged velocity and the time average of the ensemble-averaged turbulent fluctuations were obtained by integration of the ensemble-averaged periodic and the ensemble-averaged turbulent fluctuations,

$$\bar{c} = \frac{1}{T_R} \int_0^{T_R} \bar{c}(t) dt \quad \text{and} \quad \bar{c}' = \frac{1}{T_R} \int_0^{T_R} \bar{c}'(t) dt$$

The ensemble-averaged periodic, and the time-averaged and the ensemble-averaged turbulent fluctuations at the different radial positions downstream of the rotors are presented normalized by the time-averaged velocities at the respective radial position.

Discussion of Results

Time-Averaged Turbulent Fluctuations. To provide an initial overview of the flow through the turbine, the time-averaged turbulent fluctuations at the two measurement positions downstream of every rotor are presented in Fig. 3 for the three Re numbers investigated. Some important information about the flow can be gleaned from these data.

The largest turbulent fluctuations occur in the endwall regions. These large turbulent fluctuations, which are ascribed to the rotor secondary flows, extend from the tip significantly farther into the blade channel than from the hub. This is due to the radial pressure gradient, which tends to elongate the tip passage vortex toward midspan, and tends to squeeze the hub passage vortex onto the hub. Downstream of Rotor 1, especially at Position A in the midspan and in the tip region, a significant decrease of the turbulent fluctuations occurs with increasing Re number, in particular with the increase from 120,000 to 170,000. This strong drop of the turbulent fluctuations with increasing Re number downstream of Rotor 1 suggests laminar separation on either the first-stage stator or the first-stage rotor at a Re number of 120,000. Downstream of Rotors 2-4 no significant Re number dependence of the turbulent fluctuations occurs. The slight increase of the turbulent fluctuations with increasing Re number, observed in particular in the endwall regions, is of the same order of magnitude as the measurement error incurred by the constant-density calibration of the hot-film probes. Therefore, the turbulent fluctuations downstream of Rotors 2-4 are considered Re number independent.

Comparing these results to those of an earlier investigation reported by Binder et al. (1989) in which results of hot-film probe measurements made at one circumferential position downstream of Rotors 2, 4, and 5 were reported, good agreement was found for the time-averaged turbulent fluctuations downstream of Rotor 2 over the entire Re number range and for the time-averaged turbulent fluctuations downstream of Rotor 4 for the lowest Re number investigated, $Re = 120,000$. In the earlier investigation, however, a strong decrease of the turbulent (and also of the periodic) fluctuations was observed

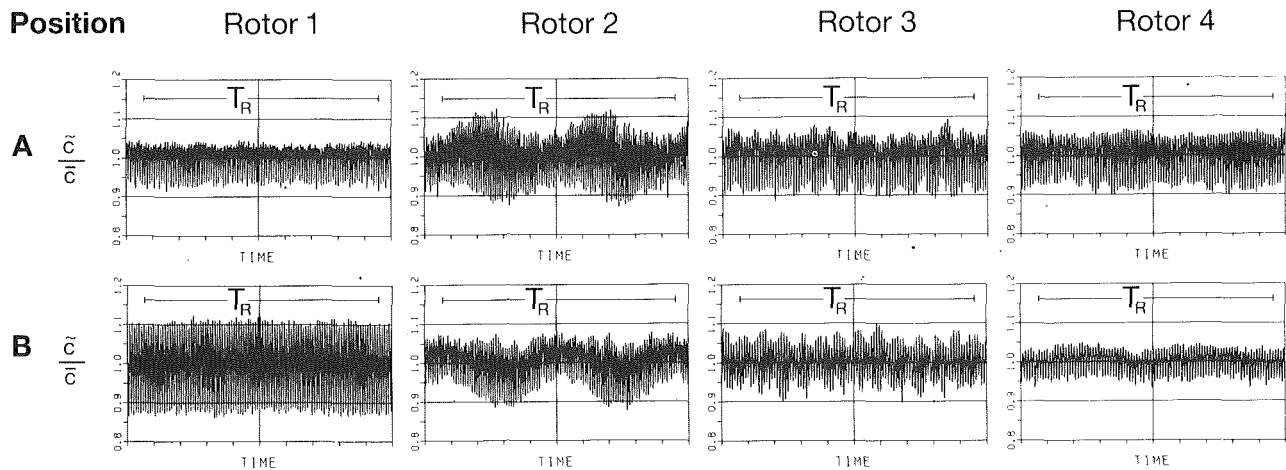


Fig. 4 Ensemble-averaged periodic fluctuations at midspan downstream of Rotors 1-4 ($Re = 170,000$, Positions A and B)

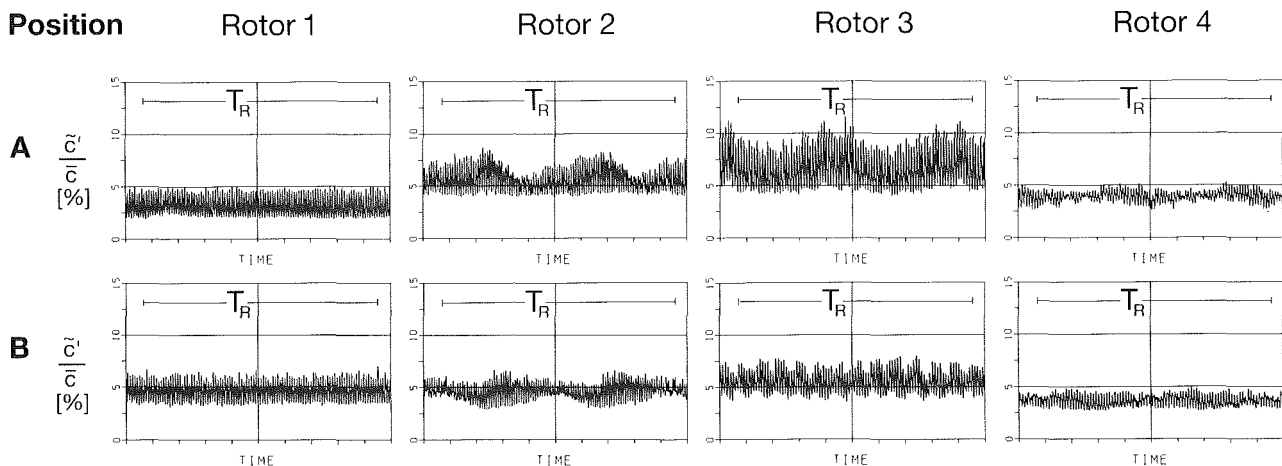


Fig. 5 Ensemble-averaged turbulent fluctuations at midspan downstream of Rotors 1-4 ($Re = 170,000$, Positions A and B)

downstream of Rotor 4 when the Re number was increased from 120,000 to 170,000. To find an explanation for this significantly different Re number behavior downstream of Rotor 4, the steady wall pressure measurements downstream and upstream of Rotor 4 as well as the steady surface pressure measurements on Stators 4 and 5 were scrutinized, but no significant Re number dependence was found for any of these measurements. It was thus concluded that the strong decrease of the turbulent fluctuations with increasing Re number observed in the earlier investigation was most likely due to a measurement error.

Ensemble-Averaged Periodic and Turbulent Fluctuations. The ensemble-averaged periodic and turbulent fluctuations at midspan downstream of Rotors 1-4 are shown in Figs. 4 and 5 for the two circumferential positions and a rig Re number of 170,000. The length of the abscissa corresponds to slightly more than one rotor revolution. In the traces of the periodic fluctuations, the downward pointing peaks identify the rotor wakes characterized by a velocity deficit compared to the velocity in the rotor core flows that are identified by the upward pointing peaks. In the traces of the turbulent fluctuations, however, the upward pointing peaks denote the rotor wakes characterized by increased turbulent fluctuations compared to the rotor core flows that are identified by the downward pointing peaks. It can be seen that significant differences in the amplitude of both the periodic fluctuations, i.e., the velocity deficits in the wakes, and the turbulent fluctuations occur between the two circumferential positions downstream of every rotor. These differences are most striking downstream of the first-stage rotor where the velocity deficit in the wake

is about 10 percent of the mean velocity at Position A and about 22 percent of the mean velocity at Position B. Correspondingly, the turbulent fluctuations are significantly larger at Position B than at Position A. These differences clearly show the influence of the first-stage stator exit flow on the flow through the first-stage rotor.

Significantly amplitude-modulated periodic and turbulent fluctuations are a salient feature of the flow downstream of Rotor 2 and, albeit to a lesser extent, also downstream of Rotors 3 and 4. The amplitude modulation of the periodic and the turbulent fluctuations comes about because of the influence the wakes that are shed by the rotor blade row immediately upstream of the one investigated exert on the flow through the next downstream rotor blade row (Binder et al., 1989). The mechanism of this wake-induced, downstream rotor-rotor interaction will be described in detail later in this paper. That the amplitude-modulated fluctuations are indeed the result of a downstream rotor-rotor interaction can easily be inferred by comparing the number of nodes and antinodes occurring over one rotor revolution to the difference in the blade count between a particular rotor blade row and the rotor blade row immediately upstream of it. The differences in the blade count for Rotor 1/Rotor 2, Rotor 2/Rotor 3, and Rotor 3/Rotor 4 are 2, 12, and 2, respectively. Correspondingly, downstream of Rotors 2, 3, and 4 the number of nodes and antinodes occurring over one rotor revolution are 2, 12, and 2, respectively, as can be seen from Fig. 4. The two trough-two peak undulation over one rotor revolution of the turbulent fluctuations downstream of Rotor 3 at Position A reveals the influence of the Rotor 1-Rotor 2 interaction on the flow through

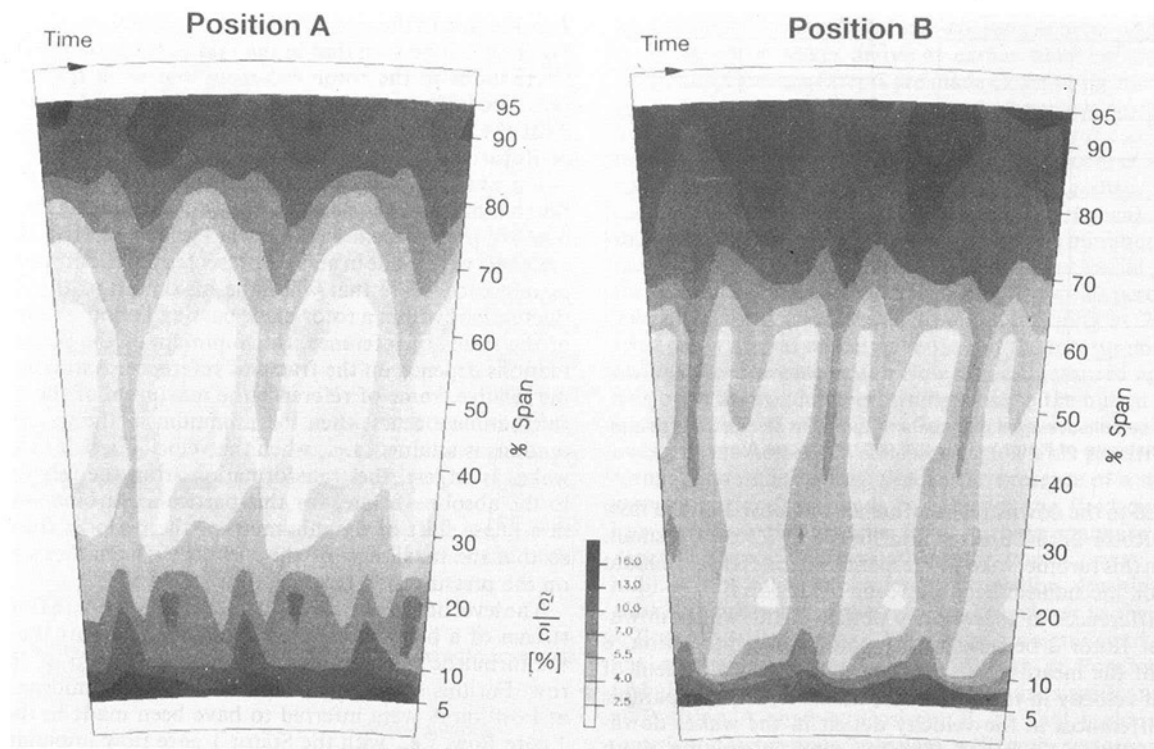


Fig. 6 Contour plot of the ensemble-averaged turbulent fluctuations downstream of Rotor 1 ($Re = 220,000$, Positions A and B)

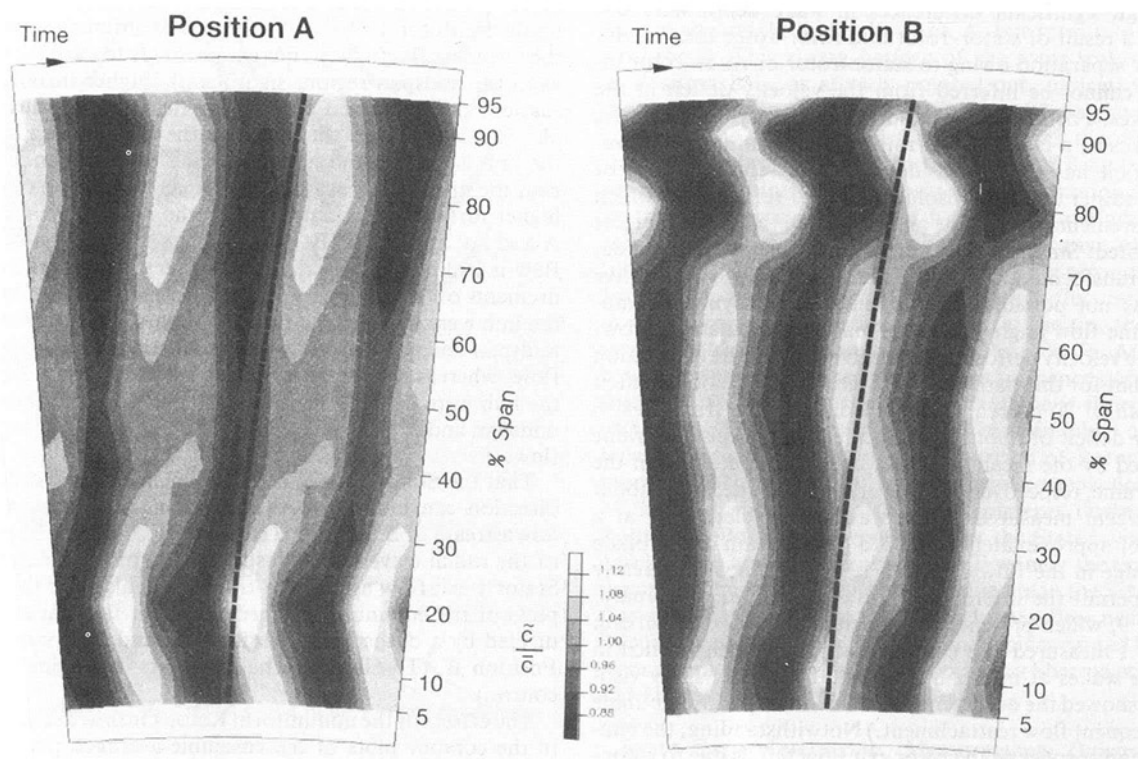


Fig. 7 Contour plot of the ensemble-averaged periodic fluctuations downstream of Rotor 1 ($Re = 220,000$, Positions A and B)

Rotor 3. This influence is, however, only noticed in the turbulent fluctuations and not in the periodic fluctuations.

Significant upstream interaction, i.e., a strong influence of a rotor blade row on the flow through an upstream rotor blade row, is not observed. Only downstream of Rotor 2 at Position B can a weak influence of a downstream rotor blade row, Rotor 3, be detected in the wake measurements. This is to say

that superimposed on the dominating 2 node-antinode structure a weak 12 node-antinode structure can be identified in the periodic fluctuations downstream of Rotor 2. Recalling that the difference in the blade count between Rotor 2 and Rotor 3 is 12, this weak 12 node-antinode structure in the periodic fluctuations downstream of Rotor 2 shows the upstream influence of Rotor 3 on the flow through Rotor 2.

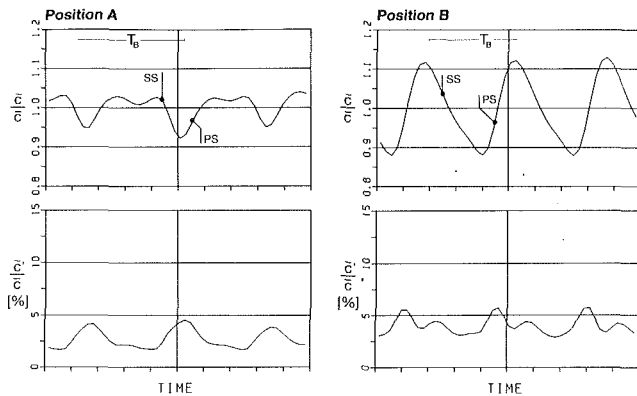


Fig. 8 Ensemble-averaged periodic and turbulent fluctuations at midspan downstream of Rotor 1 ($Re = 220,000$, Positions A and B)

Compared to the downstream influence of Rotor 1 on the flow through Rotor 2, this upstream influence of Rotor 3 is small. Hence, in this turbine wake-induced interaction is the dominant interaction mechanism between rotor blade rows.

The differences in the velocity deficit in the wakes downstream of Rotor 2 because of this rotor wake interaction, 8 percent of the mean velocity in the nodes and 20 percent of the mean velocity in the antinodes, however, are comparable to the differences in the velocity deficit in the wakes downstream of Rotor 1 because of stator-rotor interaction. Both effects, stator-rotor and rotor-rotor interaction, are therefore of comparable significance for the flow through this turbine.

Although significant differences in wake depth were observed as a result of stator-rotor and rotor-rotor interaction, blade row separation owing to stator-rotor or rotor-rotor interaction cannot be inferred from the velocity deficit in the rotor wakes. For in order to apply the velocity deficit in the rotor wakes as a criterion for rotor blade separation, the velocity deficit has to be considered in the relative frame of reference rather than the absolute frame of reference in which the measurements were made and for which the measurements are presented. Since no flow angle measurements were made, an exact transformation from the absolute frame to the relative frame was not possible. Consequently, simplifying assumptions on the flow angle had to be made to calculate approximately the velocity deficit in the relative frame. The calculation showed that for this particular turbine, a wake velocity deficit at midspan of 20 percent in the absolute frame translates to a velocity deficit of about 10–12 percent in the relative frame normalized by the mean velocities in the absolute and in the relative frame, respectively. However, a velocity deficit of about 10–12 percent measured in the wakes of a blade row at a distance of approximately 0.7 chord downstream of the blade trailing edge in the flow direction is by itself not sufficiently large to permit the inference of flow separation. (Compare, e.g., Fig. 9, which presents the velocity contours downstream of Stator 1 measured in a cascade test. The velocity deficit in the stator wakes at midspan is about 10 percent. Flow visualization showed the occurrence of a laminar separation bubble and subsequent flow reattachment.) Notwithstanding, the temporal nonuniformity of the rotor exit flow that is due to rotor-rotor interaction significantly influences the boundary layer transition on the immediate downstream stator, as results of surface hot-film gage measurements on the stator vanes of this turbine showed (Schröder, 1990).

Stator-Rotor Interaction (Measurements Downstream of Rotor 1). Contour plots of the ensemble-averaged periodic and turbulent fluctuations downstream of Rotor 1 are presented in Figs. 6 and 7 for a Re number of 220,000. (The radial positions at which the measurements were made are indicated by the short lines at the right boundary of the contour plots.)

Turning first to the contour plots of the turbulent fluctuations, Fig. 6, it can be seen that in the midspan region the turbulent fluctuations in the rotor wakes as well as in the rotor core flows are higher at Position B than at Position A; see also Fig. 8 for the turbulent and the periodic fluctuations downstream of Rotor 1 at 50 percent span.

The phase difference between the minimum of the periodic fluctuations and the maximum of the turbulent fluctuations that are presented in Fig. 8 comes about because the measurements were made in and are presented for the absolute frame of reference. Note that while the maximum of the turbulent fluctuations within a rotor blade passing period is independent of the frame of reference, the minimum of the periodic fluctuations depends on the frame of reference. Assuming that in the relative frame of reference the maximum of the turbulent fluctuations occurs when the minimum in the periodic fluctuations is attained, i.e., when the velocity deficit in the rotor wakes is largest, the transformation from the relative frame to the absolute frame, for this particular turbine, will result in a phase shift of the minimum of the periodic fluctuations so that the maximum of the turbulent fluctuations is found on the pressure side flank of the rotor wake.

The level of the turbulent fluctuations in the core flow downstream of a blade row reflects for the most part the level of the turbulent fluctuations in the flow upstream of the blade row. For this reason the measurements in the midspan region at Position A were inferred to have been made in the Stator 1 core flow, i.e., with the Stator 1 core flow impinging upon the Rotor 1 blades, and the measurements in the midspan region at Position B were inferred to have been made in the Stator 1 wake flow, i.e., with the Stator 1 wake flow impinging upon the Rotor 1 blades. At both circumferential positions, the turbulent fluctuations increase strongly toward the tip with, as in the midspan region, significantly higher turbulent fluctuations occurring at Position B. The turbulent fluctuations also increase toward the hub, but the high fluctuations near the hub do not extend as far into the blade channel as those near the tip. In contrast to the midspan and the tip region, the higher turbulent fluctuations near the hub occur at Position A and not at Position B. This suggests that the Stator 1 wake flow is inclined against the radial direction so that the measurements obtained downstream of Rotor 1 at Position A near the hub were made in the Stator 1 wake flow and those in the midspan and in the tip region were made in the Stator 1 core flow, whereas the measurements obtained at Position B near the hub were made in the Stator 1 core flow and those in the midspan and in the tip region were made in the Stator 1 wake flow.

That the Stator 1 wake is indeed inclined against the radial direction can be seen from the velocity contours measured downstream of Stator 1 in a cascade test, Fig. 9. The positions of the radial traverses downstream of Rotor 1 relative to the Stator 1 exit flow as inferred from the analysis of the contour plots of the ensemble-averaged turbulent fluctuations are indicated by a dashed line, Position A, and by a straight line, Position B. (The lines are half a Stator 1 spacing apart, of course.)

The effects of the nonuniform Rotor 1 inflow are also evident in the contour plots of the ensemble-averaged periodic fluctuations, Fig. 7. The dashed lines in Fig. 7 indicate the times at which fluid particles leaving the rotor blade trailing edge at the same instant of time should arrive at the hot-film probe if both flow angle and flow velocity corresponded to their respective design values.

Turning first to the flow at midspan (see also Fig. 8), significantly different wake shapes and wake velocity deficits are observed at Positions A and B. At Position A (with the Stator 1 core flow impinging upon the Rotor 1 blades) the velocity deficit in the rotor wakes was found to be approximately 10 percent of the mean velocity, and the rotor wakes had not

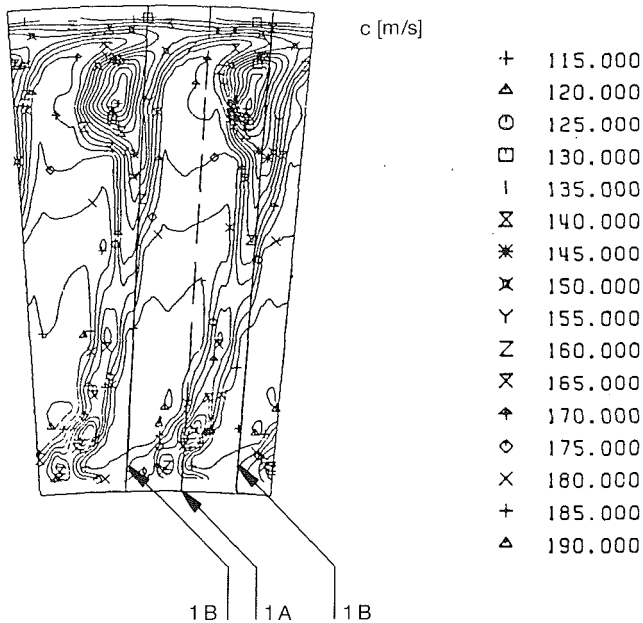


Fig. 9 Velocity contours downstream of Stator 1 measured in a cascade test ($Re = 180,000$)

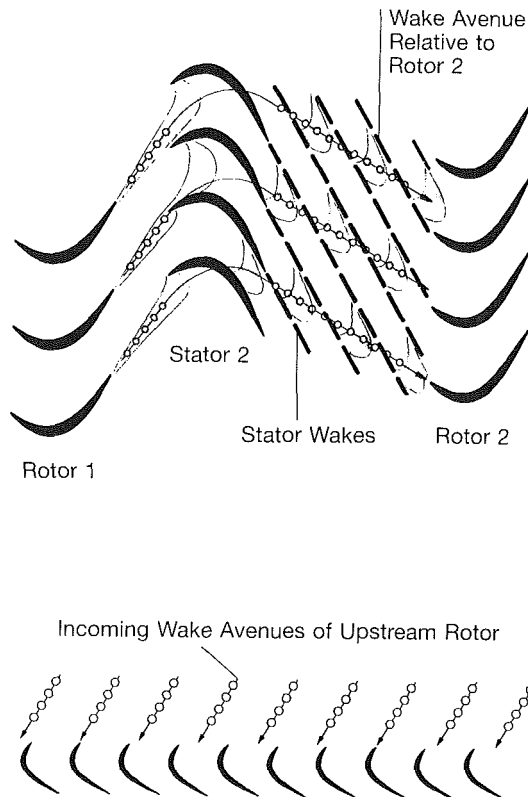


Fig. 10 Schematic illustration of the Rotor 2 inflow conditions

coalesced at the measurement position. At Position B (with the Stator 1 wake flow impinging upon the Rotor 1 blades), however, the velocity deficit in the rotor wakes was significantly larger than at Position A, approximately 22 percent of the mean velocity. Also in contrast to Position A, the rotor wakes had coalesced. This shows clearly that both significant temporal and spatial nonuniformities exist downstream of a turbine stage.

The most salient differences between the two circumferential positions, however, occur in the endwall regions. Regarding first the measurements in the hub region at Position A, it can

be seen that in the region from 40 percent span to 20 percent span the rotor wakes arrive at earlier times at the hot-film probe as the measurements are made closer to the hub, whereas in the region from 20 percent span to 5 percent span the rotor wakes arrive at later times at the hot-film probe as the measurements are made closer to the hub. Therefore, at 20 percent span, the rotor wakes arrive earlier at the measurement probe than at any other spanwise location. Thus, the wake traces in the radial direction, i.e., the locations of the minimum velocity in the rotor blade passing periods at different radial positions, form into single zigzags with a sharp turn at 20 percent span. These wake traces indicate flow underturning at 20 percent span (early arrival of the wake flow at the measurement probe owing to a decrease in the flow angle, measured against the axis of rotation) and overturning close to the hub at 5 percent span (late arrival of the wake flow at the measurement position owing to an increase in the flow angle). This pattern of overturning and underturning reveals the presence of a strong hub passage vortex (that tends to overturn the fluid close to the hub and to underturn the fluid at some spanwise position, depending upon the strength of the vortex, away from the hub). At the other circumferential position, Position B, only weak underturning of the rotor wakes, closer to the hub than at Position A, is observed. This suggests a significantly stronger hub channel vortex at Position A than at Position B. The turbulent fluctuations in the hub region are significantly higher at Position A than at Position B, so that regions of high turbulent fluctuations correlate well with regions of strong rotor wake distortion, i.e., strong overturning and underturning of the rotor wakes due to the hub passage vortex.

In the tip region, the wake traces in the radial direction form an almost straight line at Position A, but form into zigzags at Position B. This zigzag pattern of the rotor wakes observed at Position B is, as already pointed out, indicative of wake distortion due to rotor secondary flow. The wake traces observed at the two circumferential positions therefore reveal strong secondary flow influence at Position B and only weak secondary flow influence at Position A. This notion is enforced by the occurrence of lumps of high turbulent fluctuations in the tip region at Position B that are indicative of the high turbulent fluctuations associated with strong secondary flows. In contrast, no such lumps of high turbulent fluctuations occur in the tip region at Position A. Thus, at the tip, the stronger secondary flow influence occurs at Position B. At the hub, however, the stronger secondary flow influence occurs at Position A. This reflects the influence of the inclined Stator 1 wake (note that the analysis of the contour plots of the turbulent fluctuations measured downstream of Rotor 1 in conjunction with the results of velocity measurements downstream of Stator 1 showed that the measurements downstream of Rotor 1 at Position A were made in the Stator 1 wake flow near the hub and in the Stator 1 core flow near the tip, whereas the measurements at Position B were made in the Stator 1 core flow near the hub and in the Stator 1 wake flow near the tip). Reduced secondary flow influence in turbines caused by stator-rotor interaction has also been reported by Sharma et al. (1988) and Hebert and Tiederman (1990).

Rotor-Rotor Interaction (Measurements Downstream of Rotor 2).

In the discussion of the measurements made at midspan downstream of Rotors 1-4, it was pointed out that amplitude-modulated periodic and turbulent fluctuations owing to wake-induced, downstream rotor-rotor interaction were a salient feature of the flow downstream of Rotor 2 and, albeit to a lesser extent, also downstream of Rotors 3 and 4. To describe qualitatively the mechanism of wake-induced rotor-rotor interaction, a schematic illustration of the Rotor 2 inflow conditions is presented in Fig. 10 (Binder et al., 1989). The wakes shed by the Rotor 1 blades are cut and distorted by the Stator 2 vanes and thereby formed into wake segments that

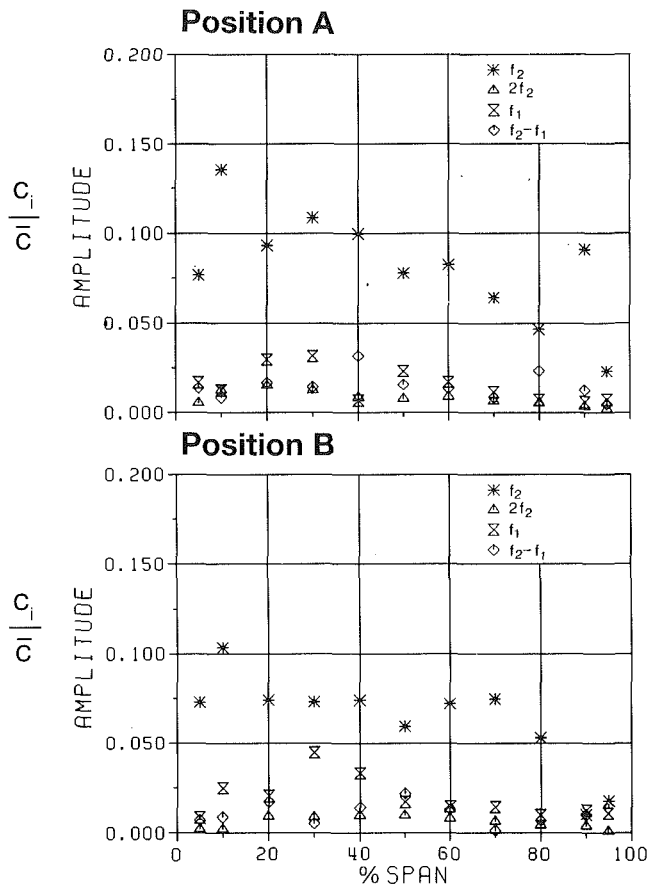


Fig. 11 Magnitudes of the Fourier coefficients of the ensemble-averaged periodic fluctuations at Rotor 2 blade passing frequency, twice Rotor 2 blade passing frequency, Rotor 1 blade passing frequency, and Rotor 1-Rotor 2 difference blade passing frequency ($Re = 170,000$, Positions A and B)

are convected downstream with the Stator 2 flow. The thick, broken lines indicate the Stator 2 wakes, and therefore the flow direction in the absolute frame of reference. Regarded from the relative frame of reference, the Rotor 1 wake segments are arranged in wake avenues marked in Fig. 10 by lines and circles. Owing to the different blade counts of Rotors 1 and 2, the Rotor 1 wake segments following these wake avenues will enter subsequent Rotor 2 blade channels at different positions relative to the Rotor 2 leading edge. The hot-film probe measurements made in the stationary frame downstream of Rotor 2 are therefore indicative of the sensitivity to the circumferential position of entry of the Rotor 1 wake segments into the Rotor 2 blade channel.

The rotor-rotor interaction occurs across the entire span. To illustrate this, the magnitudes of the Fourier coefficients of the ensemble-averaged periodic fluctuations downstream of Rotor 2 are presented in Fig. 11 for four blade passing frequencies; namely, the Rotor 2 blade passing frequency, twice the Rotor 2 blade passing frequency, the Rotor 1 blade passing frequency, and the Rotor 1-Rotor 2 difference blade passing frequency. It can be seen that for both circumferential positions across the entire span, but in particular from hub to midspan, the coefficients at the Rotor 1 blade passing frequency are second in magnitude only to the coefficients at the Rotor 2 blade passing frequency. Measured in terms of relative influence, i.e., comparing the magnitudes of the coefficients at the Rotor 1 blade passing frequency to the magnitudes of the coefficients at the Rotor 2 blade passing frequency, the effect of the Rotor 1 exit flow onto the Rotor 2 flow is stronger at Position B than at Position A. The strongest influence is noted at Position B and 30 percent span where the magnitude of the

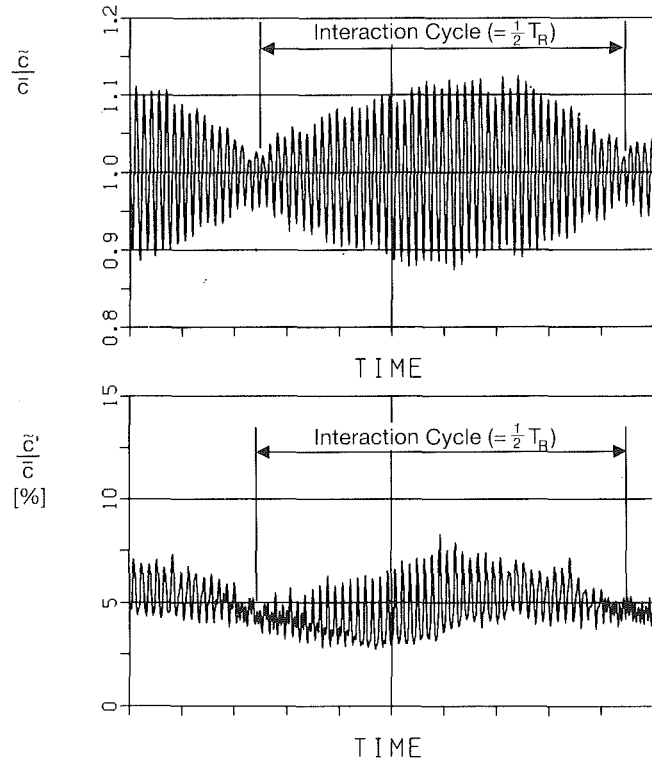


Fig. 12 Ensemble-averaged periodic and turbulent fluctuations downstream of Rotor 2 at Position B and 30 percent span ($Re = 170,000$)

coefficient at the Rotor 1 blade passing frequency attains 60 percent of the magnitude of the coefficient at the Rotor 2 blade passing frequency. It can furthermore be seen that the magnitude of the coefficients at the Rotor 1-Rotor 2 difference frequency is smaller at most spanwise locations than the magnitude of the coefficients at the Rotor 1 blade passing frequency.

The different influence of the Rotor 1 flow onto the Rotor 2 flow is the result of the Stator 2-Rotor 2 interaction, for the two measurement positions downstream of Rotor 2 were selected such that their distance in circumferential direction equaled a multiple of the Stator 1 spacing and a multiple and one half of the Stator 2 spacing. Therefore, any difference observed in the measurements made downstream of Rotor 2 is solely the result of Stator 2-Rotor 2 interaction.

For a more detailed discussion of the phenomena associated with rotor-rotor interaction, the ensemble-averaged periodic and turbulent fluctuations at Position B and 30 percent span, i.e., the location of strongest interaction, are presented in Fig. 12. Regarding first the periodic fluctuations, it can be seen that the velocity deficit in the Rotor 2 wakes varies from 5 to 25 percent of the mean velocity. It can furthermore be seen that the trace of the periodic fluctuations is almost symmetric about the instant of time at which the periodic fluctuations are smallest. This is to say that the periodic fluctuations increase in the first half of the interaction cycle in almost the same manner as they decrease in the second half of the interaction cycle. The interaction cycle denotes the period of time a stationary observer sees elapse between recurring identical positions of the Rotor 1 blades to the Rotor 2 blades and is defined to start at the instant of time when the smallest periodic fluctuations occur. Note that since the difference in blade number between the two rotor blade rows is two, a stationary observer will watch identical positions of the Rotor 1 blades to the Rotor 2 blades twice per rotor revolution; therefore, for Rotor 1 and Rotor 2 the interaction cycle is half as long as the time required for one rotor revolution. Turning next to

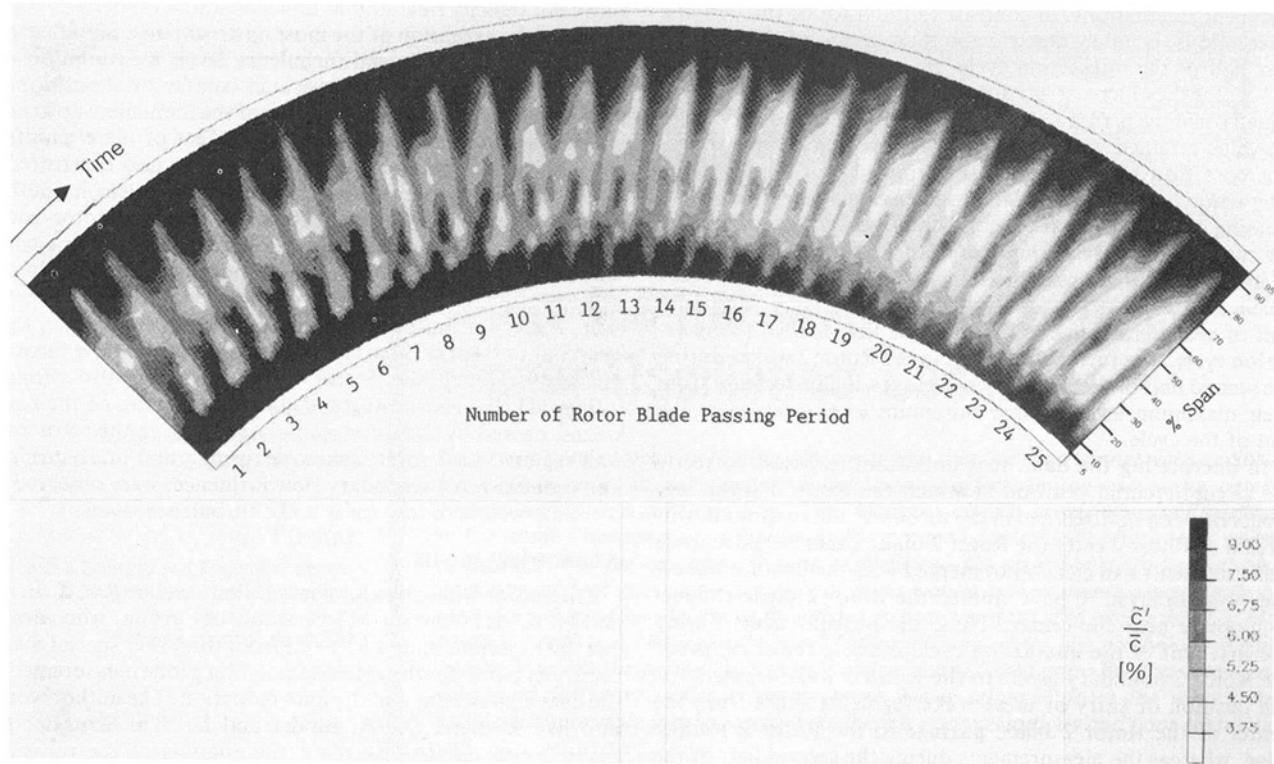


Fig. 13 Contour plot of the ensemble-averaged turbulent fluctuations downstream of Rotor 2 at Position B

the turbulent fluctuations, a peculiarity is observed around the instant of time with the smallest periodic fluctuation: A second peak per rotor blade passing period appears in the turbulent fluctuations, in addition to the one peak that identifies the increased turbulence levels of the Rotor 2 wake. This second peak is most pronounced in the sense of being equal in magnitude to the peak associated with the Rotor 2 wake when the periodic fluctuations are smallest. It can be discerned in the turbulent fluctuations for about 16 blade passing periods (of one interaction cycle) from approximately 4 blade passing periods prior to the occurrence of the smallest periodic fluctuations to approximately 12 blade passing periods thereafter.

The unfolding of this second peak is best illustrated by regarding a contour plot of the turbulent fluctuations downstream of Rotor 2, Fig. 13. Presented are the turbulent fluctuations corresponding to the first 25 blade passing periods of the traces of the periodic and turbulent fluctuations shown in Fig. 12. Note that a stationary observer downstream of a turbine blade row will see the rotor exit flow in the following order: suction side flank of the rotor wake, rotor wake, pressure side flank of the rotor wake, and finally the rotor core flow. Furthermore it has to be kept in mind that for a stationary observer the circumferential position of entry of the Rotor 1 wake segments into the Rotor 2 blade channel will shift cyclically from the pressure side of the blade leading edge to the center of the blade channel, then to the suction side of the blade leading edge, and finally back to the pressure side of the blade leading edge (cf. Fig. 10). The contour plot shows clearly the large turbulent fluctuations in the endwall regions that are ascribed to the rotor secondary flows. Turning the attention to the region extending from 20 to 60 percent span (where the secondary flow influence was presumed small) a "normal" rotor exit flow structure, i.e., high turbulence levels during the rotor blade passing period identifying the rotor wake and low turbulence levels identifying the rotor core flow, is observed for the first three rotor blade passing periods. During blade passing periods 4–6 ramification of rotor wake fluid happens at midspan. Next, the point of ramification moves gradually

closer to the hub. At midspan, the branch of highly turbulent fluid (compared to the core flow turbulence level) moves away from the pressure side flank of the Rotor 2 wake, rotor blade passing periods 7–9. This gradual moving away from the pressure side flank of the Rotor 2 wake strongly suggests that this branch of highly turbulent fluid identifies the Rotor 1 wake segments. This is to say that as the position of entry of the Rotor 1 wake segment into the Rotor 2 blade channel shifts from the pressure side of the blade leading edge to the center of the blade channel, the fluid of rather high turbulent fluctuations associated with the Rotor 1 wake segments separates from the Rotor 2 wakes, and is found in the blade channel center between two rotor blades. Another few blade passing periods later, blade passing periods 10 to 18, the branch of highly turbulent fluid, i.e., the Rotor 1 wake fluid, in the center of the Rotor 2 blade passage has completely separated from the pressure side flank of the Rotor 2 wake. It has also moved closer to the suction side flank of the Rotor 2 wake. At this instant of time, a double-peak structure occurs in the traces of the turbulent fluctuations from 30 percent span to 50 percent span, as was exemplarily shown for 30 percent span. During the next few blade passing periods, the lump of turbulent fluid in the center of the blade passage gradually merges into the suction side flank of the Rotor 2 wake, and the double-peak structure in the trace of the turbulent fluctuations diminishes.

The contour plot of the turbulent fluctuations clearly shows that blade passing periods exist with Rotor 1 wake segments not having merged into Rotor 2 wakes. Therefore, the second peak in the turbulent fluctuations has to be ascribed to Rotor 1 wake segments that are convected through the Rotor 2 blade channel without merging into the Rotor 2 wakes. This analysis of the contour plot of the turbulent fluctuations downstream of Rotor 2, in conjunction with the corresponding traces of the turbulent and the periodic fluctuations, elucidates that the downstream rotor-rotor interaction is indeed a wake-induced interaction.

Returning to the analysis of the turbulent fluctuations at 30 percent span, Fig. 12, it can be seen that the trace of the

turbulent fluctuations, in contrast to the trace of the periodic fluctuations, is not symmetric about any point of time. In the first half of the interaction cycle, the turbulence levels in the Rotor 2 wakes increase gradually from their lowest value attained when the periodic fluctuations are smallest to their highest value attained when the periodic fluctuations are largest. The core flow turbulence levels during this first half of the interaction cycle, however, first decrease gradually before increasing markedly. For the second half of the interaction cycle, the turbulence levels in the Rotor 2 core flows first continue to increase and then remain almost constant. Hence, the turbulence levels in the Rotor 2 core flows are higher in the second half of the interaction cycle than in the first half of the interaction cycle. The turbulence levels in the Rotor 2 wakes during the second half of the interaction cycle gradually decrease from their maximum level to their minimum level attained at the end of the cycle.

In interpreting the data, it is important to assess correctly the circumferential position at which the Rotor 1 wake segments that can be discerned in the turbulent fluctuations downstream of Rotor 2 enter the Rotor 2 blade channel. Since these wake segments had clearly not merged with the Rotor 2 wakes, they were inferred to have entered the Rotor 2 blade channel somewhere near the center. Thus, the measurements during the first half of the interaction cycle indicate the response of the Rotor 2 boundary layers to the Rotor 1 wake segments as the position of entry of these wake segments shifts from the center of the Rotor 2 blade passage to the Rotor 2 leading edge, whereas the measurements during the second half of the interaction cycle indicate the response of the Rotor 2 boundary layers to the Rotor 1 wake segments as the position of entry of these wake segments shifts from the Rotor 2 leading edge to the center of the blade channel. Therefore, during the first half of the interaction cycle, the blade suction side boundary layer will be affected by the Rotor 1 wake segments, whereas during the second half of the interaction cycle the blade pressure side boundary layer will be affected by the Rotor 1 wake segments. This may explain the greater variations of the turbulent fluctuations observed during the first half of the interaction cycle, for wake-induced transition has been observed significantly to affect the suction side boundary layer of blade rows operating in the Re number regime typical for low-pressure turbines (Schröder, 1990; Hodson and Addison, 1989). However, this analysis does not help fathom why a strong sensitivity to the position of impingement of the Rotor 1 wake segments upon Rotor 2, similar to the one observed in the turbulent fluctuations, is not observed in the periodic fluctuations.

Conclusion

Hot-film probe measurements were made downstream of every rotor blade row of a five-stage low-pressure turbine to investigate unsteady flow phenomena in multistage low-pressure turbines. Rotor-rotor interaction and stator-rotor interaction were observed to have a profound influence on the flow through the turbine. Interaction of rotors of different turbine stages occurred owing to the influence the wakes shed by one rotor blade row exerted on the flow through the next downstream rotor blade row. This wake-induced rotor-rotor interaction resulted in strongly amplitude-modulated periodic and

turbulent velocity fluctuations downstream of every rotor blade row with the exception of the most upstream one. Significantly different wake depths and turbulence levels measured downstream of every rotor blade row at circumferential positions a multiple plus one half of the spacing of the immediate upstream stator blade row apart evidenced the effect of the circumferentially nonuniform stator exit flow upon the next downstream rotor blade row. The variation in time of the velocity deficit in the wakes downstream of Rotor 2 owing to rotor-rotor interaction during one rotor revolution was found to be comparable to the variation in space of the velocity deficits in the wakes downstream of Rotor 1 owing to stator-rotor interaction. Therefore, stator-rotor and rotor-rotor interaction were observed to be of comparable significance to the flow through this multistage turbine. Stator-rotor interaction also strongly influenced the overturning and the underturning of the rotor wakes, caused by the rotor secondary flows, in the rotor end-wall regions. Low rotor wake overturning and underturning, i.e., reduced rotor secondary flow influence, were observed to correlate well with low rotor wake turbulence levels.

Acknowledgments

The author would like to thank J. Reifenschneider, K. Britz, and H. Kneißl from the MTU turbine test group, who carried out the experiment, and R. Göhl from the MTU special measurements group for the excellent hot-film probe measurements, the data acquisition, and the data reduction. The author would also like to thank Dr. A. Binder and Dr. Th. Schröder for many useful discussions about the analysis of the measurements.

References

- Binder, A., Förster, W., Kruse, H., and Rogge, H., 1985, "An Experimental Investigation Into the Effect of Wakes on the Unsteady Turbine Rotor Flow," *ASME Journal of Engineering for Gas Turbines and Power*, Vol. 107, pp. 458-466.
- Binder, A., Förster, W., Mach, K., and Rogge, H., 1987, "Unsteady Flow Interaction Caused by Stator Secondary Vortices in a Turbine Rotor," *ASME JOURNAL OF TURBOMACHINERY*, Vol. 109, pp. 251-257.
- Binder, A., Schröder, Th., and Hourmouziadis, J., 1989, "Turbulence Measurements in a Multistage Low-Pressure Turbine," *ASME JOURNAL OF TURBOMACHINERY*, Vol. 111, pp. 153-161.
- Doorly, D. J., and Oldfield, M. L. G., 1985, "Simulation of the Effects of Shock Wave Passing on a Turbine Rotor Blade," *ASME Journal of Engineering for Gas Turbines and Power*, Vol. 107, pp. 998-1006.
- Guenette, G. R., Epstein, A. H., Giles, M. B., Haimes, R., and Norton, R. J. G., 1989, "Fully Scaled Transonic Turbine Rotor Heat Transfer Measurements," *ASME JOURNAL OF TURBOMACHINERY*, Vol. 111, pp. 1-7.
- Hebert, G. J., and Tiederman, W. G., 1990, "Comparison of Steady and Unsteady Secondary Flows in a Turbine Stator Cascade," *ASME JOURNAL OF TURBOMACHINERY*, Vol. 112, pp. 625-632.
- Hodson, H. P., and Addison, J. S., 1989, "Wake-Boundary Layer Interactions in an Axial Flow Turbine Rotor at Off-Design Conditions," *ASME JOURNAL OF TURBOMACHINERY*, Vol. 111, pp. 181-192.
- Lefcort, M. D., 1965, "An Investigation Into Unsteady Blade Forces in Turbomachines," *ASME Journal of Engineering for Power*, Vol. 87, pp. 345-354.
- Schröder, Th., 1989, "Measurements With Hot-Film Probes and Surface Mounted Hot-Film Gauges in a Multistage Low-Pressure Turbine," 1989 European Propulsion Forum, pp. 15.1-15.27.
- Schröder, Th., 1990, "Investigation of Boundary Layer Transition and Separation Phenomena in a Multistage Low-Pressure Turbine Using Surface Mounted Hot-Film Gauges," Invited Lecture, presented at the 35th ASME International Gas Turbine and Aeroengine Congress and Exposition, June 11-14, Brussels, Belgium, in preparation to be submitted for publication.
- Sharma, O. P., Renaud, E., Butler, T. L., Milsaps, K., Jr., Dring, R. P., and Joslyn, H. D., 1988, "Rotor-Stator Interaction in Multi-stage Axial-Flow Turbines," Paper No. AIAA-88-3013.

Wind Tunnel Wall Effects in a Linear Oscillating Cascade

D. H. Buffum

NASA Lewis Research Center,
Cleveland, OH 44135

S. Fleeter

Thermal Sciences and Propulsion Center,
School of Mechanical Engineering,
Purdue University,
West Lafayette, IN 47907

Experiments in a linear oscillating cascade reveal that the wind tunnel walls enclosing the airfoils have, in some cases, a detrimental effect on the oscillating cascade aerodynamics. In a subsonic flow field, biconvex airfoils are driven simultaneously in harmonic, torsion-mode oscillations for a range of interblade phase angle values. It is found that the cascade dynamic periodicity—the airfoil-to-airfoil variation in unsteady surface pressure—is good for some values of interblade phase angle but poor for others. Correlation of the unsteady pressure data with oscillating flat plate cascade predictions is generally good for conditions where the periodicity is good and poor where the periodicity is poor. Calculations based upon linearized unsteady aerodynamic theory indicate that pressure waves reflected from the wind tunnel walls are responsible for the cases where there is poor periodicity and poor correlation with the predictions.

Introduction

Oscillating cascade experiments play an important role in the development of advanced cascade unsteady aerodynamic analyses, providing data used both to evaluate existing analyses and to provide direction for future modeling efforts.

Both linear and annular cascades have been used to investigate the aerodynamics of airfoils driven in controlled, harmonic, fixed interblade phase angle traveling-wave mode oscillations. Certain advantages and disadvantages are associated with these two types of facilities. In particular, a highly two-dimensional flow field may be obtained in a linear cascade while, in an annular cascade, undesirable three-dimensional effects may be problematic. However, while the annular cascade appears to be inherently dynamically periodic, i.e., the temporal fluctuations in the flow field vary from passage to passage according to the interblade phase angle, periodicity is less certain in the linear cascade due to the finite extent of the cascade and the boundaries introduced by the wind tunnel walls. The potential for wall interference is indicated by a number of papers devoted to the effects of wind tunnel walls on a single oscillating airfoil, for example, Jones (1943) and Runyan et al. (1955).

Carta (1983) was the first researcher to investigate the dynamic periodicity of a linear oscillating cascade. His cascade consisted of 11 NACA 65-series airfoils staggered at 30 deg with 1.33 solidity. Airfoil surface unsteady pressures were measured at reduced frequency values ranging from 0.14 to 0.30 over a wide range of interblade phase angles with a low subsonic inlet Mach number, $M \approx 0.18$. Good dynamic periodicity was generally found except for in-phase oscillations, where circumferential gradients in the phase of the unsteady pressure coefficient were found. Carta attributed this to an acoustic resonance condition in the cascade.

Contributed by the International Gas Turbine Institute and presented at the 36th International Gas Turbine and Aeroengine Congress and Exposition, Orlando, Florida, June 3–6, 1991. Manuscript received at ASME Headquarters February 20, 1991. Paper No. 91-GT-133. Associate Technical Editor: L. A. Riekert.

In the present study, the steady and unsteady aerodynamics of an oscillating, linear cascade are investigated in a low-solidity configuration. The cascade solidity, 0.65, was chosen to be representative of an advanced propeller model, which fluttered during wind tunnel performance tests (Mehmed et al., 1982). For an inlet Mach number of 0.55, the torsion mode biconvex airfoil oscillating cascade aerodynamics are quantified for reduced frequencies as high as 0.64 and a range of interblade phase angles. To help determine the validity of the data, an investigation is made into the steady state and dynamic periodicity of the cascade. Then the unsteady airfoil surface pressure data are correlated with the predictions of the linearized subsonic oscillating cascade analysis of Smith (1972). Insight into the effect of the wind tunnel walls on the cascade unsteady aerodynamics is gained from the theoretical acoustic wave generation properties of an oscillating cascade.

Oscillating Cascade Facility

The NASA Lewis Transonic Oscillating Cascade, Fig. 1, combines a linear cascade wind tunnel capable of inlet flow approaching Mach one with a high-speed airfoil drive system

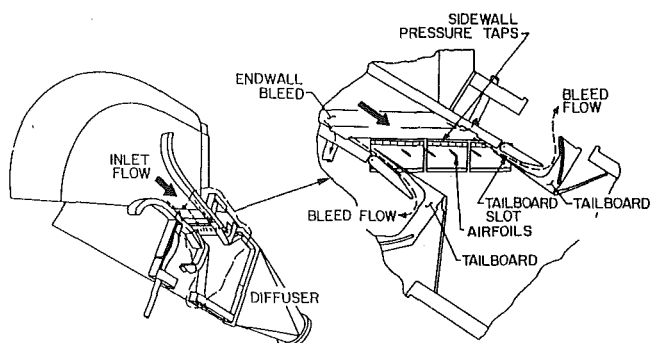


Fig. 1 Oscillating cascade facility

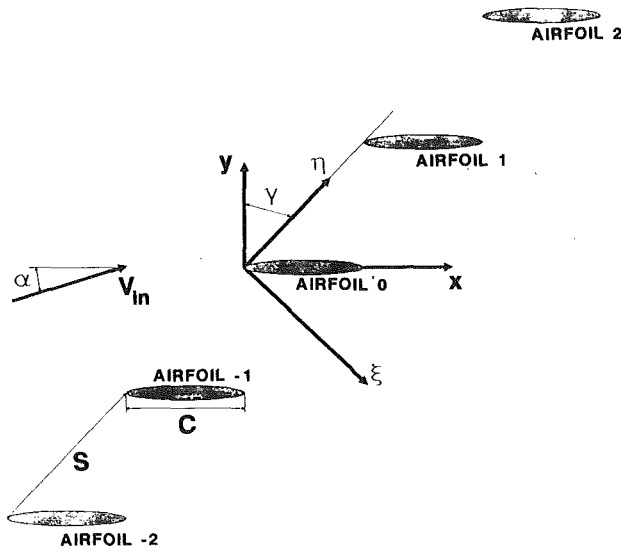


Fig. 2 Cascade geometry

that imparts torsion-mode oscillations to the cascaded airfoils at specified interblade phase angles and realistic high reduced frequency values.

Air drawn from the atmosphere passes through a smooth contraction inlet section into a constant area rectangular test section of 9.78 cm span, which measures 58.6 cm along the stagger line. Upstream of the test section, suction is applied through perforated walls to reduce the boundary layer thickness. Tailboards are used to adjust the cascade exit region static pressure and also form bleed scoops, which further reduce upper and lower wall boundary layer effects. Downstream of the test section, the air is expanded through a diffuser into an exhaust header. The exhaust system, part of a central air facility at Lewis, maintains a 30 kPa pressure downstream of the flow control valves. The cascade inlet and the airfoil angles may be adjusted over a wide range of incidence and stagger angle combinations.

The facility features a high-speed mechanism that drives the four airfoils in controlled torsional oscillations. Four stainless steel barrel cams, each having a six-cycle sinusoidal groove machined into its periphery, are mounted on a common rotating shaft driven by a 74.6 kW electric motor. A cam follower assembly, consisting of a titanium alloy connecting arm with a stainless steel button on one end, is joined on the other end to an airfoil trunnion. The button fits into the cam groove, thus coupling the airfoil to the camshaft. Lubrication of the cam/follower assembly is provided by an oil bath. The amplitude of the torsional airfoil motion is 1.2 deg as dictated by the cam and follower geometry. The drive system is con-

Table 1 Airfoil and cascade geometry

Airfoil	
Type	biconvex, no camber
Surface radius of curvature	27.4 cm
Leading and trailing edge radii of curvature	0.025 cm
Chord, C	7.62 cm
Maximum thickness / chord	0.076
Elastic axis	midchord
Dynamic pressure transducer locations, % chord	12,25,40,60,75,88
Cascade	
Number of airfoils	4
Airfoil spacing, S	11.72 cm
Solidity, C/S	0.65
Stagger angle, γ	45 degrees
Mean flow incidence angle, α_0	2 degrees
Amplitude of oscillation, α_1	1.2 degrees

figured for oscillations at a chosen interblade phase angle by fixing the cams at the required relative positions on the shaft. A reduced frequency of 0.64 is achieved at 0.55 inlet Mach number with an oscillation frequency of 250 Hz.

Airfoils and Instrumentation

Figure 2 illustrates the airfoil and cascade geometry, which is summarized in Table 1. Four uncambered, 7.6 percent thick biconvex airfoils are used to create a low-solidity ($C/S=0.65$) cascade. The stagger angle is 45 deg. and the airfoils oscillate about the midchord.

Airfoils instrumented with static pressure taps are used to measure the airfoil surface steady pressure distributions. There are 16 chordwise measurement locations, with a higher density in the leading edge region used to capture the higher gradients there. Rows of sidewall static pressure taps located upstream and downstream of the cascaded airfoils are used to determine the mean inlet and exit pressures.

Flush-mounted high-frequency-response miniature pressure transducers are used to measure the unsteady surface pressures on the oscillating airfoils. Two airfoils are instrumented, each having six transducers mounted symmetrically about the midchord on one airfoil surface. These transducers, having active sensor diameters of 1.3 percent of the airfoil chord, are epoxied into milled slots and potted in room-temperature-vulcanizing rubber for isolation from airfoil strain. A thin coating of rubber is also used to fair the transducer surface into the airfoil contour.

From static and dynamic calibrations, the pressure transducers were found to be highly linear in response over the frequency and pressure ranges of interest. However, the pressure transducers may produce undesirable signals as a consequence of the airfoil motion. This effect was quantified by oscillating the instrumented airfoils under no-flow conditions.

Nomenclature

C = airfoil chord
 C_m = unsteady aerodynamic moment coefficient

$$= \int_0^1 (x_{ea}^* - x^*) \Delta C_p(x^*) dx^*$$

 C_p = unsteady pressure coefficient
 $= p_1 / (\rho_{in} V_{in}^2 \alpha_1)$
 \bar{C}_p = steady pressure coefficient = $(\bar{p}_{in} - p_0) / (\rho_{in} V_{in}^2)$
 \tilde{C}_p^n = unsteady pressure influence coefficient for the n th airfoil
 e = unit vector
 k = reduced frequency = $\omega C / V_{in}$

M_{in} = cascade inlet Mach number
 N = limit of summation
 \bar{p}_{in} = mean inlet static pressure
 p_j = j th harmonic of airfoil surface static pressure
 S = airfoil spacing
 V_{in} = inlet velocity
 x = airfoil chordwise coordinate
 x^* = nondimensional airfoil chordwise coordinate = x/C
 x_{ea}^* = nondimensional elastic axis location = 1/2
 α_j = j th harmonic of incidence angle

β = interblade phase angle (positive when airfoil $n+1$ leads airfoil n)
 γ = stagger angle
 ΔC_p = unsteady pressure difference coefficient
 δC_p = dynamic periodicity magnitude difference
 $\delta \phi$ = dynamic periodicity phase difference
 ρ_{in} = inlet density
 ω = airfoil oscillation frequency

The response of each transducer was found to be a linear function of the airfoil acceleration, implying that the acoustic response, which varies with the airfoil velocity magnitude, is dominated by the acceleration response. Thus calibration data were obtained to correct the oscillating airfoil pressure data for acceleration effects.

The time-variant position of the reference oscillating airfoil is determined by a capacitance-type proximity sensor, which produces a voltage proportional to the air gap between it and an adjacent object. This sensor is positioned to face a six-cycle sinusoidally shaped cam mounted on the airfoil drive camshaft so as to be in phase with the reference airfoil motion.

Data Acquisition and Analysis

Conventional instrumentation is used to quantify the steady flow field. An average of the upstream sidewall static pressures along with the atmospheric pressure (total) are used to calculate the inlet Mach number. Steady flow airfoil surface static pressures are calculated from an average of approximately 100 samples. The steady pressure coefficient is defined in Eq. (1):

$$\bar{C}_p(x) = \frac{p_{in} - p_0(x)}{\rho_{in} V_{in}^2} \quad (1)$$

p_{in} is the mean inlet static pressure, p_0 is the time-averaged airfoil surface static pressure at the chordwise coordinate x , and ρ_{in} and V_{in} are the inlet values of density and velocity.

Unsteady signals are recorded on magnetic tape for postexperiment processing. During tape playback, the signals are simultaneously digitized at rates sufficient to capture at least three harmonics of the oscillation frequency, with 32,768 samples taken per channel. Each channel of data is divided into contiguous blocks, each block typically with 2048 samples, and then Fourier decomposed to determine the first harmonic of each block of data. The first harmonic pressure of each block is referenced to the airfoil motion by subtracting from it the phase of the first harmonic motion signal of the same block. Once all of the blocks from a channel are decomposed in this manner, the first harmonic block results are averaged and the complex-valued acceleration response is subtracted vectorally. Statistical analysis of the block results is used to estimate uncertainties for the average first harmonic values.

In these experiments, the motion of the n th airfoil is defined by the change in the incidence angle with time:

$$\alpha^n(t) = \alpha_0 + \alpha_1 \Re \{ e^{i(\omega t + n\beta)} \} \quad (2)$$

where α_0 is the mean incidence angle, α_1 is the torsional oscillation amplitude, ω is the frequency, β is the interblade phase angle, and \Re denotes the real part.

The complex-valued unsteady pressure coefficient is defined as

$$C_p(x) = \frac{p_1(x)}{\rho_{in} V_{in}^2 \alpha_1} \quad (3)$$

p_1 is the first harmonic airfoil surface static pressure. The dynamic pressure difference coefficient is the difference between the lower and upper surface unsteady pressure coefficients:

$$\Delta C_p = C_{pl} - C_{pu} \quad (4)$$

Linearized Analysis

The experimental dynamic pressure difference coefficient data are correlated with the predictions of a computer program published by Whitehead (1987), which is based on the analysis of Smith (1972). This is a semi-analytical technique for determining the unsteady forces on an infinite cascade of flat plate airfoils subject to harmonic disturbances in an inviscid, isentropic, subsonic, unsteady flow. The analysis assumes that the airfoils are at zero mean incidence and the unsteadiness

creates small disturbances to a uniform mean flow, resulting in a linear system of equations with constant coefficients. Additional analytical results, which will be used in the results section, are derived below.

Wave Generation by an Oscillating Cascade. The linearized conservation equations for mass and momentum may be expressed as

$$\frac{\partial \mathbf{q}}{\partial t} + \mathbf{A} \frac{\partial \mathbf{q}}{\partial \xi} + \mathbf{B} \frac{\partial \mathbf{q}}{\partial \eta} = 0 \quad (5)$$

where \mathbf{q} is the matrix of perturbation variables

$$\mathbf{q} = \begin{pmatrix} p_1 \\ u_1 \\ v_1 \end{pmatrix} \quad (6)$$

and the coefficient matrices \mathbf{A} and \mathbf{B} are constant, depending on the uniform mean flow.

$$\mathbf{A} = \begin{pmatrix} u_0 & \rho_0 a_0^2 & 0 \\ 1/\rho_0 & u_0 & 0 \\ 0 & 0 & u_0 \end{pmatrix} \quad (7)$$

$$\mathbf{B} = \begin{pmatrix} v_0 & 0 & \rho_0 a_0^2 \\ 0 & v_0 & 0 \\ 1/\rho_0 & 0 & v_0 \end{pmatrix} \quad (8)$$

u_0 and v_0 are the ξ and η components of the mean flow velocity, ρ_0 is the mean density, and a_0 is the mean speed of sound.

For an infinite cascade of equally spaced airfoils oscillating harmonically at a fixed interblade phase angle, the dependent variables depend harmonically on the spatial position and time. Thus the perturbations are expressed as

$$\mathbf{q} = \begin{pmatrix} p_1 \\ u_1 \\ v_1 \end{pmatrix} = \begin{pmatrix} \bar{p}_1 \\ \bar{u}_1 \\ \bar{v}_1 \end{pmatrix} e^{i(\omega t + l\xi + m\eta)} = \bar{\mathbf{q}} e^{i(\omega t + l\xi + m\eta)} \quad (9)$$

where l and m are the axial and circumferential wavenumbers and the quantities with overbars are complex. Substituting these perturbation expressions into Eq. (5) and differentiating results in

$$(\omega \mathbf{I} + l\mathbf{A} + m\mathbf{B})\bar{\mathbf{q}} = 0 \quad (10)$$

where \mathbf{I} is the identity matrix.

Equation (10) may be rearranged in the form of an eigenvalue problem, Eq. (11), with the axial wavenumber l being the eigenvalue.

$$(-\mathbf{A}^{-1}(\omega \mathbf{I} + m\mathbf{B}) - \mathbf{I})\bar{\mathbf{q}} = 0 \quad (11)$$

The eigenvalues are

$$l = \frac{-(\omega + mv_0)}{u_0} \quad (12)$$

and

$$j = \frac{u_0(\omega + v_0 m) \pm a_0 \sqrt{(\omega + v_0 m)^2 - (a_0^2 - u_0^2) m^2}}{a_0^2 - u_0^2} \quad (13)$$

As shown by Smith, the first eigenvalue, Eq. (12), corresponds to convection of vorticity by the mean flow with no associated pressure fluctuations. This solution is of no further interest for this application. However, the eigenvalues of Eq. (13), corresponding to irrotational pressure perturbations, are of interest.

The tangential wave number must satisfy cascade dynamic periodicity according to the interblade phase angle β . Hence

$$mS = \beta + 2\pi r \quad (14)$$

where S is the cascade spacing and r is an integer specifying the mode of the wave.

The nature of the acoustic waves produced by the cascade depends upon the term under the radical in Eq. (13). Let δ be that term:

$$\delta = (\omega + v_0 m)^2 - (a_0^2 - u_0^2) m^2. \quad (15)$$

When $\delta = 0$, the acoustic resonance condition, only one wave is created, which propagates in the circumferential direction. The resonant values of the interblade phase angle are determined by solving Eq. (15), with $\delta = 0$, for m , then using Eq. (14) to determine β for $r = 0$. The result is:

$$\beta_r^\pm = \frac{2kMS}{C(1-M^2)} (M \sin(\alpha_0 + \gamma) \pm \sqrt{1 - M^2 \cos^2(\alpha_0 + \gamma)}). \quad (16)$$

When $\delta > 0$, both values of l as specified by Eq. (13) are real; thus there are two acoustic waves that propagate undiminished, one going upstream and the other downstream. This behavior is termed superresonant when the mean flow field is subsonic.

The final case is $\delta < 0$, the subsonic cascade subresonant condition. l is now complex, and may be expressed as $l = l^R + il^I$ with the real and imaginary parts determined from Eq. (13) to be

$$l^R = \frac{u_0(\omega + v_0 m)}{a_0^2 - u_0^2} \quad (17)$$

and

$$l^I = \frac{\pm a_0 \sqrt{|(\omega + v_0 m)^2 - (a_0^2 - u_0^2) m^2|}}{a_0^2 - u_0^2}. \quad (18)$$

In this case, the pressure perturbation is of the form

$$\begin{aligned} p_1 &= \bar{p}_1 e^{i(\omega t + (l^R + il^I)\xi + m\eta)} \\ &= \bar{p}_1 e^{-l^I \xi} e^{i(\omega t + l^R \xi + m\eta)} \end{aligned} \quad (19)$$

Thus the wave decays exponentially with ξ , depending upon the imaginary part of l :

$$\frac{|p_1(\xi)|}{|\bar{p}_1|} = e^{-|l^I \xi|} \quad (20)$$

where, from Eq. (19), $|\bar{p}_1|$ is equal to $|p_1(\xi = 0)|$. The absolute value of the exponent disallows the nonphysical case of an amplifying wave.

The axial and tangential wave numbers specify the acoustic wave propagation direction relative to ξ' , η' coordinates, which are parallel to the fixed ξ , η coordinate system but moving with the mean flow velocity (Whitehead, 1987). Relative to the ξ' , η' coordinates, the waves propagate at an angle

$$\theta' = \tan^{-1} \left(\frac{-m}{-l^R} \right) \quad (21)$$

with the speed of sound. The wave propagation vector V_p in the ξ , η coordinate system is therefore the sum of the steady flow velocity vector and the wave propagation vector relative to the moving coordinate system,

$$V_p = (u_0 + a_0 \cos \theta') \mathbf{e}_\xi + (v_0 + a_0 \sin \theta') \mathbf{e}_\eta. \quad (22)$$

It follows that the direction of propagation θ in the ξ , η coordinate system is

$$\theta = \tan^{-1} \left(\frac{v_0 + a_0 \sin \theta'}{u_0 + a_0 \cos \theta'} \right). \quad (23)$$

Influence Coefficient Technique. In this analysis, the superposition principle is valid since the system of governing small disturbance equations is linear. The unsteady pressure difference coefficient on a reference airfoil (airfoil 0) for fixed values of the inlet Mach number, reduced frequency, and cascade geometry may be expressed as the sum of the effects of the oscillations of the reference airfoil itself and the other airfoils in the cascade, Eq. (24).

$$\Delta C_p(x, \beta) = \sum_{n=-N}^N \Delta \hat{C}_p^n(x) e^{in\beta} \quad (24)$$

where the complex-valued influence coefficient $\Delta \hat{C}_p^n$ expresses the influence that the oscillations of airfoil n have on the pressure difference coefficient of the reference airfoil. $N = \infty$ for an infinite cascade.

By inversion of Eq. (24), an expression for the influence coefficients is

$$\Delta \hat{C}_p^n(x) = \frac{1}{2\pi} \int_{-\pi}^{\pi} \Delta C_p(x, \beta) e^{-in\beta} d\beta. \quad (25)$$

Unsteady aerodynamic influence coefficients may thus be determined from oscillating cascade analyses by integrating the analytical predictions over the complete interblade phase angle interval. Using these influence coefficients for a finite value of N in Eq. (24) then enables analytical results for a finite number of airfoils oscillating in an infinite cascade to be determined.

Results

The effect of wind tunnel walls on the aerodynamics of a low-solidity linear oscillating cascade is investigated using experimental and analytical techniques. For a mean inlet Mach number of 0.55 and 2 deg mean incidence, the airfoil surface steady pressure coefficient distributions are presented first, followed by dynamic periodicity data and correlation of the unsteady pressure difference coefficient data with linearized analysis predictions. Linearized analysis is then used to ascertain the effects of the wind tunnel walls on the cascade unsteady aerodynamics.

Steady-State Aerodynamics. For a linear cascade to be a valid simulation of a turbomachine blade row, the cascade must exhibit good passage-to-passage periodicity for the steady flow field. Thus airfoil surface steady pressure distributions are obtained for multiple passages in the low solidity cascade. In Fig. 3, steady pressure coefficient data are presented for the center cascade passage and the two adjacent passages. Good cascade periodicity is apparent, with the only significant differences found at the leading edge of the airfoil upper surface.

The upper surface pressure coefficient distribution peaks near the leading edge and the pressure difference tends toward zero near the trailing edge. There is negligible loading beyond 50 percent of chord. Using the method of Kline and McClintock (1953), a 95 percent confidence interval of ± 0.003 is estimated for these pressure coefficients. The mean exit region static pressure divided by the inlet total pressure was 0.8251.

Unsteady Aerodynamics. Figure 4 illustrates typical sub-

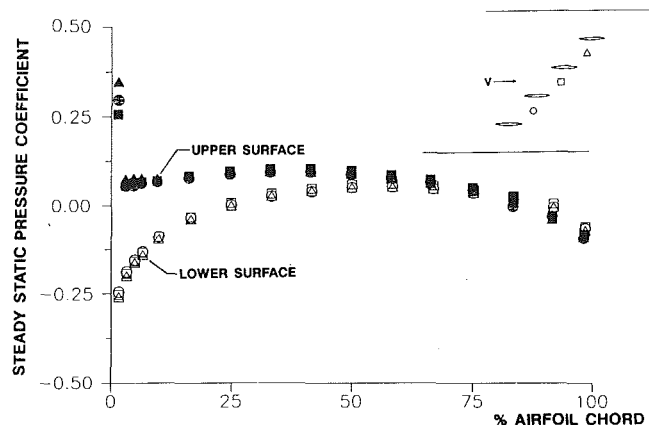


Fig. 3 Airfoil surface steady pressure coefficient distributions, $M = 0.55$, $\alpha_0 = 2$ deg

k	β_r^-	β_r^+
0.40	-14.6	37.0
0.64	-23.3	59.1

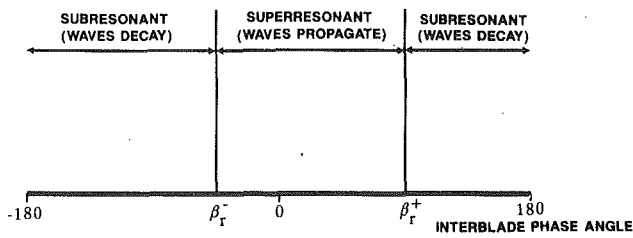


Fig. 4 Modes of subsonic oscillating cascade wave propagation

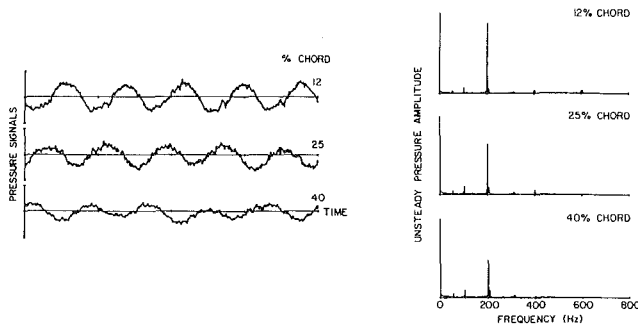


Fig. 5 Time-variant signals and averaged pressure spectra

sonic cascade behavior in terms of the wave propagation modes predicted by the linearized analysis. Acoustic resonances at positive and negative interblade phase angle values, β_r^\pm , bracket the wave-propagating superresonant region, which includes $\beta = 0$. When $\beta > \beta_r^+$ or $\beta < \beta_r^-$, the cascade is subresonant and the waves decay. Included in this figure are the resonant values of interblade phase angle, Eq. (16), for the experimental conditions.

The unsteady aerodynamic experiments discussed herein include subresonant and superresonant values of β . Airfoil surface unsteady pressure distributions are obtained for interblade phase angle values of 0, 45, -45, 90, -90, and 180 deg at reduced frequency values of 0.40 and 0.64. Sample time-variant pressure signals presented in Fig. 5 along with the resulting pressure spectra illustrate the dominance of the first harmonic component as typically found in the signals. 95 percent confidence intervals of ± 5 percent in magnitude and ± 3 deg in phase are estimated for the mean value of the unsteady pressure coefficients.

Dynamic Periodicity. Oscillating cascade data were first obtained by positioning the two instrumented airfoils to measure the unsteady pressures on the airfoil surfaces that define the center passage of the cascade. The dynamic periodicity of the cascade was investigated by subsequently positioning the instrumented airfoils to measure the opposite surfaces of the two center airfoils positions, thus giving dynamic pressure measurements for both surfaces of the two most centrally located airfoils.

First harmonic unsteady pressure coefficient periodicity data are presented in Fig. 6 for $k = 0.40$ and $\beta = -45$ deg. To simplify the discussion of these results, the two instrumented airfoils will be referred to as *A* and *B* as labeled in the figure. The data indicate that the dynamic periodicity is excellent in both magnitude and phase for the airfoil upper surface. Although the lower surface periodicity is good, the magnitudes tends to be larger on airfoil *A*, particularly over the forward half of the airfoil. There are also small but noticeable phase differences in the midchord region on the lower surface.

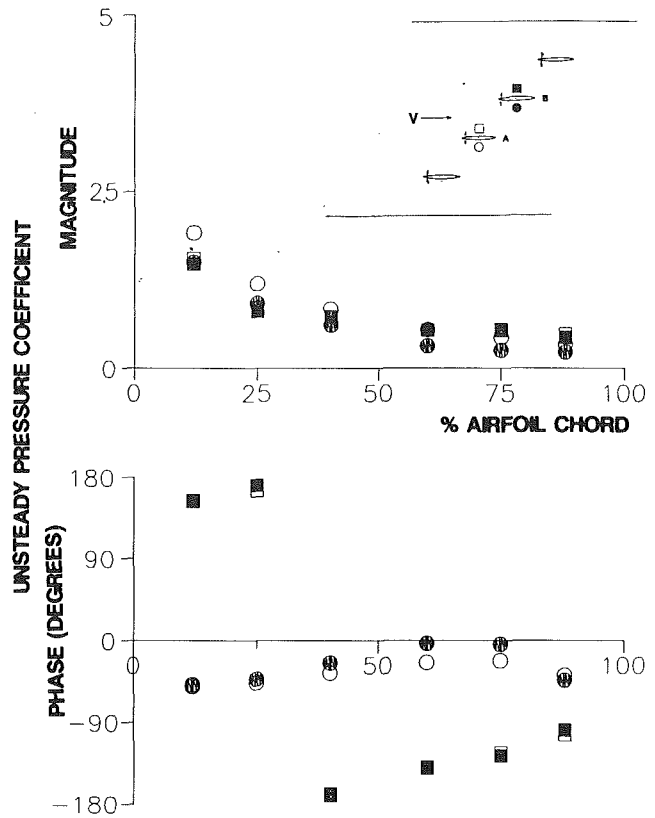


Fig. 6 Cascade dynamic periodicity, $k = 0.40$, $\beta = -45$ deg

To aid the presentation of the periodicity data, two new quantities are defined. The dynamic periodicity magnitude and phase differences, δC_p and $\delta\phi$, are defined in Eqs. (26) and (27) for each airfoil surface. Ideally, both of these quantities will be zero.

$$\delta C_p = \frac{|C_p^A| - |C_p^B|}{\frac{1}{2}(|C_p^A| + |C_p^B|)_{x/C=0.12}} \quad (26)$$

$$\delta\phi = \phi_p^A - \phi_p^B \quad (27)$$

Figure 7 presents the dynamic periodicity data determined from the data presented in Fig. 6. Both the excellent upper surface periodicity and defects in the lower surface periodicity are clearly revealed.

The oscillating cascade periodicity is now investigated as a function of reduced frequency and interblade phase angle using the quantities δC_p and $\delta\phi$. Reduced frequency crossplots of the periodicity data for $k = 0.40$ and 0.64 are presented in Figs. 8-13 for several values of interblade phase angle. Beginning with $\beta = 0$ deg, Fig. 8, the dynamic periodicity is generally poor in both magnitude and phase for these superresonant conditions, and reduced frequency has little effect on the results. The dynamic periodicity is improved somewhat for $\beta = 45$ deg, Fig. 9, but the small values of $\delta\phi$ occurring over the forward half of the airfoil are in contrast to the very large values of $\delta\phi$ at 60 and 75 percent of chord on the upper surface. Reduced frequency again has little effect on the results even though $k = 0.40$ corresponds to a subresonant condition and $k = 0.64$ is superresonant. In contrast, the periodicity is generally good for $\beta = -45$ deg, Fig. 10, where both reduced frequencies are subresonant. There, all of the values of $\delta\phi$ are acceptably small as are the values of δC_p , except for the lower surface $k = 0.40$ results. When $\beta = 90$ deg, the periodicity is poor in both magnitude and phase for both subresonant conditions, Fig. 11. But for $\beta = -90$ deg, Fig. 12, dynamic periodicity is generally good for these subresonant conditions except for the upper

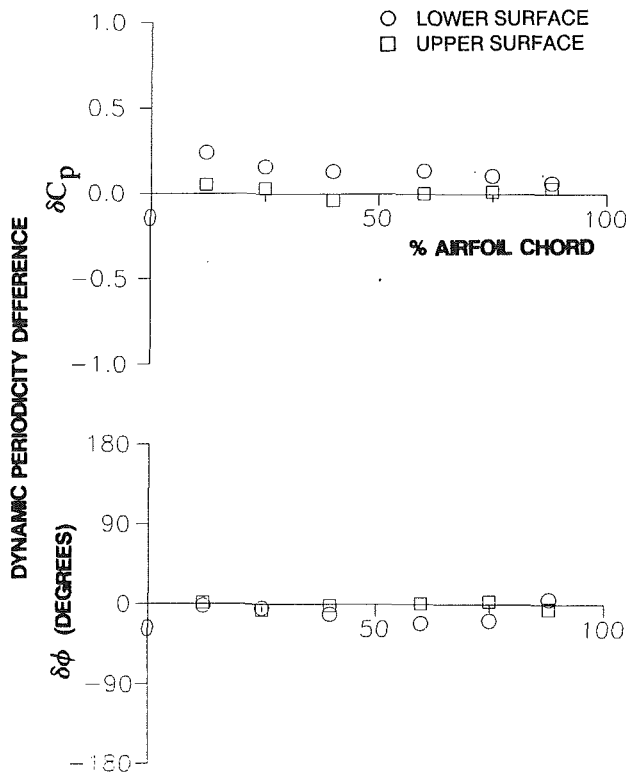


Fig. 7 Dynamic periodicity difference, $k = 0.40$, $\beta = -45$ deg

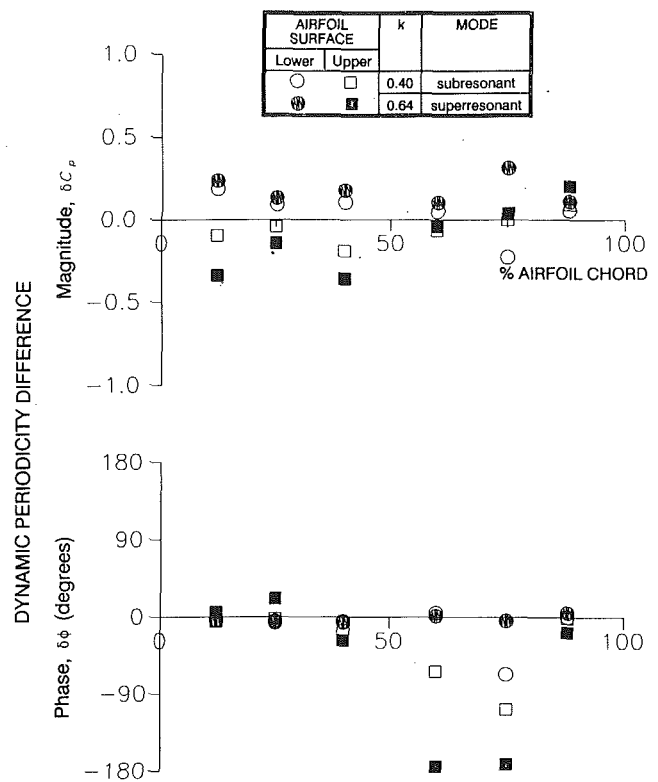


Fig. 9 Dynamic periodicity difference, $\beta = 45$ deg

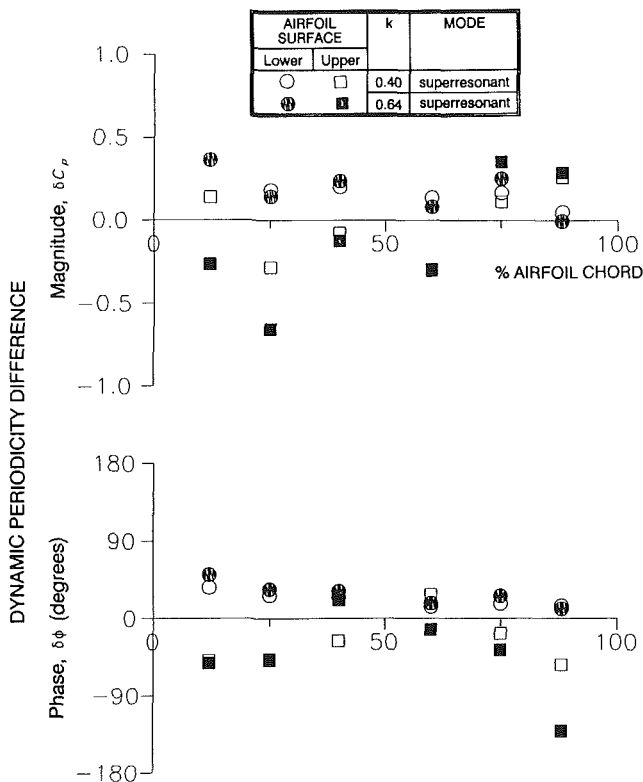


Fig. 8 Dynamic periodicity difference, $\beta = 0$

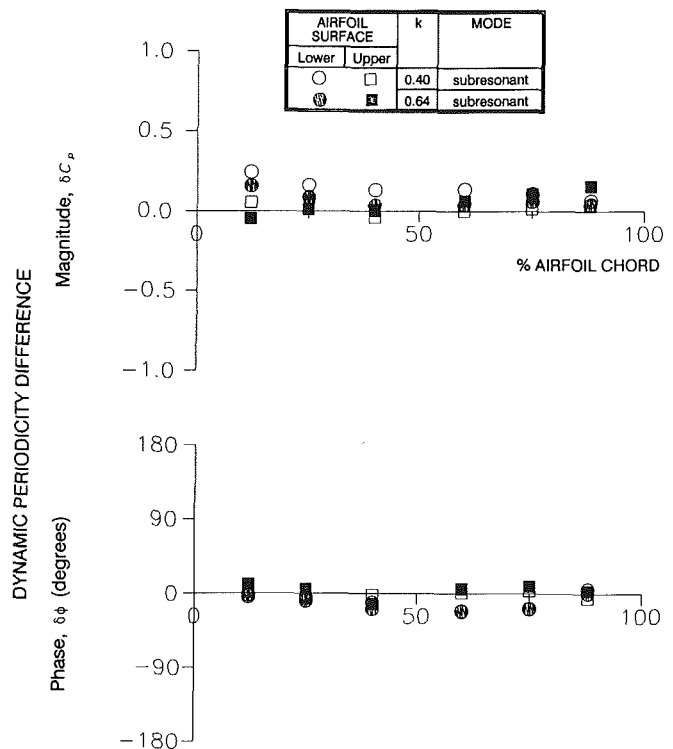


Fig. 10 Dynamic periodicity difference, $\beta = -45$ deg

surface magnitude difference at 12 percent of chord. Finally, for out-of-phase oscillations (subresonant), Fig. 13, the magnitude differences are small, but the phase differences are not. Again, reduced frequency has little effect on the results.

To summarize these data, the dynamic periodicity is largely a function of the interblade phase angle, and the periodicity is acceptable only for $\beta = -45$ deg and $\beta = -90$ deg. For both

values of reduced frequency, these values of β are predicted to be subresonant. However, subresonance does not guarantee good dynamic periodicity: For example, the periodicity is poor for $\beta = 90$ deg, a subresonant value of the interblade phase angle for both values of reduced frequency.

Correlation With Linearized Analysis. The experimental dynamic pressure difference coefficient data are correlated

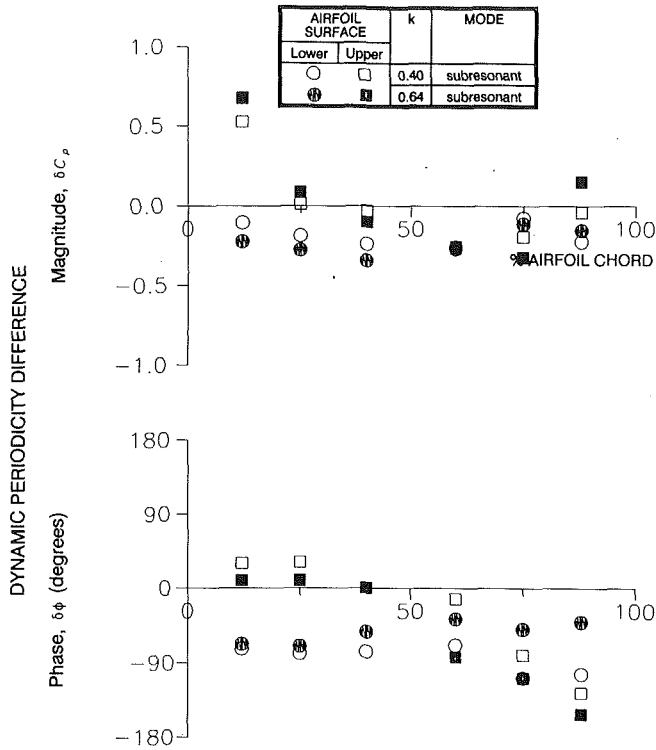


Fig. 11 Dynamic periodicity difference, $\beta = 90$ deg

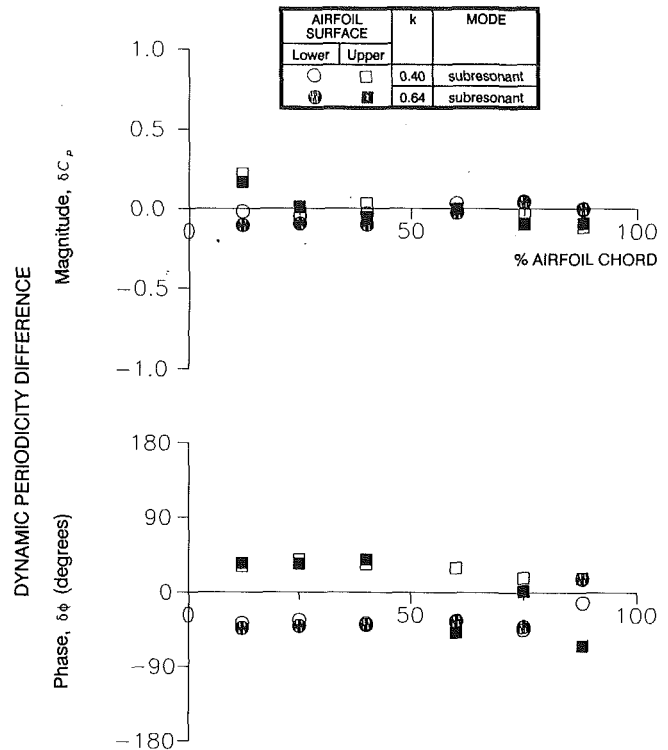


Fig. 13 Dynamic periodicity difference, $\beta = 180$ deg

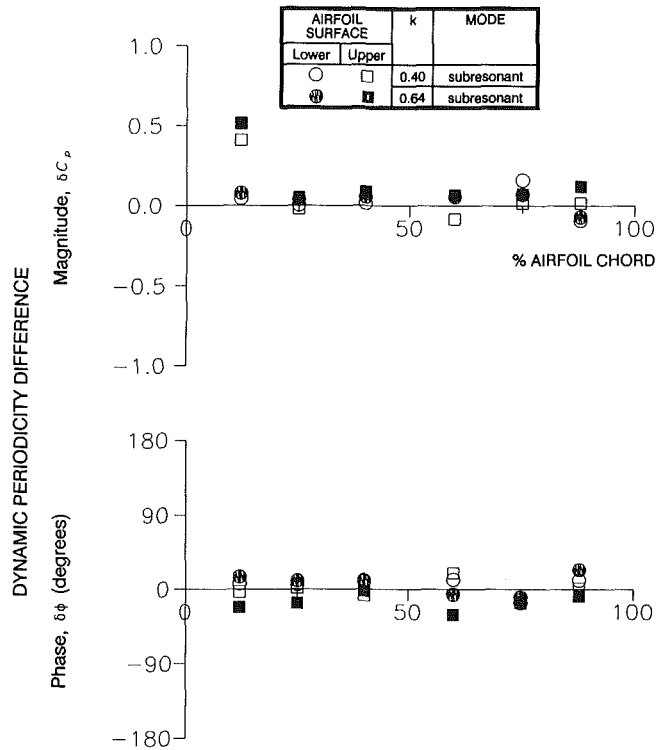


Fig. 12 Dynamic periodicity difference, $\beta = -90$ deg

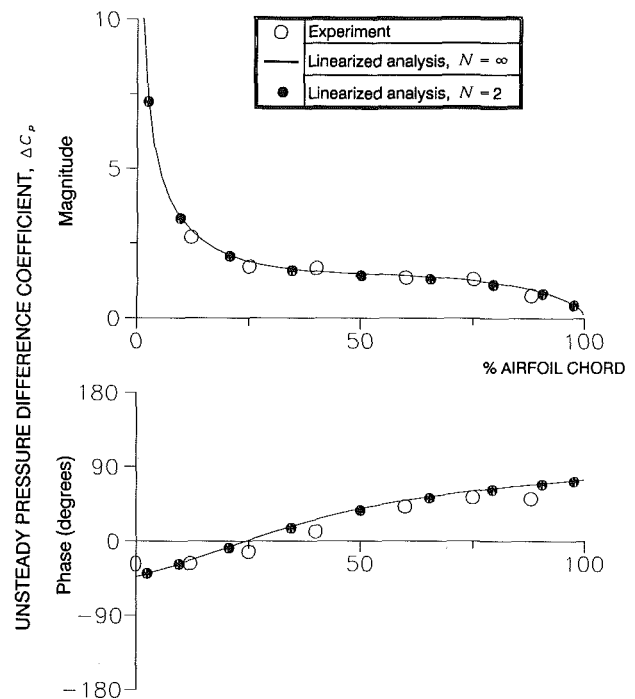


Fig. 14 Unsteady pressure difference coefficient distribution, $k = 0.64$, $\beta = -45$ deg

with the predictions of the linearized unsteady cascade analysis for an infinite number of airfoils. In addition to the infinite cascade predictions, influence coefficient predictions for the effects of five oscillating airfoils ($N=2$ in Eq. (24)) will be presented.

For a reduced frequency of 0.64 and a range of interblade phase angle values, Figs. 14–19 present correlations of the experimentally determined airfoil surface unsteady pressure difference coefficient distributions with the linearized analysis

predictions. For conditions where the cascade dynamic periodicity is good, $\beta = -45$ deg and $\beta = -90$ deg, the correlations between the analytical results and the experimental data are good, Figs. 14 and 15. Conversely, the data-analysis correlations are generally poor for conditions where the periodicity is poor, $\beta = 45$, 90, and 180 deg, Figs. 16–18. At those conditions, the phase angle data-analysis correlation is consistently poor, with the experimentally determined phases leading the predictions except near the trailing edge. An exception is $\beta = 0$

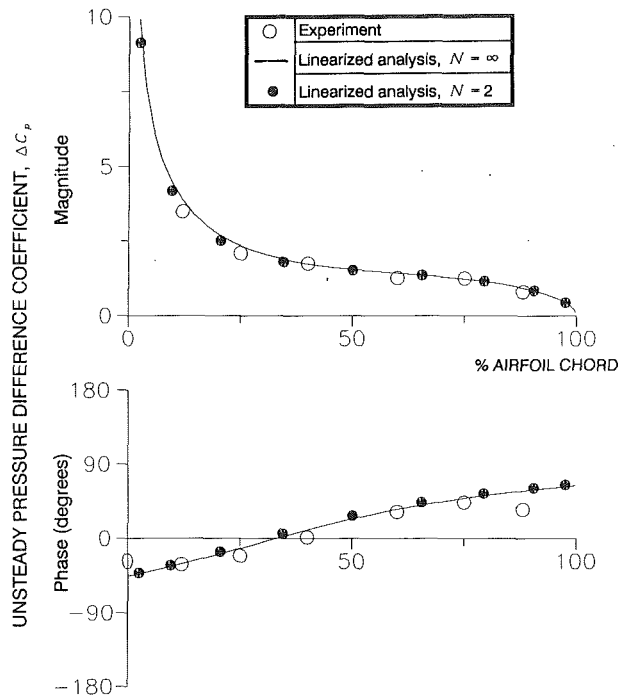


Fig. 15 Unsteady pressure difference coefficient distribution, $k = 0.64$, $\beta = -90$ deg

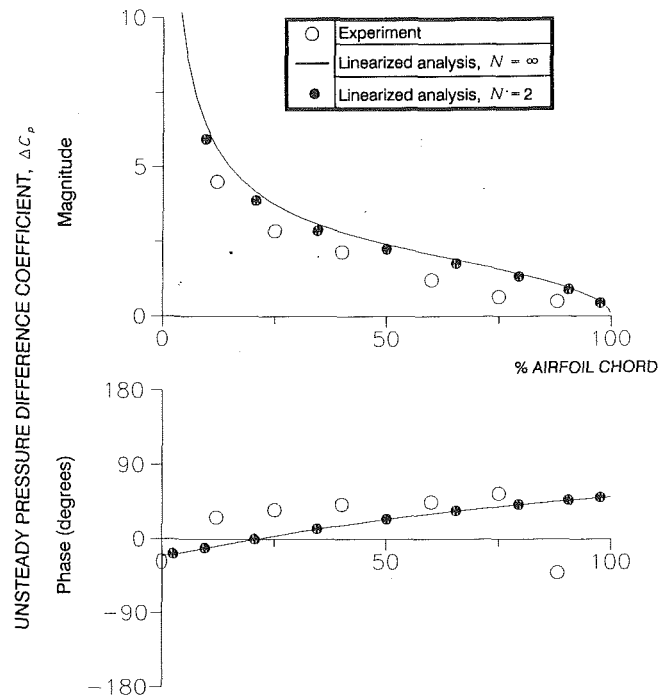


Fig. 17 Unsteady pressure difference coefficient distribution, $k = 0.64$, $\beta = 90$ deg

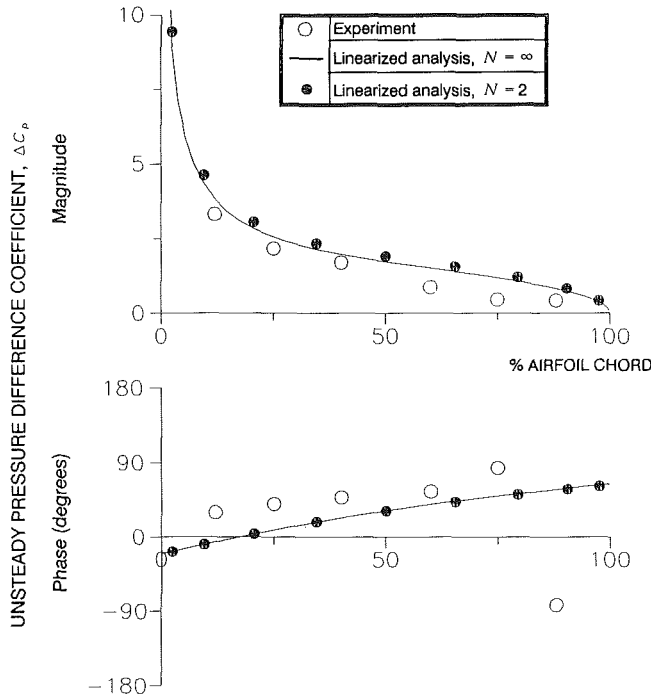


Fig. 16 Unsteady pressure difference coefficient distribution, $k = 0.64$, $\beta = 45$ deg

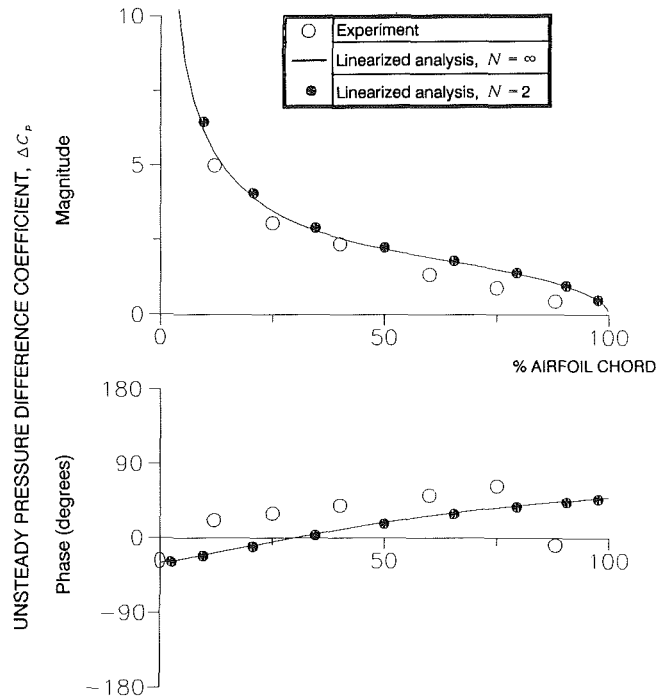


Fig. 18 Unsteady pressure difference coefficient distribution, $k = 0.64$, $\beta = 180$ deg

deg, Fig. 19, for which the data-analysis correlation is good despite poor dynamic periodicity.

The analytical influence coefficient predictions for $N = 2$ are generally in very good agreement with the predictions for an infinite cascade. This indicates that only a few oscillating airfoils are required to model an infinite cascade under these conditions. To consider this further, the imaginary part of the unsteady aerodynamic moment coefficient is presented as a function of interblade phase angle in Fig. 20. Linearized analysis results are shown for $N = \infty$, $N = 6$, and $N = 2$. The predictions for $N = 2$ and $N = 6$ are in very good agreement with

the infinite cascade results except in the vicinity of the acoustic resonances. At those points, a large number of terms in the Fourier series are required to describe the rapidly changing moment coefficient. This indicates that acoustic resonances will not occur in linear oscillating cascade experiments due to the limited number of airfoils.

Wind Tunnel Wall Effects. The cascade dynamic periodicity and correlation of the experimental data with the linearized analysis have been shown to vary greatly with interblade phase angle. How these correlations can be very good for some

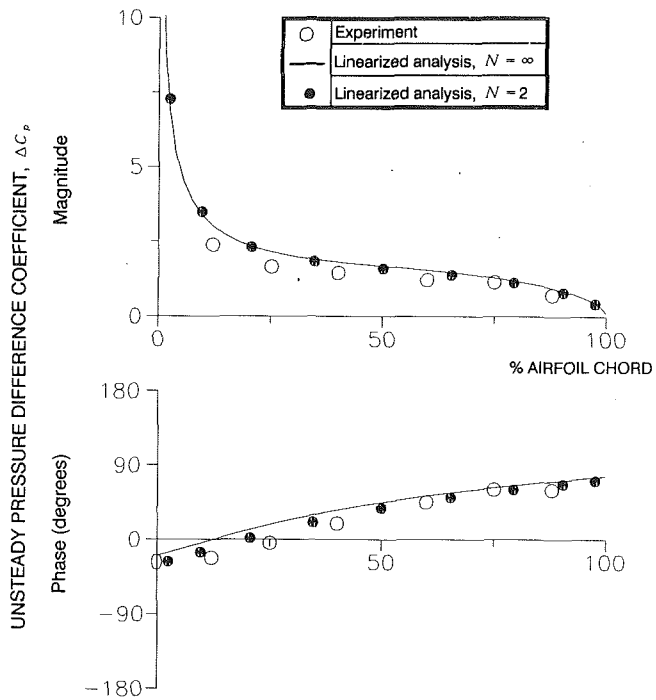


Fig. 19 Unsteady pressure difference coefficient distribution, $k = 0.64$, $\beta = 0$

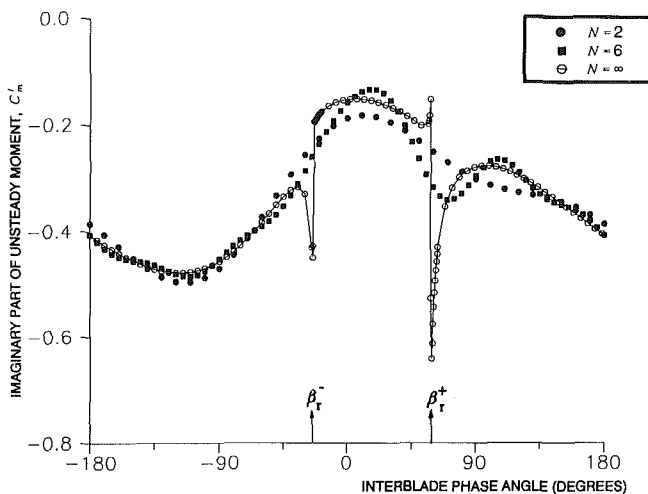


Fig. 20 Imaginary part of unsteady aerodynamic moment coefficient as predicted by linearized analysis

interblade phase angles but poor for others leads one to question the effects of the wind tunnel walls on these results. In this section, linearized analysis is used to gain insight into the oscillating cascade/wind tunnel wall interactions.

The calculated direction of acoustic wave propagation θ is shown in Fig. 21 for the low-solidity cascade geometry with $M = 0.55$ and $k = 0.64$. For any one value of β in the superresonant region, two waves are produced, one traveling upstream (in the $-\xi$ direction) and the other going downstream (in the ξ direction). Outside this region, the oscillating cascade produces subresonant waves, which travel downstream. Acoustic resonances occur at the boundaries between the subresonant and superresonant regions, with pressure disturbances propagating along the cascade in the $\pm\eta$ directions.

Values of the initial magnitude of the outgoing pressure disturbance, computed using Whitehead's computer program, are presented in Fig. 22 in the format of an unsteady pressure coefficient magnitude at the leading edge of the cascade,

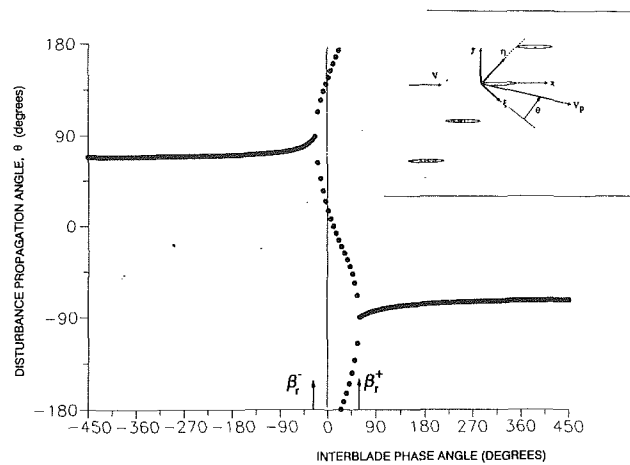


Fig. 21 Pressure disturbance propagation direction

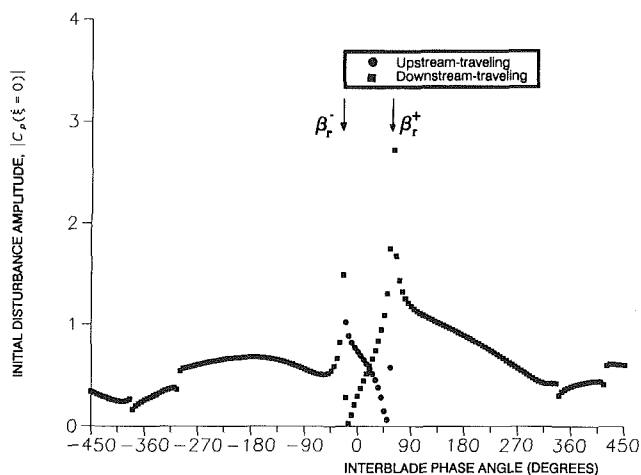


Fig. 22 Initial pressure disturbance amplitude

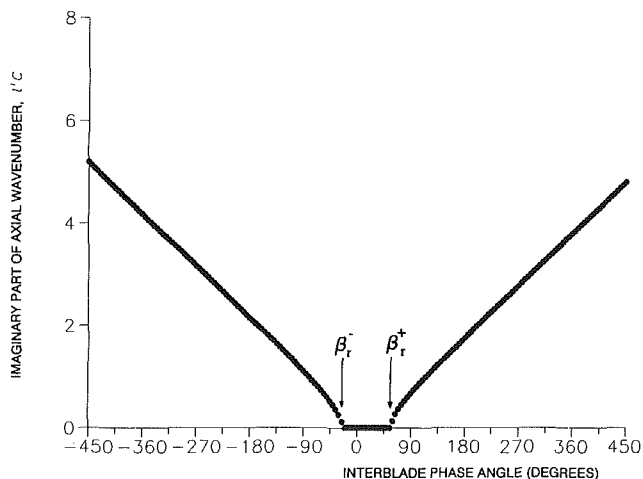


Fig. 23 Imaginary part of axial wavenumber

$|C_p'(\xi = 0)|$. Peaks in the largest initial disturbance amplitudes are found in the vicinity of the acoustic resonances, $\beta = \beta_r^\pm$. Outside the near-resonance regions, relatively large amplitudes occur at positive subresonant values of the interblade phase angle, $\beta > \beta_r^+$, but in general the amplitudes are of the same order of magnitude throughout the interblade phase angle range.

The disturbances will propagate or decay exponentially with distance from the cascade according to the imaginary part of the axial wavenumber, l'' , Eq. (20). As shown in Fig. 23, $l'' = 0$

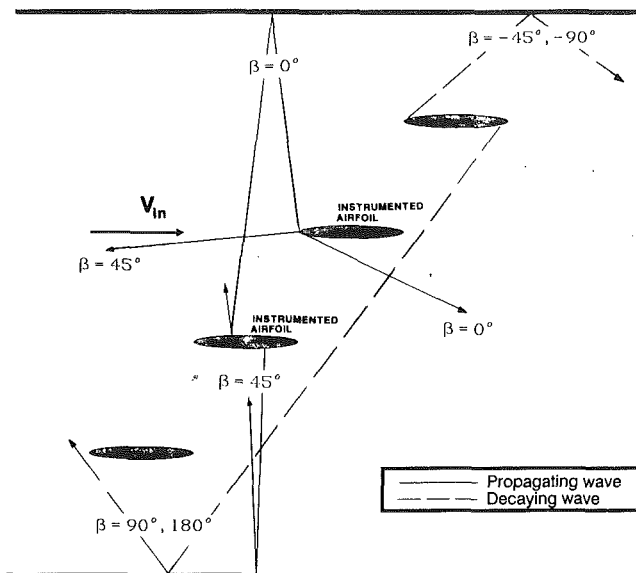


Fig. 24 Interaction of pressure disturbances with wind tunnel walls

in the superresonant region, hence superresonant disturbances propagate away from the cascade without attenuation. Outside this region, l' is nonzero and increases monotonically with $|\beta|$; thus the subresonant waves decay exponentially with distance away from the cascade.

Now the interaction of the predicted waves with the wind tunnel walls is considered. For $\beta = -45$ deg and $\beta = -90$ deg, interblade phase angles where the data-analysis correlation is good, decaying waves traveling at $\theta \approx 81$ deg with $|C_p(\xi = 0)| \approx 0.5$ are predicted. As shown in the schematic of Fig. 24, these waves are directed at the cascade upper wall. The waves are assumed to reflect specularly from the wall so that the reflected disturbances propagate away from the cascade and thus will have no effect on the oscillating cascade aerodynamics.

The data-analysis correlation is also good for $\beta = 0$ deg, a superresonant condition, but this is considered fortuitous because the cascade periodicity is poor. The upstream-traveling wave for this condition, Fig. 24, is directed at the cascade upper wall so that reflected waves travel back into the cascade and potentially affect the cascade unsteady aerodynamics and dynamic periodicity.

The data-analysis correlation is poor for $\beta = 45$ deg, the other superresonant condition. In this case, the downstream-traveling wave is predicted to interfere with the cascade after reflection off the lower wind tunnel wall, Fig. 24.

Decaying waves are predicted for $\beta = 90$ deg and $\beta = 180$ deg, interblade phase angles for which there is poor correlation between the data for all airfoils oscillating and the theory. Despite the poor correlation, the waves are predicted to reflect off the lower wind tunnel wall and propagate upstream without intersecting an airfoil, Fig. 24. This discrepancy may be due to limitations of the linearized analysis, in particular, the assumption of a uniform mean flow.

Summary and Conclusions

Steady and unsteady airfoil surface pressure distributions have been obtained in a low-solidity linear cascade oscillating at reduced frequencies up to 0.64 with 0.55 inlet Mach number. The airfoils were driven in simultaneous torsion-mode oscillations for a range of interblade phase angles. Steady and

unsteady airfoil surface pressure distributions were measured, the latter using flush-mounted miniature pressure transducers. Discrete Fourier analysis techniques were used to analyze the unsteady pressure data and determine the first harmonic components. Periodicity of the cascade was determined by measuring the steady and unsteady pressures on the airfoil surfaces defining the two passages at the center of the cascade. The unsteady pressure difference coefficient data were correlated with flat plate cascade predictions. In addition, an analysis based on linearized unsteady aerodynamic theory was used to predict characteristics of the acoustic waves generated by the cascade.

It was found that the cascade dynamic periodicity is good for some values of interblade phase angle but poor for others. For conditions where the periodicity was good, interblade phase angle values of -45 and -90 deg, the correlation of the data with the flat plate cascade analysis was also good. But, for the remaining values of interblade phase angle, the periodicity was poor and the data-analysis correlation was generally poor. A subsequent analysis predicted that, at interblade phase angle values of -45 and -90 deg, the cascade produced waves that reflected off the wind tunnel upper wall in a direction away from the cascade, so that these reflected waves did not interfere with the cascade unsteady aerodynamics. At those values of interblade phase angle where the periodicity was poor, the analysis often indicated that waves were reflecting off the wind tunnel walls back into the cascade, and therefore interfered with the cascade unsteady aerodynamics.

To make this a reliable facility for the investigation of oscillating cascade aerodynamics, the effects of the wind tunnel walls must be reduced. An effort is currently under way to replace the solid tunnel walls in the vicinity of the cascade with acoustically treated walls as developed to reduce aircraft gas turbine engine noise (Groeneweg and Rice, 1987). The effectiveness of the acoustic treatment will be investigated in part by repeating the experiments reported upon herein.

Acknowledgments

This research was supported by the Propeller and Acoustics Technology Branch and the Turbomachinery Technology Branch of the Propulsion Systems Division at the NASA Lewis Research Center. The assistance of Vincent Verhoff, Robert Olsey, and Bernadette Orahoske in completion of the experiments is gratefully acknowledged.

References

- Buffum, D. H., and Fleeter, S., 1990, "Aerodynamics of a Linear Oscillating Cascade," NASA TM 103250.
- Carta, F. O., 1983, "Unsteady Aerodynamics and Gapwise Periodicity of Oscillating Cascaded Airfoils," *ASME Journal of Engineering for Power*, Vol. 105, pp. 565-574.
- Groeneweg, J. F., and Rice, E. J., 1987, "Aircraft Turbofan Noise," *ASME JOURNAL OF TURBOMACHINERY*, Vol. 109, pp. 130-141.
- Jones, W. P., 1943, "Wind Tunnel Interference Effect on the Values of Experimentally Determined Derivative Coefficients for Oscillating Airfoils," Aeronautical Research Council Reports and Memoranda No. 1912.
- Kline, S. J., and McClintock, F. A., 1953, "Describing Uncertainties in Single-Sample Experiments," *Mechanical Engineering*, Jan., pp. 3-8.
- Mehmed, O., Kaza, K. R. V., Lubomski, J. F., and Kielb, R. E., 1982, "Bending-Torsion Flutter of a Highly Swept Advanced Turboprop," NASA TM 82975.
- Runyan, H. L., Woolston, D. S., and Rainey, A. G., 1955, "Theoretical and Experimental Investigation of the Effect of Tunnel Walls on the Forces of an Oscillating Airfoil in Two-Dimensional Subsonic Compressible Flow," NACA Report 1262.
- Smith, S. N., 1972, "Discrete Frequency Sound Generation in Axial Flow Turbomachines," Aeronautical Research Council Reports and Memoranda No. 3709.
- Whitehead, D. S., 1987, "Classical Two-Dimensional Methods," *AGARD Manual on Aeroelasticity in Axial Flow Turbomachines, Vol. 1: Unsteady Turbomachinery Aerodynamics*, AGARDograph No. 298, pp. 3-1-3-30.

Computational Study of Stall Flutter in Linear Cascades

A. Abdel-Rahim¹

F. Sisto

George Meade Bond Professor,
Fellow ASME

S. Thangam

Professor,
Mem. ASME

Department of Mechanical Engineering,
Stevens Institute of Technology,
Hoboken, NJ 07030

Aeroelastic interaction in turbomachinery is of prime interest to operators, designers, and aeroelasticians. Operation at off-design conditions may promote blade stall; eventually the stall pattern will propagate around the blade annulus. The unsteady periodic nature of propagating stall will force blade vibration and blade flutter may occur if the stall propagation frequency is entrained by the blade natural frequency. In this work a computational scheme based on the vortex method is used to simulate the flow over a linear cascade of airfoils. The viscous effect is confined to a thin layer, which determines the separation points on the airfoil surfaces. The preliminary structural model is a two-dimensional characteristic section with a single degree of freedom in either bending or torsion. A study of the relationship between the stall propagation frequency and the blade natural frequency has been conducted. The study shows that entrainment, or frequency synchronization, occurs, resulting in pure torsional flutter over a certain interval of reduced frequency. A severe blade torsional amplitude (of order 20 deg) has been computed in the entrainment region, reaching its largest value in the center of the interval. However, in practice, compressor blades will not sustain this vibration and blade failure may occur before reaching such a large amplitude. Outside the entrainment interval the stall propagation is shown to be independent of the blade natural frequency. In addition, computational results show that there is no entrainment in the pure bending mode. Rather, "de-entrainment" occurs with similar flow conditions and similar stall frequencies, resulting in blade buffeting in pure bending.

1 Introduction

Axial flow compressors are generally required to operate over a certain range of volume flow rates. If the flow rate is reduced at constant rotational speed, the angle attack in the front stages will increase, eventually reaching the stall inception angle. Then the flow will separate from the blade surface forming a stall cell. The blades, instead of all stalling together, stall in separate blade patches or "cells." These stall cells act as partial flow blockage; as consequence, the angle of attack on the neighboring blade near the pressure side is reduced, and the angle of attack on the other neighboring blade is increased. This effect causes the stall cell to propagate circumferentially in the direction of rotation of the rotor but at a speed lower than the rotor speed. Stall cells, traveling around the blade row, load and unload each blade at the frequency of encountering the cells.

The unsteady periodic blade loading, due to rotating stall, may affect the operation of the turbomachine in two ways. The stall degrades the overall performance, due to the drop of the lift, or reduction in mean flow deflection, caused by flow separation from blade surfaces. The most serious problem related to propagating stall is the destructive nature of the associated blade vibratory motion. If the compressor is op-

erated for a long period of time, the blade may fail to sustain this dynamic loading resulting in blade fatigue. Experimental observations on a single-stage axial compressor by Huppert et al. (1952) showed substantial stresses on the stator blade roots. Huppert found that the rotational speed of the stall regions increased linearly with the rotational speed of the compressor rotor and he attributed the failure of several stator blades to rotating stall. Three distinct stall cells were found when the compressor was operated in the stall condition. The number of stall cells increased with further reduction of flow coefficient; five stable stall cells were observed.

Rainey (1953) conducted an experiment of stall flutter on a single wing. His results showed, at small angle of attack, random bending response in the fundamental bending mode with very little excitation of the torsion mode. At slightly higher angle of attack the time history showed about the same type of bending trace, but the torsion trace indicated a fairly clean sinusoidal variation at about the frequency of the fundamental torsion mode. Yershov (1971) reported that fatigue cracks were detected in the blades of an axial compressor stage after half an hour of operation under propagating stall conditions.

The unsteady aerodynamic forces due to propagating stall can produce two types of blade vibration. Forced vibration occurs in which the blade structure is free to respond to these forces without interactive effects. However, if the blade amplitude is large enough and the stall frequency comes close to one of the blade natural frequencies, the stall frequency may entrain with the blade frequency (i.e., frequency synchroniz-

¹Present address: Mansoura University, Egypt.

Contributed by the International Gas Turbine Institute and presented at the 36th International Gas Turbine and Aeroengine Congress and Exposition, Orlando, Florida, June 3-6, 1991. Manuscript received at ASME Headquarters January 18, 1991. Paper No. 91-GT-5. Associate Technical Editor: L. A. Riekert.

ation occurs) resulting in stall flutter, self-excited aeroelastic instability as described by Sisto et al. (1990).

The aerodynamics of propagating stall in axial flow compressors has been investigated by many researchers. Emmons et al. (1959) conducted experiments on an axial compressor and found that propagating stall begins as a few small cells. As the compressor is throttled further, the cells grow in size until at some point they break down into additional cells. Further throttling results in cell agglomeration into one large cell occupying more than half the circumference. Typically one large stall cell appears in the flow annulus prior to encountering surge. At surge the net integrated throughflow oscillates in time.

The aerodynamic response to prescribed blade motion had been investigated by Sisto (1955) and Whitehead (1960). They used an analytical model for a cascade of airfoils at zero mean incidence with imposed harmonic motions and interblade phase angle at various reduced blade frequencies. Their models were based on a flat plate cascade, and assumed airfoil wakes as narrow strips extended in the direction of the airfoil chords from the trailing edges to downstream infinity. In addition, Sisto (1967) solved the same model with the assumption of a fully stalled cascade. He fixed the separation points on the leading edges, and used conformal transformation to solve the Laplace equation for the acceleration potential with harmonic time dependent motion.

The physical problem of stall flutter calls for a model that considers the actual flow near the boundaries. In terms of the incompressible inviscid flow computation, the unsteady separation points have to be simulated in order to obtain a practical solution. Some attempts have been made to treat the moving separation points for a single airfoil (e.g., Sisto and Perumal, 1974; Tokel and Sisto, 1978). Recently, the concept of confining the effect of viscosity of the neighborhood of the airfoil boundaries (inner flow) and treating the flow away from the airfoils as inviscid incompressible flow (outer flow) has led to the so-called vortex method.

The vortex method models the solid boundaries as vortex sheets whose vorticity can be convected away from the boundary surfaces downstream of the separation points. The flow velocities and pressure at the edge of the inner region can be employed to solve the unsteady boundary layer equation for the location of the separation points. Lewis and Porthouse (1982) used the vortex method without inner region for a three-blade cascade. In their vortex method model, the viscous diffusion is incorporated by random distribution of all shed vortices and the entire sequence of computations is repeated for each time step. Their model did not detect stall propagation, perhaps because of large computer storage and time needed for a practical computation.

Spalart (1984) used a vortex method similar to that of Lewis and Porthouse (1982) but with the inner region incorporated and coupled to an integral boundary layer solver to determine the instantaneous separation points. Spalart (1984) was able to detect the stall propagation in rigid airfoil cascade. Most recently Sisto et al. (1989) studied a computational model based on vortex method for the imposed vibration problem with different inlet flow angles and stagger angles.

In this work a computational investigation is performed for stall flutter in either the bending or torsional mode in a cascade of airfoils and an experiment for torsional vibration is used to verify the numerical results. The basic computational model for the aerodynamic part is adapted from Jonnavithula et al. (1990) and Sisto et al. (1989). The boundary layer solver is improved by incorporating unsteady and curvature effects in the momentum integral equation. Since this study is based on a two-dimensional model, the structural part is formulated in terms of lumped masses, stiffness, and damping coefficients. This model can be viewed as equivalent to the inertial and elastic properties of a typical blade element along a cantilevered blade span. These "typical section" parameters can be estimated separately by analyzing the actual cantilever blade dynamics. This is assumed to be done beforehand and the lumped parameters are then taken as fixed quantities.

2 Formulation and Method of Solution. A schematic of the physical configuration and the coordinate system is shown in Fig. 1.

The equations of motion of an incompressible Newtonian fluid are: the continuity equation

$$\nabla \cdot \mathbf{V} = 0 \quad (1)$$

and the momentum equation

$$D_t \mathbf{V} = -\frac{1}{\rho} \nabla P + \nu \nabla^2 \mathbf{V} \quad (2)$$

where

$$\mathbf{V} = (u, v), \text{ and } D_t = \frac{\partial}{\partial t} + \mathbf{V} \cdot \nabla.$$

For a cascade of airfoil, the boundary condition on each airfoil is taken to be

$$\mathbf{V} = \mathbf{V}_b \quad (3)$$

The initial condition at $t = t_0$ is

$$\mathbf{V} = \mathbf{V}_0 \quad (4)$$

The corresponding vorticity transport equation is

$$D_t \omega = \nu \nabla^2 \omega \quad (5)$$

Nomenclature

A_b = airfoil cross-sectional area
 C = blade bending stiffness
 c = blade chord
 D = blade damping coefficient
 f = frequency
 H = boundary layer shape factor
 h = blade bending displacement
 J = blade centroidal moment of inertia
 j = complex constant ($= \sqrt{-1}$)
 K = reduced frequency $= \pi fc/U$
 M = number of airfoils in stall period
 m = blade mass
 N_c = number of stall cells
 N_f = number of free vortices

P = pressure
 p = stall cell wavelength
 s = distance along the airfoil surface
 t = time
 u, v = velocity components
 x, y = Cartesian coordinates
 z = complex coordinate $= x + iy$
 V = flow velocity
 U = upstream velocity
 α = inflow angle
 β = stagger angle
 Γ = vortex strength
 Θ = torsional displacement
 ν = fluid kinematic viscosity
 ζ = complex coordinate
 ρ = fluid density

σ = interblade phase angle
 ψ = stream function
 Ω = angular velocity of the airfoil
 ω = vorticity

Subscripts

b = blade
 e = edge of the boundary layer
 f = free vortex
 n = normal vector, or natural
 s = stall, or surface

Superscripts

b = bending
 m = blade order in stall cell
 t = torsion

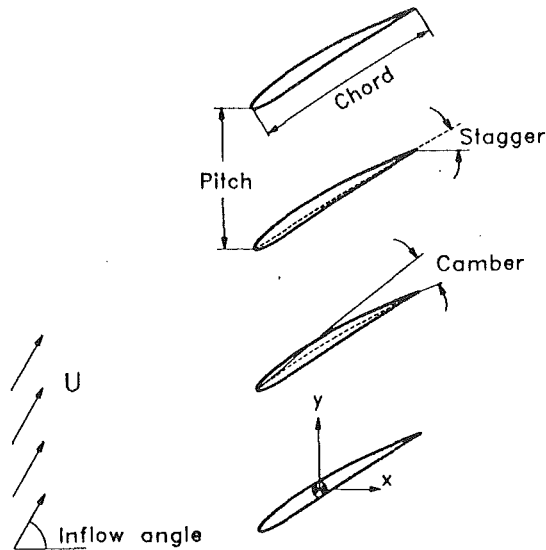


Fig. 1 Schematic of the airfoil cascade and related nomenclature

where $\omega = \nabla \times \mathbf{V}$ and the boundary condition for the vorticity equation can be written (Spalart, 1984) as

$$\oint \nu \frac{\partial \omega}{\partial n} = -2A_b D_t \Omega_b \quad (6)$$

The vorticity within the airfoil,

$$\omega = 2\Omega_b \quad (7)$$

where Ω_b is the angular blade velocity in torsional motion.

Usually turbomachines are designed to operate at high Reynolds number. Therefore, the flow over a cascade can be effectively divided into two regions. The boundary region, very thin and near the airfoil, is where the viscous effects are confined. The remaining flow field can be considered as inviscid and irrotational. The interaction between the two regions has been matched in such a way that the boundary conditions on each airfoil are satisfied.

From analytic function theory, the irrotational flow field of an ideal fluid can be represented by a sum of analytic functions, which have singularities at discrete points. The analytic function, such as the potential function (or alternately the stream function), can be built up by summing over logarithmic singularities at the boundary of the solid bodies in the field; one class of these singularities is vortices.

In this work the airfoils are replaced by vortex sheets called "boundary vortices" placed a small distance from the boundaries, in order to be able to convect some or all boundary vortices in case of partially or fully separated flow. This vortex sheet encloses the airfoil rather than lying on the boundary where the fluid and the airfoil velocities are equal (no-slip boundary condition) and thus the vortices would never convect into the flow field. It is known from the analytic function theory, that if the real or the imaginary part of an analytic function is constant on the boundary of a domain and it has no singularities within it, the function will be a constant over the whole domain. This can be applied in the case of cascade airfoils by extending the flow field to replace the airfoils. In this unsteady study the airfoils are vibrating and the stream functions, along the airfoil boundaries are not constant but rather a function of the boundary velocity. The streamline pattern frozen at a given instant of time may display streamlines crossing the airfoils.

In propagating stall analysis, each vortex in the computational domain is considered as a member of an infinite column of vortices with identical strengths and with pre-imposed period p typically equal to about four or five blade pitches. Physically, the imposed period can be used as a model for a compressor

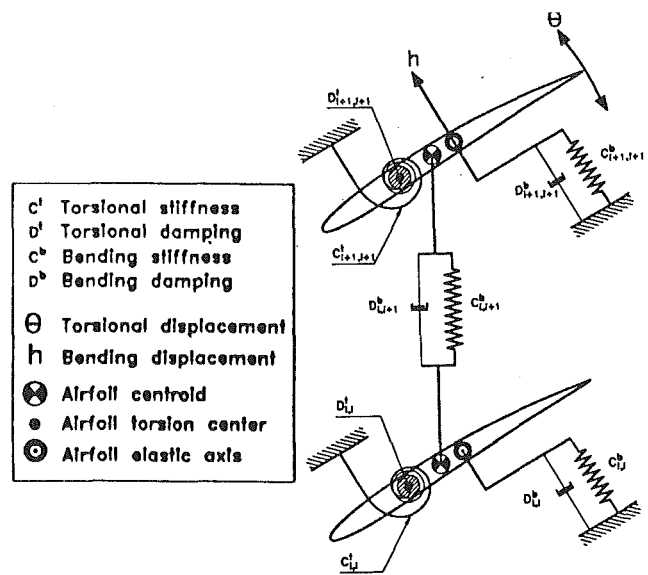


Fig. 2 Schematic of the blade structural model

with circumferential length equal to N_c times p (where N_c is an integer and represents the total number of presumably identical stall cells).

The stream function of such an array of vortices of strength Γ located at $z_o + jnp$ (where $n = 0, \pm 1, \pm 2, \dots, \pm \infty$) at the field point z is given by

$$\psi(z) = \frac{\Gamma}{4\pi} \log \left[\left| \sin \frac{2\pi j(z - z_o)}{p} \right|^2 + \epsilon^2 \right] \quad (8)$$

where ϵ is a small constant introduced to render the complex logarithm nonsingular at the points z close to $z_o + jnp$. It should be noted that ϵ is used only for computational purposes has no physical meaning.

Boundary Conditions

Usually axial flow turbomachinery blades are twisted, tapered, and connected to each other by one or more stiffening rings or shrouds. In order to investigate the flow in those machines, a three-dimensional model for both the aerodynamics and blade structure needs to be implemented. The blade may vibrate in each of several coupled modes of predominant bending and/or predominant torsion.

In this study a representative blade element is identified as a two-dimensional airfoil. Usually this characteristic section is chosen at 80 percent of the blade span, and may vibrate in bending normal to the chord and/or in the chordwise direction. From the airfoil shape, the blade is stiffer in the chordwise direction compared to its stiffness normal to its chord; hence, in this study, the bending mode of vibration is considered to be normal to the airfoil chords only. The airfoils may also vibrate in torsion around their torsion centers. These two modes of vibration (bending and torsion) are coupled due to the offset between the centroidal and torsion centers. (In the case of a cylindrical beam with two axes of symmetry this offset is zero, and the two modes would be structurally uncoupled.) Each blade is represented by a concentrated mass at its centroid and an offset between the centroid and the torsion center. A schematic of the blade structural model used in this analysis is shown in Fig. 2. The cantilevered blade elements are assumed to be rigid and equivalent structural bending and torsional stiffness and damping acting on the blade elements are represented by linear spring-dashpot systems connected to ground. The interblade structural coupling is represented by an equivalent linear spring-dashpot system connecting the consecutive

blade centroids. (This coupling is not studied in the present report.)

In bending vibration the instantaneous location of the airfoil boundary points as a function of time can be written as

$$z_i(t) = z_i(t_0) + jh(t)e^{j\beta} \quad (9)$$

Upon differentiating the above equation, the bending velocities at the boundary points are

$$\dot{z}_i(t) = j\dot{h}(t)e^{j\beta} \quad (10)$$

In torsional vibration the instantaneous location of the airfoil boundary points as a function of time can be written as

$$z_i(t) = z_i(t_0)e^{j\Theta(t)} \quad (11)$$

and the corresponding torsional velocities are

$$\dot{z}_i(t) = jz_i(t_0)\dot{\Theta}(t)e^{j\Theta(t)} \quad (12)$$

where $z_i(t_0)$ are the airfoil complex coordinates at the initial time t_0 measured from its centroid, assumed here to coincide with the torsion center (cf. Fig. 2). $h(t)$, $\dot{h}(t)$, $\Theta(t)$, and $\dot{\Theta}(t)$ are the instantaneous displacement and velocity for bending and torsional vibrations, respectively. The stream function on the boundary of the airfoil in oscillatory motion can be expressed as

$$\delta\psi|_s = \int_{s_0}^{(s_0+\delta s)} (\mathbf{v} - \mathbf{n}) ds \quad (13)$$

The induced difference of the stream function at the boundary points ξ_{i+1} , γ_i of blade b due to all free "old" vortices in the field (denoted by $\theta\psi^{\text{old}}$) is given by:

$$\begin{aligned} \Delta\psi^{\text{old}} &= \psi_{i+1}^{\text{old}} - \psi_i^{\text{old}} \\ &= \sum_{k=1}^{N_f} \frac{\Gamma_k}{4\pi} \left\{ \log \left[\left| \sin \frac{\pi j(\xi_{i+1} - z_k)}{p} \right|^2 + \epsilon^2 \right] \right. \\ &\quad \left. - \log \left[\left| \sin \frac{2\pi j(\xi_i - z_k)}{p} \right|^2 + \epsilon^2 \right] \right\} \quad (14) \end{aligned}$$

where N_f is the number of free vortices in the field (previously convected from the airfoils). For a period of M blade pitches the induced difference of stream function due to bound vortices (denoted by $\theta\psi^{\text{bound}}$) on blade b is given by:

$$\begin{aligned} \Delta\psi^{\text{bound}} &= \psi_{i+1}^{\text{bound}} - \psi_i^{\text{bound}} \\ &= - \sum_{l=1}^M \sum_{k=1}^{N_f} \frac{\Gamma_k^l}{4\pi} \left\{ \log \left[\left| \sin \frac{2\pi j(\xi_{i+1} - \zeta_k^l)}{p} \right|^2 + \epsilon^2 \right] \right. \\ &\quad \left. - \log \left[\left| \sin \frac{2\pi j(\xi_i - \zeta_k^l)}{p} \right|^2 + \epsilon^2 \right] \right\} \quad (15) \end{aligned}$$

where ζ_k^l are the instantaneous coordinates of points k on blade l and N_b is the number of the boundary points chosen to represent the vortex sheet on the airfoil. The stream function ψ_u due to uniform flow with complex conjugate velocity $u - jv = Ue^{-ja}$ can be written as

$$\Delta\psi_u = \text{Imag} \left[Ue^{-ja}(\xi_{i+1} - \xi_i) \right] \quad (16)$$

Therefore,

$$\theta\psi^{\text{bound}} = -\nabla\psi^{\text{old}} - \Delta\psi_u + \Delta\psi_s \quad (17)$$

Blade Structural Dynamics

The airfoils are taken to be typical elements of counterpart axial flow compressor blades. Each airfoil element represents

a typical section of a cantilevered blade fixed at the compressor hub. The equivalent bending and torsion stiffness and damping coefficients can be determined from the structural analysis of an actual blade geometry. In this work it is assumed that the elastic blade parameters are known prior to the computations. It is worth noting, generally, that there is coupling between the two modes of vibration due to the offset of the blade elastic and mass axes. It is assumed in this study that this offset is equal to zero; hence the vibration modes are structurally uncoupled. It is important that the effect of this structural coupling be investigated in future work, along with aerodynamic coupling.

Since the bending and torsional modes of the present study are uncoupled, the two modes of vibration can be represented by two separate systems of second-order ordinary differential equations. For a stall cell wavelength encompassing M blades, the bending or torsion response can be represented as a system of M coupled, second-order ordinary differential equations with periodic conditions. For the i th airfoil the equation of motion for the bending mode is

$$\begin{aligned} \text{Lift}_i(t) &= m_i\ddot{h}_i - D_{i,i+1}^b\dot{h}_{i+1} - D_{i,i-1}^b\dot{h}_{i-1} \\ &\quad + (D_{i,i+1}^b + D_{i,i}^b + D_{i,i-1}^b)\dot{h}_i - C_{i,i+1}^b h_{i+1} \\ &\quad - C_{i,i-1}^b h_{i-1} + (C_{i,i-1}^b + C_{i,i}^b + C_{i,i-1}^b)h_i \end{aligned}$$

and for the torsion mode it is

$$\begin{aligned} \text{Moment}_i(t) &= J_i\ddot{\Theta}_i - D_{i,i+1}^t\dot{\Theta}_{i+1} - D_{i,i-1}^t\dot{\Theta}_{i-1} \\ &\quad + (D_{i,i+1}^t + D_{i,i}^t + D_{i,i-1}^t)\dot{\Theta}_i - C_{i,i+1}^t\Theta_{i+1} \\ &\quad - C_{i,i-1}^t\Theta_{i-1} + (C_{i,i+1}^t + C_{i,i}^t + C_{i,i-1}^t)\Theta_i \end{aligned}$$

where h is the bending displacement, normal to the airfoil chord, Θ is the torsional displacement (positive counterclockwise) and $i = 1, 2, 3, \dots, M-1, M$. The initial conditions at $t = 0$ are given by $h_i = 0$, $\dot{h}_i = 0$, $\Theta_i = 0$, and $\dot{\Theta}_i = 0$ for a time-marching type of solution. In this time-domain implementation the aerodynamic forces and moments are calculated and then used in the above equations to determine the blade displacement and velocities for the next time increment. These velocities and displacement then serve to determine the aerodynamic forces.

Results and Discussion

The objective of this computational study is to investigate, or ultimately to define, the region in which the unsteady aerodynamic forces due to the propagating stall in a linear cascade have frequencies close to the blade natural frequencies and in which stall flutter may appear. In the computations, the aerodynamic parameters (e.g., the inflow velocity and angle) are kept unchanged and the blade structural frequency is varied. The midrange of the blade frequencies is chosen to equal the rigid-blade stall propagation frequency. A series of computations for stall flutter has been performed on a cascade of airfoils in pure torsional vibration or pure bending vibration. The airfoil center of gravity is used as the center of rotation in the pure torsional mode, while in pure bending the airfoils were free to vibrate normal to the airfoil chords. The cascade of airfoils consist of NACA0008 thickness distribution with 10 deg circular arc camber. The stagger angle ($\beta = 0$ deg), and the inlet flow angle ($\alpha = 55$ deg) are chosen to be within the stable region of propagating stall for a stall cell periodicity of three-blade pitches (cf. Jonnavithula et al., 1990). The spring stiffnesses are varied to cover a wide range of the blade natural frequency, the "blade frequency."

The program performs the computations at each time step ($\Delta t = 0.05$) for a full duration of 400 time units for torsional or bending vibration. Most of the computations were performed using 64-bit arithmetic in a CYBER-205 supercomputer. A typical computation required 100 minutes of CPU time. An equivalent calculation at 32-bit precision in a VAX-8700 took about 28 hours of CPU time. The outputs at each

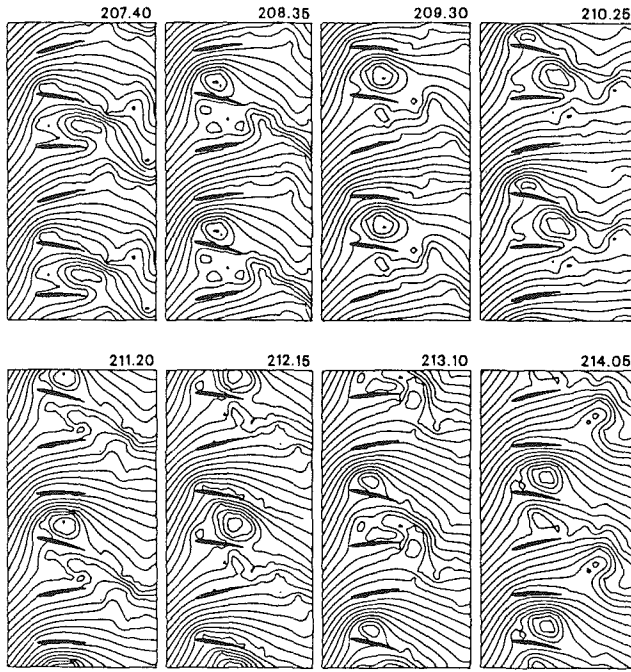


Fig. 3 Instantaneous streamline pattern for a three-blade cascade in torsional vibration at consecutive times over a single period of oscillation [$\alpha = 55$ deg, $\beta = 0$ deg, $K_{\eta(\text{vacuum})} = 0.13$ Hz]

time step are the vibrational blade response and the unsteady aerodynamic lift and moment coefficients for each blade in the cascade. The time signal of the displacement and the lift are then post-processed using the Fast Fourier Transform (FFT) technique to determine the frequency content in each signal.

Torsional Degree of Freedom

An extensive investigation for stall flutter in torsional vibration is performed for the case of stagger angle $\beta = 0$ deg inflow angle $\alpha = 55$ deg, and blade reduced frequency ranges between $0.25 \leq K_n \leq 0.60$. To facilitate the presentation of results, all the parameters were normalized using the airfoil chord as a unit length and inflow velocity as a unit velocity, and the corresponding time unit was c/U . Figure 3 shows the instantaneous streamline pattern for consecutive times over one period of the blade oscillation ($t \approx 7.6$ time units). The plots are extended for additional three blade passages in the vertical direction to help in the visualization of stall propagation. It is seen from these plots that the blades are experiencing a severe torsional vibration and the stall cell is passing the blades at about the same time interval. In fact, these streamlines demonstrate one of the cases that indicate synchronization of the blade and stall frequencies.

Figure 4 shows the torsional displacement spectra for the three blades in the cascade. Each plot displays a definite peak of about 15 deg in magnitude at the blade frequency, which is a slightly higher than the input value due to the apparent mass of the air. Figure 5 shows the corresponding moment spectra, which also display peaks at the same frequency as the peaks of the displacements.

Figure 6 shows the influence of the blade reduced frequency on the stall propagation frequency. This figure displays clearly the region of the entrainment of both frequencies on the 45 deg dashed line. The two dotted vertical lines on the left and right of the entrainment region represent a sudden transition of the stall propagation frequency to entrain and "de-entrain" with blade frequency, respectively.

It is seen that these two transitions are different in length and the manners in which the propagation frequency is en-

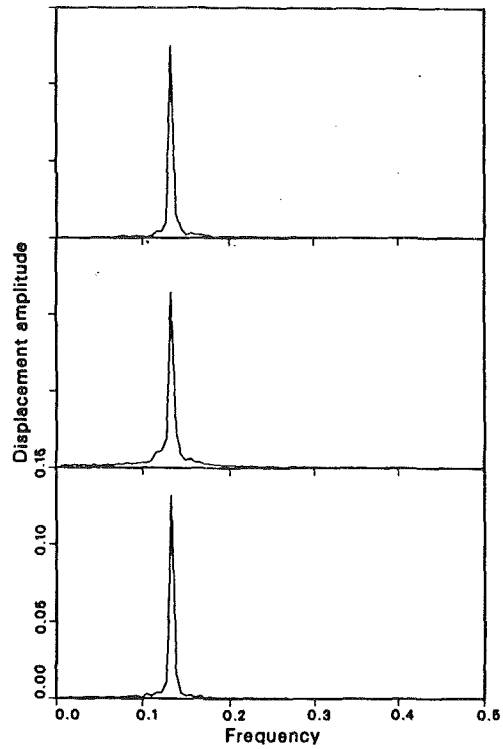


Fig. 4 Displacement spectra for a cascade in torsional vibration [other details are the same as in Fig. 3]

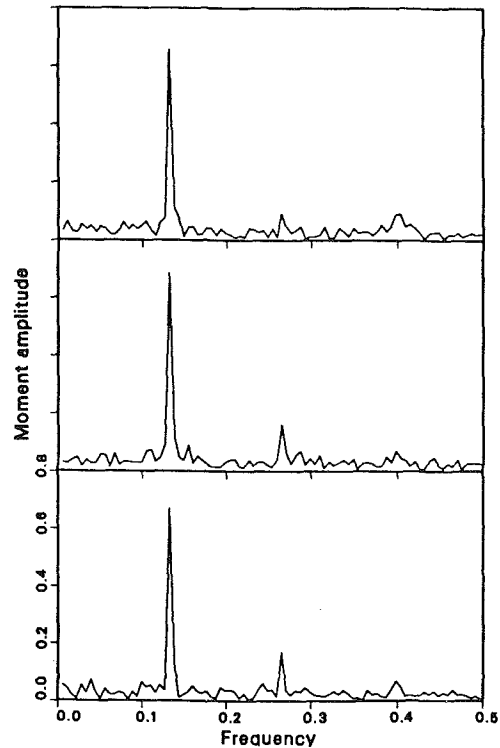


Fig. 5 Moment spectra for a cascade in torsional vibration [other details are the same as in Fig. 3]

trained and "de-entrained" are opposite in character. The subregion on $\Delta K_n = 0.05$ width up to the left of entrainment is considered as a "pre-entrainment" region and the subregion of the same interval to the right of entrainment as "post-entrainment" region. This may be explained in view of the blade frequency magnitudes at each of the transitions; the blade frequency is small in the pre-entrainment region and larger in

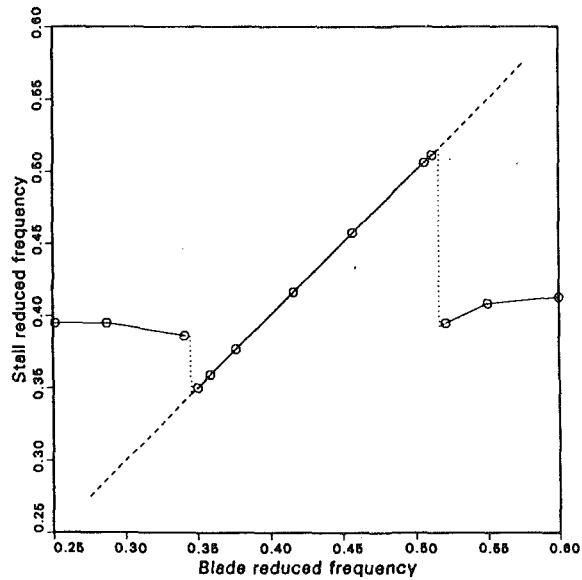


Fig. 6 Influence of blade reduced frequency on stall reduced frequency for a cascade in torsional vibration [other details are the same as in Fig. 3]. The plot shows that the entrainment of frequencies occurs on a certain interval of blade frequency.

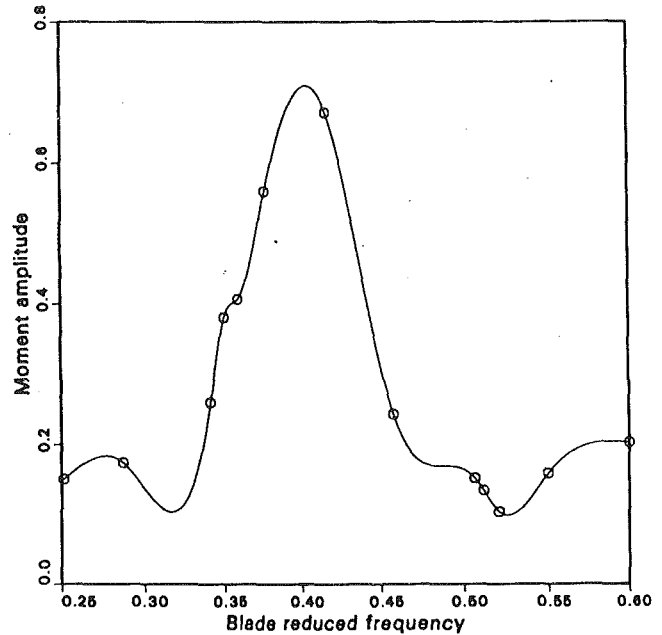


Fig. 8 Influence of blade reduced frequency on the blade moment amplitude for a cascade in torsional vibration [other details are the same as in Fig. 3]. The plot shows a substantial moment amplitude at the entrainment.

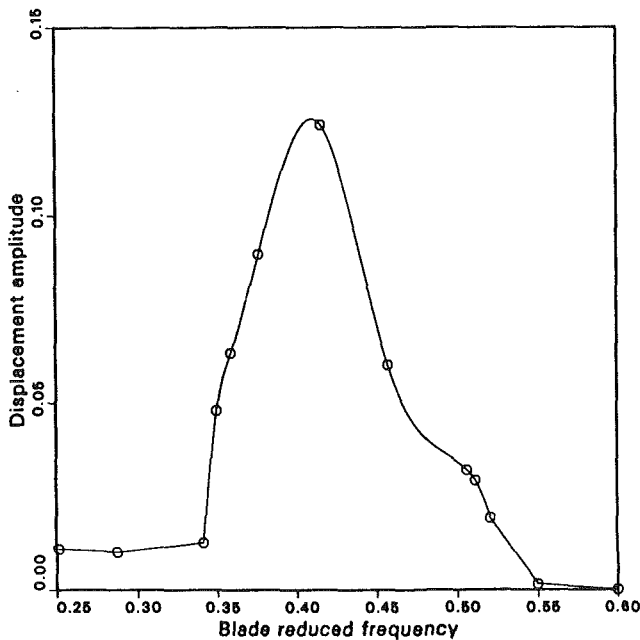


Fig. 7 Influence of blade reduced frequency on the blade displacement amplitude for a cascade in torsional vibration [other details are the same as in Fig. 3]. The plot shows a substantial displacement amplitude at the entrainment.

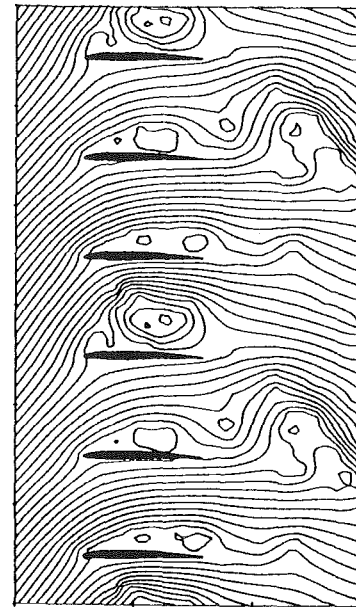


Fig. 9 Instantaneous streamline pattern for a three-blade cascade in bending vibration [$t = 400$, $\alpha = 55$ deg, $\beta = 0$ deg, $K_{n(\text{vacuum})} = 0.123$ Hz]

the post-entrainment regions. In the pre-entrainment the blades have a large amplitude relative to that of the post-entrainment, and the aerodynamic forces are controlled primarily by the blade vibration. On the other hand, in the post-entrainment the blade vibration has less effect on the flow, and the stall propagation characteristics are similar to that of a rigid blade cascade.

In Fig. 7 the influence of the blade frequency on the torsional blade amplitude is shown. The amplitudes correspond to the peak values of the torsional displacement spectra similar to those shown in Fig. 4. The results shown resemble that of an externally forced mass spring system resonance curve in which

the amplitude reaches its peak when the forcing frequency sweeps past the blade natural frequency. The results shown in this graph are for the case where the forcing frequency is kept constant (its analog in this nonlinear system is the stall frequency for a rigid cascade) and a series of blades with increasing natural frequencies are considered. However, in case of the cascade the stall propagation frequency is entrained with the blade frequency (in the region, $\Delta K_n \approx 0.34$ to 0.52), and each point in this region resembles the peak of the linear system resonance curve. In Fig. 8 the influence of the blade frequency on the aerodynamic moment amplitude is shown. As can be seen the moment reaches its peak at the same blade frequency as the peak of the displacement.

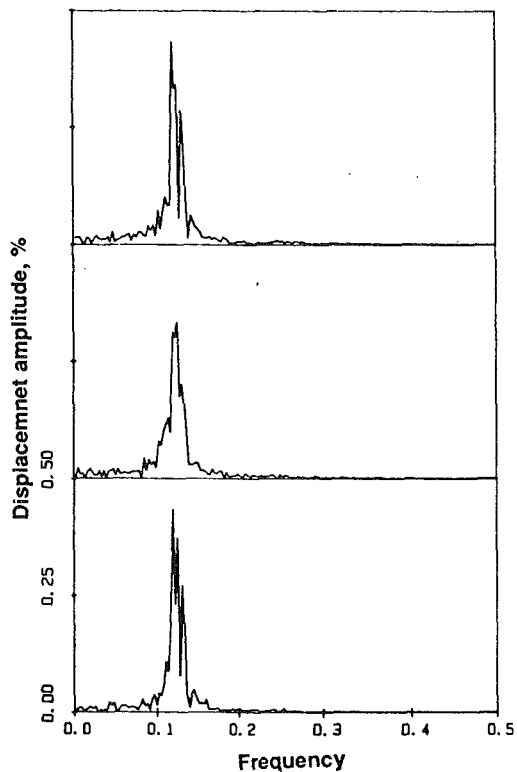


Fig. 10 Displacement spectra for a three-blade cascade in bending vibration [other details are the same as in Fig. 9]

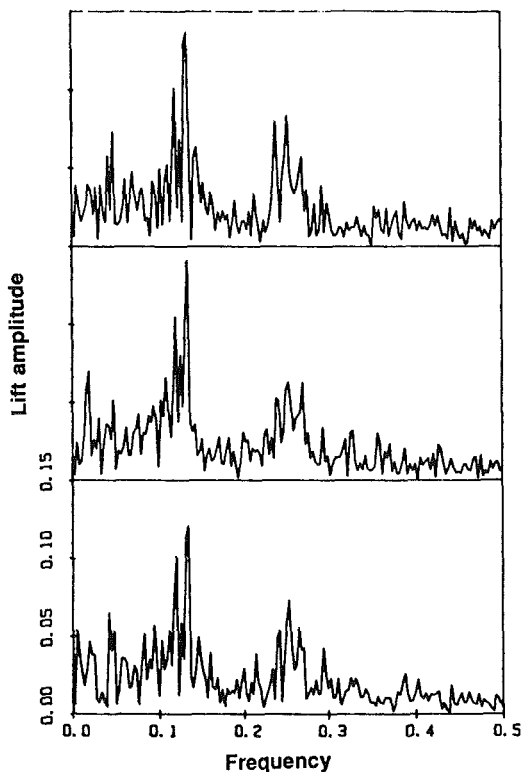


Fig. 11 Lift spectra for a three blade cascade in bending vibration [other details are the same as in Fig. 9]

Bending Degree of Freedom

An investigation for stall flutter in bending is carried out for the case of stagger angle $\beta = 0$ deg, inflow angle $\alpha = 55$ deg, and blade reduced frequency ranges between $0.15 \leq \Delta K_n$

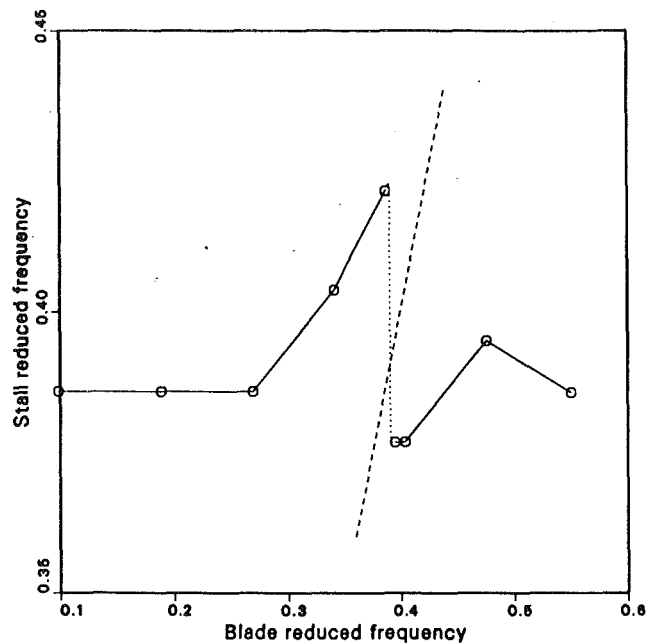


Fig. 12 Influence of blade reduced frequency on the stall reduced frequency for a cascade in bending vibration [other details are the same as in Fig. 9]. The plot shows the "de-entrainment" of the stall frequency.

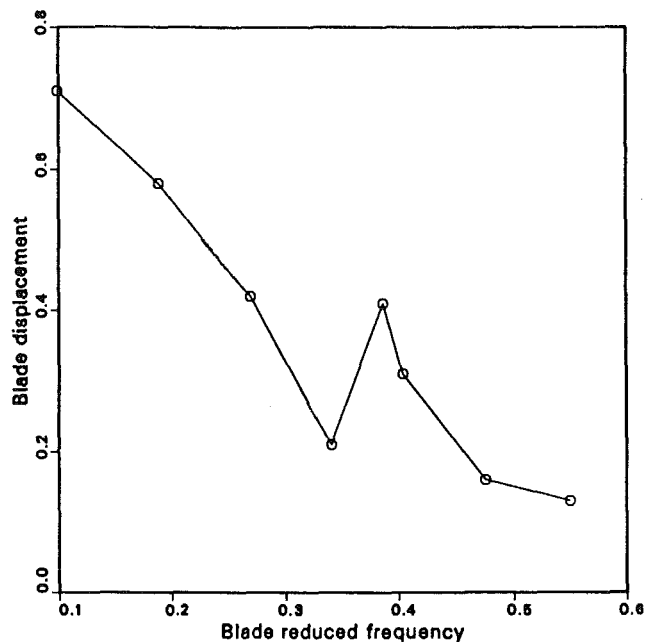


Fig. 13 Influence of blade reduced frequency on the displacement of a cascade in bending vibration [other details are the same as in Fig. 9]

≤ 0.75 . A sample of streamline pattern is shown in Fig. 9 for the case of three-blade cascade and $\alpha = 55$ deg, $\beta = 0$ deg, $f_n = 0.123$ Hz, at $t = 400$. It is seen from the streamlines that all the blades are stalling and frequency spectra for displacement and lift are shown in Figs. 10 and 11, respectively. It is seen from these figures that the frequency at the peaks corresponds to the blade frequency for the displacement spectra, and that of propagating stall for the lift.

Figure 12 shows the effect of blade reduced frequency on stall reduced frequency. It is shown that when the blade and stall frequencies are further apart, that stall frequency is constant and independent of the blade frequency. In the narrow region, when the blade frequency approaches the stall fre-

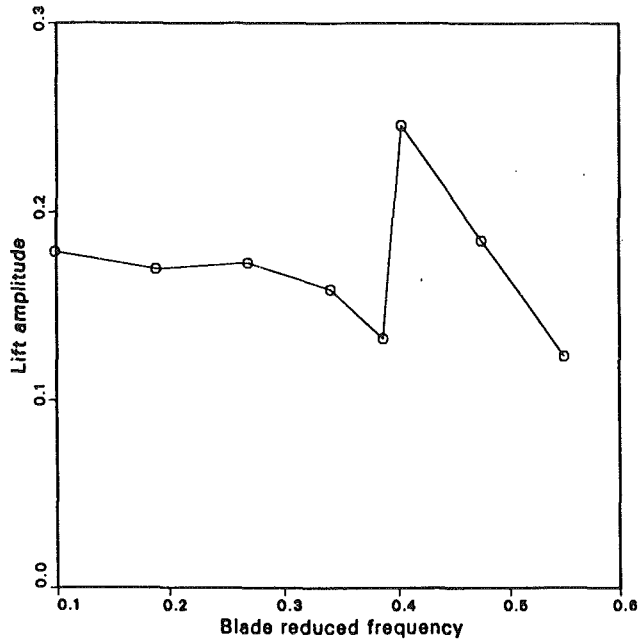


Fig. 14 Influence of blade reduced frequency on the lift amplitude for a cascade in bending vibration [other details are the same as in Fig. 9]

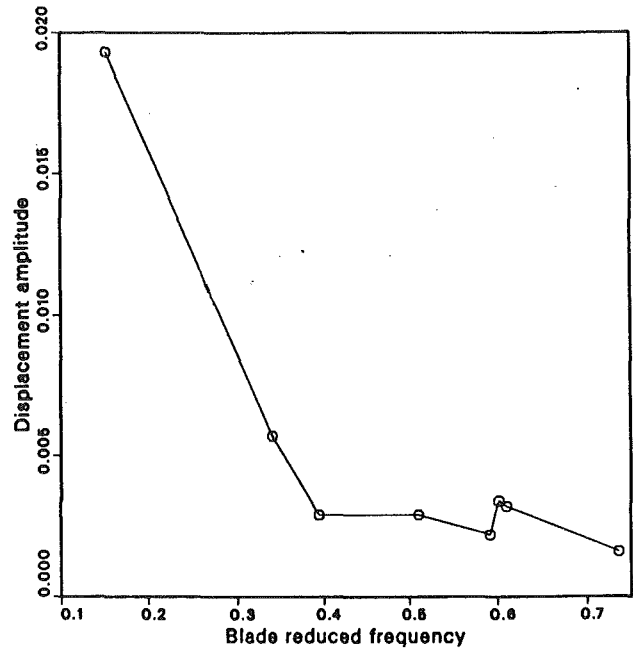


Fig. 16 Influence of blade reduced frequency on the blade displacement amplitude for a two blade cascade in bending vibration [other details are the same as in Fig. 9]

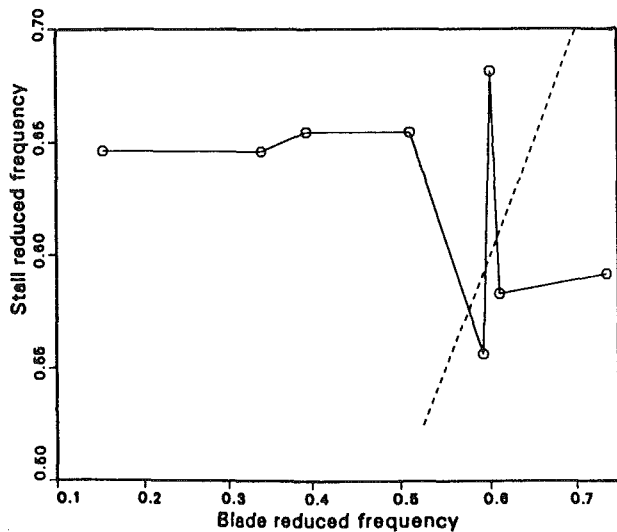


Fig. 15 Influence of blade reduced frequency on the stall reduced frequency for a two blade cascade in bending vibration showing the "de-entrainment" of the stall frequency [other details are the same as in Fig. 9]

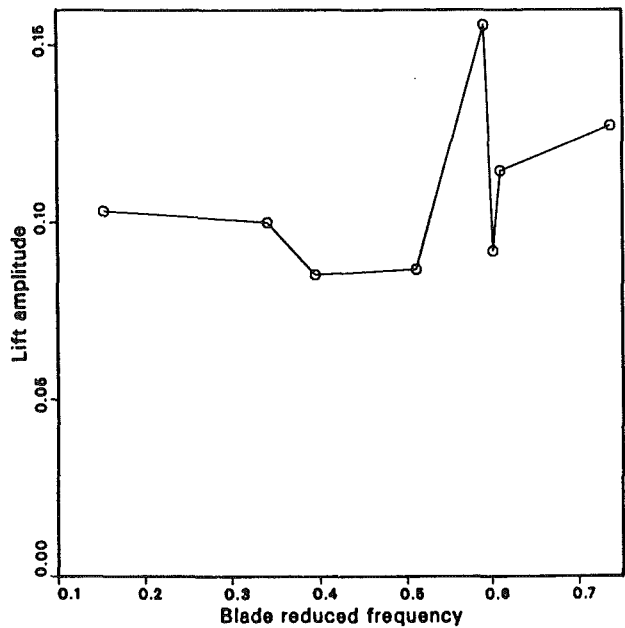


Fig. 17 Influence of blade reduced frequency on the lift amplitude for a two-blade cascade in bending vibration [other details are the same as in Fig. 9]

quency, the latter begins to change and the de-entrainment of both frequency occurs, even though entrainment would occur under similar circumstances in the torsional mode, as was shown in the previous section. Since the mechanism of bending and torsional vibrations are different in nature, the interaction of the flow and structure is also different and this can be explained as follows. In the case of torsional vibration the instantaneous flow incidence on each blade increases with the blade torsional displacement (positive counterclockwise) and the blade vibration would be expected to control the flow separation from the blade surface. The effect of torsional velocity on local incidence is variable along the blade chord, being zero at the center of rotation, and hence does not exert such a profound effect on the instantaneous incidence. Therefore, it is possible for the stall propagation frequency to synchronize with that of the vibration resulting in self-sustained

vibration of "torsional stall flutter." On the other hand, in the case of bending vibration the instantaneous incidence depends primarily on the blade bending vibration frequency, the larger the blade velocity would be at constant vibration amplitude. But at large blade frequency the blades are stiffer and can be considered as nearly rigid; the structural effect on the flow field will be negligible.

In the de-entrainment region, Fig. 13 shows a small increase of the blade bending displacement, and Fig. 14 shows also a small increase in the lift. These small changes in the blade bending displacement and lift can be explained by the fact that there is little interaction between the structure and the aero-

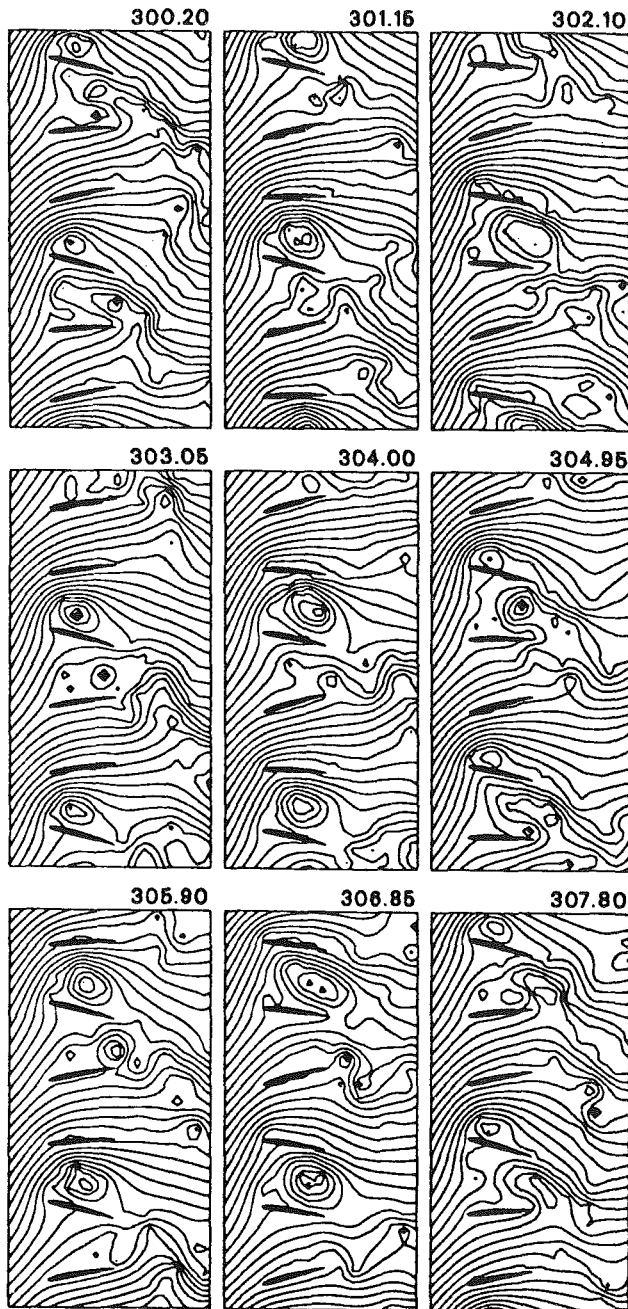


Fig. 18 Instantaneous streamline pattern for a six-blade cascade in torsional vibration at consecutive time over a single period of oscillation [$t = 400$, $\alpha = 55$ deg, $\beta = 0$ deg, $K_{n(\text{vacuum})} = 0.13$ Hz]

dynamics when the blade bending frequency approaches the stall propagation frequency. Rather, the blades will respond to a random vibration at their natural frequencies, resulting in blade buffeting as described in Sisto et al. (1990). The results for a two-blade cascade vibrating in bending are shown in Figs. 15–17. As can be seen, the behavior of the cascade is similar to that of the three-blade cascade.

Computational Assumption of Periodicity

For reasons of computational economy, it is not currently feasible to compute the propagating stall/stall flutter instability with periodicity enforced over a large number of blade pitches comparable to the number of blades in typical annular blade row. Thus, there is an area of uncertainty as to the proper number of blades used to specify the period, or wavelength,

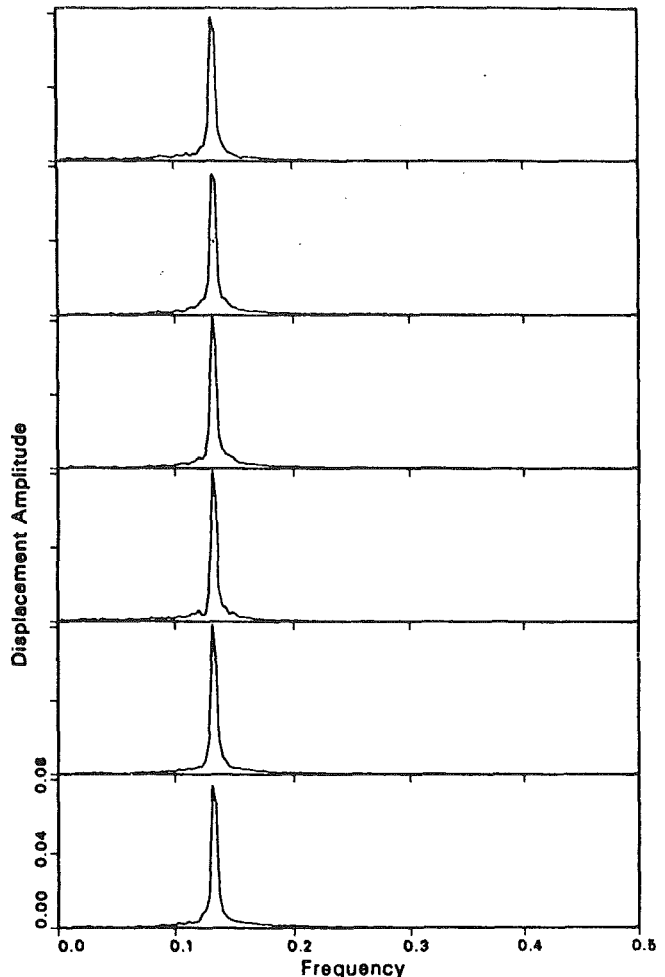


Fig. 19 Displacement spectra for a six-blade cascade in torsional vibration [other details are the same as in Fig. 18]

of these fluid and structure phenomena. In the future, when the full three-dimensional structural model can be taken to include the disk, this uncertainty may be partially resolved, since the bladed-disk structure displays a sequence of combined modes with different numbers of diametral nodes. The number of such nodes in effect represents a circumferential wavelength, which in turn will govern the number of stall patches and thus determine the number of blades in a period.

Some important information on the relative stability of different assumed wavelengths, or stall periods, is obtained from Figs. 18–20. In the first figure a six-bladed cascade shows a streamline patterns, which computationally has displayed three-blade periodicity. With periodicity enforced over a six-blade interval, the predicted phenomena could have displayed one, two, three, or six-blade periodicity. This result should be compared with the flow field shown the Fig. 3 wherein a periodicity of three blade passages was enforced. Thus the question of relative stability can be determined computationally, and this capability can be enlarged in the future. Figures 19 and 20 show similar behavior for the torsional displacements and moments.

Concluding Remarks

The present study has indicated clearly that the flexibility of the blade structure does in fact exert a degree of control over the stall propagation within the entrainment interval of frequencies. Thus the propagating stall phenomenon in a completely rigid set of airfoils is far from identical in all aspects when the real blade structure is considered.

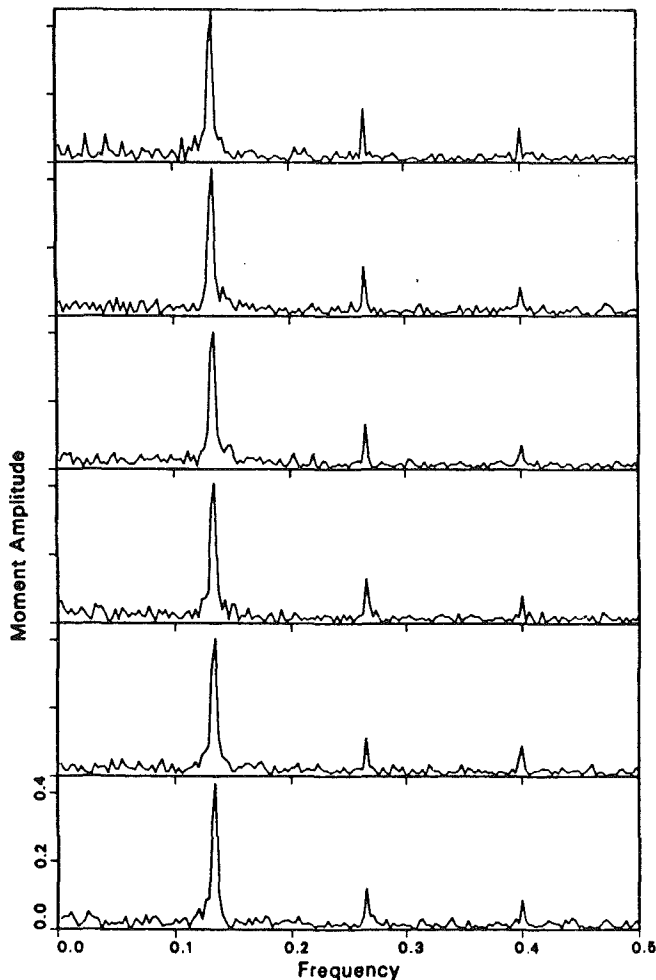


Fig. 20 Moment spectra for a six-blade cascade in torsional vibration [other details are the same as in Fig. 18]

In case of a cascade experiencing torsional vibration, it is found that the stall propagation frequency is entrained with the blade natural frequency in a definite interval. However, in the case of bending vibration, the stall propagation frequency is de-entrained with the blade frequency. One may conclude, according to this computational investigation, that the stall flutter is more likely to occur in the torsional mode of vibration rather than in the bending mode.

Because the magnitude of the frequency interval over which entrainment occurs cannot be expressed analytically, the computational models are required to explore the effect of aeroelastic interaction on stall propagation. A parametric study of this problem is required using computational solutions of the nonlinear unsteady aeroelastic model. It should be noted that the flow separation from the airfoil boundary controls the stall and its propagation in many aspects and the available data for

the unsteady flow separation on curved profiles in cascades are very limited.

The parameters mentioned below, for bending and torsional vibrations in airfoil cascades, should be included in the parametric study to understand fully the aerolastic problem in turbomachines. The recommended computational study should include the effect of inflow angle and cascade stagger on the blade vibration and stall propagation. The stall cell wavelength should be used as a parameter to model a real axial compressor cascade. Intrablade coupling should be introduced by allowing two degrees of freedom and by separating the mass and elastic axes. Additional elastic coupling due to blade twist also needs to be explored computationally in a three-dimensional extension of the structural model.

References

- Emmons, H. W., Kronauer, R. E., and Rockett, J. A., 1959, "A Survey of Stall Propagation—Experiment and Theory," *ASME Journal of Basic Engineering*, Vol. 81, pp. 409-416.
- Ericsson, L. E., and Reding, J. P., 1973, "Stall Flutter Analysis," *Journal of Aircraft*, Vol. 10, pp. 5-13.
- Evans, R. L., 1978, "Boundary Layer Development on an Axial Flow Compressor Stator Blade," *ASME Journal of Engineering for Power*, Vol. 100, pp. 287-293.
- Huppert, M. C., Johnson, D. F., and Costilow, E. L., 1952, "Preliminary Investigation of Compressor Blade Vibration Excited by Rotating Stall," Lewis Flight Propulsion Laboratory Report, NACA RM E52J15, Dec.
- Jeffers, J. D., II, and Meece, C. E., Jr., 1974, "F100 Fan Stall Flutter Problem Review and Solution," *Journal of Aircraft*, Vol. 12, pp. 350-357.
- Jonnvithula, S., Sisto, F., and Thangam, S., 1990, "Computational and Experimental Investigations of Rotating Stall in Compressor Cascades," *AIAA Journal*, Vol. 28, No. 11, pp. 1945-1952.
- Lewis, R. I., and Porthouse, D. T. C., 1982, "A Generalized Numerical Method for Bluff Body and Stalling Aerofoil Flow," *ASME Paper No. 82-GT-70*.
- Moore, F. K., 1984, "A Theory of Rotating Stall of Multistage Axial Compressors; Part I—Small Disturbances," *ASME Journal of Engineering for Gas Turbine and Power*, Vol. 26, pp. 313-320.
- Rainey, A. G., 1953, "Some Observations on Stall Flutter and Buffeting," Langley Aeronautical Laboratory Technical Report NACA RM L53E15, June.
- Simpson, R. L., 1985, "Two Dimensional Turbulent Separated Flow," *AGARD-AG-287*, Vol. 1, June.
- Sisto, F., 1955, "Unsteady Aerodynamic Reactions of Airfoils in Cascade," *Journal of Aeronautical Sciences*, Vol. 22.
- Sisto, F., 1967, "Linearized Theory of Nonstationary Cascades at Fully Stalled or Supercavitated Conditions," *ZAMM*, Vol. 47, pp. 531-542.
- Sisto, F., and Ni, R. H., 1971, "Quasi-Static Moment Measurements for Airfoils in an Annular Cascade," *AIAA Paper No. 71-301*.
- Sisto, F., and Perumal, P. V. K., 1974, "Lift and Moment Prediction for an Oscillating Airfoil With a Moving Separation Point," *ASME Journal of Engineering for Power*, Vol. 96, pp. 372-378.
- Sisto, F., Wu, W., Thangam, S., and Jonnvithula, S., 1989, "Computational Aerodynamics of Oscillating Cascade With the Evolution of Stall," *AIAA Journal*, Vol. 27, No. 4, pp. 462-471.
- Sisto, F., Thangam, S., and Abdel-Rahim, A., 1990, "Computational Prediction of Stall Flutter in Cascaded Airfoils," *AIAA Journal*, Vol. 29, No. 7, pp. 1161-1167.
- Spalart, P. R., 1984, "Two Recent Extensions of Vortex Method," *AIAA Paper No. 84-0343*.
- Tokel, H., and Sisto, F., 1978, "Dynamic Stall of an Airfoil With Leading Edge Bubble Separation Involving Time Dependent Re-attachment," *ASME Paper No. 78-GT-194*.
- Whitehead, D. S., 1960, "Force and Moment Coefficients for Vibrating Airfoils in Cascade," British Aerospace Research Council R & M 3254.
- Yershov, V. N., 1971, "Unstable Conditions of Turbodynamics—Rotating Stall," Foreign Technology Division, WP-AFB document number FTD-MT-24-04-71, Aug.

The Effect of Steady Aerodynamic Loading on the Flutter Stability of Turbomachinery Blading

T. E. Smith

Sverdrup Technology, Inc.,
Lewis Research Center Group,
Brook Park, OH 44142

J. R. Kadambi

Department of Mechanical and Aerospace
Engineering,
Case Western Reserve University,
Cleveland, OH 44106

An aeroelastic analysis is presented that accounts for the effect of steady aerodynamic loading on the aeroelastic stability of a cascade of compressor blades. The aeroelastic model is a two-degree-of-freedom model having bending and torsional displacements. A linearized unsteady potential flow theory is used to determine the unsteady aerodynamic response coefficients for the aeroelastic analysis. The steady aerodynamic loading was caused by the addition of (1) airfoil thickness and camber and (2) steady flow incidence. The importance of steady loading on the airfoil unsteady pressure distribution is demonstrated. Additionally, the effect of the steady loading on the tuned flutter behavior and flutter boundaries indicates that neglecting either airfoil thickness, camber, or incidence could result in nonconservative estimates of flutter behavior.

Introduction

It is well known that airfoil geometry and steady loading have a strong influence on the unsteady aerodynamic response of cascades. So as the design of modern turbomachinery becomes more stringent to meet specific fatigue and life requirements, the design/analysis for aeroelastic problems will also become more important. It is popularly believed that the modeling of shaped airfoils as unloaded flat plates results in conservative estimates of flutter prediction. The development of an aeroelastic model that accounts for blade thickness, camber, and flow incidence effects is required to determine whether this belief is correct and to identify the conditions where it may fail.

The axial-flow turbomachinery blade designer often attempts to model dynamic aeroelastic instabilities through the use of simplified structural and aerodynamic models. Blade-row flutter analyses (Kaza and Kielb, 1982; Kielb and Kaza, 1983; Srinivasan and Fabunmi, 1984) often employ flat plate, small-disturbance theory (Smith, 1972; Adamczyk and Goldstein, 1978) to model the unsteady aerodynamic forces acting on vibrating blades. These small-disturbance theories do not account for the effect of airfoil thickness, camber, and flow incidence on the unsteady aerodynamic/response of the cascade.

Accounting for airfoil shape and steady loading requires that a more accurate aerodynamic analysis be done. Verdon and Caspar (1982, 1984) have developed an unsteady aerodynamic theory based on a linearization of the unsteady full potential equation. Their method accounts for the effects of blade geometry (i.e., thickness, camber) and steady loading

(i.e., flow incidence) on the unsteady potential field within the cascade. Results presented by Verdon (1987) imply that the unsteady aerodynamic response of the cascade is strongly dependent upon the steady flow field within which the blade vibrates. An alternative method for solving the same equation set on practical airfoil geometries has been reported by Whitehead (1982). This technique solves the linearized unsteady potential equation discretized using the finite element method.

The purpose of the current work is to present an aeroelastic analysis scheme that utilizes an unsteady aerodynamic formulation to account for the mentioned steady aerodynamic loading effect on the cascade unsteady aerodynamic behavior. The objective is to study the effect of airfoil shape and steady aerodynamic loading on the tuned flutter characteristics of the cascade. An advantage of this method is that the use of the linearized aerodynamic theory permits the effect of variations in aerodynamic and aeroelastic conditions on flutter characteristics to be examined at reasonable computational cost.

The approach utilizes a two-degree-of-freedom (DOF) structural dynamic model of the blade and two-dimensional linearized unsteady potential theory to model the fluid within the cascade. This analysis is presented for a cascade of blades, which are representative of compressor blading. The effects of changes in airfoil shape and steady flow incidence are studied to assess their associated impact on the cascade flutter stability.

Analytical Development

Aeroelastic Formulation. The model of the turbomachinery blading in this study follows a "typical section" approach wherein the blade is modeled as a rigid airfoil having two DOF. This model assumes the airfoil motion at a representative spanwise location is made up of a bending motion (h) normal to the blade chord and a torsional motion (α) about the elastic axis of the airfoil. Positive directions for these DOF and the

Contributed by the International Gas Turbine Institute and presented at the 36th International Gas Turbine and Aeroengine Congress and Exposition, Orlando, Florida, June 3-6, 1991. Manuscript received at ASME Headquarters February 20, 1991. Paper No. 91-GT-130. Associate Technical Editor: L. A. Riekert.

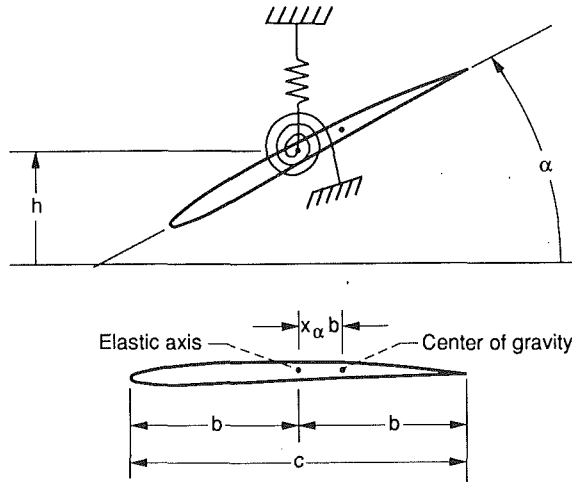


Fig. 1 Typical section airfoil degrees of freedom

resulting forces are indicated in Fig. 1. A full development of the following equations of motion can be found in Bendikson and Friedman (1980).

The dynamic equations of motion for this two DOF blade model are shown below.

$$\begin{bmatrix} m & S_\alpha \\ S_\alpha & I \end{bmatrix} \begin{Bmatrix} \dot{h} \\ \dot{\alpha} \end{Bmatrix} + \begin{bmatrix} K_h & 0 \\ 0 & K_\alpha \end{bmatrix} \begin{Bmatrix} h \\ \alpha \end{Bmatrix} = \begin{Bmatrix} L \\ M \end{Bmatrix} \quad (1)$$

The airfoil section mass and moment of inertia are m and I , and lumped springs of stiffness K_h and K_α act at the elastic axis. Inertial coupling may be present due to an offset in the

elastic axis from the airfoil center of gravity, and is modeled as a static mass unbalance S_α . The forcing term on the right-hand side of Eq. (1) represents the unsteady aerodynamic forces and moments present during airfoil oscillation.

The vibration of the blade is assumed to occur as small-amplitude and simple harmonic in time, such that the blade displacement vector is

$$\begin{Bmatrix} h \\ \alpha \end{Bmatrix} = \begin{Bmatrix} h_o \\ \alpha_o \end{Bmatrix} e^{i\omega t} \quad (2)$$

The motion-dependent unsteady aerodynamic loads are modeled as first-order harmonic in time:

$$\begin{aligned} L &= \rho W^2 c \left(L_h \frac{h_o}{c} + L_\alpha \alpha_o \right) e^{i\omega t} \\ M &= \rho W^2 c^2 \left(M_h \frac{h_o}{c} + M_\alpha \alpha_o \right) e^{i\omega t} \end{aligned} \quad (3)$$

The unsteady aerodynamic coefficients L_h , L_α , M_h , M_α are complex quantities, which relate the aerodynamic forces and their phase to the corresponding driving motion. For a fixed cascade geometry, these coefficients are strongly dependent upon the cascade operating parameters, relative Mach number M_R , incidence angle i , and the aeroelastic parameters, reduced frequency k and interblade phase angle σ .

Substitution of Eqs. (2) and (3) into Eq. (1) results in an aeroelastic equation, which describes the blade/fluid system dynamics. This equation is nondimensionalized by using the nondimensional parameters δ , x_α , r_G , and k . The bending DOF h is also nondimensionalized by the blade chord c and the frequency is normalized by the torsional natural frequency ω_α . The nondimensional flutter equation that results is:

Nomenclature

a = fluid sonic velocity	M_h = unsteady aerodynamic moment coefficient due to blade bending motion	W = fluid inlet relative velocity at leading edge
b = blade semichord length	M_R = fluid inlet relative Mach number	x_α = offset of airfoil elastic axis from center of gravity nondimensionalized by blade semichord
$\bar{C}_p = (\bar{P} - \bar{P}\alpha)/(1/2\rho w^2)$ = steady static pressure coefficient	M_α = unsteady aerodynamic moment coefficient due to torsional motion	α = blade torsional displacement about elastic axis
$\Delta\bar{C}_p = \bar{P}/(1/2\rho w^2)$ = unsteady pressure coefficient	m = blade mass per unit span	β = cascade stagger angle measured from axial direction
$c = 2b$ = blade chord length	N = number of blades in rotor	$\delta = \frac{m}{\pi\rho b^2}$
h = chordwise normal bending displacement	P = steady static pressure	= blade/fluid mass ratio
$I = mr_G^2 b^2$ = blade section moment of inertia about elastic axis	\bar{P} = first harmonic unsteady pressure	ϵ = airfoil camber angle, deg
i = fluid steady flow incidence angle, deg; also $\sqrt{-1}$	P_∞ = steady static pressure far upstream	μ = real portion of complex eigenvalue (Eq. (6))
K_h = spring stiffness for bending	$r_G = \sqrt{\frac{I}{mb^2}}$	ν = imaginary portion of complex eigenvalue (Eq. (6))
K_α = spring stiffness for torsion	= blade section radius of gyration about elastic axis	ρ = fluid mass density
$k = \frac{\omega b}{W}$ = reduced frequency	$S_\alpha = x_\alpha mb$ = static mass moment coupling term	σ = interblade phase angle, deg
based on semichord	s = root locus eigenvalue (Eq. (6)); also cascade gap	ω = oscillation frequency, rad/s; also complex eigenvalue
L_h = unsteady aerodynamic lift force per unit span	t = time	$\omega_h = \sqrt{\frac{K_h}{m}}$
L_l = unsteady aerodynamic lift coefficient due to blade bending motion	U = rotor blade velocity at leading edge	= natural frequency of blade bending motion
L_α = unsteady aerodynamic lift coefficient due to blade torsional motion	V = fluid absolute velocity at leading edge	$\omega_\alpha = \sqrt{\frac{K_\alpha}{m}}$
M = unsteady aerodynamic moment per unit span about elastic axis		= natural frequency of blade torsional motion

$$\left(\frac{\omega}{\omega_\alpha}\right)^2 \left(\begin{bmatrix} 1 & X_\alpha \\ \frac{2X_\alpha}{r_G^2} & 1 \end{bmatrix} + \frac{1}{\delta\pi k^2} \begin{bmatrix} L_h & L_\alpha \\ \frac{4M_h}{r_G^2} & \frac{4M_\alpha}{r_G^2} \end{bmatrix} \right) \begin{Bmatrix} \frac{h_o}{c} \\ \alpha_o \end{Bmatrix} = \begin{bmatrix} \left(\frac{\omega_h}{\omega_\alpha}\right)^2 & 0 \\ 0 & 1 \end{bmatrix} \begin{Bmatrix} \frac{h_o}{c} \\ \alpha_o \end{Bmatrix} \quad (4)$$

This equation indicates that when using a frequency domain (harmonic) approximation for the blade motion and aerodynamic forces, the motion-dependent forces appear as an “apparent inertia” term in the equations of motion.

The compressor rotor within this work is assumed to be represented by an unwrapped infinite two-dimensional cascade of airfoils. The cascade for this analysis is assumed to vibrate as a “tuned” rotor. A tuned rotor consists of identical blades, with each blade having the same in-vacuum natural frequencies and mode shapes. Such a rotor, when vibrating within a flowing fluid, will have all the blades experiencing the same amplitude of motion, with a constant phase angle between neighboring blades. These phase angles are referred to as “interblade phase angles” and they describe a traveling wave around the periphery of the rotor.

The interblade phase angles are limited to a discrete set of angles as described by Lane (1956):

$$\sigma_j = \frac{2\pi(j-1)}{N} \text{ for } j = 1, \dots, N \quad (5)$$

This equation implies that a rotor having N blades may vibrate with any one of N possible interblade phase angle modes.

Aerodynamic Formulation

The aerodynamic forces present on the blade are calculated using the two-dimensional linearized unsteady potential approach of Verdon and Caspar (1984). The unsteady potential flow within the cascade is assumed to be a first-order harmonic perturbation about the nonuniform steady full potential flow. This expansion involves products of both the steady potential and the first-order harmonic potential. Thus, the variations in the steady potential field caused by airfoil shape and flow incidence are coupled to the unsteady flow problem through the governing unsteady field equations.

The approach requires solution of the two-dimensional steady-state full potential equation on a blade-to-blade computational mesh. The method described by Caspar (1983) is used to calculate the steady full potential flow within the blade passages. The unsteady potential flow is then calculated using this steady full potential flow as the mean flow for the cascade.

A complete discussion of this method including some example results may be found in Verdon and Caspar (1984). A comparison of this linearized unsteady potential method with experimental results from two-dimensional oscillating cascades has been reported in Verdon and Usab (1986). A comparison of the unsteady pressures due to torsional vibration of a large-scale compressor rotor has also been reported by Hardin et al. (1987) showing excellent agreement.

Flutter Solution

Flutter occurs as a dynamic instability in which the blade motion becomes self-excited by extracting energy from the flowing fluid. This condition may develop when the aerodynamic forces become in-phase with and eventually lead the blade motion. If no other dissipation mechanism exists for the self excitation (e.g., structural damping), the motion will become unstable.

The determination of aeroelastic stability requires the solution of Eq. (4). This equation represents a complex eigenvalue problem, which is solved for the eigenvalues, ω_1, ω_2 . Solution of this second-order equation is accomplished by determining the roots of the quadratic characteristic equation.

The resulting eigenvalues will be complex, and they are converted to root locus form by

$$S = i \left(\frac{\omega}{\omega_\alpha} \right) = \mu + i\nu \quad (6)$$

The real part of this eigenvalue (μ) represents a measure of the aerodynamic damping ratio, and the imaginary part of this eigenvalue (ν) represents the damped natural frequency normalized by the torsional natural frequency. The system will be in a flutter condition when the real part of either eigenvalue (μ_1 or μ_2) becomes equal to or greater than zero. For a tuned rotor, the eigenvalue problem of Eq. (4) is solved N times, for each of the corresponding interblade phase angles of Eq. (5).

The aerodynamic forces are dependent upon several aeroelastic parameters, the most important of which are the reduced frequency k , relative Mach number M_R , and cascade interblade phase angle σ . Therefore, an iterative eigensolution must be used to determine the condition when flutter will occur, i.e., when $\mu = 0$. The flutter iteration for a specified blade geometry and cascade configuration involves prescribing either a Mach number or a reduced frequency, and varying the other parameter while calculating all interblade phase angles for the rotor.

The present method involved specifying a Mach number where a flutter point is desired, and iterating on the reduced frequency until an unstable eigenvalue was obtained for one of the phase angles of the full rotor. An initial guess for the flutter reduced frequency is made and the eigenvalues for all interblade phase angles are calculated. The most unstable eigenvalue (eigenvalue with largest μ) is used to continue in a Newton iteration until convergence.

The algorithm is expressed as

$$k_F^{(n+1)} = k_F^{(n)} - \left(\frac{\Delta k_F}{\Delta \mu} \right)^{(n)} \mu^{(n)} \quad (7)$$

where n signifies the iteration level, k_F is the flutter reduced frequency, and μ is the real portion of the eigenvalue for the most unstable interblade phase angle mode. It has been found that this procedure usually converges within from four to six iterations.

Application of Method

Compressor Cascade. The application of this aeroelastic model is presented for a cascade of blades representative of current compressor blade designs. The airfoil shape used for this work is a NACA 0006 series airfoil thickness distribution applied along a circular arc mean camber line. The camber was varied by changing the height of the camber line. The camber angle is represented as ϵ , which is the difference in the inlet metal and exit metal angles at the airfoil leading and trailing edges. An illustration of the compressor cascade denoting the cascade nomenclature is include as Fig. 2. The cascade parameters chosen to represent this compressor cascade are listed in Table 1.

The airfoil inertial properties were determined using numerical integration to calculate the airfoil center of gravity, moment of inertia, and radius of gyration. A number of airfoils were studied in this work, ranging in camber angles from 0 to 30 deg. The elastic axis for all the airfoils was chosen to be at midchord. The airfoil properties for all of the camber angles studies are included in Table 2.

The aeroelastic analyses were conducted to determine the effect of (1) airfoil shape and (2) steady flow incidence on the flutter behavior of a tuned cascade. Flutter was determined by solving the eigenvalue problem of Eq. (4), which includes

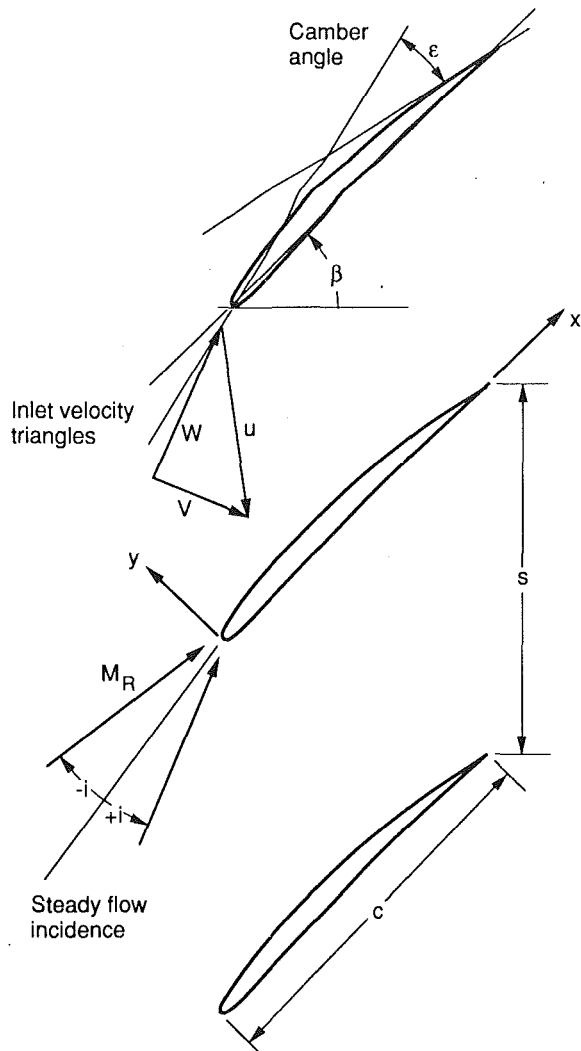


Fig. 2 Cascade geometry and nomenclature

Table 1 Cascade description

Airfoil thickness distribution	NACA 0006
Cascade stagger angle, β , deg	45
Cascade solidity, c/s	1.0
Blade-fluid mass ratio, μ	330
Frequency ratio, ω_h/ω_α	0.30
Radius of gyration, r_G	Varied
E.A. - C.G. offset, x_α	Varied
Number of blades, N	12
Elastic axis location	0.5, 0.0

Table 2 Cambered airfoil inertial properties

Camber angle, ϵ , deg	Center of gravity		r_G	x_α
	x	y		
0	0.4180	0.0000	0.4953	-0.1640
5	.4180	.0083	.4955	-.1640
10	.4179	.0165	.4962	-.1642
15	.4179	.0248	.4981	-.1642
20	.4178	.0331	.5016	-.1644
25	.4177	.0415	.5045	-.1646
30	.4175	.0498	.5088	-.1652

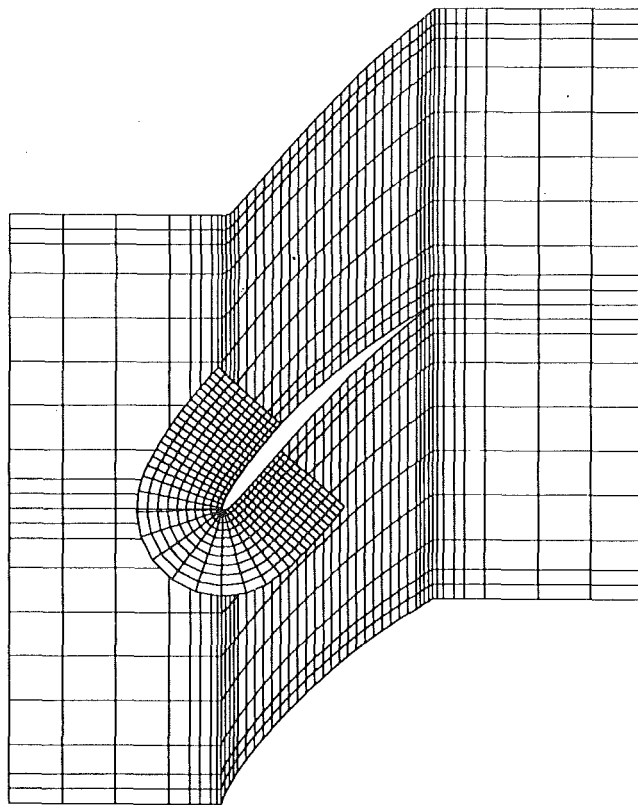


Fig. 3 Unsteady aerodynamic computational meshes

not only aerodynamic properties of the system, but also the structural dynamic properties. This method of analysis was chosen because it is similar to the type of analysis that a designer may use during initial component design analysis. For all cases, the inlet relative Mach number was limited to subsonic values such that no shocks would appear within the cascade. This was done so that the effect of variations in the mean potential field due to blade shape and incidence could be studied, where there were no flow discontinuities occurring in the potential field.

Aerodynamic Analysis

The aerodynamic analysis method employed in this work requires that two-dimensional computational meshes be used to perform the finite-difference solution of the governing equations. The current method uses a blade-to-blade *H*-type computational mesh to capture the global flow behavior over a single blade passage. A local *C*-type grid is then required to resolve the flows more accurately around the leading edge region of the blade. An example of these global and local computation meshes is included as Fig. 3 for a cascade having 20 deg camber angle. A dependence upon local mesh discretization was encountered during the analysis, so the leading edge local mesh was refined until successive flow solutions indicated a convergence to a steady surface pressure distribution about the blade. The meshes used for all the analyses were of size 75×30 for the global mesh and 70×11 for the local mesh.

The steady full potential flow on the cascade was computed using the method described previously. Calculations were performed for Mach numbers up to $M_R = 0.7$. The calculated static pressure coefficient C_p is shown in Fig. 4 for an inlet Mach number of 0.60 for NACA 0006 airfoils having camber angles of 0, 10, and 20 deg. Calculations were also performed for a NACA 0006 with 10 deg camber cascade at incidence

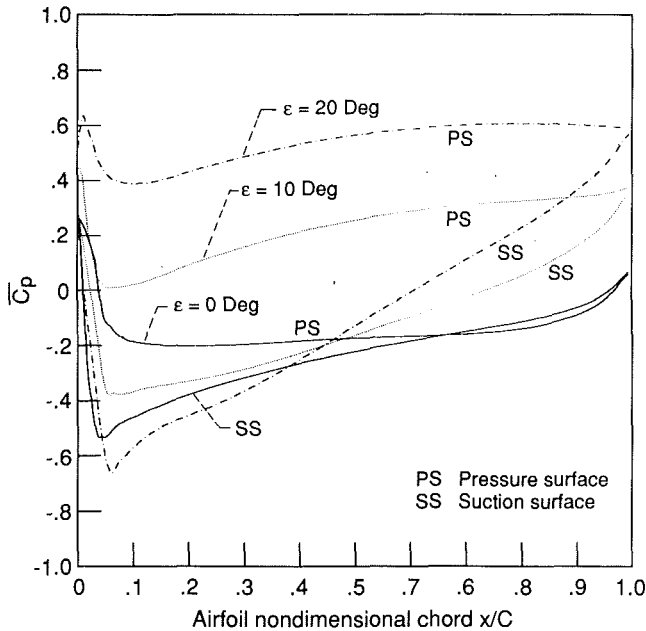


Fig. 4 Steady surface pressure distributions (NACA 0006 airfoils, $M = 0.60$, $i = 0$ deg)

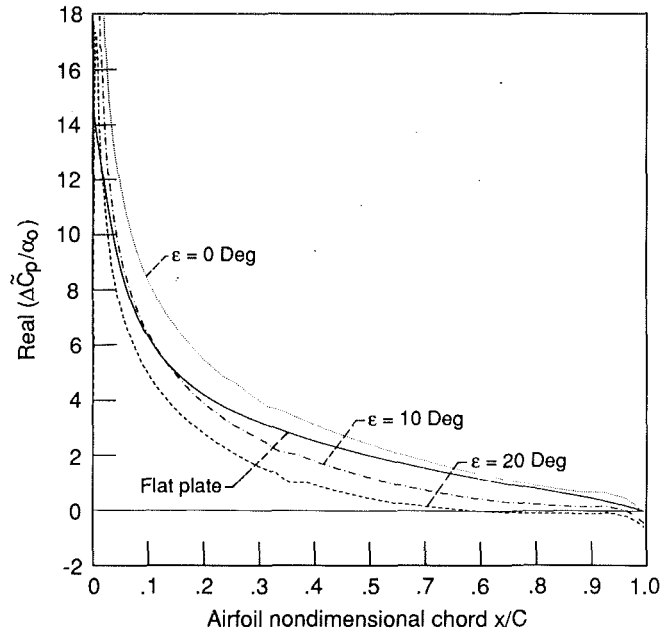


Fig. 6 Unsteady surface pressure distributions—real part (NACA 0006 airfoils, $M = 0.60$, $i = 0$ deg, $\sigma = 60$ deg)

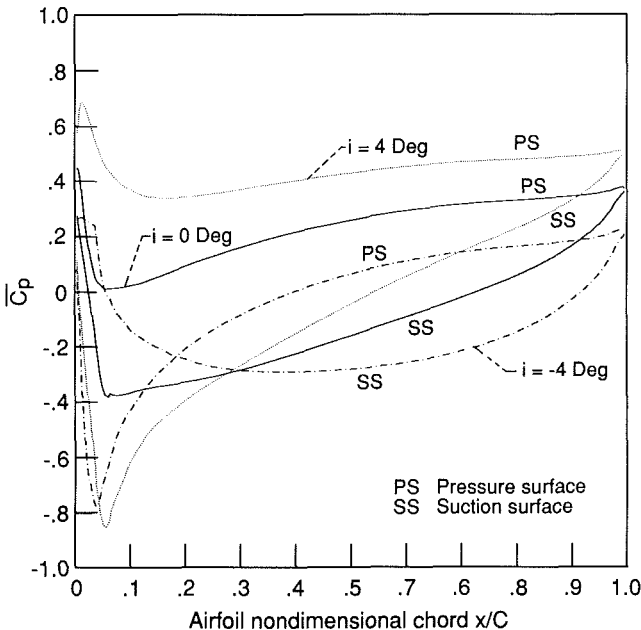


Fig. 5 Steady surface pressure distributions (NACA 0006 airfoils, $M = 0.60$, $\epsilon = 0$ deg)

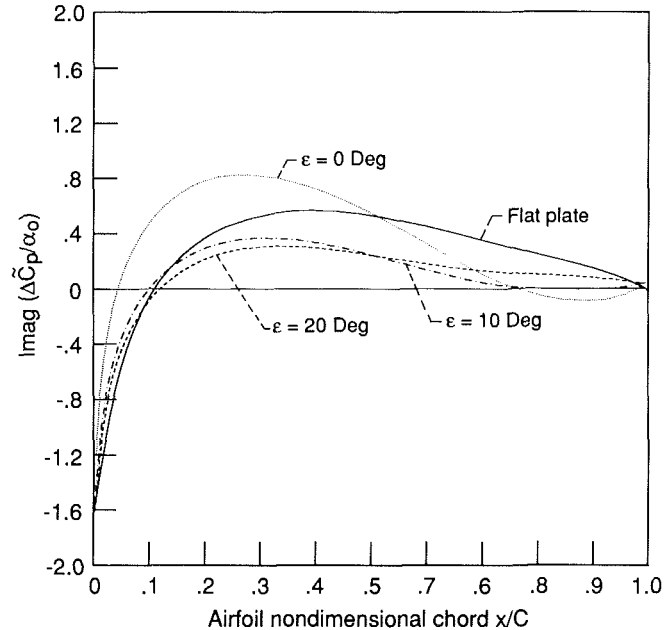


Fig. 7 Unsteady surface pressure distributions—imaginary part (NACA 0006 airfoils, $M = 0.60$, $i = 0$ deg, $\sigma = 60$ deg)

angles of -4 , 0 , and 4 deg as shown on Fig. 5. This figure shows the off-design effects such as the large expansion near the leading edge for the 4 deg incidence case and underexpansion, which occurs for the -4 deg case. These conditions may be encountered during partial speed operation of the compressor.

The unsteady pressures due to torsional motion of the airfoil about the elastic axis were calculated for airfoils having camber angles of 0 , 10 , and 20 deg. The inlet Mach number was 0.60 and the incidence angle for all cases was 0 deg. The reduced frequency was $k = 0.22$ and the interblade phase angle was $\sigma = 60$ deg. Plots showing the unsteady surface pressure coefficient difference across the airfoil are shown in Fig. 6 (real part) and Fig. 7 (imaginary part). The results from a flat plate

airfoil modeled using the same method are also included for reference. The unsteady pressure coefficient is normalized by the magnitude of the torsional motion.

It is important to observe that two basic effects are present for this unsteady flow problem. There is an influence due to the dependence of the unsteady potential equation on the underlying steady potential field. In addition, there is also the effect of changes in the airfoil surface boundary condition for airfoils of different camber. A determination of which of these two effects is more important is not obvious based on these results.

Therefore, an analysis was conducted to study the effect of flow incidence (changing steady potential field alone) for the same cambered airfoil under the same operating conditions.

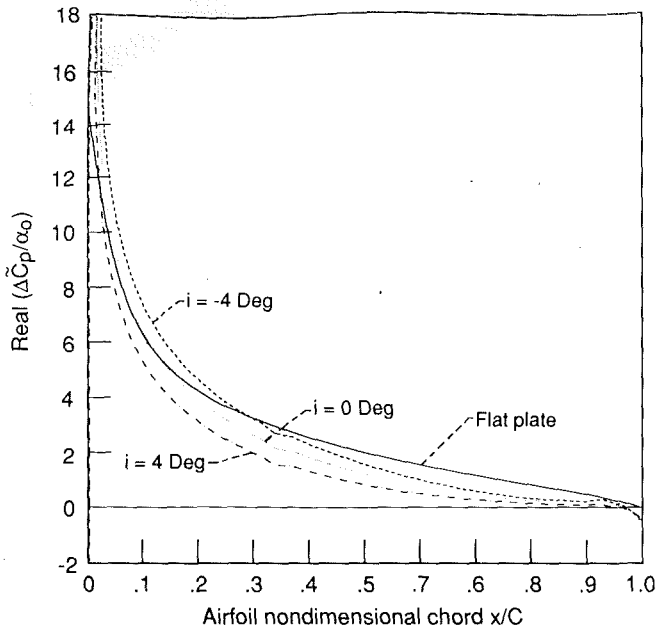


Fig. 8 Unsteady surface pressure distributions—real (NACA 0006 airfoils, $M = 0.60$, $\epsilon = 0$ deg, $\sigma = 60$ deg)

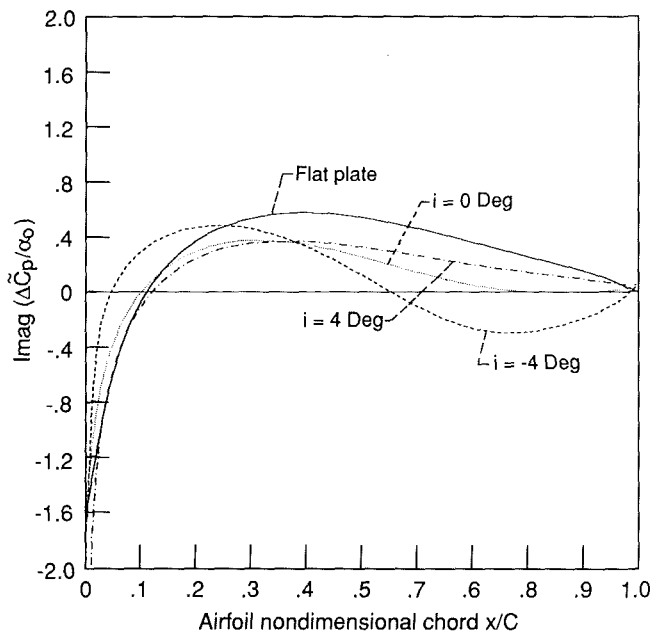


Fig. 9 Unsteady surface pressure distributions—imaginary part (NACA 0006 airfoils, $M = 0.60$, $\epsilon = 10$ deg, $\sigma = 60$ deg)

Results showing the unsteady pressure difference caused by torsional motion for a 10 deg cambered airfoil at three different incidence angles are included on Figs. 8 and 9. As before, the reduced frequency was $k = 0.22$ and the interblade phase angle was 60 deg. Both positive and negative incidence angles are included to simulate off-design operating conditions. These unsteady pressure results resemble those presented for camber angle changes, although the imaginary pressure seem to depend more strongly upon incidence, particularly in the region from midchord aft to the trailing edge.

Aeroelastic Analysis

The dependence of unsteady surface pressures on the steady aerodynamic loading level has been studied in the previous

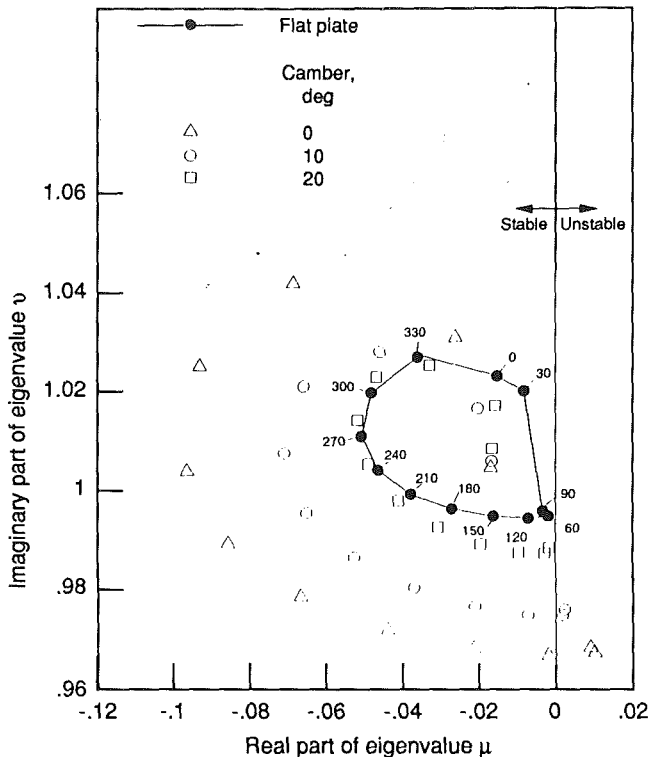


Fig. 10 Tuned rotor root locus showing effect of airfoil camber (torsion mode, $M = 0.60$, $i = 0$ deg, $k = 0.22$)

section. In the current section, an investigation of the same effect on the overall aeroelastic stability is presented. The flutter solution for the cascades was determined by solving Eq. (4) for a range of camber angles and operating Mach numbers. The solution of this tuned aeroelastic eigenvalue problem is required for all interblade phase angles that occur for the rotor, in this case $N = 12$. The resulting set of complex eigenvalues form the locus of roots, where one root will become most unstable.

This root locus has been calculated for the sample rotor operating at a relative Mach number of 0.60 and a reduced frequency of $k = 0.22$. The four cases analyzed consisted of a flat plate airfoil, and NACA 0006 airfoils having 0, 10, and 20 deg camber. The root locus shown on Fig. 10 shows the four loci corresponding to these cascades, where the eigenvalues corresponding to the torsional DOF are shown, as this was that most unstable mode of vibration. The modes corresponding to bending motion of the blade were always more stable than those corresponding to torsional motion of the blade. The numbers on the plot represent the interblade phase angle modes for the tuned rotor. These calculations show a large difference between the flat plate airfoil and the 0 deg camber airfoil rotors where the only difference is due to the airfoil thickness distribution. The rotor of uncambered airfoils is the most unstable, with increasing airfoil camber causing the rotor to become more stable.

The above result implies that the modeling of a low cambered compressor under the assumption that a flat plate aerodynamic representation is valid may not always be as conservative as is often assumed. Additionally, the effect of increasing airfoil camber appears to cause the rotor to become more stable. In fact, these results imply that the flat plate results always underpredict the flutter condition when compared to the results when airfoil shape and flow incidence are considered.

A similar calculation was performed to determine the root locus for the NACA 0006 10 deg camber airfoil at incidence angles of -4 , 0 , and 4 deg. As before, the relative Mach

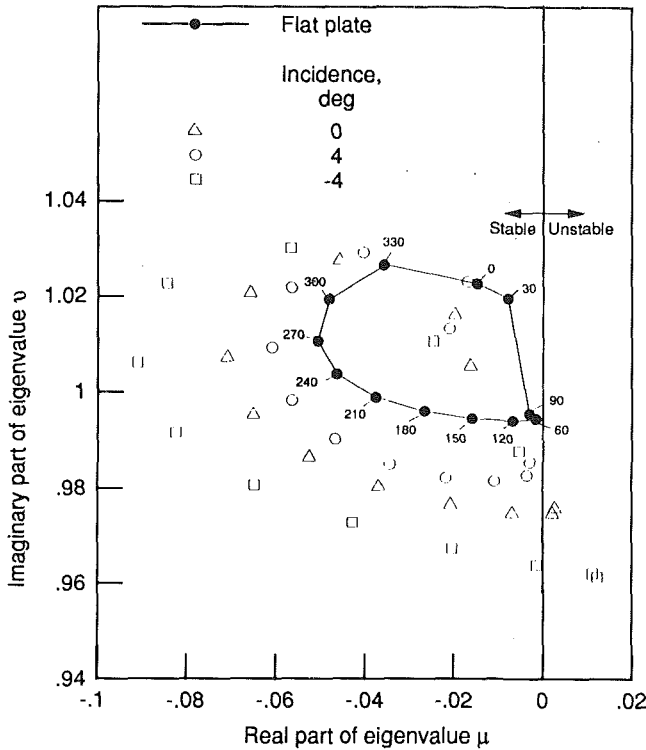


Fig. 11 Tuned rotor root locus showing effect of flow incidence (NACA 0006 airfoil, $\epsilon = 10$ deg, torsion mode, $M = 0.60$, $k = 0.22$)

number was 0.6 and the reduced frequency $k = 0.22$. The root loci are shown on Fig. 11 for the flat plate cascade and the 10 deg camber airfoil at negative and positive incidence levels. These calculations were performed to determine the effect of off-design conditions due to inlet flow angle variations on the rotor stability. These results indicate that positive flow incidence makes the rotor become more stable when compared to zero incidence. Likewise, negative incidence causes a strong destabilization of the rotor, as shown by the large spread of the -4 deg incidence eigenvalues relative to the zero incidence case. Obviously none of these characteristics would be identified using flat plate small-disturbance aerodynamic theories.

Flutter Analysis

The aeroelastic stability analysis for the rotor was studied in order to determine the effect of airfoil camber and flow incidence on the flutter behavior. The iterative flutter search method was implemented in order to perform the flutter analysis more efficiently. The effect of parametric changes in airfoil camber angle on the flutter boundary for a tuned rotor operating at inlet Mach numbers of 0.5 to 0.7 was studied. Figure 12 shows the flutter boundaries for these operating conditions where the fluttering mode was a torsional mode in all cases. Note the apparent linearity of the flutter reduced frequency with increasing airfoil camber. The flutter reduced frequencies for the flat plate are also shown on this figure as symbols. Note that the flat plate results are constant with changes in camber angle.

The effect of variations in the mean flow incidence angle on the flutter characteristics was also determined. The flutter boundaries for the tuned rotor operating at a Mach number of 0.6 is shown on Fig. 13 as a function of positive and negative mean flow incidence angles. This figure includes the results for the NACA 0006 airfoils having camber angles of 0, 10, and 20 deg. Additionally, the flat plate flutter point is also shown on this figure as a point. Usually, the designer considers

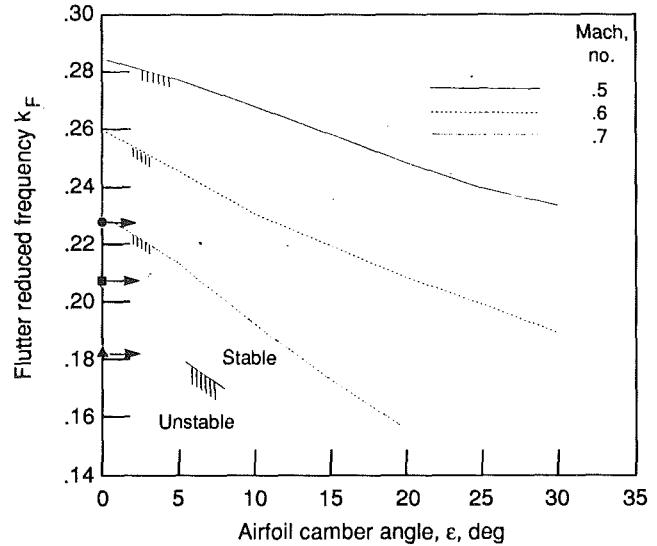


Fig. 12 Effect of airfoil camber angle on flutter boundary (NACA 0006 airfoil, torsion mode, $l = 0$ deg); symbols denote flat plate results

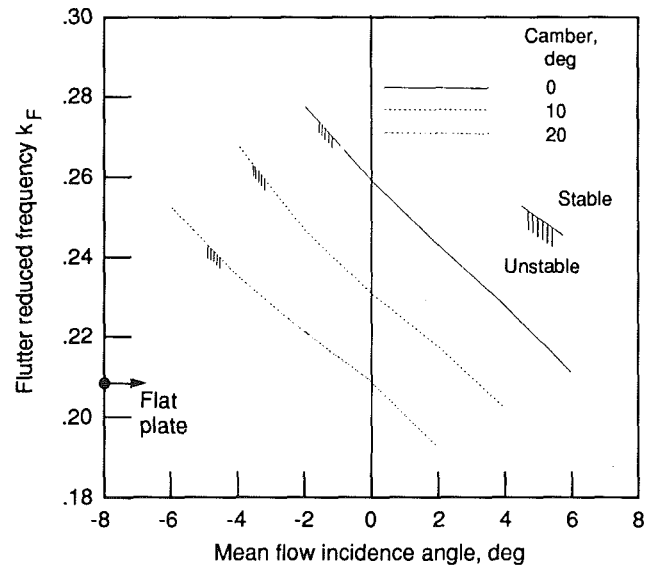


Fig. 13 Effect of mean flow incidence on flutter boundary (NACA airfoils, torsion mode, $M = 0.60$)

a lower flutter reduced frequency as better, because it permits higher relative fluid velocities. This figure indicates that operating at off-design negative incidence angles (engine deceleration, approaching choking) can have an undesirable effect on the rotor stability. These calculations were performed using inviscid potential flow theory, and the authors realize the limitations of inviscid flow models when applied to flows at high incidence angles.

Computer Time

The use of the linearized unsteady aerodynamic theory presents a significant advantage over other recent unsteady CFD methods because of its rapid computational time. The current implementation computes one set of unsteady aerodynamic coefficients (i.e., L_h and M_h) in about 8 CPU seconds on the NASA Lewis Cray X-MP computer. The calculation of a full tuned rotor root locus required approximately 180 CPU sec-

onds. The iterative flutter solution for one Mach number and incidence angle required approximately 1600 CPU seconds. These figures represent a cost advantage of more than an order of magnitude reduction in CPU time when compared to other recently proposed CFD methods.

Conclusions

A numerical study of the influence of steady aerodynamic loading on the flutter behavior of a tuned compressor rotor was performed. The results of this analysis imply the following:

1 Airfoil camber and thickness have a strong influence on the unsteady surface pressures induced by airfoil oscillation.

2 The effect of steady flow incidence on the unsteady surface pressures can be as strong or stronger than the effect of airfoil camber alone.

3 The impact of steady aerodynamic loading caused by airfoil camber, thickness, and flow incidence, is significant with respect to rotor flutter calculations when compared to a traditional flat-plate aerodynamic analysis.

4 Unloaded flat plate results indicated a strong difference from the analyses which accounted for airfoil shape, implying that the flat plate assumption would not properly predict the occurrence of flutter.

5 The presented results indicate that the effect of airfoil camber angle and steady flow incidence shows a fairly linear behavior with respect to flutter boundaries within the range of parameters which may be considered during the design process.

The intent of this work was not to present a complete flutter analysis for a specific class of turbomachinery. The objective was to demonstrate the effect of some practical design parameters on the overall aeroelastic stability of rotors. The continued development of state-of-the-art unsteady aerodynamic models for turbomachinery flows is making the task of aeroelastic analysis of real-world blading more practical.

Acknowledgments

This work was supported under NASA contract No. NAS3-25266, George Stefko and Oral Mehmed, technical monitors.

References

- Adamczyk, J. J., and Goldstein, M. E., 1978, "Unsteady Flow in a Supersonic Cascade With Subsonic Leading-Edge Locus," *AIAA Journal*, Vol. 16, pp. 1248-1254.
- Bendiksen, O., and Friedmann, P., 1980, "Coupled Bending-Torsion Flutter in Cascades," *AIAA Journal*, Vol. 18, pp. 194-201.
- Caspar, J. R., 1983, "Unconditionally Stable Calculation of Transonic Potential Flow Through Cascades Using an Adaptive Mesh for Shock Capture," *ASME Journal of Engineering for Power*, Vol. 105, pp. 504-513.
- Hardin, L. W., Carta, F. O., and Verdon, J. M., 1987, "Unsteady Aerodynamic Measurements on a Rotating Compressor Blade Row at Low Mach Numbers," *ASME JOURNAL OF TURBOMACHINERY*, Vol. 109, pp. 499-507.
- Kaza, K. R. V., and Kielb, R. E., 1982, "Flutter and Response of a Mistuned Cascade in Incompressible Flow," *AIAA Journal*, Vol. 20, pp. 1120-1127.
- Kielb, R. E., and Kaza, K. R. V., 1983, "Aeroelastic Characteristics of a Cascade of Mistuned Blades in Subsonic and Supersonic Flows," *ASME Journal of Vibration, Acoustics, Stress, and Reliability of Design*, Vol. 105, pp. 425-433.
- Lane, F., 1956, "System Mode Shapes in the Flutter of Compressor Blade Rows," *Journal of the Aeronautical Sciences*, Vol. 23, pp. 54-66.
- Smith, S. N., 1972, "Discrete Frequency Sound Generation in Axial Flow Turbomachines," Aeronautical Research Council, ARC-R/M-3709.
- Srinivasan, A. V., and Fabunmi, J. A., 1984, "Cascade Flutter Analysis of Cantilevered Blades," *ASME Journal of Engineering for Gas Turbines and Power*, Vol. 106, pp. 34-43.
- Verdon, J. M., and Caspar, J. R., 1982, "Development of a Linear Unsteady Aerodynamic Analysis for Finite-Deflection Subsonic Cascades," *AIAA Journal*, Vol. 20, pp. 1259-1267.
- Verdon, J. M., and Caspar, J. R., 1984, "A Linearized Unsteady Aerodynamic Analysis for Transonic Cascades," *Journal of Fluid Mechanics*, Vol. 149, pp. 403-429.
- Verdon, J. M., and Usab, W. J., 1986, "Application of a Linearized Unsteady Aerodynamic Analysis to Standard Cascade Configurations," NASA CR-3940.
- Verdon, J. M., 1987, "The Unsteady Aerodynamic Response to Arbitrary Modes of Blade Motion," *Unsteady Aerodynamics and Aeroelasticity of Turbomachines and Propellers, Proceedings of the Fourth International Symposium, Aachen, West Germany, Sept, 6-10, 1987*, Rheinsch-Westfallische Technische Hochschule Aachen, pp. 313-334.
- Whitehead, D. S., 1982, "The Calculation of Steady and Unsteady Transonic Flow in Cascades," Cambridge University Engineering Department, Report CUED/A-Turbo/TR 118.

An Unsteady Lifting Surface Theory for Ducted Fan Blades

R. M. Chi

Senior Research Engineer,
Applied Mechanics Research,
Department of Propulsion and Flight
Systems,
United Technologies Research Center,
East Hartford, CT 06108

A frequency domain lifting surface theory is developed to predict the unsteady aerodynamic pressure loads on oscillating blades of a ducted subsonic fan. The steady baseline flow as observed in the rotating frame of reference is the helical flow dictated by the forward flight speed and the rotational speed of the fan. The unsteady perturbation flow, which is assumed to be potential, is determined by solving an integral equation that relates the unknown jump in perturbation velocity potential across the lifting surface to the upwash velocity distribution prescribed by the vibratory motion of the blade. Examples of unsteady pressure distributions are given to illustrate the differences between the three-dimensional lifting surface analysis and the classical two-dimensional strip analysis. The effects of blade axial bending, bowing (i.e., circumferential bending), and sweeping on the unsteady pressure load are also discussed.

Introduction

Advanced commercial and military engines have low aspect ratio fan blades that are often highly swept. Aeroelastic analysis of these fan blades using the classical two-dimensional strip theory, which was developed for high aspect ratio straight blades, becomes fundamentally questionable. In fact, even for high aspect ratio straight blades, the two-dimensional strip theory is inherently limited for those vibration problems that exhibit large spanwise gradient of vibration amplitude.

Analytical prediction of three-dimensional unsteady aerodynamic flows associated with vibration of ducted rotating blades was pursued by many researchers. McCune (1958a, 1958b, 1972) and Okurounmu and McCune (1970, 1974) studied steady and unsteady lifting line and lifting surface theories for subsonic and transonic flows with limited results. Homicz and Lordi (1981) and Lordi and Homicz (1981) studied the steady loading problem for subsonic relative flows. Namba (1974, 1977), Namba and Ishikawa (1983) and Kodama and Namba (1989) studied the subsonic and transonic unsteady flow problems for helical blades. In all these works, the sonic cylinder at part-span location is considered, but none allows the steady mean flow nonuniformity in the flow field for unsteady pressure load calculations.

Many researchers have studied three-dimensional unsteady aerodynamics and aeroacoustics for unducted propeller blades that are closely related to the ducted fan blade problem. Busemann (1952) studied the zone of influence for compressible flows in the rotating environment. Hanson (1982, 1983), Runyan (1973), Williams (1990), and Williams et al. (1990) also solved the unsteady aerodynamic problem for propellers using the linearized potential flow model. In propeller aeroacoustic research, Long (1983a, 1983b), Farassat (1984a,

1984b), Das (1984), and Long and Watts (1984) used the same type of linear potential flow model.

In a transonic theory formulation for ducted fan blades, Chi (1985, 1986) developed an analytical framework that treats the nonuniform mean flow velocity field as a spatial distribution of simple harmonic sources and doublets. It is essentially a generalization of the transonic small disturbance theory for the fixed wing problem by Landahl (1961) to the rotating fan blade configuration. To maintain the analytical framework of the well-established transonic small disturbance theory, the unsteady perturbation velocity potential is used by Chi (1985) as the explicit unknown variable. The unsteady perturbation pressure is simply related to the perturbation potential by the linearized Bernoulli equation. This makes Chi's theory different from others that directly choose the unsteady perturbation pressure as the unknown variable. To establish the solution technique for solving the perturbation velocity potential together with the perturbation pressure, the subsonic axial flow problem that corresponds to a constant subsonic relative flow for each radial station was investigated in detail by Chi (1990a). The subsonic theory, solution procedure, and representative results are given in this paper.

Theory

Helical Baseline Flow. As shown in Fig. 1, the helical flow pattern specified by the forward flight speed and the fan rotational speed is taken as the baselined steady flow about which all flow perturbations are defined. Throughout the paper, the fan case radius R_T is used to nondimensionalize all coordinates, parameters, and physical variables as required. This is equivalent to set R_T equal to unity.

At each radial location, a helix can be drawn with a pitch measured in the axial flow direction equal to the axial flow velocity multiplied by 2π and divided by the rotational speed Ω . A three-dimensional helical blade can be generated by spec-

Contributed by the International Gas Turbine Institute and presented at the 36th International Gas Turbine and Aeroengine Congress and Exposition, Orlando, Florida, June 3-6, 1991. Manuscript received at ASME Headquarters February 20, 1991. Paper No. 91-GT-131. Associate Technical Editor: L. A. Riekert.

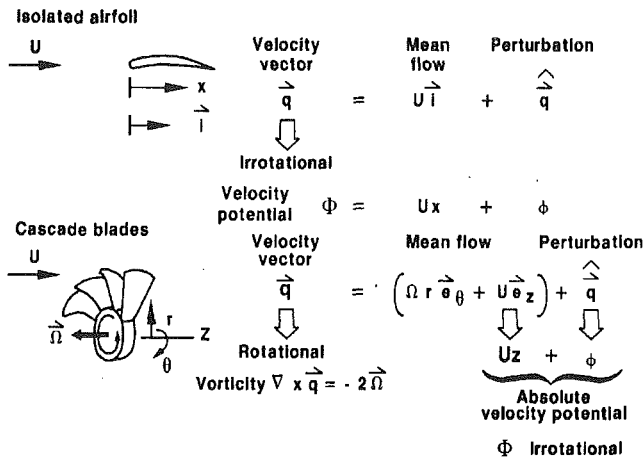


Fig. 1 Small perturbation concept

ifying first an arbitrary space curve called the helical blade generator inside the flow annulus originating from a point on the hub surface and extending to the fan case surface, and then assigning at each radial station the leading edge and trailing edge locations along its helix. The mathematical representation of the helical blade is given by

$$z = \frac{U}{\Omega} \theta + \sigma(r) \quad (1)$$

where $\sigma(r)$ is the helix number that can be interpreted as the axial shift of the helix at a radial station relative to the origin of the cylindrical coordinate system fixed to the spinning rotor (see Fig. 2). The helical blade generator can be made to coincide with, for example, the leading edge locus, the midchord locus, or the trailing edge locus of a real fan blade.

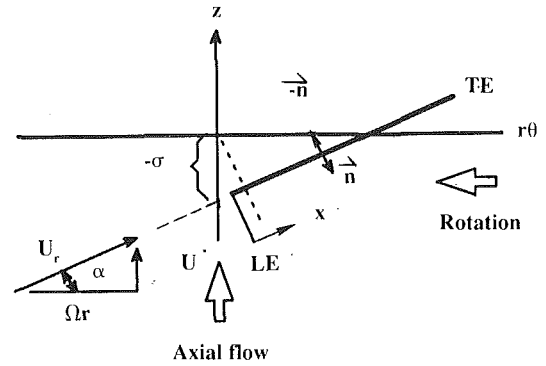


Fig. 2 Helical blade section

The helical blade generated for a forward flight condition according to the procedure described above will not cause flow disturbances in an inviscid flow, because the mean flow velocity is everywhere tangent to the helical surface. Flow disturbances can only be produced by sources such as blade thickness, camber, incidence angle, blade vibration, flow path convergence, and flight vehicle pitch and yaw motion. The inclusion of these disturbance sources in formulating transonic flow analysis is discussed by Chi (1985). Here, we consider exclusively perturbations due to vibration of unloaded blades by leaving out other disturbance sources.

Governing Equations. For an observer in the cylindrical coordinate system fixed to the rotating fan, the partial differential equation that governs the perturbation velocity potential ϕ for an oscillation frequency ω is the convective wave equation:

Nomenclature

α = undisturbed speed of sound	N_b = number of blades	y' = local coordinate normal to helix and tangent to helical surface
$[A]$ = influence matrix	N_d = number of nodal diameters	z = engine axis coordinate, positive looking rearward
b_n = mode coefficient	N_{mode} = number of mode functions	α = stagger angle; $\tan \alpha = U/\Omega r$
C or C_r = blade chord at constant radius r	p = perturbation pressure	$\beta_{rel} = (1 - M_{rel}^2)^{1/2}$
C_a = axial chord	q = velocity vector	Δ = jump across helical surface
d_n^j = coefficient of shifted Chebyshev polynomial of order n	r = radial coordinate	θ = circumferential coordinate whose positive direction is opposite to the direction of rotation
e_θ = unit vector in θ direction	r = upwash point	$\pi = 3.1415926$
e_z = unit vector in z direction	r_o = load point	ρ = undisturbed air density
$f(x)$ = displacement normal to the helical chord at constant radius	real = real part	$\sigma(r)$ = helix number as a function of r
$g(r_o, r)$ = cascade source solution	R = compressible radius	ϕ = perturbation velocity potential
$G(r_o, r)$ = duct source solution	R_H = fan hub radius, i.e., blade root radius	ω = oscillation frequency
H_n = potential mode function	R_T = fan tip radius, i.e., fan case radius	Ω = rotational speed of fan rotor
i = unit vector in x direction	S_ϕ = surface area	∇^2 = Laplacian operator
imag = imaginary part	T_n^* = shifted Chebyshev polynomial of order n	
K = kernel function	TE = trailing edge	
K_s = singular part of kernel function	U = forward flight speed of fan rotor	
LE = leading edge	U_r = relative flow velocity defined by $[U^2 + (\Omega r)^2]^{1/2}$	
M = axial flow Mach number	W = upwash velocity	
M_r = relative flow Mach number defined by $[1 + (\Omega r/U)^2]^{1/2} M$	x = local coordinate along helical chord measured from leading edge	
n = unit vector normal to helical chord pointing into fluid from suction side	y = local coordinate normal to helical chord at constant radius	
		Subscripts
		I = imaginary part
		n = mode index
		r = at radial location with radius r
		rel = relative
		R = real part

$$\nabla^2 \phi - \frac{1}{\alpha^2} \mathfrak{D}^2 \phi = 0 \quad (2)$$

where

$$\nabla^2 = \frac{1}{r} \frac{\partial}{\partial r} \left(r \frac{\partial \phi}{\partial r} \right) + \frac{1}{r^2} \frac{\partial^2}{\partial \theta^2} + \frac{\partial^2}{\partial z^2}$$

$$\mathfrak{D} = i\omega + \Omega \frac{\partial}{\partial \theta} + U \frac{\partial}{\partial z}$$

The unsteady perturbation pressure is related to the perturbation velocity potential by the linearized Bernoulli equation:

$$p = -\rho \left(i\omega \phi + \Omega \frac{\partial \phi}{\partial \theta} + U \frac{\partial \phi}{\partial z} \right)$$

$$= -\rho \left(i\omega \phi + U_R \frac{\partial \phi}{\partial x} \right) \quad (3)$$

where U_r is the relative flow velocity at a radial station, and $\partial/\partial x$ refers to the partial derivative along the helical chord.

Boundary Conditions. The boundary conditions required to solve the governing equation, Eq. (2), are the following:

- In the direction normal to the helical blade surface, the induced fluid particle velocity must match the blade vibration velocity. For an inviscid flow, the fluid particle is allowed to slide along the blade surface.
- The jump in perturbation pressure must vanish at the blade trailing edge (Kutta condition).
- The fluid velocity normal to the hub and casing surfaces must vanish.
- The unsteady flow disturbances must decay or propagate away from the fan in the rotating reference frame.

Integral Equation. By applying integral theorems, the partial differential equation, Eq. (2), in conjunction with the boundary conditions, one can derive the following integral equation that relates the blade upwash velocity $W(\mathbf{r})$ to the jump in perturbation velocity potential $\Delta\phi$ across a reference blade:

$$W(\mathbf{r}) = \int \int_{\substack{\text{reference} \\ \text{blade and wake}}} K(\mathbf{r}_o, \mathbf{r}) \Delta\phi(\mathbf{r}_o) dS_o \quad (4)$$

where the domain of surface integral covers the reference blade and its helical wake extending to downstream infinity. Here, the upwash velocity W is defined by

$$\frac{W(x)}{U} = \frac{\frac{\partial f}{\partial x} \left[1 + \left(\frac{\Omega}{U} r \right)^2 \right]^{1/2} + i \frac{\omega f}{U}}{\left[1 + \frac{(d\sigma/dr)^2}{1 + \frac{1}{\left(\frac{\Omega r}{U} \right)^2}} \right]^{1/2}}$$

where $f(x)$ is the displacement normal to the helical chord and tangent to the constant radius cylinder at a given radial station, $\partial f/\partial x$ is the chordwise slope of the displacement function, $d\sigma(r)/dr$ represents the rate of twist variation along the blade span. The kernel function $K(\mathbf{r}_o, \mathbf{r})$, which can be called the potential kernel, is related to the pressure kernel used by Namba (1974), and Namba and Ishikawa (1983) by a Fourier type integral along the helix from the load point to downstream infinity. See Chi (1990b) for the detailed proof.

Kernel Function. The "potential kernel" $k(\mathbf{r}_o, \mathbf{r})$ is defined by

$$K(\mathbf{r}_o, \mathbf{r}) = \frac{\partial^2 g}{\partial n \partial n_o}(\mathbf{r}_o, \mathbf{r}) \quad (5)$$

where the cascade source solution $g(\mathbf{r}_o, \mathbf{r})$ for an interblade phase angle σ is given by

$$g(\mathbf{r}_o, \mathbf{r}) = \sum_{k=1}^{N_b} e^{j(k-1)\sigma} G(r_o, \theta_o + [k-1] \frac{2\pi}{N_b}, z_o; r, \theta, z) \quad (6)$$

Here, the Green's function $G(\mathbf{r}, \mathbf{r}_o)$ with \mathbf{r} and \mathbf{r}_o interchanged for the annular duct that satisfies the zero radial gradient condition on the hub and case surfaces is governed by the partial differential equation

$$\nabla^2 G - \frac{1}{\alpha^2} \mathfrak{D}^2 G = \delta(\mathbf{r}, \mathbf{r}_o)$$

$$= \frac{1}{r} \delta(r-r_o) \delta(\theta-\theta_o) \delta(z-z_o) \quad (7)$$

where the adjoint operator \mathfrak{D} for the reversed flow is defined by

$$\mathfrak{D} = i\omega - \Omega \frac{\partial}{\partial \theta} - U \frac{\partial}{\partial z}$$

Equation (7) can be solved by performing a Fourier series expansion in θ and a Fourier transform in z followed by a direct solution of the resultant Bessel's equation in r . The mathematical details are given by Chi (1986). The result is

$$G(r, r_o, \theta - \theta_o, z - z_o) = \left(\frac{1}{2\pi} \right)^2 \sum_{n=-\infty}^{\infty} \quad (8)$$

$$e^{jn(\theta - \theta_o)} \int_{-\infty}^{\infty} d\alpha y_n(r, r_o, \alpha) e^{i\alpha(z - z_o)}$$

$$y_n(r, r_o, \alpha) = c \begin{cases} F_1(r) F_2(r_o) & \text{for } r < r_o \\ F_1(r_o) F_2(r) & \text{for } r > r_o \end{cases}$$

$$F_1(r) = u_1(r) u_2'(R_H) - u_2(r) u_1'(R_H)$$

$$F_2(r) = u_1(r) u_2'(R_T) - u_2(r) u_1'(R_T)$$

	$u_1(r)$	$u_2(r)$	c
$b_n^2 > 0$	$J_n(b_n r)$	$Y_n(b_n r)$	$\frac{\pi/2}{u_1'(R_H) u_2'(R_T) - u_1'(R_T) u_2'(R_H)}$
$b_n^2 < 0$	$I_n(b_n r)$	$K_n(b_n r)$	$\frac{-1}{u_1'(R_H) u_2'(R_T) - u_1'(R_T) u_2'(R_H)}$

$$b_n^2 = \frac{1}{M^2 - 1} \left[\alpha - \frac{M}{1+M} \left(\frac{\omega}{U} - n \frac{\Omega}{U} \right) \right] \left[\alpha + \frac{M}{1-M} \left(\frac{\omega}{U} - n \frac{\Omega}{U} \right) \right]$$

Here, the u_1' and u_2' represent the derivatives of u_1 and u_2 with respect to r .

As shown in Eq. (6) the cascade source solution $g(\mathbf{r}_o, \mathbf{r})$ is the Fourier sum of the duct source solution $G(\mathbf{r}_o, \mathbf{r})$. Because of the complex Fourier series format for the $\theta - \theta_o$ part of the duct Green's function $G(\mathbf{r}, \mathbf{r}_o)$ and the blade summation (i.e., k summation) part of the cascade Green's function $g(\mathbf{r}, \mathbf{r}_o)$, it is shown below that the summation of circumferential waves (i.e., summation over n) is limited to certain n values depending on two factors: the nodal diameter (ND) associated with the prescribed interblade phase angle (σ), and the number of blades in the fan rotor (N_b). Substituting Eq. (8) into Eq. (6) and noting the interchange of \mathbf{r} and \mathbf{r}_o in the substitution, one obtains

$$\begin{aligned}
g(\mathbf{r}_o, \mathbf{r}) &= \left(\frac{1}{2\pi}\right)^2 \sum_{k=1}^{N_b} e^{i(k-1)\sigma} \sum_{n=-\infty}^{\infty} e^{in(\theta_o + [k-1](2\pi/N_b) - \theta)} \\
&\times \int_{-\infty}^{\infty} d\alpha y_n(r_o, r, \alpha) e^{i\alpha(z_o - z)} \\
&= \left(\frac{1}{2\pi}\right)^2 \sum_{n=-\infty}^{\infty} \left[\sum_{k=1}^{N_b} e^{i(k-1)(\sigma + (2\pi n/N_b))} \right] \\
&\times e^{in(\theta_o - \theta)} \int_{-\infty}^{\infty} d\alpha y_n(r_o, r, \alpha) e^{i\alpha(z_o - z)}
\end{aligned}$$

The factor inside the square bracket must be equal to N_b or 0, i.e.,

$$\sum_{k=1}^{N_b} e^{i(k-1)(\sigma + (2\pi n/N_b))} = \begin{cases} N_b & \text{if } n = -ND + m \cdot N_b \\ 0 & \text{otherwise} \end{cases}$$

where the interblade phase angle σ is related to the nodal diameter ND by

$$\sigma = 2\pi \frac{ND}{N_b}$$

Therefore, the cascade Green's function becomes

$$\begin{aligned}
g(\mathbf{r}_o, \mathbf{r}) &= \left(\frac{1}{2\pi}\right)^2 \cdot N_b \cdot \sum_{\substack{n = -ND + m \cdot N_b \\ \text{for } m = 0, \pm 1, \pm 2, \dots}} e^{in(\theta_o - \theta)} \\
&\times \int_{-\infty}^{\infty} d\alpha y_n(r_o, r, \alpha) e^{i\alpha(z_o - z)}
\end{aligned}$$

which is basically N_b times the duct Green's function $G(\mathbf{r}_o, \mathbf{r})$ except that the summation over the circumferential wave number n no longer covers all possible integer values from $-\infty$ to ∞ and instead covers only those integer n values that satisfy the following relationship:

$$n = -ND + m \cdot N_b$$

where $m = 0, \pm 1, \pm 2, \dots$

In Eq. (5), which defines the potential kernel function, the normal derivative is simply the scalar product between a gradient vector quantity and the unit normal vector. Therefore, the kernel function $K(\mathbf{r}_o, \mathbf{r})$ is related to the second derivatives of the cascade Green's function $g(\mathbf{r}_o, \mathbf{r})$ as follows:

$$K(\mathbf{r}_o, \mathbf{r}) = \{n_r \ n_\theta \ n_z\} \begin{bmatrix} \frac{\partial^2 g}{\partial r \partial r_o} & \frac{1}{r_o} \frac{\partial^2 g}{\partial r \partial \theta_o} & \frac{\partial^2 g}{\partial r \partial z_o} \\ \frac{1}{r} \frac{\partial^2 g}{\partial \theta \partial r_o} & \frac{1}{r_o r} \frac{\partial^2 g}{\partial \theta \partial \theta_o} & \frac{1}{r} \frac{\partial^2 g}{\partial \theta \partial z_o} \\ \frac{\partial^2 g}{\partial z \partial r_o} & \frac{1}{r_o} \frac{\partial^2 g}{\partial z \partial \theta_o} & \frac{\partial^2 g}{\partial z \partial z_o} \end{bmatrix} \begin{Bmatrix} n_{r_o} \\ n_{\theta_o} \\ n_{z_o} \end{Bmatrix}$$

Here the unit normal components n_r , n_θ , and n_z for a helical surface described by Eq. (1) are simply

$$n_r = \frac{-d\sigma/dr}{|\nabla F|}$$

$$n_\theta = \frac{-U/\Omega r}{|\nabla F|}$$

$$n_z = \frac{1}{|\nabla F|}$$

where

$$|\nabla F| = \left[\left(\frac{U_r}{\Omega r}\right)^2 + \left(\frac{d\sigma}{dr}\right)^2 \right]^{1/2}$$

$$U_r = (U^2 + \Omega^2 r^2)^{1/2}$$

The three components n_{r_o} , n_{θ_o} , n_{z_o} are defined similarly.

Besides its dependence on the load position \mathbf{r}_o and the upwash location \mathbf{r} , the potential kernel function is also a function of the axial flow Mach number M , the nondimensional rotor speed Ω/U , the nondimensional oscillation frequency ω/U , the number of blades N_b , and the number of nodal diameters N_d .

Furthermore, in the cylindrical coordinate system, the dependence of the kernel function on \mathbf{r}_o and \mathbf{r} appears as $K(r_o, r, \theta_o - \theta, z_o - z)$. The kernel function is singular when the load point \mathbf{r}_o coincides with the upwash point \mathbf{r} . The singularity behaves like

$$K_s(\mathbf{r}_o, \mathbf{r}) = -\frac{\beta_{rel}^2}{4\pi R^3} \quad (9)$$

where β_{rel}^2 is defined by $1 - M_{rel}^2$, M_{rel} is the relative Mach number defined as $M[1 + (\Omega r/U)^2]^{1/2}$, and R is the compressible radius defined by $[(x_o - x)^2 + \beta_{rel}^2 (y_o' - y')^2]^{1/2}$.

Integral Equation Solution. For a prescribed upwash velocity distribution over the blade, the integral Eq. (4) is solved by discretizing the blade and wake surfaces and subsequently using a mode expansion procedure.

First of all, the reference blade and wake surfaces are discretized into finite size constant potential elements. The potential jump values for the wake elements are related to the potential jump value at the blade trailing edge for the same radius. This is because the pressure jump vanishes in the wake, and consequently the linearized Bernoulli Eq. (3), can be integrated to relate the potential jump in the wake to that at the blade trailing edge, i.e.,

$$\Delta\phi(x) = \Delta\phi(x_{TE}) e^{i(\omega/U_r)(x_{TE} - x)} \text{ for } x > x_{TE} \quad (10)$$

where x denotes the distance measured along the helix at a given radial station. Physically, this corresponds to vortex convection along the helical wake with the relative flow velocity U_r . Therefore, the only unknowns are the potential jumps for all the blade elements.

The jump in perturbation velocity potential $\Delta\phi$ for a given radial station is then expressed as a finite series expansion in terms of selected potential mode functions $H_n(x/c_r)$:

$$\frac{\Delta\phi(x)}{U_r c_r} = - \sum_{n=0}^{N_{mode}-1} b_n H_n\left(\frac{x}{c_r}, i \frac{\omega c_r}{U_r}\right) \quad (11)$$

The corresponding jump in perturbation pressure is also represented as a finite series expansion in terms of selected pressure mode functions:

$$\frac{\Delta p(x)}{\rho U_r^2} = \left(\frac{1-x/c_r}{x/c_r}\right)^{1/2} \sum_{n=0}^{N_{mode}-1} b_n T_n^*\left(\frac{x}{c_r}\right) \quad (12)$$

where T_n^* is the shifted Chebyshev polynomial of order n . Note that the same mode coefficients b_n are used for the potential jump and pressure jump series expansions. The series expansion for pressure satisfies the $x^{-1/2}$ type singularity at the leading edge as required for subsonic relative flows.

Substituting Eqs. (11) and (12) into the linearized Bernoulli Eq. (3), one can show that the n th potential mode function is simply related to n th pressure mode function by the following equation:

$$\begin{aligned}
H_n\left(\frac{x}{c_r}, i \frac{\omega c_r}{U_r}\right) &= e^{-i(\omega c_r/U_r)(x/c_r)} \sum_{j=0}^n d_j^n \\
&\times \int_0^{x/c_r} (1-\xi)^{1/2} \xi^{j-1/2} e^{i(\omega c_r/U_r)\xi} d\xi
\end{aligned}$$

where d_j^n are the coefficients of polynomial expansion of the shifted Chebyshev polynomial $T_n^*(x)$, i.e.,

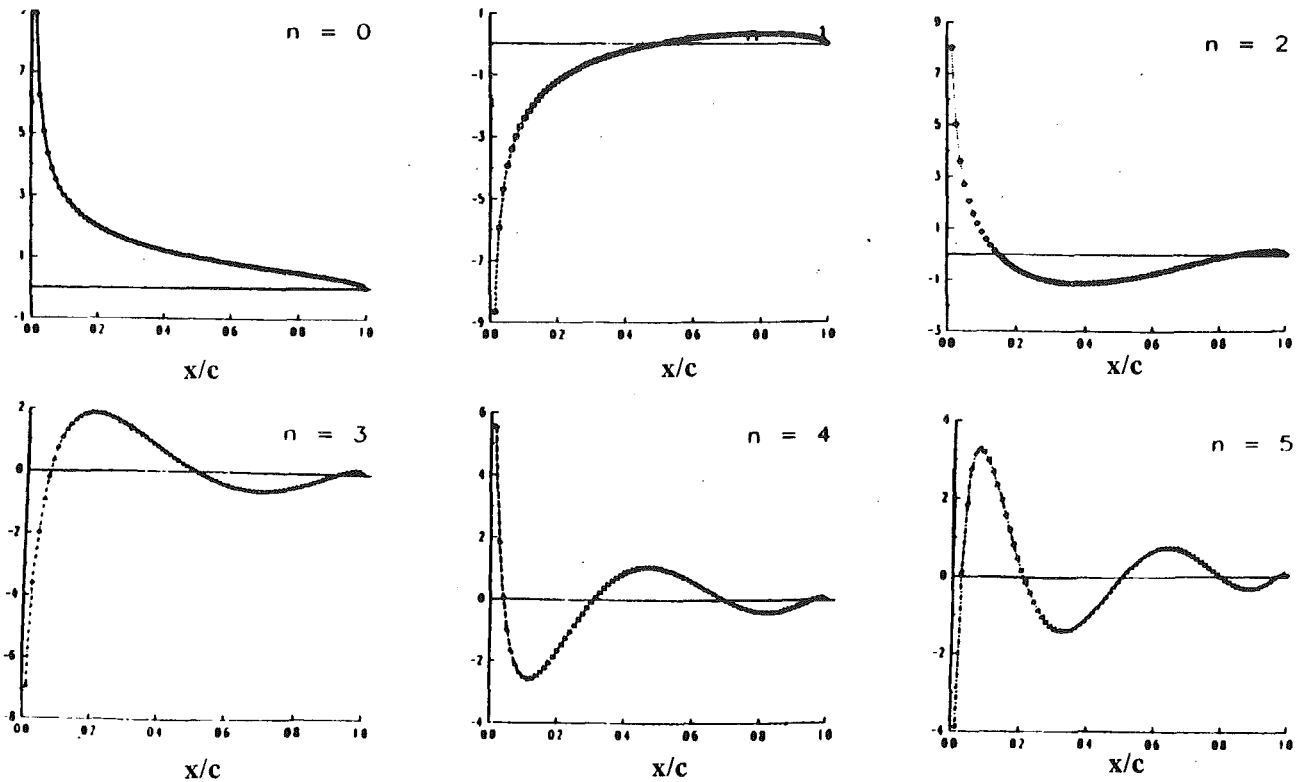


Fig. 3 Pressure mode functions $\sqrt{\frac{1-x/c}{x/c}} \cdot T_n^*(x/c)$ for $n=0, 1, 2, 3, 4, 5$

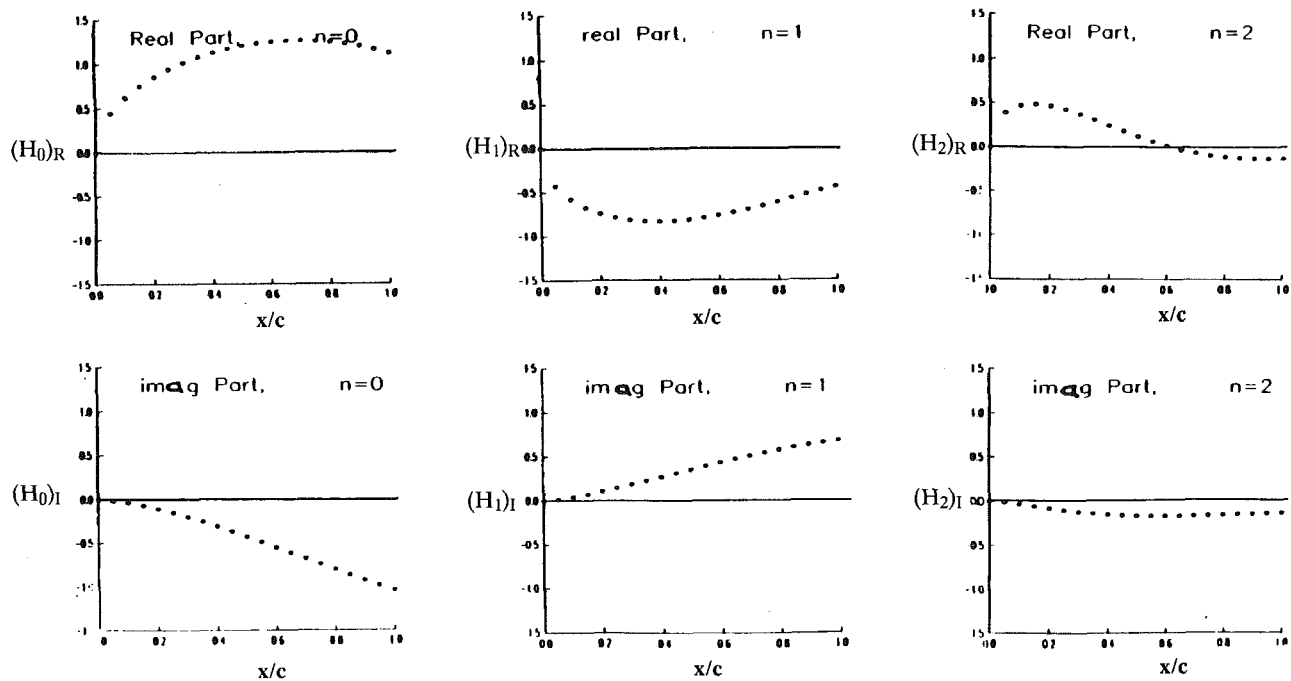


Fig. 4 Potential mode functions $H_n(x/c)$ versus x/c for $n=0, 1, 2$, assuming $\omega c/U_1=1$

$$T_n^*(x) = \sum_{j=0}^n d_j^n x^j$$

Note that the pressure mode functions are real and the potential mode functions are frequency dependent and complex.

Representative pressure mode functions are shown in Fig.

3 from the first six modes, and the corresponding potential mode functions are shown in Figs. 4, 5, and 6. Note that all pressure mode functions vanish at the trailing edge ($x=1$) and all potential mode functions vanish at the leading edge ($x=0$). See Chi (1990d) for the analytical details.

By choosing the number of modes N_{mode} equal to the number

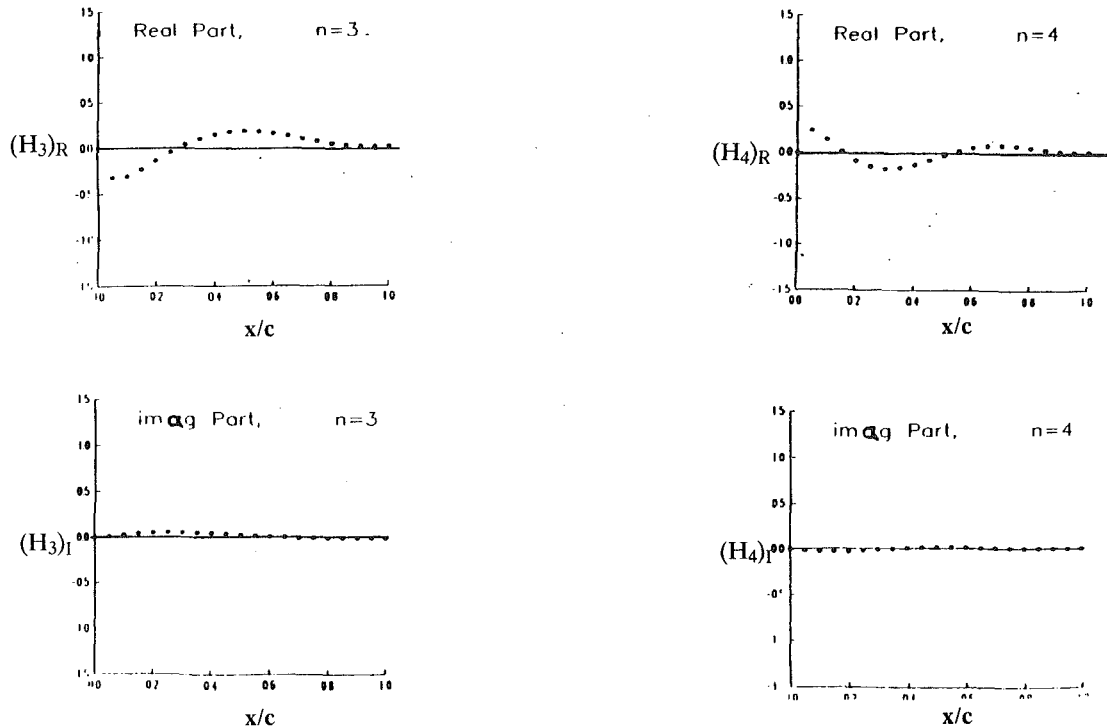


Fig. 5 Potential mode functions $H_n(x/c)$ versus x/c for $n=3$ and 4 assuming $\omega c_r/U_t=1$

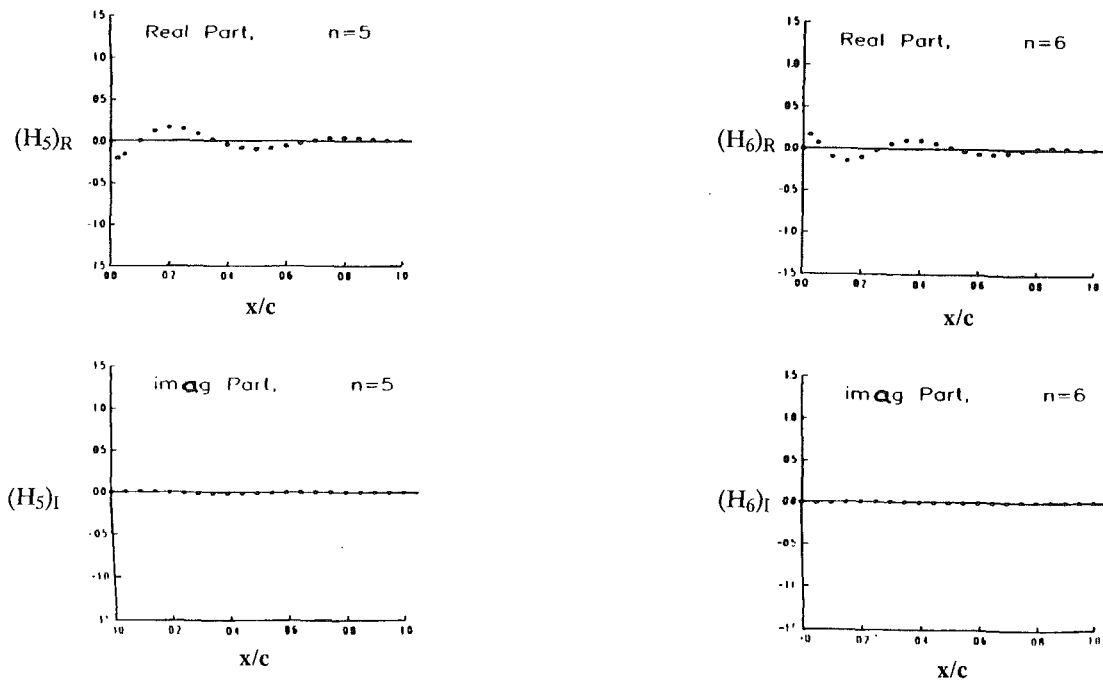


Fig. 6 Potential mode functions $H_n(x/c)$ versus x/c for $n=5$ and 6 assuming $\omega c_r/U_t=1$

of chordwise panels for each radial station and applying Eq. (11) to the centroids of the blade panels, one would obtain a linear transformation between the unknown potential jumps and the mode coefficients b_n . Then, by assuming constant $\Delta\phi$ panels in Eq. (4), one obtains the following set of simultaneous algebraic equations in which the unknowns are a collection of mode coefficients $\{b_n\}$ for all chordwise strips:

$$[A]\{b_n\} = \left\{ \frac{W}{U} \right\} \quad (13)$$

where the elements of the aerodynamic influence matrix are simply the integrals of the potential kernel function over the reference blade and wake surfaces.

Here, the number of unknowns is the same as the number of blade elements, which is equal to the sum of the numbers of mode coefficients from all chordwise strips. Then, selecting the centroids of the blade elements to match the upwash velocity on the right-hand side of Eq. (13) will yield the solution for the mode coefficients. The jumps in perturbation pressure are then calculated using Eq. (12).

Aerodynamic Influence Matrix. The calculation of the aerodynamic influence matrix [4] in Eq. (13) must be carefully handled. This is primarily due to the singular nature of the kernel function $K(\mathbf{r}_o, \mathbf{r})$ as \mathbf{r}_o approaches \mathbf{r} . The singular part of the kernel function must be integrated analytically. Besides, for certain combinations of duct sizes and flow parameters, nondecaying propagating waves will exist and the kernel function would oscillate with a finite amplitude for large $z_o - z$ values. These propagating waves must be integrated analytically over the semi-infinite wake region extending to downstream infinity.

Therefore, for a given upwash point, the surface integral given by Eq. (4) is separated into three parts: one associated with the integral over the blade panel surface whose centroid is the upwash point $W_{\text{blade singular}}$, one associated with integrals covering the rest of the blade panels $W_{\text{blade regular}}$, and one for the entire wake region W_{wake} . Therefore we have

$$W(\mathbf{r}) = W_{\text{blade singular}}(\mathbf{r}) + W_{\text{blade regular}}(\mathbf{r}) + W_{\text{wake}}(\mathbf{r})$$

Integral Over Upwash-Point Panel, $W_{\text{blade singular}}$. At the centroid of the upwash panel, the upwash velocity is matched exactly. The portion of the integral shown in Eq. (4) that covers the upwash panel element, i.e., $W_{\text{blade singular}}$, must be evaluated in two parts by writing the kernel function $K(\mathbf{r}_o, \mathbf{r})$ as

$$K(\mathbf{r}_o, \mathbf{r}) = K_s(\mathbf{r}_o, \mathbf{r}) + [K(\mathbf{r}_o, \mathbf{r}) - K_s(\mathbf{r}_o, \mathbf{r})]$$

where $K_s(\mathbf{r}_o, \mathbf{r})$ is the singular term given by Eq. (9). The first term K_s is integrated analytically as follows:

$$\int \int_{\substack{\text{upwash} \\ \text{panel} \\ \text{element}}} K_s(\mathbf{r}_o, \mathbf{r}) \Delta\phi(\mathbf{r}_o) dS_o \approx \Delta\phi \int \int_{\substack{\text{upwash} \\ \text{panel} \\ \text{element}}} K_s(\mathbf{r}_o, \mathbf{r}) dS_o$$

$$= \Delta\phi \frac{1}{\pi} \left(\frac{\beta_{\text{rel}}^2}{\epsilon^2} + \frac{1}{\delta^2} \right)^{1/2}$$

where

$$\beta_{\text{rel}}^2 = 1 - M_{\text{rel}}^2 \text{ for upwash point } \mathbf{r}$$

$$\epsilon = \frac{U_r \Delta\theta_o}{\Omega \cdot 2}$$

$\Delta\theta_o$ = panel element size in θ direction

$$\delta = \frac{\text{Area}}{4\epsilon}$$

Area = surface area of panel element

$\Delta\phi$ = potential jump for the panel element

and the second term $K - K_s$ is integrated numerically using Gaussian quadrature.

Integral Over Blade Panels Besides Upwash-Point Panel, $W_{\text{blade regular}}$ (\mathbf{r}). The kernel function is regular outside the upwash point panel, and therefore the integral $W_{\text{blade regular}}(\mathbf{r})$ is evaluated using Gaussian quadrature.

Integral Over Wake, W_{wake} (\mathbf{r}). The integral over the wake surface $W_{\text{wake}}(\mathbf{r})$ requires a special treatment because (a) the wake potential jump is related to the trailing edge potential jump by a simple exponential factor, (b) the kernel function $K(\mathbf{r}_o, \mathbf{r})$ in general oscillates indefinitely toward downstream infinity ($z_o - z \rightarrow \infty$). In the wake integral,

$$W_{\text{wake}}(\mathbf{r}) = \int \int_{\text{wake}} K(\mathbf{r}_o, \mathbf{r}) \Delta\phi(\mathbf{r}_o) dS_o$$

the potential jump in the wake $\Delta\phi$ is related to the potential jump at the trailing edge traced back along the same helix for

a fixed radius r , i.e., Eq. (10). The kernel function $K(\mathbf{r}_o, \mathbf{r})$ oscillates indefinitely toward downstream infinity with constant amplitudes and a finite number of spatial periods. Representing the spatially oscillating part of the kernel function by K_∞ , one can write the full kernel as

$$K(\mathbf{r}_o, \mathbf{r}) = K_\infty(\mathbf{r}_o, \mathbf{r}) + [K(\mathbf{r}_o, \mathbf{r}) - K_\infty(\mathbf{r}_o, \mathbf{r})]$$

Then the wake integral becomes

$$W_{\text{wake}}(\mathbf{r}) = I_\infty(\mathbf{r}) + \Delta I(\mathbf{r})$$

where

$$I_\infty(\mathbf{r}) = \int \int_{\text{wake}} K_\infty(\mathbf{r}_o, \mathbf{r}) \Delta\phi(\mathbf{r}_o) dS_o$$

$$\Delta I(\mathbf{r}) = \int \int_{\text{wake}} [K(\mathbf{r}_o, \mathbf{r}) - K_\infty(\mathbf{r}_o, \mathbf{r})] \Delta\phi(\mathbf{r}_o) dS_o$$

with the area element on a helical surface given by

$$dS_o = \left\{ \left(\frac{U}{\Omega} \right)^2 + r_o^2 \left[1 + \left(\frac{d\sigma}{dr_o} \right)^2 \right] \right\}^{1/2} dr_o d\theta_o$$

The integral $\Delta I(\mathbf{r})$ is evaluated using Gaussian quadrature. Meanwhile, the unknown $\Delta\phi(x)$ for a wake panel at a given radius is replaced by the new unknown $\Delta\phi(x_{TE})$ for the trailing edge panel at the same radius using Eq. (10).

The integral I_∞ must be evaluated analytically. Because of the use of the helical coordinate x in representing the wake potential jump in Eq. (10), it is convenient to choose r_o, x_o instead of r_o, θ_o as the independent variables in evaluating the surface integral I_∞ , i.e.,

$$I_\infty(\mathbf{r}) = \int_{R_H}^{R_T} \Delta\phi(x_{TE}(r_o)) e^{i(\omega/U_{r_o})x_{TE}(r_o)} \left\{ \left(\frac{U}{\Omega} \right)^2 + r_o^2 \left[1 + \left(\frac{d\sigma}{dr_o} \right)^2 \right] \right\}^{1/2} \frac{\Omega}{U_{r_o}} \left[\int_{x_{TE}(r_o)}^{\infty} K_\infty(\mathbf{r}_o, \mathbf{r}) e^{-i(\omega x_o/U_{r_o})} dx_o \right] dr_o$$

Here, the integral is first carried out along each helix (x_o integration) followed by an integral in the radial direction (r_o integration). The radial integral is carried out again using the Gaussian quadrature algorithm after the x_o integral inside the square bracket is evaluated analytically.

The oscillating part of the kernel function consists of a finite number of terms of the following form:

$$e^{iax_o}$$

where a is a real number. Using this asymptotic form in the square bracket term involving $K_\infty(\mathbf{r}_o, \mathbf{r})$, one needs to evaluate integrals of the following type:

$$\int_{x_{TE}(r_o)}^{\infty} e^{i(-(\omega/U_{r_o})+a)x_o} dx_o$$

which has a finite value given by

$$\frac{-e^{i(-(\omega/U_{r_o})+a)x_{TE}(r_o)}}{i \left(-\frac{\omega}{U_{r_o}} + a \right)}$$

by assuming that ω has a small but negative imaginary part. The assumption of a small but negative imaginary part of the frequency ω is a means of introducing artificial viscosity into the flow model. An assumption of a positive imaginary part of ω would have made the integral along the helix become infinitely large, and this would correspond to "negative viscosity," which is physically unrealizable.

Therefore, the K_∞ integral can be written as

Table 1 Baseline cascade properties

	Cascade A	Cascade B	Cascade C
Axial Mach Number (M)	0.5	0.3	0.5
Rotor Speed (Ω/U)	1	2.4744	1.597
Hub to Tip Ratio (R_H/R_T)	0.5	0.4	0.35
Number of Blades (N_b)	30	30	15
Special Feature	Midchord Locus is Radial	Midchord Locus is Radial	Leading Edge Locus is Radial
Axial Chord (C_a/R_T)	Constant 0.1	Constant 0.0666666	Varying Along Span
Helical Chord (C_r/R_T)	Varying Along Span	Varying Along Span	Constant 0.333333
Blade Motion	Unit Angle of Attack	Circumferential Bending	Pitching About Leading Edge
Frequency (ω/U)	0	3	2.396
Nodal Diameter (N_d)	0	6	0

$$\int_{x_{TE}(r_o)}^{\infty} K_{\infty}(\mathbf{r}_o, \mathbf{r}) e^{-i(\omega x_o/U r_o)} dx_o = \sum_j \frac{i e^{i(a_j - (\omega/U r_o)) x_{TE}(r_o)}}{a_j - \frac{\omega}{U r_o}}$$

where the summation over j includes as many terms as the flow condition dictates.

Results

Baseline Cascade Configurations. Three cascade configurations, designated as Cascade A, Cascade B, and Cascade C, are analyzed using the analysis procedures described above. The number of panels for blade discretization depends on the size of the blade and the required accuracy for the unsteady pressure jump. Generally, satisfactory results can be obtained using eight chordwise elements, six spanwise elements, and a wake axial length equal to the maximum axial extent of the blade. A typical computational runtime is thirty minutes on a VAX workstation Model 3100.

The geometric properties and flow conditions for these cascade configurations are given in Table 1. The helix numbers $\sigma(r)$ for all these baseline cascade configurations are zero so that the helical blade for these cascades always contains a straight radial line which defines the radial coordinate. All pressure jump data are normalized by the local values of $\rho U r_o^2$.

Cascade A. Cascade A has 30 high-aspect-ratio blades (aspect ratio near 5) with a constant axial chord. The midchord locus of the blade coincides with a straight radial line corresponding to zero helix number $\sigma(r)=0$.

For an axial flow Mach number $M=0.5$ and a nondimensional rotor speed $\Omega/U=1$, Lordi and Homicz (1981) calculated the sectional lift forces for a steady flow produced by a unit angle-of-attack twist of the blade. For the same flow condition, Fig. 7 shows the detailed pressure jump distributions calculated using the present three-dimensional theory and the classical two-dimensional strip theory (Chi, 1980). In the three-dimensional analysis, the blade is discretized into five steps of equal radial width and each strip is further divided into four equal chordwise elements. For each radial station, the length of the wake surface included in the analysis is equal to the blade chord for that radial station. Because of the high aspect ratio of the blade and the constancy of the blade displacement along the span, the steady pressure distributions for all radial stations exhibit very strong two-dimensional flow nature.

Cascade B. Cascade B represents a rotor of 30 high-aspect-ratio blades (aspect ratio near 6) with a constant axial chord that is one-third smaller than the Cascade A blade. The midchord locus is again radially straight. For an axial flow Mach

number 0.3 and a nondimensional rotor speed Ω/U equal to 2.4744, Namba and Ishikawa (1983) calculated the pressure jump distributions due to the six nodal diameter circumferential bending vibration of forward traveling wave type at a reduced frequency ω/U equal to 3.0. The first bending mode shape of a cantilever beam was used to represent the radial variation of the bending displacement amplitude. However, the displacement amplitude at the blade tip was not clearly stated in his paper.

Assuming the amplitude of the circumferential bending displacement at the blade tip is unity relative to the fan case radius, the three-dimensional unsteady pressure distributions are calculated using six aerodynamic strips with four chordwise blade elements and twenty wake elements for each strip. In Fig. 8, the three-dimensional results are compared with the two-dimensional strip theory. Because of the large variation of bending displacement amplitude from the blade root section to the blade tip section, a strong radial flow interaction apparently brings down the two-dimensional strip theory load near the blade tip by more than 50 percent. On the other hand, near the hub, the unsteady load is increased from its minimum two dimensional load (exactly zero at the hub because zero local blade motion) to a moderate level.

Cascade C. Cascade C represents a fan rotor of 15 blades with an aspect ratio near 2. The blade chord remains constant (chord normalized by fan case radius equal to 0.333333) along the span so that the axial chord decreases radially outward. The leading edge locus is a straight radial line which is also the pitching axis of the blade. This cascade configuration was used by Williams (1990) in his low Mach number propfan airload calculations.

For an axial flow Mach number 0.5 and a nondimensional rotor speed 1.597, Fig. 9 shows the calculated three-dimensional pressure jump distributions compared to the two-dimensional strip theory load due to a zero nodal-diameter pitching oscillation about the straight leading edge locus at a reduced frequency ω/U equals to 2.396. In the three-dimensional analysis, the blade span is divided into six strips and each strip is further discretized into eight chordwise elements. The wake length included is twice the blade chord at each radial station. The strong two-dimensional nature of the unsteady pressure is clearly seen primarily because the pitching amplitude is constant along the blade span.

With the same flow condition and pitching oscillation frequency, calculation is made by introducing a linear pitching amplitude distribution along the span (zero pitching at the root and unit pitching angle at the tip). This variation of Cascade C is designated as Cascade D. The result is shown in Fig. 10. The pitching airload is reduced near the tip and the hub load is increased because of the enhancement of the three-dimen-

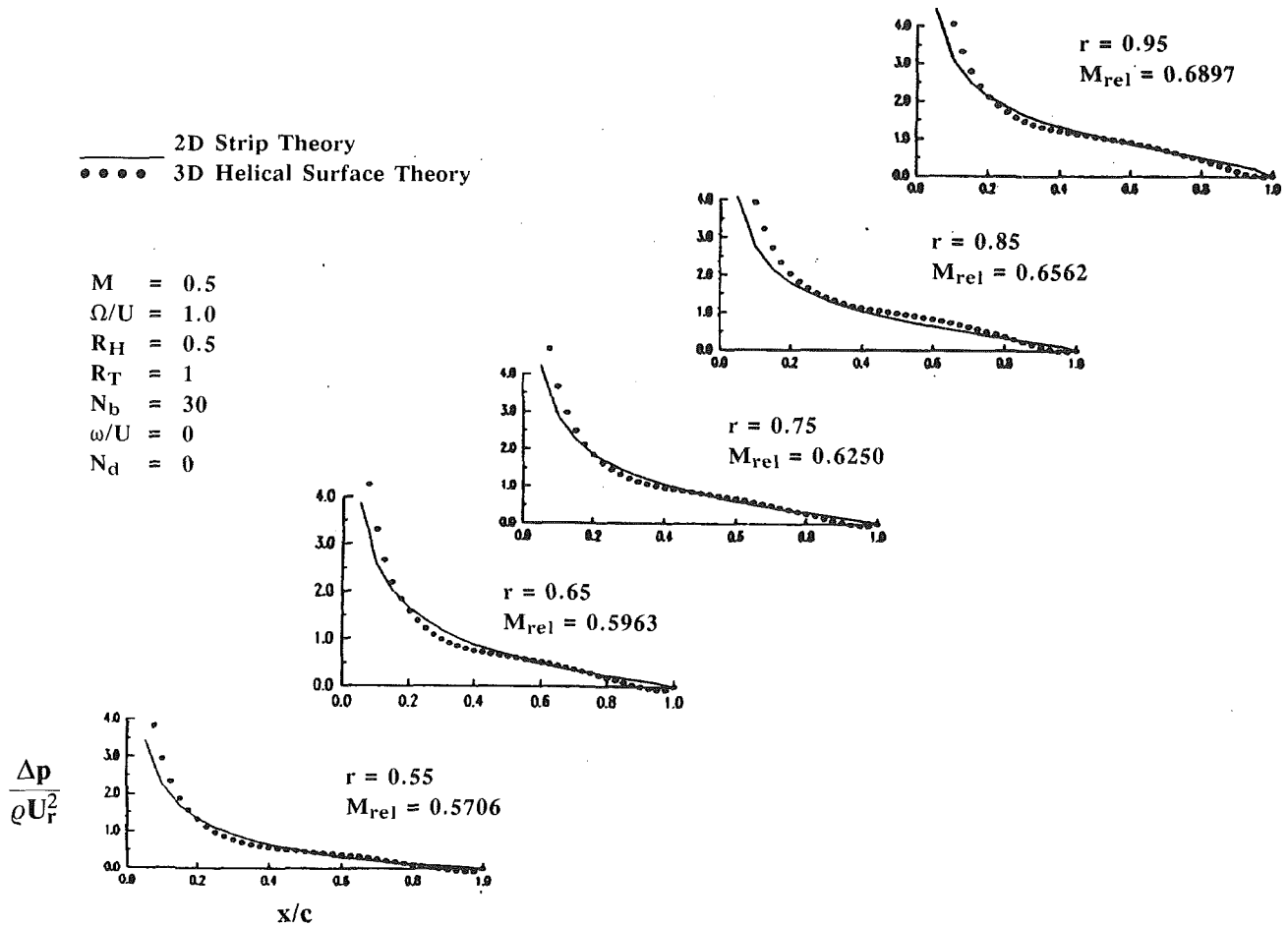


Fig. 7 Cascade A—Steady pressure jump distributions for unit angle of attack: two-dimensional versus three-dimensional

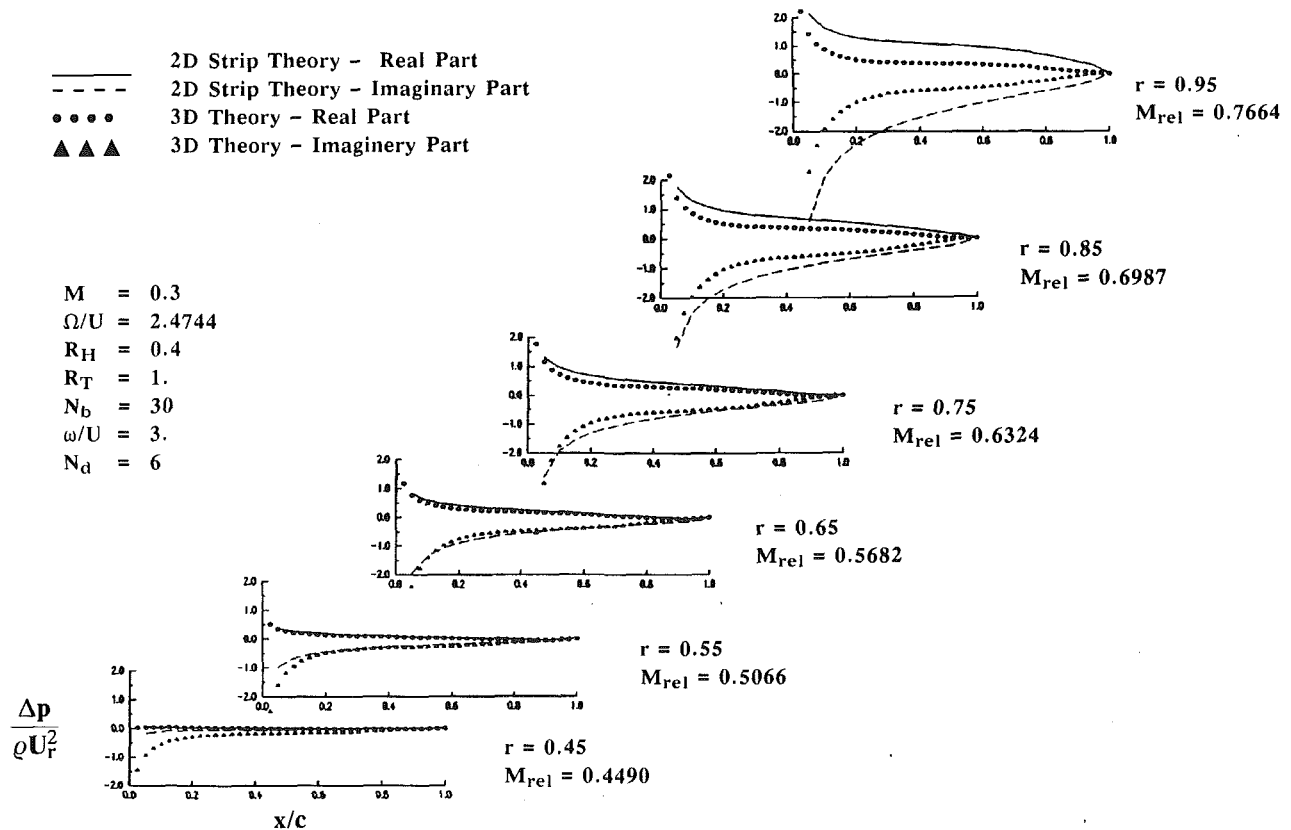


Fig. 8 Cascade B—Unsteady pressure jump distributions for bending vibration: two-dimensional versus three-dimensional

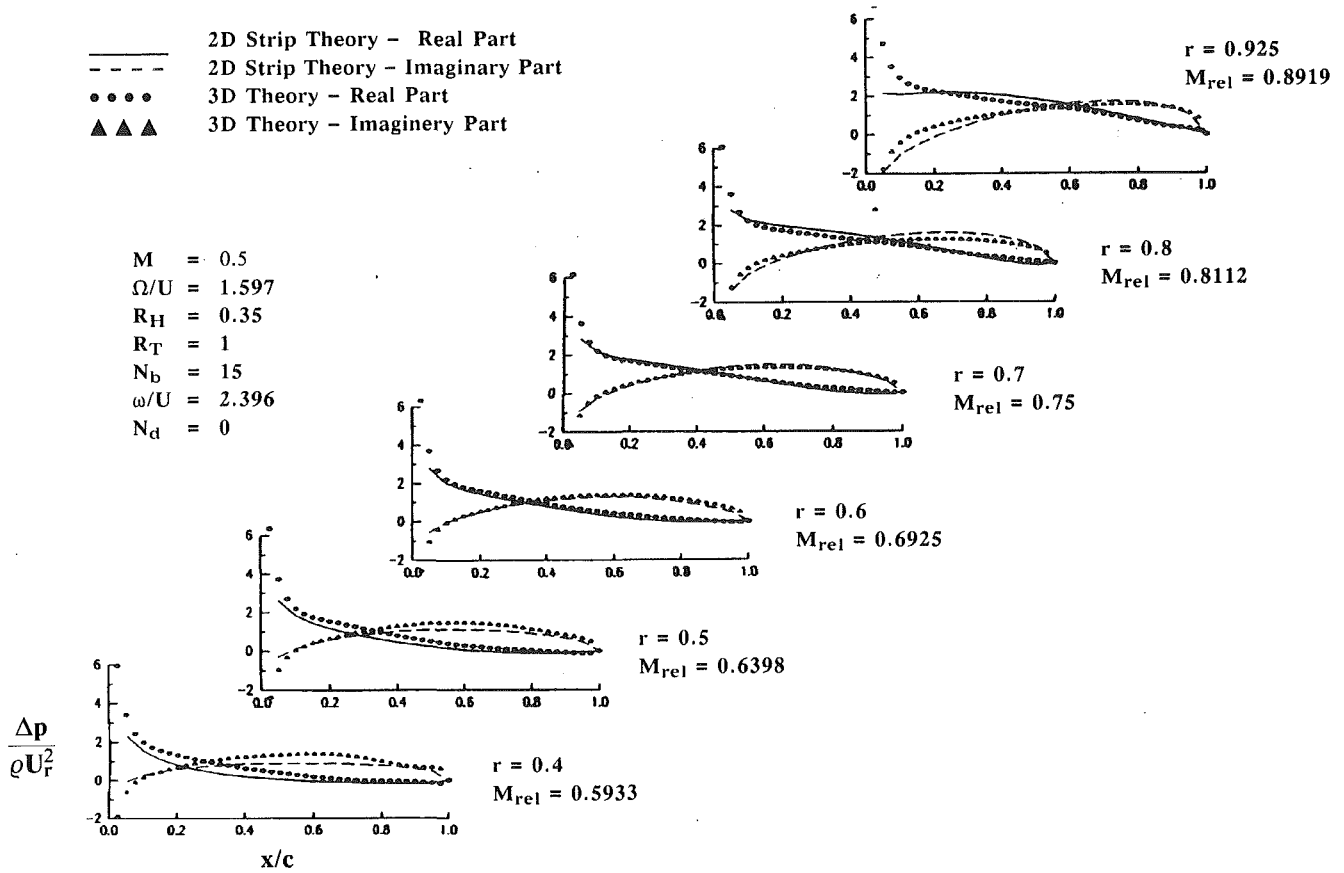


Fig. 9 Cascade C—Unsteady pressure jump distributions for unit angle of attack pitching oscillation about leading edge: two-dimensional versus three-dimensional

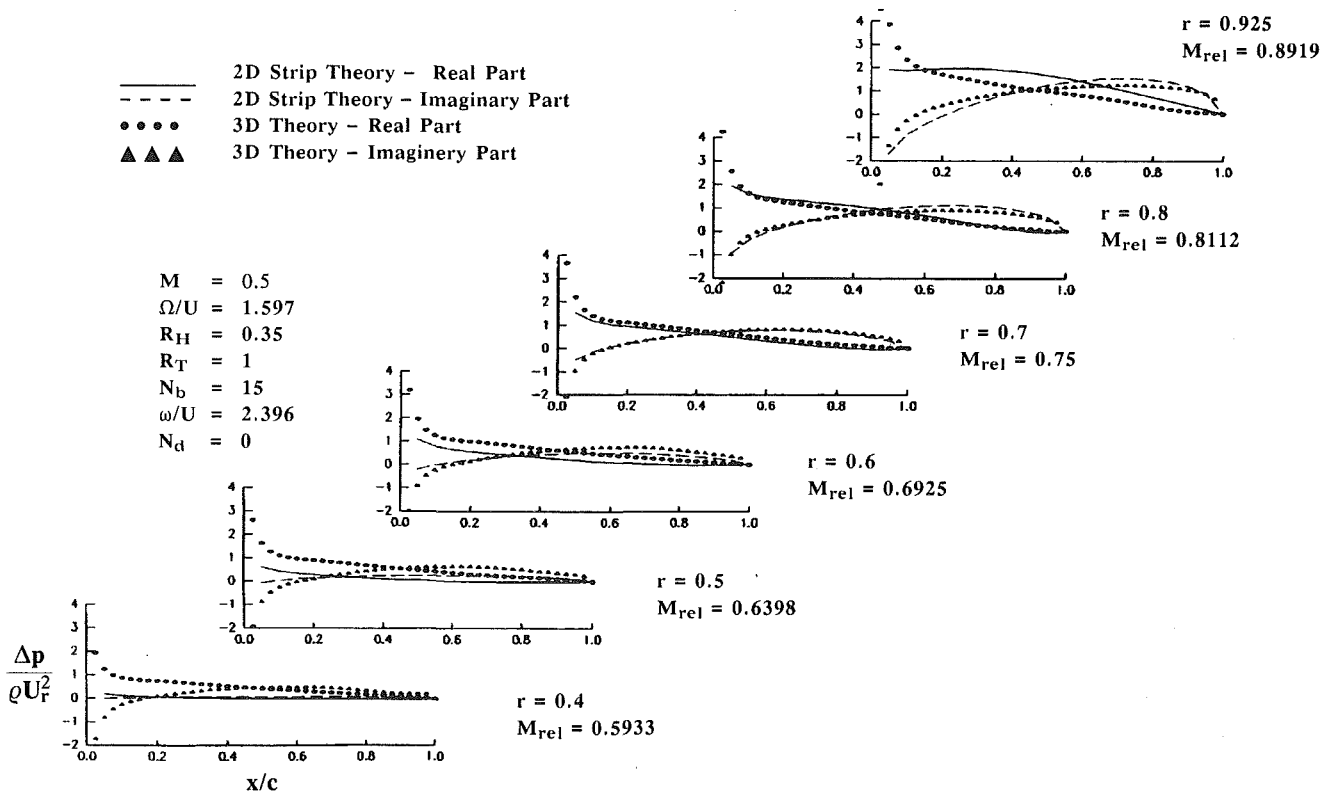


Fig. 10 Cascade D—Unsteady pressure jump distributions for linear pitching oscillation: two-dimensional versus three-dimensional

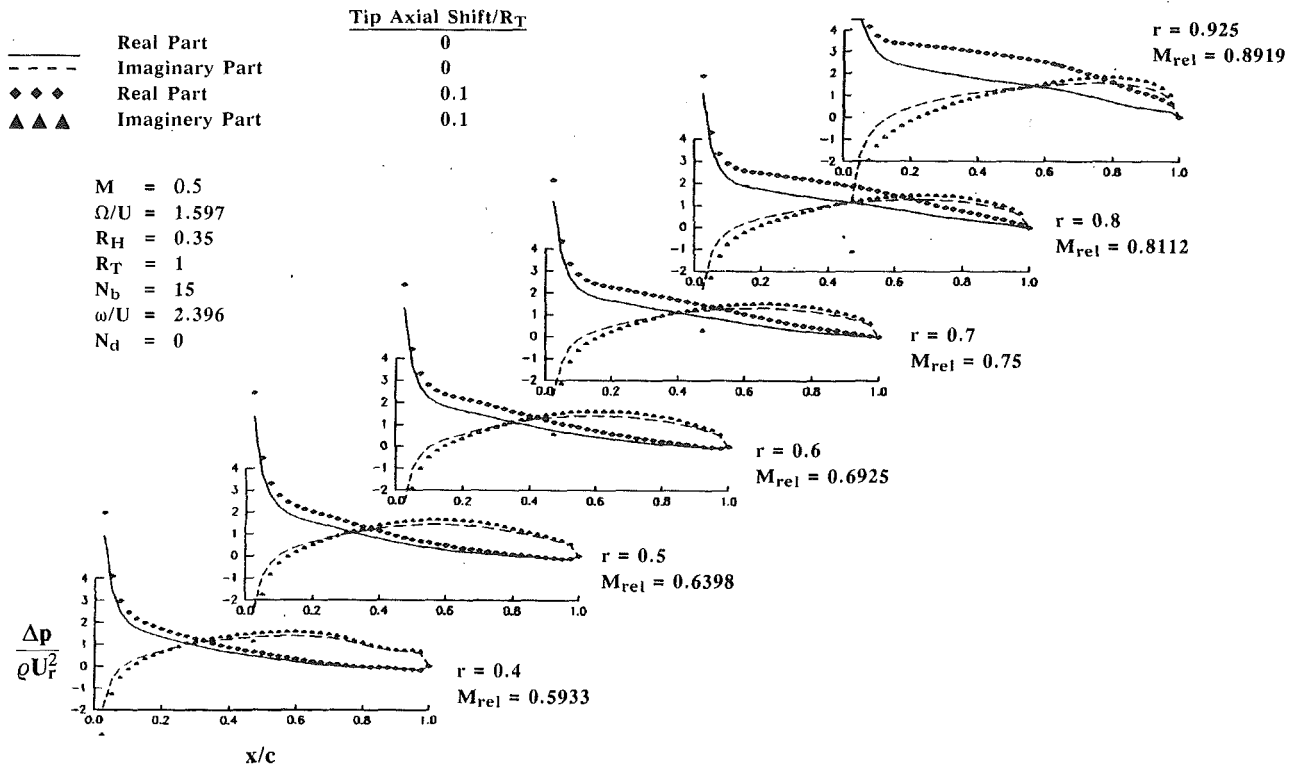


Fig. 11 Effect of axial bending of cascade C blades on three-dimensional unsteady pressure jump distributions

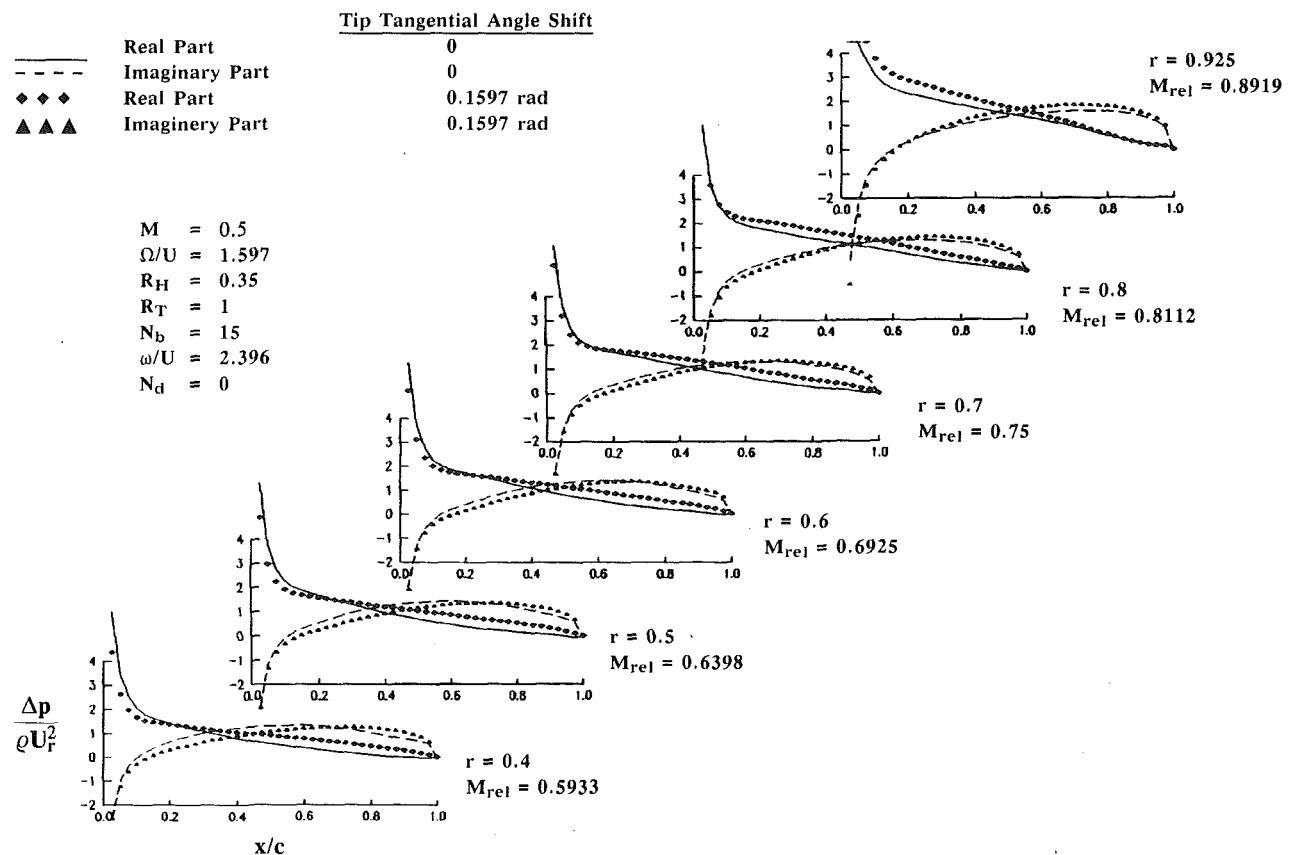


Fig. 12 Effect of tangential bowing of cascade C blades on three-dimensional unsteady pressure jump distributions

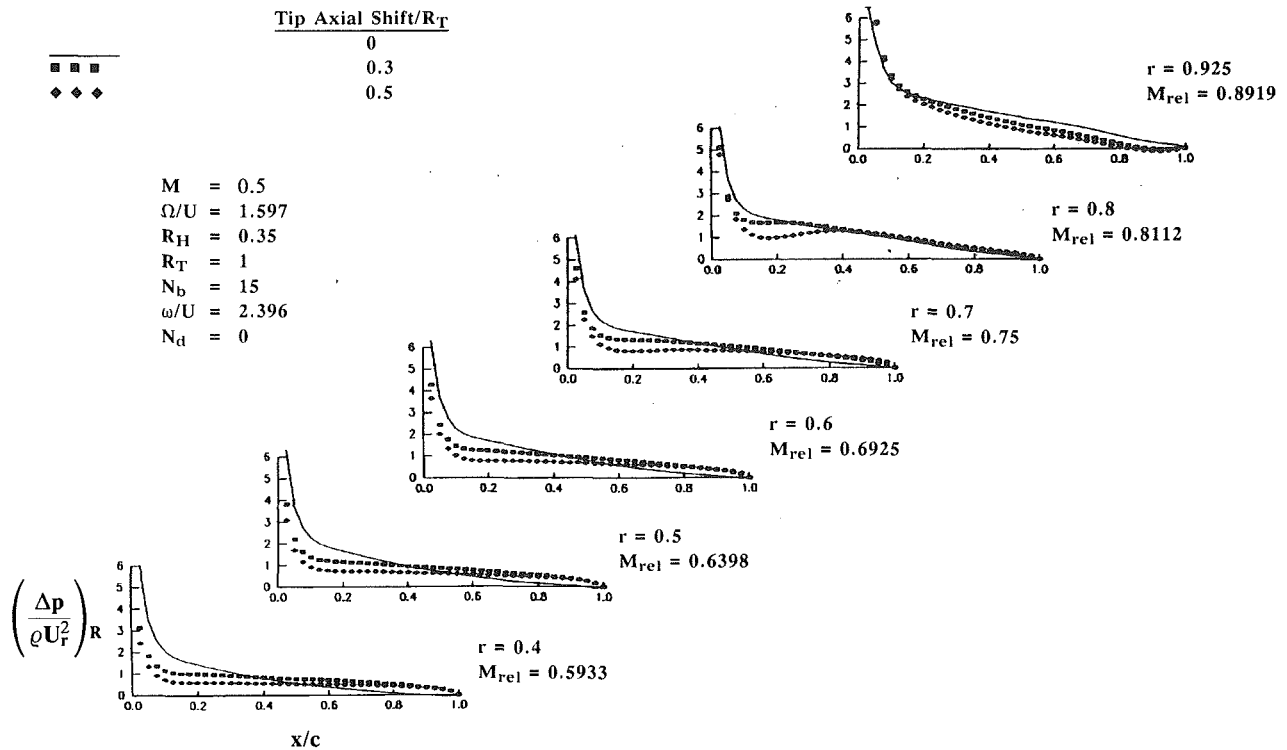


Fig. 13 Effect of linear backward sweep of cascade C blades on real part of three-dimensional unsteady pressure jump distributions

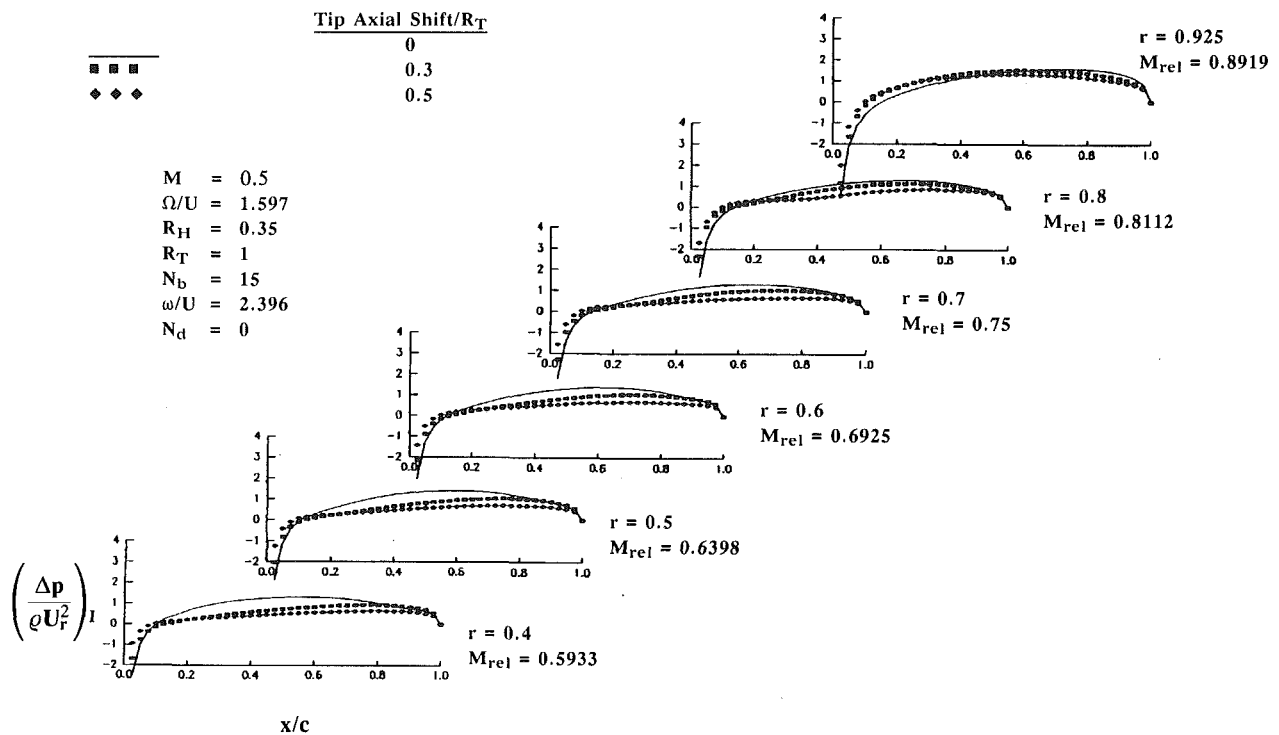


Fig. 14 Effect of linear backward sweep of cascade C blades on imaginary part of three-dimensional unsteady pressure distributions

sional radial flow interaction by the significant radial variation of the blade displacement amplitude.

Effect of Bending, Bowing, and Helical Sweep. To study the effect of blade bending (in the engine axis direction), bowing (in the circumferential direction), and sweeping (by sliding blade sections along the helix at each radial station), the Cascade C baseline blade configuration is bent axially, bowed (i.e., bent circumferentially), and swept and three-dimensional un-

steady aerodynamic analyses are carried out. Any of these blade deformations will introduce a nonzero helix number distribution $\sigma(r)$ along the blade span. As the blades are deformed, the pitching axis for each radial station still remains at its own leading edge in order to make a sensible airload comparison.

Axial Bending. In Fig. 11, the three-dimensional pressure jump distributions for the baseline Cascade C rotor are com-

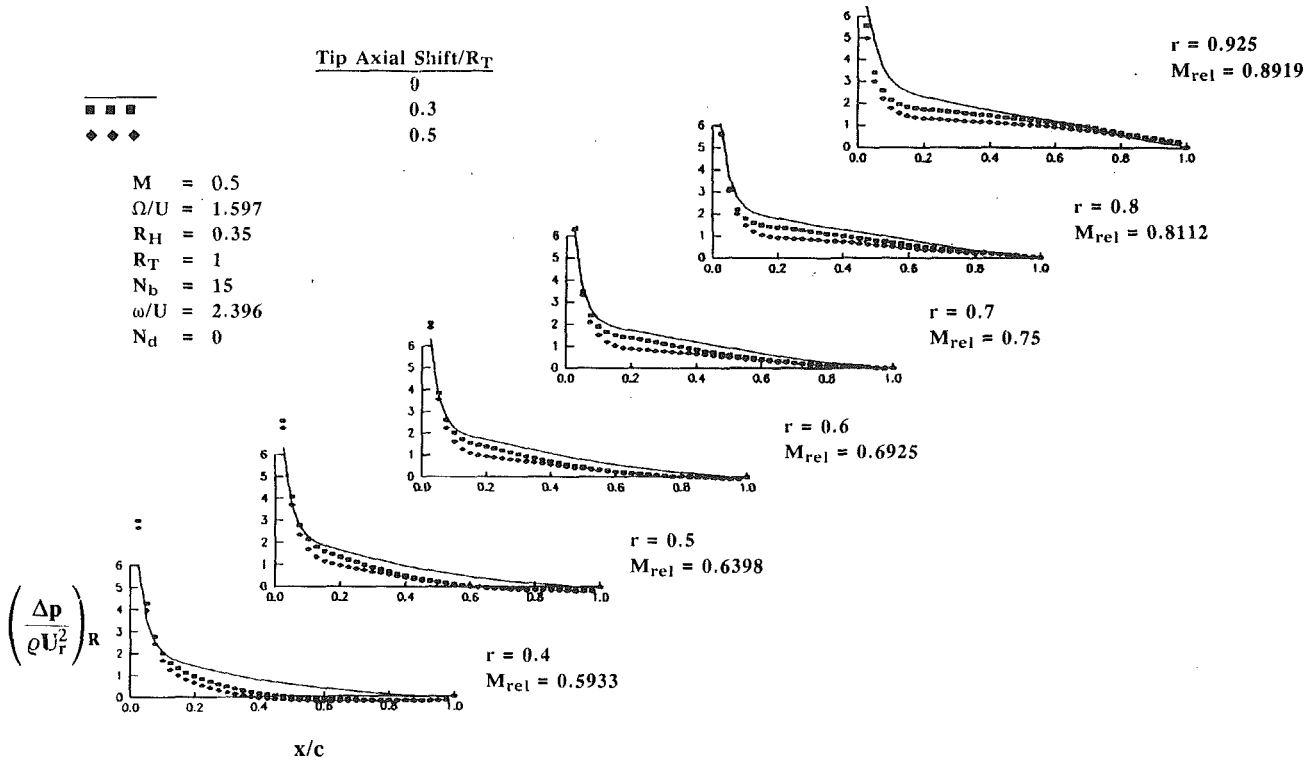


Fig. 15 Effect of linear forward sweep of cascade C blades on real part of three-dimensional unsteady pressure distributions

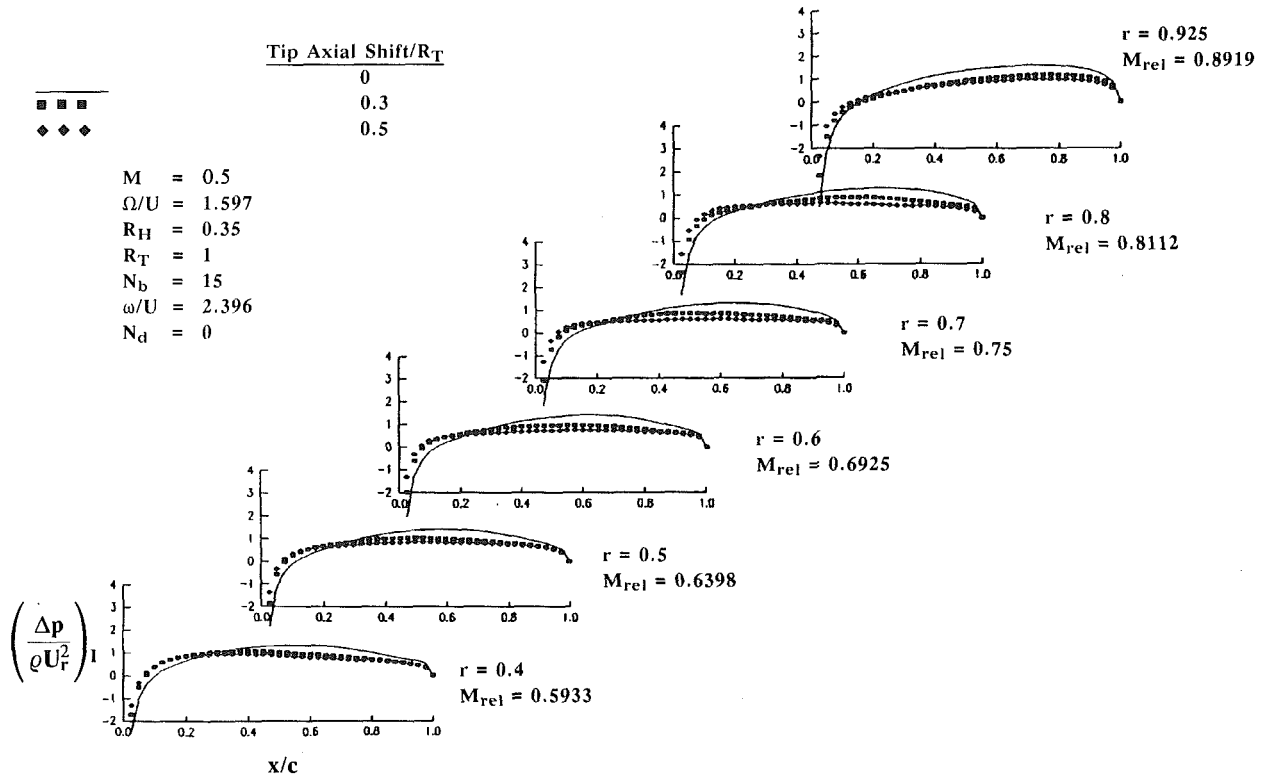


Fig. 16 Effect of linear forward sweep of cascade C blades on imaginary part of three-dimensional unsteady pressure distributions

pared with those for an axially bent rotor. The amount of axial bending is distributed linearly along the blade span with zero bending at the blade root and the maximum axial backward bending distance equal to 10 percent of the fan case radius. The majority of the unsteady airload distribution pattern shows an increase in its magnitude due to backward bending of the blades.

Bowing (i.e., Circumferential Bending). Figure 12 shows the comparison between the pressure jump distributions for the baseline Cascade C rotor and those for a circumferentially bowed rotor. The amount of circumferential bending is distributed linearly along the blade span with zero bowing at the blade root and a maximum circumferential angle movement of 9.15 degrees opposite to the direction of rotation at the

blade tip. The airloads are seen to increase for the outer span and decrease for the inner span due to the circumferential shift of the blades.

Sweep. The baseline Cascade C blades are swept by sliding the helical chord along the helix forward or backward at each radius. Blade sweeping defined in this manner maintains the zero helix number associated with the baseline blades and simply changes the leading edge and trailing edge locations of each blade section along the helix.

For blades with backward sweep, Figs. 13 and 14 show the real and imaginary parts of the pressure jump distributions, respectively. Two swept configurations are analyzed: One corresponds to an axial shift of 30 percent of the fan case radius, and another 50 percent of the fan case radius. Backward sweep is seen to reduce the airload in general. For blades with forward sweep, similar results are shown in Figs. 15 and 16.

Conclusions

An analytical method has been developed to compute subsonic unsteady pressure jump distributions on oscillating blades of an ducted engine fan. The method utilizes an aerodynamic kernel function that absorbed the fan hub and case boundary conditions and the interblade influences so that an integral equation that relates the potential jump across the lifting surface to the upwash distribution can be solved by discretizing only the blade and wake surfaces.

Representative results calculated for three standard cascade configurations are given covering zero to high frequency oscillations due to bending as well as torsional motion. One of the baseline cascade configurations is further deformed to allow the effect of blade axial bending, bowing (i.e., circumferential bending), and sweeping on unsteady airloads to be clearly observed.

The three-dimensional effect is generally important for low-aspect-ratio, swept blades for obvious reasons. For high-aspect-ratio blades, the three-dimensional effect is also important, because the radial variation of the vibration mode shape is in general large enough to trigger significant spanwise unsteady flow interactions that usually reduce the airload for the outer span and elevate the airload for the inner span sections.

Acknowledgments

This work is sponsored by Pratt and Whitney Division and United Technologies Research Center of the United Technologies Corporation. The author wishes to thank Gary R. Hilbert and Michael C. Romanowski of Pratt and Whitney Aircraft, and Professor Marc H. Williams of Purdue University for many stimulating discussions.

References

Busemann, A., 1952, "Theory of the Propeller in Compressible Flow," *Proceedings of the Third Midwestern Conference on Fluid Mechanics*, The University of Minnesota, pp. 267-286.

- Chi, R. M., 1980, "Unsteady Aerodynamics in Stalled Cascade and Stall Flutter Prediction," ASME Paper No. 80-C2/Aero-1.
- Chi, R. M., 1985, "Formulation of Three Dimensional Unsteady Aerodynamics Theory for Rotating Fan Blades," UTRC R85-152294-1.
- Chi, R. M., 1986, "Green's Function for Three Dimensional Unsteady Flow About Rotating Fan Blades," UTRC R86-152294-1.
- Chi, R. M., 1990a, "Three-Dimensional Subsonic Unsteady Lifting Surface Theory for Ducted Fan," UTRC R90-255135-1.
- Chi, R. M., 1990b, "Notes on Unsteady Aerodynamic Theory-Subsonic 3D Plane Wing," UTRC R90-152294-1.
- Chi, R. M., 1990c, "Kernel Function for Unsteady Aerodynamic Flow in a Ducted Fan," UTRC R90-255135-2.
- Chi, R. M., 1990d, "A Mode Expansion Technique for Unsteady Aerodynamic Applications," UTRC R90-255135-3.
- Das, A., 1984, "A Unified Approach for the Aerodynamics and Acoustics of Propellers in Forward Motion," in: *Aerodynamics and Acoustics of Propellers*, AGARD CP-366.
- Farassat, F., 1984a, "A New Aerodynamic Integral Equation Based on an Acoustic Formulation in the Time Domain," *AIAA J.*, pp. 1337-1340.
- Farassat, F., 1984b, "Theoretical Analysis of Linearized Acoustics and Aerodynamics of Advanced Supersonic Propellers," in: *Aerodynamics and Acoustics of Propellers*, AGARD CP-366.
- Hanson, D. B., 1982, "Compressible Lifting Surface Theory for Propeller Performance Calculation," AIAA Paper No. 82-0020.
- Hanson, D. B., 1983, "Compressible Helical Surface Theory for Propeller Aerodynamics and Noise," *AIAA J.*, Vol. 21, pp. 881-889.
- Homicz, G. F., and Lordi, J. A., 1981, "Three-Dimensional Theory for the Steady Loading on an Annular Blade Row," *AIAA J.*, Vol. 19, pp. 492-500.
- Kodama, H., and Namba, M., 1990, "Unsteady Lifting Surface Theory for a Rotating Cascade of Swept Blades," *ASME JOURNAL OF TURBOMACHINERY*, Vol. 112, pp. 411-417.
- Landahl, M. T., 1961, *Unsteady Transonic Flow*, Pergamon Press, London.
- Long, L. N., 1983a, "The Aerodynamics of Propellers and Rotors Using an Acoustic Formulation in the Time Domain," AIAA Paper No. 1821.
- Long, L. N., 1983b, "The Compressible Aerodynamics of Rotating Blades Based on an Acoustic Formulation," NASA TP 2197.
- Long, L. N., and Watts, G. A., 1984, "A General Theory of Arbitrary Motion Aerodynamics Using an Aeroacoustics Approach," in: *Aerodynamics and Acoustics of Propellers*, AGARD CP-366.
- Lordi, J. A., and Homicz, G. F., 1981, "Linearized Analysis of the Three-Dimensional Compressible Flow Through a Rotating Annular Blade Row," *Journal of Fluid Mechanics*, Vol. 103, pp. 413-442.
- McCune, J. E., 1958a, "A Three-Dimensional Theory of Axial Compressor Blade Rows—Application in Subsonic and Supersonic Flows," *Journal of Aerospace Sciences*, pp. 544-560.
- McCune, J. E., 1958b, "The Transonic Flow Field on an Axial Compressor Blade Row," *Journal of Aerospace Sciences*, pp. 616-626.
- McCune, J. E., 1972, "Lifting-line Theory for Subsonic Axial Compressor Rotors," MIT GTL Report No. 110.
- Namba, M., 1974, "Lifting Surface Theory for a Rotating Subsonic or Transonic Blade Row," ARC R.&M. No. 3740.
- Namba, M., 1977, "Three-Dimensional Analysis of Blade Forces and Sound Generation for an Annular Cascade in Distorted Flows," *J. of Sound and Vibration*, Vol. 50, No. 4, pp. 479-508.
- Namba, M., and Ishikawa, A., 1983, "Three-Dimensional Aerodynamic Characteristics of Oscillating Supersonic and Transonic Annular Cascades," *ASME Journal of Engineering for Power*, Vol. 105, pp. 138-146.
- Okurounmu, O., and McCune, J. E., 1970, "Three-Dimensional Vortex Theory of Axial Compressor Blade Rows at Subsonic and Transonic Speeds," *AIAA J.*, Vol. 8, No. 7, pp. 1275-1283.
- Okurounmu, O., and McCune, J. E., 1974, "Lifting Surface Theory of Axial Compressor Blade Rows: Part I—Subsonic Compressor; Part II—Transonic Compressor," *AIAA J.*, Vol. 12, No. 10, pp. 1363-1380.
- Runyan, H. L., 1973, "Unsteady Lifting Surface Theory Applied to a Propeller and Helicopter Rotor," Ph.D. Thesis, Loughborough University of Technology, United Kingdom.
- Williams, M. H., 1990, "An Unsteady Lifting Surface Method for Single Rotation Propellers," NASA CR-4302.
- Williams, M. H., Cho, J., and Dalton, W. N., 1990, "Unsteady Aerodynamic Analysis of Ducted Fans," to appear in *AIAA Journal of Propulsion and Power*.

Optical Measurements of Unducted Fan Flutter

A. P. Kurkov

O. Mehmed

NASA Lewis Research Center
Cleveland, OH 44135

The paper describes a nonintrusive optical method for measuring flutter vibrations in unducted fan or propeller rotors and provides detailed spectral results for two flutter modes of a scaled unducted fan. The measurements were obtained in a high-speed wind tunnel. A single-rotor and a dual-rotor counterrotating configuration of the model were tested; however, only the forward rotor of the counterrotating configuration fluttered. Conventional strain gages were used to obtain flutter frequency; optical data provided complete phase results and an indication of the flutter mode shape through the ratio of the leading- to trailing-edge flutter amplitudes near the blade tip. In the transonic regime the flutter exhibited some features that are usually associated with nonlinear vibrations. Experimental mode shape and frequencies were compared with calculated values that included centrifugal effects.

Introduction

Optical measurement of flutter vibrations (Nieberding and Pollack, 1977) has been used in turbo-machinery for a number of years. However, because this method requires the proximity of a wall next to the blade tips, it is unsuitable for unducted fans and propellers. To measure the steady-state deflections for these rotors, Kurkov (1988, 1990) applied another method in which a laser beam is directed across the rotational plane to a photodetector. As illustrated in Fig. 1, the laser and the detector are positioned remotely so that they do not interfere with the flow. As the beam is chopped by the rotor, a series of pulses are generated (Fig. 2). These pulses are indicative of the instantaneous positions of the blades.

The paper illustrates the use of this method to measure unsteady displacements during flutter of an unducted fan model installed in a high-speed wind tunnel. Because of the complexity of the flutter in the transonic region, additional information provided by the displacement data was essential for interpreting flutter modes.

Beyond the flutter instrumentation aspects, the paper presents new experimental data in the transonic flutter regime for a composite unducted fan model rotor. Particular attention is placed on reporting features that, in general, are associated with nonlinear vibrations, since the nonlinear aspects of flutter in the transonic region are of current interest. Bendiksen (1990) has presented some results obtained by a simultaneous solution of nonlinear aerodynamic and structural equations. The flutter mode arrived at by Bendiksen is essentially chordwise bending with the strong participation of the trailing edge.

Most of the results that are relevant for comparison with theoretical solutions are presented in the section entitled "Flutter Modes." The more detailed results presented in the section entitled "Flutter Spectra" illustrate some of the dynamic as-

pects of flutter as well as techniques used in the analysis. Therefore, the material in this section should also be of interest to the data analyst.

Following the usual practice, the performance and blade

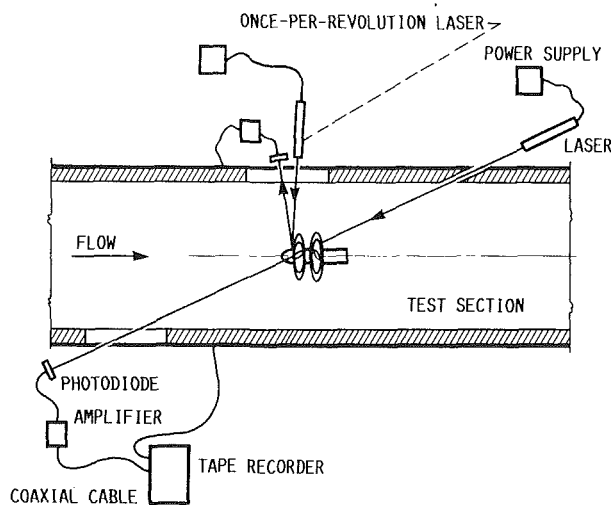


Fig. 1 Test schematic

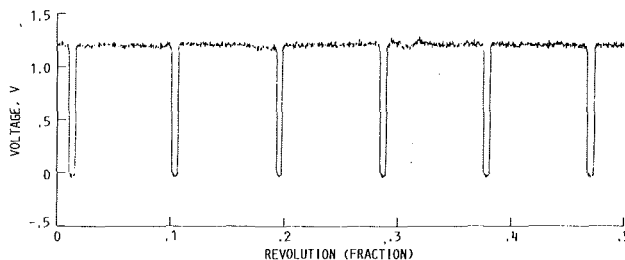


Fig. 2 Blade-tip pulses

Contributed by the International Gas Turbine Institute and presented at the 36th International Gas Turbine and Aeroengine Congress and Exposition, Orlando, Florida, June 3-6, 1991. Manuscript received at ASME Headquarters January 25, 1991. Paper No. 91-GT-19. Associate Technical Editor: L. A. Riekert.

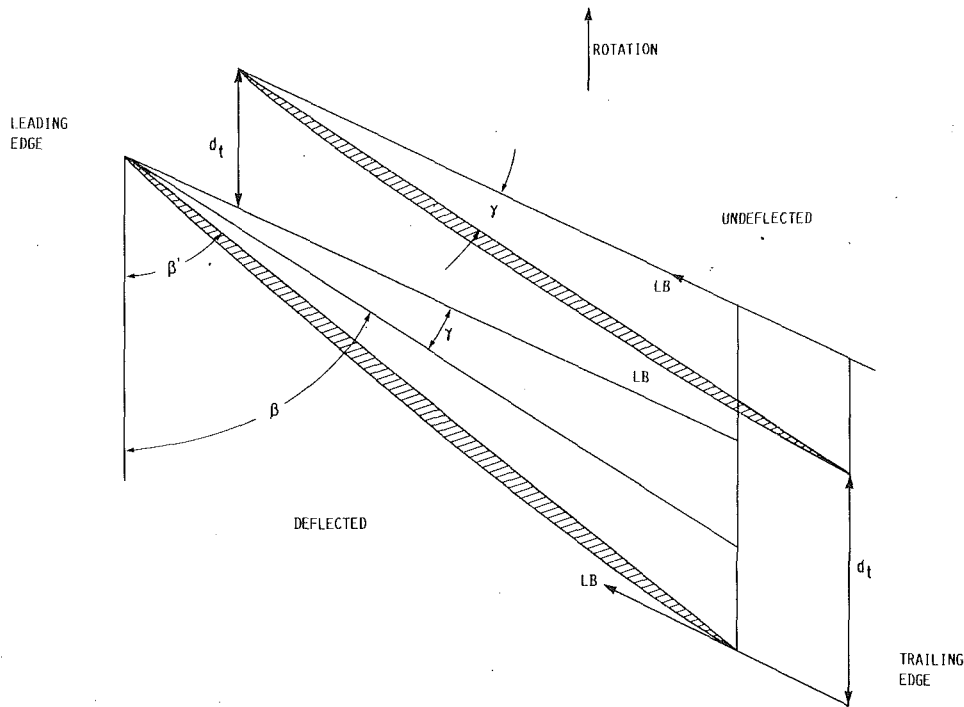


Fig. 3 Geometry of laser beam and blade section; d_t denotes measured deflection; γ denotes laser beam incidence; β' and β denote deflected and undeflected blade angles

element parameters in this report were calculated by using the free-stream conditions. However, for accurate comparison with theoretical results, these parameters should be adjusted for the axial flow acceleration due to the nacelle forebody. The experimental data of Podboy and Krupar (1989) obtained with the same nacelle and similar blades indicate that the axial velocity at the tip increased by about 6.5 percent of the free-stream velocity.

Experimental Measurements

The same equipment can be used to measure the steady-state deflections (Kurkov, 1988) and the flutter vibrations. The only difference is that the steady-state deflections remain essentially constant for every revolution, whereas vibratory deflections vary (excluding the integral engine-order vibrations). The steady-state component of the signal is obtained by averaging blade pulse times measured with respect to the once-per-revolution pulse over a number of revolutions (typically about 100). The dynamic pulse-displacement times are obtained by subtracting the averaged steady-state times from the original pulse times.

The geometry of deflection measurement in plane perpendicular to the blade pitch (Z) axis is given in Fig. 3. The coordinate system in this figure is fixed with respect to the undeflected blade, and therefore, the laser beam is rotated relative to the undeflected blade to depict the intersection of the beam and the deflected blade. The experimentally measured displacements are along the arc (centered with respect to the rotational axis) subtended by the vector d_t (Fig. 3). The geometric relationships for various degrees of approximations are given by Kurkov (1988). The relationships still hold for a single-degree-of-freedom flutter, provided that either the instantaneous dynamic deflection or the vibratory amplitude is substituted for the steady-state deflection.

In this paper deflections are left essentially in the same form as they are defined in the experiment. Therefore, for comparison with experimental data, the calculated displacements along the major axes are used to derive the displacements that

are equivalent to the experimentally measured displacements as shown in Fig. 3.

In the experiment only the forward rotor fluttered. Therefore, during the alignment of the laser beam it was necessary to bypass the rear rotor by tilting it slightly toward the axis. It was also desirable to intersect a blade with the laser beam in the plane approximately perpendicular to the pitch axis and to form some small positive incidence angle γ relative to the blade chord in the plane of intersection. These requirements could be satisfied provided that the blade-beam intersection occurred somewhat past the 12 o'clock position (facing the rotor). The beam intersection time was minimized by focusing the beam on the intersecting blade. Optical line filters were used to cut down the extraneous light. The silicon photodiode detector and the amplifier were manufactured by United Detector Technology, and the helium-neon laser by Aerotech.

The displacement data were recorded during the test on a magnetic tape by using a frequency-modulated wideband II magnetic recorder (Honeywell 101). The frequency bandwidth was 500 kHz. The desired real-time digitizing speed was achieved by reducing the tape speed on playback. A concurrent computer model 5450 was used to digitize and process the data.

Since the displacement data were digitized at a near-constant rate of 12,000 points per revolution, it was convenient to express absolute displacements in digitized units (i.e., in $1/12,000$ th of the revolution fraction). Similarly, in most cases it was convenient to express frequency in engine orders E , since in this way a clear distinction is made between the forced response and the self-excited vibrations.

Figure 4 illustrates the blade planform and the first three natural modes calculated for a stationary blade in a vacuum. The calculated frequencies are also given in the figure. The blade was designed by General Electric as one of the model blades (designated F21) for its unducted fan engine. It has a graphite/glass shell and a half-span titanium spar. Tip diameter is 61.8 cm and tip sweep angle is 45 deg. There were 13 blades on the forward and 10 on the aft rotor. More information on this and related blades and tests is available (Balan et al., 1988).

At the time of these tests there were three active strain gages

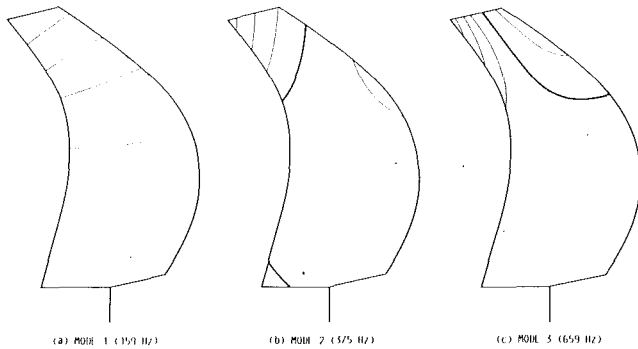


Fig. 4 Nonrotating blade mode shapes

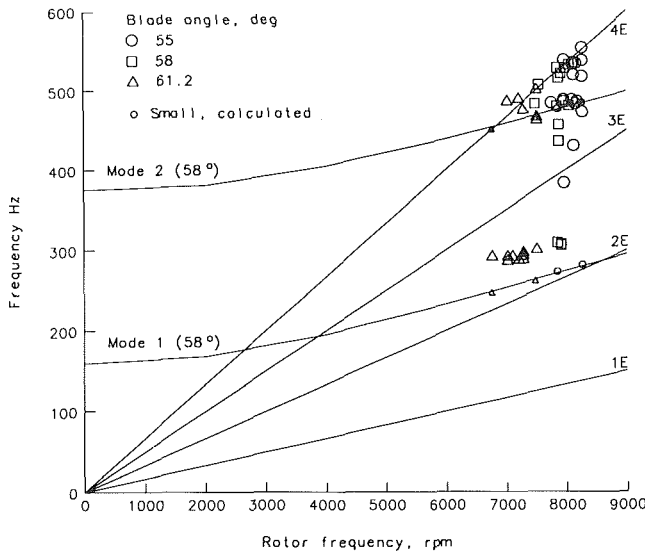


Fig. 5 Campbell diagram

on the forward rotor on three different blades (denoted as channels 4, 6, and 12). These gages were mounted near a blade tip and were sensitive to twist deformation and rather insensitive to bending.

Except for the windmill points, flutter was approached for a set wind tunnel Mach number by increasing rotational speed. For the windmill points flutter was approached by increasing the tunnel Mach number. These steps were reversed to get out of flutter. The shutdown was triggered automatically when the stress limit was exceeded, except for windmill points, when it was performed manually.

Flutter Modes

As already mentioned, there were two distinct flutter modes. During the preliminary analysis of the flutter data, it became apparent that in the higher frequency mode flutter occurred over a fairly wide frequency range. In order to examine the reason for this variation, the subsequent flutter points were selected so that they spanned the full observed frequency range. Some of the points selected for the detailed analysis were from the dual-rotor tests. As a rule, however, the data from the single-rotor tests were favored.

Figure 5 presents the Campbell diagram that includes all the data points discussed in this report; however, no distinction is made between the dual and the single-rotor tests. The frequencies for the first two modes were calculated for the blade setting angle of 58 deg. In order to illustrate variations in frequencies with the blade setting angle, two points for $\beta = 55$ deg and 61.2 deg were also included.

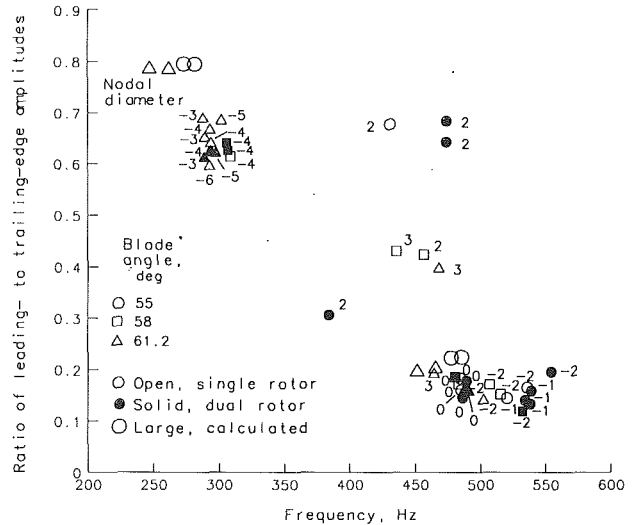


Fig. 6 Ratios of leading- to trailing-edge flutter amplitude and nodal diameters

The displacement spectral results were available for both the leading and trailing edges at a near-tip span. Consequently, by taking the ratio of the leading- to trailing-edge flutter amplitudes, an indication of the flutter mode shape could be obtained. This ratio was also calculated from the natural mode shape for the associated mode. The calculated natural mode shape included the centrifugal effects, but it did not include the effect of added mass due to air density or the modification of the deflected shape due to air loads.

In order to locate the two points properly in the finite element model that correspond to the intersection of the laser beam and the blade contour in the experiment, a similar procedure as for the steady-state deflections (Kurkov, 1988) was adopted. The deflected points were obtained by intersection of a line representing the laser beam and the deflected contours of the leading and trailing edges. Two deflected shapes were considered. The first one included only the centrifugal steady-state deflection. The second one included both the centrifugal and modal deflections represented by the vibratory amplitude. In order to approximate the experimental conditions the modal deflections were scaled so that they were small relative to the centrifugal. The simulated experimental modal amplitudes were obtained as the difference between the tangential displacements (d_i in Fig. 3) associated with the second and first deflection calculations. (Note that both deflection calculations were evaluated relative to the undeflected finite element blade contour.) Because most of the steady-state deflection for these blades was caused by centrifugal forces, and because the agreement between the calculated and measured deflections for the particular blade was good (Kurkov, 1988), this procedure should give a good representation of the equivalent experimental leading- to trailing-edge amplitude ratio.

Modal ratio results are presented in Fig. 6. The calculated results are shown by the large open symbols (in Fig. 5 they were shown by small open symbols). They were obtained for the two extreme blade setting angles β of 55 deg and 61.2 deg and for the rotational speeds that span the experimental range for the associated blade angles. Thus they illustrate calculated variation in frequencies and modal ratio for the experimental range of rotational speeds and blade angles. Also noted in the figure are the predominant nodal diameters associated with each point. They were obtained from the overall displacement spectra as described in the next section.

The cluster of points near the first natural frequency appears to be associated with the single-degree-of-freedom flutter mode, since both the frequency and the mode shape deviate by a

relatively small amount from the calculated values for the first mode. This differs from previous experience with another advanced propfan composite model, where the experimental flutter frequencies were between the first two natural modes (Mehmed and Kaza, 1986; Kaza et al., 1987). Note that the second mode for these blades was mainly torsion, rather than second bending as for the current blades. The experimental flutter frequency for a composite blade reported by Crawley and Ducharme (1989) was also between the first two in-vacuum natural modes; however, the second mode for this blade was second bending.

Predominant nodal diameters for this group of points in Fig. 6 range from -3 to -6 . The slight shift in frequencies is of the order of the variation caused by the change in the rotational speed or the blade setting angle β , as shown by the large open symbols. The solid symbols correspond to the dual-rotor configuration.

Although most of the plotted points in Fig. 6 are associated with the primary response (or the dominant peak), some points associated with the secondary response (or minor peaks) were also plotted. Therefore, this figure also includes some points for which the stress level was relatively low, of the order of 2 kN/cm^2 rather than the 4 to 6 kN/cm^2 for most of the flutter points. This permitted a more complete documentation of all the modes and frequencies and revealed some of the changes in response with deeper penetration into the flutter region. (Note that the current flutter theories can only deal with flutter inception.)

The second group of points in Fig. 6 is clustered to the right and slightly below the second natural mode. This mode has a nodal line near the tip as shown in Fig. 4. As a result, the displacement of the trailing edge is much higher than that of the leading edge. The phase angle in both the experimental and calculated displacements is such that the center of rotation is in front of the leading edge. The spread in frequency for this mode is larger than can be attributed to the speed or the blade setting angle variation. The frequency spread is particularly large for the -2 nodal diameter. It is 64 Hz , which is about twice what would be expected from a calculated in-vacuum frequency variation for the range of experimental variables. Note, however, that in the experimental variables circles fall to the right of triangles, Fig. 6, as predicted by the in-vacuum modes. The mode shape for all points is reasonably close to the calculated shape, particularly taking into account the fact that the displacement amplitude at the leading edge is fairly small and, therefore, may not be accurate.

The response away from the immediate vicinity of the two natural frequencies is, in general, secondary and of low stress or displacement amplitude level. However, it does illustrate the rather wide possible range of nonintegral-order, self-excited vibrations in the transonic flow regime. These points correspond to positive nodal diameters of 2 and 3 . Only one of these points, the 3 -nodal-diameter, $\beta = 61.2 \text{ deg}$ point with the amplitude ratio of 0.2 , is near the natural mode. (Note that without the knowledge of amplitude ratio, the group of points with positive nodal diameters would not stand out from the zero and negative nodal diameter points clustered around the second natural mode.)

The frequency spread of the higher flutter mode was examined further by plotting the tip relative Mach numbers for these points in terms of frequency in Fig. 7 and in terms of advance ratio J in Fig. 8. (Advance ratio J is defined as the ratio of the free-stream axial velocity and a product of the rotational frequency n and the tip diameter D .) Below a relative Mach number of about 0.98 , the predominant response is the zero-nodal-diameter mode with some secondary response at the -1 mode at frequencies about 50 Hz higher. Above the relative Mach number of 0.98 , the -2 -nodal-diameter mode appears at the high end of the frequency range. The frequency gap evident in Fig. 7 at low relative Mach numbers is ultimately

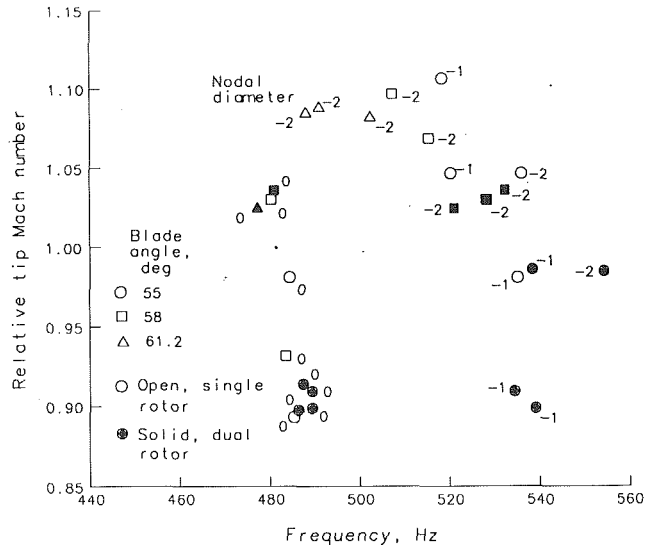


Fig. 7 Relative tip Mach numbers and nodal diameters for second flutter mode

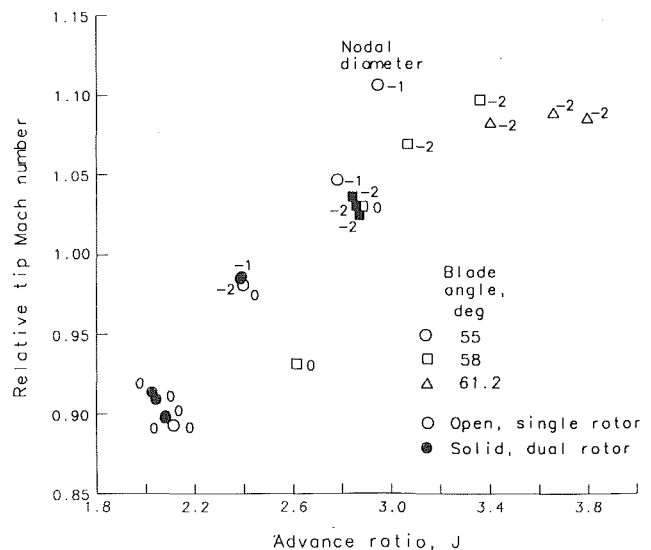


Fig. 8 Second-flutter-mode stability boundary

closed by the -2 -nodal-diameter points at the high limit of the relative Mach number. Despite this frequency spread for different nodal diameters and relative Mach numbers, the flutter data correlate fairly well in Fig. 8, where the independent variable is the advance ratio J , which is essentially a measure of the relative flow angle. For a given value of J , the higher value of the blade setting angle corresponds to a higher incidence. The two points that seem to deviate from the others illustrate the incidence effect on the flutter. The square, corresponding to a blade setting angle of 58 deg at $J = 2.6$, indicates a drop in the flutter boundary because of the high incidence (it is the low end of J for this value of β), and the circle, corresponding to a blade setting angle of 55 deg at $J = 2.94$, indicates a rise in the flutter boundary because of the low incidence (it is the high end of J for this β).

During the spectral analysis of the displacement data, it was noticed that for a number of flutter points associated with the higher flutter frequencies the flutter frequency fell close to a four-engine-order response. However, none of these points have the -4 -nodal-diameter phase relationship that is necessary for the $4E$ forced response mode. In Fig. 9 the data from Fig. 8 are plotted in terms of engine-order frequency. However,

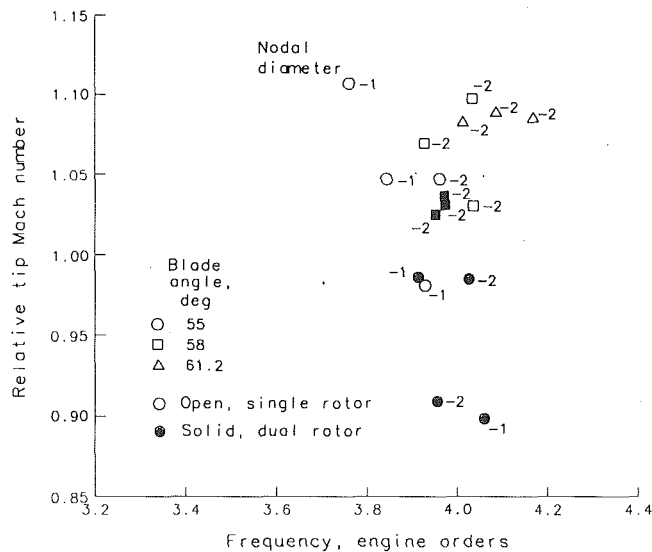


Fig. 9 High-frequency branch of second flutter mode expressed in engine orders

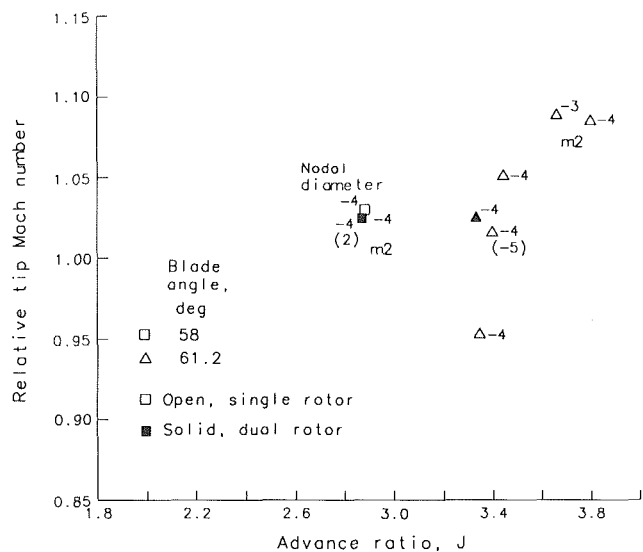


Fig. 10 First-flutter-mode stability boundary

since the 0-nodal-diameter points are clustered in a narrow frequency range in Fig. 8, they were not included in Fig. 9. (They would scatter in the range from 3.55 E to 3.88 E in Fig. 9.) Except for the two highest Mach number points (which were the windmill points) for β of 55 deg and 61.2 deg with nodal diameters of -1 and -2 , respectively, and the -1 -nodal-diameter, $\beta = 55$ deg point at 3.84 E , all the points cluster within 0.1 E of the 4 E frequency. However, on the whole, the frequency spread for the -1 -nodal-diameter, $\beta = 55$ deg points in Fig. 9, is not narrower than that in Fig. 7. It appears, therefore, that the response for this mode may be unrelated to the 4 E excitation.

The two right-most points in Fig. 9 for $\beta = 61.2$ deg and -2 nodal diameters, which are farthest from the 4 E frequency, are reasonably close to the lower-frequency (about 485 Hz), 0-nodal-diameter cluster of points in Fig. 7. However, the remaining -2 -nodal-diameter points, which are associated with the higher frequency range in Fig. 7, are all closely clustered about the 4 E line in Fig. 9. This suggests a possible interaction between the -2 -nodal-diameter mode and the 4 E response, which is only possible for nonlinear vibrations. This should

also warrant some caution when interpreting flutter frequency close to an observed integral engine-order response.

The stability boundary for the first flutter mode is presented in Fig. 10. For $\beta = 58$ deg, and for the highest Mach number point for $\beta = 61.2$ deg, the response in the first flutter mode was secondary to the response in the second flutter mode. For the point corresponding to the highest J ($\beta = 61.2$ deg windmill), the spontaneous amplitude growth was simultaneous for both flutter modes. The part of the flutter boundary formed by these points is marked by $m2$ (i.e., second mode) in Fig. 10. Flutter strictly associated with the first mode occurred in a narrow range of J . As for second-mode flutter, the effect of incidence was destabilizing. A large increase in mistuning was noticed for the lowest Mach number (or the highest incidence) points.

The reduced frequency based on the semichord at 80 percent of the span was in the range 0.2 to 0.22 for the first flutter mode and 0.34 to 0.41 for the second.

Flutter Spectra

The spectral analysis of data obtained in a stationary reference frame, such as the flutter displacement data, was documented previously (Kurkov, 1984), and hence, only a brief overview is given here. One of the features of the displacement data is that the sampling rate cannot be varied arbitrarily as it is fixed by the rotational speed and the number of blades. Since the flutter frequency is usually greater than the rotational frequency, if each individual blade is analyzed separately, the resulting spectra will be folded several times in the region to the left of $1/2 E$ frequency. On the other hand, if all the blades are included as they are sampled, the sampling rate per revolution is then equal to the number of blades, and the folding frequency, expressed in engine orders, is increased to half the number of blades. This sampling method is therefore the choice method in most cases and was used in this study.

The other feature of the displacement spectra is that the observed frequency associated with flutter is shifted away from the true flutter frequency by an exact multiple of engine orders. This shift, expressed in engine orders, is equal to the nodal diameter wave of the flutter mode. The shift is to the right for positive nodal diameters and to the left for negative.

The spectral analysis of the displacement data was optimized by selecting a nearly integral number of cycles in the time domain. This was possible because of the use of Singleton's (1969) algorithm. For the most part, no such optimization was carried out for the strain gage spectra. In order to facilitate the comparison with the displacement spectra, only the low end of the strain gage spectra was displayed.

In this test, the frequency was determined from the strain gage spectra. With the frequency known, the displacement spectra yielded the nodal diameters associated with the flutter mode. Several nodal diameters associated with a single flutter frequency signify mistuning (Whitehead, 1966). The flutter amplitude and phase distribution around the rotor in this case are nonuniform and must be obtained by superposition of several nodal diameter modes.

Note that the integral order response cannot be detected in the displacement spectra because of the nature of the sampling process. Hence all the responses in these spectra, in the absence of any sources, are associated with self-excited vibrations.

The next several figures illustrate the flutter history for the point in Fig. 7 with a frequency of 502.3 Hz, a relative Mach number of 1.081, and $\beta = 61.2$ deg. The strain gage and displacement spectra of fully developed flutter corresponding to 7512 rpm and a tunnel Mach number of 0.8 are given in Fig. 11 and 12. In order to illustrate the difference in the flutter displacement amplitudes at the leading and trailing edges, both spectra are plotted in Fig. 11. The stress in Fig. 12 was normalized with respect to the highest peak, 7.14 kN/cm² (dashed

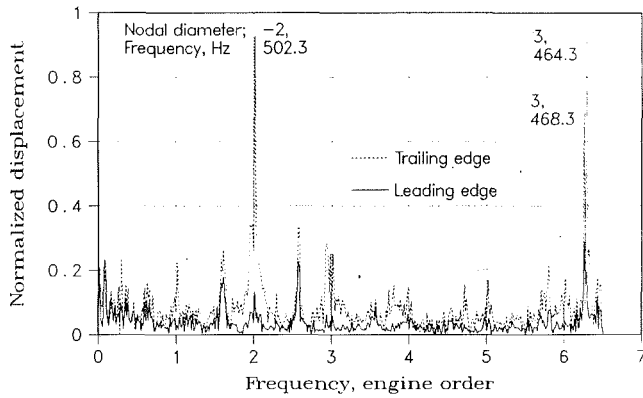


Fig. 11 Displacement spectra at 7512 rpm: blade setting angle, β , 61.2 deg; Mach 0.8; normalization constant, 6.96/12,000 revolution

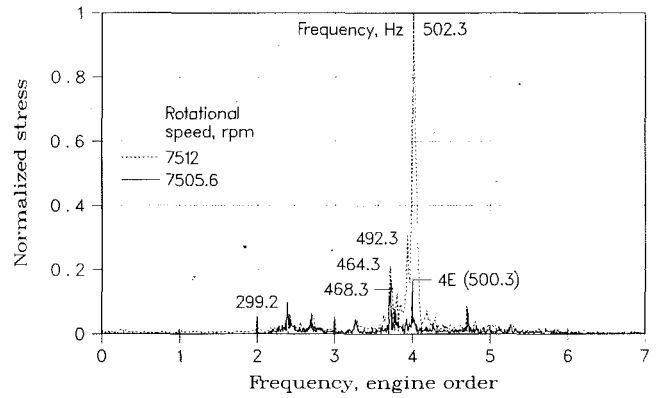


Fig. 14 Blade-tip stress spectra at 7512 and 7505.6 rpm: blade setting angle, β , 61.2 deg; Mach 0.8; normalization stress, 4.84 kN/cm² (channel 4)

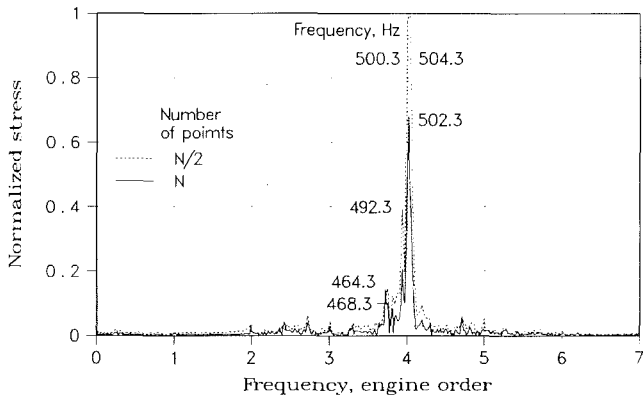


Fig. 12 Blade-tip stress spectra at 7512 rpm: blade setting angle, β , 61.2 deg; Mach 0.8; normalization stress, 7.14 kN/cm² (channel 4)

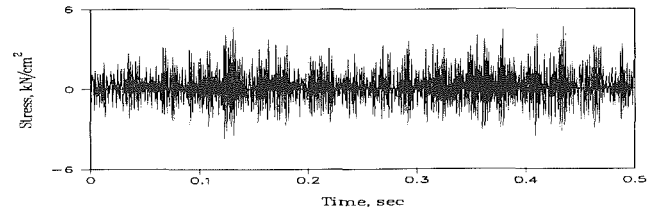


Fig. 15 Blade-tip stress (channel 6) at 7505.6 rpm: blade setting angle, β , 61.2 deg; Mach 0.8

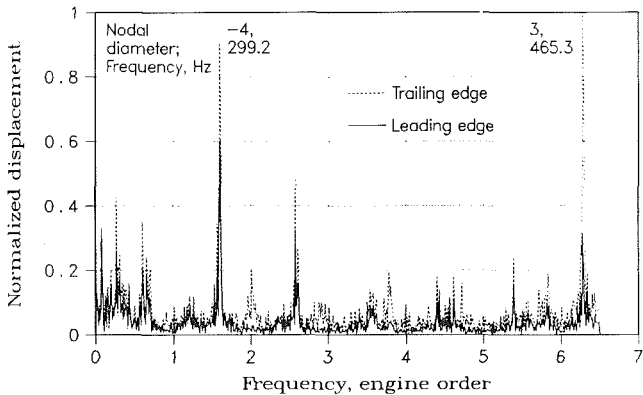


Fig. 13 Displacement spectra at 7505.6 rpm: blade setting angle, β , 61.2 deg; Mach 0.8; normalization constant, 5.368/12,000 revolution

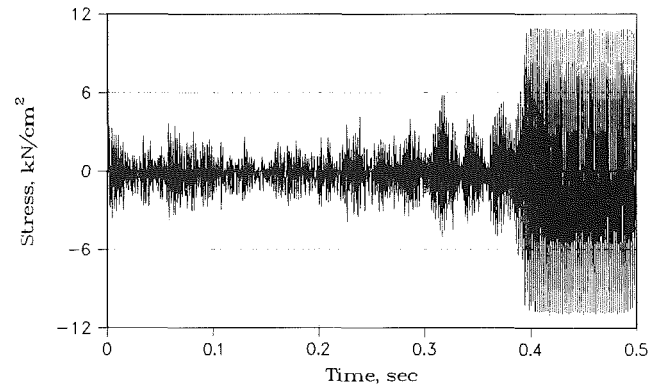


Fig. 16 Blade-tip stress (channel 6) at 7512 rpm, showing spontaneous flutter (beyond 0.4 sec signal is clipped): blade setting angle, β , 61.2 deg; Mach 0.8

line). Unless stated otherwise, when referring to Fig. 12 the solid curve corresponding to N ($N = 8192$) points is implied.

The flutter peak at 4.012 E or 502.3 Hz in the strain gage spectrum (Fig. 12) is shifted by 2 E to the left in the displacement spectrum (Fig. 11). Such a shift implied (Kurkov, 1984) that the mode is -2 nodal diameters. The two peaks in Fig. 11 at 6.26 and 6.29 E correspond to 3.74 and 3.71 E (or 468.3 and 464.3 Hz) peaks in Fig. 12. The fact that the fractional parts of the corresponding engine-order frequencies in these two figures add up to 1 indicates that the two peaks in the displacement spectrum are folded about 6.5 E (or one-half the number of samples per revolution). Taking into account folding, the frequency shift for these two peaks relative to the strain gage spectrum is 3 E and, therefore, they correspond to 3 nodal diameters. The strain gages are less sensitive to these

modes than the displacements (Fig. 11) compared with the 502.3 Hz mode. In fact, if the displacement data were not available, these modes would probably be overlooked.

Figure 13 presents the displacement spectrum obtained for a slightly lower rotational speed of 7505.6 rpm. (The tunnel Mach number was 0.8, the same as for Figs. 11 and 12.) The corresponding strain gage spectrum is plotted as a solid line in Fig. 14, superimposed on the 7512-rpm spectrum (dashed line). The 4.012 E , 502.3-Hz mode could not be detected in the strain gage spectrum in Fig. 14. Instead, there was a noticeable response at 4 E frequency and nonintegral responses at 2.39 E and 3.72 E corresponding to frequencies of 299.2 Hz and 465.2 Hz (essentially overlapping the 464.3-Hz peak). The two associated peaks in the displacement spectra (Fig. 13) are at 6.28 E and 1.61 E . They are folded about 6.5 E and 0 E , respectively, and correspond to nodal diameters of 3 and -4 . As expected, the response associated with 4 E frequency in the strain gage spectrum is absent in Fig. 13. (Because of the -4 -nodal-diameter phase required by the 4 E forced excitation, this response would be expected at 0 E .)

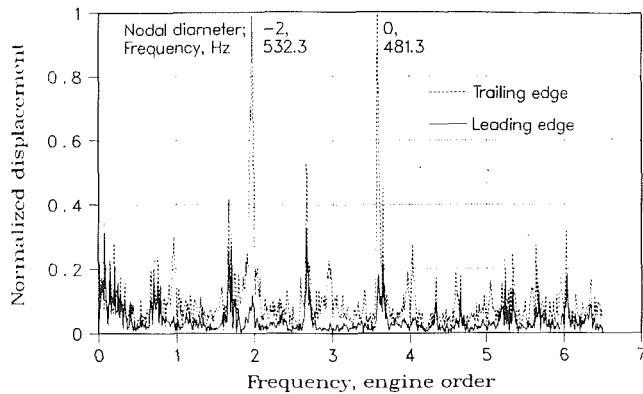


Fig. 17 Dual-rotor displacement spectra: blade setting angles, β , 58.1 deg (forward) and 58.6 deg (aft); Mach 0.7; rotational speeds, 8052.5 rpm (forward) and 6397 rpm (aft)

The raw stress levels at these two rotational speed are illustrated in Figs. 15 and 16. The signal was clipped beyond 0.4 s in the last figure because the tape recorder amplifier saturated. The analysis did not include the interval beyond the clipping point. (Even if the signals were not clipped, it would probably not be wise to include any appreciable portion of the high-amplitude region, as it is uncertain at which point the autosutdown started to affect the flutter amplitude.)

In order to indicate the frequency content during the spontaneous growth period for this flutter point, an additional stress spectrum was obtained covering only the second half of the time period that is associated with the first spectrum. This resulted in half the resolution of the previous spectrum but gave more weight to the higher stress data sampled near the end of the interval. The two spectra are compared in Fig. 12. The peak response for the second ($N/2$) spectrum is split evenly between the two frequency lines. By using Braun's interpolation rule (Kurkov, 1984) we can conclude that the frequency for this sampling period is centered about 502.3 Hz and that the true amplitude is about 1.4 times higher than the shown peak height. On the other hand, the flutter peak associated essentially with 464.3 Hz ($3.71 E$) remained the same, and hence this mode did not participate in the spontaneous growth. It appears that the frequency band associated with the growth of the stress extends about $0.2 E$ on either side of the $4 E$ frequency.

Another example that includes spontaneous flutter growth is given in Figs. 17 and 18. For this point both rotors were installed. The rotational speeds for the forward and aft rotors were 8052.5 and 6397 rpm, respectively, and the corresponding blade setting angles were 58.1 deg and 58.6 deg. The tunnel Mach number was 0.7 and the relative tip Mach number was 1.033. Again, the time domain for spectral analysis extended up to the instant when the strain gage signal was clipped. The peaks at $3.97 E$ and $3.58 E$ (or 532.3 and 481.3 Hz) in Fig. 18 correspond to -2 and 0 nodal diameters, respectively (Fig. 17). From the leading- and trailing-edge spectra in Fig. 17, it follows that the mode shapes associated with these two peaks are reasonably close.

In order to determine which of the two modes is responsible for the spontaneous amplitude growth, similarly as before, the spectral analysis was repeated including only the last $N/4$ fraction of the original N -point time domain ($N = 8192$). Comparison of the spectra in Fig. 18 shows that the $3.97 E$ mode and the region of about $0.2 E$ on either side of it experienced growth, whereas the $3.59 E$ mode was virtually unaffected.

The spontaneous growth of flutter amplitude was noticed only for -1 and -2 nodal diameters. For the -1 nodal diameter, the additional requirement is that the relative tip Mach number be higher than 1. (No points of significant stress level

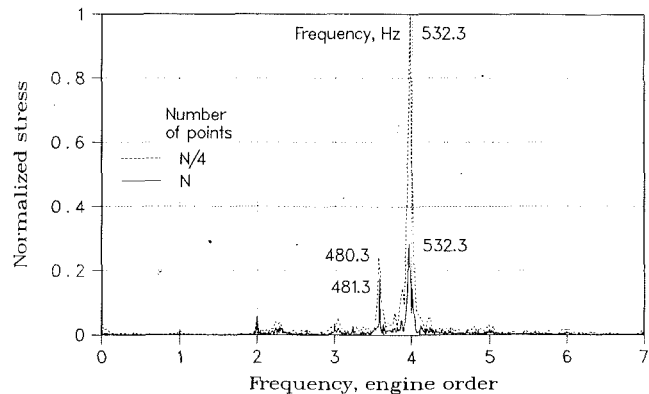


Fig. 18 Dual-rotor stress spectra (channel 12): blade setting angles, β , 58.1 deg (forward) and 58.6 deg (aft); Mach 0.7 rotational speeds, 8052.5 rpm (forward) and 6397 rpm (aft)

occurred below this Mach number of -2 nodal diameters.) For the -2 -nodal-diameter mode, rapid spontaneous flutter growth occurred for the five points closest to the $4 E$ frequency (Fig. 9), the two dual-rotor $\beta = 58$ deg points, the two single-rotor $\beta = 58$ deg points, and the one $\beta = 61.2$ deg point. The flutter growth was more gradual for the two $\beta = 61.2$ deg points farther from $4 E$.

For the remaining flutter points, no spontaneous amplitude growth was encountered up to about the 6 -kN/cm² level, when the test would usually terminate. (On a few occasions, however, the test was terminated at a lower stress level.) Regardless of whether or not spontaneous growth was observed, corresponding to each flutter point there was always a region of a low-stress-level response with one or several well-established traveling waves that could be observed in the displacement spectrum and could be maintained indefinitely. It appears, therefore, that a limit cycle sets in virtually at the flutter inception and that the observed rapid spontaneous growth is a transition to a higher amplitude limit cycle (provided that the blade does not fail). This suggests that nonlinearities have a role, not only in limiting the amplitude, but also in its growth.

Because only the low ends of the strain gage spectra were displayed in the figures, the higher harmonics fell beyond the displayed range of frequencies. However, these harmonics were clearly visible in all the linear spectra. At high stress level for the second flutter mode, the second harmonic was observed to be about one-third of the first. The stress wave shape was somewhat triangular. The second harmonic in the displacement spectra was much less significant but was observed in some spectra at twice the nodal diameter of the first.

Space limitations do not allow presentation of spectral results for all points; however, the two flutter points for which the detailed results were presented were selected to illustrate some of the more complicated features associated with the particular flutter mode, as well as to illustrate the method of analysis to deal with these complexities.

Concluding Remarks

Flutter blade vibrations at the near-tip span were successfully measured and monitored during a wind tunnel test of an unducted fan model by an optical method. The method relies upon the chopping of the laser beam by the blades rather than upon the reflection of a light beam by the blade tips. The traveling-wave nodal diameter modes were determined from the overall displacement spectra given the frequency, which was measured by strain gages. Because of the presence of mistuning, and because of the incomplete strain gage coverage of the rotor blades, this information would have been difficult, if not impossible, to obtain from the strain gage data alone.

Two distinct flutter modes were present. One was associated with the first natural mode and the other with the second. An indication of a flutter mode shape was obtained from the displacement data as the ratio of the leading- to trailing-edge flutter amplitudes. For each mode this ratio was in the neighborhood of the corresponding calculated value obtained from a finite element code that accounted only for centrifugal loads. For both modes, however, the experimentally determined amplitude ratios were lower and frequencies were somewhat higher than the calculated values. The frequency spread for the first flutter mode for the range of nodal diameters encountered in the test was relatively small; however, it was rather large for the second flutter mode, particularly for the -2 -nodal-diameter group, which also occurred at a high relative Mach number. For this traveling-wave mode, most flutter points occurred close to the $4E$ frequency. Past a certain flutter amplitude level, rapid spontaneous amplitude growth was observed for these points. In addition to the well-defined flutter frequency peak, the amplitude growth was also evident in a frequency band of about $0.2E$ on either side of $4E$. The $4E$ forced response was evident in the strain gage spectra away from the flutter region. Its source is unknown. For the high tip relative Mach numbers, spontaneous growth was also observed for the -1 -nodal-diameter group. The second-flutter-mode points corresponding to the zero nodal diameter occurred at the lower relative Mach numbers and were all close to the second natural frequency.

Some evidence of secondary response at nonintegral engine orders was noticed and associated with the positive interblade phase angles at frequencies that were, in general, close to the second natural mode but with a much higher leading- to trail-

ing-edge amplitude ratio. This ratio was essential in sorting out these points.

For both flutter modes, high incidence was found to be destabilizing.

References

- Balan, C., Sullivan, T., Frost, R., Hoff, G., Janardan, B., and Whitfield, C., 1988, "Modern Counterrotating Blade Concepts Performance Testing in NASA Wind Tunnels," Report GE TM87-528, NASA Contract NAS3-24080.
- Bendiksen, O. O., 1990, "Aeroelastic Problems in Turbomachines," AIAA Paper No. 90-1157-CP.
- Crawley, E. P., and Ducharme, E. H., 1990, "Parametric Trends in the Flutter of Advanced Turboprops," ASME JOURNAL OF TURBOMACHINERY, Vol. 112, pp. 741-750.
- Kaza, K. R. V., Mehmed, O., Narayanan, G. V., and Murthy, D. V., 1987, "Analytical Flutter Investigation of a Composite Propfan Model," NASA TM-88944; also Paper No. AIAA-87-0738.
- Kurkov, A. P. 1984, "Formulation of Blade-Flutter Spectral Analyses in Stationary Reference Frame," NASA TP-2296.
- Kurkov, A. P., 1988, "Optical Measurement of Propeller Blade Deflection," NASA TP-2841.
- Kurkov, A. P., 1990, "Optical Measurement of Unducted Fan Blade Deflections," ASME JOURNAL OF TURBOMACHINERY, Vol. 112, pp. 751-758.
- Mehmed, O., and Kaza, K. R. V., 1986, "Experimental Classical Flutter Results of a Composite Advanced Turboprop Model," NASA TM-88792.
- Nieberding, W. C., and Pollack, J. L., 1977, "Optical Detection of Blade Flutter in YF-100 Turbofan Engine," ASME Paper No. 77-GT-66; NASA TM X-73573.
- Podboy, G. G., and Krupar, M. J., 1989, "Laser Velocimeter Measurement of the Flow Field Generated by an Advanced Counterrotating Propeller," AIAA Paper No. 89-0434.
- Singleton, R. C., 1969, "An Algorithm for Computing the Mixed Radix Fourier Transform," *IEEE Transactions, Audio and Electroacoustics*, Vol. AU-17, No. 2, pp. 93-103.
- Whitehead, D. S., 1966, "Torsional Flutter of Unstalled Cascade Blades at Zero Deflections," Report ARC-R&M-3429, British Aeronautical Research Council, London, United Kingdom.

S. R. Manwaring¹

S. Fleeter

Thermal Sciences and Propulsion Center,
School of Mechanical Engineering,
Purdue University,
West Lafayette, IN 47907

Rotor Blade Unsteady Aerodynamic Gust Response to Inlet Guide Vane Wakes

A series of experiments is performed in an extensively instrumented axial flow research compressor to investigate the fundamental flow physics of wake-generated periodic rotor blade row unsteady aerodynamics at realistic values of the reduced frequency. Unique unsteady data are obtained that describe the fundamental unsteady aerodynamic gust interaction phenomena on the first-stage rotor blades of a research axial flow compressor generated by the wakes from the inlet guide vanes. In these experiments, the effects of steady blade aerodynamic loading and the aerodynamic forcing function, including both the transverse and chordwise gust components, and the amplitude of the gusts, are investigated and quantified.

Introduction

Periodic aerodynamic excitations generate unsteady aerodynamic forces and moments on turbomachinery blading. At the resonance conditions where the aerodynamic excitation frequency matches a blade natural frequency, catastrophic vibrational responses of the blading may occur. In the design process, Campbell diagrams are utilized to predict the occurrence of the resonant conditions in the operating range of the blade row. Unfortunately, accurate predictions of the amplitude of the blade vibration at these resonances cannot currently be made due to the inability of mathematical models to predict the unsteady aerodynamics accurately, i.e., the aerodynamic forcing function to the blade row and the resulting unsteady aerodynamics acting on the blading. As a result, empirical correlations are currently used to indicate the blade row response to an excitation, with varying degrees of success.

On a first principles basis, forced response unsteady aerodynamics are analyzed by first defining the forcing function in terms of harmonics. The periodic response of an airfoil row to each harmonic is then assumed to be comprised of two components. One is due to the harmonic components of the unsteady aerodynamic forcing function being swept past the nonresponding airfoil row, termed the streamwise and transverse gust responses. The second, the self-induced unsteady aerodynamics, arises when a vibrational response of the airfoil row is generated.

The gust and motion-induced unsteady aerodynamic models involve many physical and numerical assumptions. Therefore, experimental modeling of the fundamental distortion and wake-generated blade row periodic unsteady aerodynamic response,

including both the forcing function and the resulting blade row unsteady aerodynamics, is needed for validation and enhancement of theoretical and numerical models.

Unsteady aerodynamic gust experiments of direct interest to turbomachines have been performed in low-speed research compressors. Fleeter et al. (1978, 1980) investigated the effects of airfoil camber and rotor-stator axial spacing on the unsteady aerodynamics of a stator vane row of a single-stage low-speed research compressor. Capece et al. (1986) and Capece and Fleeter (1987) performed measurements in a three-stage low-speed research compressor to investigate the effect of steady airfoil loading and detailed aerodynamic forcing function waveshape on the unsteady aerodynamic response of a stator vane row. Gallus et al. (1980) performed measurements at the midspan of a low camber vane of a single-stage axial flow compressor. The unsteady lift coefficients corresponding to the first five harmonics of rotor blade wake passing were measured with five transducers embedded in each vane surface.

Gust experiments performed in rotor blade rows include the following. With regard to inlet flow distortions, O'Brien et al. (1980) utilized six dynamic pressure transducers embedded on each rotor blade surface to measure the unsteady aerodynamic response to a distorted inlet flow field. However, the periodic rotor blade row inlet flow field was not measured and, thus, the unsteady aerodynamic gust forcing function was not quantified. Hardin et al. (1987) measured low reduced frequency oscillating airfoil aerodynamics on the rotor of a single-stage compressor and also stated that they performed similar distortion experiments, although the results were not presented.

Manwaring and Fleeter (1989, 1991) experimentally investigated the unsteady aerodynamic rotor blade row gust response generated by low reduced frequency inlet distortions and wake type disturbances. The major advantage of rotor-based unsteady gust experiments over stationary blade row experiments is that the unsteady aerodynamic forcing function is located in the stationary reference frame. This enables a

¹Current address: Engineer, Aerodynamics Research Laboratory, General Electric Aircraft Engines, Cincinnati, OH.

Contributed by the International Gas Turbine Institute and presented at the 36th International Gas Turbine and Aeroengine Congress and Exposition, Orlando, Florida, June 3-6, 1991. Manuscript received at ASME Headquarters February 20, 1991. Paper No. 91-GT-129. Associate Technical Editor: L. A. Riekert.

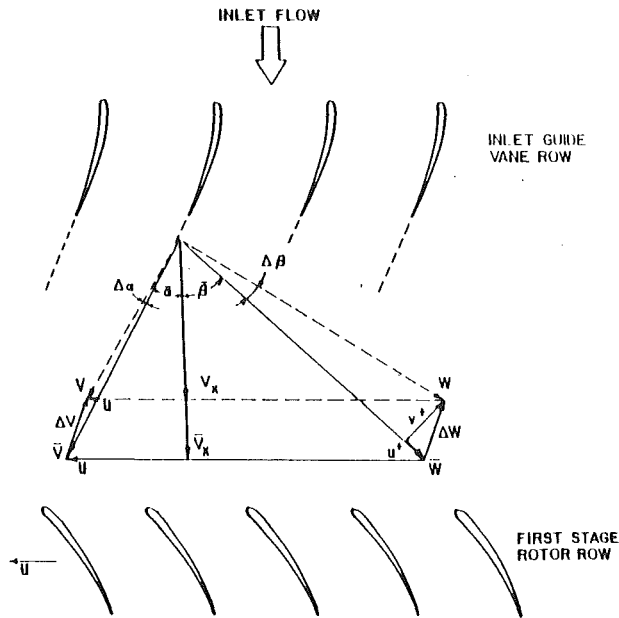


Fig. 1 Schematic of IGV wake-generated transverse and streamwise unsteady velocities, u^+ and v^+

wide range of forcing function to be more easily generated, without large detrimental effects on compressor overall performance.

In this paper, the rotor blade row fundamental unsteady aerodynamic flow physics generated by period wakes are investigated at realistic values of the reduced frequency. In particular, the effects of the detailed unsteady aerodynamic forcing function, including both the transverse and chordwise gust components and the gust amplitude, as well as steady aerodynamic loading on the unsteady aerodynamic gust response of the first-stage rotor blade row, are investigated. This is accomplished by means of a series of experiments performed in an extensively instrumented axial flow research compressor. Unique unsteady aerodynamic data are obtained that describe both the detailed unsteady aerodynamic forcing function generated by the wakes from the IGVs and the resulting first-stage rotor blade row unsteady aerodynamic gust response.

In these experiments, the primary data obtained define the midspan chordwise distributions of both the steady and unsteady pressure on the rotor blade surfaces, with the aerodynamic forcing function generated in the stationary reference frame. These forcing functions are measured with a rotating cross hot-wire probe, with these data then analyzed to determine the streamwise and transverse velocity components, u^+ and v^+ , shown in Fig. 1. The resulting unsteady aerodynamic gust generated rotor blade surface unsteady pressure chordwise distributions are measured with embedded ultraminiature high-response dynamic pressure transducers. The blade surface

Table 1 Overall airfoil and compressor characteristics

	ROTOR	STATOR	IGV
Airfoil type	C4	C4	C4
Number of Airfoils	43	31	36
Chord, C (mm)	30	30	30
Solidity, C/S	1.14	1.09	0.96
Camber, θ	28.0	27.7	36.9
Stagger Angle, γ	36.0	-36.0	21.0
Inlet Metal Angle, β_1	50.0	30.0	0.0
Aspect Ratio	2.0	2.0	2.0
Thickness/Chord (%)	10.0	10.0	10.0
Flow Rate (kg/s)		2.03	
Design Axial Velocity (m/s)		24.4	
Design Rotational Speed (RPM)		2250	
Number of Stages		3	
Design Stage Pressure Ratio		1.0	
Inlet Tip Diameter (mm)		420	
Hub/Tip Radius Ratio		0.714	
Stage Efficiency (%)		85	

steady pressure chordwise distributions are measured with blade surface static taps ported to a rotor-based Scanivalve system.

Research Compressor

The Purdue Axial Flow Research Compressor models the fundamental turbomachinery unsteady aerodynamic multi-stage interaction phenomena, which include the incidence angle, the velocity and pressure variations, the aerodynamic forcing function waveforms, the reduced frequency, and the unsteady blade row interactions. The compressor is driven by a 15 hp dc-electric motor at a speed of 2250 rpm. Each identical stage contains 43 rotor blades and 31 stator vanes having a British C4 airfoil profile, with the first-stage rotor inlet flow field established by a variable setting inlet guide vane (IGV) row of 36 airfoils. The overall compressor and airfoil characteristics are defined in Table 1.

The compressor aerodynamic performance is determined utilizing a 48 port Scanivalve system, thermocouples, and a venturi orifice to measure the required pressures, temperatures, and flow rate, respectively. The Scanivalve transducer is calibrated each time data are acquired, thus automatically compensating for zero and span shifts of the transducer output. A 95 percent confidence interval, root-mean-square error analysis of 20 samples is performed for each steady data measurement.

Instrumentation

Both steady and unsteady rotor blade row data are required. These are acquired with the rotor-based instrumentation system schematically depicted in Fig. 2. The steady data quantify

Nomenclature

b = rotor blade semichord
 \bar{C}_1 = rotor blade steady loading = $\int_0^c (\bar{C}_{p, \text{pressure}} - \bar{C}_{p, \text{suction}}) dx$
 \bar{C}_p = rotor blade steady pressure coefficient
 C_p = rotor blade unsteady pressure coefficient
 $C_{\Delta p}$ = rotor blade unsteady pressure difference coefficient

\bar{i} = rotor blade mean incidence angle
 k = reduced frequency = $\omega b / \bar{V}_x$
 p = digitized ensemble-averaged unsteady pressure
 P_s = rotor blade surface steady pressure
 \hat{p} = first harmonic complex unsteady pressure
 \hat{u}^+ = streamwise gust first harmonic component

\hat{v}^+ = transverse gust first harmonic component
 V_x = mean axial velocity
 ΔV = absolute velocity vector difference from mean value
 ΔW = total unsteady velocity
 $\bar{\beta}$ = relative mean flow angle
 $\Delta \beta$ = relative flow angle difference from mean value
 ω = forcing function frequency, rad

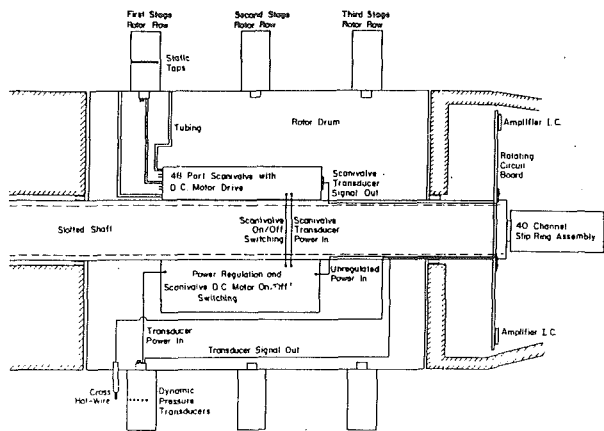


Fig. 2 Rotor-based instrumentation

the rotor row mean inlet flow field and the resulting rotor blade midspan steady loading distribution. The unsteady data define the periodic aerodynamic forcing function and the resulting midspan blade surface periodic unsteady pressure distributions.

The inlet flow field, both steady and unsteady, is measured with a rotating cross hot-wire probe. Disturbances in the stationary frame of reference, i.e., the IGV wakes, are the unsteady aerodynamic forcing functions to the first-stage rotor row. The rotor periodic unsteady inlet flow field generated by these disturbances is measured with a cross hot-wire mounted in the rotor frame of reference. The probe is axially mounted 30 percent of rotor chord upstream of the rotor leading edge plane. A potential flow field analysis determined this axial location to be such that leading edge potential effects are negligible for all steady loading levels. The probe is angularly aligned to obtain rotor relative velocity and flow angle data. The cross hot-wire probe was calibrated and linearized for velocities from 18.3 m/s to 53.4 m/s and ± 35 deg angular variation, with the accuracy of the velocity magnitude and flow angle were determined to be 4 percent and ± 1.0 deg, respectively. Centrifugal loading effects on the rotating hot-wire sensor resistances and, thus, the responses, were found to be negligible.

The detailed steady aerodynamic loading on the rotor blade surfaces is measured with a chordwise distribution of 20 midspan static pressure taps, 10 on each surface. The static pressure at the rotor exit plane, measured with a rotor drum static tap, is used as the blade surface static pressure reference. These static pressure measurements are made using a rotor-based 48 port constant speed drive Scanivalve system located in the rotor drum.

The measurement of the midspan rotor blade surface unsteady pressures is accomplished with 20 ultraminiature, high-response transducers embedded in the rotor blades at the same chordwise locations as the static pressure taps. To minimize the possibility of flow disturbances associated with the inability of the transducer diaphragm to maintain the surface curvature of the blade exactly, a reverse mounting technique is utilized. The pressure surface of one blade and the suction surface of the adjacent blade are instrumented, with transducers embedded in the nonmeasurement surface and connected to the measurement surface by a static tap. The embedded dynamic transducers are both statically and dynamically calibrated. The static calibrations show good linearity and no discernible hysteresis. The dynamic calibrations demonstrate that the frequency responses, in terms of gain attenuation and phase shift, are not affected by the reverse mounting technique. The accuracy of the unsteady pressure measurements, determined from the calibrations, is ± 4 percent.

The rotor-based static pressure Scanivalve transducer, ro-

tating cross hot-wire probe, and 20 blade surface dynamic pressure transducers are interfaced to the stationary frame-of-reference through a 40 channel slip ring assembly. On-board signal conditioning of the transducer output signals is performed to maintain a good signal-to-noise ratio through the slip rings. The remaining 17 channels of the slip-ring assembly are used to provide excitation to the transducers and on/off switching to the Scanivalve d-c motor.

Data Acquisition and Analysis

Steady Data. The rotor blade surface static pressure data, measured with the rotor-based Scanivalve system, are defined by a root-mean-square error analysis of 20 samples with a 95 percent confidence interval. The reference for these midspan blade pressure measurements is the static pressure at the exit of the rotor measured in the rotor drum. Thus, the blade surface and the reference static pressures are measured at different radii. Hence, a correction for the resulting difference in the radial acceleration is applied in calculating the blade surface static pressure coefficient:

$$\bar{C}_p = \frac{\bar{P}_s - \bar{P}_{\text{exit}}}{1/2\rho U_t^2} \quad (1)$$

where U_t is the rotor blade tip speed.

Periodic Data. The periodic data of interest are the harmonic components of the aerodynamic forcing function to the first-stage rotor blade row together with the resulting rotor blade surface unsteady pressures and unsteady pressure differences. These are determined by defining a digitized ensemble-averaged periodic unsteady aerodynamic data set consisting of the rotating cross hot-wire probe and blade surface dynamic pressure transducer signals at each steady operating point. In particular, these time-variant signals are digitized with a high-speed A-D system at a rate of 100 kHz and then ensemble averaged.

The key to this averaging technique is the ability to sample data at a preset time, accomplished by an optical encoder mounted on the rotor shaft. The microsecond range step voltage signal from the encoder is the data initiation time reference and triggers the high-speed A-D multiplexer system. To reduce significantly the random fluctuations superimposed on the periodic signals of interest, 200 averages are used. A Fast Fourier Transform (FFT) algorithm is then applied to these ensemble-averaged signals to determine the harmonic components of the unsteady aerodynamic forcing function and the resulting rotor blade surface harmonic unsteady pressures and pressure differences.

The unsteady inlet flow field to the rotor row is measured with the rotating cross hot-wire probe, which quantifies the relative velocity and flow angle. The velocity triangle relations depicted in Fig. 1 are then used to determine the unsteady inlet flow field to the rotor, in particular, the streamwise and transverse velocity components, u^+ and v^+ , respectively. These are then Fourier decomposed to determine the first harmonic of the streamwise and transverse velocity components, termed the streamwise and transverse gust components, \hat{u}^+ and \hat{v}^+ .

The various unsteady aerodynamic gust mathematical models reference the gust-generated airfoil aerodynamic response to a transverse gust at the leading edge of the airfoil. However, in the experiments described herein, the time-variant data are referenced to the initiation of the data acquisition shaft trigger pulse. Thus, for consistency with the models, the periodic data are further analyzed and referenced to a transverse gust at the leading edge of the first stage rotor blade. This is accomplished by assuming that: (1) the aerodynamic forcing function remains fixed in the stationary reference frame; and (2) the forcing function does not decay from the rotating hot-wire probe axial location to the rotor row leading edge plane.

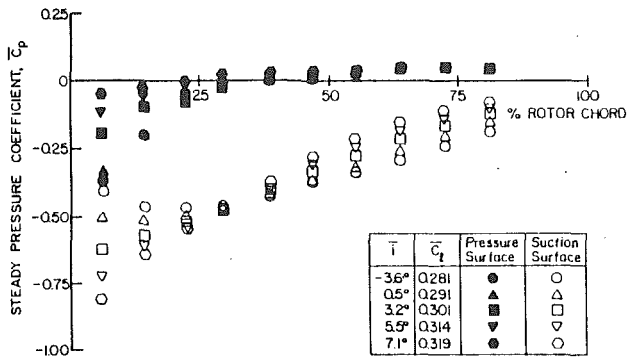


Fig. 3 Steady pressure chordwise distributions for five steady loading levels

The rotor blade surface unsteady pressure data, measured with the embedded high response pressure transducers, are analyzed to determine the harmonics of the chordwise distribution of the unsteady pressure coefficient, C_p , and the unsteady pressure difference coefficient, $C_{\Delta p}$. These are defined in Eq. (2) and are specified from the Fourier coefficients of the digitized ensemble-averaged dynamic pressure transducer signals.

$$C_p = \frac{\hat{p}}{\rho \bar{V}_x^2 \left(\frac{\hat{\theta}^+}{\bar{V}_x} \right) \bar{\beta}} \quad (2a)$$

$$C_{\Delta p} = C_{p, \text{pressure}} - C_{p, \text{suction}} \quad (2b)$$

where $\hat{\theta}^+$ is the first harmonic transverse gust component, \bar{V}_x is the mean axial velocity, and $\bar{\beta}$ is the relative mean flow angle in rad.

The final forms of the gust-generated rotor blade row unsteady aerodynamic data define the chordwise distribution of the harmonic complex unsteady pressure and pressure difference coefficients. Also included as a reference are predictions from the transverse gust analysis of Smith (1971). This model analyzes the unsteady aerodynamics generated on a flat plate airfoil cascade at zero incidence by a transverse gust convected with an inviscid, subsonic, compressible flow.

Results

A series of experiments are performed to investigate and quantify the effects on the unsteady aerodynamic gust response of the first-stage rotor blade row due to the detailed variation of the unsteady aerodynamic forcing function generated by the IGV wakes. Forcing function effects include both the transverse and chordwise gust components, defined by the ratio of the amplitudes of the first harmonic streamwise-to-transverse gust components, $|\hat{u}^+/\hat{\theta}^+|$, and the gust amplitude, defined by the ratio of the first harmonic transverse gust magnitude to mean axial velocity, $|\hat{\theta}^+/\bar{V}_x|$. The ratio of the streamwise-to-transverse gust amplitude, $|\hat{u}^+/\hat{\theta}^+|$, was varied by changing the IGV setting angle. The level of steady aerodynamic loading, characterized by the mean incidence angle, was varied as a parameter. The variation in the rotor blade steady loading was obtained by holding the rotor speed constant and varying the mass flow rate and, thus, the mean flow incidence angle to the rotor blade row.

Periodic Aerodynamic Forcing Function. Four distinct 36-per-revolution aerodynamic forcing functions to the first-stage rotor blade row are generated, characterized by nominal first harmonic streamwise-to-transverse gust amplitude ratios of 0.29, 0.37, 0.45, and 0.55. The unsteady aerodynamic gust generated from the IGV wake first harmonic has nominal reduced frequency values between 5 and 6. The Fourier decomposition of these IGV wake aerodynamic forcing functions to

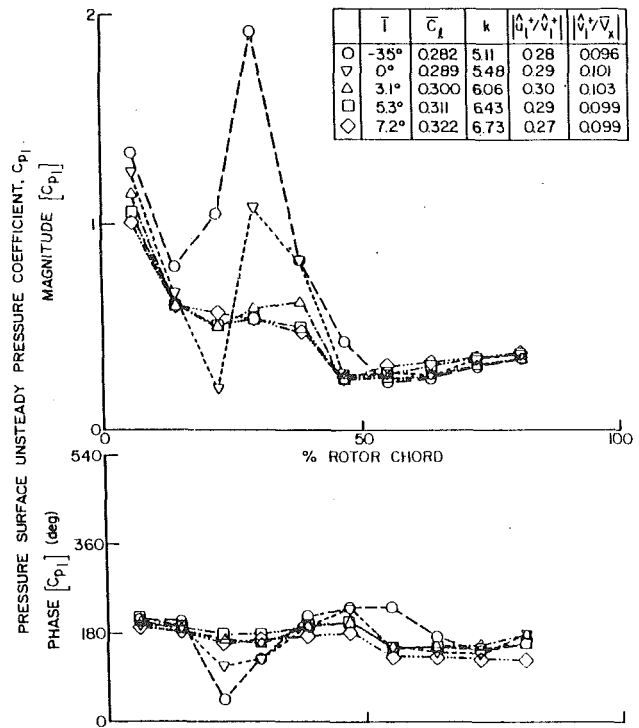


Fig. 4 Steady loading effect on blade pressure surface unsteady response for a nominal first harmonic $|\hat{u}^+/\hat{\theta}^+|$ of 0.29

the first-stage rotor row shows a dominant 36-per-rev excitation fundamental harmonic with smaller higher harmonics. As the gust amplitude ratio increases, the transverse harmonic gust amplitudes become smaller while the streamwise harmonic gust amplitudes becomes larger with respect to the mean axial velocity.

Blade Surface Steady Pressures. The effect of steady aerodynamic loading as characterized by the mean incidence angle on the rotor blade surface steady pressure coefficient is shown in Fig. 3. The level of steady loading only affects the steady pressure distribution on the pressure surface over the front 40 percent of the chord. On the suction surface, the steady loading variation has a large effect on the steady pressure distribution over the entire suction surface. Also, these data give no indication of suction surface flow separation. It should be noted that these surface steady pressure distributions are not affected by the characteristics of the periodic unsteady aerodynamic forcing function.

Rotor Row Periodic Aerodynamic Response. The periodic aerodynamic responses of the first-stage rotor blade row to the IGV wake first harmonic forcing function are presented in the format of the chordwise distribution of the complex unsteady pressure coefficient on the individual rotor blade surfaces as well as the corresponding complex unsteady pressure difference coefficient generated by the 36-per-rev IGV wake first harmonic forcing function, with the steady loading level as a parameter.

Pressure Surface Unsteady Pressure. The effect of steady aerodynamic loading level on the IGV wake-generated first harmonic complex unsteady pressure distribution on the rotor blade pressure surface is shown in Figs. 4, 5, 6, and 7 for nominal streamwise-to-transverse gust amplitude ratios of 0.29, 0.37, 0.45, and 0.55, respectively. The first harmonic gust amplitude, characterized by $|\hat{\theta}^+/\bar{V}_x|$ values of approximately 0.1, is small compared to the mean axial velocity.

For each gust amplitude ratio value, the form of the dimensionless unsteady pressure coefficient specified in Eq. (2)

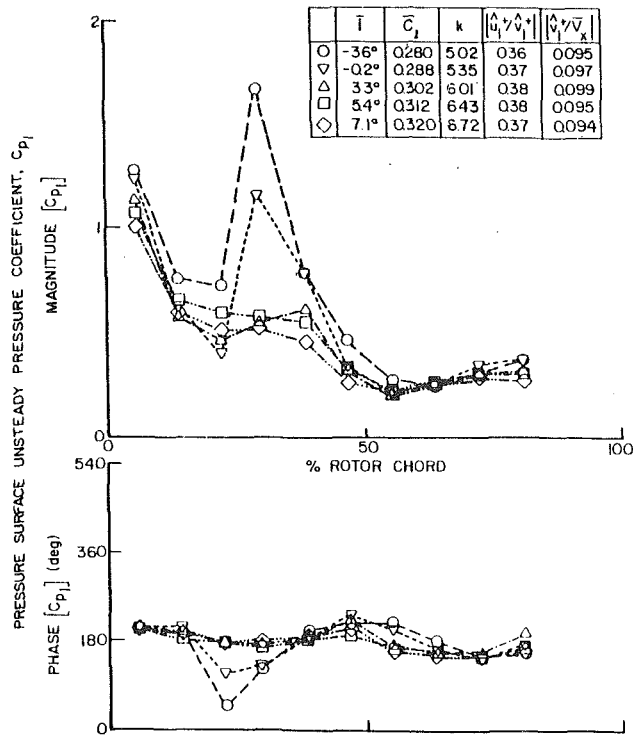


Fig. 5 Steady loading effect on blade pressure surface unsteady response for a nominal first harmonic $|\hat{u}^+/\hat{v}^+|$ of 0.37

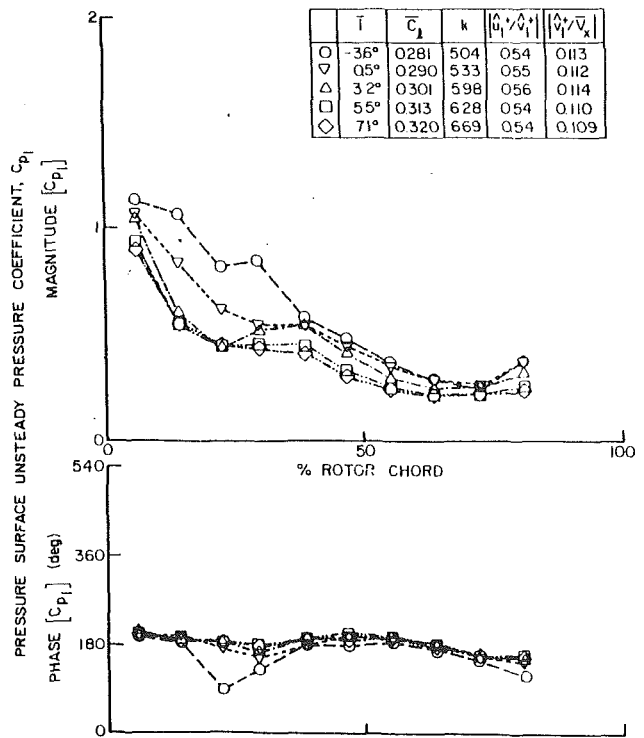


Fig. 7 Steady loading effect on blade pressure surface unsteady response for a nominal first harmonic $|\hat{u}^+/\hat{v}^+|$ of 0.55

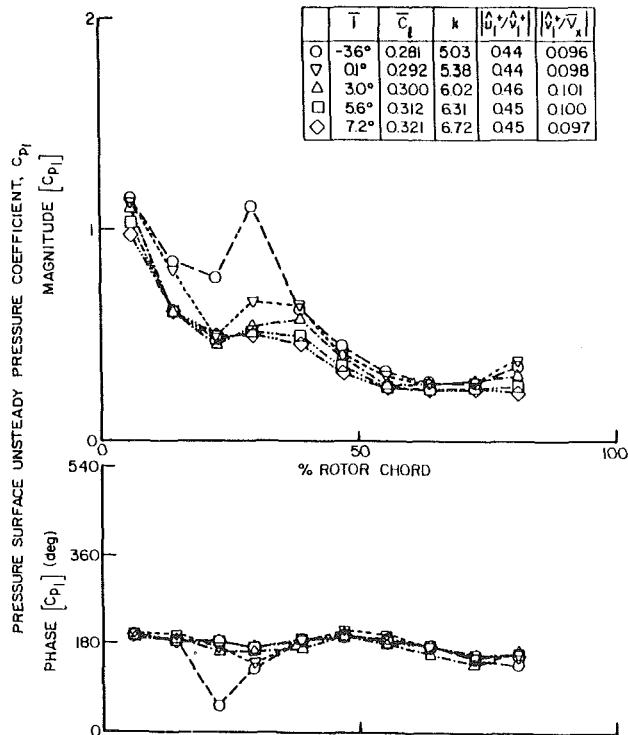


Fig. 6 Steady loading effect on blade pressure surface unsteady response for a nominal first harmonic $|\hat{u}^+/\hat{v}^+|$ of 0.45

results in a compression of the unsteady pressure magnitude data over the entire pressure surface for all gust amplitude ratios and all but the two lowest steady loading levels. For these two loading cases, large variations are found in the magnitude data in the neighborhood of the quarter chord, with these variations decreasing with increasing gust amplitude ratio. This corresponds to the previously noted effects of steady

loading on the rotor blade surface steady pressure wherein loading primarily influences the front part of the pressure surface. Namely, the steady pressure coefficient value for the rotor drum hub steady pressure coefficient upstream of the rotor row is approximately -0.24 , thereby indicating that the mean flow field accelerates around the pressure surface leading edge before decelerating (diffusing) for the two lowest mean incidence angles, i.e., the steady pressure coefficient decreases and then increases.

The level of steady loading has only a minimal effect on the pressure surface unsteady pressure phase, the exception being the two lowest steady loading levels in the front chord region. Also as $|\hat{u}^+/\hat{v}^+|$ increases, the decrease in phase in the 25 percent chord region becomes less for the two low steady loading levels, while the three highest steady loading levels in the front chord region and all steady loading levels in the aft chord region remain relatively unaffected by the gust amplitude ratio.

Suction Surface Unsteady Pressures. The effect of steady aerodynamic loading on the IGV wake-generated first harmonic complex unsteady pressure on the rotor blade suction surface is shown in Figs. 8, 9, 10, and 11 for the four nominal gust amplitude ratio values.

The unsteady pressure coefficient magnitude on the entire suction surface is a strong function of the level of steady aerodynamic loading. This corresponds to the previously presented suction surface steady pressure data variation with mean incidence angle. For all gust amplitude ratios, the front-to-midchord region data show a decreasing-increasing magnitude trend with chord, with the minimum magnitude chordwise location moving forward with increasing steady loading. This minimum corresponds to the minimum in the steady pressure chordwise distribution, Fig. 5, wherein the chordwise location of the change from accelerating to decelerating mean flow moves forward with increasing mean incidence. Thus, similar to the pressure surface unsteady response in the front chord region at negative mean incidence angle, the unsteady gust interacts with the accelerating mean flow field around the

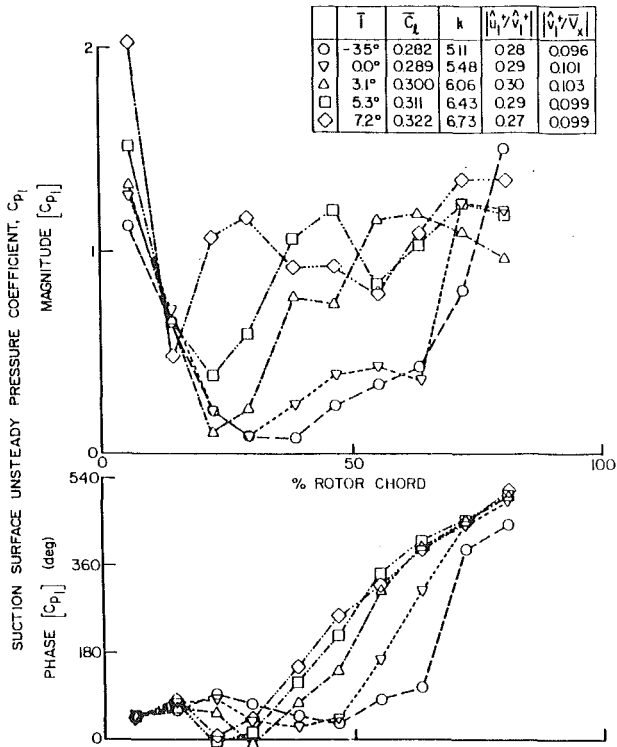


Fig. 8 Steady loading effect on blade suction surface unsteady response for a nominal first harmonic $|\hat{u}^+/\hat{v}^+|$ of 0.29

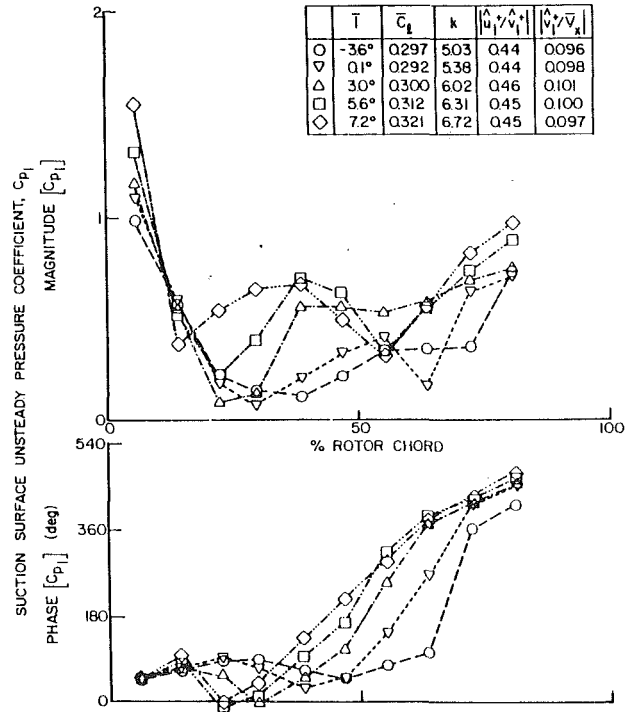


Fig. 10 Steady loading effect on blade suction surface unsteady response for a nominal first harmonic $|\hat{u}^+/\hat{v}^+|$ of 0.45

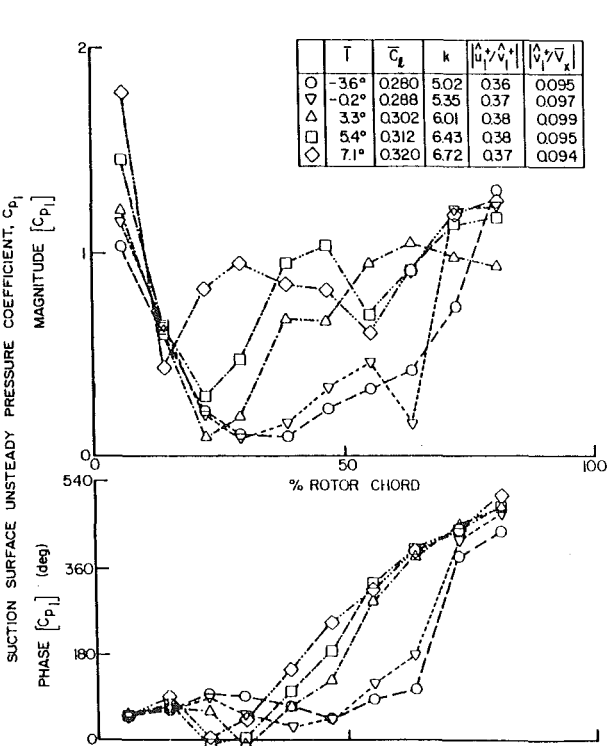


Fig. 9 Steady loading effect on blade suction surface unsteady response for a nominal first harmonic $|\hat{u}^+/\hat{v}^+|$ of 0.37

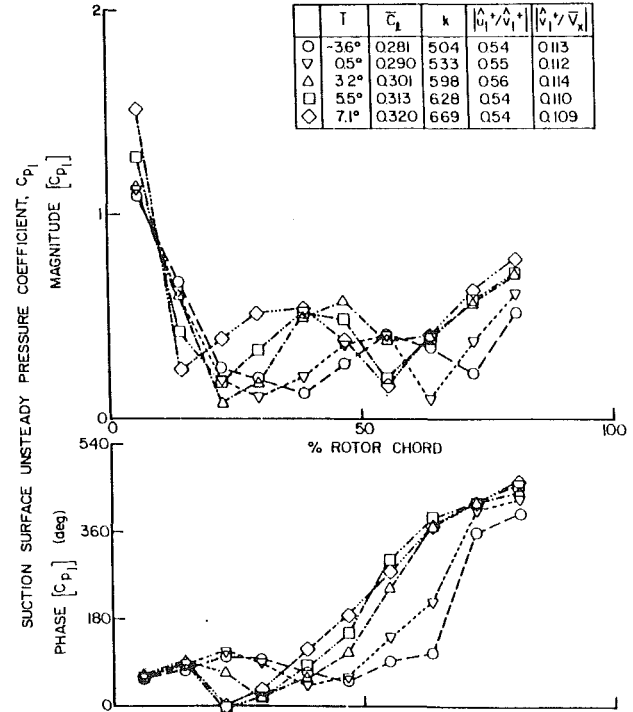


Fig. 11 Steady loading effect on blade suction surface unsteady response for a nominal first harmonic $|\hat{u}^+/\hat{v}^+|$ of 0.55

suction surface in the front chord region. In the mid-to-aft chord region, the gust amplitude ratio alters the effect of steady loading on the chordwise distributions of the unsteady pressure response. Namely, for the large gust amplitude ratios, a decreasing-increasing unsteady pressure magnitude trend with chord occurs, with the minimum moving forward with in-

creasing steady loading. As $|\hat{u}^+/\hat{v}^+|$ decreases, this increasing-decreasing magnitude trend with chord becomes smoother and the data increase dramatically in magnitude in the aft half chord. Thus, for this higher camber suction surface, the mean flow field interacts with the unsteady gust over the entire blade surface, with the gust amplitude ratio affecting the response over the aft half of the surface.

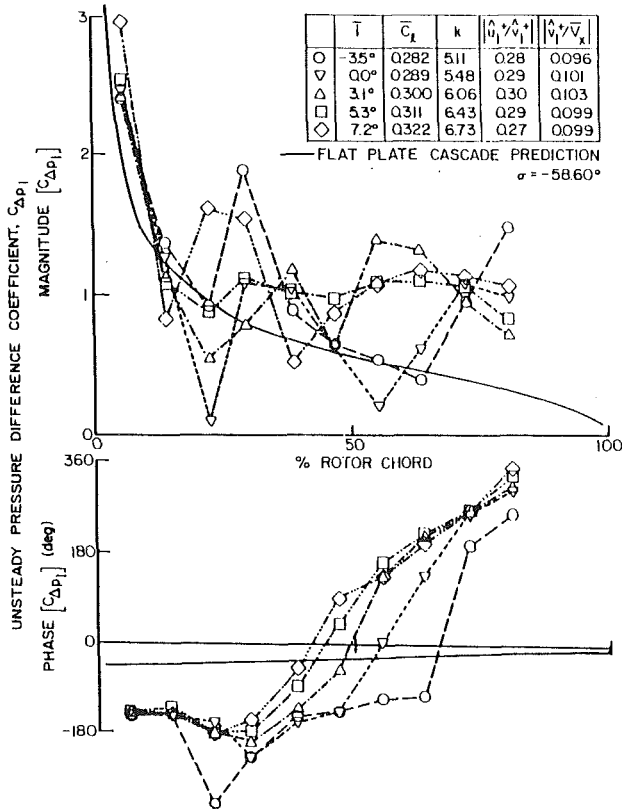


Fig. 12 Steady loading effect on blade unsteady pressure difference response for a nominal first harmonic $|\hat{u}^+ / \hat{v}^+|$ of 0.29

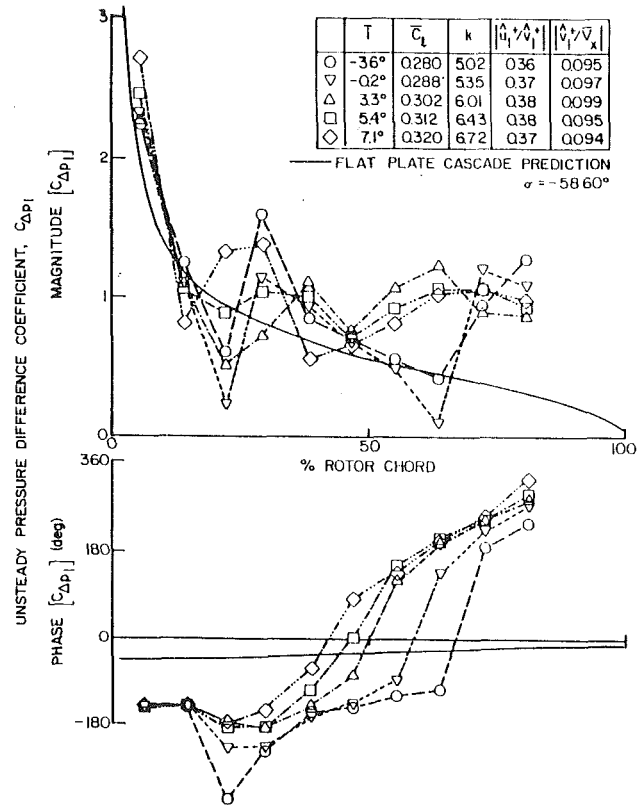


Fig. 13 Steady loading effect on blade unsteady pressure difference response for a nominal first harmonic $|\hat{u}^+ / \hat{v}^+|$ of 0.37

Nearest to the leading edge, the magnitude data increase with increasing steady loading level. As noted previously, this steady loading trend is attributed to the IGV wake first harmonic gust interacting with the mean accelerating flow field around the blade leading edge. Hathaway et al. (1987) have experimentally demonstrated the interaction of a rotor wake with a downstream stator row. They found that from approximately -20 to 10 percent of the downstream stator chord, the rotor wake-generated unsteady velocity magnitude increases, with the increase becoming larger as steady loading increases. This indicates that the wake-generated gust magnitude increases due to the interaction with the accelerating mean flow field around the blade leading edge.

With regard to the phase of the unsteady pressure, the streamwise-to-transverse gust amplitude ratio has minimal effect, with steady loading primarily affecting the phase on the aft three quarters of the chord. As the mean incidence angle is increased from the low loading level, the chordwise variation of the phase data on the aft part of the surface becomes linear, with the extent of this linear distribution increasing with increasing mean incidence. This linear chordwise distribution indicates the existence of a wave phenomenon, with a convective velocity equal to the mean axial velocity through the blade row (20.5 m/s). This mean axial velocity wave phenomenon has been experimentally detected by other authors (Fleeter et al., 1980; Hodson, 1985) but is yet to be physically explained.

Summarizing these blade surface steady loading and gust amplitude ratio effects, for the low camber pressure surface in the chordwise region where the mean flow field does not accelerate, i.e., the mid-to-aft chord region for all steady loading levels and the front chord region for the three high steady loading levels, the data compress for all gust amplitude ratios, indicating that steady loading as characterized by the mean flow incidence is a key mechanism for the low camber unsteady aerodynamic wake response. However, in an accelerating mean

flow field, i.e., the front chord region for the two low steady loading levels, mean flow field interactions with the unsteady gust are also important. As the gust amplitude ratio increases, this interaction lessens. On the higher camber suction surface, the interaction between the mean flow field and the unsteady gust affects the unsteady aerodynamic response over the entire blade surface for all steady loading levels and streamwise-to-transverse gust amplitude ratios. Also, the gust amplitude ratio has a large effect on these interactions over the aft half of the blade surface.

Unsteady Pressure Differences. The steady loading effect on the first harmonic of the complex unsteady pressure difference across the rotor blade camberline is shown in Figs. 12, 13, 14, and 15 for the nominal streamwise-to-transverse gust amplitude ratios of 0.29, 0.37, 0.45, and 0.55, respectively. Also presented as a reference are the flat plate cascade, inviscid, transverse gust predictions of Smith (1971) and Whitehead (1987).

The effects of steady loading on the previously presented individual pressure and suction surface magnitude and phase data are still apparent, with the suction surface effects being dominant. For example, analogous to the high gust amplitude steady loading trends on the suction surface for the high gust amplitude ratio, the unsteady pressure difference magnitude data show two decreased magnitude regions, one in the front chord region and the other in the mid-to-aft chord region, with the chordwise location of the magnitude minima moving forward with increased steady loading. Also, the chordwise location where the rapid increase in value of the phase data begins to occur moves forward with increasing steady loading similar to the suction surface, whereas for the low steady loading level, the phase decreases sharply at 25 percent rotor chord per the pressure surface trends. Similar to the steady loading trends in the suction surface aft chord region, as the gust amplitude ratio decreases, the magnitude data increase.

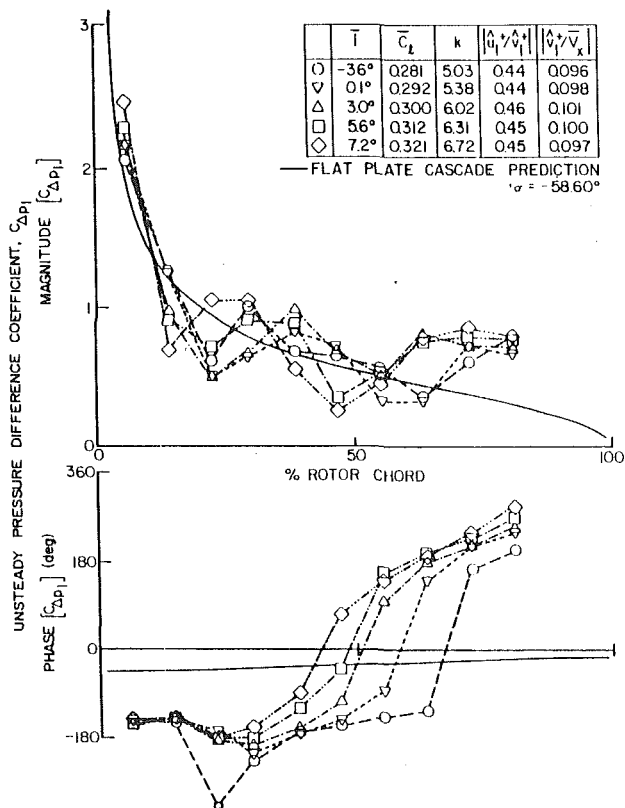


Fig. 14 Steady loading effect on blade unsteady pressure difference response for a nominal first harmonic $|\hat{u}^+/\hat{v}^+|$ of 0.45

These steady loading effects cause the chordwise distribution of the unsteady pressure difference magnitude and phase data to differ greatly from the flat plate cascade predictions, with the magnitude data not just decreasing with increasing chord and the phase data not remaining nearly constant with chord per the predictions. The lowest steady loading level, which most closely approximates the prediction model no loading condition, shows fair comparison with the magnitude data, except in chord regions where strong gust interactions with the steady flow field occur, i.e., the pressure surface interaction at 25 percent chord and the suction surface interaction in the aft chord. The prediction differs from the phase data by approximately 90 deg over the entire blade except, once again, in the 25 percent and aft chord region.

Effect of Gust Amplitude. The previous results considered the periodic aerodynamic response of the first-stage rotor blade row to relatively small amplitude IGV wake first harmonic gusts, with the ratio of the transverse gust to mean axial velocity on the order of 0.1. The effect of larger amplitude gusts, $|\hat{u}^+/\bar{V}_x|$ on the order of 0.3, on the blade surface unsteady pressure response, including the effect of steady loading, are presented in Figs. 16 and 17, where the effect of operation at the five nominal steady loading levels is also included. In particular, these figures present the chordwise distribution of the complex unsteady pressure coefficient on the pressure and suction surfaces generated by large amplitude 36-per-rev IGV wake first harmonic forcing functions.

The effect of the larger amplitude gusts on the pressure surface unsteady pressure response is demonstrated by comparing the high-amplitude gust generated response with that resulting from the low-amplitude gust of the same nominal streamwise-to-transverse gust amplitude ratio value, Figs. 5 and 16. Nearly identical unsteady pressure magnitude and phase responses are shown for both gust amplitudes except in the 25

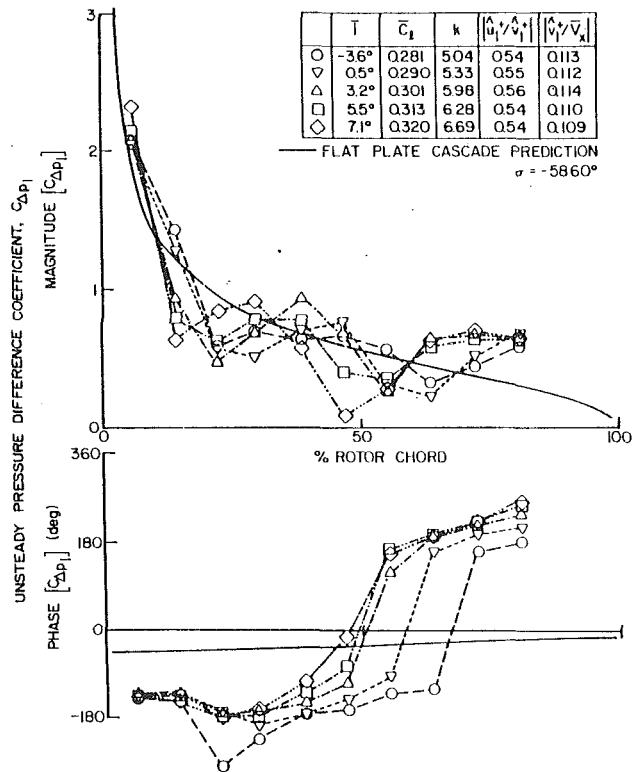


Fig. 15 Steady loading effect on blade unsteady pressure difference response for a nominal first harmonic $|\hat{u}^+/\hat{v}^+|$ of 0.55

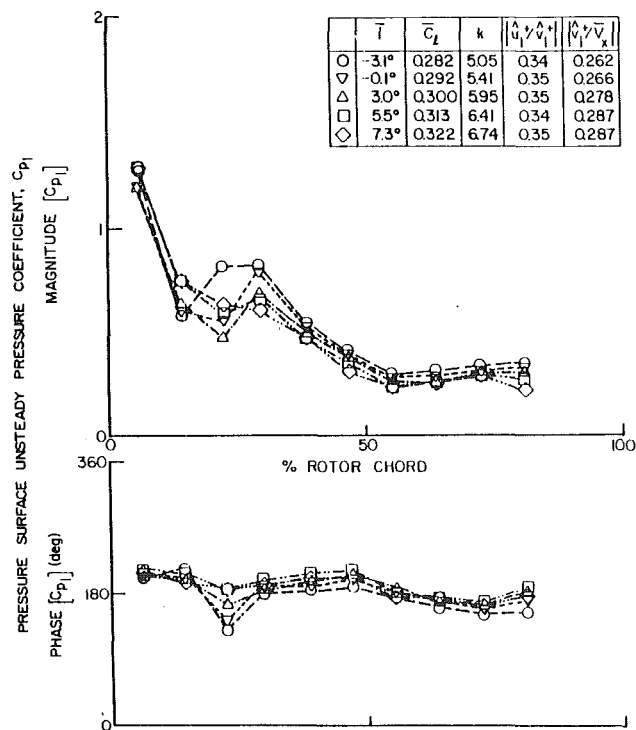


Fig. 16 Steady loading effect on blade pressure surface response for large-amplitude gusts

percent chord region for the lowest two mean flow incidence angles. In this front chord region at negative mean flow incidence, the interaction between the accelerating mean flow field and the unsteady gust is weaker for the larger amplitude

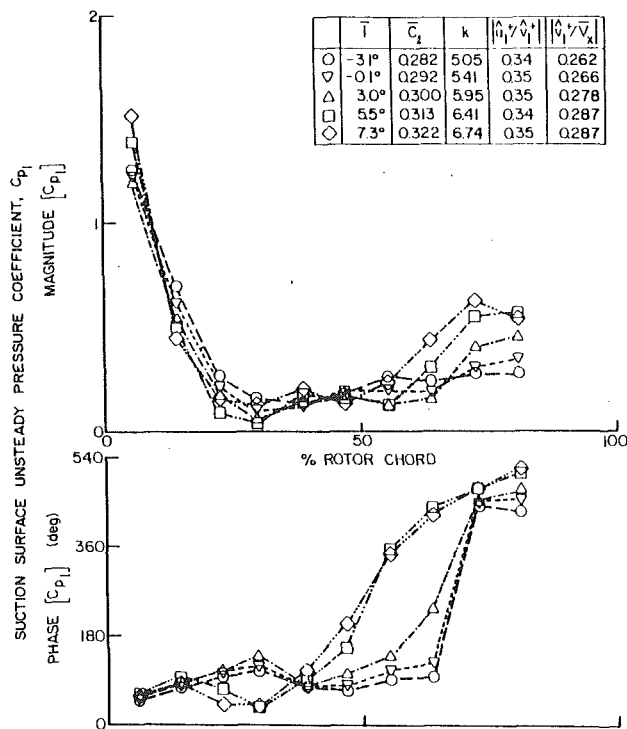


Fig. 17 Steady loading effect on blade suction surface response for large-amplitude gusts

gust, as evidenced by the decrease in the magnitude and phase variation.

The effect of large-amplitude gusts on the suction surface unsteady pressure response is seen by comparing the high and low-amplitude gust-generated response for equivalent gust amplitude ratio values, Figs. 9 and 17. The phase data are unaffected by the gust amplitude, with the steady loading effect on the phase chordwise distributions being nearly equivalent. However, the magnitude data are greatly affected by the gust amplitude, particularly over the aft three quarters of the surface. The high-amplitude gust magnitude data are greatly decreased compared to the low-amplitude gust magnitude data, with the steady loading effect being greatly reduced. Thus, similar to the pressure surface front chord region at negative mean flow incidence, the interaction of high-amplitude gusts with the mean flow is weaker than the interaction of low-amplitude gusts with the mean flow.

Summary and Conclusions

The rotor blade row fundamental unsteady aerodynamic flow physics generated by periodic wakes were investigated at realistic values of the reduced frequency. In particular, the effects of the detailed unsteady aerodynamic forcing function, including both the transverse and chordwise first harmonic gust components and the gust amplitude, as well as steady aerodynamic loading on the unsteady aerodynamic gust response of the first-stage rotor blade row, were investigated and quantified. This was accomplished by means of a series of experiments performed in an extensively instrumented axial flow research compressor.

The rotor blade surface steady loading distributions were quantified with surface static pressure taps and a rotor-based Scanivalve system. The aerodynamic forcing function to the rotor blade row was determined with a rotating cross hot-wire probe, with the aerodynamic gust-generated rotor blade surface unsteady pressure chordwise distributions measured with embedded ultraminiature high-response dynamic pressure transducers.

The detailed IGV wake-generated unsteady aerodynamic results of these experiments are summarized in the following.

Forcing Function

- The IGV wake forcing function shows a dominant 36-per-rev, with smaller higher harmonic content.

Blade Surface Steady Pressures

- Steady loading affects the steady pressure distribution on the front portion of the blade pressure surface and over the entire suction surface.
- The unsteady gust amplitude ratio and magnitude have negligible effect on the steady pressure distribution.

Pressure Surface Response

- The unsteady pressure phase data are nearly independent of the steady loading level and the gust amplitude ratio except in the front chord region at negative mean flow incidence.
- The selected unsteady pressure nondimensionalization compresses the magnitude data with regard to mean flow incidence angle for each gust component amplitude ratio except in the front chord region for negative mean flow incidence.
- Increasing the gust amplitude ratio results in weaker interactions between the mean and unsteady flow fields in the front chord region at negative mean flow incidence.
- Large-amplitude gusts reduce this interaction between the unsteady gust and the accelerating mean flow field.
- The magnitude of the unsteady pressure response on the blade pressure surface, i.e., the low camber surface, is thus primarily affected by the level of steady loading as characterized by the mean flow incidence angle except in the accelerating mean flow field of the front chord region at negative mean flow incidence.

Suction Surface Response

- The unsteady pressure phase data are nearly independent of the gust component amplitude ratio, with increased mean incidence, resulting in a linear chordwise distribution, which corresponds to a wave phenomenon convected at the mean axial velocity of the flow through the rotor blade row.
- The selected unsteady pressure nondimensionalization does not compress the magnitude data with regard to mean flow incidence angles.
- The mid-to-aft chord magnitude data are a strong function of the gust amplitude ratio, with the increase in magnitude with increasing steady loading becoming smaller with increasing gust amplitude ratio.
- Large-amplitude gusts reduce these mean flow field interactions with the unsteady gust, similar to the pressure surface.
- The magnitude of the unsteady pressure response on the blade suction surface, i.e., the higher camber surface, is thus affected by both the steady flow field interactions and the gust amplitude ratio.

Unsteady Pressure Difference Response

- The unsteady pressure difference data reflect the effects of loading on the pressure and suction surface unsteady data, with the suction surface effects being dominant.
- These steady loading effects cause the chordwise distribution of the magnitude and phase data to differ greatly from the flat plate cascade predictions.
- The lowest steady loading level data were correlated with flat plate cascade predictions, with the unsteady aerodynamic response correlation being fair.

Acknowledgments

Research sponsored by the Air Force Office of Scientific Research (AFSC) under Contract No. F49620-88-C-0022. The United States Government is authorized to reproduce and dis-

tribute reprints for governmental purposes notwithstanding any copyright notation hereon.

References

- Capece, V. R., and Fleeter, S., 1987, "Unsteady Aerodynamic Interactions in a Multi-stage Compressor," *ASME JOURNAL OF TURBOMACHINERY*, Vol. 109, pp. 420-428.
- Capece, V. R., Manwaring, S. R., and Fleeter, S., 1986 "Unsteady Blade Row Interactions in a Multi-stage Compressor," *AIAA Journal of Propulsion*, Vol. 2, No. 2, pp. 168-174.
- Fleeter, S., Bennett, W. A., and Jay, R. L., 1980, "The Time-Variant Aerodynamic Response of a Stator Row Including the Effects of Airfoil Camber," *ASME Journal of Engineering for Power*, Vol. 102, pp. 334-343.
- Fleeter, S., Jay, R. L., and Bennett, W. A., 1978, "Rotor Wake Generated Unsteady Aerodynamic Response of a Compressor Stator," *ASME Journal of Engineering for Power*, Vol. 100, pp. 664-675.
- Gallus, H. E., Lambertz, J., and Wallman, Th., 1980, "Blade-Row Interaction in an Axial-Flow Subsonic Compressor Stage," *ASME Journal of Engineering for Power*, Vol. 102, pp. 169-177.
- Hardin, L. W., Carta, F. O., and Verdon, J. M., "Unsteady Aerodynamic Measurements on a Rotating Compressor Blade Row at Low Mach Number," *ASME JOURNAL OF TURBOMACHINERY*, Vol. 109, No. 4, pp. 499-507.
- Hathaway, M. D., Suder, K. L., Okiishi, T. H., Strazisar, A. J., and Adamczyk, J., 1987, "Measurements of the Unsteady Flow Field Within the Stator Row of a Transonic Axial-Flow Fan. II—Results and Discussion," ASME Paper No. 87-GT-227.
- Hodson, H. P., 1985, "Measurements of Wake-Generated Unsteadiness in the Rotor Passages of Axial Flow Turbines," *ASME Journal of Engineering for Gas Turbines and Power*, Vol. 107, pp. 467-476.
- Manwaring, S. R., and Fleeter, S., 1990, "Inlet Distortion Generated Periodic Aerodynamic Rotor Response," *ASME JOURNAL OF TURBOMACHINERY*, Vol. 112, No. 2, pp. 298-307.
- Manwaring, S. R., and Fleeter, S., 1991, "Forcing Function Effects on Rotor Periodic Aerodynamic Response," *ASME JOURNAL OF TURBOMACHINERY*, Vol. 113, pp. 312-319.
- O'Brien, W. F., Cousins, W. R., and Sexton, M. R., 1980, "Unsteady Pressure Measurements and Data Analysis Techniques in Axial-Flow Compressors," *Measurement Methods in Rotating Components of Turbomachinery*, ASME, pp. 195-210.
- Smith, S. N., 1971, "Discrete Frequency Sound Generation in Axial Flow Turbomachines," ARC R&M 3709.
- Suder, K. L., Hathaway, M. D., Okiishi, T. H., Strazisar, A. J., and Adamczyk, J., 1987, "Measurements of the Unsteady Flow Field Within the Stator Row of a Transonic Axial-Flow Fan. I—Measurement and Analysis Technique," ASME Paper No. 87-GT-226.
- Whitehead, D. S., 1987, "Classical Two-Dimensional Methods," *AGARD Manual on Aeroelasticity in Axial Flow Turbomachines, Vol. 1: Unsteady Turbomachinery Aerodynamics*, AGARDograph No. 298, pp. 3-1-3-30.